Atomistic and Continuum Level Modeling of Laser-Induced Microstructuring, Surface Morphology Modification, and Acoustic Activation of Surface Processes

---

A Dissertation

Presented to
the faculty of the School of Engineering and Applied Science
University of Virginia

---

in partial fulfillment of the requirements for the degree of
Doctor of Philosophy

by
Maxim V. Shugaev

May 2019

Approval Sheet

The dissertation
is submitted in partial fulfilment of the requirements
for the degree of
Doctor of Philosophy

(Maxim Shugaev)
Author

The dissertation has been read and approved by the examining committee:

Leonid V. Zhigilei
Advisor

Patrick E. Hopkins

James M. Howe

Gary J. Shiflet

Eugene B. Kolomeisky

Alexey E. Romanov

Accepted for the School of Engineering and Applied Science:

Craig H. Benson, Dean, School of Engineering and Applied Science

May 2019

Abstract

Short pulse laser irradiation has the ability to bring material into a state of strong electronic, thermal, phase, and mechanical non-equilibrium and trigger a sequence of structural transformations leading to the generation of complex multi-scale surface morphologies, unusual metastable phases and microstructure that cannot be produced by any other means. High resolution and accuracy of laser-induced modification of material properties makes this technique indispensable for practical applications; however, better theoretical understanding of fundamentals of laser interaction with matter, non-equilibrium processes caused by ultrafast energy deposition, generation of crystal defects, and modification of surface morphology under highly non-equilibrium conditions created by the laser irradiation is vital for further advancement of laser-based processing methods.

In this work, a combination of large-scale atomistic simulations and theoretical analysis is used to reveal the mechanisms responsible for the laser-induced generation of crystal defects and the sensitivity of the structural modifications to the target crystallographic orientation, which is reported in experimental studies. The peculiarities of melting and solidification occurring under conditions of strong superheating/undercooling as well as the relaxation of intense laser-induced thermal stresses are found to result in emission of dislocations from the melting front, formation of dislocations during crystal growth, generation of growth twins and high concentration of vacancies. The effect of the choice of interatomic potential on the results of atomistic simulations of short pulse laser processing is illustrated by considering high-temperature properties of Ti predicted by nine potentials suggested in literature for this metal. Spatial confinement by a solid transparent overlayer in short pulse laser processing is revealed to suppress of the generation of unloading tensile waves in the irradiated target, leading to suppression of photomechanical spallation and cavitation, decrease of the maximum melting depth, and reduction or elimination of the emission of dislocations from the melting front. The stabilizing effect of the overlayer prevents complete melting near the interface and facilitates formation of a thin layer of slightly misoriented grains. Apart from the microstructure modification, large-scale atomistic simulations have provided insights into the mechanisms of laser-induced sub-surface cavitation and photomechanical spallation, and suggested a novel

mechanism of the generation of Laser-Induced Periodic Surface Structures (LIPSS) in the phase explosion regime.

The relaxation of laser-induced stresses on the scale of entire laser spot is accompanied not only by generation of crystal defects and ablation but also by formation of intense bulk and surface acoustic waves (SAWs) that are shown in recent experimental studies to affect surface processes at atomic/molecular level. This observation is surprising since there is a large mismatch between the typical SAWs frequency and characteristic vibrational modes of atoms and molecules on a surface. A plausible explanation of this phenomenon is suggested by the results of our study of acoustically activated surface diffusion and desorption of small clusters. We have found that nonlinear wave evolution accompanied by generation of high frequency harmonics capable of direct coupling with vibrational modes of surface species is largely responsible for the acoustic activation of surface diffusion and desorption of atomic clusters. Moreover, atomistic simulations performed for graphene on a catalytic Cu substrate demonstrate and explain an acoustically-activated motion of graphene sheets on the substrate.

Contents

Acknowledgments

I would like to first express my sincerer appreciation and gratitude to my advisor, Prof. Leonid Zhigilei, for his outstanding mentorship and support throughout my graduate program. After joining the Computational Materials Group in 2012 as a visiting scholar and during my PhD program started from 2014, Leo has been helping me in development of my professional skills and made himself available for discussions even when he was extremely busy. Despite sometimes I am a person whom is not very easy to deal with, Leo was always patient and kind. Discussions with Leo were always insightful and helped to succeed in particular research projects. Also, I appreciate very much the opportunity to work on a variety of projects that helped me to gain knowledge in a broad range of topics. I can never thank Leo enough for the tremendous impact on completing this thesis.

I would also like to thank other members of my dissertation committee, Profs. Patrick Hopkins, James Howe, Gary Shiflet, Eugene Kolomeisky, and Alexey Romanov, for their kind acceptance to serve as members of my dissertation committee and their precious time in reading this long dissertation.

Another person who helped me to start with acoustics related projects is Prof. Vladimir Zaitsev. His broad experience as well as readiness to share his knowledge and fruitful discussions was indispensable for me to step in into this new area. Vlad, thank you so much for your time and your help.

Furthermore, I am grateful to all my former and current colleagues from the Computational Materials Group: Dr. Cheng-Yu Shih, Dr. Bernard Wittmaack, Dr. Chengping Wu, Dr. Eaman Karim, Miao He, Prof. Alexey Volkov, Dr. Richard Salaway, Dr. Marshall Tabetah, Dr. Wu Han, Hao Huang, Chaobo Chen, Dr. Kaushik Joshi, Mikhail Arefev, Geng Shaoning, Lingyu Guo. I had very close collaboration with Dr. Cheng-Yu Shih, Dr. Chengping Wu, Dr. Eaman Karim, and Miao He in several projects both included and not included in this thesis. It was very interesting and resultful to work with you. Moreover, I would like to thank collaborators who have performed experimental verification on my work: group of Dr. J.-P. Colombier, group of Dr. Henry Helvajian, Dr. Iaroslav Gnilitskyi, group of Dr. Nikolay

Polushkin, and group of Dr. Rantej Bali. Also, Helge Heinrich has helped to perform SEM and TEM characterization of samples produced by our collaborators.

I would like to give a special thanks to all my friends both ones I met at UVa and in Russia. I would especially like to thank Dr. Bernard Wittmaack, Dr. Cheng-Yu Shih, Chaobo Chen, and Hao Huang who have been among my closest friends at UVa, I will remember the fun time I have shared with you. Also, I would like to thank Mikhail Moiseev from Russia who worked with me on development of Lattice Boltzmann model for simulation of boiling.

In addition to all of those who have guided and helped me during my time at UVa, I also would like to deeply thank the person who first introduced me to the world of computer modeling and laser interaction with matter, Dr. Nadezhda Bulgakova. The skills and foundation developed in my undergraduate and master program under her mentorship have helped me to succeed in my study at UVa.

Finally, I want to give the greatest thanks to my parents and my brother who has encouraged and supported me all this time. Staying for almost seven years away from the home, I deeply miss you, and I express my sincerer appreciation for calling me almost every day, hearing your voice is very encouraging and always gives me energy to make one more step and face new challenges. These few words cannot express the appreciation I have.

List of publications

[1]* M. He, C. Wu, M. V. Shugaev, G. D. Samolyuk, and L. V. Zhigilei, Computational study of short-pulse laser-induced generation of crystal defects in Ni-based single-phase binary solid-solution alloys, J. Phys. Chem. C, in press, 2019.

[2] M. V. Shugaev, M. He, S. A. Lizunov, Y. Levy, T. J.-Y. Derrien, V. P. Zhukov, N. M. Bulgakova, and L. V. Zhigilei, Insights into laser-materials interaction through modeling on atomic and macroscopic scales, in Advances in the Application of Lasers in Materials Science, Springer Series in Materials Science, Edited by M. Dinescu. D. B. Geohegan, A. Miotello and P. M. Ossi (Springer Nature Switzerland AG, 2018), pp. 107-148.

[3]* N. I. Polushkin, V. Oliveira, R. Vilar, M. He, M. V. Shugaev, and L. V. Zhigilei, Phase-change magnetic memory: Rewritable ferromagnetism by laser quenching of chemical disorder in $Fe_{60}Al_{40}$ alloy, *Phys. Rev. Applied* **10**, 024023, 2018

[4]* J. Ehrler, M. He, M. V. Shugaev, N. I. Polushkin, S. Wintz, V. Liersch, S. Cornelius, R. Hübner, K. Potzger, J. Lindner, J. Fassbender, A. A. Ünal, S. Valencia, F. Kronast, L. V. Zhigilei, and R. Bali, Laser-rewriteable ferromagnetism at thin-film surfaces, ACS Appl. Mater. Interfaces **10**, 15232-15239, 2018.

[5]* C.-Y. Shih, R. Streubel, J. Heberle, A. Letzel, M. V. Shugaev, C. Wu, M. Schmidt, B. Gökce, S. Barcikowski, and L. V. Zhigilei, Two mechanisms of nanoparticle generation in picosecond laser ablation in liquids: the origin of the bimodal size distribution, Nanoscale **10**, 6900-6910, 2018. A figure from this paper is featured on the **back cover of the journal issue**

[6]* C.-Y. Shih, C. Wu, H. Wu, M. V. Shugaev, and L. V. Zhigilei, Atomistic simulations of the generation of nanoparticles in short-pulse laser ablation of metals: The effect of background gas and liquid environments, in Pulsed Laser Ablation: Advances and Applications in Nanoparticles and Nanostructuring Thin Films, Edited by I. N. Mihailescu and A. P. Caricato (Pan Stanford, 2018), pp. 421-466.

[7] M. V. Shugaev, I. Gnilitskyi, N. M. Bulgakova, and L. V. Zhigilei, Mechanism of single-pulse ablative generation of laser-induced periodic surface structures, Phys. Rev. B **96**, 205429, 2017.

[8]* C.-Y. Shih, M. V. Shugaev, C. Wu, and L. V. Zhigilei, Generation of subsurface voids, incubation effect, and formation of nanoparticles in short pulse laser interactions with bulk metal targets in liquid: Molecular dynamics study, J. Phys. Chem. C **121**, 16549-16567, 2017. A figure from this paper is featured on the **cover of the journal issue**

[9] M.V. Shugaev, C.-Y. Shih, E.T. Karim, C. Wu, and L.V. Zhigilei, Generation of nanocrystalline surface layer in short pulse laser processing of metal targets under conditions of spatial confinement by solid or liquid overlayer, *Appl. Surf. Sci.* **417**, 54, 2017.

[10]*C.-Y. Shih; C. Wu, M.V. Shugaev, L.V. Zhigilei, Atomistic modeling of nanoparticle generation in short pulse laser ablation of thin metal films in water, *J. Colloid Interface Sci.,* **489**, 3, 2017. This is an **invited paper**

[11] M.V. Shugaev, C. Wu, O. Armbruster, A. Naghilou, N. Brouwer, D.S. Ivanov, T.J.-Y. Derrien, N.M. Bulgakova, W. Kautek, B. Rethfeld, L.V. Zhigilei, Fundamentals of Ultrafast Laser-Material Interaction, *MRS Bull.* **41**, 960, 2016. This is an **invited review paper +** a figure from this paper is featured on the **cover of the journal issue**

[12] X. Sedao, M.V. Shugaev, C. Wu, T. Douillard, C. Esnouf, C. Maurice, S. Reynaud, F. Pigeon, F. Garrelie, L.V. Zhigilei, and J.-P. Colombier, Growth twinning and generation of high-frequency surface nanostructures in ultrafast laser-induced transient melting and resolidification, *ACS Nano* **10**, 6995–7007, 2016. **First 2 authors are co-first authors**

[13] E.T. Karim, M.V. Shugaev, C.Wu, Z. Lin, H. Matsumoto, M. Conneran, J. Kleinert, R.F. Hainsey, and L.V. Zhigilei, Experimental characterization and atomistic modeling of interfacial void formation and detachment in short pulse laser-processing of metal surfaces covered by solid transparent overlayers, *Appl. Phys. A* **122**, 407, 2016.

[14] M.V. Shugaev, A.J. Manzo, C. Wu, V.Yu. Zaitsev, H. Helvajian, and L.V. Zhigilei. Strong enhancement of surface diffusion by nonlinear surface acoustic waves, *Phys. Rev. B* **91**, 235450, 2015.

[15] E.T. Karim, M. Shugaev, C. Wu, Z. Lin, R.F. Hainsey, and L.V. Zhigilei, Atomistic simulation study of short pulse laser interactions with a metal target under conditions of spatial confinement by a transparent overlayer, *J. Appl. Phys.* **115**, 183501, 2014. A figure from this paper is featured on the **cover of the journal issue**

* publications not directly related to projects considered in this thesis.

1. Introduction

The emergence of ultrashort pulse lasers has opened up new opportunities for high-precision processing of a wide range of materials, including dielectrics, semiconductors, and metals, enabling numerous applications in fields ranging from micromachining to photonics and life sciences [1-3]. The ability of ultrashort lasers to confine energy deposition in small regions of irradiated targets, usually tens to hundreds of nanometers in depth and microns to tens of microns in diameter, makes it possible to perform selective material modification and, at the same time, provides unique opportunities for investigation of material behavior and properties under extreme conditions of strong electronic excitation, rapid heating and cooling, and ultrafast mechanical deformation. A hierarchy of intertwined processes triggered by ultrashort laser pulses in metals, dielectrics, and semiconductors [2,4] is schematically illustrated in Figure 1 [5]. The laser-induced processes can be roughly separated into three groups, highlighted by different colors in the figure, namely, laser excitation of optically active electronic states in the irradiated material and the initial ultrafast processes occurring in response to the electronic excitation (yellow), rapid nonequilibrium phase transformations triggered by the energy transfer from the excited electrons to atomic vibrations (green), and the subsequent cooling and solidification of the surface region of the irradiated target (turquoise).

In semiconductors and dielectrics, a high concentration of free electrons promoted across the bandgap by laser excitation may lead to non-thermal phase transformations induced by transient modification of interatomic bonding [6,7]. Meanwhile, the excited electrons in semiconductors and dielectrics, as well as conduction band electrons in metals, are capable of effective laser energy absorption, which may bring the material to plasma states or even produce a Coulomb explosion due to the electron emission and charging of a surface region of a dielectric target [8]. The hot electrons then conduct energy deeper into the irradiated target and, on the picosecond time scale, thermalize with the lattice through electron−phonon coupling [9]. The energy transfer from electrons to lattice vibrations can lead to rapid heating with rates exceeding 10^{14} K/s, resulting in homogeneous melting [10,11] or even formation of a supercritical fluid [12]. The lattice heating leads to the rapid melting and resolidification, spallation, ablation, and generation of crystal defects occurring on the time scale of hundreds of picoseconds to nanoseconds. Depending on the laser fluence and material properties, the laser-induced processes may include complex hydrodynamic motion and material redistribution in the surface region of the irradiated target [13-16] as well as generation of unusual microstructure in the subsurface region [17].

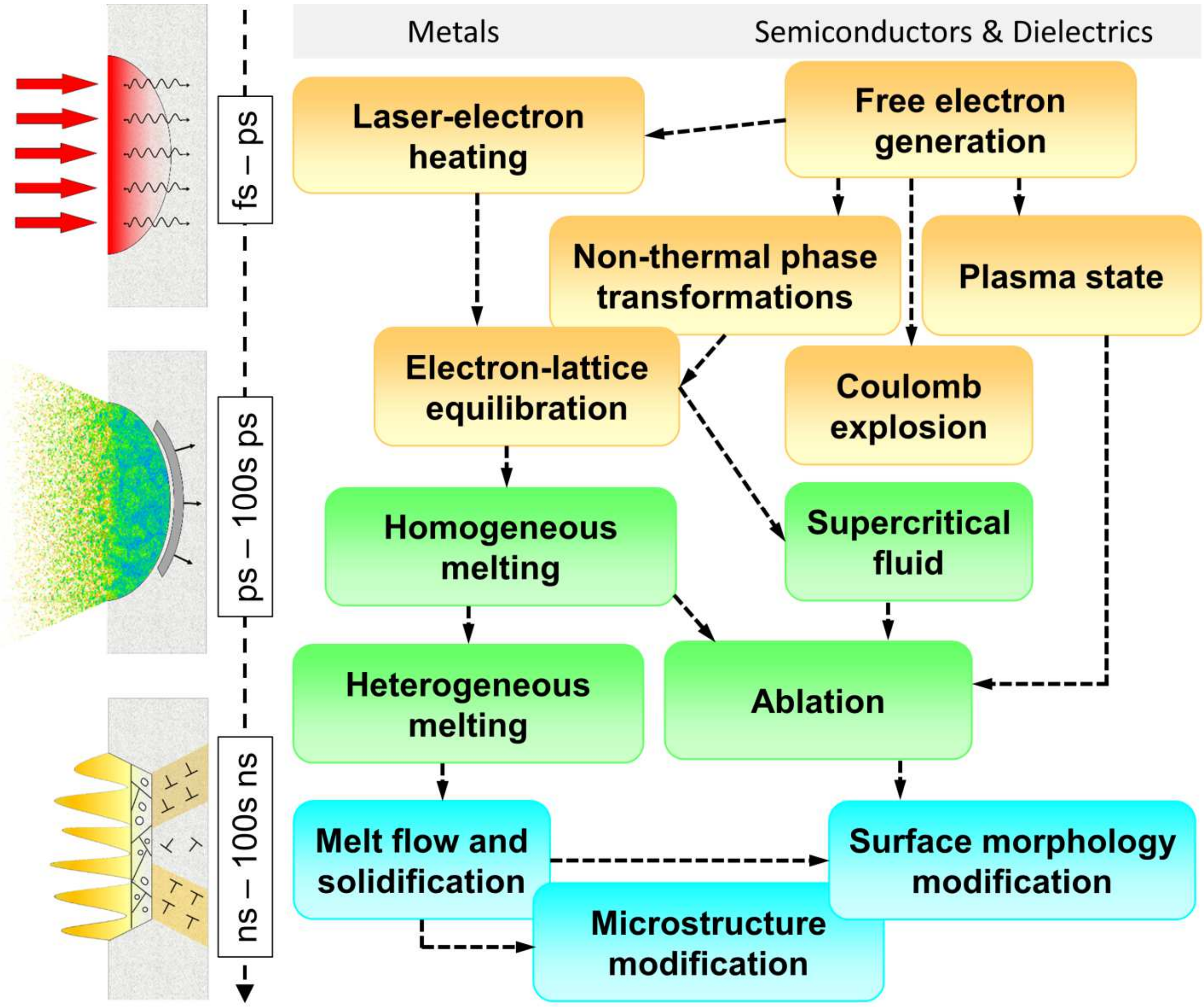

Figure 1. Typical pathways of energy dissipation and phase transformations following the excitation of a material by an ultrashort laser pulse. Note: ns, nanosecond; ps, picosecond; fs, femtosecond. Adapted from Ref. [5].

In particular, the interaction of the laser-induced compressive stresses with the free surface of the irradiated sample can result in the generation of a tensile wave sufficiently intense to cause the formation subsurface voids. The growth and percolation of the voids may lead to the separation and ejection of a top layer from the target. Analogous to the term “spallation,” commonly used to describe the dynamic fracture that results from the reflection of a shock wave from the back surface of a sample, material ejection driven by the relaxation of laser-induced stresses is commonly referred to as photomechanical spallation (admittedly, "cavitation" would be a more appropriate term when the photomechanical processes take place in the melted part of the target). Further increase in the laser fluence above the spallation threshold results in the separation and ejection of thinner layers and/or multiple droplets from the target, and, at a sufficiently high laser fluence, induces a transition to a different ablation regime commonly referred to as "phase explosion" or "explosive boiling." In this regime, the melted surface region of the irradiated target is overheated above the limit of thermodynamic stability of the liquid phase [18-20], leading to a rapid decomposition of the overheated melted material into a mixture of vapor and liquid droplets. An explosive release of vapor, rather than the relaxation of photomechanical stresses, provides the main driving force for the collective ejection of the overheated surface region of the target in the regime of phase explosion. In the case of ablation by longer laser pulses, in the absence of stress confinement, spallation is not activated, and explosive boiling is the mechanism responsible for the direct transition from the regime of surface melting and evaporation to the phase explosion [6,20].

The extreme temperature and pressure conditions created by the rapid laser energy deposition may cause generation of unusual metastable phases [21-23] as well as complex surface morphology [3,24-26] produced in the course of photomechanical spallation [27,28] or explosive decomposition of superheated material into a vapor-droplet mixture [18-20]. When the temperature drops below the equilibrium melting point, resolidification starts. In metals, strong laser energy localization combined with large thermal conductivity results in high cooling rates of up to 10^{12} K/s [17,29], which bring the material into a state of strong undercooling. The ultrahigh rates of laser-induced cooling and the resulting resolidification, combined with the generation and relaxation of strong compressive stresses generated by the fast laser heating of the absorption region [27,28], create conditions for the formation of unusual metastable phases and unique material microstructures that are difficult if not impossible to produce by any other processing methods. In particular, metallic glass formation in systems not previously considered as glass formers has been demonstrated in ns- and ps-pulse laser quenching [29,30]. Recent examples of exotic phases produced by lasers include a dense body-centered-cubic Al phase [21] and new tetragonal polymorphs of silicon [22] formed through ultrafast confined microexplosions generated by fs laser pulses tightly focused inside a sapphire (α-Al_2O_3) crystal and at the interface between a transparent amorphous silicon dioxide layer (SiO_2) and an opaque crystalline Si substrate, respectively. An unusual amorphous carbon phase featuring a large fraction of sp^3-bonded carbon and a propensity for nano-/microdiamond nucleation has been generated by nanosecond laser treatment of amorphous carbon films [23].

Generation/annealing of crystal defects, grain refinement, formation of metastable structures, such as recently reported polyicosahedral structures [31] and growth twinning [32], strongly impact surface properties such as optical reflectivity, hardness, wear and corrosion resistance as well as enhanced catalytic activity, potentially impacting the use of the treated materials [33-38]. In addition, high cooling rate creates conditions for rapid quenching and freezing of the transient liquid structures generated in laser spallation or ablation [31,39] leading to formation of complex multilevel surface morphology. Short pulse laser-induced modification of a surface morphology provides unique opportunities for many practical applications with examples including tuning the surface wetting properties from superhydrophilic [40] to superhydrophobic [41], and even superwicking, making water and other fluids to move uphill, against the gravity forces [42], fabrication of black (strongly enhanced broadband absorption) [43] or colored (wavelength-selective reflection) metals [44], as well as strong enhancement of photoelectron and thermal emission from surfaces [45].

The continuous progress in the advancement of laser applications is increasingly relying on thorough theoretical understanding of laser-induced processes that control the structural and phase transformations responsible for material modification, selective removal and/or transfer. Experimental diagnostics capable of resolving the laser-induced processes on femto-/picosecond time-scales and simultaneously on sub-micrometer length-scales, however, are currently limited to specific systems and irradiation conditions [46-48]. Even with the advancement of existing and the development of new time-resolved diagnostic methods, the experimental probing alone is unlikely to completely uncover the relationships between numerous processes involved in laser-matter interactions, which take place simultaneously or sequentially with overlap in time and space. Numerical simulation of processes occurring in laser-irradiated materials is an indispensable tool for understanding the complex phenomena of laser-materials interactions, especially when materials are driven far out of electronic, thermal, and mechanical equilibrium [5,49].

The relaxation of laser-induced stresses on the scale of entire laser spot is accompanied not only by generation of crystal defects and ablation but also by formation of intense bulk and surface acoustic waves (SAWs), Figure 2. One important feature of SAWs is that they can propagate along a thin surface layer of a substrate with little dissipation and transfer energy far from the laser spot. This characteristic of SAWs has been utilized in many practical applications, including signal processing [50], chemical sensing [51,52], nondestructive evaluation of mechanical properties [53,54], and microscale manipulation of fluid flow in microfluidics devices [55,56]. Moreover, a number of recent experimental studies indicate that SAWs may affect surface processes at atomic/molecular level. In particular, SAWs and bulk waves have been shown to enhance catalytic activity in heterogeneous catalysts [57-65], induce structural transformations and changes in surface morphology [65-72], desorb atomic clusters and molecules from surfaces [65-72], and guide surface diffusion [73,74]. These observations are unexpected and surprising as there is a large mismatch between the relatively low frequencies of SAWs, typically less than 100 MHz, and the vibration frequencies characteristic for individual atoms and molecules on the surface, on the order of 1 THz. Therefore, a detailed theoretical and computational study is needed to make sense of these surprising observations and to provide convincing explanation of the mechanism of acoustic activation of surface processes.

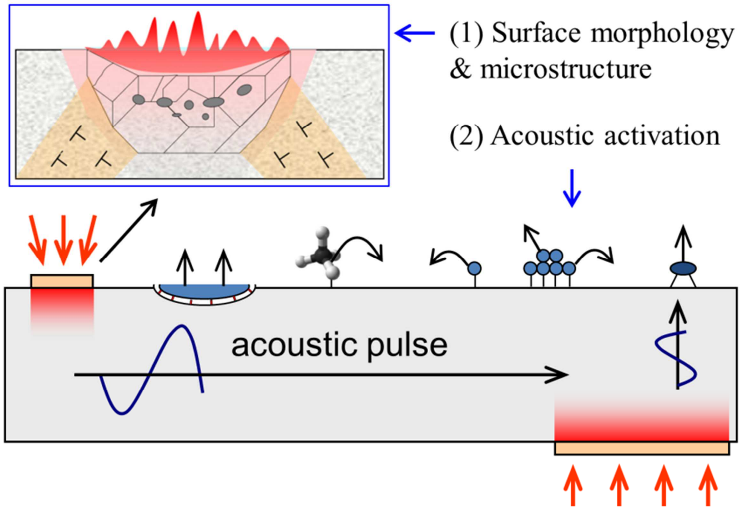

Figure 2. Schematic illustration of acoustic activation of surface processes by acoustic pulses generated in laser irradiation in addition to surface morphology and microstructure modification. Adopted from Refs. [75,76].

The primary goal of this dissertation is to elucidate the processes and mechanisms responsible for modification of surface microstructure/morphology and acoustic activation of surface processes in short pulse laser irradiation. A brief description of the computational models used in this dissertation, newly developed methods, and procedures used to calculate particular properties of material in atomistic simulations is provided in **Section 2**. The subject of this work consists of three interrelated parts: (1) laser-induced modification of subsurface microstructure, (2) laser-induced modification of surface morphology, (3) acoustic activation of surface processes, discussed in Sections 3, 4 and 5, respectively. **Section 3** first discusses the effect of crystallographic orientation of an irradiated target on emission of dislocations in short pulse laser processing, proposes a novel mechanism of dislocation generation during crystal growth, describes the origin of vacancy supersaturation, elucidates the mechanism of growth twins formation observed in experimental study by our collaborators, and provides an extensive theoretical an computational analysis of growth twinning. Next, the effect of interatomic potential on results of atomistic simulations of short pulse laser irradiation is illustrated, and a number of high temperature properties of Ti interatomic potentials are computed. Finally, the effect of a spatial confinement by a solid transparent overlayer on microstructure produced in laser processing is analyzed, and the final microstructure is compared with one obtained for irradiation in vacuum and in presence of a liquid overlayer. **Section 4** discusses two topics: fundamentals of photomechanical spallation and mechanism of generation of Laser-Induced Periodic Surface Structure (LIPSS) in the phase explosion regime. **Section 5** is focused on revealing the mechanisms responsible for acoustic activation of surface processes. In particular, a series of continuum level simulations is first completed to assess the efficiency of Surface Acoustic Wave (SAW) generation in nonablative regime of laser irradiation. Next, an atomistic approach for modeling of free propagation of SAWs is designed and used for a detailed analysis of intrinsic features corresponding to linear and nonlinear evolution of SAW. Before our study, the method of molecular dynamics (MD) has never been applied for description of free propagation of SAWs, and prior works were limited to either periodic shaking of surface to produce a wide spectrum of bulk and surface waves [77] or displacing a thin layer of material [78] according to the analytical solution [79]. The newly designed approach has helped us to reveal the crucial role of nonlinear wave evolution in enhancement of surface diffusion of small clusters observed in experiments. The nonlinear sharpening of the SAW profile corresponds to the generation of high frequency harmonics, which are able of directly couple with natural vibrational modes of these clusters. This explanation is also demonstrated to be valid for acoustically activated desorption. Finally, the SAW induced motion of graphene sheets on Cu substrate is demonstrated and explained. This dissertation then concludes with a summary and suggestions for future work in **Section 6**.

2. Methods

Abstract: Computer simulations and theoretical analysis of laser-materials interactions are playing an increasingly important role in the advancement of modern laser technologies and broadening the range of laser applications. The small size of the laser modified zone as well as ultrashort time scales of the investigated processes makes experimental investigation of defect formation during ultrashort laser irradiation extremely difficult and underlines the increasingly important role of computer modeling in providing a reliable physical interpretation of *ex situ* characterization of the microstructure [17,32,80].

The highly non-equilibrium nature of the processes induced by short pulse laser irradiation as well as atomic resolution required for accurate description of defect generation and evolution without prior assumptions suggest atomistic modeling as an indispensable and consummate tool for investigation of microstructure and surface morphology modification during ultrafast laser processing [17,81-84]. Moreover, molecular dynamics (MD) method opens unprecedented opportunities for investigation of the influence of intense SAWs on atomic level processes, such as diffusion, desorption, catalytic activity, and structure modification. Meanwhile, the high computational cost of atomistic simulations limits the spatial and temporal scales accessible in the modeling. Thus, computationally cheaper continuum-level or coarse-grained models, capable to describe entire irradiated spot and surrounding material, are necessary for mapping the atomistic predictions to the experimental conditions.

2.1. Atomistic models

2.1.1. Atomistic modeling of laser irradiation of metals

This subsection provides an overview of a hybrid computational model combining a continuum-level description of the laser excitation and subsequent relaxation of the conduction band electrons in metals with the classical MD method capable to describe rapid non-equilibrium melting, cavitation in liquid, spallation, solidification under conditions of deep undercooling, and generation of a high density of crystal defects in a course of this process. The basic concepts of the model are summarized below.

Method of molecular dynamics (MD)

Classical molecular dynamics (MD) method is a computational technique describing process under the study by tracking motion of individual atoms, molecules, or coarse-grained particles in the system [85,86]. The temporal evolution of a system of interacting particles is defined by solving the system of classical equations of motion:

$$m_i \frac{d^2 \bar{r}_i}{dt^2} = \overline{F}_i = -\frac{\partial U(\bar{r}_1, \bar{r}_2, \ldots, \bar{r}_N)}{\partial \bar{r}_i} \qquad (2.1),$$

where m_i and $\bar{r}_i$ are the masses and positions of particles, $\overline{F}_i$ is the force acting i from other particles, and $U(\bar{r}_1, \bar{r}_2, \ldots, \bar{r}_N)$ is the energy of interparticle interactions in the system with N particles. After setting the initial conditions, such as initial positions and velocities, solution of Eq. 2.1 provides a set of trajectories that describes the evolution of the system and its thermodynamic parameters.

In our study, 7-th order predictor-corrector algorithm [87] (k = 8) is used for integration of equations of motion. The algorithm includes two stages: prediction of the system state on the next time step and correction based on the evaluated value of forces. For each particle positions, velocities, and values of k-2 higher order derivatives are tracked and at each "prediction" stage are updated according to the following equation (Taylor expansion):

$$\bar{q}_{i,n}^{t+\widetilde{\Delta t}} = \sum_{j=n}^{j-k} C_j^n \cdot \bar{q}_{i,j}^{t} \qquad (2.2),$$

$$\bar{q}_{i,n} = \frac{\Delta \mathrm{t}^{\mathrm{n}}}{n!} \frac{d^n \bar{r}_i}{dt^n},$$

where $\Delta \mathrm{t}$ is the time step, and C_j^n are the binomial coefficients. After the coordinates $\bar{q}_{i,0} = \bar{r}_i$ are updated, the interparticle forces are calculated for the next configuration, and the error is computed as:

$$\Delta \bar{q}_i^{t+\Delta t} = \frac{\bar{F}(t+\Delta t)}{2m_i} \Delta t^2 - \bar{q}_{i,2}^{t+\widetilde{\Delta t}} \qquad (2.3).$$

The corrected values of $\bar{q}_{i,n}$ at the next time step are computing with using filter values C_i:

$$\bar{q}_{i,n}^{t+\Delta t} = \bar{q}_{i,n}^{t+\widetilde{\Delta t}} + C_i \Delta \bar{q}_i^{t+\Delta t} \qquad (2.4).$$

The optimal values of C_i are summarized in Table 1 for a number of values k and p, which represents the order of derivative used to compute the error term. In particular, for MD p = 2 since when force is evaluated the second derivative is used for computing the error. When system is initialized, the values of higher order derivatives are set to be zero.

Table 1. The values of C_i for Gear predictor-corrector algorithm. Adapted from Ref. [87].

p	k	C_0	C_1	C_2	C_3	C_4	C_5	C_6	C_7
1	3	5/12	1	1/2					
	4	3/8	1	3/4	1/6				
	5	251/720	1	11/12	1/3	1/24			
	6	95/288	1	25/24	35/72	5/48	1/120		
	7	19087/60480	1	137/120	5/8	17/96	1/40	1/720	
	8	5257/17280	1	49/40	203/270	49/192	7/144	7/1440	1/5040
2	4	1/6	5/6	1	1/3				
	5	19/120	3/4	1	1/2	1/12			
	6	3/20	251/360	1	11/18	1/6	1/60		
	7	863/6048	665/1008	1	25/36	35/144	1/24	1/360	
	8	1925/14112	19087/30240	1	137/180	5/16	17/240	1/120	1/2520
3	5	1/4	1/2	5/4	1	1/4			
	6	3/80	19/40	9/8	1	3/8	1/20		
	7	221/5040	9/20	251/240	1	11/24	1/10	1/120	
	8	2185/46368	863/2016	95/96	1	25/48	49/336	1/48	1/840
4	6	1/30	1/10	1	5/3	1	1/5		
	7	16/630	3/20	19/20	3/2	1	3/10	1/30	
	8	11/630	221/1260	9/10	251/180	1	11/30	1/15	1/210

Despite the basic idea of MD is quite simple, various optimization techniques must be applied to make the simulation computationally feasible. In particular, computing all vs. all interactions in a system has $O(N^2)$ complexity, and using a potential cutoff together with a neighbor list (Verlet list) [88], cell list, or combination of these algorithms is needed to reduce the complexity to $O(N)$ [85,89]. In addition, tabulation of force table, using of half list of interactions [85], and advanced multiple time step integration algorithms [90] as well as usage of features of modern hardware and capabilities of parallel computing enable further extension of temporal and special limits accessible in atomistic simulations. However, even with the above-described optimizations, the computational cost of atomistic simulations remains relatively high, Figure 3. The typical system sizes and duration of simulations accessible in MD are on the scale of hundreds of nanometers and nanoseconds, and usually only a small part of an experimental system can be simulated.

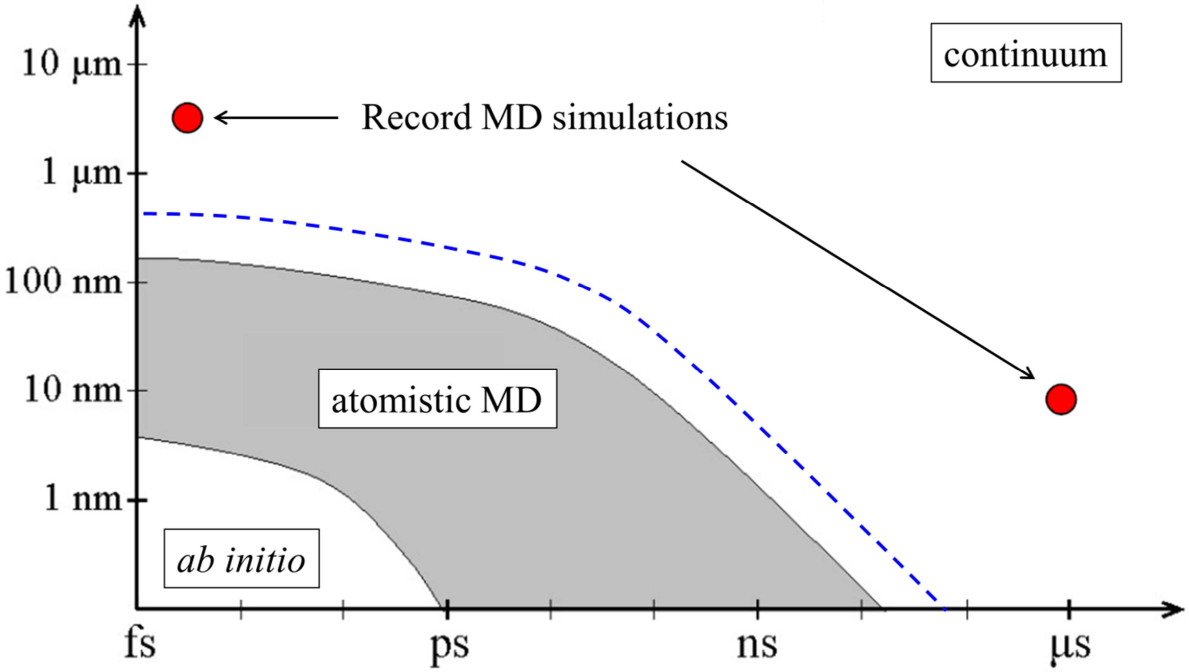

Figure 3. Schematic illustration of spatial and temporal scales accessible in atomistic simulations. The scales accessible through large scale parallel computing are illustrated by dashed blue line. Adapted from Ref. [91].

Under conditions when the analytical (continuum-level) description of spatially confined laser ablation is hindered by the complexity and highly nonequilibrium nature of laser-induced processes, the molecular dynamics computer simulation technique can serve as a useful alternative approach, capable of providing atomic-level insights into the laser-induced processes. The main advantage of the MD technique is that no assumptions are made on the processes or mechanisms under study. The only input in the MD model is the interatomic interaction potential that defines the equilibrium structure and thermodynamic properties of the material. The interatomic potentials are typically designed via ab-initio calculation and fitted to reproduce basic material properties of interests. Once the interatomic potential is chosen and initial conditions are defined, the MD trajectories (positions and velocities) are obtained through numerical solution of the equations of motion for all atoms in the system without any further assumptions. This advantage makes MD an ideal technique for exploring non-equilibrium processes and revealing new physical phenomena. However, as pointed out in Section 3.4, since all material properties are hidden within the interatomic potential, it may be very simple to obtain erroneous results in an MD simulation, and in particular cases computing of material parameters and knowledge of their effect on the simulation may be needed for interpretation of MD predictions.

Two temperature model (TTM)

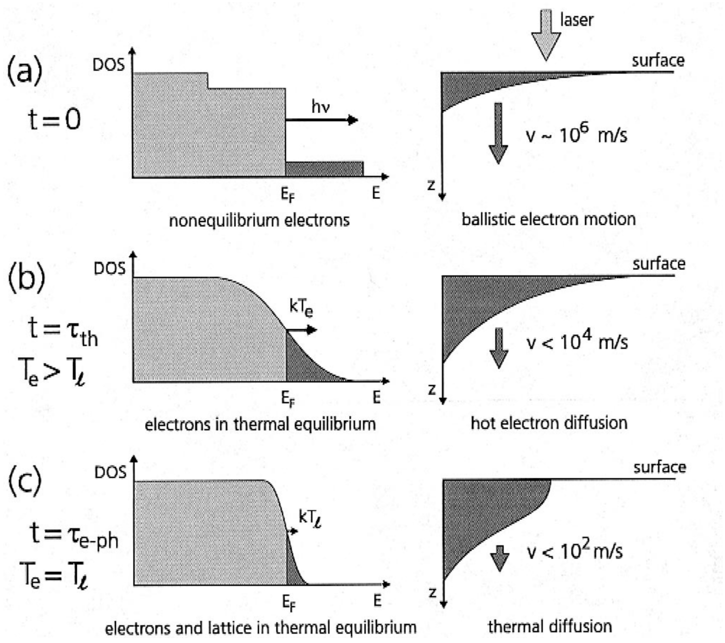

Figure 4. Three distinguished relaxation phases of optically excited electrons in metals: (a) photon absorption, (b) electron-electron relaxation is completed, and (c) electron-phonon relaxation is completed. Adapted from Ref. [92].

The energy of a short laser pulse couples mainly to electrons of the irradiated material. In metals, the presence of conduction band electrons enables the direct absorption of laser energy by electrons undergoing collisions with nuclei (i.e., by inverse bremsstrahlung). This process is followed by electron-electron equilibration proceeding within 10s of femtoseconds [92]. Before electron-electron equilibration, the absorbed energy is redistributed by excited electrons in a ballistic regime [92,93]. Studies targeted at the revealing the ultrafast dynamics of nonequilibrium electrons in metals under ultrashort pulse laser irradiation [94,95] demonstrate a stepwise shape of the electron density distribution in the vicinity of the Fermi level with the step size multiple to the photon energy, $h\nu$, immediate after laser irradiation. However, the shape of the distribution changes to the equilibrium Fermi-Dirac distribution after several tens of femtoseconds. At the next stage the evolution of the system is governed by heat diffusion in the electron system and by equilibration of hot electrons with phonons on the picosecond time scale. At this stage the system has two distinct temperatures: electron and phonon temperatures. In literature the phonon temperatures is commonly referred as lattice temperature. The above-described stages are schematically illustrated in Figure 4.

Two-temperature model (TTM) [9,96] has been proposed as a simplified approximation accounting for the absorption of laser energy, two temperature stage resulted by laser irradiation, electron heat conduction to the bulk of the target, and rapid heating of lattice through the electron-phonon collisions. The model is represented by two coupled heat diffusion equations for electronic and phononic subsystems:

$$\begin{cases} C_e \frac{\partial T_e}{\partial t} = \nabla[k_e \nabla T_e] - g \cdot (T_e - T_l) + S \\ C_l \frac{\partial T_l}{\partial t} = \nabla[k_l \nabla T_l] + g \cdot (T_e - T_l) \end{cases} \qquad (2.5),$$

where T_e and T_l are the temperatures of the electronic and phononic (lattice) subsystems; C_e and C_l are the electron and lattice heat capacities; k_e, k_l, and g are the electron and lattice thermal conductivity and the electron-phonon coupling parameter, and S is a source term describing energy deposition through laser irradiation. The energy attenuation with depth, z, is described according to Beer-Lambert law, and the Gaussian temporal shape of the laser pulse, which is a good approximation for femtosecond laser pulses, is assumed:

$$S = \frac{2I_{abs}\sqrt{ln2}}{\sqrt{\pi}\tau} exp\left(-4ln2 \cdot \left(\frac{t}{\tau}\right)^2\right) \cdot \frac{e^{-z/\lambda_0}}{\lambda_0} \qquad (2.6),$$

where τ is the pulse duration computed as full width at half maximum (FWHM), λ_0 is the absorption depth computed as a sum of the optical absorption depth and ballistic depth, $\lambda_0 = \lambda_{opt} + \lambda_b$, and I_{abs} is the absorbed laser fluence, which is approximated as $I_{abs} = (1 - R)I_0$ in this dissertation in the case of comparison with experimental conditions. I_0 is the incident laser fluence, and R is the reflectivity coefficient. More accurate description of reflectivity with accounting for the temporal evolution of the electron temperature may be provided through Drude model [49]. In particular, this method has been used in one of our recent studies to estimate absorbed energy for irradiation of Au target in water environment [97]. However, as pointed out in the supplemental materials to Ref. [97], the uncertainty resulted by the choice of the ballistic depth results in variation of the absorbed laser fluence for a given incident fluence in a wide range, which can be eliminated only with using an explicit description of the ballistic electron transport based on the solution of Boltzmann transport equation for electrons [98].

Therefore, in all reported simulations we use absorbed rather than incident fluence. Also when λ_0 and τ become comparable or smaller that the size of the mesh and time step used in the simulation, which is the case for continuum-level simulations reported in this dissertation and for Cr with $\lambda_0 = 9.6$ nm. Therefore, the integral form of Eq. 2.6 should be used:

$$S = I_{abs} \cdot \frac{erf\left(2\sqrt{ln2}\cdot(t+dt)/\tau\right) - erf\left(2\sqrt{ln2}\cdot t/\tau\right)}{2dt} \cdot \frac{e^{-z/\lambda_0} - e^{-(z+h)/\lambda_0}}{h} \qquad (2.7),$$

where h is the mesh size, dt is time step, and erf is error function. In all simulations all pulses shifted by 2.5τ to insure complete absorption of energy corresponding to a given value of I_{abs}.

In early TTM based simulations g was approximated as a constant, and C_e as $C_{e0}T_e$ [92,99,100]. However, later studies with explicit consideration of the density of states for particular materials have provided more accurate temperature dependent values of C_e and g [101], which are used in our study. Several approximations to describe the dependence of the electron thermal conductivity, k_e, on the electron and lattice temperature are described in Ref. [102]. In our study, the electron thermal conductivity is taken similarly to Ref. [101] as $k_e = v_F^2 C_e \tau_c/3$, where v_F is the Fermi velocity. The collision frequency of free electrons is approximated via the sum of electron-electron and electron-phonon scattering rates as $\tau_c^{-1} = \tau_{e-e}^{-1} + \tau_{e-ph}^{-1} = AT_e^2 + BT_l$ [101]. The value of the coefficient A can be estimated based on free electron model [103]. The coefficient B can be set as a constant or described as a function of the lattice temperature and the materials phase state, so that the experimental temperature dependences of thermal conductivity of the solid and liquid under conditions of electron-phonon equilibrium are reproduced in the simulation. Lattice thermal conductivity k_l is usually neglected in simulations based on TTM model since for metals k_e exceeds k_l by one or two orders of magnitude. However, in some specific cases such as heat diffusion near metal-dielectric interface phononic heat capacity may prevail within several nanometers from the interface, especially for metals with weak electron-phonon coupling as pointed out in Section 3.6.

Hybrid TTM-MD model

Although the MD method is capable of providing detailed information on the microscopic mechanisms of laser ablation, several modifications have to be made in order to apply the classical MD for simulations of laser interactions with metals. In particular, a realistic description of the laser coupling to the target material, the kinetics of thermalization of the absorbed laser energy, and the fast electron heat conduction should be incorporated into the MD technique. These processes can be accounted for by incorporating the MD method into the general framework of the two-temperature model (TTM) [9,96] commonly used in the simulations of short pulse lase interactions with metals.

The idea of the combined TTM-MD model [39,102,104] is schematically illustrated in Figure 5 and is briefly explained below. TTM is used to describe absorption of laser energy by electrons with following energy redistribution and equilibration with phonon system at picosecond time scale. To overcome the limitations of this continuum level approach in description of ultrafast phase transformations, morphology changes, and microstructure modification, the top part of the irradiated target, where these processes take place, is simulated with classical molecular dynamics model, which replaces the equation for lattice. Meanwhile, the temperature evolution in the remaining part of the target is described with TTM approach. The size of this part, L_{TTM}, is selected to be 2-5 μm to ensure negligible temperature change at the bottom of the system. At the interface between TTM-MD and TTM parts a heat conducting pressure wave transmitting boundary condition [105,106] is applied to ensure non-reflecting propagation of the laser-induced stress wave from the MD region of the computational system to the bulk of the target. The size of TTM-MD part, L_{TTM-MD}, is selected to ensure that its bottom part remains solid throughout the simulation.

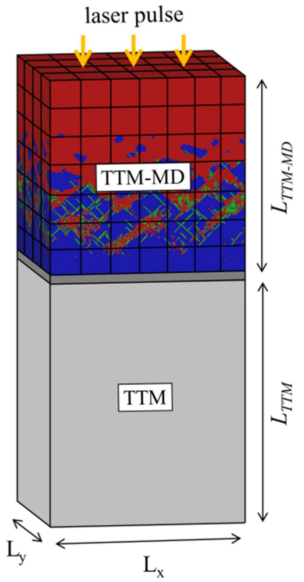

Figure 5. A schematic representation of a hybrid TTM-MD approach. A snapshot from a simulation reported in Section 3.6 is used to represent the hybrid part. A nonreflecting boundary condition is illustrated by dark gray rectangle at the interface between TTM-MD and TTM parts.

The system of TTM equations is integrated simultaneously with MD, and MD domain is decomposed into cells according to the mesh used in TTM. The three-dimensional solution of the diffusion equation for T_e is used in simulations of laser spallation and ablation, where the dynamic material decomposition may result in lateral density and temperature variations. The size of the cells in our simulations is selected to be 1-1.5 nm in z direction and 4-6 nm in lateral directions. The energy exchange between electron subsystem in TTM and MD part is described by adding extra contribution to the force acting on each atom [102]:

$$m_i \frac{d^2\bar{r}_i}{dt^2} = \bar{F}_i + \xi m_i \bar{v}_i^{th} \qquad (2.8),$$

$$\xi = \frac{1}{n}\sum_{k=1}^{n} gV_{cell} \cdot \left(T_e^k - T_l^{cell}\right) / \sum_i^N m_i \left(\bar{v}_i^{th}\right)^2 \qquad (2.9),$$

$$T_l^{cell} = \sum_i^N m_i (\bar{v}_i^T)^2 / 3k_B (N_{cell} - 1) \qquad (2.10),$$

where V_{cell} is the cell volume, T_l^{cell} is the local lattice temperature computed for each cell, $\bar{v}_i^{th}$ is the thermal velocity of the atom defined as $\bar{v}_i^{th} = \bar{v}_i - \bar{v}^c$, $\bar{v}_i$ is the actual velocity of atom i, and $\bar{v}^c$ is the velocity of center of mass of a cell which the atom i belongs to. Since explicit Euler algorithm is used to solve TTM equations, the maximum time step is limited: $\Delta t_{TTM} \leq 0.125h^2 C_e/k_e$. High thermal conductivity of metals results in maximum Δt_{TTM} to be in a range of 0.01-0.1 fs, which one-two orders of magnitude smaller that the time step used in MD, 1-5 fs. Therefore, each MD step corresponds to n TTM steps. The expansion, density variation, and, at higher fluences, disintegration of the irradiated target predicted in the MD part of the model are accounted for through the corresponding changes of the parameters of the TTM equation for electron temperature. Cells containing less than 10% atoms are disabled. Liquid and crystal regions produced in the simulations of ultrafast melting and solidification are identified with local order parameter described in more details in Ref. [102].

As pointed out above, the most severe limitation of MD is huge computational cost that limits spatial and temporal scales of the simulation and does not allow to model entire laser spot. The processes occurring at the scale of laser spot can then be evaluated through a “mosaic” approach based on combining the results of a series of atomistic simulations with periodic boundary conditions in lateral directions performed for a range of local fluences chosen from the laser beam profile [39], Figure 6. However, this approximation may fail when lateral material and energy redistribution play an important role, for example in the case of LIPSS formation discussed in Section 4.2

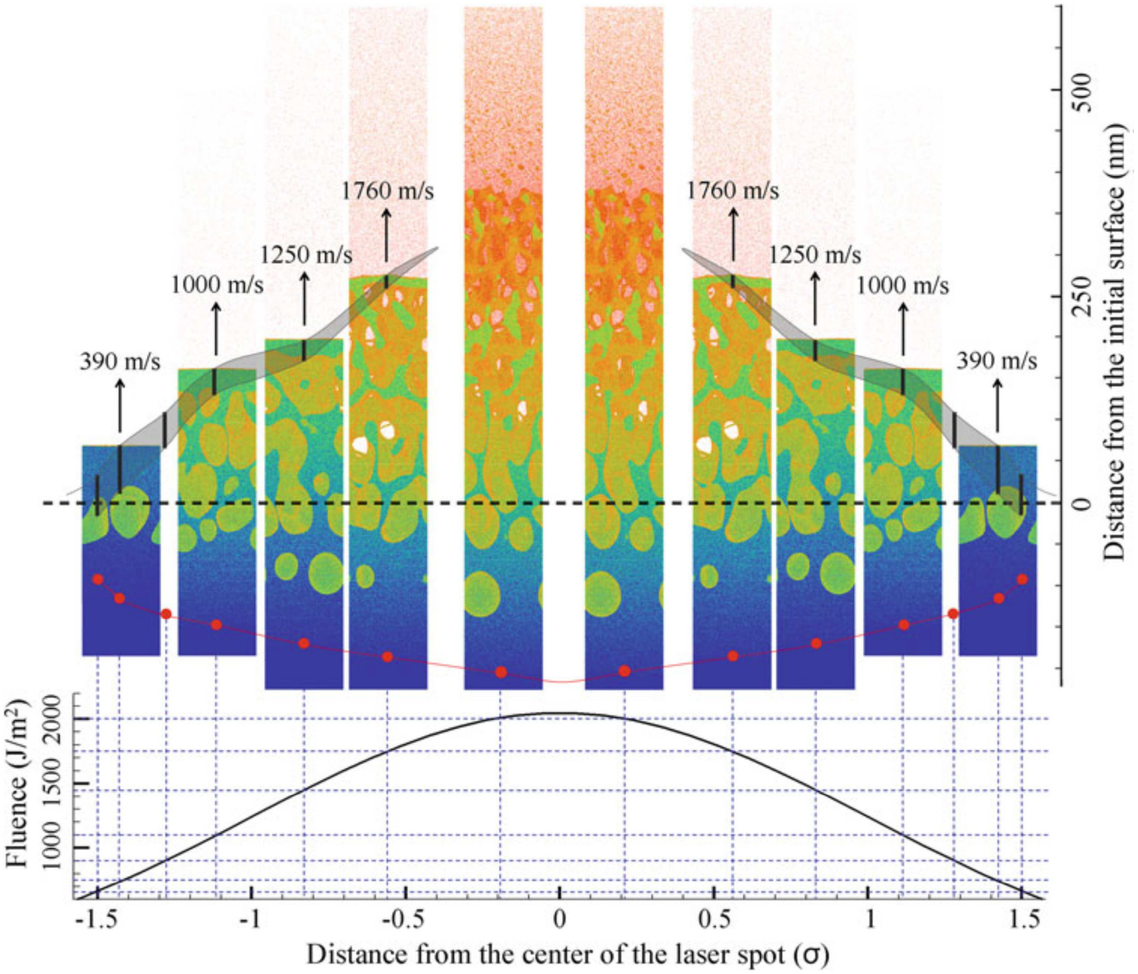

Figure 6. The integral visual picture of melting, generation of subsurface voids and material ejection from an Al target irradiated by a 100 fs laser pulse. The laser beam has a Gaussian spatial profile with a peak absorbed laser fluence of 2050 J/m^2, as shown in the bottom part of the figure. The representation of the laser-induced processes at the scale of the whole laser spot is based on a "mosaic approach", where snapshots from individual TTM-MD simulations taken at the same time of 150 ps after the laser pulse are aligned with locations within the laser spot that correspond to the values of local fluence used in the simulations, as shown by the thin vertical and horizontal dashed lines. The atoms in the snapshots are colored by their potential energy, from blue for low energy atoms in the bulk of the target to red for the vapor-phase atoms. The red dots connected by the red line mark the location of the melting front. The thicknesses and locations of the top void-free layers are shown by black bars for simulations performed in the spallation regime and, in the case of the lowest fluence of 650 J/m^2, just below the spallation threshold. For two local fluences, 650 and 900 J/m^2, the locations of the melting front and the void-free layers are marked without showing the corresponding snapshots. The velocities of the top void free layers at 150 ps are provided in the figure. Adapted from Ref. [39].

Computational representation of the transparent overlayer

Two different methods developed in this work for representation of the transparent overlayer are illustrated in Figure 7. In both implementations, the properties of fused silica are used in parameterization, and the overlayer is assumed to be sufficiently thick to ensure that the pressure wave generated in the overlayer due to the laser energy absorption by the metal target does not reflect from the top surface of the overlayer and come back to the metal-overlayer interface during the time of the simulation. For a 10 μm thick overlayer and the speed of sound of 5900 m/s in fused silica [107], it takes more than 3 ns for the reflected wave to reach the interface. In the irradiation regimes considered in this work (from the threshold for surface melting up to several times the threshold), the time scale of laser-induced structural and phase transformations does not exceed several nanoseconds, and the reflected pressure wave would not affect the transformations for overlayers with thickness on the order of tens of micrometers.

In the first method, illustrated in Figure 7a, the overlayer is not represented with atomic resolution but introduced through a dynamic acoustic impedance matching boundary condition that accounts for the displacement of the metal overlayer interface in response to the thermal expansion and phase transformations occurring in the surface region of the metal target. The dynamic boundary condition in this case takes the form of an imaginary plane that interacts with the Ag atoms through the Lennard-Jones (LJ) potential defined as a function of the distance between an Ag atom and the imaginary plane. The imaginary plane moves in response to forces acting on it from the Ag atoms as well as an additional force F_{NRB} that mimics the elastic response of the overlayer to forces acting from the side of the metal target. This additional force is proportional to the instantaneous velocity v of the imaginary plane and acts in the opposite direction, $F_{NRB} = -ZSv$, where S is the surface area of the interface and Z is the acoustic impedance of the overlayer material. For the silica overlayer, the acoustic impedance is calculated as $Z = \rho_{SiO_2} c_{SiO_2}$, where $\rho_{SiO_2} =$ 2200 kg/m^3 and $c_{SiO_2} =$ 5900 m/s are the experimental values of density and speed of sound in fused silica [107]. The mass assigned to the imaginary plane is equal to the total mass of Ag atoms in a single (001) atomic plane and the equation of motion is solved for the plane together with the integration of the equations of motion for all the atoms.

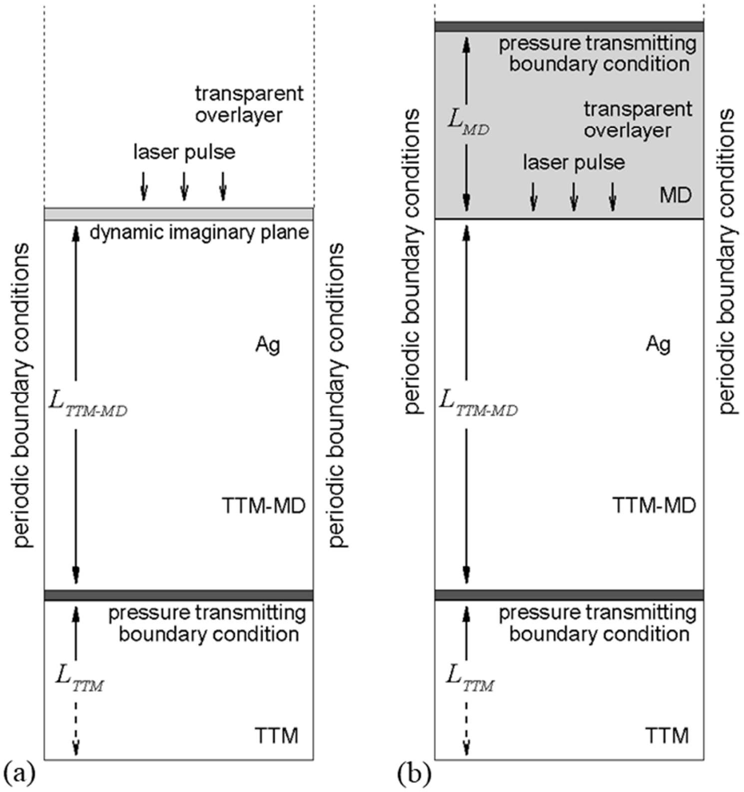

Figure 7. Schematic sketches of two alternative computational setups designed for simulations of laser interactions with a Ag target covered by a transparent overlayer. In both setups, the top layer of the Ag target with thickness of L_{TTM-MD} is represented by the atomistic TTM-MD model, whereas the heat conduction in the deeper part of the substrate is simulated with TTM equations solved in the region with thickness of L_{TTM}. The transparent overlayer is represented by a dynamic imaginary plane in (a) and by a model adapting an atomistic MD description of a part of the overlayer adjacent to the Ag target in (b). The dynamic pressure-transmitting boundary conditions are applied at the bottom of the TTM-MD region and, in (b), at the top of the MD part of the overlayer to mimic non-reflective propagation of laser-induced pressure waves through the boundaries. In both setups, the partial propagation of the laser-induced pressure wave into the silica overlayer and the work of adhesion between the overlayer and the Ag film are reproduced. Adapted from Ref. [108].

The parameters of the LJ potential describing the interaction between a Ag atom and the imaginary plane are fitted to reproduce the experimental value of the work of adhesion between the Ag substrate and silica overlayer as well as the local stiffness under uniaxial compression at the interface defined by an arithmetic average of the elastic constant C_{11} for FBD EAM Ag (C_{11} = 124 GPa, Ref. [107]) and fused silica (C_{11} = 76.6 GPa, calculated from experimental values of longitudinal wave velocity and density, Ref. [107]). The work of adhesion for Ag-silica interface at 773 K, W_{adh} = 0.43 J/m^2 (Ref. [109]) is used to fit the value of the LJ parameter defining the energy scale of the potential, ε. This parameter is chosen so that the energy of the

Ag-silica interface, γ_{Ag-SiO_2}, satisfies the following definition of the work of adhesion: $W_{adh} = \gamma_{Ag} + \gamma_{SiO_2} - \gamma_{Ag-SiO_2}$, where $\gamma_{Ag} = 0.72$ J/m^2 is the energy of free (001) surface of Ag calculated at 773K for the FBD EAM potential and $\gamma_{SiO_2} = 0$ since the energy of the imaginary surface of silica after separation from Ag is zero. The parameter defining the length scale of the potential, σ, is then chosen to reproduce the local stiffness to uniaxial compression, C_{11}, as described above. The fitting yields the following parameters of the LJ potential: σ = 2.42 Å and ε = 0.224 eV.

While the representation of the overlayer by the method based on the imaginary plane provides a computationally efficient description of the partial reflection of the laser-induced pressure wave from the metal-silica interface and reproduces the experimental work of adhesion between the metal substrate and silica overlayer, this method is not free of limitations. In particular, the boundary condition can only reproduce the elastic response of the overlayer, and no plastic deformation or melting of the overlayer is allowed. Moreover, in the simulations performed under irradiation conditions leading to the transient surface melting and resolidification of the metal target, the imaginary plane is observed to promote nucleation of hcp (hexagonal close packed) and fcc (face centered cubic) crystallites with close packed crystallographic planes oriented parallel to the imaginary plane.

In order to relax the assumption of an ideal “indestructible” overlayer, an alternative method, illustrated in Figure 7b, is developed. In this method, a part of the overlayer adjacent to the metal target is simulated with an atomistic MD method. In the present work, we do not attempt to provide an accurate description of the silica structure and silica-Ag interfacial structure, as such description would necessitate the use of a reactive force field that would substantially increase the computational cost of the simulations. Instead, the silica substrate is simulated as an fcc crystal with atoms interacting through LJ potential. The parameters of the LJ potential, σ = 4.41 Å and ε = 0.237 eV, and the atomic mass of 113.5 Da are chosen so that the values of the elastic constant, $C_{11} = 75$ GPa, melting temperature, T_m = 1825 K, and density, ρ_{SiO_2} = 2200 kg/m^3 of the model material are in a good agreement with experimental values for fused silica (C_{11} = 76.6 GPa, T_m = 1938 K, ρ_{SiO_2} = 2200 kg/m^3, Ref. [107]).

The cross-interaction between the atoms in the overlayer and Ag is also described by the LJ potential. The LJ parameter σ is chosen so that the equilibrium interatomic distance for the cross-interaction would be an arithmetic average of the ones in the substrate and the overlayer. Similarly to the case where the overlayer is represented by an imaginary plane (described above), the LJ parameter ε is fitted to the work of adhesion for the Ag-silica interface at 773 K, $W_{adh} =$ 0.43 J/m^2, Ref. [109]. With the calculated surface energies of $\gamma_{Ag} = 0.72$ J/m^2 and $\gamma_{SiO_2} = 0.39$ J/m^2, the parameter ε is chosen to reproduce the energy of the Ag-silica interface, $\gamma_{Ag-SiO_2} = \gamma_{Ag} + \gamma_{SiO_2} - W_{adh} = 0.68$ J/m^2. The fitting yields the following parameters of the LJ potential for the Ag-silica cross-interaction: σ = 3.53 Å and ε = 0.111 eV.

The size of the part of the overlayer represented with atomistic resolution, L_{MD} in Figure 7b, is 100 nm in simulations performed at absorbed laser fluences of 900 and 1000 J/m^2, and 200 nm at 3000 and 6000 J/m^2. In contrast to the metal substrate, where the heat transfer is dominated by the electrons and is reproduced with the TTM equations, the vibrational heat transfer in the glass overlayer is treated directly by the MD model. The value of the thermal conductivity of the model overlayer material, k = 0.85 Wm^{-1}K^{-1}, is calculated from the evolution of the temperature profiles predicted in a non-equilibrium MD simulation of a 411 nm long system with an initial temperature of 300K and a temperature of 1000K fixed at one end of the system. The conductivity of the model material is comparable to the experimental one for fused silica, 1.38 Wm^{-1}K^{-1}, Ref. [107]. The characteristic length of thermal diffusion in the simulated overlayer on the timescale of the simulation, $t_{sim} = 1$ ns, is $L_{th} = \sqrt{2D_T t_{sim}} =$ 57 nm, where $D_T = k/c_v$ ~ 1.7×10^{-6} m^2/s is the thermal diffusivity, k is the thermal conductivity, $c_v = 3R$ is the heat capacity, and R is the ideal gas constant. Therefore, for $L_{MD} =$ 100 – 200 nm, $L_{th} < L_{MD}$ and the heat transfer through the upper boundary of the computational system in Figure 7b is neglected in the simulations. A pressure transmitting boundary condition [105,106], similar to the one applied at the bottom of the TTM-MD region of the metal target, is applied to the top monolayer of the fcc crystal representing the MD part of the overlayer.

2.1.2. Atomistic modeling of SAW propagation

A brief description of the MD model developed for the first atomistic simulations of free (nonlinear) propagation of SAWs is provided below. The following subsections discuss the general idea of the computational method developed for the atomistic simulations of free propagation of nonlinear acoustic waves, the constraints imposed on the choice of parameters of the computational setup by the peculiarities of the nonlinear SAWs, and the method used to generate the waves.

Computational "synchrotron" for atomistic simulations of nonlinear acoustic waves

The general idea of the computational method developed for simulation of the wave profile evolution during the propagation in a nonlinear medium is illustrated in the schematic shown in Figure 8. From the first sight the schematic resembles a synchrotron for particle acceleration. Drawing on this analogy, the generation of the initial wave at the source in the computational "synchrotron" corresponds to the particle injection in the real synchrotron, the gradual evolution of the wave profile and shock formation during the propagation away from the source corresponds to the particle acceleration by the magnetic field, and the material modification by the shock wave generated in the computational "synchrotron" corresponds to the ejection and utilization of the accelerated particle in applications. This general setup depicted in Figure 8 is utilized in our work in simulations of both bulk and surface acoustic waves. The implementation of each of the three components of the computational "synchrotron" is briefly outlined below.

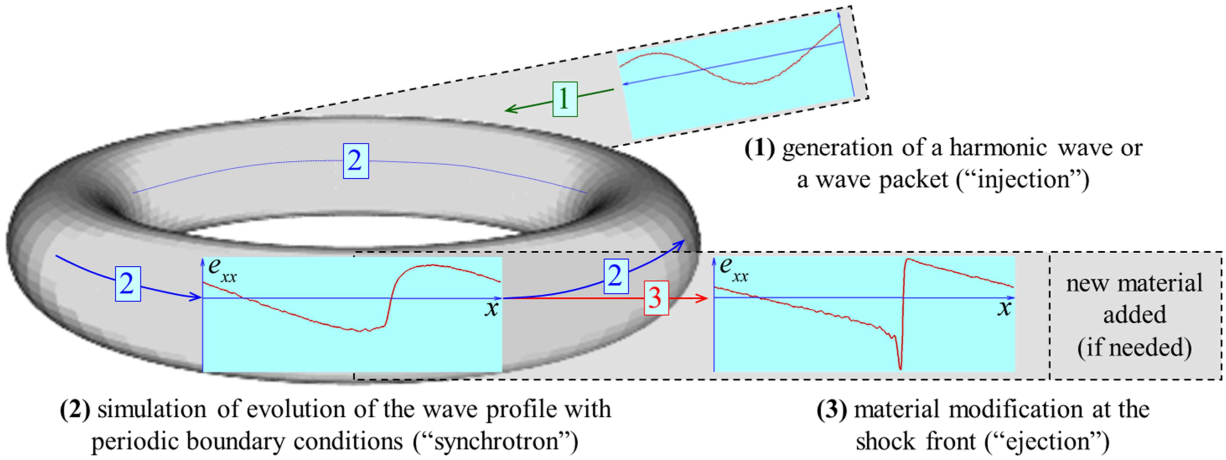

Figure 8. Schematic representation of the interactions between different components of the proposed computational "synchrotron" approach to simulation of the generation of SAWs, their nonlinear propagation and structural modification of the surface region (see description in the text).

[1] "injection": Depending on the purpose of the simulation, a continuous sinusoidal wave with a given frequency or a wave packet representing a SAW pulse generated by an external optical or electromechanical stimulus can be generated in the MD computational system at the start of the simulation. As explained in a subsection below, the generation of the wave packets or periodic waves can be done by assigning instantaneous displacements and velocities to all atoms in the system according the corresponding solutions of continuum-level equations derived for the corresponding linear (harmonic) SAWs or bulk wave.

[2] "synchrotron": Once the initial wave is generated, the gradual evolution of the wave profile during the propagation in a nonlinear medium can be simulated in a computational setup adopting periodic boundary conditions in the direction of the wave propagation. In the case of a periodic wave, the length of the computational system in this direction must be multiple of the wavelength. This approach makes it possible to perform analysis of the long-term evolution of the wave profile without the need for extending the size of the computational system to match the distance covered by the wave. Since periodic boundary conditions are applied along the direction of the wave propagation, the increasing time in the simulation corresponds to the linearly increasing distance from the source of the wave under typical experimental conditions. The non-linear sharpening of the wave and the generation of a shock front can leads to the onset of an active SAW energy dissipation, as discussed in Section 5.2. While the energy deposition due to the wave dissipation can be offset by maintaining a constant temperature throughout the substrate with a specially designed thermostating procedure, any irreversible structural material modification or "damage" caused by the propagating wave would immediately render the "reuse" the damaged material in the "synchrotron" mode of the simulation impossible.

[3] "ejection": When the strain magnitude at the shock front, increasing due to the nonlocal nonlinearity of SAWs [110-112], reaches the levels sufficient for generation of irreversible material modification, the realistic modeling of the wave propagation through the pristine material away from the source can no longer be done with periodic boundary conditions applied in the direction of wave propagation. In this case, the periodic boundary conditions should be switched off and, if needed, new material could be added and equilibrated in front of the propagating wave. In order to extend the time-scale of the simulations and avoid the linear increase of the number of atoms in the system with simulation time, the material behind the propagating acoustic pulse can be removed, so that the MD computational system of a fixed size remains stationary in the reference frame of the moving front of the wave. This approach is similar to the "moving window" technique [113] that has been successfully applied in investigations of bulk shock waves in gases [114], liquids [115] and crystals [116-118], as well as in the analysis of detonation front instabilities [119]. Note that the addition of new material and the "moving window" approach are only needed when the long-term evolution of the wave after the damage is produced is of interest. In many cases, when the conditions for the onset of surface damage and the nature of surface modification are of interest, the simulation can be completed before the wave front reaches the outer boundary of the computational system. This scenario is exemplified by a simulation discussed in Section 5.2 performed for strongly nonlinear regime, where a gradual evolution of a SAW in the computational "synchrotron" produces a shock wave that are sufficiently strong to cause the generation of several zones of localized plastic deformation in the surface region of the substrate.

Details of MD computational setup

The main goal of the simulations reported in this subsection is to explore, using the general computational approach outlined in the previous section, the new opportunities provided by the atomistic modeling in the investigation of linear and nonlinear propagation of SAWs. The computational systems considered in the simulations, therefore, are chosen to be simple but representative of different classes of real materials. In particular, the simulations will be performed with two pairwise interatomic potentials that reproduce materials with positive and negative values of the parameter of local nonlinearity [120] (*e.g.*, metals and fused silica, respectively), so that qualitatively different evolution of the wave profile (*e.g.*, compression and extension of a SAW pulse for metals and silica, respectively) could be studied.

The material with positive value of the parameter of local nonlinearity is described by the common Lennard-Jones (LJ) potential, with parameters σ and ε defining the length and energy scales of the interatomic interactions and a cutoff function [121] used to ensure that the interactions vanish at a cutoff distance of $r_c = 3\sigma$. The negative value of the parameter of local nonlinearity are reproduced, somewhat counterintuitively, by a harmonic pair potential (considered between nearest neighbors) with the equilibrium interatomic distance and the force constant (second derivative of the potential function at the equilibrium distance) matching those of the LJ potential. For a one-dimensional (1D) chain of particles interacting via a harmonic (parabolic) potential, the dependence of the elastic energy density on strain is also ideally parabolic. Consequently, the propagation of waves in the 1D chain is perfectly linear and does not result in the generation of higher frequency harmonics or other nonlinear effects. In a bulk three-dimensional (3D) crystal described by the harmonic pair potential, however, the anharmonic quadratic terms in the stress-strain dependence do appear due to purely structural reasons and the sign of these terms is opposite to the one in the material described by the LJ potential. Namely, the tensile deformation leads to the effective stiffening of the material described by the harmonic potential while the material softens if the LJ potential is used. This contrasting behavior makes it possible to perform an initial exploration of the effect of the sign of the acoustic nonlinearity on the evolution of SAW profiles with simple and computationally efficient pairwise potentials. For results produced with LJ potential, all the physical quantities are presented in reduced units scaled by the LJ length and energy parameters, σ and ε, and the atomic mass m. In particular, the time, velocity, and temperature are expressed in units of $\tau = (m\sigma^2/\varepsilon)^{1/2}$, $v = \sigma/\tau = (\varepsilon/m)^{1/2}$, and $T = \varepsilon/k_B$, respectively, where k_B is the Boltzmann constant. Otherwise, real units are used.

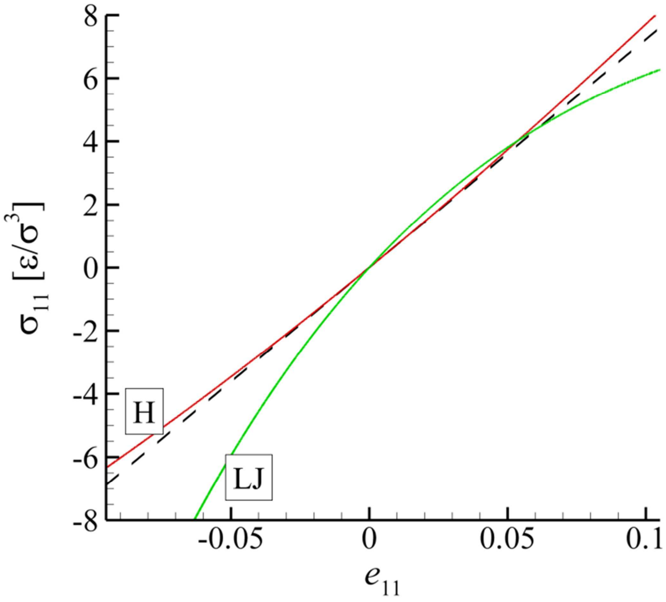

Figure 9. The dependence of σ_{11} strain on e_{11} for a crystal described with LJ (green) and Harmonic (red) potentials. Linear dependence of strain on stress is outlined with a dashed line.

The MD simulations are performed for a computational system shown schematically in Figure 10. It represents a surface region of a substrate with fcc crystal structure and (001) crystallographic orientation of the surface. The periodic boundary conditions are applied along x and y directions, parallel to the free surface of the substrate. In the direction of the SAWs propagation, the minimum system size, L_x, is defined by the spatial periodicity of the simulated SAW and varies between 12 and 1200 fcc unit cells (18.6σ to 1860σ) in simulations with corresponding values of SAW wavelength. The constraint on the minimum size of the computational system in the y direction, parallel to the front of the propagating SAW, is imposed by the use of the periodic boundary condition, which requires the size of the system to be at least twice larger than the cutoff distance of the interatomic interaction potential, *i.e.*, $L_y > 2r_c$. To minimize the computational time, L_y is chosen to be close to the minimum value, $L_y = 7.8\sigma$, which corresponds to 5 fcc unit cells.

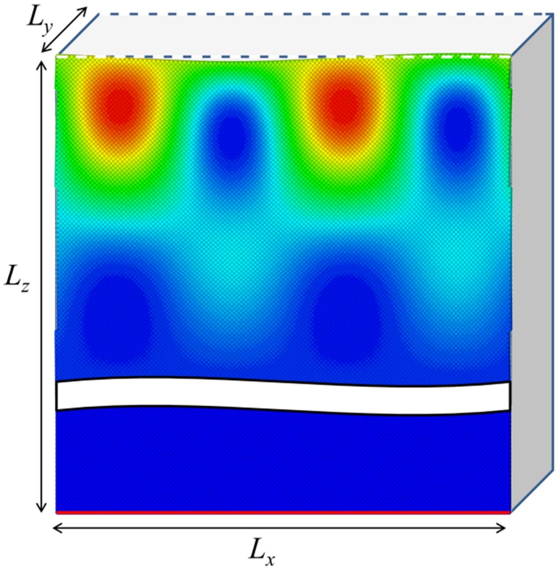

Figure 10. The schematic representation of the computational system used in the simulations of free propagation of SAWs. The color shows an instantaneous distribution of kinetic energy in the field of an initial sinusoidal SAW propagating in the direction of x-axis. The blue and red colors correspond to low and high values of the kinetic energy.

The choice of the depth of the computational system, L_z, and the type of the boundary conditions suitable for the bottom of the simulated system requires particular attention. In contrast to earlier MD simulations of SAWs [77,78,122], where the close-to-sinusoidal wave profiles are generated and maintained through dynamic boundary conditions applied at [77,122] or very close [78] to the surface, the simulations of free nonlinear wave propagation require the dynamic representation of much deeper part of the substrate. The elastic field of a SAW decays exponentially into the bulk of the substrate (oscillations superposed on the exponential envelope may appear in anisotropic crystals) and the energy carried by the SAW is largely concentrated within a surface layer with a thickness on the order of the SAW wavelength λ. One may expect, therefore, that a depth of the MD simulation system exceeding one or two wavelengths would be sufficient for reproducing the unperturbed propagation of the SAW in an infinitely thick substrate. The first MD simulations performed for systems with $L_x = 2\lambda - 4\lambda$, however, reveals a rather strong influence of the finite depth of the computational system on the wave propagation, even though the wave energy density decreases at these depths down to less than $10^{-4} - 10^{-7}$ of that at the upper surface.

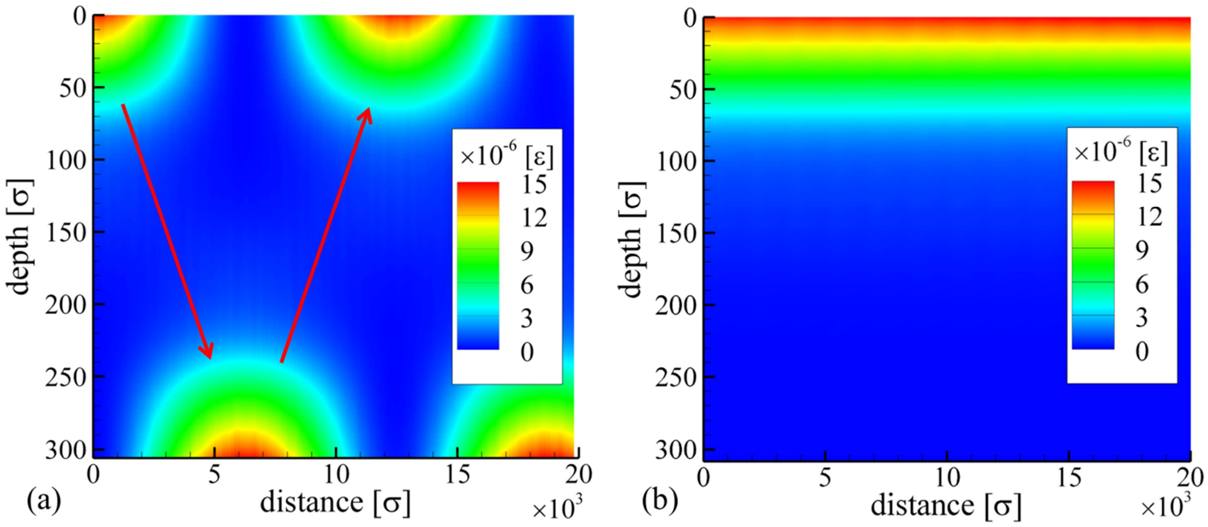

Figure 11. Contour plots showing the evolution of the kinetic energy in MD simulations of SAWs propagating in two systems of the same depth of $L_z = 2\lambda$ but different boundary conditions applied at the bottom of the computational system, free boundary in (a) and rigid boundary in (b). The horizontal axis shows the distance passed by the wave, which is linearly related to the time of the simulation. The vertical axis represents the depth under the surface where the initial wave is generated at the start of the simulation. The color corresponds to the kinetic energy per atom averaged over one SAW wave period and surface subdomains with one fcc unit cell in *x* direction and 4 fcc unit cells in *z* direction. The simulations are performed for SAWs with wavelength of $\lambda = 155\sigma$, strain amplitude of $e_0 = 8\times10^{-5}$, and zero temperature of the substrate. Periodic energy exchange between the dynamically coupled SAWs propagating along the two free surfaces of the system is observed in panel (a) and schematically outlined by red arrows, while no such energy redistribution is seen in panel (b), where the rigid boundary condition is applied at the bottom.

In the simulations where the free boundary condition is used at the bottom of the computational system, a strong linear coupling between the upper and the bottom surfaces is found to create an effective channel of linear energy exchange between the SAWs propagating along the upper and bottom surfaces. As a result, the wave energy is periodically transferred from one surface to another in a manner similar to the energy exchange between two coupled identical oscillators, as can be seen in Figure 11a. For the sample thickness of $L_z = 2\lambda$, the period of the energy exchange corresponds to the distance of about 39λ covered by the wave. Certainly, the efficiency of coupling between the SAWs propagating along the two surfaces can be reduced by increasing the sample thickness, leading to the increase in the energy exchange period. This effect is illustrated in Figure 12, where different rates of the energy leakage from the original waves generated in the top surface regions to the waves induced at the bottoms of the computational systems are shown for different values of L_z equal to 2λ, 3λ, and 4λ. Despite the marked decrease in the rate of the energy exchange with increasing depth of the system, however, the raise of the bottom wave amplitude on the time scale of the simulation is still significant at $L_z = 4\lambda$ and, eventually, all the energy of the original wave will be fully transferred to the energy of the wave propagating along the opposite side of the system.

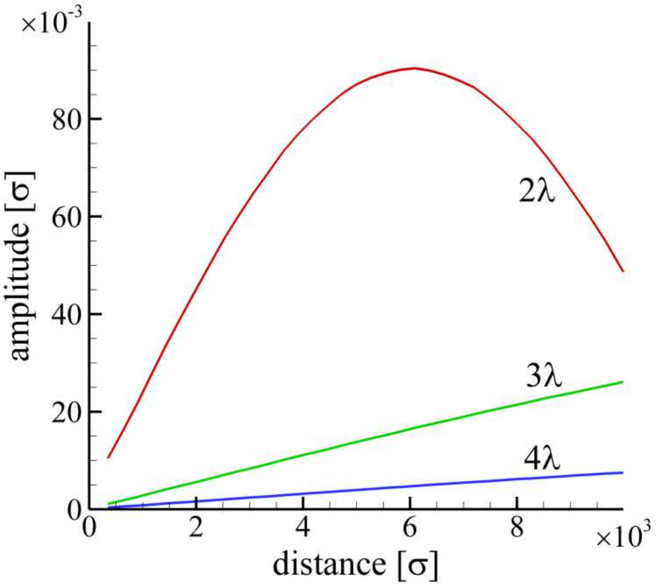

Figure 12. The dependence of the amplitudes of the SAWs induced near the free bottom surfaces of computational systems with different depths, L_z, equal to 2λ, 3λ, and 4λ. All three simulations are performed for SAWs with wavelength of $\lambda = 155\sigma$, strain amplitude of $e_0 = 8\times10^{-5}$, and zero temperature of the substrate. The curve for $L_z = 2\lambda$ corresponds to the panel (a) in Figure 11. These examples illustrate the reduction in the rate of energy exchange between the SAWs propagating along the upper and bottom surfaces of the substrate. They also show that even with the relatively weak coupling between the two waves at $L_z = 4\lambda$, the cumulative energy exchange may be rather efficient.

A simple and radical solution to the problem of the energy leakage from a SAW propagating along the top surface of a computational system of finite size is to apply the rigid boundary condition at the bottom of the computational system, thus eliminating the possibility of the excitation of the second SAW. Indeed, as shown in Figure 11b, the application of rigid boundary condition results in a complete disappearance of the energy leakage from the SAW propagating along the top surface region of the computational system. The elimination of the resonant coupling to the bottom surface of the system, however, does not mean that the computational setup with the rigid boundary condition is free of artifacts introduced by the finite depth of the system. In particular, one of the important consequences of the finite depth of the system (with either rigid or free boundary conditions applied at the bottom) is the appearance of extra frequency dispersion. Indeed, since the characteristic depth of the SAW energy localization is proportional to the wavelength, the presence of the opposite boundary has different effect on waves of different frequencies. It is well known that, for nonlinear wave transformation, the phase mismatch between the interacting harmonics in a dispersive media can drastically change the resultant wave profile. In particular, an efficient generation of co-propagating higher frequency harmonics is prevented, and no shock fronts are formed in dispersive optical materials. It should be verified, therefore, that the depth of the system is sufficiently large for preventing the introduction of strong dispersion and ensuring a realistic representation of the propagation of SAW on a substrate of infinite depth. To revel the effect of the depth of the computational cell on the wave propagation and generation of higher-frequency harmonics, three simulations are performed for the same SAW with $\lambda = 155\sigma$ and different depth of the computational system, L_z equal to 2λ, 3λ and 4λ. The evolution of the second harmonic of the wave, shown for the three simulations in Figure 13, demonstrates a substantial effect of the depth for the transition from 2λ to 3λ, while the results predicted with 3λ and 4λ are almost identical.

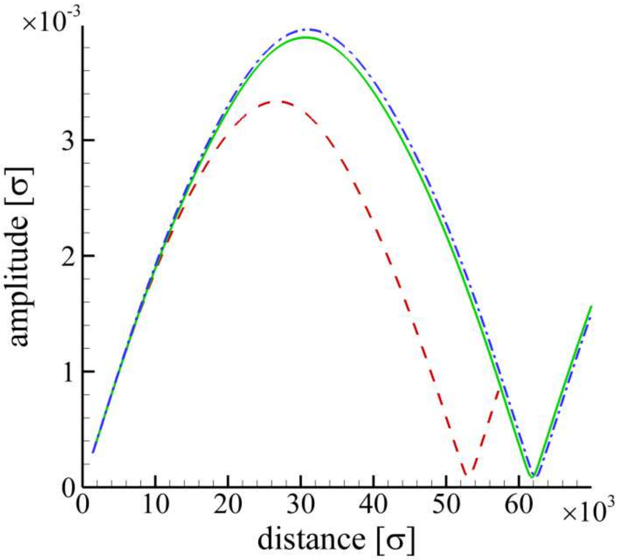

Figure 13. The evolution of the second harmonic of the surface acoustic wave for the depth of the rigid bottom equal to 2λ (red dashed line), 3λ (green solid line), and 4λ (blue dash-dot line). The wavelength is 155σ, strain amplitude of $e_0 = 2\times10^{-5}$, and zero temperature of the substrate. This plot demonstrates rather significant difference between the cases 2λ and 3λ, while the evolution of the second harmonic is almost the same for 3λ and 4λ system depth.

Based on these observations, and given the fact that the increase in depth of the simulated system leads to the corresponding increase in the computational cost of the atomistic simulations, the depth of 3λ and the rigid boundary condition at the bottom of the computational system are chosen in this work as a reasonable compromise between the minimization of the artifacts related to the finite depth of the system and ensuring computational efficiency the simulations.

Generation of SAWs

It is known that sufficiently good understanding of the behavior of a running initially sinusoidal surface wave is important for understanding more complex cases. On the other hand, consideration of an initially sinusoidal wave makes it possible to exclude unnecessary computational costs by applying periodical boundary conditions to a system with horizontal size precisely corresponding to the wave length of the fundamental harmonic. To create an initially sinusoidal SAW in the sample, it is desirable to ensure the distribution of the displacements and velocities of the particles in the initial moment $t = 0$ as close as possible to the actual distribution for a running harmonic wave with the chosen frequency. Any other initial distribution would correspond to the excitation of a wide spectrum of spatial and frequency harmonics propagating in both (left and right) directions in the form of both SAWs and bulk waves.

The derivation of the solution of wave equation for surface waves is based on an approach suggested in Ref. [123]. In particular, the solution for surface waves is written with assuming unknown imaginary direction of wave propagation defined based on the boundary condition imposed on the surface. Such an approach significantly simplifies the derivation of the solution for anisotropic media. Below we provide a derivation of a solution for Rayleigh wave propagating in a cubic crystal along the direction [100] in the plane (001), for which an analytical form is known from a previous study [78], and in a cubic crystal along the direction $[11\bar{2}]$ in the plane (111), which is more complicated and has not been reported in literature. Out of a variety of SAWs, we consider only Rayleigh wave solution for which displacement within the wave occurs in a plane perpendicular to the surface and parallel to the wave propagation direction.

For anisotropic medium the wave equation is written in the following form with using Einstein notation:

$$\rho \frac{\partial^2 u_i}{\partial t^2} = c_{ijlm} \frac{\partial^2 u_m}{\partial x_j \partial x_l} \tag{2.11}$$

where ρ is density, u_i is displacement along a particular coordinate axis x_i, and c_{ijlm} is a stiffness tensor. The solution of the equation for a SAW can be written as:

$$u_j = A_j exp[ik \cdot (x_1 cos\alpha_1 + x_2 cos\alpha_2 + x_3 cos\alpha_3 - ct)] \tag{2.12}$$

where $cos\alpha_1$ and $cos\alpha_2$ define the direction of propagation of the wave on the surface; $cos\alpha_3$ defines a complex angle of the wave propagation perpendicular to the surface; c and k is speed of the wave and spatial angular frequency; and A_j is the wave amplitude. Therefore, after substitution of Eq. 2.12 in Eq. 2.11 we obtain:

$$k^2 A_m \left(c_{ijlm} cos\alpha_j cos\alpha_l - \delta_{im}\rho c^2\right) = 0 \qquad (2.13).$$

In the following calculations we use $cos\alpha_1 = 1$, $cos\alpha_2 = 0$, $cos\alpha_3 = q$, and $\rho c^2 = R$.

100: For a wave propagating along the direction [100] in the plane (001) Eq. 2.13 is written as:

$$k^2 A_m \begin{pmatrix} C_{11} + q^2 C_{44} - R & 0 & q(C_{12} + C_{44}) \\ 0 & (1 + q^2)C_{44} - R & 0 \\ q(C_{12} + C_{44}) & 0 & C_{44} + q^2 C_{11} - R \end{pmatrix} = 0 \qquad (2.14),$$

were C_{11}, C_{12}, and C_{44} are three nonzero components of stiffness tensor in a cubic crystal. This gives a system of equations with respect to unknown amplitudes. The condition of non-trivial solution is that the determinant is equal to zero:

$$det \begin{vmatrix} C_{11} + q^2 C_{44} - R & 0 & q(C_{12} + C_{44}) \\ 0 & (1 + q^2)C_{44} - R & 0 \\ q(C_{12} + C_{44}) & 0 & C_{44} + q^2 C_{11} - R \end{vmatrix} = 0 \qquad (2.15).$$

This condition can be split into two: $(1 + q^2)C_{44} - R = 0$, which gives a solution for a shear wave propagation along the surface and polarized in x_2 direction, and:

$$(C_{11} + q^2 C_{44} - R)(C_{44} + q^2 C_{11} - R) - q^2 (C_{12} + C_{44})^2 = 0 \qquad (2.16),$$

which has four solutions for waves with exponentially decreasing amplitude at $-\infty$ and $+\infty$:

$$q_{1,2,3,4} = \pm\sqrt{\frac{-b \pm \sqrt{b^2 - 4ac}}{2a}} \qquad (2.17),$$

$$a = C_{11}C_{44},\ b = C_{11}(C_{11} - R) + C_{44}(C_{44} - R) - (C_{12} + C_{44})^2,\ c = (C_{11} - R)(C_{44} - R)$$

For waves propagating in a solid half space at $z > 0$ we select two roots with positive imaginary part. The total solution is written as a superposition of solutions corresponding to these roots:

$$u_j = \sum_{n=1}^{2} A_j^{(n)} C_n exp[ik \cdot (x_1 + q_n x_3 - ct)] \qquad (2.18).$$

A_2^1 and A_2^2 are equal to zero for a Rayleigh wave solution. Out of seven remaining constants only five are independent, and one of them corresponds to the wave amplitude, a_0. Therefore, we set the following values $A_1^{(1)} = A_3^{(1)} = a_0$, $A_3^{(1)} = \gamma_1$, $A_3^{(2)} = \gamma_2$, $C_1 = 1$, $C_2 = C$, where:

$$\gamma_n = -\frac{q_n(C_{12}+C_{44})}{C_{11}q_n^2-R} \quad (2.19).$$

The values of the remaining constants, C and R, are calculated based on the boundary condition (zero stress at a free boundary):

$$\sigma_{i3} = c_{i3lm}\frac{\partial u_m}{\partial x_l}\bigg|_{x_3=0} = 0 \quad (2.20),$$

$$C = -\frac{C_{12}+C_{33}\gamma_1 q_1}{C_{12}+C_{33}\gamma_2 q_2} \quad (2.21),$$

$$\gamma_1 + \gamma_2 C + q_1 + q_2 C = 0 \quad (2.22).$$

Numerical solution of Eq. 2.22 allows to derive the value of R. In the earlier work by Stoneley [79], Eq. 2.22 is simplified to a cubic equation, which can be solved analytically:

$$(1 - R/C_{44})(1 - C_{12}^2/C_{11}^2 - R/C_{11})^2 = R^2(C_{11} - R)/C_{11}^3 \quad (2.23).$$

111: Analytical expressions for the displacement and velocities in the Rayleigh wave available in literature [79,124] are limited by $\{001\}$ surface for cubic and orthorhombic and $\{0001\}$ surface for hexagonal crystals. Therefore, to have an ability to study Rayleigh wave propagation on $\{111\}$ surface we have derived a corresponding solution of the wave equation and a numerical procedure for wave generation. For the case of (111) surface, the stiffness tensor is rotated prior applying Eqs. 2.11and 2.13 to have x_3 perpendicular to the surface and x_1 parallel to $[11\bar{2}]$. The stiffness tensor in this case is modified, and its nonzero components are calculated as:

$$C'_{11} = C'_{22} = (C_{11} + C_{12} + 2C_{44})/2$$

$$C'_{33} = (C_{11} + 2C_{12} + 4C_{44})/3$$

$$C'_{12} = (C_{11} + 5C_{12} - 2C_{44})/6$$

$$C'_{13} = (C_{11} + 2C_{12} - 2C_{44})/3$$

$$C'_{44} = C'_{55} = (C_{11} - C_{12} + C_{44})/3$$

$$C'_{66} = (C_{11} - C_{12} + 4C_{44})/6$$

$$C'_{15} = -C'_{25} = -C'_{46} = -(C_{11} - C_{12} - 2C_{44})\sqrt{2}/6 \quad (2.24),$$

which leads to the following equation for existence of a nontrivial solution:

$$det\begin{vmatrix} C'_{11}+2C'_{15}+q^2C'_{44}-R & 0 & C'_{15}+q(C'_{13}+C'_{44}) \\ 0 & C'_{66}-2C'_{15}q+q^2C_{44}-R & 0 \\ C'_{15}+q(C'_{13}+C'_{44}) & 0 & C'_{44}+q^2C'_{33}-R \end{vmatrix}=0 \quad (2.25).$$

It is noticeable that on (111) surface Rayleigh wave solution exists only for propagation in $[11\bar{2}]$ and $[\bar{1}\bar{1}2]$ directions. Moreover, since C'_{15} is not equal to zero, wave profile does not have a mirror symmetry with respect to the direction of wave propagation that, as shown both in experimental studies [125,126] and by our simulations, affects nonlinear evolution and formation of a shock front.

Solution of Eq. 2.25, similar to the previously considered case, can be split into shear wave polarized along x_2 and Rayleigh wave solution with motion in (x_1, x_3) plane. The second one results in the following equation:

$$(C'_{11}+2C'_{15}+q^2C'_{44}-R)(C'_{44}+q^2C'_{33}-R)-\left(C'_{15}+q(C'_{13}+C'_{44})\right)^2=0 \quad (2.26),$$

which can be rewritten as:

$$aq^4+bq^3+cq^2+dq+e=0 \quad (2.27),$$

$$a=C'_{33}C'_{44},\ b=2C'_{15}C'_{33},\ c=C'_{11}C'_{33}-C'^2_{13}-2C'_{13}C'_{44}-R(C'_{33}+C'_{44}),$$

$$d=-2C'_{15}(C'_{13}+R),\ e=C'_{11}C'_{44}-C'^2_{15}-(C'_{11}+C'_{44})R+R^2.$$

Solution of this equation produces four values of q, two with positive and two with negative imaginary part. For waves propagating in a solid half space at $z > 0$ we select two roots with positive imaginary part and write the total solution with using Eq. 2.18. Using the same notation as in the (100) case, the unknown constants are calculated as:

$$\gamma_n=-\frac{C'_{15}+q_n(C'_{13}+C'_{44})}{C'_{44}+C'_{33}q_n^2-R} \quad (2.28).$$

$$C=-\frac{C'_{13}+C'_{33}\gamma_1q_1}{C'_{13}+C'_{33}\gamma_2q_2} \quad (2.29),$$

and the value of R is computed based on iterative solution of the following equation:

$$C'_{15}(1+C)+C'_{44}(\gamma_1+\gamma_2C+q_1+q_2C)=0 \quad (2.30).$$

As an example, Rayleigh wave solutions for (001) and (111) surfaces are plot in Figure 14. The oscillating behavior of the profile is resulted by crystal anisotropy and is not present in isotropic solids. Also, the plot illustrates that the structure of the wave may strongly be affected by the orientation of the substrate. The SAWs are incorporated into MD system by adding an extra displacement and velocities, calculated as time derivatives of displacements, to a thermalized system. Positions of atoms in the ideal crystal are used for evaluation of displacements for each individual atom. After wave is incorporated to the system, free dynamics simulation allows tracking evolution of the wave and its effect on surface species, as discussed in Sections 5.2 and 5.3.

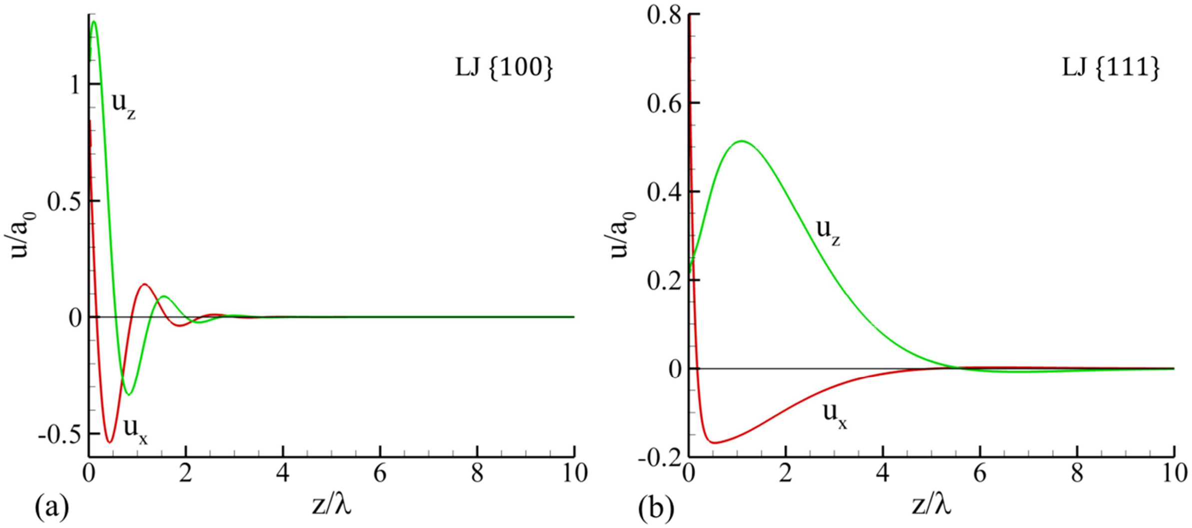

Figure 14. The dependence of x (red) and z (green) components of displacement on depth at $x = 0$ and $t = 0$ for Rayleigh wave solution on $\{001\}$ surface $[100]$ direction and $\{111\}$ surface $[11\bar{2}]$ direction. a_0 is the wave amplitude, and λ is the wavelength.

2.2. Continuum-level models

Despite the above-described advantages of MD in description of highly non-equilibrium processes induced by short pulse laser irradiation in description of surface morphology and microstructure modification, the high computational cost of atomistic simulations limits the spatial and temporal scales accessible in the modeling. Thus, computationally cheaper continuum-level models, capable to describe entire irradiated spot and surrounding material, are necessary for mapping the atomistic predictions to the experimental conditions. Also, these models are vital for quick evaluation of the physical conditions reached for a particular setup.

2.2.1. *TTM model with accounting for kinetics of melting and solidification*

The data on the kinetics of melting and resolidification processes and the conditions for the onset of growth twinning in Section 3.2 obtained in the atomistic simulations are incorporated into the conventional TTM model adopted for a quick evaluation of the laser fluence dependence of the thickness of the surface layer affected by the growth twinning. The equations of TTM model are solved using the backward (implicit) Euler algorithm based on block tridiagonal matrix inversion.

The motion of the solid–liquid interface is described by the following equations:

$$\frac{dX_I}{dt} = V_I(T_I) = \int_0^L V_I\big(T(x,t)\big) f(x)\, dx \qquad (2.31),$$

$$S_I = V_I(T_I)\Delta H_f f(x - X_I) \qquad (2.32),$$

$$f(x) = \frac{1}{\sqrt{2\pi\sigma^2}} exp\left(-\frac{x^2}{2\sigma^2}\right) \qquad (2.33),$$

where X_I is the position of the solid-liquid interface, V_I is the velocity of the interface, T_I is the lattice temperature at the interface, L is the size of the computational system set to ensure that the interface is covered by the integration, ΔH_f is the heat fusion of the target material S_I is the energy source term added to TTM equation for the lattice temperature to account for the heat released or absorbed due to movement of the solid–liquid interface, $f(x)$ is the Gaussian function that approximates the Dirac delta function defining the position of the interface, and σ is the thickness of the interface taken to be 2 nm.

The temperature dependence of the velocity of the liquid-crystal interface is described by the Wilson-Frenkel expression [127]:

$$V_I = V_0 exp(-E_a\Omega_a/k_B T)[1 - exp(-\Delta G_v(T)\Omega_a/k_B T)] \qquad (2.34),$$

where V_0 is a prefactor, E_a is the activation energy per unit volume, $\Delta G_v = G_v^l - G_v^s$ is the free energy difference between the liquid and solid phases per unit volume, Ω_a is the atomic volume of the solid phase at the equilibrium melting temperature T_m, and k_B is the Boltzmann constant. The value of ΔG_v is approximated as $\Delta G_v \approx \Delta H_f(1 - T/T_m)$. It has been shown that Eq. 2.34 provides an adequate description of the velocity of crystallization front in fcc metals down to ~$0.6T_m$ [128,129], *i.e.*, in the range of temperatures realized in the simulations of laser melting and resolidification [17,104]. As an example, we put velocities of solidification computed in MD for three low index (100), (011), and (111) orientations of the solid-liquid interface with using Ni EAM potential [130]. The fitting parameters V_0 and E_a (Eq. 2.34) are summarized in Table 2. To account for the fast homogeneous melting of crystals superheated above $\sim 1.2T_\mathrm{m}$ [11,131], the regions of the target where the lattice temperature exceeds $1.2T_\mathrm{m}$ are set to undergo instantaneous melting.

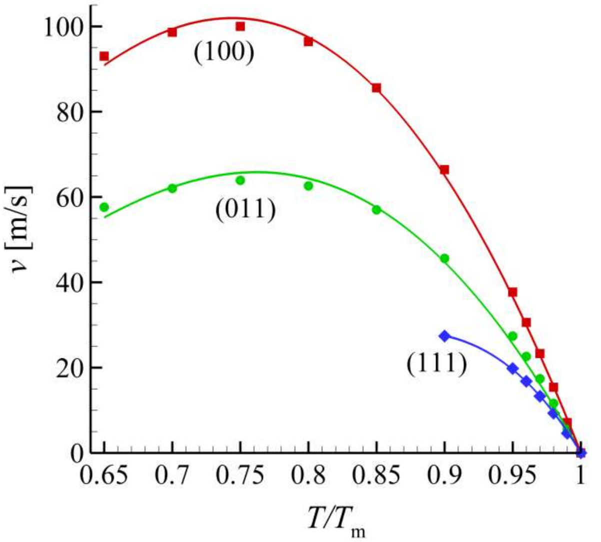

Figure 15. The velocity of solid-liquid interface at different levels of undercooling in Ni described by EAM interatomic potential [130]. Three low index (100), (011), and (111) orientations of the solid-liquid interface are considered. The fitted curves with parameters from Table 2 are plot by solid lines. Since growth twins are generated in Ni (111) for solidification at undercooling level below $0.87T_\mathrm{m}$ (Sections 3.2 and 3.3), which reduces the velocity of solidification, the line is extended only to $0.9T_\mathrm{m}$.

Table 2. The parameters of curves fitted in Figure 15 with using Eq. 2.34.

	Ni, 100	Ni, 011	Ni, 111
v_0, m/s	6450	6130	5550
E_a, eV	0.340	0.382	0.400

In addition to the estimation of the depth of the region affected by growth twinning in Section 3.2, the above-described model is successfully used to study thermodynamic conditions produced in laser irradiation of $Fe_{60}Al_{40}$ alloy and predict the spatial extend of a region with magnetic disordered phase in our study of phase-change magnetic memory [132,133], not reported in this dissertation.

2.2.2. 2D thermoelasticity model

The fast rate of energy deposition in short pulse laser processing applications may result not only in the rapid melting and resolidification of a surface region of an irradiated target but also lead to the generation of strong stresses within the absorption region. The laser-induced stresses are particularly high in the regime of stress confinement [27,28,104,134], when the time of the laser heating (defined by the laser pulse duration, τ_p, or the time of the electron-phonon equilibration, $\tau_{e\text{-}ph}$, whichever is longer) is shorter than the time required for the mechanical relaxation (expansion) of the heated volume, $\tau_s \sim L_p/C_s$, where C_s is the speed of sound in the target material and L_p is the effective depth of the laser energy deposition. The relaxation of the initial compressive stresses generated by the laser energy deposition can result in the emergence of an unloading tensile component of the stress wave that is sufficiently intense to cause the formation subsurface voids [17,135-138] or separation of a surface layer from the target in a process commonly called photomechanical spallation [27,28,104,134] (Section 4.1). At lower laser fluencies, the relaxation of laser-induced stresses in the vicinity of a free surface of the target can result in the co-emission of longitudinal, shear, and surface acoustic waves (SAWs) that can be utilized in many practical applications, including nondestructive evaluation of mechanical properties and surface defects [53,139,140], acoustic desorption [67-69,71,72], and acoustic activation of surface diffusion [73,74,78].

The computational description of the dynamic evolution of thermoelastic stresses and the emission of stress waves can be described in the framework of the thermoelasticity model [141-145], which combines thermal model based on heat diffusion equation and thermoelastic wave equation:

$$C_p\rho\frac{\partial T}{\partial t} = \nabla k_{th}\nabla T + S - \alpha_L T C_{iimn}\frac{\partial^2 u_m}{\partial t\partial x_n} \quad (2.35),$$

$$\rho\frac{\partial^2 u_i}{\partial t^2} = \frac{\partial \sigma_{ij}}{\partial x_j} = C_{ijmn}\left[\frac{\partial^2 u_m}{\partial x_j\partial x_n} - \delta_{mn}\alpha_L\frac{\partial T}{\partial x_j}\right] \quad (2.36),$$

$$\sigma_{ij} = C_{ijmn}\left[\frac{\partial u_m}{\partial x_n} - \delta_{mn}\alpha_L(T - T_0)\right] \quad (2.37),$$

where T, C_p, ρ, k_{th}, u_i, σ_{ij}, α_L, and C_{ijmn} are temperature, heat capacity, density, thermal conductivity, displacement, stress tensor, linear thermal expansion coefficient, and stiffness tensor, respectively. S is a source term describing laser interaction with mater. The transient heating/cooling induced by adiabatic compression/expansion of the material during the wave propagation is accounted for by including an additional source term in the form of $-\alpha_L T C_{iimn}\frac{\partial^2 u_m}{\partial t\partial x_n}$ to the heat diffusion equation, Eq. 2.35. In literature, the stress tensor is commonly formulated for the case of isotropic material [143,145]:

$$\sigma_{ij} = \delta_{ij}\lambda\cdot\left(\frac{\partial u_k}{\partial x_k}\right) + \mu\cdot\left(\frac{\partial u_i}{\partial x_j} + \frac{\partial u_j}{\partial x_i}\right) - 3\delta_{ij}B\alpha_L(T - T_0) \quad (2.38),$$

where $\lambda = B - 2G/3$ and $\mu = G$ are Lamé constants, B and G are bulk and shear moduli of the material. This formulation of the thermoelasticity model is suitable for the description of an irradiation process not only in Cartesian but also in cylindrical coordinates [145]. The Eq. 2.38, however, is not valid for description of highly anisotropic materials, *e.g.*, single crystal silicon, where the description provided by Eqs. 2.35-2.37 has to be applied.

Eq. 2.36 is solved using an Explicit Euler method with $\theta = C_{11}\Delta t^2/\rho\Delta x^2 = 0.6$. Despite implicit schemes are not limited by using $\theta \leq 0.6$, they introduce strong numerical dispersion and require special consideration in 2D/3D cases. For the thermal part (Eq. 2.35) Explicit Euler or Alternating Direction Implicit (ADI) algorithms are used depending on the condition $\zeta = k_{th}\Delta t/C_p\rho\Delta x^2 < 0.25$. ADI algorithm is slightly slower than explicit Euler but allows performing simulations with $\zeta = 25 - 50$ that accelerates overall simulation. Implicit formulation of a free boundary condition suggested in Ref. [146] is used and provides a stable solution for all range of elastic parameters.

The above described model is applied in Section 5.1 to study the efficiency of SAWs generation in thermoelastic regime. As discussed in Sections 5.3 and 5.5, sufficiently strong SAWs are capable to enhance surface diffusion and result in motion of graphene sheets. Despite irradiation in high fluence regime is demonstrated experimentally to produce very strong, up to 10^{-2} strain amplitude [120], surface acoustic waves, the efficiency of SAWs generation in thermoelastic and non-ablative regimes is typically considered as low. However, the regimes below the damage threshold are attractive for practical applications since the target can be irradiated repeatedly to generate not only one SAW pulse, but a sequence of pulses, which can be used for activation of surface processes.

The capabilities of the thermoelasticity model, implemented in our study, are illustrated in Figure 16, which provides a snapshot of laser-generated elastic waves in a silica glass plate. The simulation is performed for an absorbed fluence of 10 J/cm^2, a laser spot diameter of 21 μm, and the characteristic absorption depth assumed to be 10 μm based on the depth of grooves observed in experiments. This simulation is motivated by an intriguing experimental observation of the spatial distribution of laser-induced damage in a silica glass plate undergoing laser cutting [147]. This study demonstrates the generation of damage lines on the rear surface of the plate, which are located not directly underneath the laser spot but at ~37° degree angle. The rear surface damage is attributed in Ref. [147] to the interaction of a shear wave emitted from the irradiated spot and a surface Rayleigh wave generated due to reflection of a longitudinal wave from the rear surface. To verify this hypothesis, thermoelasticity modeling of the generation of stress waves in a silica glass substrate is performed in Cartesian coordinates for a two-dimensional geometry. Laser-induced heating of the target triggers generation of a variety of acoustic waves that interact with the free surfaces of the silica glass plate and create a complex dynamic pattern of transient stresses within the plate, as depicted in Figure 16. The calculations, however, do not support the original explanation of the rear surface damage suggested in Ref. [147], as the reflection of the longitudinal waves from the bottom surface of the plate does not produce Rayleigh waves of any significant magnitude. Therefore, an alternative explanation of the experimental observations is needed.

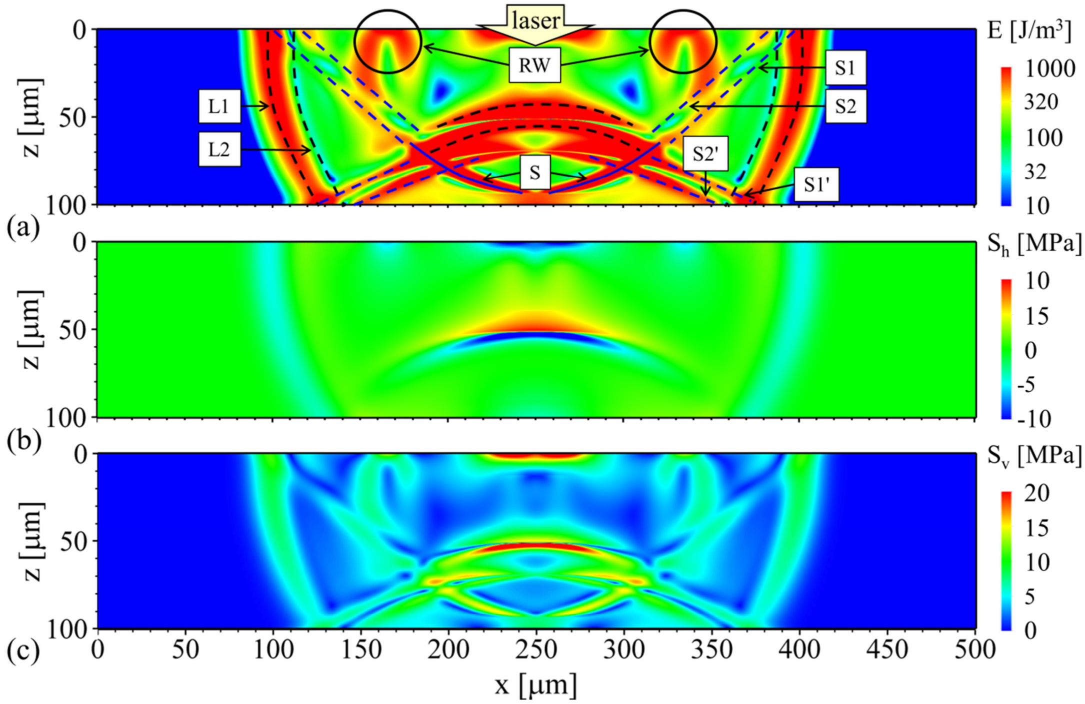

Figure 16. Generation of elastic waves in a silica substrate irradiated by a laser pulse at 10 J/cm^2. The energy density (a), hydrostatic stress (b), and Von-Misses stress (c) are plotted for a time of 25 ns after the laser pulse. In (a), the longitudinal and shear waves are schematically outlined by black and blue lines, respectively. Rayleigh waves, longitudinal compressive, longitudinal tensile, and shear waves generated by rapid laser heating are marked as RW, L1, L2, S, respectively. Shear waves emitted due to interaction of L1 and L2 waves with top and bottom free surfaces are marked as S1, S2, S1´, S2´. By the time of 25 ns, L1 and L2 waves are already reflected from the bottom free surface and propagate upwards. The thermal stresses generated by laser heating cannot be completely relaxed by the material expansion towards the free surface and, therefore, are still present in the vicinity of the irradiated area. Adapted from Ref. [49].

2.3. New methods designed in this work

2.3.1. Langevin non-reflecting boundary condition

In MD simulations of laser interaction with a bulk target, the region of the target that can be represented with atomic resolution is typically small and does not exceed several hundreds of nanometers. The propagation of laser-generated stress waves from the region of the laser energy deposition to the bulk of the target can be effectively mimicked with utilization of so-called non-reflecting boundary (NRB) conditions [105,106]. This approach, however, is only applicable for simulation of non-reflecting propagation of planar [32,39,81] or spherical circular [82,148] waves. For a system that cannot be expected to have a planar wave front, in particular in the case of spatially modulated laser energy deposition considered in a work discussed in Section 4.2, the traditional NRB is inapplicable. To model the non-reflecting propagation of the nonplanar pressure wave, we designed an alternative formulation of NRB based on the Langevin equation, which is briefly descried below.

The basic idea of NRB is to ensure the absorption of incoming elastic waves through the application of an external dumping force to boundary atoms, $F_{NRB} = -ZS_a v$, where Z is the acoustic impedance of the target or substrate material, S_a is the effective area per each boundary atom, and v is the velocity of atoms perpendicular to the boundary. In the traditional NRB [39,81,105] all atoms move together, and the atomic velocities and forces are averaged over all boundary atoms. In contrast, to model non-reflecting propagation of a wave with a nonplanar front, we can treat motion of each boundary atom independently [106]. One difficulty with this approach, however, is that the application of the dumping force to each atom independently not only affects the collective atomic motion associated with the stress wave but also effectively dampens the thermal motion of the boundary atoms. Due to the strong cooling of the boundary region, this approach is only applicable under conditions where the temperature near the boundary is zero [106]. In order to minimize the computational cost of the simulations, however, it is preferable to limit the MD part of the model to a region where the laser-induced structural and phase transformations take place, while the heating and heat transfer that do not cause structural changes can be described at the continuum level. This requirement means that the temperature increase can be substantial at the location of the non-reflecting boundary. As a result, the velocity v corresponds not only to a coherent motion of the boundary layer but also to a thermal motion of individual atoms, which should not be damped. In order to compensate for the loss of the thermal energy, the equation of motion for a boundary atom i can be expressed in a form similar to Langevin dynamics equation with the dumping constant ZS_a:

$$m\frac{d^2z_i}{dt^2} = F_i^z - ZS_a v_i^z + \eta(t) \quad (2.39),$$

$$\langle \eta(t)\eta(t') \rangle = 2ZS_a k_B T\delta(t - t') \quad (2.40),$$

where the boundary is assumed to be perpendicular to z direction, m is the atomic mass, v_i^z and F_i^z are z components of the velocity of atom i and force acting on atom i, η is the a delta-correlated stationary Gaussian process with zero mean and variance defined by the second equation, and T is the average temperature of the boundary atoms, which can be taken from the solution of the TTM equation at the location of the boundary. Note that, in contrast to NRB described in Refs. [39,81,105,106], the force F_i^z accounts for the interactions with all the neighboring atoms, not just the ones located further away from the boundary than the atom i. Therefore, in this case, S_a is defined as the total area of the boundary divided by the number of boundary atoms. Since a high value of dumping force may cause instability of the boundary, this value can be reduced by increasing the number of monoatomic layers included in the Langevin nonreflecting boundary (LNRB) layer, which reduces the effective atomic area S_a. In the simulation reported in Section 4.2, the LNRB thickness of three monoatomic layers is found to ensure stable behavior of the boundary condition.

The results of testing of the performance of the LNRB are shown in Figure 17. The first test simulation is performed for a Cr system with dimensions of 4.1nm × 4.1nm × 19 nm described with EAM potential [81], periodic boundary conditions applied in lateral directions, free boundary used at the top, and the LNRB imposed at the bottom of the computational system. The system is equilibrated at 300 K prior to the test simulation. A strong plane compressive wave with magnitude of 19 GPa is generated at one end of a 19-nm-thick Cr slab by applying an 800m/s extra velocity to a 1.5-nm-thick top surface layer. As can be seen from the contour plot shown in Figure 17a, the compressive wave propagates with relatively weak reflection, where the reflected wave remains within the range of ±1GPa. The reflection can be further minimized by introducing pressure dependence of the acoustic impedance Z. The performance of the LNRB for nonplanar waves is illustrated in Figure 17b, where a sequence of pressure plots from the large scale atomistic TTM-MD simulation with a periodically modulated absorption pattern, discussed in the Section 4.2, is shown. Overall, we can conclude that the modified formulation of the boundary condition provides an efficient and simple way to simulate nonreflecting propagation of nonplanar waves.

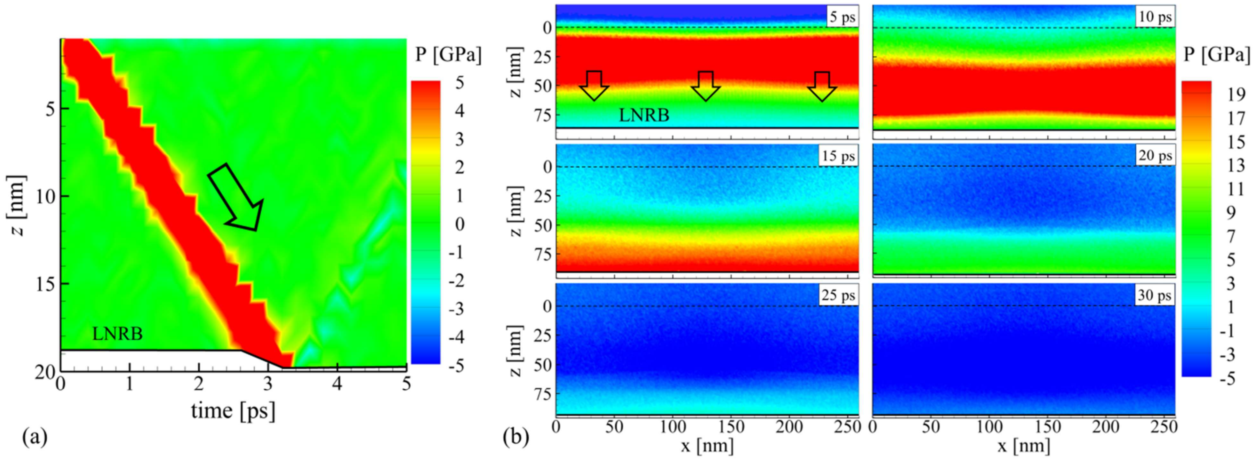

Figure 17. The results of testing the LNRB performance in a simulation of a nonreflecting propagation of an 18-GPa-strong compressive planar wave (a) and in a TTM-MD simulation of laser ablation described in Section 4.2, where a nonplanar wave is generated (b). In (a), a free boundary condition is applied at the top of the system, at z = 0, and the LNRB is initially located at z = 19 nm. In (b), the horizontal dashed line shows the initial position of the surface of the irradiated Cr target, and the LNRB is located at z = 87 nm. In both panels, the arrows show the direction of the pressure wave propagation. Adapted from Ref. [149]

2.3.2. Calculation of a step free energy

This subsection is focused on the calculation of free energy of steps on $\{111\}$ surface of FCC crystal that is an important parameter for estimation of the density of growth twins during crystal growth discussed in Section 3.3.

Capillarity waves method for step free energy calculation

The basic approximation of step free energy, which is used in several publications to calculate the probability of nucleation [150-152], is a product of a surface free energy by the spacing between (111) planes:

$$\beta = \gamma h \tag{2.41}$$

More accurate consideration of the geometry of the steps [153] suggests that the step free energy can be approximated as $\beta_A = \left(\gamma_{100} - \gamma_{111}/\sqrt{3}\right) \cdot a_0$ and $\beta_A = a_0\gamma_{111}/\sqrt{3}$ for $[2\bar{1}\bar{1}]$ and $[1\bar{1}0]$ steps respectively, were γ_{100} and γ_{111} are the free energies of (100) and (111) surfaces, which in our case can be considered as a solid-liquid interface free energies. For small anisotropy of surface free energy, where γ_{100} and γ_{111} are approximately equal, this estimation gives $0.52\gamma h$ and $0.71\gamma h$. However, a direct measurement of a step free energy for silicon [154] suggests about an order of magnitude difference between the measured value and the simple estimation based on Eq. 2.41. Since the probability of nucleation has exponential dependence on the step free energy, for correct description of the nucleation process it is vital to use a reliable value of step free energy.

The method of step free energy calculation suggested in this section is based on the capillarity wave approach that, in the case of 2D interface, gives an accurate value of solid liquid interface free energy [155-157]. The basic idea of this method is decomposition of the interface roughness as a set of harmonics which contribute $k_B T/2$ to the total energy based on the equipartition principle. The energy of each harmonic depends on the wavelength and interface stiffness, and thus, the interface energy can be calculated based on the Fourier spectrum of the interface roughness. In the case of 1D interface similar analysis can be done to obtain the step free energy. First, we consider a circular interface with small fluctuations. The energy increase due to the presence of fluctuations can be expressed as:

$$\Delta E = \int_0^{2\pi} \beta(\varphi)\left[\sqrt{[r'(\varphi)]^2 + [r(\varphi)]^2} - r_0\right] d\varphi \approx \frac{1}{2r_0} \int_0^{2\pi} \beta(\varphi)[r'(\varphi)]^2 d\varphi \qquad (2.42),$$

where $\beta(\varphi)$ is step free energy, r_0 is the initial radius of the interface, $r(\varphi)$ and $r'(\varphi)$ is the distance and its derivative between the interface and the origin, which can be expressed in terms of Fourier amplitudes:

$$r(\varphi) = \sum_n r_n e^{in\varphi} \text{ and } r_n = \frac{1}{N}\sum_j r(\varphi_j) e^{-in\varphi_j} \qquad (2.43).$$

Thus, the energy increase is:

$$\Delta E \approx \frac{1}{2r_0} \int_0^{2\pi} \beta(\varphi)\left|in \sum_n r_n e^{in\varphi}\right|^2 d\varphi = \frac{\beta(2\pi)^2}{2L} \sum_n n^2 |r_n|^2 \qquad (2.44),$$

were β is the average step free energy, L is the total interface length. Based on the equipartition principle:

$$\frac{2\beta}{L}\pi^2 n^2 \langle |r_n|^2 \rangle = \frac{k_B T}{2} \qquad (2.45),$$

the final expression can be derived:

$$n^2\langle|r_n|^2\rangle = \frac{k_B TL}{4\beta\pi^2} \qquad (2.46).$$

This equation is in agreement with the result obtained in ref. [158], where a radial deviation from the mean perimeter is mapped to a straight interface with fluctuations that also implies smallness of fluctuations.

If the shape of the 1D interface between solid and liquid is not circular, and the fluctuations are not small, as demonstrated in Figure 18 and Figure 19f, the above approximation is not valid anymore, and more general approach should be considered. For an arbitrary parametric contour a shape can be decomposed into orthonormal basis based on the Elliptic Fourier transform [159]:

$$x(l) = \sum_n A_n cos\left(\frac{2\pi nl}{L}\right) + B_n sin\left(\frac{2\pi nl}{L}\right)$$

$$y(l) = \sum_n C_n cos\left(\frac{2\pi nl}{L}\right) + D_n sin\left(\frac{2\pi nl}{L}\right) \qquad (2.47),$$

where l is the cumulative length along the curve, and A_n, B_n, C_n, D_n are Elliptic Fourier coefficients that are calculated by the following formulas:

$$A_n = \frac{L}{2n^2\pi^2}\sum_{p=1}^{k}\frac{x_p - x_{p-1}}{l_p - l_{p-1}}\left[cos\left(\frac{2\pi nl_p}{L}\right) - cos\left(\frac{2\pi nl_{p-1}}{L}\right)\right]$$

$$B_n = \frac{L}{2n^2\pi^2}\sum_{p=1}^{k}\frac{x_p - x_{p-1}}{l_p - l_{p-1}}\left[sin\left(\frac{2\pi nl_p}{L}\right) - sin\left(\frac{2\pi nl_{p-1}}{L}\right)\right]$$

$$C_n = \frac{L}{2n^2\pi^2}\sum_{p=1}^{k}\frac{y_p - y_{p-1}}{l_p - l_{p-1}}\left[cos\left(\frac{2\pi nl_p}{L}\right) - cos\left(\frac{2\pi nl_{p-1}}{L}\right)\right]$$

$$D_n = \frac{L}{2n^2\pi^2}\sum_{p=1}^{k}\frac{y_p - y_{p-1}}{l_p - l_{p-1}}\left[sin\left(\frac{2\pi nl_p}{L}\right) - sin\left(\frac{2\pi nl_{p-1}}{L}\right)\right] \qquad (2.48),$$

where x_p, y_p, l_p are x, y coordinates and cumulative length of the curve at the point p. An example of a contour decomposition based on the Elliptic Fourier transform is shown in Figure 19; higher harmonics add new features to the shape of the contour. The length increase introduced by n-th harmonic can be calculated numerically based on the formula:

$$\Delta l_n = \int_0^L\left[\sqrt{x'^2 + y'^2} - \sqrt{(x' - x'_n)^2 + (y' - y'_n)^2}\right]\frac{2\pi dl}{L} \qquad (2.49),$$

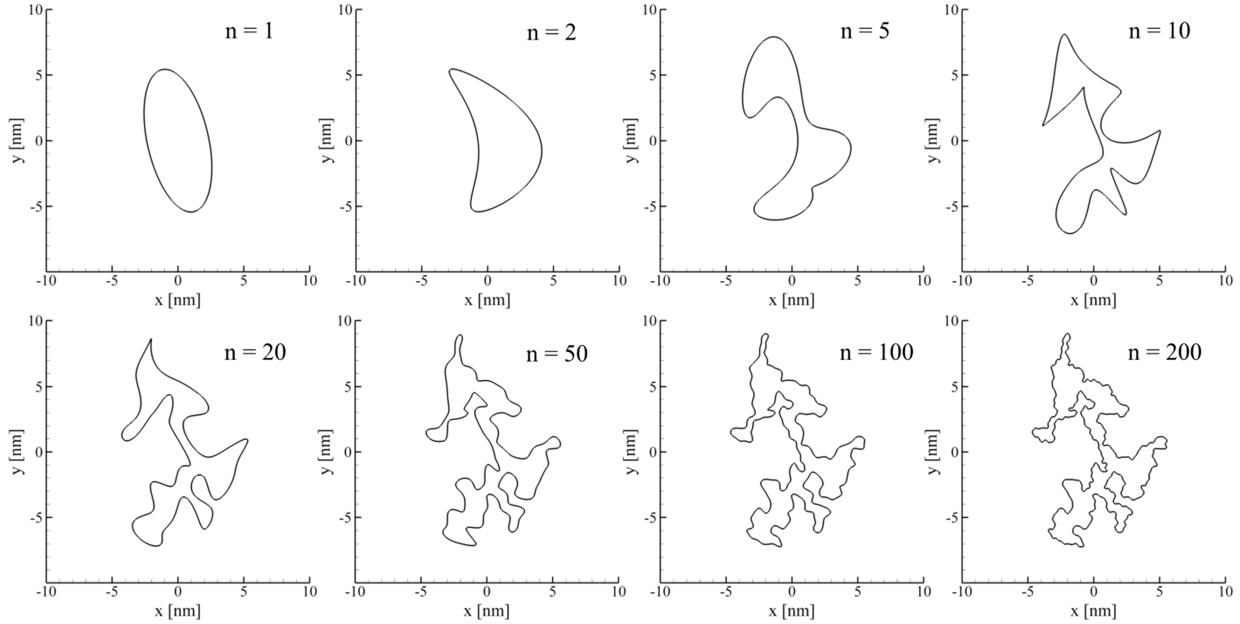

Figure 18. A representation of a shape of the contour based on 1, 2, 5, 10, 20, 50, 100 and 200 harmonics of Elliptic Fourier transform. This contour corresponds to a step on solid-liquid (111) interface extracted from the modeling at the melting temperature.

The energy increase introduced by n-th harmonic is then a product of the length increase by the step free energy. Thus, based on the equipartition principle:

$$\Delta E_n = \beta\langle\Delta l_{\mathrm{n}}\rangle = \frac{k_B T}{2} \qquad (2.50),$$

This formula provides a way to calculate the step free energy for step lines with arbitrary shape.

If the magnitude of higher harmonics is small, the shape of the contour is approximately is circular, and Eq. 2.49 gives the result predicted in Eq. 2.46. For convenience, Eq. 2.47 can be rewritten in the following way to make the calculation more compact:

$$x(\varphi) = \sum_n C_{xn} cos(n\varphi + \varphi_{xn})$$

$$y(\varphi) = \sum_n C_{yn} cos(n\varphi + \varphi_{yn}) \qquad (2.51),$$

where $\varphi = 2\pi nl/L$, and C_{xn}, C_{yn}, φ_{xn}, φ_{yn} are the new coefficients which can be expressed in terms of A_n, B_n, C_n, D_n. If the amplitude of higher harmonics is small, the Eq. 2.49 can be approximated in the same manner as Eq. 2.44:

$$\Delta l_n \approx n^2 \int_0^{2\pi} \frac{C_{xn}^2 \sin^2(n\varphi+\varphi_{xn})+C_{yn}^2 \sin^2(n\varphi+\varphi_{xn})}{\sqrt{x'^2+y'^2}} d\varphi \approx \frac{(2\pi n)^2}{2L}\left(C_{xn}^2+C_{yn}^2\right) \qquad (2.52)$$

and thus:

$$\frac{k_B T L}{4\beta\pi^2} = n^2\langle C_{xn}^2 + C_{yn}^2\rangle = n^2\langle |r_n|^2\rangle \qquad (2.53).$$

Thereby the general approach can reproduce the Eq. 2.46 if the deviation of the contour shape from a circle is small.

Extraction of step lines

The formalism described in the previous subsection provides a method of step free energy calculation based on the shape of step lines. However, this approach requires extraction of step lines from a sequence of MD snapshots that is done based on the algorithm described in this subsection. The steps of the algorithm are illustrated in Figure 19. The first step is extraction of monoatomic (111) layers that are located in the vicinity of solid-liquid interface. This extraction is performed based on the atomic number density distribution along the direction perpendicular to the interface. The distribution is obtained based on dividing the MD sample into layers of thickness 0.01 nm with following counting atoms in each layer and normalizing the value based on the average density of solid. The noise is reduced by a Gaussian blur filter with σ equal to 0.02 nm. The distribution obtained for a particular MD snapshot is plot in Figure 19a. Based on the figure, in the liquid part the density is almost constant, but the solid part includes alternating regions of high and low density, which correspond to atomic (111) layers. Near the interface a transition behavior is observed: the amplitude of these oscillations decreases, and the density approaches the constant value. Thus, the extraction of the monoatomic layers can be done based on the local minima of the density distribution. The examination of the density distribution starts in the liquid part with following motion in the direction of solid. The extraction of layers begins when the density in the local minimum drops below 0.85. The following local minima are considered as boundaries between monoatomic layers which are extracted until the density in a local minimum drops below 0.015. The extracted layers are separated by lines in Figure 19a.

The next step is demarcation of solid and liquid within one monoatomic layer which is done based on the 2D angular order parameter:

$$\Psi_k = \left|\frac{1}{N_k}\sum_j e^{6i\phi_{kj}}\right|^2 \qquad (2.54),$$

where N_k is the number of nearest atoms within the layer, ϕ_{kj} is the angle between the vector connecting k-th and j-th atom, and [10] direction. The value of cutoff distance is chosen equal to 0.35 nm which lies between the first and the second nearest neighbor shells. The parameter has the maximum value when the angel between each neighbor and [10] direction is multiple to $\pi/6$ that corresponds to the ideal triangular lattice. The value of the local parameter is averaged among nearest neighbors to reduce the thermal noise as suggested in Ref. [160]:

$$\overline{\Psi_i} = \frac{1}{N_{ij}+1}\left(\Psi_i + \sum_j \Psi_j\right) \qquad (2.55).$$

Figure 19b shows a monoatomic layer colored based on the value of the local order parameter. Atoms with order parameter below 0.45 are considered as a part of liquid, otherwise they are recognized as a solid. Further reduction of thermal noise is achieved by assuming that atoms of solid/liquid cannot have less than three solid/liquid nearest neighbors, otherwise the atom is set as a liquid/solid. The enlarged view of the system after blanking atoms of liquid is shown in Figure 19c. Clusters of solid/liquid with the size less than 8 atoms are not taking into consideration in the further analysis. Points of solid-liquid 1D interface are put in the middle between nearest neighbors recognized as solid and liquid and depicted in the plot as blue dots.

The next part of the algorithm solves the problem of connection the interface points into lines which is done based on the Amenta reconstruction algorithm [161] that can be described by the following way. When a Delaunay triangulation is applied to the union of the original set of points and the Voronoi diagram vertexes that are used as an approximation of medial axes, the edges connect the original set of points to form segments of the reconstructed curve (the crust). This Delaunay triangulation is shown in Figure 19d, and the reconstructed curve is presented in Figure 19e. At this stage the major part of the points is connected by the correct way, however, there are several parts of the curve that are not reconstructed properly. The last part in the line extraction algorithm is correction of the errors in the line reconstruction that includes several steps applied sequentially: removing lines connecting two triple points (points with 3 edges), removing dangling points (points with 1 edge) in the vicinity of triple points, transforming triple points to a dangling points and regular points (points with 2 edges) by deleting the longest edge, removing short lines with the length less or equal to 5 segments, connecting two nearest dangling points if the distance between them is less than 3 nm. The final interface lines, after correction the errors, is shown in Figure 19f. The suggested algorithm performs extraction of step lines from a sequence of MD snapshots that allows to accomplish automatic data acquisition and collect significant statistics for the further analysis. The parameters of the algorithms are adjusted for Ni and may require fine turning for other materials.

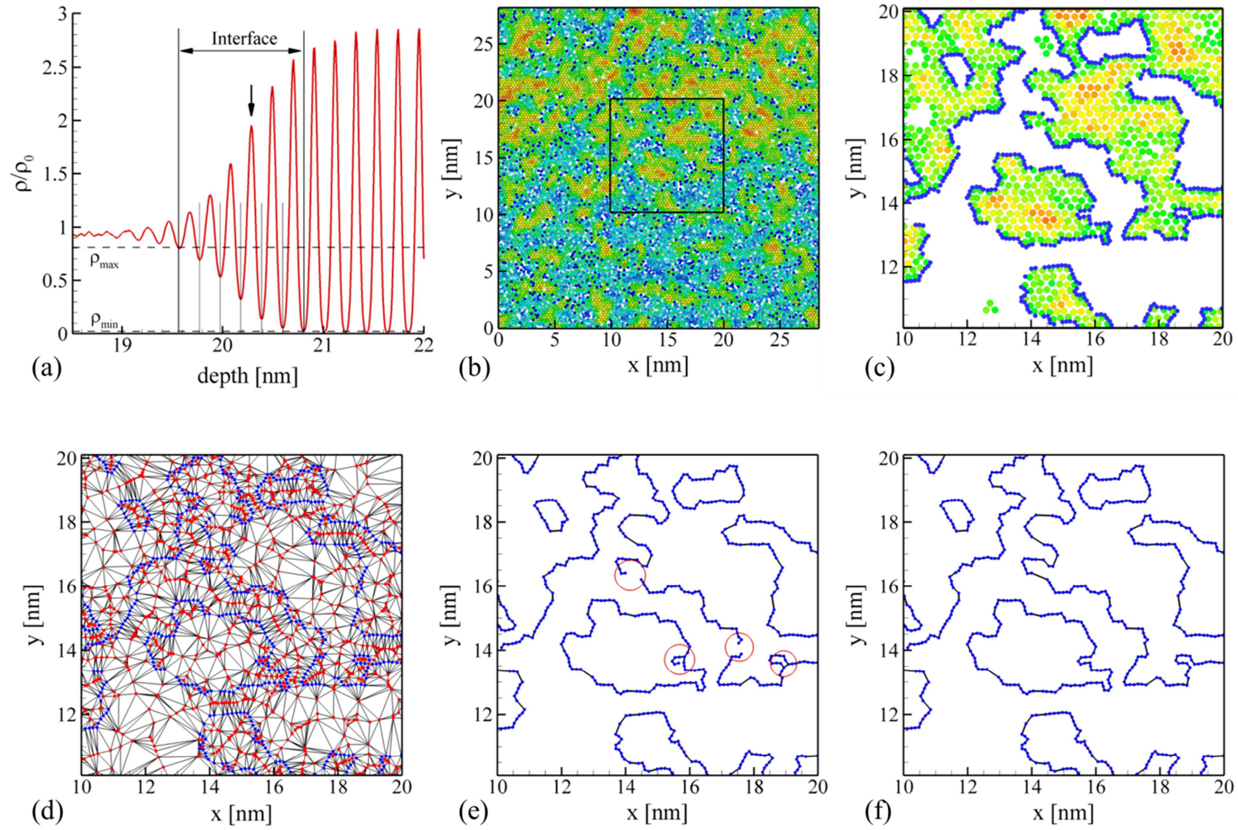

Figure 19. The algorithm of steps extraction. (a) Normalized atomic number density distribution which is used for extraction of monoatomic (111) layers. The arrow points out the layer that is used as an example in the following plots. (b) A monoatomic (111) layer colored based on the 2D angular order parameter. The gradation of the color from red to blue corresponds to the range of this parameter between 0 and 1. (c) Enlarge part of Figure 19b outlined by a black square. The atoms with the order parameter below 0.45 are considered as a liquid and blanked. Blue dots are put in the middle point of each pair of neighboring atoms recognized as a solid and liquid. These interface points are used to reconstruct the 1D interface between solid and liquid which is considered as a step. (d) Delaunay triangulation of the point set that combines interface points (blue) and Voronoi diagram vertexes (red) produced by these points. (e) Results of Amenta reconstruction which is performed based on the Delaunay triangulation (Figure 19d). The reconstructed interface lines connect the interface points. The errors in the interface reconstruction are outlined by red circles. (f) The interface lines after correction of the errors.

Calculation of the Step Free Energy

A framework described in the two previous subsections is applied to calculate step free energy of Ni. An atomistic simulation was performed at the melting temperature during 200 ps to collect the information about the equilibrium solid liquid-interface. The snapshots are saved every 4 ps and used for step lines data acquisition with applying the extraction algorithm described in the previous subsection. Only closed contours with the length above 20 nm are considered in the further analysis. The shape of each contour is decomposed based on the Elliptic Fourier transform (Eq. 2.47 and 2.48), and the contour length increase introduced by each harmonic is calculated based on Eq. 2.49. Figure 20 shows the averaged contour length increase based on the harmonic wavelength which is calculated for the entire output produced in the MD simulation. Based on the equipartition principle the length increase should be the same for each harmonic. The small values at short wavelengths may be explained by inaccuracy in the line extraction. Thus, the average value of the contour length increase, which is shown by a dashed line in the plot, is calculated for harmonics with wavelength between 10 and 30 nm and equal to 1.03 nm. The increase in the density of harmonics per unit change in the wavelength with decrease of the wavelength is considered during this averaging by introducing weights.

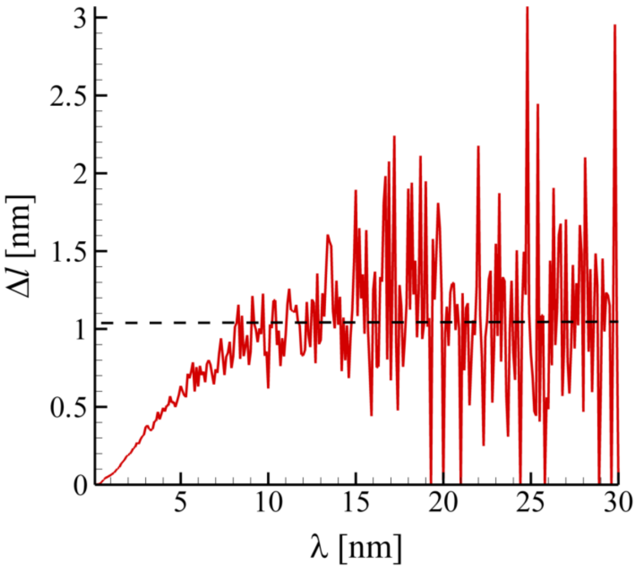

Figure 20. The dependence of an average step length increase produced by a certain Elliptic Fourier transform harmonic on the wavelength of this harmonic. The dashed line depicts the average value calculated for harmonics with wavelengths from 10 to 30 nm.

Calculation of the step free energy based on Eq. 2.50 gives the value 0.071 eV/nm. To make a comparison with the estimation based on Eq. 2.41, the solid-liquid interface free energy is calculated based on the capillarity waves method [155-157]. The acquired values are 0.356 and

0.351 J/m^2 for γ_{100} and γ_{111} respectively, thus, the predicted value of β is 0.46 eV/nm. This more than 6-fold discrepancy is in agreement with the comparison done for silicon in Ref. [154], which reports more than order of magnitude difference between the estimated and measured values of β. The reason of so small value of step free energy may be resulted by underestimation of the entropic contribution in Eq. 2.41. As pointed out in Ref. [154], step free energy and interface free energy are not directly related, and at roughening temperature the step free energy drops to zero while the interface free energy remains finite.

2.4. Calculation of material properties in MD

2.4.1. The temperature dependence of vacancy concentration

In order to assess the significance level of the concentration of vacancies generated at the rapidly propagating solidification front, the equilibrium values of vacancy concentration as a function of temperature are estimated based on the Arrhenius expression:

$$n_{eq} = exp\left(-\frac{G_f(T)}{k_B T}\right) \qquad (2.56),$$

where $G_f(T) = H_f(T) - TS_f(T)$ is the change of Gibbs free energy associated with forming a vacancy. The vacancy formation enthalpy $H_f(T)$ in Ni described by Mishin [130] and Cr described by Johnson [81] EAM potential is calculated in a series of NPT simulations as the enthalpy difference between systems with and without vacancies. The obtained temperature dependence of enthalpy of vacancy formation is fitted to the following equation:

$$H_f = H_f^0 + AT^2 + Be^{-C/T} \qquad (2.57)$$

as shown by the red lines in Figure 21. Based on the fitting parameters H_f^0, A, B, and C, which are summarized in Table 3, the entropy and free energy of vacancy formation can be expressed in the form:

$$G = -T\int\frac{H(T)dT}{T^2}, S = -\left(\frac{\partial G}{\partial T}\right)_P \qquad (2.58),$$

$$G_f = H_f^0 - TS_f^0 - AT^2 - \frac{BT}{C}e^{-C/T} \qquad (2.59),$$

$$S_f = S_f^0 + 2AT + B(T^{-1} + C^{-1})e^{-C/T} \qquad (2.60).$$

Since Eq. 2.57 is written in a form that does not account for the low temperature behavior of entropy, the condition of zero entropy at 0 K cannot be used to derive the value of the integration parameter S_f^0. Instead, we use the concentration of vacancies at the melting point computed by Miao He in atomistic simulations performed for a large crystal system with thickness of 10 nm. Periodic boundary conditions are applied in the lateral directions, and two free surfaces are created perpendicular z. The simulation is performed at constant lateral size and temperature T_m, and the free surfaces acts as sources and sinks of vacancies. After around 20 ns the number of vacancies in the crystal reaches the equilibrium value. This equilibrium vacancy concentration, n_{eq}^{Tm}, is applied in Eq. 2.56 along with H_f at T_m obtained from Eq. 2.57, to calculate the entropy of vacancy formation at the melting temperature, thus the parameter S_f^0 can be estimated from Eqs. 2.59 and 2.60. It should be pointed out that the dependence of the vacancy formation entropy on temperature in Eq. 2.60 is valid for temperatures exceeding the Debye temperature, and require spatial consideration in the low temperature range. Thus, S_f^0 should not be confused as the entropy of vacancy formation at zero temperature.

After fitting of all the parameters in Eqs. 2.57-2.60, the equilibrium vacancy concentration is calculated as a function of temperature from Eq. 2.56, as illustrated in Figure 21. Comparison of these values with the concentration of vacancies generated during solidification under conditions of deep undercooling confirms that the rapid propagation of solidification front produces the concentration of vacancies exceeding the equilibrium value at a particular temperature by 1-2 orders of magnitude (Section 3.1). Meanwhile, in the vicinity of the melting temperature, due to extremely small velocity of solidification front and high mobility of vacancies, the vacancy concentration is reduced towards the equilibrium value at melting temperature.

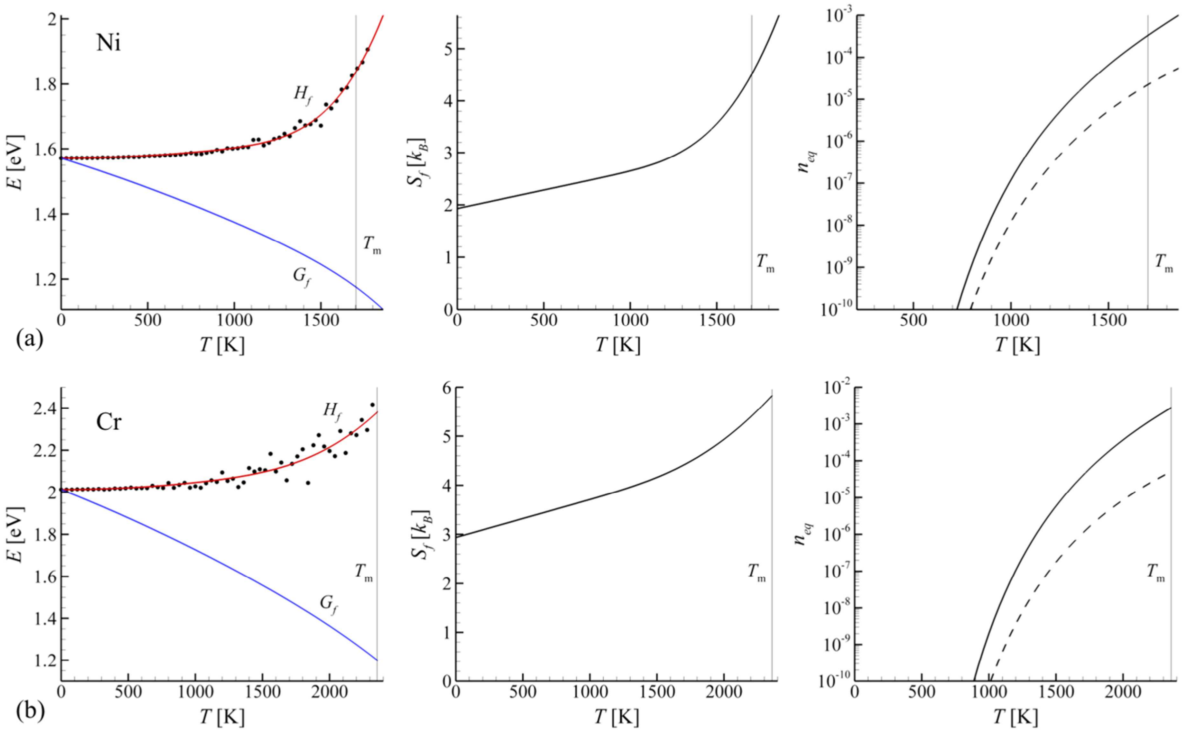

Figure 21. The enthalpy, free energy, entropy of vacancy formation, and the equilibrium concentration of vacancies at different temperatures for Ni (a) and Cr (b). The concentration of vacancies predicted based only on the enthalpy of vacancy formation at 0 K, H_f^0, is shown by a dash line. The fitting parameters are summarized in Table 3.

Table 3. Fitting parameters used in Eqs. 2.57-2.60 to describe the temperature of vacancy formation enthalpy, entropy, and free energy in Ni and Cr.

	H_f^0 [eV]	S_f^0 [k_B]	A [eV/K^2]	B [eV]	C [K]	n_{eq}^{Tm}
Ni	1.57	1.93	3.06×10^{-8}	306	12690	3.3×10^{-4}
Cr	2.01	2.94	3.33×10^{-8}	48.4	13140	2.9×10^{-3}

2.4.2. Surface tension calculation

In our study, surface tension is computed with Test Area Method (TA) [162], which is based on free energy perturbations. Following the derivation from Ref. [163], the difference in Helmholtz free energy of two systems (0) and (1) can be expressed as:

$$\Delta F_{0\to1} = F_1 - F_0 = -k_B T ln(Z_1/Z_0) = -k_B T ln\left(\frac{\int dr^N exp(-U_1/k_B T)}{\int dr^N exp(-U_0/k_B T)}\right) \qquad (2.61).$$

The configuration energy U_1 can be considered as a perturbation of the configuration energy U_0, *i.e.* $U_1 = U_0 + \Delta U$, where ΔU is a difference in the potential energy of two systems. Therefore, the free energy difference can be expressed based on a canonical average of ΔU:

$$\Delta F_{0\to 1} = -k_B T ln\langle exp(-\Delta U/k_B T)\rangle_0 \qquad (2.62).$$

Turning our attention back to the calculation of surface free energy, Ref. [162] has suggested using a pair of symmetric perturbations preserving the total volume of the system, *i.e.* increase/decrease of the interface surface area by ΔA combined with decrease/increase of the system length perpendicular to the interface by $\sqrt{\Delta A}$:

$$\gamma = \left(\frac{\partial F}{\partial A}\right)_{NVT} \approx \frac{\Delta F_{0\to 1} - \Delta F_{0\to -1}}{2\Delta A}$$

$$\gamma = -\frac{-k_B T}{2\Delta A}\left[ln\langle exp(-\Delta U_{0\to 1}/k_B T)\rangle_0 - ln\langle exp(-\Delta U_{0\to -1}/k_B T)\rangle_0\right] \qquad (2.63).$$

The sampling is performed in NVT coexistence system composed of liquid and vapor with periodical boundary conditions applied in all three directions. The lateral size, parallel to the liquid-vapor interface, is chosen to be equal to approximately 4 nm in all our simulations. The thickness of the liquid part is chosen between 6 and 12 nm to make sure that two interfaces are not affected by each other, which correspond to 4000-8000 atoms. The MD setups for these simulations are prepared in the following way. A liquid system is created by rapid hitting to the temperature 1.5-2 T_m followed by cooling to the melting point and volume equilibration along *z* axis at constant pressure and temperature for 50 ps. After the liquid system is generated, it is expanded along z-direction to 25 nm to create an empty volume, which during the following equilibration is filled in by vapor. On the next step, the system is heated/cooled to the destination temperature within 300-600 ps (depending on the temperature difference), the equilibration of vapor takes approximately 200 ps. The data acquisition is performed during the following 5 ns MD run, and a canonical ensemble is created with utilization Nose-Hoover chain thermostat [80]. The values of ΔU are collected every 0.1 ps and averaged according to Eq. 2.63 to evaluate the value of surface tension at a particular temperature. The error bar is estimated as a standard deviation of the mean assuming that an independent atomic configuration is generated every 5 ps. The relative change of the surface area in perturbations is chosen to be 2×10^{-4}.

2.4.3.Critical point calculation

A critical point of a material is a crucial parameter for description of the material behavior under conditions where formation of a supercritical fluid takes place. However, calculation of critical point in MD is not a straightforward task and requires reconstruction of a liquid-vapor coexistence curve (binodal line). In our study, we use a series of NVT liquid-vapor coexistence simulations to calculate the equilibrium densities of vapor and liquid phases in the temperature range starting from ~0.6 to 0.9 T_c. The typical setup used in the simulations is shown in Figure 22a. The MD system preparation procedure is the same as one described in the previous subsection for surface tension evaluation. To obtained the density profile we divide the entire system into 0.1 Å thick layers and count the number of atoms in each layer with following averaging during the 5 ns data acquisition run. As an example, the final density profile for Ti EAM potential (MUA3) [164] is depicted in Figure 22a. The value of vapor and liquid densities are calculated by averaging the data points corresponding to these phases.

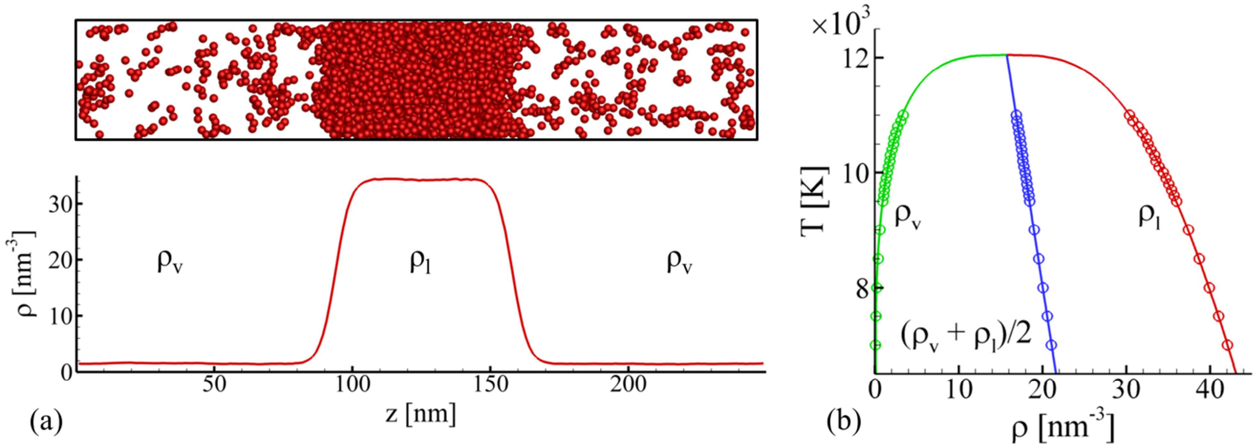

Figure 22. (a) The system setup used in calculation of the critical point and the density profile obtained for MUA3 potential at 10^4 K. (b) The liquid and vapor densities calculated for Ti EAM potential (MUA3) [164], solid lines depict fitted curves.

When the above procedure is applied for a range of temperatures, a set of points corresponding to liquid-vapor coexistence is produced. On the next step the sum and difference of vapor and liquid densities are fitted according to the dependencies predicted from renormalization group theory, as described in Ref. [165,166]:

$$(\rho_l - \rho_v)/2 = A_0(T_c - T)^{\beta} + A_1(T_c - T)^{\beta+\theta} \quad (2.64),$$

$$(\rho_l + \rho_v)/2 = \rho_c + B_1(T_c - T) \quad (2.65),$$

where A_0, A_1, B_1, critical temperature T_c, and critical density ρ_c are fitting parameters, β critical exponent is equal to 0.326, and θ exponent of correction to the scaling is equal to 0.54. Figure 22b shows liquid and vapor densities and the fitted curves for Ti EAM potential as an example. When the critical temperature and density are found, critical pressure P_c is computed in a separate NVT simulation performed at the critical point.

Given the difficulty of liquid-vapor interface stabilization in vicinity of the critical point, the calculations are performed for temperatures below 0.9 T_c. More accurate calculation of the critical point may be performed with utilization of NVT Plus Test Particle Method proposed in Ref. [166]. In this method, simulations are performed not for coexistence but for a single phase system, and the coexistence equilibrium densities are calculated by matching the chemical potential of liquid and vapor phases. Since no difficulties with interfaces present in this approach, points in the direct vicinity of the critical point can be extensively probed, even at the temperature 0.9995 T_c [166], that provides a superior accuracy. However, this approach requires performing several simulations to reconstruct chemical potential lines at each temperature point. In addition, the accuracy of this method is reaching the point where the effect of system size plays a role, and simulations with several systems have to be performed to push the accuracy limit. Thus, acquisition of each temperature point requires performing tens of MD simulations that inclined us to use less accurate coexistence method: otherwise thousands of simulations would be required to calculate the critical points for the all Ti potentials considered in Section 3.4.

2.4.4. Melting point calculation

Knowledge of the melting point is essential for analysis of computational results, such as understanding kinetics of homogeneous melting or investigation of microstructure generated in resolidification. Thus, in our work the melting point is calculated for several interatomic potentials, in particular Section 3.4 reports results for a number of Ti potentials. The melting temperature is calculated in coexistence free dynamics simulations with utilizing the concept described in Ref. [160]. The flowing iterative procedure is applied. First, after an expected melting temperature, T_{m0}, is picked, a crystal with corresponding lattice parameter is generated by equilibration of the system in NσT ensemble for 30 ps under zero stress with periodic boundary conditions applied in all directions. For simulations reported in Section 3.4 the system size is approximately 4.4 nm × 4.4 nm × 44 nm for BCC (43940 atoms) and 4.1 nm × 4.2 nm × 43 nm for HCP phases (40320 atoms). After the crystal is generated, it is heated up to approximately 1.1-1.15 T_{m0} within 20 ps with constant system dimensions along 2 directions (x and y) and zero stress applied along the third one (z-direction). Zero stress condition allows avoiding generation of pressure waves when a free boundary condition is imposed on the next step.

The created system is used for a free dynamics simulation with free boundary imposed in z-direction and constant system size along x- and y-directions. Overheating and presence of free boundaries creates 2 melting fronts propagating from the boundaries, cooling the system down and driving it to the equilibrium. It is important to maintain a constant system size along lateral direction instead of keeping constant zero pressure since solid-liquid interface tension creates additional stresses resulting in artificial compression/tension of the system if pressure control condition is imposed. The initial overheating is chosen (1) to be sufficient to melt 30-50% of the system and (2) to be below the onset of homogeneous melting. The total time of the simulation is chosen 6250 ps to ensure complete equilibration and collection of statistically reliable data. First 750 ps are excluded for the system equilibration, while during the following 5500 ps values of the instantaneous system temperature are collected for further averaging. If the system is completely melted or stay solid, another value of the expected melting temperature is picked, otherwise the average temperature is used as a new value of the expected melting temperature, and the iteration repeated again. When the difference between the expected melting temperature and the average temperature is less than 5 K the iterative procedure is stopped. We have chosen $(2\bar{1}\bar{1}0)$ solid-liquid interface orientation rather than (0001) in HCP samples to avoid complications in melting/resolidification process that in the second case proceeds through subsequent nucleation of steps on closed packed planes followed by their motion and can be sucked at the different temperature than the melting point.

The above described procedure provides a simple, accurate, and robust method of melting temperature evaluation, which is applied in our study for a number of potentials, in particular for Ti potentials Table 6 in Section 3.4. An accuracy of the procedure is examined by comparison of our results evaluated for MUA1 potential with values of melting temperature provided in Ref. [164], where another procedure based on a series of constant temperature coexistence simulations is applied [167]. The listed values, 1765±1 K for HCP and 1918±1 K for BCC phases, are in an excellent agreement with our results, 1766.2 K for HCP and 1917.8 K for BCC phases. The standard error of the melting temperature evaluation in our method, estimated from the averaging procedure, is less than 0.1 K that is one order of magnitude smaller than in Ref. [164]. There can be systematic errors, which are more difficult to consider, resulted, for instance, by presence of temperature gradients inside the sample or a slight inaccuracy in determining the initial lateral dimensions of the system. Nevertheless, a simple estimation shows that temperature equilibration requires only hundreds of picoseconds, and the melting temperature only slightly depends on lateral compression since it does not create a volumetric pressure. Thus, the effect of those factors is relatively weak, and results of subsequent iterations converge to almost the same value.

Another advantage of the proposed approach is the number of simulations which need to be performed in order to calculate the melting temperature. The procedure described in Ref. [167] requires tens of simulations to accurately reproduce the dependence of the solid liquid interface velocity near the melting point. However, our procedure requires only 2-3 iterations to complete, and results of the first iteration give the value of melting temperature within ~1 K from the final value calculated in subsequent iterations even if the assumed $T_{\mathrm{m}0}$ is off by ~100 K.

3. Laser-induced modification of subsurface microstructure and defect generation

Abstract: In short pulse laser irradiation of metals the absorbed energy is localized within thin, tens to hundreds of nanometers, subsurface layer before is transferred to lattice vibration on the picosecond time scale. Rapid heating with the rate exceeding 10^{14} K/s leads to homogeneous melting of localized surface or internal regions of the target and generation of strong compressive stresses, which can reach 10s of GPa for heating under conditions of spatial confinement as discussed later. In addition, very localized energy deposition produces sharp temperature gradients leading to rapid quenching of the transiently melted material. In strongly absorbing materials such as metals or semiconductors, a combination of shallow depth of the laser energy deposition with high thermal conductivity of the irradiated material can lead to cooling rates approaching and even exceeding 10^{12} K/s [17,29]. The cooling rates can be even higher, in excess of 10^{13} K/s [82], when the laser energy deposition is confined not only within the thin surface layer of the irradiated target, but also in the lateral dimensions, creating conditions for even faster two- or three-dimensional heat transfer from the absorption region.

The ultrahigh rates of laser-induced cooling and the resulting resolidification, combined with the generation and relaxation of strong compressive stresses generated by the fast laser heating of the absorption region [27,28], create conditions for the formation of unusual metastable phases and unique material microstructures that are difficult if not impossible to produce by any other processing methods. In particular, this section considers emission of dislocations as a result of relaxation of initial thermal stresses and reveals the effect of target crystallographic orientation on this process (Section 3.1). Next, generation of dislocations during solidification under conditions of deep undercooling is analyzed and explained (Section 3.1). In addition to formation of dislocations, our study has demonstrated formation of growth twins confirmed by our experimental collaborators (Section 3.2). Thorough theoretical and computational analysis has revealed the mechanism of growth twinning (Section 3.3). Next, we look into details on the effect of interatomic potential on the microstructure predicted in short pulse laser processing and provide several specific examples (Section 3.4). Finally, the effect of a spatial confinement by a solid transparent overlayer on microstructure produced in laser

processing is analyzed (Section 3.5), and the final microstructure is compared with one obtained for irradiation in vacuum and in presence of a liquid overlayer (Section 3.6).

3.1. The effect of crystallographic orientation on laser-induced generation of dislocations in Ni

Abstract: The results of the large-scale atomistic simulations confirm the significant influence of the crystal orientation on the formation of sub-surface defects and provide detailed information on the defect configurations generated in (100), (011) and (111) targets. In the case of (001) surface, no emission of dislocations is observed when the resolved shear stress reaches the maximum value. The emission of dislocations from the solid-liquid interface and formation of stacking faults, however, takes place in targets with (011) and (111) surface orientations, with the latter exhibiting the highest density of dislocations activated in 3 different {111} slip planes and interacting with each other to produce complex dislocation reactions. These results are in a good qualitative agreement with experimental observations and are explained based on resolved shear stress analysis performed for different dislocation systems. In addition to the prompt dislocation emission during the dynamic relaxation of laser-induced stresses, the generation of dislocation loops and other crystal defects is also observed in the slower process of resolidification of the transiently melted surface regions of the irradiated targets. Based on the analysis of the defects generation during advancing the solid-liquid interface, the new mechanism of dislocation and vacancy clusters formation is proposed. Overall, the results of the simulations clarify the mechanisms responsible for the laser-induced generation of crystal defects and explain the sensitivity of the structural modification of metal surfaces to the crystallographic orientation of irradiated targets.

Introduction

Laser-induced surface modification is widely used in numerous modern processing and fabrication techniques including surface hardening, annealing, and alloying [168-172]. The enhancement of surface properties is achieved by microstructure and composition modification of the thin surface layer. Particularly, generation/annealing of crystal defects, grain refinement, formation of metastable structures such as recently reported polyicosahedral structures [31], and growth twinning [32] strongly affect the mechanical properties of the material. The shallow depth of the laser energy deposition and a steep temperature gradient produced by ultrashort laser pulses allow very selective microstructure modification within a layer with thickness from tens to hundreds of nanometers [173-176]. High resolution and accuracy of laser-induced modification of material properties makes this technique indispensable for practical applications; however, better theoretical understanding of fundamentals of laser interaction with matter, non-equilibrium processes caused by ultrafast energy deposition, and generation of crystal defects under these highly non-equilibrium conditions is vital for further advancement of laser-based processing techniques.

Resent experimental studies of laser irradiation of polycrystalline Ni targets, reported in Ref. [177], have demonstrated a very strong effect of the crystallographic orientation of grains on the microstructure modification and generation of defects in the subsurface region of the target. To reveal the mechanisms responsible for the laser-induced generation of crystal defects and explain the sensitivity of the structural modification of metal surfaces to the crystallographic orientation of irradiated targets, we performed a serious of large-scale atomistic simulations of laser irradiation of Ni targets with (100), (011), and (111) surface orientation. In this section we explain the effect of target crystallographic orientation on dislocation emission and defect generation during crystal regrowth based on the results of large-scale atomistic simulations and the theoretical analysis of the maximum resolved shear stresses built during laser irradiation. The modeling confirms the strong effect of the crystal orientation on the microstructure modification and provides an important insight into the mechanisms of the microstructure evolution.

Computational setup

The effect of a target crystallographic orientation on laser-induced generation of crystal defects is studied in a series of large scale atomistic simulations performed with a hybrid atomistic-continuum model [102] (Section 2.1.1), which combines a continuum level description of laser excitation and subsequent relaxation of the conduction band electrons based on two temperature model (TTM) [9,96] with classical Molecular Dynamics (MD) approach to simulate highly non-equilibrium processes of ultrafast phase transformations (melting and resolidification) and microstructure modification. The computational setup used in the simulations of laser irradiation is schematically illustrated in Figure 23. The top 150 nm of the target, where active generation of defects takes place, is represented by a TTM-MD model. The simulations are performed for single crystal targets with (100), (011), and (111), surface orientations. The system size in lateral directions (perpendicular to the surface) is about 100 nm

× 100 nm, and periodic boundary conditions are applied in these directions. The systems consist of 162, 153, and 150 million atoms for (100), (011), and (111) targets, respectively. This system size is sufficient enough to eliminate the effect of periodic boundary condition on the process of dislocation emission. In particular, as demonstrated later, the distance between emitted dislocations is much smaller than 100 nm. At the bottom of the TTM-MD part, a pressure wave transmitting, heat conducting boundary condition [106] is applied to ensure a nonreflecting propagation of a laser-induced pressure pulse and a heat transfer into the bulk of the target, where the heat conduction is described by classical TTM equations. Before running the simulations, MD systems were equilibrated for 70 ps at the temperature 300 K.

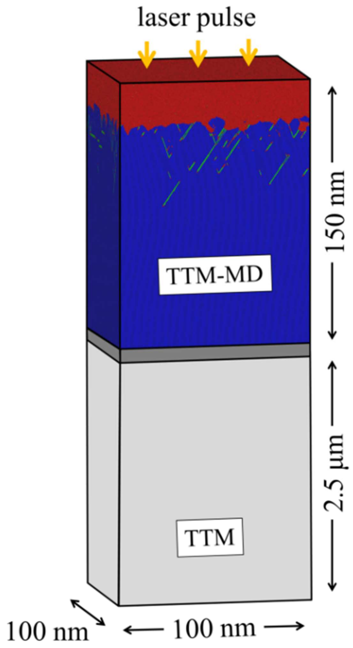

Figure 23. Schematic sketch of the computational setup used in the MD simulations of laser irradiation. The top part of the system is represented by TTM-MD model, whereas the temperature evolution in the deeper part is described by TTM equations. At the bottom of the TTM-MD region pressure wave transmitting boundary is imposed. The background corresponds to the snapshot of MD part in the simulation with (111) target orientation at 50 ps. The atoms are colored based on the local crystal structure environment: blue, green, and red colors correspond to FCC, HCP and unidentified local crystal structure environment, respectively. With this coloring scheme, a single green layer and a double green layer represent a twin boundary and a stacking fault in the FCC structure. Unidentified atoms correspond to liquid, solid-liquid interface, dislocation cores, and point defects.

The interatomic interaction in the MD part is described by the Embedded Atom Method (EAM) potential in the form proposed by Mishin and parametrized for Ni [130]. This potential is fitted to the experimental values of lattice parameter, elastic constant, and vacancy formation and migration energies. In addition, this potential provides a more accurate [130,178], in respect to other available Ni potentials, description of stacking fault and twin boundary energy, which are important for accurate description of emission and evolution of partial dislocations, and generation of growth twins. The microstructure produced in atomistic simulations is analyzed with the crystal structure analysis tool [179,180], which is capable to determine atomic local crystal structure environment and extract dislocation lines.

The laser irradiation of a material is described through a source term included in the TTM equation for electrons that reproduced laser excitation of conduction band electrons. The absorbed laser fluence is 600 J/m^2, which is slightly above the melting threshold; pulse duration is 50 fs. The source term reproduces a Gaussian temporal profile, shifted by 125 fs to ensure complete absorption of laser energy, and exponential intensity attenuation with depth according to Beer-Lambert law with optical absorption depth 14.5 nm assumed for Ni at the wavelength 800 nm [181]. A complete set of Ni parameters used in TTM is provided elsewhere [32].

To study generation of crystal defects under controlled conditions, additional atomistic simulations are accomplished with smaller computational cell, 29 nm × 29 nm × 66 nm, which consists of 4.6 million atoms. The initial system configuration is composed of 11 nm single crystal solid part surrounded by liquid. The solid and liquid parts of the systems were thermalized independently and combined together to create a system with flat solid-liquid interface. Periodic boundary conditions are applied along lateral directions, and outer surfaces of liquid are kept free to ensure pressure relaxation during resolidification. The simulation demonstrating the mechanism of vacancy formation is performed at 0.8 T_m (the melting temperature is 1701 K [182]). The lateral size of the system is chosen to fit the equilibrium lattice constant at 300 K, which corresponds to the conditions built during laser irradiation when the material does not have enough time to relax in lateral directions. A series of simulations targeted at the investigation of the concentration of vacancies generated by solidification under conditions of deep undercooling are performed with laterally relaxed systems.

Thermodynamics of laser irradiation and evolution of the microstructure

The fast rate of energy deposition by short laser pulses leads to ultrafast heating, homogeneous melting, and generation of compressive stresses. As an example of the laser-induced processes followed by laser irradiation, let us consider temperature and pressure evolution in a bulk Ni (100) target shown in the form of contour plots in Figure 24. During the laser irradiation, the laser energy is first absorbed by conduction band electrons and then transferred to phonons during the electron-phonon equilibration, which occurs on the picosecond time scale. Fast electron-phonon relaxation in Ni leads to confinement of the thermal energy in approximately top ~50 nm layer of the target that leads to the strong overheating of the material reaching $1.27T_m$ (the melting temperature T_m = 1701 K [182]). This overheating exceeds the limit of thermodynamic stability found to be ~(1.20 – 1.25) T_m for Au [102,183], Ag [17], Ni [11,102,104,184], as well as Ni-Fe and Ni-Cr solid solution alloys [185]. Therefore, a massive homogeneous nucleation of liquid regions inside the top 20 nm superheated crystal layer occurs within the time interval between 10 and 20 ps. Ultrafast melting significantly cools the top part, and at approximately 50 ps, when the temperature near the solid-liquid interface drops below the melting point due to the heat conduction to the bulk, resolidification process starts. Comparison of the results of simulations with different target orientations demonstrates almost the same values of the maximum melting depth, temperature, compressive and tensile stresses in all considered cases that is not surprising since target orientation does not affect thermodynamic properties of the material. However, since the speed of solidification front strongly depends on the interface orientation [128], the time of complete resolidification is very different and equal to 400, 490 and 720 ps for (100), (011), and (111) targets, respectively.

The ultrafast heating leads not only to homogeneous melting of the top part of irradiated surface but also to generation of compressive stresses. The laser-generated stresses are particularly high in the regime of stress confinement [27,28,134], when the time of the laser heating (defined by the laser pulse duration, τ_p, or the time of the electron–phonon equilibration, τ_{e-ph}, whichever is longer) is shorter than the time required for the mechanical relaxation (expansion) of the heated volume, *i.e.*, $max\{\tau_p, \tau_{e-ph}\} \leq L_p/C_s$, where C_s is the speed of sound in the target material and L_p is the effective depth of the laser energy deposition. With $\tau_{e-ph} \approx 10$ ps [186], $L_p \approx 50$ nm [187], and $C_s \approx 5080$ m/s [188], the condition for a partial stress confinement is satisfied, and the laser heating leads to the buildup of high compressive stresses in the surface region of the target, Figure 24b. Relaxation of the stress by expansion of the material toward the free surface creates a tensile wave which follows the compressive one (Figure 24b). Rapid homogeneous melting of the surface region adds to the compression as the molten material has a higher specific volume, as can be seen for a secondary spike in the compressive stresses upon melting in Figure 24b. The strong pressure gradient drives the emission of an intense compressive wave propagating into the bulk of the target, while the expansion of the material towards the free surface creates an unloading tensile component of the stress wave that follows the compressive one (Figure 24b). The tensile stresses associated with the unloading wave can induce emission of dislocations from the solid-liquid interface [49,83,189] as well as cavitation in the molten part of the target followed by photomechanical spallation [27,28,134] (Section 4.1) for higher laser fluence.

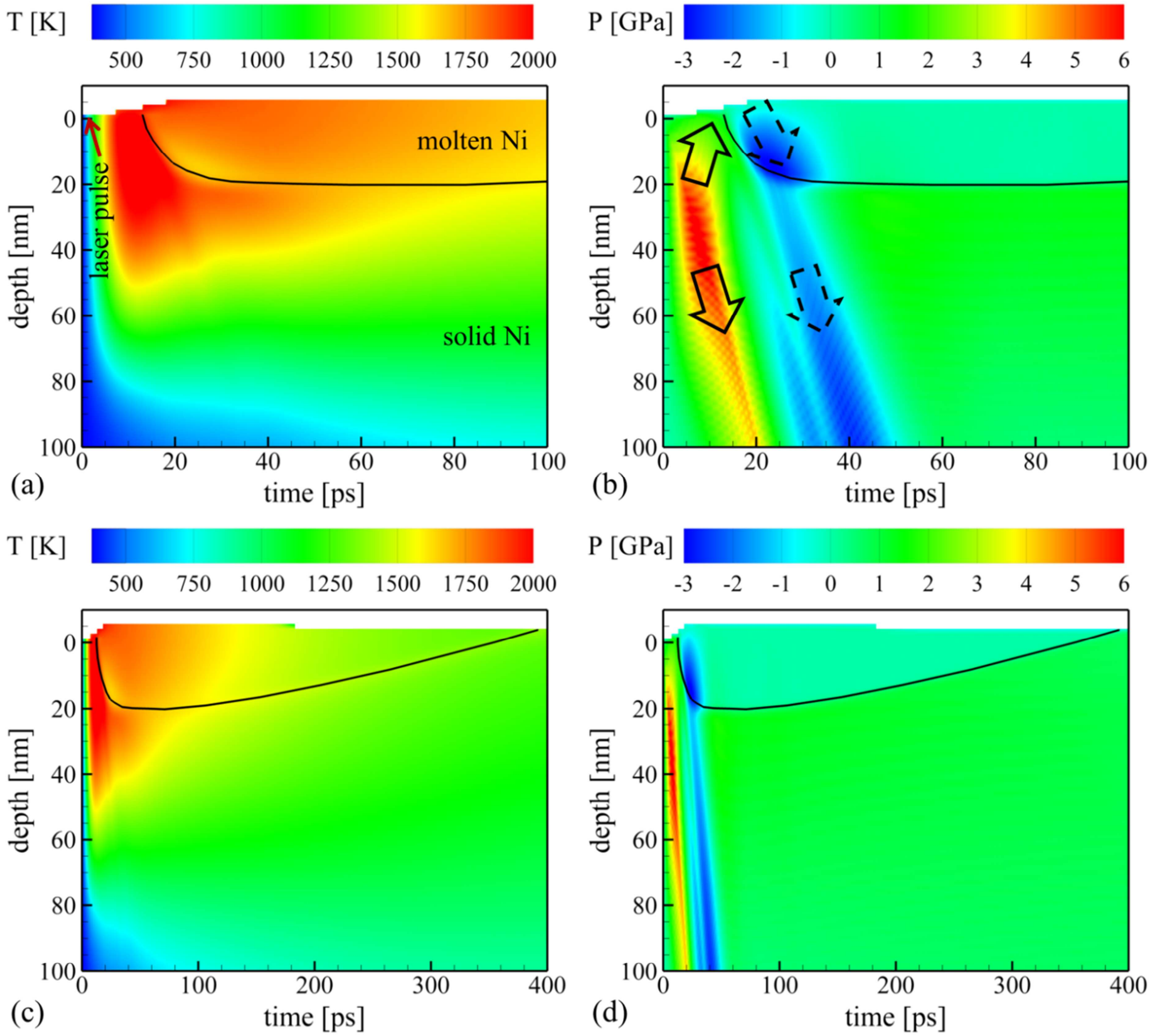

Figure 24. Contour plots of temporal and spatial evolution of temperature (a,c) and pressure (b,d) in a bulk Ni target irradiated by a 50 fs laser pulse at an absorbed laser fluence of 600 J/m^2, which is slightly above the melting threshold. Black line outlines the solid-liquid interface; solid and dashed black arrows in (b) show the direction of propagation of compressive and tensile stress waves.

Following the initial dynamic relaxation of the laser-induced stresses, the pressure in the molten part of the target quickly relaxes down to zero. The thermoelastic stresses in the crystalline part of the target, however, cannot completely relax by uniaxial expansion in the direction normal to the free surface, while the lateral expansion of the heated part of the target is constrained by the surrounding cold material. Thus, when the tensile wave propagates though the hot material, strong shear stress can be generated in some slip systems followed by emission of dislocations, as discussed in the next subsection. In addition, some residual quasi-static compressive stresses are present below the crystal-liquid interface in Figure 24b and remain in the target after complete resolidification of the surface region (Figure 24d), until it is cooled to the original temperature.

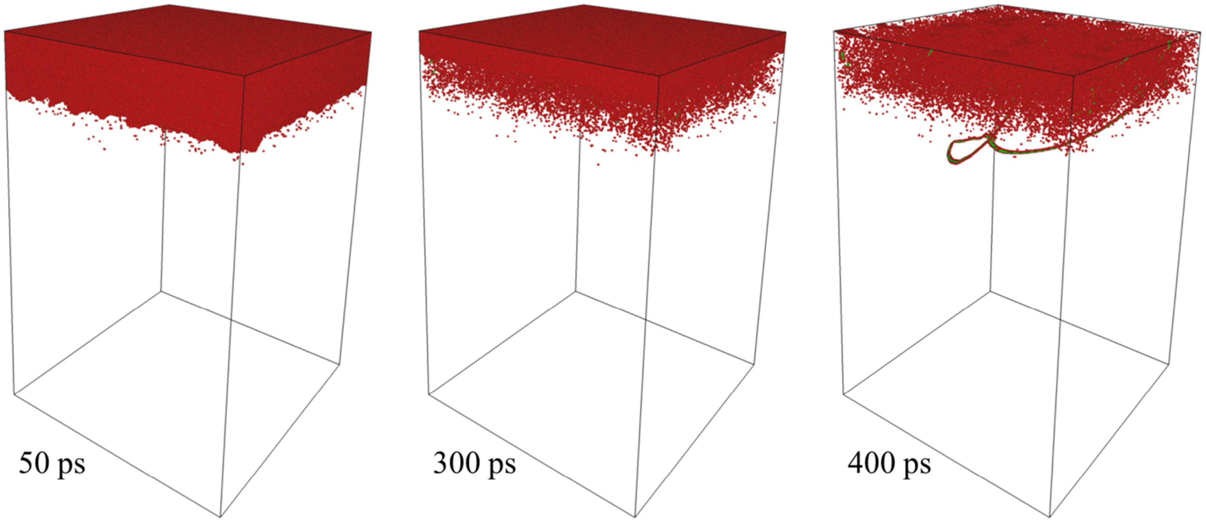

Figure 25. Snapshots of atomic configurations generated after irradiation of Ni (100) target. Atoms with FCC local crystal structural environment are blanked to expose the defect structures. The remaining atoms are colored by their local crystal structural environment: green and red colors correspond to HCP and unidentified local crystal structure environment, respectively. With this coloring scheme, a single green layer and a double green layer represent a twin boundary and a stacking fault in the FCC structure. Unidentified atoms correspond to liquid, solid-liquid interface, dislocation cores, and point defects. The resolidification process is completed by 450 ps after the laser pulse, and the top 3.5 nm surface layer is blanked in all snapshots to expose the underlying defect structure in the snapshot shown for 400 ps, where the surface roughness of ~1 nm is observed.

Ultrafast melting and resolidification as well as strong thermal stresses leads to generation of crystal defects and modifies the microstructure of the irradiated target, as depicted in Figure 25. Surprisingly, during first 50 ps, when a tensile wave is generated and the resolved shear stress reaches the maximum value, there is no emission of dislocations. However, the last snapshot shows presence of dislocations (green ribbons outlined by red) that suggest nucleation of dislocations during resolidification. The detailed description of the mechanism of dislocation formation during crystal growth, proposed in the current work, is provided in a subsection below.

In addition, solidification under the condition of deep undercooling creates a strong vacancy supersaturation, as depicted by numerous red dots in Figure 25.

The evolution of microstructure in (011) Ni target is depicted in Figure 26. In contrast to the previous case, numerous Shockley partial dislocations are emitted at the initial stage in two slip planes. The energy cost of stacking fault formation during expansion of dislocation loops is compensated by the work done by the external stresses. However, at later time the stress drops down during relaxation and cooling the material, and, thus, stacking faults become unstable. The minimum shear stress that leads to expansion of stacking faults can be estimated from the energy balance: $\tau_S \approx \gamma_T/h$, where γ_T is the twin energy, h is the spacing between $\{111\}$ planes. For the EAM potential used in the MD simulation $\gamma_T \approx 68$ mJ/m^2 [130], and $h \approx 2.07$ Å at the melting temperature. These values give approximately 0.3 GPa that is reached at approximately 40 ps leading to shrinking of stacking faults and emission of trailing partial dislocations to cancel the stacking faults. At the moment 300 ps only split dislocations remain in the system. It is noticeable that dislocations formed during resolidification have vertical arrangement and correspond to the set of slip planes that are not activated during the emission of dislocations at the initial stage. The configuration of dislocations formed during crystal growth is discussed in a subsection below. At approximately 300 ps, dislocations reach the bottom of the computational cell and stop; however, it does not affect the microstructure evolution in the top part of the target and cannot be avoided without significant increase of the system size and, thus, the computational cost of the simulation.

The results for (111) Ni target are shown in Figure 27. For this target orientation, numerous partial dislocations are also emitted at the initial stage in three slip planes when the resolved shear stress reaches the maximum value. Similar to (011) target orientation, at the later time when the stress drops down, the stacking faults either retreat back of form split dislocations. Since emission of dislocations takes place in three slip planes, the generated dislocation network is more complicated than in the previous case and numerous dislocation reactions are observed. At approximately 200 ps dislocations reach the bottom of the computational cell, but, as mentioned above, it does not affect the microstructure evolution in the top part and cannot be avoided without significant increase of the computational cost.

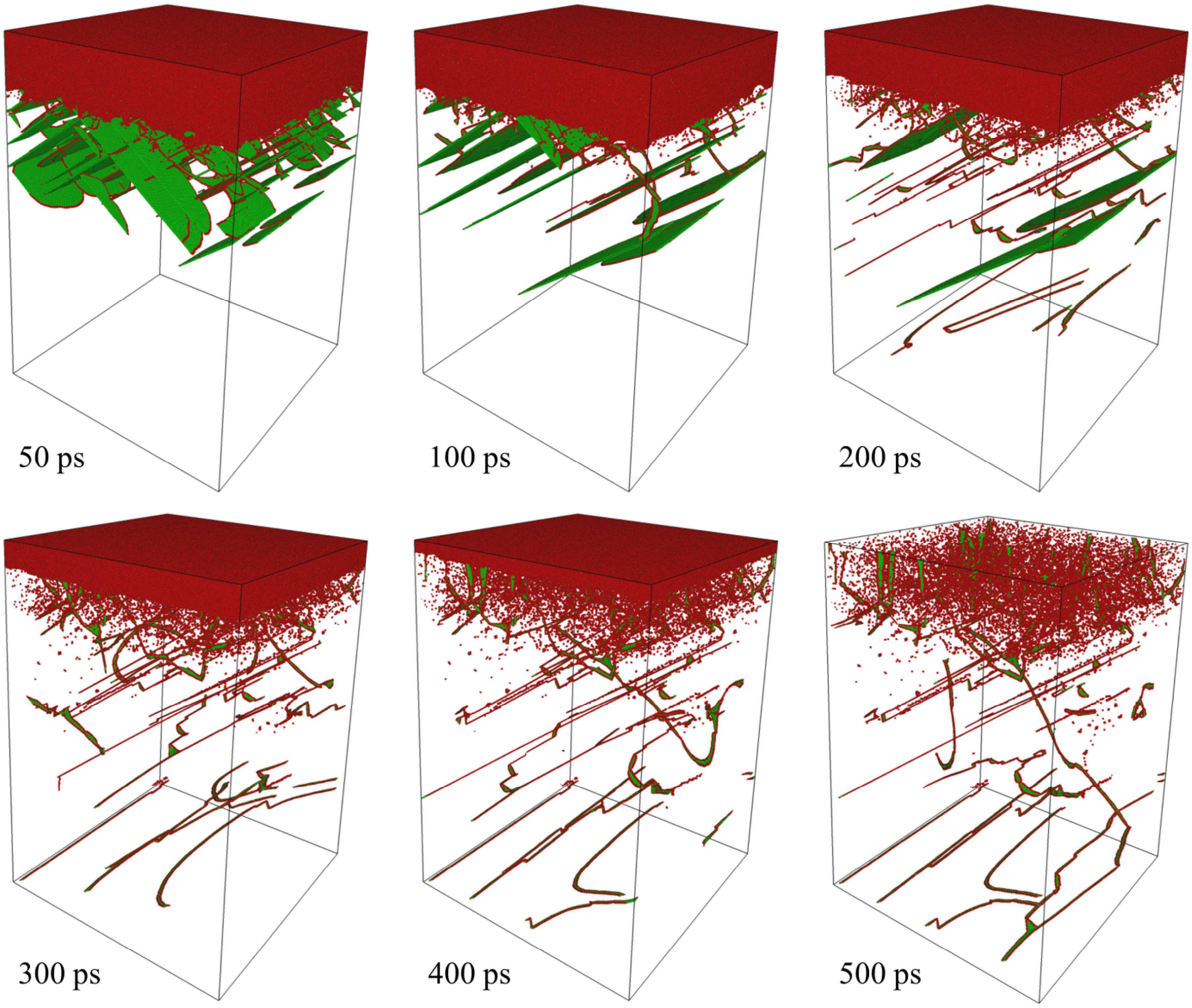

Figure 26. Snapshots of atomic configurations generated after irradiation of a (011) target. The coloring scheme is the same as in Figure 25. The resolidification process is completed by 500 ps after the laser pulse, and the top 3.5 nm surface layer is blanked in all snapshots to expose the underlying defect structure in the snapshot shown for 500 ps, where the surface roughness of ~1 nm is observed.

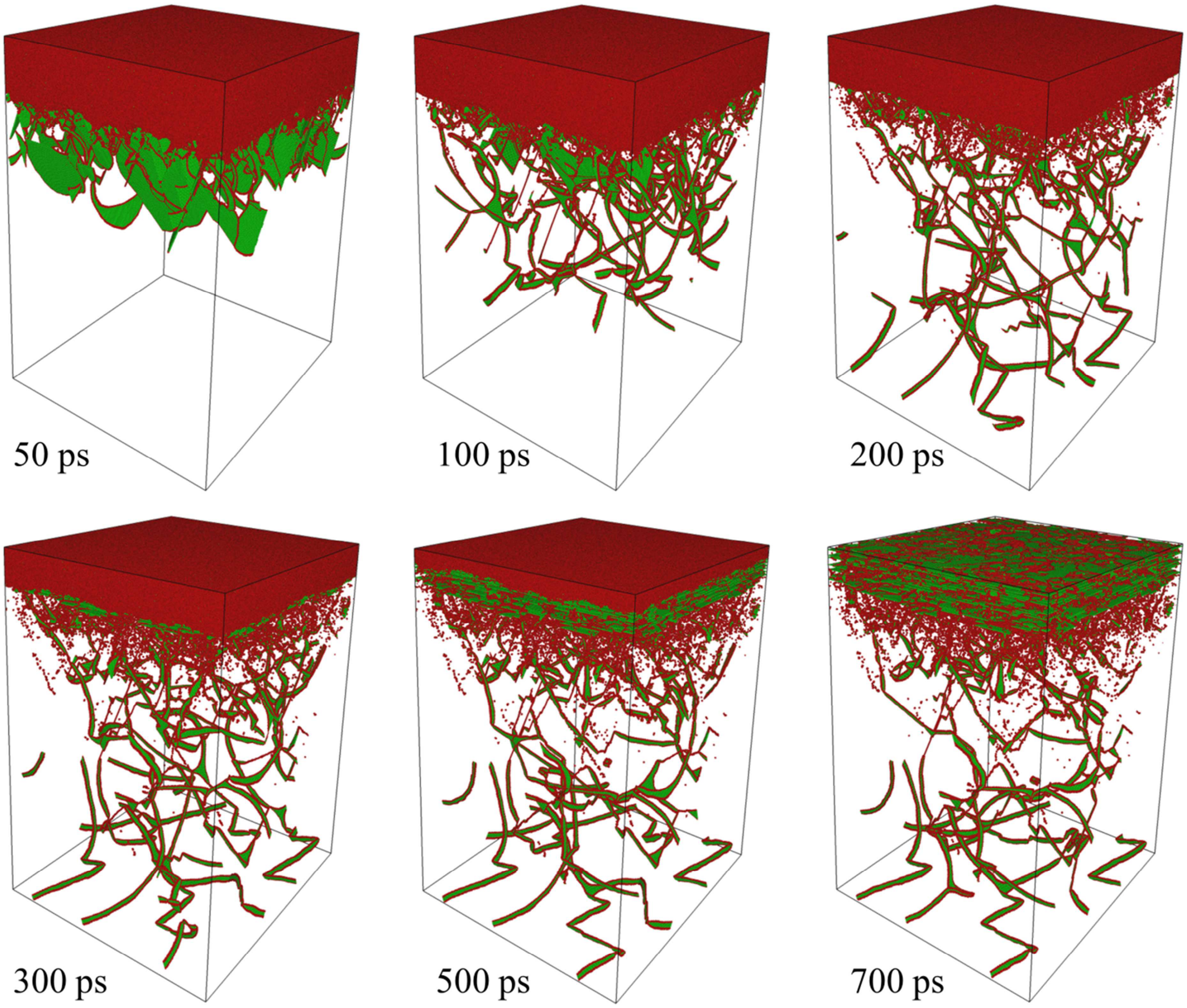

Figure 27. Snapshots of atomic configurations generated after irradiation of a (111) target. The coloring scheme is the same as in Figure 25. The resolidification process is completed by 720 ps after the laser pulse, and the top 3.5 nm surface layer is blanked in all snapshots to expose the underlying defect structure in the snapshot shown for 700 ps, where the surface roughness of ~2 nm is observed.

One noticeable effect, which is only present in (111) Ni target, is formation of high density of twin boundaries at the final stage of resolidification process. According to Figure 27, at the initial stage, from 50 to 200 ps, the resolidification process proceeds through epitaxial regrowth of crystal. However, when the temperature near the solidification front drops below ~0.86 T_m, the defect structure of the resolidified region is changed abruptly, and, as shown in the last three snapshots in Figure 27, numerous coherent twin boundaries, Σ3 {111}, are formed in planes parallel to the (111) solid-liquid interface. The comparison of this nanotwinned structure with experimental results and detailed description of the mechanism of growth twinning during solidification under the condition of deep undercooling are provided in Sections 3.2 and 3.3 in Ref. [32,150].

The final configuration of dislocations after complete resolidification in Ni targets with (100), (011), and (111) surface orientation is demonstrated in Figure 28. The plots shows presence of two types of dislocations: perfect dislocations split into two partials and prismatic dislocation loops composed of Frank partial, Stair-rod, and Shockley partial dislocations. In (100) target the major part of dislocations is located in the top 20 nm layer, the region affected by melting, because the dislocations are generated only during resolidification. When the distance between the ends of the dislocation reaches the critical value, the dislocation loop starts expanding under the residual thermal stresses. This critical distance may be estimated based on $L_c \approx 2\alpha Gb/\tau$ [190], where G is shear modulus of the material, b is Burgers vector, τ is the resolved shear stress, α is the numerical constant with typical value 0.5 – 1.5. By taking the maximum resolved shear stress in slip systems for perfect dislocation generated by residual thermal stress equal to 0.6 GPa in (100) target, the value of L_c can be estimated as approximately 60 nm, which in a reasonable agreement with onset of the dislocation loop expansion shown in Figure 28a. In the target with (011) surface orientation, the density of dislocations is higher than in the previous case, and since dislocations are emitted at the initial stage of laser irradiation, they present both in the deeper part of the target and in the top region affected by melting. Also this plot clearly illustrates the vertical arrangement of dislocation formed during resolidification. In the case of (111) surface orientation (Figure 28c), dislocation are also present both in the top and deeper part of the target. However, the most noticeable feature is an extremely high density of dislocations in the top region affected by melting, which is equal approximately to 5×10^{17} m^{-2}. As discussed above, this region contains high density of growth twin boundaries, and since incoherent twin boundaries are formed by Shockley partial dislocations, numerous dislocations are recognized during the crystal structure analysis.

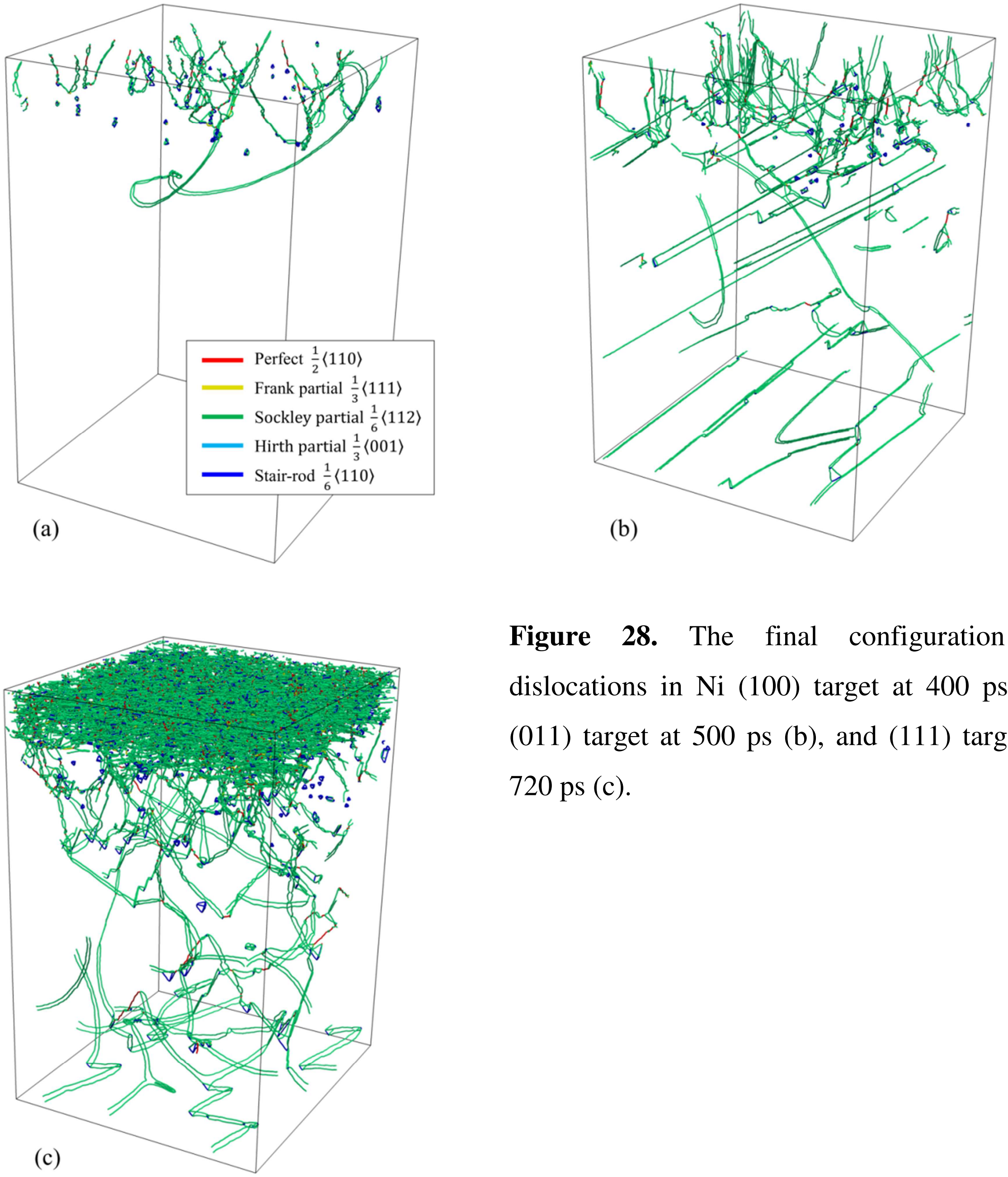

(a) (b) (c)

Figure 28. The final configuration of dislocations in Ni (100) target at 400 ps (a), (011) target at 500 ps (b), and (111) target at 720 ps (c).

Effect of crystallographic orientation on emission of dislocations

Relaxation of laser-induced thermal stresses, as described above, is accompanied by generation of a tensile wave, which propagating through a solid-liquid interface leads to active emission of partial dislocations in targets with (011) and (111) surface orientations. Meanwhile, no dislocations are generated (100) target at the initial stage. This section provides an explanation of the effect of crystallographic orientation on emission of dislocations based on the values of the resolved shear stress in FCC slip systems estimated theoretically and measured in simulations.

Theoretical approximation of the resolved shear stress

Emission of dislocations takes place when a resolved shear stress in a particular slip system reaches the critical value. Slip in FCC crystal structure occurs along close packed planes, $\{111\}$, in the direction $\langle 110\rangle/2$ for perfect and $\langle 112\rangle/2$ for Shockley partial dislocations [190]. Figure 29 illustrates the slip systems for each considered surface orientation. Each $\{111\}$ plane has 3 slip directions for perfect dislocations, which correspond to close packed directions marked on the plot by arrows, and 3 directions for Shockley partial dislocations.

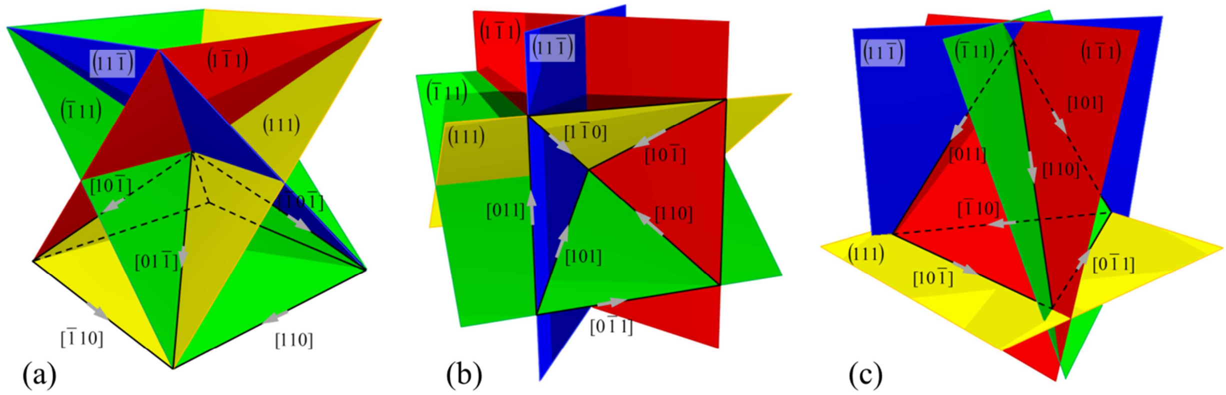

Figure 29. A schematic sketch of slip systems in FCC targets with (100) (a), (011) (b), and (111) (c) surface orientation. The colored planes represent arrangement of close packed planes in a FCC target, the vectors show close packed directions.

During ultrafast laser irradiation, material is expanded uniaxially along the direction perpendicular to the surface (z direction). The relaxation of the lateral stresses takes much longer time since the typical size of the laser spot is significantly larger than the depth of the region where laser energy is deposited. In the following analysis, the values of resolved shear stresses created during laser irradiation are estimated based on a simplified ideal system that is tensed in the z direction under the condition of zero strain in lateral directions. Since volumetric compression does not create shear stresses, the zero level of strain can be shifted to subtract the initial thermal strain.

The value of stress can be calculated based on the Hook's law [190], $\sigma_{ij} = C_{ijmn}e_{mn}$, where C_{ijmn} is the stiffness tensor, σ_{ij} and e_{ij} are the stress and strain tensors. Since uniaxial compression of a cubic crystal affects only normal components of the stress tensor keeping other components equal to zero, the final set of equations for a target with (100) surface orientation can be written in the fallowing way:

$$\begin{cases} \sigma_{xx} = C_{11}e_{xx} + C_{12}e_{yy} + C_{12}e_{zz} = C_{12}e \\ \sigma_{yy} = C_{12}e_{xx} + C_{11}e_{yy} + C_{12}e_{zz} = C_{12}e \\ \sigma_{zz} = C_{12}e_{xx} + C_{12}e_{yy} + C_{11}e_{zz} = C_{11}e \end{cases} \quad (3.1),$$

where *e* is the strain applied in *z* direction. The values of the resolved shear stress can be calculated by projection of the strain tensor on a particular slip system:

$$\tau = \sigma_{ij} \cdot cos(\theta_{in}) \cdot cos(\theta_{jd}) \quad (3.2),$$

where θ_{in} and θ_{jd} are angles between *i* direction and slip system normal *n*, and *j* direction and slip direction *d*. Based on Figure 29a, for a target with (001) surface orientation all slip planes are identical. Since σ_{xx} and σ_{yy} are equal, and [*mn*0] is perpendicular to *z* axis, the resolved shear stress in all slip planes in [*mn*0] direction is equal to zero. The shear stress in other slip systems for perfect dislocations is the same and equal to:

$$\tau_{perfect}^{100} = (\sigma_{zz} - \sigma_{xx})/\sqrt{6} \quad (3.3).$$

For slip systems corresponding to partial dislocations, there are also two cases:

$$\tau_{partial}^{100} = \left(2\sigma_{zz} - \sigma_{xx} - \sigma_{yy}\right)/3\sqrt{2} = \sqrt{2}(\sigma_{zz} - \sigma_{xx})/3 = 2\tau_{perfect}^{100}/\sqrt{3} \quad (3.4).$$

$$\tau_{partial}^{\prime 100} = (2\sigma_{xx} - \sigma_{xx} - \sigma_{zz})/3\sqrt{2} = (\sigma_{zz} - \sigma_{xx})/3\sqrt{2} \quad (3.5).$$

Only the absolute value of shear stress is important, the sign shows the direction of the shear and, thus, dropped in Eq. 3.5. Since $\tau_{partial}^{\prime 100} < \tau_{perfect}^{100} < \tau_{partial}^{100}$, only partial dislocations can be emitted in the direction [*mn2*]. When the resolved shear stress reaches the critical value in a particular slip system, emission of dislocations prevents further increase of the stress and limits emission in other slip systems. By combining Eqs. 3.1 and 3.4, the maximum value of the resolved shear stress reached in (100) target can be estimated as:

$$\tau_{partial}^{100} = \sqrt{2}(C_{11} - C_{12}) \cdot e/3 \quad (3.6).$$

The equations for stresses generated in a target with (011) surface orientation can be derived by rotation of the stiffness tensor to the new coordinate system:

$$C'_{i'j'm'n'} = C_{ijmn} \cdot cos(\theta_{ii'}) \cdot cos(\theta_{jj'}) \cdot cos(\theta_{mm'}) \cdot cos(\theta_{nn'}) \qquad (3.7),$$

where $\theta_{ii'}$, $\theta_{jj'}$, $\theta_{mm'}$, and $\theta_{nn'}$ are angles between axes of the old and new coordinate systems. The final equations for (011) target orientation can be written as following:

$$\begin{cases} \sigma_{xx} = C_{11}e_{xx} + C_{12}e_{yy} + C_{12}e_{zz} = C_{12}e \\ \sigma_{yy} = C_{12}e_{xx} + \frac{C_{11}+C_{12}+2C_{44}}{2}e_{yy} + \frac{C_{11}+C_{12}-2C_{44}}{2}e_{zz} = \frac{C_{11}+C_{12}-2C_{44}}{2}e \\ \sigma_{zz} = C_{12}e_{xx} + \frac{C_{11}+C_{12}-2C_{44}}{2}e_{yy} + \frac{C_{11}+C_{12}+2C_{44}}{2}e_{zz} = \frac{C_{11}+C_{12}+2C_{44}}{2}e \end{cases} \qquad (3.8),$$

For this target orientation there are two pairs of identical slip planes. In the first pair (green and yellow planes in Figure 29b), the maximum resolved shear stress is reached for partial dislocations in the directions $[211]$ and $[\bar{2}11]$:

$$\tau_{partial}^{011} = \sqrt{2}(\sigma_{zz} - \sigma_{xx})/3 = \sqrt{2}(C_{11} + 2C_{44} - C_{12}) \cdot e/6 \qquad (3.9).$$

In the second pair (red and blue planes in Figure 29b), the maximum resolved shear stress is reached for partial dislocations in the directions [112], [121], $[\bar{1}12]$, and $[\bar{1}21]$:

$$\tau_{partial}^{\prime 011} = \sqrt{2}(\sigma_{yy} - \sigma_{xx})/3 = \sqrt{2}(C_{11} - 2C_{44} - C_{12}) \cdot e/6 \qquad (3.10).$$

The equations for stresses generated in a target with (111) can derive similar to (011) case by rotation of the stiffness tensor (Eq. 3.7):

$$\begin{cases} \sigma_{xx} = \frac{C_{11}+C_{12}+2C_{44}}{2}e_{xx} + \frac{C_{11}+5C_{12}-2C_{44}}{6}e_{yy} + \frac{C_{11}+2C_{12}-2C_{44}}{3}e_{zz} = \frac{C_{11}+2C_{12}-2C_{44}}{3}e \\ \sigma_{yy} = \frac{C_{11}+5C_{12}-2C_{44}}{6}e_{xx} + \frac{C_{11}+C_{12}+2C_{44}}{2}e_{yy} + \frac{C_{11}+2C_{12}-2C_{44}}{3}e_{zz} = \frac{C_{11}+2C_{12}-2C_{44}}{3}e \\ \sigma_{zz} = \frac{C_{11}+2C_{12}-2C_{44}}{3}e_{xx} + \frac{C_{11}+2C_{12}-2C_{44}}{3}e_{yy} + \frac{C_{11}+2C_{12}+4C_{44}}{3}e_{zz} = \frac{C_{11}+2C_{12}+4C_{44}}{3}e \end{cases} \qquad (3.11).$$

In the case of (111) target orientation the resolve shear stress in (111) plane (yellow plane in Figure 29c) is zero for all slip directions; other three planes are identical. The maximum shear stress is reached for partial dislocations in directions [211], [121], [112] in $(\bar{1}11)$, $(1\bar{1}1)$, $(11\bar{1})$ planes, respectively:

$$\tau_{partial}^{111} = 2\sqrt{2}(\sigma_{zz} - \sigma_{xx})/9 = 4\sqrt{2}C_{44} \cdot e/9 \qquad (3.12).$$

The EAM Ni potential used in the in the current work have the following values of elastic constants: C_{11} = 241.3 GPa, C_{12} = 150.8 GPa, C_{11} = 127.3 GPa [130]. Thus, the values of resolved shear stress produced by e strain in z direction under the condition of zero strain in lateral directions can be calculated as: $\tau_{partial}^{100} \approx 42.7e$, $\tau_{partial}^{011} \approx 81.3e$, $\tau_{partial}^{\prime 011} \approx 38.7e$, $\tau_{partial}^{111} \approx 80.8e$. Despite the values of the elastic moduli are temperature dependent, a slight variation of the obtained values of the resolves shear stresses does not change the overall picture. The predicted values of the resolved shear stresses for the considered systems are in a good agreement with the microstructure evolution discussed in the previous subsection. In the case of (100) target orientation, the resolved shear stress has the lowest value that suggests no emission of dislocations. For a target with (011) orientation, the stress is about twice larger in (111) and $(\bar{1}11)$ (green and yellow planes in Figure 29b), which, indeed, correspond to emission dislocations, as shown in Figure 26. In other planes the resolved shear stress is much lower, and dislocations are not emitted. For a target with (111) surface orientation, the stress has also high value in 3 identical slip planes, $(\bar{1}11)$, $(1\bar{1}1)$, $(11\bar{1})$ which correspond to emission of dislocations in Figure 27. Thus, the simple analysis of shear stresses generated in slip systems is capable to provide an insight into dependence of dislocation emission on the target crystallographic orientation.

Emission of dislocations during laser processing

The evolution of the resolved shear stress during laser irradiation in the slip system where the stress reaches the maximum value is shown in Figure 30 for 3 considered surface orientations. The maximum value of the resolved shear stresses are 1.73, 1.73, and 2.00 GPa for (100), (011), and (111) surface orientations, respectively. The comparison of these values leads to a contradiction: the maximum shear stress in (011) target is approxinatly the same as in (100); however, in the last case dislocations do not nucleate at the initial stage, Figure 25. In addition, in the vicinity of the solid-liquid interface, where dislocations are emitted due to the lower nucleation barrier, the values of the resolved shear stress are substantially lower in (011) case compared with (100) target.

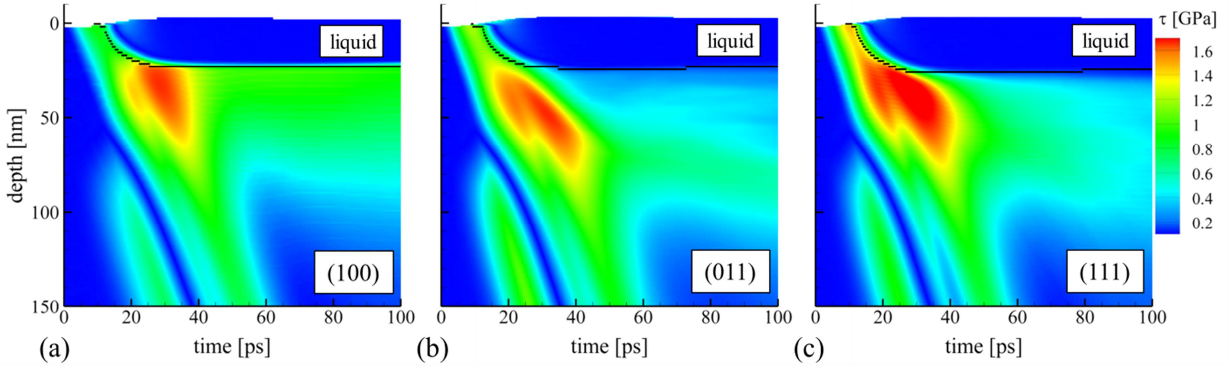

Figure 30. Contour plots showing spatial and temporal evolution of resolved shear stress in Ni (100) (a), (011) (b), and (111) (c) for a slip system where the resolved shear stress reaches the maximum value, and emission of dislocations is observed. The black solid curve separates the melted region from the solid part.

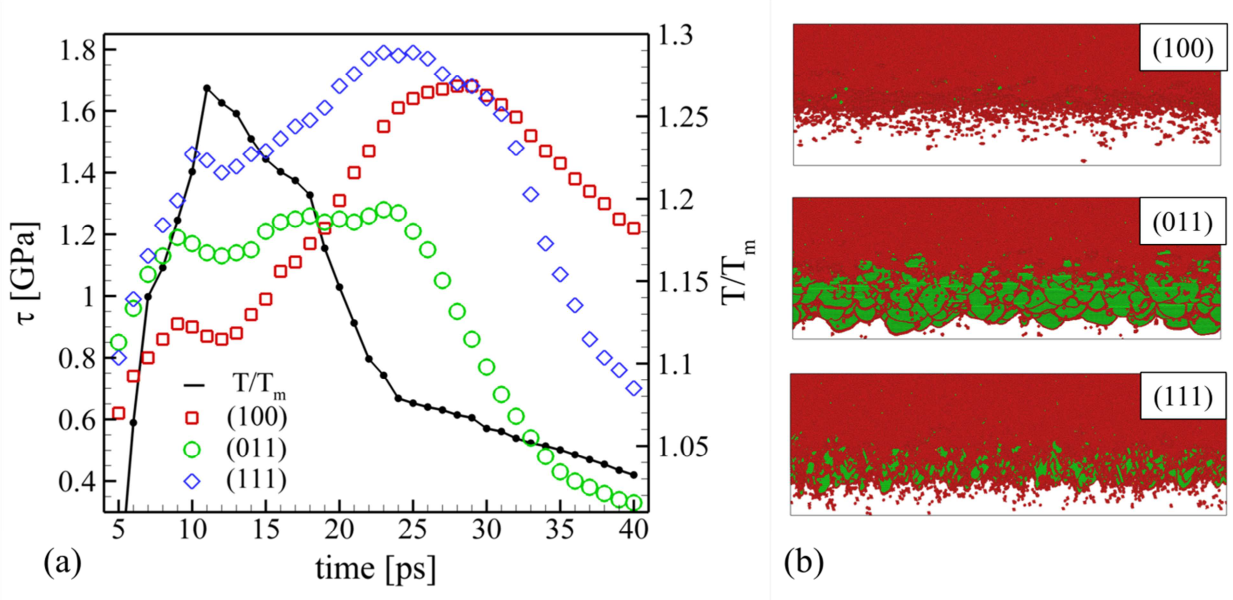

Figure 31. (a) The evolution of the maximum value of a resolved shear stress within 5 nm from the solid-liquid interface in Ni (100) (red squares), Ni (011) (green circles), and Ni (111) (blue diamonds) for a slip system where the resolved shear stress reaches the maximum value, and emission of dislocations is observed. The temperature near the interface in Ni (100) is shown by a black line. (b) Snapshots of atomic configurations generated at 20 ps after laser irradiation. The coloring scheme is the same as in Figure 25. Active emission of Shockley partial dislocations is observed only in (011) and (111) targets.

This puzzle can be resolved by recalling that emission of dislocations is a thermally assisted process. The critical shear stress required for emission of dislocations rapidly drops with the temperature increase [191]. Thus, dislocations are formed only when the temperature near the interface is sufficiently high. Figure 31a shows the evolution of temperature and resolved shear stresses near the interface. At the time between 7 and 20 ps, the resolved shear stress in (011) and (111) cases is substantially larger than in (100) target, and it would reach even higher value if there was no relaxation by emission of dislocations, as shown in Figure 31b. At the later stage, when the temperature near the interface drops down during ultrafast melting, dislocations are not emitted in (100) target even if the shear stress reaches 1.6 GPa.

The analysis of the resolved shear stress generated under the uniaxial expansion, which is performed in the previous subsections, suggests approximately twice stronger response of (011) and (111) targets on the same deformation. Thus, during expansion of the target, the resolved shear stress is always higher in (011) and (111) cases. When it reaches the critical value, dislocation emission starts, and further increase of the stress is suppressed. Since in (111) target dislocations are generated in 3 slip systems, dislocation reactions impede growth of the dislocation loops. Thus, the shear stress in the target with (111) orientation reaches higher value than in (011) case. In (100) target, stronger expansion of the material is required to achieve a sufficiently high value of shear stress that requires longer time, and as a result the maximum values of the shear stress is reached only at the moment 28 ps, when the top part of the target is melt, and the temperature is too low for dislocation emission.

Generation of dislocations during crystal growth

The discussion of the microstructure evolution during laser processing in a subsection above has revealed several interesting questions. First, in the case of (100) surface orientation, dislocations are not emitted initially when the resolved shear stress reaches the maximum value but generated later during resolidification. Second, in the case of (011) target the dislocations formed during crystal growth have vertical arrangement, which is different from the arrangement of dislocations emitted at the initial stage. This subsection describes the mechanism of dislocation generation during crystal growth and discusses the effect of the target orientation of the configuration of dislocations formed during resolidification.

Generation of dislocations in Ni (100)

Analysis of atomic configurations generated during laser irradiation of Ni (100) targets at the moment 50 and 100 ps shows absence of dislocations. The first dislocations appear at the time 150-200 ps, Figure 25, and grow forming the configuration shown in Figure 28a. Tracking the dislocation evolution suggests that the dislocations are generated not by diffusion and aggregation of vacancies but directly near the solid-liquid interface. To understand the mechanism of dislocation formation, the interface roughness is compared with the configuration of defects generated in the target to the moment 200 ps. The results of the comparison, shown in Figure 32, demonstrate a strong correlation: partial dislocations nucleate only in troughs. Also, the concentration of vacancies is lower in the elevated parts colored by red compared with deeper parts colored by green and blue.

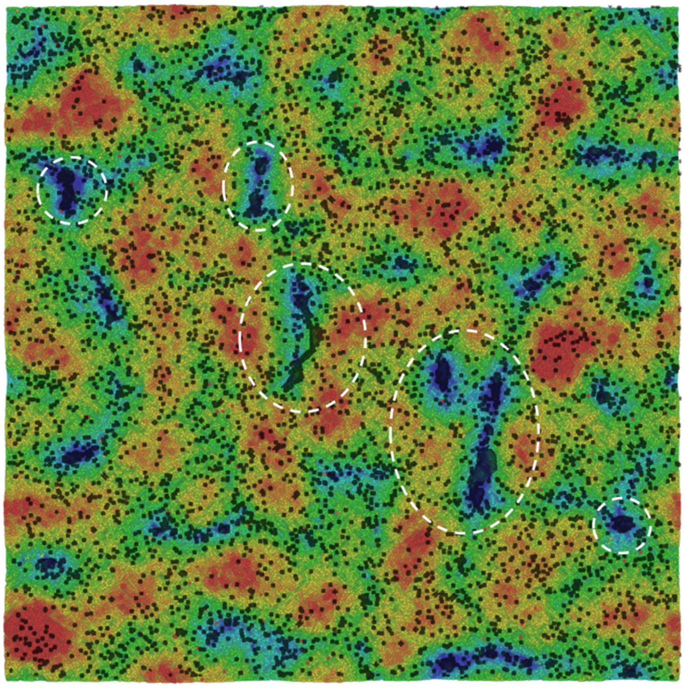

Figure 32. Correlation of formation of vacancies and dislocations with surface elevation. This plot can be considered as a view from bulk to the interface region at 200 ps after laser irradiation. The solid-liquid interface is colored based on the elevation: gradation from red to blue corresponds to 5 nm. Vacancies are plot as dark spots; partial dislocations are represented by large dark regions that are outlined by white dashed ellipses. The concentration of vacancies is smaller in elevated parts colored by red in comparison with deeper parts colored by green and blue. Dislocations also nucleate only in troughs.

Figure 33 illustrates evolution of the solid-liquid interface roughness after laser irradiation, compared with values estimated from the interface stiffness based on the capillarity wave theory and results of atomistic simulations under controlled conditions. Ultrafast melting creates a very rough interface containing numerous troughs, as shown in Figure 32. At the beginning of resolidification, the roughness slightly decreases; however, it remains approximately twice higher compared with the atomistic modeling of resolidification with initially flat interface. Besides this very rough interface generated by ultrafast melting, the roughness of the solid-liquid interface during resolidification is always larger compared with the equilibrium value even for simulations with initially flat interface, which can be explained by pinning the interface by defects formed during advancing the interface. Moreover, as shown in Figure 34, the temperature increase due to the interface motion has biased profile: the average temperature in front of the solid-liquid interface (liquid fraction in a range 0.5-0.9) is lower compared to the value behind the interface (liquid fraction in a range 0.1-0.5). Since in the temperature range 0.75-1.0 T_m the velocity of the solid liquid interface increases with the temperature decrease Figure 15, the temperature difference near the interface leads to a growth instability, which results in faster growth of elevated parts compared with deeper ones.

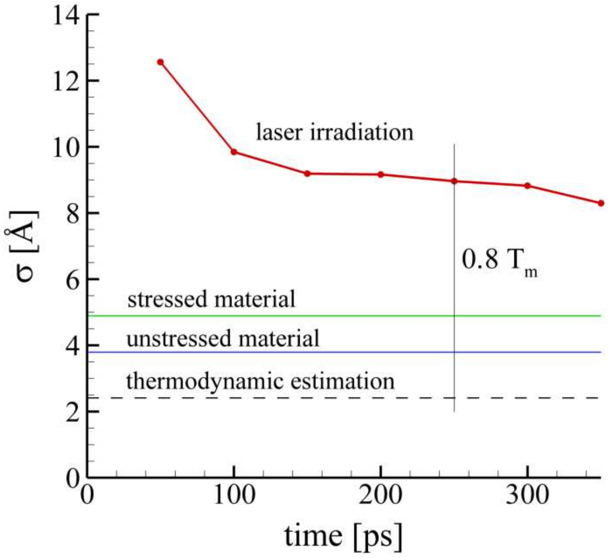

Figure 33. The evolution of the standard deviation of solid-liquid interface elevation (red) in (100) Ni target after laser irradiation. The values are compared with the results obtained in atomistic simulations at constant temperature 0.8 $\mathrm{T_m}$ with initially flat solid-liquid interface. The green line show the result of a simulation with the system size in lateral directions equal to the equilibrium size at 300 K, which corresponds to absence of lateral material relaxation in the simulations of laser irradiation. The blue line corresponds to the simulation with relaxed material in lateral directions. The dashed line depicts the interface roughness expected at the melting point which is calculated based on the interface stiffness.

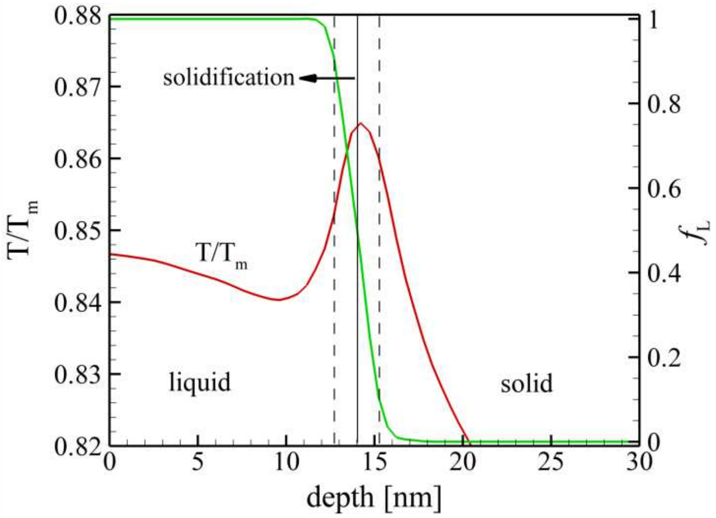

Figure 34. The temperature profile in the vicinity of the solid-liquid interface in the modeling of laser irradiation of Ni (100) target at 200 ps. The red and green lines show the temperature and the fraction of liquid, respectively. The solid black line depicts the position of the interface (liquid fraction is 0.5), dashed lines outlines the region with the fraction of liquid in the range 0.1-0.9.

To reveal the origin of the connection between defect generation and the interface roughness, the formation of defects is studied in additional small scale atomistic simulation under controlled conditions with initially flat solid-liquid interface. The snapshots of atomic configurations that demonstrate formation of a cluster of vacancies are shown in Figure 35. The deeper part of the interface, formed by fluctuations, propagates slower and at some point is pinned. When the solid-liquid interface passes this part, it is sealed. Since the density of liquid is less than for solid, the isolated part corresponds to a cluster of 41 vacancies, which after rearrangement creates a prismatic dislocation loop depicted in Figure 36. This loop can be represented as a Frank dislocation loop partially split into Stair-rod and Shockley partial dislocations.

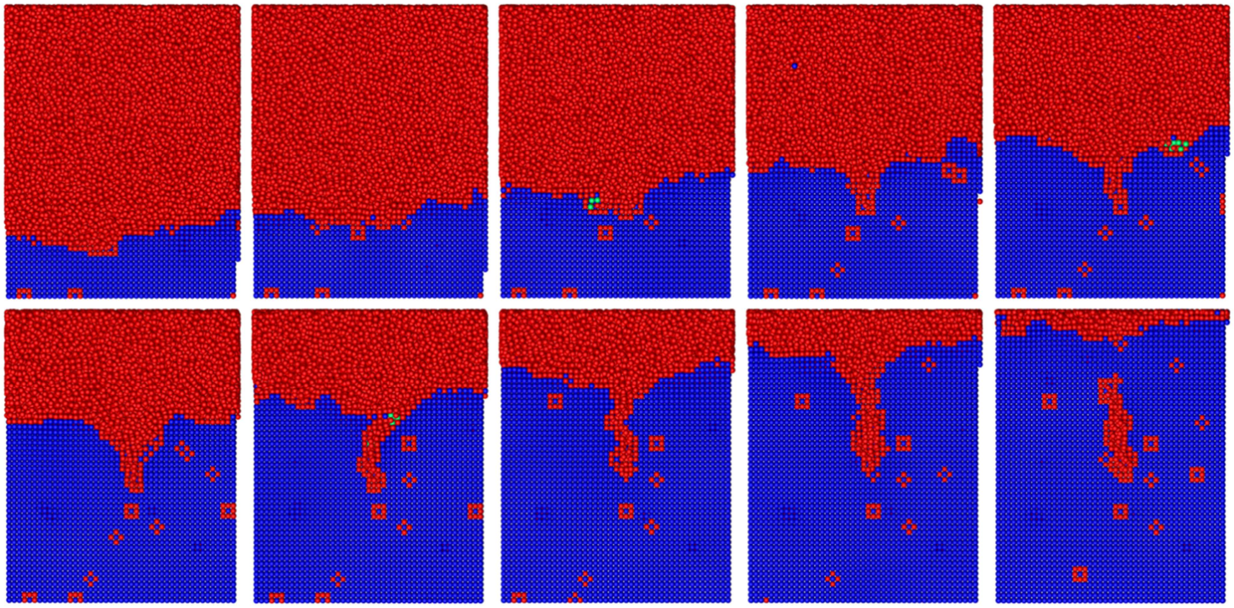

Figure 35. Formation of a cluster of vacancies during resolidification in a small scale atomistic simulation performed under controlled conditions at 0.8 T_m. The snapshots are plot with 10 ps time interval; each snapshot represents an enlarged cross section of the cluster with the box size 8 by 10 nm. The coloring scheme is similar to Figure 25, but atoms with FCC local crystal structure environment are not blanked but shown by blue color.

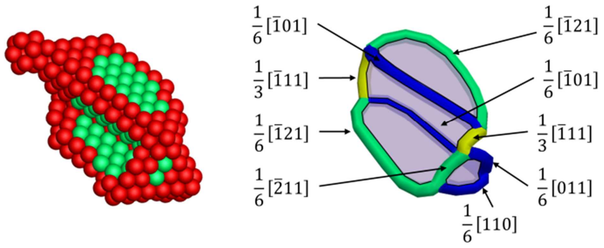

Figure 36. A prismatic dislocation loop formed after rearrangement of a cluster of 41 vacancies depicted in Figure 35. The atomic snapshot corresponds to the time 140 ps after the last snapshot in Figure 35. The coloring scheme is the same as in Figure 25. The right part of the figure shows the schematic representation of the dislocation loop. Dislocations are colored based on the type: Shockley partials are green, Frank partials are yellow, Stair-rod are blue. Grey planes represent stacking faults.

In the modeling of laser irradiation, the solid-liquid interface is very rough and contains numerous troughs generated during ultrafast melting. Formation of a dislocation during resolidification is illustrated on the cross section of a trough, shown in Figure 37. Similar to the previous case, the deeper part of the interface moves slower. However, when the interface passes this part, it is sealed not ideally but with a missing plane that leads to formation of a stacking fault and generation of a Frank partial dislocation. This mechanism explains generation of dislocations during crystal growth in Ni (100) target. This Frank partial dislocation can be split into Stair-rod and Shockley partial dislocations to minimize the energy. The configuration of the dislocation at 200 ps is presented in Figure 38.

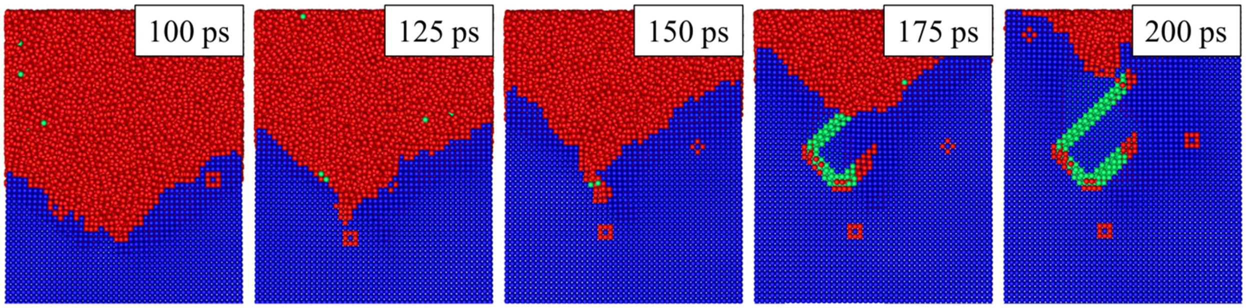

Figure 37. Formation of a partial dislocation during resolidification of (100) target after laser irradiation. Each snapshot represents an enlarged cross section of the dislocation with the box size 8 by 10 nm. The coloring scheme is similar to Figure 25, but atoms with FCC local crystal structure environment are not blanked but shown by blue color.

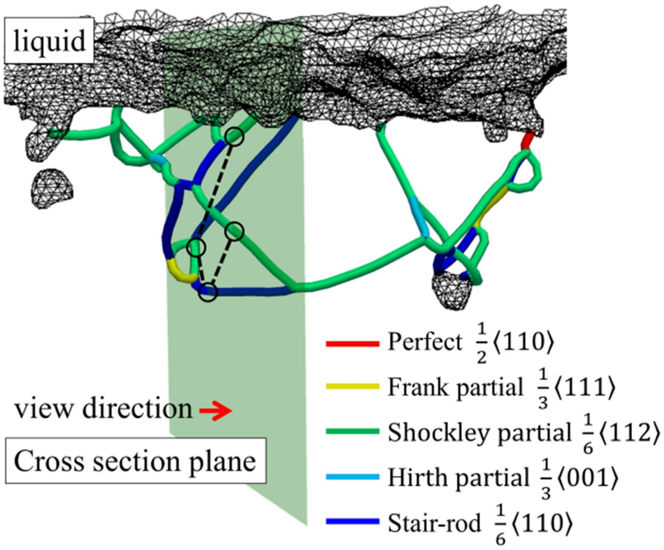

Figure 38. The configuration of dislocations in the snapshot depicted in Figure 37 at 200 ps. Dislocations are colored by their type. The triangulated area corresponds to liquid and clusters of vacancies. The cross section plane of Figure 37 is shown by green; the intersections of the plane with dislocations are marked by black circle, and intersections with stacking faults are shown by dashed lines.

Advancement of the solid-liquid interface increases the length of the dislocations connected to the interface. To avoid a significant increase of the relative contribution of stacking fault energy to the total energy during dislocation growth, the ends of dislocations connected by stacking faults should not significantly spread in lateral directions. Several dislocation loops that fulfil this condition and grow almost vertically are present in the final microstructure illustrated in Figure 28a. These loops consist of interacting Shockley partial and Stair-rod dislocations, similar to Figure 36, and can reach the length 5 nm in the vertical direction. Another possibility is formation of dislocation configurations where only perfect (or split dislocations) are connected to the solid-liquid interface. It can be achieved, for example, by splitting Frank partial dislocation into perfect and Shockley partial (Figure 38, perfect dislocation). After this rearrangement, the dislocations can grow with advancing the solid liquid interface without significant increase of the stacking fault area. The major part of the dislocations in Figure 28a has this configuration.

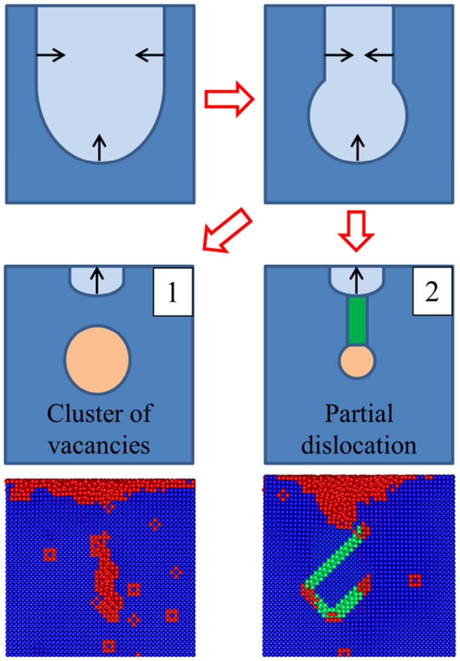

Figure 39. A schematic sketch of the defect generation mechanisms. The plot shows a cross section of the system; arrows illustrate the process of solidification. A cavity generated during advancing the solid-liquid interface can be sealed forming a cluster of vacancies (1). Edges of a trough can be fold with a missing plane forming a stacking fault and generating a partial dislocation (2). The snapshots below illustrate the atomic configuration in each case; the coloring scheme is the same as in Figure 35.

Summing-up the results presented in Figure 35 and Figure 37, the mechanism of defects generation during crystal growth can be described as a sequence of steps that are outlined in Figure 39. Deeper parts of the solid-liquid interface, generated by ultrafast melting or formed by fluctuations, grow slower compared with elevated parts and sealed when the interface passes them. A cavity (1) can be ideally sealed creating a cluster of vacancies, which later may be rearranged into a dislocation loop or dissolve into individual vacancies. Edges of a trough (2) growing toward each other can be folded with a missing plane, especially if the material is laterally compressed. This process creates a stacking fault and generates a partial dislocation.

Folding with a missing plane is only possible for troughs due to their elongation. A cavity cannot be sealed with a missing plane that is consistent with results of small scale simulations with initially flat interface where only cavities are generated, and formation of clusters of vacancies takes place. The reported mechanism is different form classically described formation of prismatic dislocation loops by diffusion and aggregation of vacancies.

Configuration of growth dislocations

The arrangement of dislocations formed during crystal growth may be different from the configuration of dislocations emitted at the initial stage. For example, Figure 28b (011 target) shows that dislocations in the sub-surface part, which is affected by transient melting and following resolidification, have vertical arrangement in contrast to dislocations emitted at the beginning. Also, since in the case of (100) surface orientation (Figure 28a) the vertical orientation is not very pronounced as in the previous case, the configuration of growth dislocations is expected to depend on the target orientation. This subsection discusses the main factors affecting the growth of dislocations during resolididfication.

Since dislocations cannot terminate inside a crystal, they grow with advancement of the solid-liquid interface. During this process, the total energy of a dislocation segment, which depends on the length and arrangement of the dislocation, is minimized. Arrangement of dislocations along close-packed directions is preferable since this configuration corresponds to the lowest energy of the dislocation core and allows splitting of a perfect dislocation into two Shockley partials. In the case of (011) surface orientation there is a close-packed direction perpendicular to the surface, as shown in Figure 29b, which allows both the length minimization and arrangement of dislocations along the close-packed direction. Thus, even if dislocations are emitted initially in (111) and $(\bar{1}11)$ planes (green and yellow planes in Figure 29b), during resolidification dislocations do not continue grow in the direction they were emitted but change their orientation to a vertical one.

In the case of (100) surface orientation, close-packed directions have either 0 or 45 degree angle to the solid-liquid interface, as shown in Figure 29a. It leads to a competition between the vertical configuration corresponding the shortest dislocation length and arrangement along close-packed directions under the 45 degree angle to the interface, which decreases the energy of a dislocation and allows splitting into two partials for further energy minimization. As shown in Figure 28a, some dislocation segments are arranged along close-packed directions and split. However, other segments are not split and have the arrangement close to the vertical one.

Generation of vacancies

Ultrafast energy deposition during laser processing results in not only ultrafast melting and resolidification of the top part of an irradiated target, building up a strong compressive and tensile stresses, and emission of dislocations, but also generates a high concentration of vacancies which can reach the level 10^{-3} of lattice cites. This subsection discusses the effect of the target crystallographic orientation on generation of vacancies.

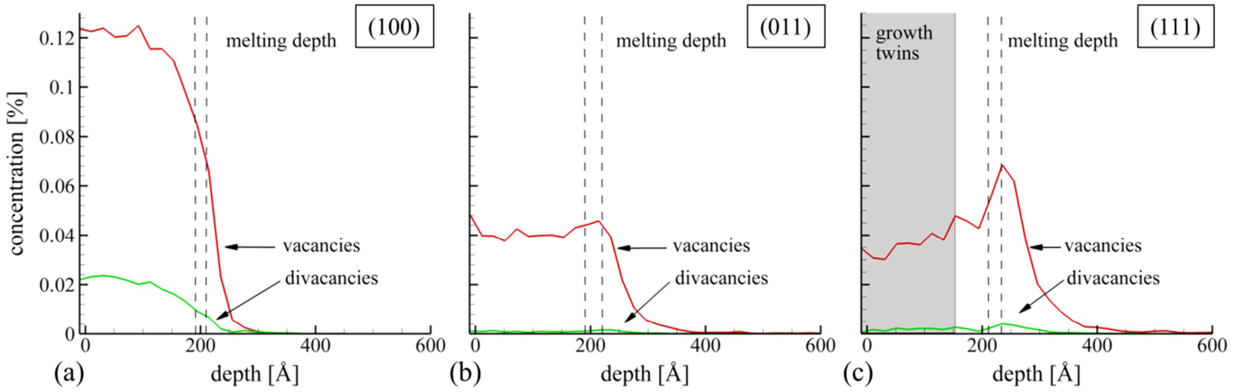

Figure 40. The concentration of vacancies (red) and divacancies (green) in Ni (100) target at 400 ps (a), Ni (011) at 500 ps (b), and Ni (111) at 720 ps (c), which correspond to the end of resolidification.

The concentration of vacancies and divacancies in the irradiated targets after complete resolidification is shown in Figure 40. In the target with (100) surface orientation, ultrafast melting and following resolidification generates very high concentration of vacancies, which reaches 0.12% of lattice cites for vacancies and 0.024% for divacancies. The maximum concentration of vacancies in (011) and (111) targets are 0.048% and 0.068%, respectively. These concentrations are larger than the equilibrium vacancy concentration at the melting point, 0.033%, and exceed the equilibrium vacancy concentration at ~$0.8T_m$, the temperature at the solidification front, by 1-2 orders of magnitude (Section 2.4.1).

To estimate the characteristic vacancy diffusion path, we have computed the vacancy diffusion coefficient in a series of small-scale simulations with a single vacancy performed at different temperatures. The computed prefactor and the diffusion barrier are 1.48×10^{-5} m^2/s and 1.31 eV, respectively. Therefore, at the melting temperature the vacancy diffusion can be estimated as 1.9×10^{-9} m^2/s that gives ~1 nm diffusion path on the time scale of 100 ps, and vacancies almost do not move on the simulation timescale. Thus, in Figure 40 following regions with different vacancy formation mechanism can be identified: vacancies below the melting depth formed at the initial stage (1), and vacancies above the melting depth formed during crystal regrowth (2). In addition, in targets with (011) and (111) surface orientation vacancies at the depth grater 250 Å are mostly produced by dislocation climb (3).

Formation of vacancies at the initial stage cannot be described by diffusion form the solid-liquid interface since the mobility of vacancies is very low: even at the temperature 1.3 T_m, the maximum temperature reached in the simulation, the diffusion coefficient can be estimated as 1.5×10^{-8} m^2/s. Thus, the vacancies below the melting depth must be generated as Frenkel pairs with following escape of interstitials, which have much higher mobility compared to vacancies, into the liquid as discussed in Ref. [81]. At the temperature close to the lattice stability limit, the lattice is significantly distorted, and Frenkel pairs can be formed with much lower barrier compared to a cold crystal. Since the concentration of defects formed by creation of a vacancy-interstitial pairs in the vicinity of homogeneous melting onset can reach 10^{-3}, Ref. [192] suggests formation of Frenkel pairs as the first stage of a homogeneous melting process: the point defects form clusters that growth rapidly and irreversibly if contain more than 10 atoms. At the end of homogeneous melting, remaining clusters of point defects can be clearly seen below the melted part of the target as shown in Figure 31b. Homogeneous melting rapidly cools the sub-surface part of the target, and remaining interstitials escape the solid part of the target leaving high concentration of vacancies in the region below the melting front.

In contrast to the target with (100) surface orientations, in (011) and (111) cases the concentration of vacancies remains high even at the depth 250-300 Å, and several vacancies are present at the depth greater than 400 Å. These vacancies are generated by dislocation climb. As discussed in subsection above, numerous dislocations are generated in targets with (011) and (111) surface orientations at the time scale several tens of picoseconds. Since the dislocations are emitted in several slip planes, interaction of dislocations generates jogs which produce a tail of vacancies during following motion of dislocations as illustrated in Figure 41. In addition, dislocation reactions such as annihilation of dislocations on neighboring planes also generate vacancies. Figure 27 depicts several lines of vacancies produced by dislocations.

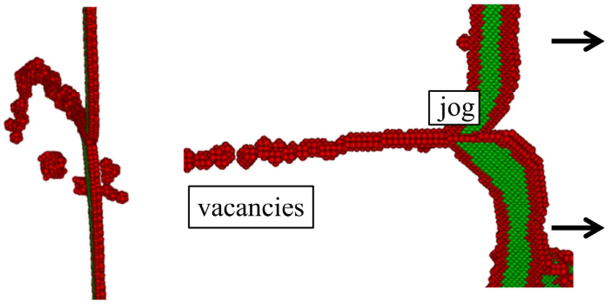

Figure 41. Formation of a tail of vacancies by motion of a dislocation with an atomic jog. The coloring scheme is the same as in Figure 25.

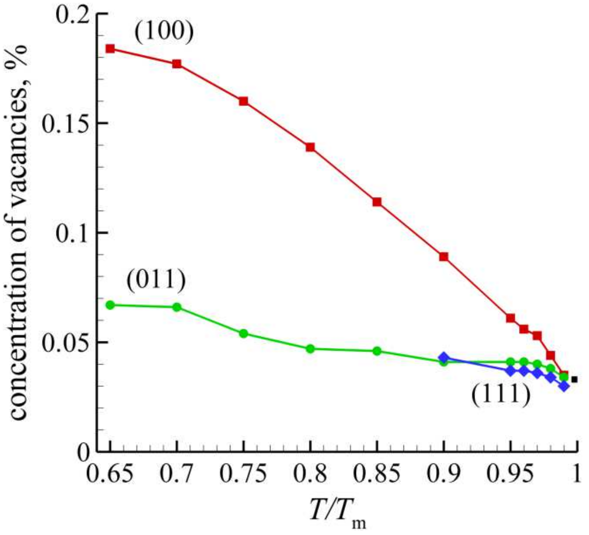

Figure 42. The concentration of vacancies generated during resolidification under conditions of strong undercooling is investigated in a series of atomistic coexistence simulations of Ni system described by the EAM Mishin potential [130]. In contrast to results shown in Figure 40, the concentration of vacancies is computed based on the total number of missing atoms in a particular atomic plain, and vacancies, divacancies, and vacancy clusters are not distinguished. Three low index (100), (011), and (111) orientations of the solid-liquid interface are considered. We do not show the size of the error bar because it is comparable with the size of symbols representing each point. The equilibrium vacancy concentration at the melting point is marked by black square.

During resolidification under the condition of deep undercooling, fast advancing the solid-liquid interface generates high concentration of vacancies. The effect of crystallographic orientation of the solid-liquid interface on the produced vacancy supersaturation in solidification under conditions of deep undercooling is assessed in a series of atomistic simulations of solidification under controlled conditions. Figure 42 shows the dependence of the vacancy concentration on temperature and crystallographic orientation. In the vicinity of the melting point the produced concentration of vacancies is close to the equilibrium vacancy concentration at the melting point, 0.033%, and increases with increasing the level of undercooling. Similarly to results of large scale TTM-MD simulations, the concentrations of vacancies produced in systems with (011) and (111) crystallographic orientations are similar and much lower to one produced in (100) target. Thus, the different concentration of the vacancies in TTM-MD simulations is the result of the interface orientation rather than specific conditions realized in simulations.

Connection to experiment

The results of recent electron backscatter diffraction (EBSD) analysis of the microstructure of polycrystalline Ni targets irradiated by femtosecond laser pulses, reported in Ref. [177], demonstrate a strong effect of the crystallographic orientation of grains in the polycrystalline targets on the generation and accumulation of crystal defects in the surface region, Figure 43. The provided EBSD-generated band slop maps show very high degree of lattice distortion in the regions with (111) surface orientation which related by the authors to the high concentration of dislocations.

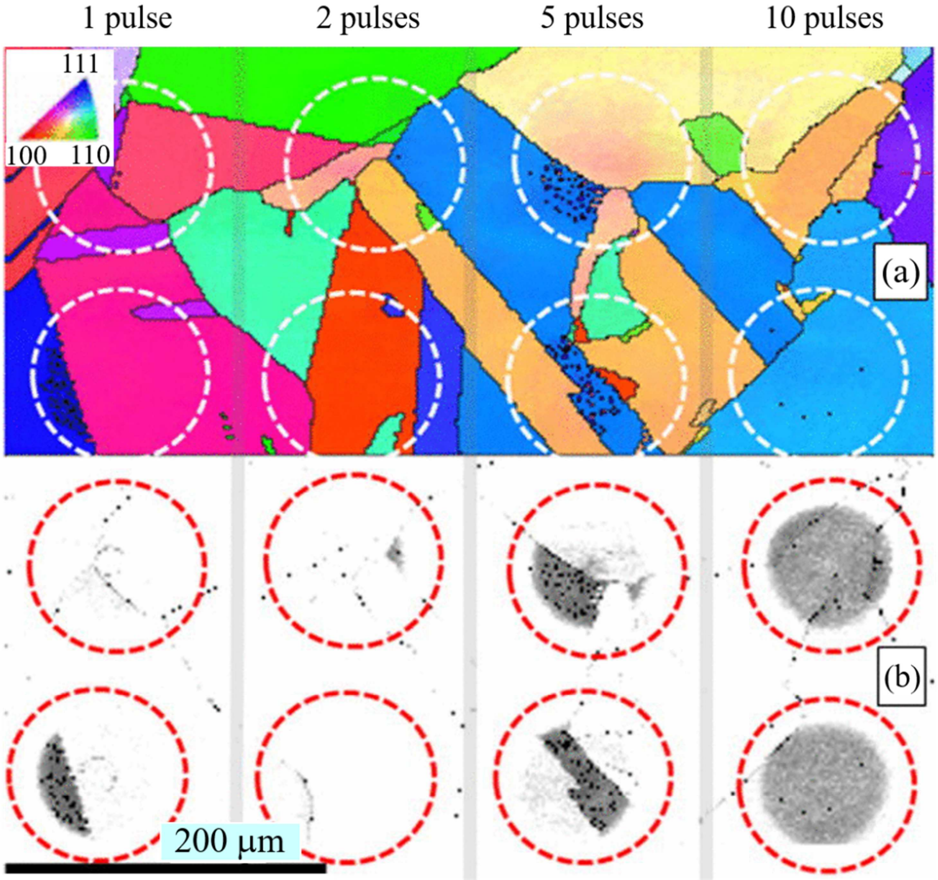

Figure 43. Electron Backscatter Diffraction (EBSD) orientation map and band slope map reflecting the presence of defects in a polycrystalline Ni target irradiated by 50 fs laser pulses at incident fluence of 0.3 J/cm^2. The number of pulses applied to spots shown in each row is indicated at the top of the figure. The figure is adapted from Ref. [177].

The experimentally observed trend is in a good qualitative agreement with results of large-scale atomistic simulations of laser irradiation of Ni targets, reported in this paper. Modeling demonstrates very strong effect of the target crystallographic orientation on the microstructure modification. As illustrated in Figure 28a, simulation predicts minor modification in (100) target, where dislocations only form during solidification. Since in (011) and (111) targets dislocations are emitted during initial relaxation of thermal stresses, they exhibit higher density of dislocations (Figure 28b and Figure 28c), especially (111) case.

Formation of a layer with high density of growth twins during laser processing of a target with (111) surface orientation, discussed in Section 3.2, is compared with experimental results in Ref. [32]. At similar irradiation conditions as in the simulation, the experiment demonstrates formation of a 30 nm nanotwinned layer composed by 5-6 twinned domains. This result in a very good agreement with modeling, which predicts generation of a 15 nm nanotwinned layer composed by 4-5 twinned domains. As suggested in Ref. [32] and Section 3.2, the finial thickness of the twinned domains may be increased during motion of incoherent twin boundaries on the later time scale not included in the MD simulation. Formation of a nanotwinned layer for other surface orientations is not demonstrated both by the simulations and the experiment [32].

Summary

In order to reveal the physical origin of the sensitivity of the laser-induced surface modification to the crystallographic orientation of irradiated surface, a series of large-scale atomistic simulations of femtosecond laser irradiation of Ni targets with (001), (011), and (111) surface orientations is performed. The results of the simulations do confirm the strong effect of the target orientation on the microstructure modification, observed experimentally [177], and provide a detailed description of the defect configuration generated for each surface orientation.

The results of the resolved shear stress analysis performed for different slip systems explain absence of dislocation emission in the case of (100) target and confirm generation of dislocations in two slip planes in (011) and in three slip planes in (111) cases. The theoretically predicted value of the maximum resolved shear stress in (100) target is almost twice lower than in the case of (011) and (111) targets if the same strain is applied. This stronger response leads to faster growth of the shear stress and onset of dislocation emission in (011) and (111) targets before the temperature of the overheated material drops down during homogenous melting of the top part. In (100) target the maximum resolved shear stress is reached only when the temperature near the solid-liquid interface drops almost to the melting point that leads to higher critical shear stress required for dislocation emission. Therefore, in (100) case no dislocations are generated during the initial relaxation of thermal stresses.

In addition to the prompt dislocation emission during the dynamic relaxation of laser-induced stresses, the generation of dislocation loops takes place during resolidification of the transiently melted top region of the irradiated targets. The simulation with (100) surface orientation demonstrates the strong correlation of the crystal defect generation with the solid-liquid interface roughness: for instance, dislocations are formed only in troughs. Based on the analysis of crystal defect generation, the new mechanism of dislocation and vacancy clusters formation during advancing the solid-liquid interface is proposed. Due to the growth instability, deeper parts of the solid-liquid interface grow slower and can be sealed when the interface passes them. After sealing, a cavity creates a cluster of vacancies, which during the following evolution is either rearranged into a prismatic dislocation loop or dissolved. Edges of a trough can be folded with a missing plane that creates a Frank partial dislocation, which can be split into combination of Shockley partials Stair-rod dislocation.

Highly non-equilibrium conditions built during laser irradiation leads not only to active formation of dislocations but also to generation of a high concentration of vacancies, which can reach the level 10^{-3}. In the modeling, three mechanisms of vacancies formation are identified. First, overheating the material close to the lattice stability limit creates numerous pairs of vacancies and interstitials. Interstitials readily escape the solid part due to high mobility, creating a region with high concentration of vacancies right below the melting depth. Second, dislocation climb in the case of (011) and (111) surface orientation is a source of vacancies in the deeper part of the target. Last, fast advancing the solid-liquid interface under the condition of deep undercooling generates high concentration of vacancies in the region experienced transient melting during laser irradiation. Resolidification of a target with (111) crystal orientation under the condition of deep undercooling leads to generation of a high density of growth twins, which is discussed in more details in Section 3.2 and Ref. [32].

The results of large-scale atomistic simulations predict minor modification of the microstructure for (100), moderate for (011), and strong for (111) target orientations that is in a good qualitative agreement with the available experimental data. Overall, the reported results clarify the mechanisms responsible for the laser-induced generation of crystal defects and explain the sensitivity of the structural modification of metal surfaces to the crystallographic orientation of irradiated surfaces.

3.2. Generation of growth twins in laser irradiation of Ni (111)[1]

Abstract: The structural changes generated in surface regions of single crystal Ni targets by femtosecond laser irradiation are investigated experimentally and computationally for laser fluences that, in the multipulse irradiation regime, produce sub-100 nm high spatial frequency surface structures. Detailed experimental characterization of the irradiated targets combining electron back scattered diffraction analysis with high-resolution transmission electron microscopy reveals the presence of multiple nanoscale twinned domains in the irradiated surface regions of single crystal targets with (111) surface orientation. Atomistic- and continuum-level simulations performed for experimental irradiation conditions reproduce the generation of twinned domains and establish the conditions leading to the formation of growth twin boundaries in the course of the fast transient melting and epitaxial regrowth of the surface regions of the irradiated targets. The observation of growth twins in the irradiated Ni (111) targets provides strong evidence of the role of surface melting and resolidification in the formation of high spatial frequency surface structures. This also suggests that the formation of twinned domains can be used as a sensitive measure of the levels of liquid undercooling achieved in short pulse laser processing of metals.

Introduction

High-precision machining of materials with ultrashort laser pulses [1,193,194] is a powerful enabling technology actively used in a broad range of applications in the fields of photonics, biomedical and life sciences [44,195,196]. The preparation and functionalization of material surfaces on the nanometer scale are of prime importance for the advancement of these applications. Micro and nanostructural changes strongly impact surface properties such as optical reflectivity, hydrophobicity, hardness, wear and corrosion resistance, potentially impacting the use of the treated materials [33-35]. Laser-induced surface modification is the result of material response to the extreme conditions of rapid highly localized heating and cooling created in the surface region of irradiated targets by ultrafast laser irradiation. Under multipulse exposition, high densities of crystal defects and subsurface voids can be accumulated during successive thermomechanical loading of the material leading to irreversible surface damage and ablation [17,81,197-202].

---

[1] Results of this work are reported in Ref. [32]. The experimental portion of this work is done by the group of Jean-Philippe Colombier.

While single pulse irradiation can readily alter the surface topography, multiple-pulse irradiation can cause interference between the incident laser light and surface scattered electromagnetic waves, potentially involving surface plasmon excitation [203-206], thus giving rise to periodic modulation of surface morphology with periods close to the laser wavelength, known as Laser-Induced Periodic Surface Structures (LIPSS), or more accurately, Low Spatial Frequency LIPSS (LSFL) [204]. Further details on LIPSS are provided in Section 4.2. In addition, another kind of LIPSS with a periodicity significantly smaller than the laser wavelength, down to $\Lambda \approx \lambda/10$, can be produced. These surface structures are often referred to as High Spatial Frequency LIPSS (HSFL) and can be oriented parallel or perpendicular to the laser polarization [207,208]. The origin of such structures is much less understood and a number of alternative mechanisms have been proposed, including the coherent superposition of scattered and refracted waves [205], laser-induced surface plasma waves [209,210], surface oxidation and higher harmonic generation [211], surface self-organization [212], and coherent nanobubble formation in the subsurface region [136,213]. One general question of fundamental importance is whether the HSFL formation is essentially associated with phase transformations triggered by ultrafast laser irradiation. Since the contrast of HSFL is relatively weak, and the time of the laser melting and resolidification can be very short [104,214,215], the direct time-resolved probing of the laser-induced processes is difficult [214-217]. Nevertheless, a reliable interpretation to the results from *ex situ* analysis of laser-processed samples requires an improved understanding of the connections between the rapid highly nonequilibrium phase transformations and the ensuing surface modifications produced by the laser irradiation. In this subsection we combine experimental characterization of single crystal Ni targets irradiated in the regime where HSFL are produced with a thorough computational and theoretical analysis of laser-induced melting and resolidification processes. The generation of growth twin boundaries is found to be a clear indicator of the role of melting and a sensitive measure of the degree of undercooling reached at the solidification front in laser interactions with Ni (111) targets.

Experiment Results

The experimental portion of this work is done by our collaborators from the group of Jean-Philippe Colombier. A detailed description of experimental results is given in Ref. [32], and below we provide a brief summary relevant to discussion of computational results. Ni (111) surface is irradiated with 46 laser pulses at 1900 J/m^2, level of incident fluence that, when converted to the absorbed fluence using reflectivity of 0.7 [168], exceeds the melting threshold predicted in atomistic simulations. The scanning electron microscopy (SEM) image shows the formation of HSFL in the 5 μm wide central part of the laser spot. A two-dimensional FT spectrum analysis of the SEM images asserts the periodicity of the HSFL is Λ = 70–90 nm.

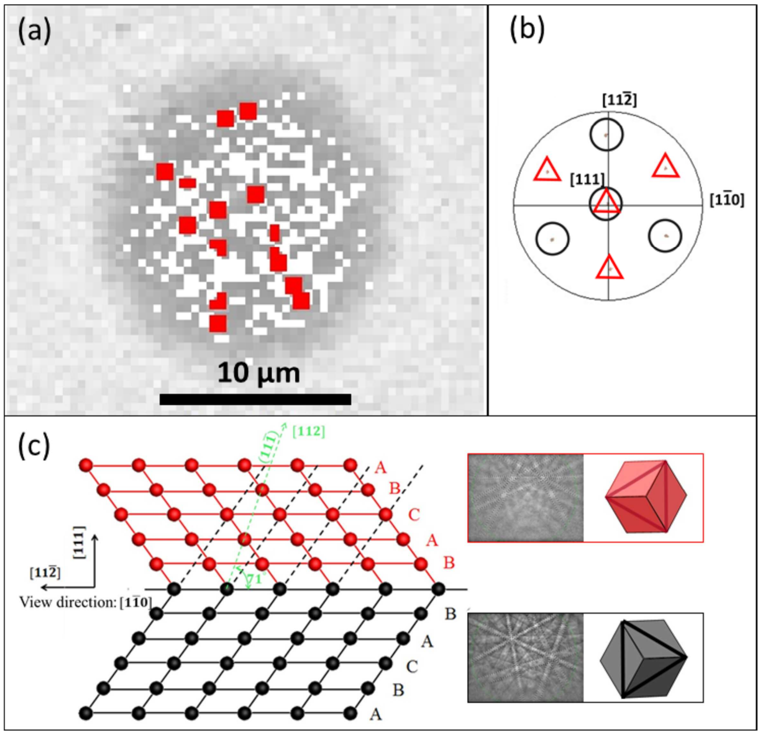

Figure 44. Crystal structure modification in the central area of the laser spot on a Ni (111) crystal irradiated by 46 laser pulses at an incident laser fluence of 1900 J/m^2. (a) EBSD map reflects the lattice distortions due to the presence of crystal defects (the greyer the larger are the distortions) and twins (red-colored spots) in the central area of the laser impact. The white-colored zones in the center of the map are the areas where EBSD indexing was not possible. (b) ⟨111⟩ pole figure from EBSD indexed crystal orientations showing the projection of the original ⟨111⟩ axes (indicated by black circles) along with the new ⟨111⟩ axes appearing due to laser-induced growth twinning (indicated by red triangles). (c) Schematic representation of atomic structure in the vicinity of a twin boundary (left panel) and Kikuchi patterns obtained from nonirradiated surface (lower right panel) and a twinned region generated by laser irradiation (upper right red panel). The corresponding cube presentations of a fcc unit cell, with (111) planes highlighted and common [111] axis pointing out from the paper plane, are also shown next to the Kikuchi patterns for the original and twined crystals. Adapted from ref. [32].

The laser-induced generation of crystal defects is characterized with electron backscatter diffraction (EBSD) and illustrated in Figure 44a. At the center of the laser spot, an area with a diameter of 15 μm rendered with dark-gray color has a higher degree of lattice distortion. The localized white color coded areas in the central part of the laser spot are places without successful EBSD indexing, which is also related to the generation of crystal defects [177]. One type of crystal defects that is prominently present within the irradiated area is the twin boundary. The twins are identified through EBSD indexing in the regions highlighted by the red color in Figure 44a. The EBSD $\langle 111 \rangle$ pole figure generated from the same surface region is displayed in Figure 44b, which sums up the orientation relationship between the lattice of original orientation and twinned lattice. The pole figure manifests clearly the projection of the twinned $\langle 111 \rangle$ axes in addition to the $\langle 111 \rangle$ axes of the original crystal. A schematic representation of the atomic arrangement in the vicinity of a twin boundary is provided in Figure 44c. The areas where the twinning is recorded with a sufficient intensity are highlighted by red color in Figure 44a. For EBSD indexation of twins, a substantial twinned volume is required to generate Kikuchi patterns typical of twinned domains, as shown in Figure 44c.

Figure 45 shows high resolution TEM images on the central part of the laser spot. The bright field (BF) image (Figure 45a) gives an overview of the zone of interest. Figure 45b is the electron diffraction pattern generated from the HSFL and its subsurface region. It reveals the characteristic signature of twinning, with two sets of diffraction patterns emanating from the original lattice and twinned lattice. The yellow dashed-line oval highlights the common (111) diffraction spot shared between the two lattices, as illustrated in Figure 44. The diffraction spot $(3\bar{3}1)$ is attributed to the original lattice and is enclosed by the green dashed-line oval. The new (twinning) diffraction spot $(0\bar{2}4)$ is outlined by the red dashed-line oval. The diffraction spots in Figure 45b are attributed exclusively to the Ni crystal, *i.e.*, no signs of oxidation and formation of NiO_x or Ni-related amorphous material are observed in this region. The three diffraction spots marked in Figure 45b are chosen to generate dark field (DF) images that are color-boxed (in yellow, green and red) and presented in Figure 45c-e, respectively. The DF image taken based on the common (111) diffraction spot (Figure 45c) appears as a matching pair to the BF image (Figure 45a). The $(3\bar{3}1)$ DF image yields a full view of the bulk and six to eight rows of laminated epilayers of lattice with original crystal orientation grown parallel to the surface. In the $(0\bar{2}4)$ DF image, another six to eight complementary rows of laminated twin layers are revealed. These roughly equally spaced layers are 4-5 nm thick and add up to a total of about 30 nm thick surface region. In order to depict the spatial distribution of the epilayers and twins, a small central region is selected from Figure 45d and e (indicated by the dashed-line boxes), the two images of this region are superimposed and represented using false colors in Figure 45f. The mechanisms responsible for the generation of the twinned structure will be elucidated below, with the aid of computational modeling.

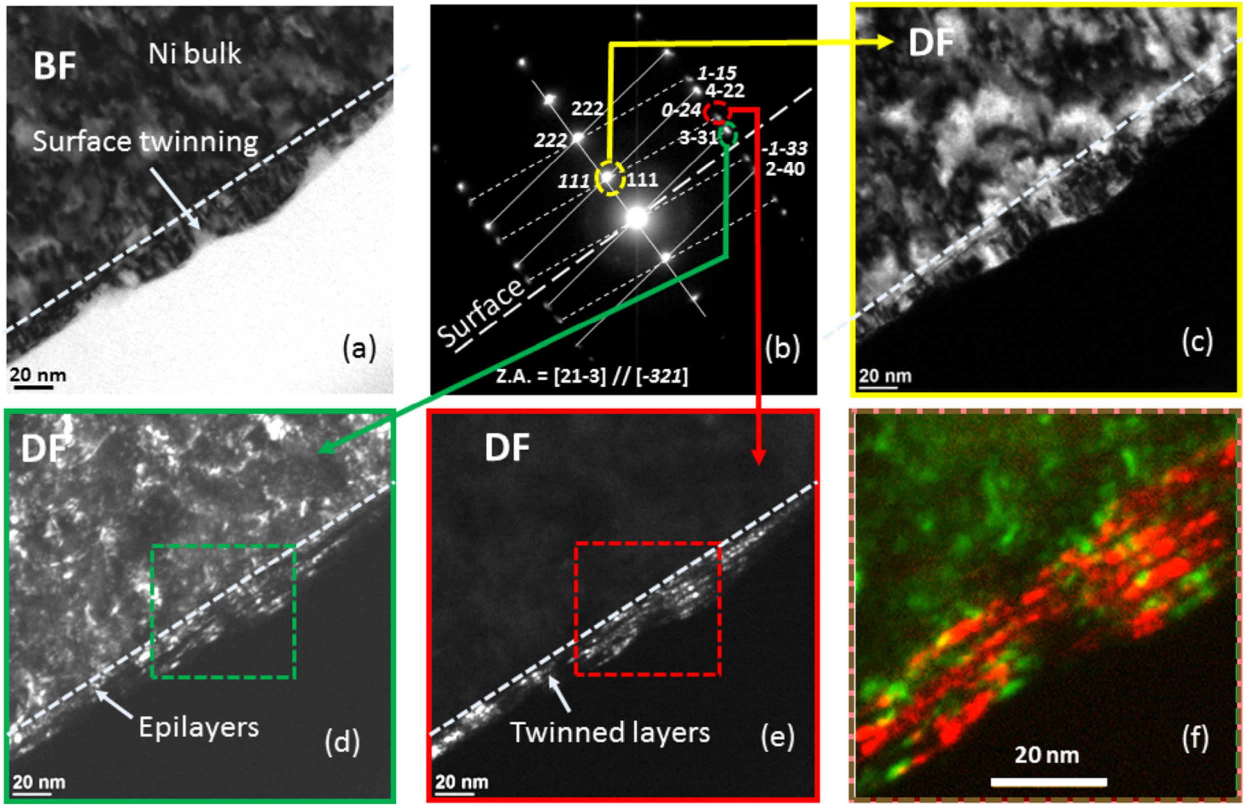

Figure 45. Results of detailed microscopy examination of the central area of irradiated spot. BF image (a). Selected area electron diffraction (SAED) showing two superimposed diffraction patterns: one highlighted by solid white lines with zone axis $[21\bar{3}]$ and diffraction spots indexed in nonitalic characters and another highlighted by thin dashed white lines with zone axis $[\bar{3}21]$ and diffraction spots indexed in italic (b). Note the mirror symmetry with respect to the common (111) plane, i.e., the initial surface of Ni substrate. Selected diffraction spots (111), $(3\bar{3}1)$, and $(0\bar{2}4)$ were used to obtain DF images shown in (c), (d), and (e), respectively. In (c), the bulk of the crystal, epilayers, and twinned domains can be identified. In (d), the bulk of the crystal and the epitaxial layers are revealed. In (e), the complementary details attributed to twinned domains can be seen. The thick dashed white lines in BF and DF images are visual guides outlining the surface region where the laser-induced twinning occurred. The areas marked by the green and red boxes in (d) and (e) are enlarged, superimposed and illustrated in (f). (f) False color image highlighting the spatial distribution of the epilayers (green) and twinned domains (red). Adapted from ref. [32].

Computational and theoretical analysis

The mechanisms and kinetics of laser-induced melting and resolidification of Ni targets are investigated in atomistic and continuum-level simulations performed for irradiation conditions used in the experiments. A single-pulse irradiation is considered in the simulations to evaluate the nature of material modification in one excitation–relaxation cycle. The atomic-level mechanisms responsible for the generation of subsurface microstructure in the course of rapid solidification of transiently melted surface regions are studied in a series of large-scale atomistic simulations, whereas a quick scan of the undercooling conditions created by the laser irradiation at different laser fluences is performed with a continuum model. The mechanisms of the experimentally observed generation of a high density of twin boundaries in the surface regions of single crystal Ni targets irradiated by femtosecond (fs) laser pulses are discussed in this section based on the results of large-scale atomistic simulations of laser interactions with Ni targets, theoretical analysis of the generation of growth twins in the course of rapid solidification under conditions of strong undercooling, and continuum-level modeling of laser-induced melting and resolidification of Ni targets at different laser fluences.

Observation of laser-induced twinning in large-scale atomistic simulations.

The general picture of the laser- induced melting and resolidification processes revealed in the three large-scale simulations using combined two-temperature model (TTM) and classical molecular dynamics method (MD) performed for Ni targets with (111) surface orientation. The details of the computational setup and the initial stage of laser irradiation are provided in Section 3.1. One notable effect that is observed in the course of the epitaxial resolidification of the target with (111) surface orientation is the formation of a high density of coherent twin boundaries, $\Sigma3$ $\{111\}$, at the final stage of the solidification process. This effect is illustrated in Figure 46, where a series of snapshots of atomic configurations in the top 30 nm surface layers of the Ni (111) target are shown. The initial stage of the resolidification process, from 50 to 200 ps, proceeds by the epitaxial regrowth of the crystal, as illustrated by a snapshot shown for 100 ps after the laser pulse. The solidification proceeds simultaneously with increasing undercooling of the melted layer (red region in Figure 46), the velocity of the crystal-liquid interface increases, and a large number of vacancies (red dots) are left behind the solidification front. The green ribbons outlined by red lines in the bottom part of the snapshot correspond to $1/2\langle 110\rangle$ dislocations split into two Shockley partials (red lines) connected by stacking faults (green ribbons). These dislocations are emitted from the melting front during the dynamic relaxation of the laser-induced stresses, as discussed in Section 3.1.

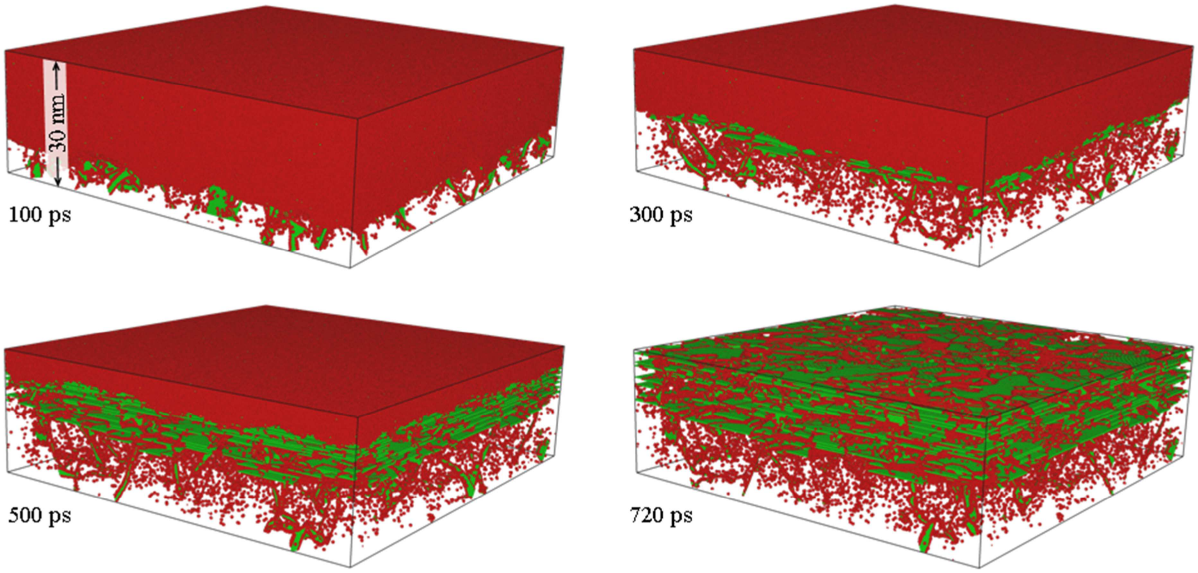

Figure 46. Snapshots of atomic configurations generated in a TTM-MD simulation of a Ni (111) target irradiated by a 50 fs laser pulse at an absorbed fluence of 600 J/m^2. Only the top 30 nm surface region of the irradiated target is shown in the snapshots. The atoms with local structural environment characteristic of fcc crystal structure are blanked to expose the defect structures. The remaining atoms are colored by their local structural environment, so that the green atoms have local structure characteristic of hcp crystals and red atoms belong to the liquid phase, make up dislocation cores, or surround point defects. With this coloring scheme, a single green layer and a double green layer correspond to a twin boundary and a stacking fault in the fcc structure, respectively. The resolidification process is completed by 720 ps after the laser pulse and the top 3.5 nm surface layer is blanked in all snapshots to expose the underlying defect structure in the snapshot shown for 720 ps, where the surface roughness of ~2 nm is observed. Adapted from ref. [32].

The defect structure of the resolidified region changes abruptly when the temperature in the vicinity of the solidification front drops down to about $0.85T_m$ at about 180 ps after the laser pulse, and a large number of coherent twin boundaries appear in the planes parallel to the advancing (111) crystal-liquid interface. The twin boundaries (green layers parallel to the surface) can be seen in the snapshot shown in Figure 46 for 300 ps, and the region affected by twinning expands as the solidification front propagates toward the surface of the target. A clear view of multiple twin boundaries with a characteristic thickness of twinned domains on the order of several nm is provided in Figure 47, where the final microstructure of the top part of the resolidified target, shown without blanking the fcc atoms, and an enlarged view of a representative vertical cross-section of the surface layer are presented.

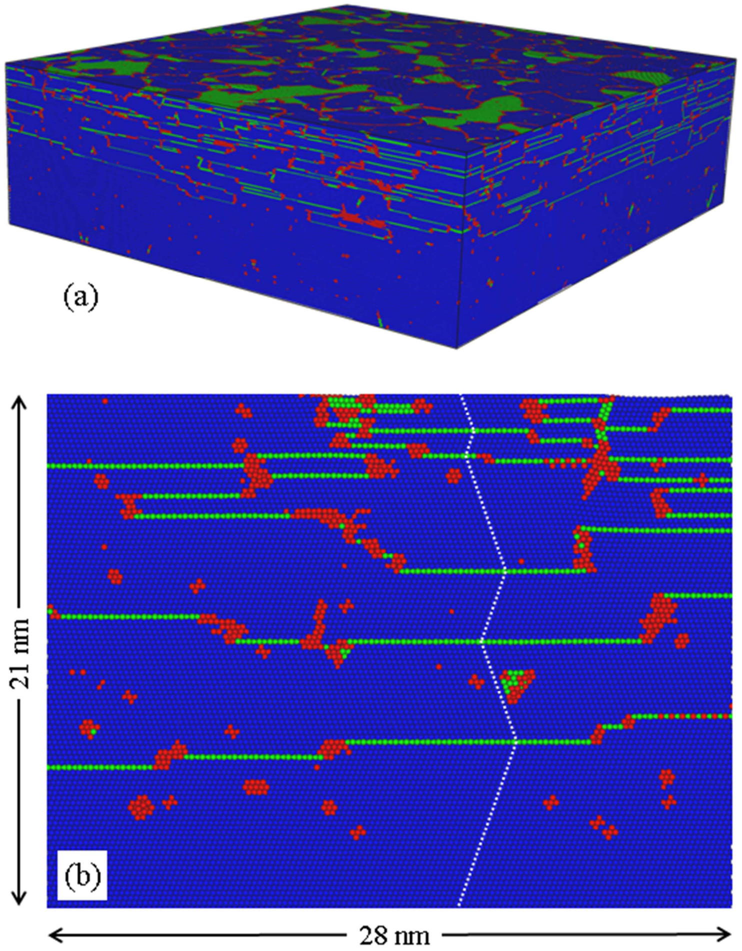

Figure 47. An alternative view of the last configuration (720 ps) of Figure Figure 46, in which the fcc atoms are shown and colored blue (a) and an enlarged view of a representative vertical cross-section of the surface layer of the resolidified target (b). Additional details of the color scheme are given in Figure 46 caption. The dashed line in (b) shows the altering orientation of atomic planes in the twinned domains. Adapted from ref. [32].

The flat islands of the coherent twin boundaries are connected with each other by incoherent twin boundary segments that remain relatively mobile after the complete solidification. One can expect that the motion of the incoherent twin boundaries would result in the disappearance of some of the smaller twinned domains upon further cooling of the surface down to the room temperature. Nevertheless, some of the twin boundaries can be expected to remain in the target as the mobility of the incoherent twin boundaries sharply drops with increasing thickness of the twinned domains [218]. To illustrate this point, the atomic configuration shown in Figure 47a has been annealed at $0.9T_\mathrm{m}$ for 1.5 ns. This temperature is much higher than the $0.76\ T_m$ recorded at the end of the resolidification process in the simulation of laser processing, which increases the mobility of incoherent twin boundaries (ITBs) and enables us to study the evolution of the crystal structure at a much shorter time scale. The initial system configuration produced by laser excitation, as well as snapshots taken at 0.5, 1, and 1.5 ns of the annealing simulation are presented in Figure 48. Since the mobility of ITBs strongly depends on the thickness of twinned domains [218], the thin domains rapidly shrink during the first 500 ps, and only sufficiently thick domains remain and slowly evolve during the remaining 1 ns. These twin domains will stay even if the annealing is performed for a longer time, which is consistent with experimental observations of twinned domains in laser processed targets. The thickness of the remaining twined domains, ~10 nm, is also close to the experimentally reported values, Figure 45. Since during laser processing when ultrafast cooling takes place the temperature drops down to 0.61 T_m in less than 1 ns, relatively thin twinned domains, with thickness less than 10 nm, may be frozen in and remain after cooling the system down to the room temperature.

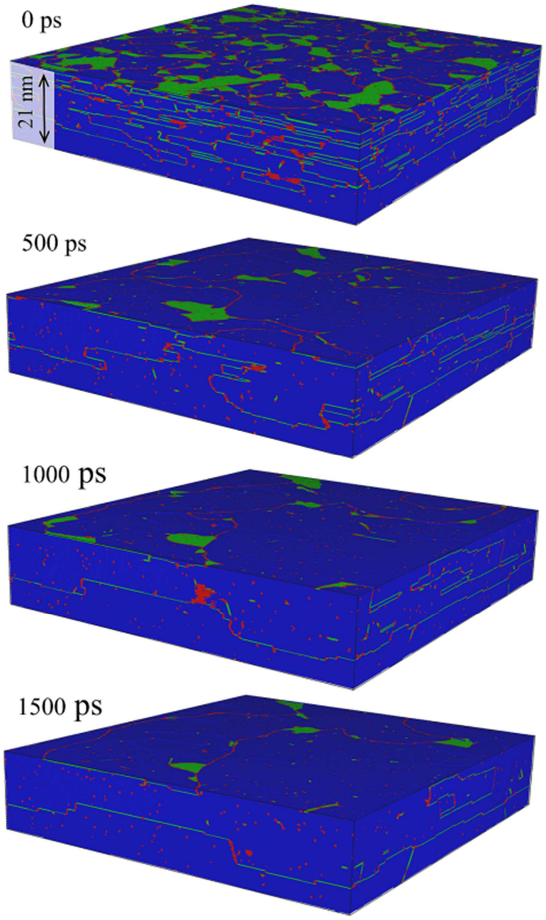

Figure 48. Snapshots of atomic configurations generated after annealing a crystal structure produced in a TTM-MD simulation of a Ni (111) target irradiated by a 50 fs laser pulse at an absorbed fluence of 600 J/m^2. Only the top 24.5 nm surface region was cut and annealed at 0.9 T_m. The atoms are colored based on the local crystal structure environment. Blue, green, and red colors correspond to FCC, HCP and unidentified local crystal structure environment, respectively. With this coloring scheme, a single green layer and a double green layer represent a twin boundary and a stacking fault in the FCC structure. Unidentified atoms correspond to dislocation cores, and point defects. The top 3.5 nm surface layer including 2 nm surface roughness is blanked in all snapshots to expose the underlying defect structure.

To make a direct connection to the experimental observation of twinning in the surface regions of the irradiated targets, the pole figures similar to the one shown in Figure 44b are calculated for the three targets that experienced laser melting and resolidification. The pole figures in Figure 49 show the projections of ⟨111⟩ directions for all fcc atoms in the top 20 nm surface regions of the resolidified targets, with the ⟨111⟩ poles corresponding to the original ⟨111⟩ directions in the single crystal targets marked by circles. In the pole figure calculated for the target with (111) surface orientation, new ⟨111⟩ poles created by the growth twinning are clearly present and marked by triangles in Figure 49a. In contrast, only the original ⟨111⟩ poles are present in the pole figures calculated for targets with (100) and (011) surface orientations, Figure 49b and Figure 49c, indicating that no twins are introduced by laser-induced melting and resolidification of these targets. The computational predictions are in a good agreement with the experimental observation of the appearance of new poles associated with twinning for targets with (111) surface orientation, Figure 44b, and the absence of twinning in targets with (100) surface orientation.

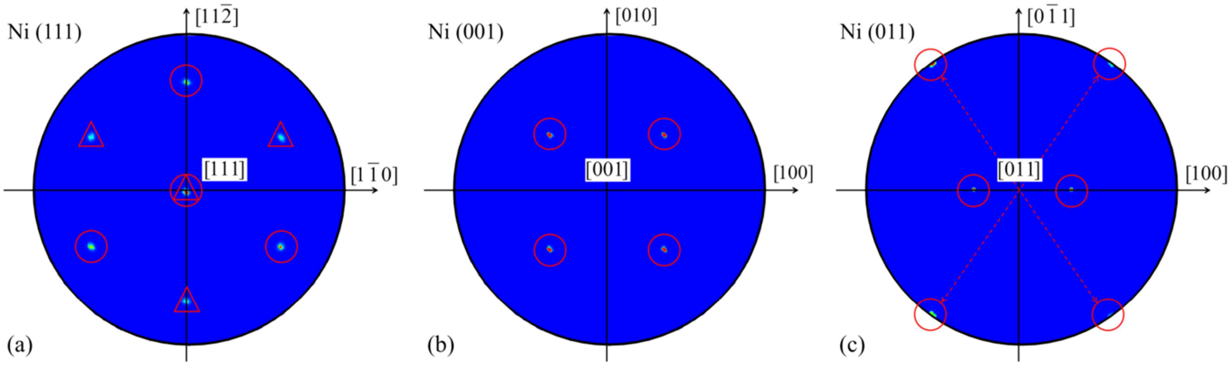

Figure 49. The ⟨111⟩ pole figures calculated for 20 nm top regions of Ni targets with (111), (100) and (110) surface orientations irradiated by 50 fs laser pulses at an absorbed fluence of 600 J/m^2. All calculations are done after complete solidification of the irradiated targets. The ⟨111⟩ poles that correspond to the original single crystal are marked by circles and the new ⟨111⟩ poles generated by twinning are marked by triangles. The twinning is only observed for (111) surface orientation of the irradiated target. Adapted from ref. [32].

Mechanisms of growth twinning under conditions of strong undercooling

In order to evaluate the conditions for the formation of Σ3 {111} growth twins in the process of rapid solidification, a series or small scale simulations is performed under fixed temperature and zero pressure conditions for a 28 nm × 28 nm × 50 nm system containing, in its initial state, a 11 nm thick crystalline slab with two (111) surfaces surrounded by liquid. No twins are observed to form in the solidification process occurring under conditions of weak undercooling, at $T > 0.86T_m$. The formation of first twin boundaries is detected at $T \approx 0.86T_m$, and the density of the twin boundaries is increasing with decreasing temperature. The threshold-like condition for the onset of the generation of the growth twins and the decreasing size of the twinned domains with increasing undercooling can be explained by a simple thermodynamic model [150] that considers the advancement of the solidification front through the nucleation and lateral growth of two dimensional atomic islands on (111) terraces of the solid-liquid interface. This model is briefly outlined and applied to the epitaxial regrowth (111) Ni targets below.

The nucleation of a new atomic layer on a (111) facet of the growing fcc crystal can produce one of the two possible stacking sequences of the close packed atomic planes, AB**C** sequence of the regular fcc structure and AB**A** sequence which, in turn, may lead to the formation of a twin boundary (AB**A**CB sequence of planes) or a stacking fault (AB**A**BCA or AB**A**CAB for the intrinsic and extrinsic stacking faults, respectively) in the growing fcc crystal. Given the more than twice higher energy of the stacking faults as compared to twins [219], we can neglect the possibility of the appearance of stacking faults in the growth process and only consider the formation of twins. The change in the free energy due to the nucleation of a round atomic island of radius r with the fcc stacking sequence of the close packed planes can be expressed as

$$\Delta G_r^{fcc}(r,T) = 2\pi r\gamma_{step} - \pi r^2 h\Delta G_v(T) \qquad (3.13),$$

where $\Delta G_v(T)$ is the free energy difference between the liquid and solid phases per unit volume, h is the spacing between $\{111\}$ planes, and γ_{step} is the free energy per unit length of a step on a $\{111\}$ solid-liquid interface. When the nucleation results in the AB**A** stacking of the planes, the extra energy associated with the faulted stacking has to be accounted for in the free energy calculation and can be approximated by the energy of the twin boundary in a bulk crystal, γ_{twin}. The energy of the circular nucleus in this case can be expressed as

$$\Delta G_r^{twin}(r,T) \approx 2\pi\gamma_{step} - \pi r^2 \cdot (h\Delta G_v(T) - \gamma_{twin}) \qquad (3.14).$$

It is apparent from the above equation that small values of undercooling, when $\Delta G_v < \gamma_{twin}/h$, the free energy is increasing for any radius of the nucleus, and no growth twins can be generated. Using the approximation of $\Delta G_v \approx \Delta \mathrm{H_f}(1 - T/T_m)$, the critical temperature below which the twin boundaries can be formed in the solidification process can be estimated as

$$T_c \approx T_m \cdot \left(1 - \frac{\gamma_{twin}}{\Delta H_f h}\right) \qquad (3.15).$$

For the EAM potential used in the MD simulations of Ni [130], γ_{twin} = 68 mJ/m^2, heat of fusion ΔH_f = 0.187 eV/atom = 2.59 × 10^9 J/m^3, h = 2.09 Å at the melting point, and the value of T_c can be estimated to be 0.87T_m. An estimation based on experimental parameters of Ni, γ_{twin} = 43 mJ/m^2 [130], ΔH_f = 2.58 × 10^9 J/m^3 [220], and h = 2.09 Å at $T \approx T_m$ [221], yields a comparable value of T_c = 0.92T_m.

From the free energy expressions given by Eqs. 3.13 and 3.14, the activation barriers for the formation of the fcc and twinned nuclei can be obtained:

$$G^*_{fcc}(T) \approx \frac{\pi\gamma^2_{step}}{h\Delta G_v(T)},\ G^*_{twin}(T) \approx \frac{\pi\gamma^2_{step}}{h\Delta G_v(T) - \gamma_{twin}} \qquad (3.16).$$

The relative probability of the nucleation of twin and fcc planes can then be expressed as the ratio of the corresponding nucleation rates:

$$\frac{I_{twin}}{I_{fcc}} \approx exp\left(\frac{\left[G^*_{fcc}(T) - G^*_{twin}(T)\right]\Omega_a}{k_B T}\right) \approx exp\left(-\frac{\pi\gamma^2_{step}\gamma_{twin}\Omega_a}{k_B T h\Delta G_v(T)[h\Delta G_v(T) - \gamma_{twin}]}\right) \qquad (3.17).$$

This equation suggests that the nucleation of twins starts when the temperature of the crystal-liquid interface drops below T_c, and the probability of the twin formation increases with increasing undercooling. These conclusions of the theoretical analysis are in a good agreement with the results of TTM-MD simulations (Figure 46 and Figure 47), where the appearance of twin boundaries is only observed when the temperature drops below 0.85T_m and the twinning domains get thinner closer to the top surface of the target, where the solidification takes place under conditions of stronger undercooling.

Laser fluence dependence of the solidification conditions and twinning

To predict the dependence of the thickness of the surface layer affected by the growth twinning on laser fluence, a series of continuum-level simulations are performed with the TTM model enhanced with a description of nonequilibrium melting and solidification as Section 2.2.1. The material parameters in the TTM equation for the electron temperature are the same as in the TTM-MD model used in the simulations described above. The lattice heat conduction is neglected, and the lattice heat capacity is assumed to be constant and equal to 3.96 × 10^6 Jm^{-3}K^{-1} [220]. The values of parameters V_0 = 2270 m/s and E_a = 4.52 × 10^9 J/m^3 (correspond to 0.326

eV/atom with Ω_a = 11.55 Å^3 obtained from MD simulations) are calculated by fitting Eq. 2.34 to the velocities predicted for (111) Ni interface in MD simulations performed under controlled temperature and pressure conditions in the range of temperatures from 0.65Tm to 0.95T_m. The simulations are performed for the values of absorbed laser fluence ranging from 500 J/m^2, just above the threshold for surface melting, up to 1300 J/m^2, close to the threshold for photomechanical spallation identified in TTM-MD simulations.

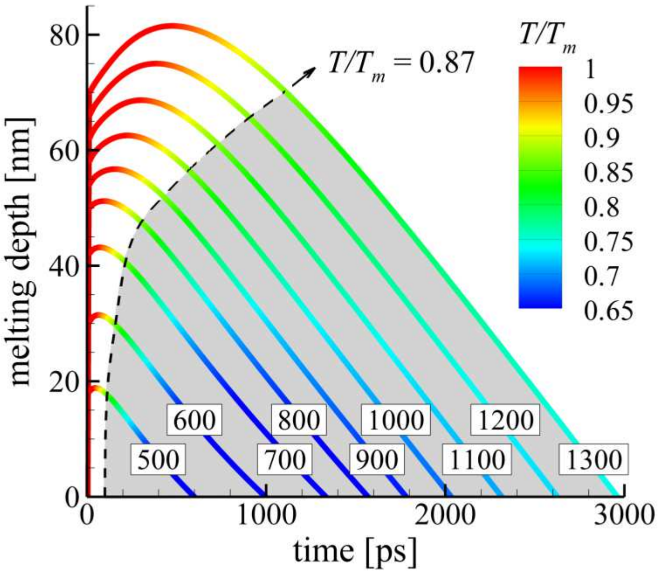

Figure 50. Evolution of the melting depth and temperature at the liquid–crystal interface predicted in TTM calculations accounting for the kinetics of nonequilibrium meting/solidification. The curves on the plot correspond to simulations of Ni targets irradiated by a 50 fs laser pulse at different values of absorbed laser fluence marked in the plot in units of J/m^2. The lines are colored according to the temperature at the solidification front. The gray region outlined by the dashed line corresponds to the conditions of strong undercooling (T < 0.87 T_m), when the growth twinning is predicted in the theoretical analysis and atomistic TTM-MD simulations. Adapted from ref. [32].

The results of the simulations are shown in Figure 50, where the evolution of the melting depth and temperature at the liquid-crystal interface are plotted for different laser fluences. The fast homogeneous melting, occurring on the time-scale of electron-phonon equilibration, is responsible for the initial jump of the melting depth and is followed by additional heterogeneous melting through the propagation of the melting front deeper into the bulk of the target at higher fluences. The melting is followed by resolidification of the target proceeding under conditions of increasing undercooling of the liquid-crystal interface below the equilibrium melting temperature. The fastest cooling and the maximum undercooling at the end of the resolidification process are realized close to the melting threshold, when the melting depth is comparable to the depth of the laser energy deposition and a steep temperature gradient is created at the liquid-crystal interface by the end of the homogeneous melting process. The cooling rate and the maximum undercooling are decreasing with increasing fluence, with the temperature of the liquid−crystal interface at the time it reaches the surface raising from its minimum of ~$0.58T_m$ at 600 J/m^2 up to ~$0.74T_m$ at 1300 J/m^2. The overall picture of the fluence dependence of the melting and resolidification processes predicted in the TTM calculations is consistent with the earlier TTM-MD simulations performed for Ni targets [104], with small quantitative differences related to the differences in the parameters adopted in the two series of simulations.

The condition for the onset of growth twinning, $T = 0.87T_m$, predicted theoretically and confirmed in the atomistic simulations, is marked in Figure 50 by the dashed line. The depth of the region affected by twinning (gray region in Figure 50) increases rapidly at laser fluences close to the melting threshold and shows signs of saturation as the laser fluence approaches the spallation threshold. Note that the decrease of the cooling rate and the levels of undercooling with increasing fluence suggest that the depth of the surface region affected by twinning may even shrink at higher laser fluences in materials with higher energies of twin boundaries, where T_c is lower, Eq. 3.15. Moreover, the weaker undercooling can be expected to result in the lower probability of the nucleation of twin boundaries, Eq. 3.17, thus increasing the average thickness of twinned domains at higher laser fluences.

The computational results provide an explanation for the increase of both the region affected by twinning and the thickness of twinned domains with increasing laser fluence observed in experiments discussed earlier. Using reflectivity of 0.7 at laser wavelength of 800 nm [168], the experimental incident laser fluences of 1900 and 3800 J/m^2 can be converted to absorbed fluences of 570 and 1140 J/m^2, respectively. The TTM calculations predict the maximum levels of undercooling at the end of resolidification of $0.58T_m$ and $0.71T_m$ at the absorbed fluences of 600 and 1100 J/m^2, respectively, thus explaining the substantially larger thickness of the twined domains observed at the higher laser fluence. Moreover, the region affected by the growth twinning is predicted to be deeper at the higher fluence, which is also qualitatively consistent with the experimental observations.

Further increase of the laser fluence beyond the spallation/ablation threshold results in removal of a hot surface material from the bulk target, leading to the increase in the cooling rate during the solidification of the remaining shallow melted region [104]. The two factors, namely, the drop in the depth of the melted region remaining after the ablation of the top layer of the target and the increase in the cooling rate, compete with each other in defining the final thickness of the twinned region. The evaluation of the dependence of the layer affected by growth twinning on laser fluence in the ablation regime is ongoing and will be reported elsewhere. Irradiation with longer laser pulses, in the range of hundreds of picoseconds and nanoseconds, produces smaller temperature gradients and cooling rates during resolidification [222], and reduces the depth of the twinned region. Continuum level TTM calculations suggest that pulses longer than 3 ns cannot produce a sufficiently strong undercooling for generation of growth twins in Ni (111) targets.

Connections between transient phase transformations and generation of HSFL

The clear experimental evidence of the laser-induced generation of a laminar subsurface structure composed of twinned domains and epilayers, combined with the mechanistic insights provided by the theoretical analysis and atomistic simulations, indicates that the growth twinning can be used as a sensitive "fingerprint" of the transient melting and resolidification induced in a fcc metal target/grain with {111} surface orientation by short pulse laser irradiation at laser fluences near the melting threshold. In the absence of growth twinning, the structural signatures of the transient melting and resolidification (e.g., generation of a high vacancy concentration in a Cr (001) target [81]) may be too weak to be detected in *ex situ* experimental characterization. We can conclude, therefore, that the growth twinning in fcc metal targets with {111} surface orientation provides the most clear marker of melting at laser fluences below the threshold for subsurface cavitation and spallation [17,104].

The generation of the subsurface twins in the irradiated Ni (111) targets correlates with the formation of HSFL in the multipulse irradiation regime. The HSFL are observed exclusively in the central part of the laser spot, where the subsurface twins are also present, suggesting a direct link between the transient melting and the formation of the HSFL. Despite the relatively small thickness of the layer experiencing laser melting and resolidification (the total thickness of the twinned domains and epilayers at the center of the laser spot measures about 30 nm), the HSFL with sub-100 nm periodicity are observed to grow entirely in the resolidified layer, with the peak-to-valley amplitude attaining 20 nm in the center. This observation suggests a substantial redistribution of the melted material in the course of repetitive laser melting and resolidification of the thin surface layer of the target. While the exact mechanisms driving the material redistribution remain the subjects of ongoing debates [136,205,207-213], the results of the present study suggest an important role of the laser-induced surface melting in the formation of HSFL. The presence of a twinned domain in the off-center part of the laser spot, where no HSFL is observed, also suggests that the development of the surface roughness may rely on the melting depth exceeding a certain minimum level. Note that HSFL studied in the experimental part are formed at a laser fluence that is substantially below the spallation/ablation threshold, and generation of HSFL is not related to the material removal from the irradiated target.

Summary

The results of a combined experimental and computational study of the short pulse laser interaction with single crystal Ni targets reveal a direct connection between the laser-induced melting/resolidification and the formation of HSFL. The occurrence of melting is evidenced by the formation of nanoscale lamellar structures of interlaying twinned domains and epilayers in the surface regions of irradiated Ni (111) targets. Atomistic- and continuum-level simulations performed for the experimental irradiation conditions reproduce the generation of twinned domains in the course of the rapid solidification of the transiently melted surface regions of the irradiated targets. Theoretical analysis of the microscopic mechanisms of the solidification process yields the conditions leading to the onset of the growth twinning and establishes the connection between the degree of undercooling and the density of twins generated at the solidification front. The laser fluence dependence of the density and thickness of the twinned domains revealed in the experimental study is explained based on the results of continuum-level simulations of nonequilibrium laser-induced melting and resolidification. Both the thickness of twinned domains and the depth of the region affected by twinning are in a good quantitative agreement with the experimental results. In multipulse irradiation regime, the appearance and growth of sub-100 nm HSFL oriented parallel to the laser polarization is observed in the thick twinned domains in the center of the laser spot, highlighting the connections between melting, melt depth, and generation of HSFL. Overall, the results of experimental characterization of laser processed targets, combined with predictions of atomistic and continuum-level simulations, provide a clear evidence of an intrinsic link between the laser-induced melting and HSFL formation.

3.3. Atomistic and Theoretical Study of Growth Twinning in (111) Ni

Abstract: Formation of growth twins during resolidification of Ni with (111) solid-liquid interface under the condition of deep undercooling, revealed in the previous section, is investigated in details in a series of atomistic simulations. The mechanism of growth twinning is discussed based on the thermodynamics analysis of twin nucleation and growth. A method of step free energy calculation designed in Section 2.3.2 and applied for Ni have opened a door for the direct comparison of the results of Molecular Dynamics (MD) simulations with theoretical predictions. A threshold like behavior for onset of twin generation, which is described by the thermodynamics analysis, is well reproduced in the modeling. However, the density of twin boundaries at the end of resolidification is demonstrated to be several times smaller than theoretically predicted values. The analysis of the crystal structure evolution has demonstrated that the density of twin boundaries generated at the stage of nucleation and growth agrees well with the thermodynamics analysis. Though, the density significantly decreases during following incoherent twin boundaries (ITB) motion in de-twinning.

Introduction

Nanotwinned metals have demonstrated superior mechanical strength (1 GPa for copper and 6.5 GPa for steel) combined with high ductility (up to ~10% strain) [151,223-229], which are typically mutually exclusive but very desired for numerous applications. This enhancement of material properties is achieved by impeding dislocation glide by coherent twin boundaries (CTB), or Σ3 {111}, and incoherent twin boundaries (ITB) [229-231] combined with mobility of ITB in de-twinning [232]. Moreover, nanotwinned metals in contrast to nanocrystalline materials have higher electrical conductivity [223,233], thermal stability [234], and fatigue resistance [235,236]. Several approaches such as generation of deformation twins by shock loading [237] and generation of high density of growth twins in a vapor and electrodeposition [151,238-240], which produce structures with sufficiently high twin density, have been reported. A recent study [32] has provided evidence of growth twins generation during propagation of {111} solid-liquid interface under condition of strong undercooling that is readily achieved in a short pulse laser processing of metals or ultrafast quenching [241].

Our study is focused on formation of growth twins during resolidification of deeply undercooled metals. The mechanism of growth twinning under these conditions has already been described based on a thermodynamics analysis of nucleation probability of twins in Ref. [150], however, this study provides a general discussion without putting material properties in the model to determine the density of twin boundaries. Also, the model has not been verified by experimental results or atomistic simulation. Meanwhile, our work reported in Ref. [32] and

Section 3.2, discusses MD simulation of laser processing of a metal target and demonstrates a very good agreement between the thermodynamics prediction and the observed undercooling that corresponds to the onset of growth twining, though, the density of twins has not been estimated and compared. One of the main obstacles that did not allow a direct comparison of the twin density predicted by the theoretical model with results of atomistic simulations or experiments is difficulty of step free energy measurement. It is very important parameter of the model that can adversely affect the predicted concentration of twins since the nucleation probability has exponential dependence on the step free energy.

In this section we provide a comparison of generation of growth twins during propagation of (111) solid-liquid interface in deeply undercooled Ni in atomistic simulations with the theoretical prediction based on the thermodynamics analysis. A method of step free energy calculations in MD simulation based on the capillarity wave approach is developed (Section 2.3.2) and applied for Ni that opens a door for direct comparison of the theoretical model and MD simulation. The threshold like behavior for onset of twin formation is in a good agreement with the thermodynamics analysis. Notwithstanding, the density of twins generated in atomistic simulations to the moment of complete resolidification at the temperatures below 0.86 T_m is appeared to be several times smaller than theoretically predicted value. The following analysis of the crystal structure evolution reveals the important role of de-twinning, which significantly decreases the density of twin boundaries, in formation of the final crystal structure and confirms correctness of the thermodynamics prediction at the stage of nucleation and growth. Annealing of the nanotwinned crystal further supports the role of de-twinning and suggests that the final crystal structure generated under conditions when twins form is significantly affected by the thermal activation of de-twinning.

Computational setup

The resolidification of deeply undercooled Ni targets is investigated in a series of atomistic simulations. The system setup is illustrated in Figure 51a. The initial system configuration is composed of a solid (111) precursor with the thickness 54 monoatomic (~11 nm) planes surrounded by liquid. The total length of the systems in the direction perpendicular to the solid-liquid interface is approximately 50 nm. The lateral sizes of the system are approximately 28 nm, which are adjusted to fit the equilibrium lattice constant at the simulation temperature. Periodic boundary conditions are applied along lateral directions. The liquid and solid parts of the systems are thermalized independently and combined together to create solid-liquid interfaces. Outer surfaces of the liquid parts are kept free to allow volume relaxation during resolidification. The total number of atoms in each simulation is ~3.4 million. The interatomic interaction is described based on EAM Ni potential [130]. This potential provides more accurate, in respect to other available Ni potentials [178], description of stacking fault and twin boundary energies, which are crucial for modeling of growth twinning. The simulations are performed in the temperature range 0.65-1.0 T_m with the temperature step 0.05 T_m; the melting temperature is 1701 K [182]. The analysis of the crystal configuration generated during resolidification is accomplished by using the crystal structure analysis tool [179,180].

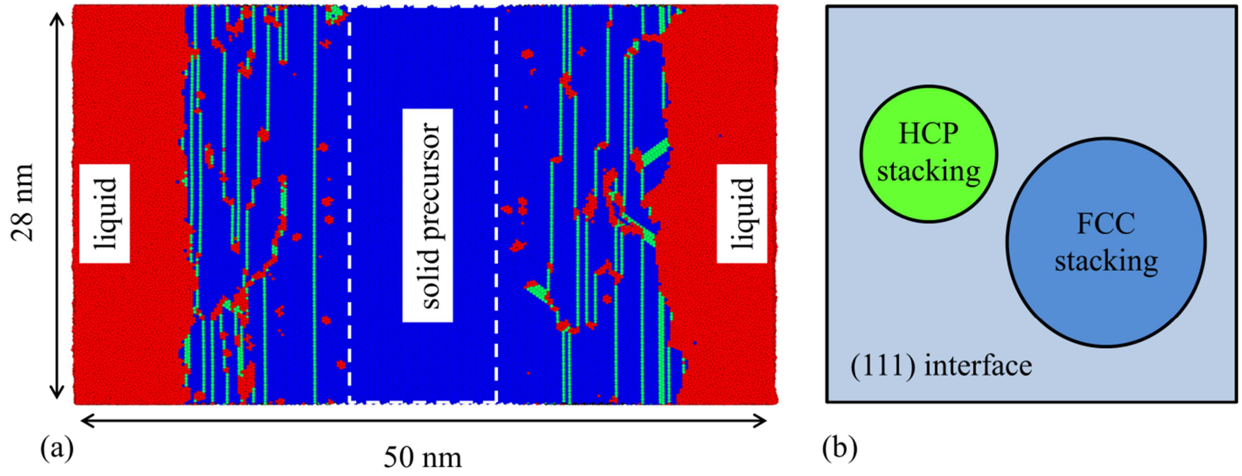

Figure 51. (a) The system setup used in MD simulations. The background corresponds to the side view of a system configuration at 300 ps and the temperature 0.76 T_m. The atoms are colored based on the local crystal structure environment. Blue, green, and red colors correspond to FCC, HCP and unidentified local crystal structure environment, respectively. With this coloring scheme, a single green layer and a double green layer represent a twin boundary and a stacking fault in the FCC structure. Unidentified atoms correspond to liquid, solid-liquid interface, dislocation cores, and point defects. The material which corresponds to the solid part of the initial system is outlined by white dashed rectangle. (b) A schematic representation of formation of nuclei with FCC and HCP local stacking sequence on (111) surface during resolidification.

Growth twinning: theoretical analysis and MD prediction

As described in Section 3.2, the resolidification process of FCC crystal in the case of (111) solid-liquid interface can be described as a nucleation of monoatomic ledges on a (111) facet with following growth in the lateral directions. The nucleation of a new layer can produce one of the two stacking sequences of closed packed atomic planes: the atoms may be arranged in a regular FCC (ABC) stacking sequence or in a sequence typical for HCP stacking (ABA). In the second case, the nucleation of the layer leads to formation of a twin boundary (ABACB sequence of planes) or a stacking fault (ABABCA or ABACAB for the intrinsic and extrinsic stacking faults, respectively). Since usually the stacking fault energy is more than trice large than the energy of a coherent twin boundary, in our analysis we consider only formation of twins. This process is schematically illustrated in Figure 51b and can be described based on the classical nucleation theory, Eqs. 3.13-3.17:

$$\frac{I_{twin}}{I_{fcc}} \approx exp\left(\frac{\left[G^*_{fcc}(T)-G^*_{twin}(T)\right]\Omega_a}{k_B T}\right) \approx exp\left(-\frac{\pi\gamma^2_{step}\gamma_{twin}\Omega_a}{k_B T h\Delta G_v(T)[h\Delta G_v(T)-\gamma_{twin}]}\right)$$

Based on the MD modeling, during resolidification the solid-liquid interface is always rough, and nucleation is not a limiting process. Thus, the number of atoms with HCP local crystal structure environment is proportional not only to the relative probability of nucleation, but also to the growth rate. The velocity of a solid-liquid interface can be described by the Wilson-Frenkel expression [127], Eq. 2.34. By assuming the same prefactors and activation energies for HCP and FCC steps, the relative velocity of growth is expressed as (the notation is the same as in Eqs. 3.13-3.17):

$$\frac{V_{HCP}}{V_{FCC}} = \frac{1-exp(-[\Delta G_v(T)-\gamma_{twin}/h]\Omega_a/k_B T)}{1-exp(-\Delta G_v(T)\cdot\Omega_a/k_B T)} \qquad (3.18).$$

The value of the step free energy required for this analysis is computed in Section 2.3.2 that allows direct comparison of the analytical prediction with MD results. Figure 52 illustrates the temperature dependence of the relative amount of HCP to the total number of atoms which is calculated based on the nucleation probability, Eq. 3.17 (red line), and corrected based on the growth velocity, Eq. 3.18 (green line). The value of T_c, which corresponds to onset of twin formation, can be estimated to be 0.87 T_m. Based on the plot, the number of atoms with HCP local crystal structure environment rapidly increases at the temperature below T_c and approaches 0.5 at approximately 0.75 T_m. The correction based on the growth velocity (Eq. 3.18) decreases the number of the HCP atoms; however, it remains on the level of 0.3-0.4 in the temperature range 0.65-0.8 T_m. This result suggests that approximately every 3-d atomic layer forms a coherent twin or stacking fault.

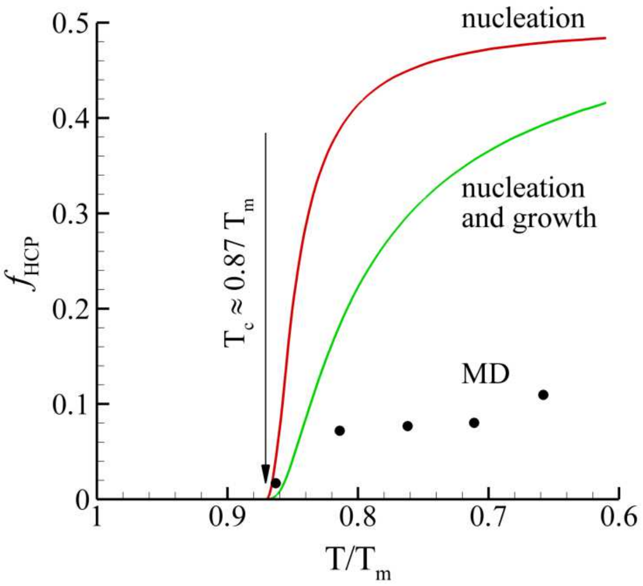

Figure 52. A comparison of the theoretical prediction of the fraction of atoms with HCP local crystal structure environment with MD results obtained at the moment of complete resolidification. The red line depicts the fraction of atoms with HCP local crystal structure environment (coherent twin boundaries) calculated solely based on the nucleation probability. The green line represents the corrected HCP fraction after considering the growth speed. The theoretically predicted threshold of twinning onset is pointed by an arrow. The results of MD simulations are illustrated as black circles.

The formation of growth twins described based on Eqs. 3.17 and 3.18 is evaluated in a series of MD simulations performed in a temperature range between 0.66 and 0.96 T_m. The relative number of atoms with HCP local crystal structure environment is depicted as black dots in Figure 52. The threshold like behavior described by Eq. 3.15 is well reproduced: the twines are generated only at the temperature 0.86 T_m and below. However, it appeared that at the moment of complete resolidification the relative number of atoms with HCP local crystal structure environment reaches only 0.08-0.1 in the temperature range 0.65-0.8 T_m. Moreover, it rapidly increases at ~0.82 T_m and stays approximately constant at the level 0.1 with increasing level of undercooling, which could be described neither by Eq. 3.17 nor Eq. 3.18 even if the matereal parameters are adjusted. For example, using larger step free energy to reproduce the relative number of atoms with HCP local crystal structure environment in the lower temperature region results in almost zero probability of twin nucleation at the temperature above 0.75 T_m. This result looks contradictive and surprising, however, further analysis, presented in the following subsection, demonstrates that the theoretical prediction, indeed, is in a good agreement with the modeling at the stage of nucleation and growth, but the density of twins drastically decreases during following motion of ITB.

Role of motion of ITB and de-twinning

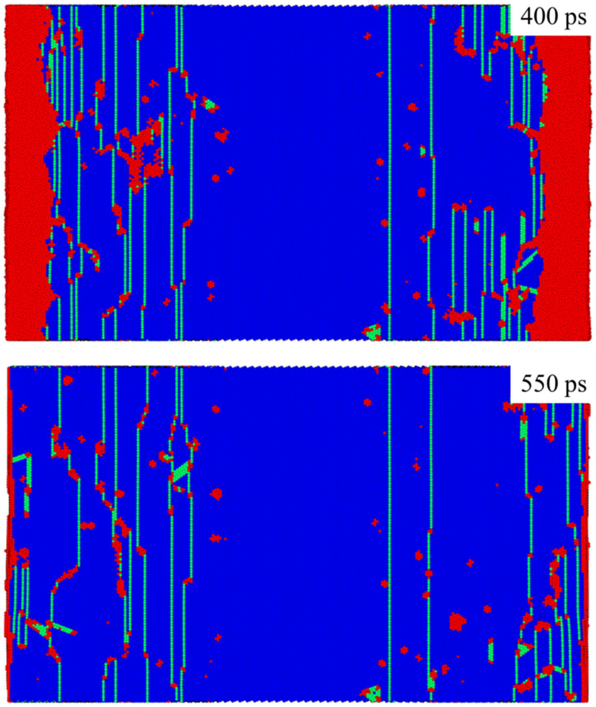

Figure 53. A side view of a system configuration at 400 ps and 550 ps which exposes motion of ITBs. The simulation is performed at 0.76 T_m, and the atoms are colored based on the local crystal structure environment. Blue, green, and red colors correspond to FCC, HCP and unidentified local crystal structure environment, respectively. With this coloring scheme, a single green layer and a double green layer represent a twin boundary and a stacking fault in the FCC structure. Unidentified atoms correspond to liquid, solid-liquid interface, dislocation cores, and point defects. The plot clearly demonstrates that the concentration of twin boundaries is the maximum near the solid liquid interface where they are generated. However, motion of ITBs leads to disappearance of small twinned domains at the later moment of time.

The comparison of theoretically predicted density of twin boundaries with results of atomistic simulations provided above has revealed a quantitative disagreement: the number of atoms with HCP local crystal structure environment, which correspond to twin boundaries and stacking faults, measured at the end of resolidification process is several times smaller than the prediction of the thermodynamics analysis (Figure 52). Further study of the evolution of the crystal structure has revealed the high density of twin boundaries in the vicinity of the solid-liquid interfaces as depicted in Figure 53. However, a comparison of two sequential system snapshots illustrates substantial decrease in the number of twin boundaries at the later moment of time, when the interface moves away. Numerous thin twinned domains generated during resolidification shrink or merge forming thick domains by motion of ITB, which are represented by arrays of Shockley partial dislocations and thus colored by red. Ref. [218] suggests that thin ITB are very mobile: atomistic simulation done for aluminum and copper at 300 K and zero external stress provides the velocity of ITB on the order of 1000 m/s for twin thickness of 3 and on the order of 100 m/s for twin thickness of 6 monoatomic layers. Since the mobility of ITB depends on the stacking fault energy [218], which have similar values for EAM Al used in the paper and for the currently used EAM Ni, this data suggests that twined domains with thickness

~6 atomic layers should shrink or merge at the time scale 100 ps at the temperature 300 K. At high temperature even thicker twinned domains can be affected since motion of twinned dislocations is described as an Arrhenius activated process. The data provided by Ref. [218] predicts very strong dependence of the ITB mobility on the twinned domain thickness and thus suggests that thick twined domains are not affected by de-twinning.

Nucleation of CTB followed by motion of ITB is illustrated in Figure 54 for one particular monoatomic (111) layer. The evolution of a fraction of atoms with HCP local crystal structure environment in respect to the total number of HCP and FCC atoms in this monoatomic layer is presented in Figure 55. At 300 ps after beginning of the simulation, when solid-liquid interface passes the illustrated layer, both FCC phase and CTB nucleate and grow. During first 25 ps the fraction of HCP atoms is fluctuating in the range 0.41-0.49 that is in a good agreement with the thermodynamics analysis accomplished in the previous subsection, which at the temperature 0.76 T_m predicts 0.45 based on the nucleation probability and 0.30 with considering the correction due to the growth speed. At 325 ps the growth process is almost completed, and the following evolution is governed by motion of ITB. The snapshots at later moments of time depict shrinking small twinned domains which are outlined by red line corresponding to twinning dislocations. At 350 ps the major part of twinned domains generated initially disappears, and the fraction of HCP atoms drops to 0.27. The remaining domains slowly shrink during the next 100 ps, and at 450 ps only one twinned domain remains and stays until the end of the simulation. The fraction of atoms with HCP local crystal structure environment drops to approximately 0.02 and remains almost constant during the last 75 ps of the simulation. The effect of ITB motion on the crystal structure is further illustrated by annealing of a crystal configuration produced at the end of resolidification in the modeling of laser irradiation of (111), as discussed in Section 3.4.

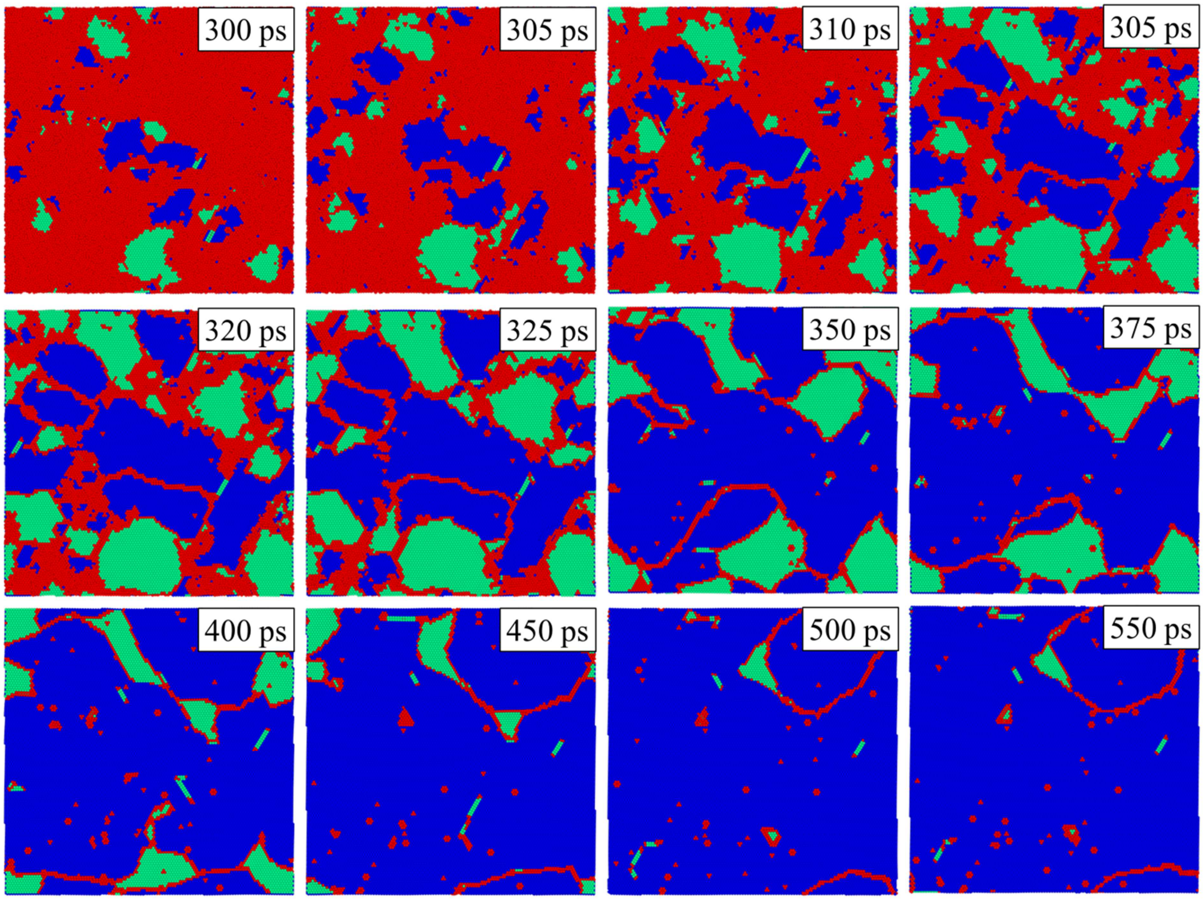

Figure 54. Nucleation and growth of FCC (blue) and HCP (green) nuclei on (111) surface followed by motion of ITB at the later stage when the solid liquid interface goes away at about 325 ps. The snapshots correspond to the top view of the MD system cut and show the same atomic layer. The simulation is performed at 0.76 T_m, and the labels represent the time in picoseconds. The atoms are colored based on the local crystal structure environment. Blue, green, and red colors correspond to FCC, HCP and unidentified local crystal structure environment, respectively. Unidentified atoms correspond to liquid, solid-liquid interface, dislocation cores, and point defects. At the initial stage the amounts of HCP and FCC atoms are approximately equal, however, at the later stage the major part of coherent twins disappears during the motion of ITB.

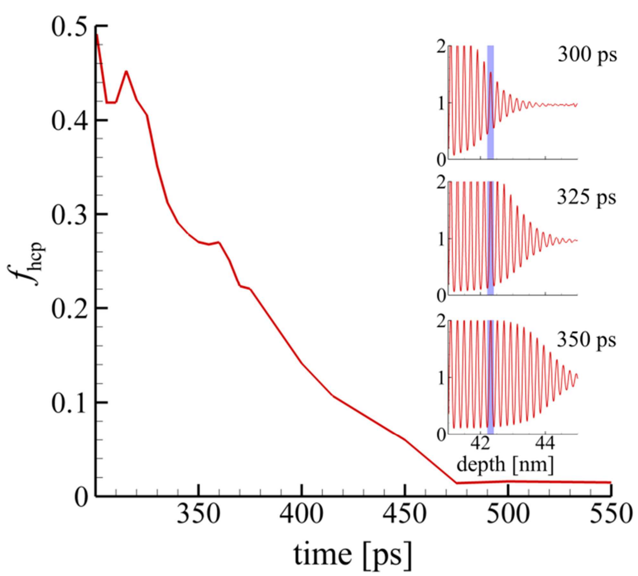

Figure 55. The evolution of the fraction of atoms with HCP local crystal structure environment (coherent twin boundaries) to the total number of FCC and HCP atoms in the top (111) monoatomic layer depicted in Figure 54. The insertion shows the normalized atomic density function at the initial stage of nucleation of solid (300 ps), the moment when the solid-liquid interface passes the layer (325 ps), and when the interface is 4-5 monolayers away from the layer (350 ps). The position of the layer is depicted by blue rectangles.

Summary

The mechanism of high density CTB formation during propagation of (111) solid-liquid interface under conditions of strong undercooling is studied both theoretically and computationally. A simple thermodynamics analysis describes generation of twins as a result of nucleation and growth of monoatomic ledges with a wrong stacking sequence of (111) planes that eventually produces twins and stacking faults. The analysis is general enough to be applicable for variety of materials; however, the current study is focused on Ni. The thermodynamic analysis has revealed the threshold like behavior for formation of twines that is well supported by the atomistic simulations where twins are not observed at small undercooling. A step free energy, which is a vital parameter in the thermodynamic description of the nucleation process, is calculated for EAM Ni [130] based on the capillarity wave method designed and described in details in the current paper.

The comparison of the theoretical prediction with the crystal configuration produced in MD simulations at the end of resolidification has revealed a quantitative discrepancy which cannot be avoided by adjustment of the parameters used in the thermodynamic analysis. Further investigation has demonstrated that nucleation and growth of twins agrees well with the theoretical prediction, while the final crystal structure is not only affected by the nucleation of twins but also by subsequent motion of ITB that leads to merging or shrinking thin twinned domains. This de-twinning process significantly reduces the density of twin boundaries and decreases the fraction of atoms that belong to CTB to less than 0.1. Thick twinned domains are not affected by the de-twinning since the mobility of ITB is strongly depends on the domain thickness. Since the motion of twinning dislocations is thermally activated process, twinned domains with a small thickness can remain in a sample if the resolidification takes place at low temperature. Therefore, ultrafast cooling rate achievable in short pulse laser irradiation suggests ultrashort pulse laser processing as a tool for surface modification capable to create a high density of twin boundaries. Also, a vapor deposition at low temperature, when formation of twins is described by the same thermodynamics model as during resolidification [151,152], can be applied to grow layers with very high density of twin boundaries.

3.4. Effect of interatomic potential on MD results

Abstract: Molecular dynamics simulation technique is a superior tool capable of providing atomic-level insights into the investigated processes. The main advantage of the MD technique is that no assumptions are made on the processes or mechanisms under study, and the only input in the MD model is the interatomic interaction potential that defines the equilibrium structure and thermodynamic properties of the material. However, this advantage is also the major drawback of MD technique since even very sophisticated interatomic potentials are not capable of reproducing all variety of material properties, and mostly only low temperature properties are examined in fitting procedure. In this section we provide several specific examples of how choice of the interatomic potential affects the computational predictions, and which parameters should be considered when potential is selected for description of laser-induced microstructure and surface morphology modification.

Evaluation of EAM Ti potentials for simulation of high-temperature behavior: melting, surface tension of the melt, and critical point

In this section we draw attention to the effect of high temperature material properties predicted by Embedded Atom Method (EAM) interatomic potentials parametrized for Ti on the accuracy of description of high temperature material behavior in atomistic simulations. The overview of a number of popular Ti EAM interatomic potentials is provided, and the advantages and drawbacks of these potentials are assessed based on the available in literature low temperature properties. A brief methodology of melting temperature, surface tension of melt, and critical point calculation is revisited and applied to examine in the first time high temperature properties of a number of Ti EAM potentials. Finally, the effect of these parameters is revealed in a series of atomistic simulations contrasting the microstructure produced in rapid solidification and the dynamics of overheated material decomposition.

Introduction

Titanium and its alloys are extensively used for aerospace and marine applications, in industry and medicine due to an excellent combination of high strength to density ratio, corrosion and fatigue resistance, ability to withstand extreme temperature, and biocompatibility [242-249]. In addition, Ti-based alloys are attractive functional materials since they exhibit shape memory effect as well as unique physical properties such as pre-transformation behaviors enriched by various martensitic transformations [250].

Molecular Dynamics (MD) simulations provide a unique capability to study microstructure modification, phase transformations, shape memory behavior, and fatigue of Ti at the atomic level [251-255]. To utilize MD approach for modeling Ti and its alloys, a number of interatomic interaction fields have been developed [164,256-262] that in most cases are fitted to reproduce low temperature properties of Ti such as lattice parameter and cohesive energies of the ground state, elastic constants, and properties of point defects since they are relatively easy to measure and to fit. However, higher temperature properties such as the melting point or phase diagram are considered in the fitting procedure only in a limited number of studies [164,261,262].

Meanwhile, accurate reproduction of high temperature behavior by interatomic potentials is crucial for a number of practical cases. Particularly, atomistic study of martensitic phase transformations in Ti is not possible until the interatomic potential can provide an accurate representation of the phase diagram. Other examples of high temperature applications of interatomic potentials include atomistic modeling of laser processing or ion bombardment. Particularly, recent large scale atomistic simulations of laser irradiation of metals have revealed mechanisms of microstructure and surface morphology modification [17,31,32,39], and nanoparticle generation [263,264].

Since there is a number of practical applications of interatomic potentials that require reproduction of high temperature behavior, it is important to have understanding of the effect of high temperature material properties, reproduced by interatomic potentials, on results of atomistic simulations. In the current article, first, we provide a methodology of high temperature material properties evaluation in MD simulations that, in contrast to properties calculated at zero temperature, requires sophisticated and thorough procedure. Next, we apply this methodology to examine high temperature properties predicted by a number of Ti interatomic potentials. Finally, to draw attention to the effect of these properties on the accuracy of atomistic computational predictions, we provide examples comparing microstructure and surface morphology modification predicted with a number of Ti potentials. Despite these examples are focused on laser-mater interactions, their conclusions are valid for other applications exhibiting high temperature material behavior. Particularly, we show the effect how microstructure produced in rapid solidification depends on the ability of interatomic potentials to reproduce particular phases of Ti and transformations between them. Also, we show the effect of high temperature material parameters on dynamics of material decomposition.

EAM potentials for Ti

In the current section we provide an overview of a number of EAM Ti potentials. EAM potentials are widely used for description of metallic systems due to their relatively low computational cost and capability to reproduce environmental dependence inherent for metallic bounding. However, despite a considerable success in reproduction of properties of metals, EAM potentials lack angular dependent interactions that may be essential in the case of *d*-metals having a significant contribution of covalent bonding. Particularly, EAM potentials have difficulties in reproduction of high stacking fault energy in FCC and HCP structures as well as solid-solid phase transitions, which are crucial for Ti. Despite some of these difficulties are overcome in the recently developed by Mendelev *et al.* EAM Ti potential [164], a number of modified EAM (MEAM) potentials, accounting for angular dependence of interatomic interactions, have been designed for Ti system [260-262].

Table 4 summarizes cohesive energy, lattice parameters, elastic properties, point defect formation energies, free surface and stacking fault energies calculated at zero temperature for a number of EAM and MEAM Ti potentials. We list interstitial formation energy, free surface and stacking fault energies only for one particular configuration since our purpose is providing a characteristic value for each interatomic potential, and additional details can be found in papers introducing these potentials. The first seven columns correspond to EAM potentials, following three columns list properties of MEAM potentials, and the last column provides a comparison with experimental values or results of DFT calculations.

Table 4. Properties of α-Ti (HCP) phase at zero temperature: cohesive energy, lattice parameters, elastic moduli, vacancy and octahedral interstitial formation energies, energies of (0001) free surface and I2 stacking fault. The values are taken from papers describing the potentials.

	MUA1 [164]	MUA2 [164]	MUA3[164]	Mishin [256]	Ackland [257]	Johnson1 [258]	Johnson2 [258]	HLTRW [261]	KLB[260]	KGN [262]	experiment and DFT
E_c [eV]	5.346	5.247	5.404	4.850	4.853	4.855	4.855	4.831	4.873	4.867	4.85 [265]
a [Å]	2.947	2.949	2.951	2.951^1	2.959	2.922	2.922	2.931	2.945	2.922	2.951 [266]
c/a	1.597	1.593	1.589	1.585^1	1.591	1.633	1.633	1.596	1.591	1.506	1.587 [266]
C_{11} [GPa]	161	160	165	178^1	180^1	184	195	174	170.1	170.0	176.1 [267]
C_{12} [GPa]	80	70	88	74^1	87.3^1	78.5	73.7	95	80.4	95.5	86.9 [267]
C_{44} [GPa]	53	54	58	51^1	51.4	41.7	48.1	58	42.1	40.4	50.8 [267]
C_{13} [GPa]	86	70	83	77	76.7	67.3	60.9	72	74.8	72.4	68.3 [267]
C_{33} [GPa]	169	165	166	191^1	217	179	207	188	187.1	190.4	191 [268] 172.5 [267]
C_{66} [GPa]	40	45	39		46.4				44.8		44.6 [267]
E_f^v [eV]	2.74	1.78	1.73	1.83	1.43	1.49	1.48	2.24	1.79	1.46	1.97 [269]
E_f^O [eV]	2.30	2.17	2.23		3.07		3.45	2.64	4.51		2.13 [269]
$E_s^{[0001]}$ [mJ/m^2]	1380^2	1920^2	2260^2	1725	993			1470	2144	2032	2048 [270]
E_{SF}^{I2} [mJ/m^2]	257	236	236	56	64			170	213		259 [270]

[1] These values are slightly different from results of later studies [271]

[2] The Ref. [164] includes a misprint, and the suggested values are not corrected from meV/Å^2 to mJ/m^2

All listed potentials are capable of reproducing relatively accurate values of the lattice parameter and elastic moduli of α-Ti. Potentials that are referred as Johnson1 and Jonson2 are ones of the first EAM potentials developed for Ti [258]. Despite these potentials account only for interactions with the first nearest neighbors, they can relatively accurately reproduce a number of Ti properties listed in the table. However, lack of a cutoff function deteriorates energy conservation in MD simulations. Also, since only interactions with the first nearest neighbors are considered, the potential is not able to reproduce not only various phases of Ti but also differentiate between HCP and FCC phase.

The abovementioned drawbacks are addressed in development of Ackland interatomic potential [257]; however, the surface energy and especially the stacking fault energy, predicted by this potential, are strongly underestimated. Thus, the threshold value of stress corresponding to emission of dislocations and formation of twins is also underestimated, and in MD simulations of plasticity the predicted density of dislocations and twin boundaries has to be larger than the expected value for real Ti. In addition, low surface energy calculated at zero temperature correlates with surface tension of melt, thus the cavitation threshold in liquid in simulations with this potential is significantly decreased that facilitates material removal in simulations of laser ablation, as shown below in this section. The problem of low surface energy is fixed in the potential referred in the table as Mishin [256], which is also capable of reproducing the accurate value of the vacancy formation energy. However, the issue with strongly underestimated stacking fault energy remains in simulations with this potential.

Recently developed by Mendelev *at al.* EAM potentials [164], referred as MUA1, MUA2, and MUA3, provide a great improvement in description of both point and planar defect energies. In addition, this is only EAM potentials listed in the table that are capable to reproduce formation not only α-Ti (HCP) but also high temperature β-Ti (BCC) phases. The first potential, MUA1, is fitted to reproduce the melting point and the temperature of α- β phase transition. The other two potentials are fitted to reproduce the energy of point defects and can be used for simulation of radiation damage. All these potentials can predict an accurate value of stacking fault energy that suggests applicability of these potentials for simulation of plasticity. In addition, the surface energy is also well reproduced for MUA2 and MUA3 potentials. Discrepancy of C_{33} elastic modulus is resulted by fitting the potentials to the value predicted in a DFT calculation that is lower than the experimental measurement. One of the drawbacks of MUA potentials is slightly higher cohesive energy compared with the experimental value. Also, even MUA1 potential predicts formation of β-Ti phase, it has difficulties in reproduction of β-α martensitic phase transformation when the temperature decreases, as noticed below in this section.

Difficulties in description of Ti properties by EAM potentials are resulted by angular dependent contribution to the interatomic bonding resulted by *d*-electrons. Thus, several MEAM potentials, explicitly accounting for this angular dependence, have been proposed. KLB potential [260] is capable of providing a significant improvement in description of Ti properties listed in the Table 4, only the interstitial formation energy is significantly overestimated. However, this potential is unable to reproduce high temperature β-Ti phase.

Development of KGN MEAM potential [262] has allowed to model martensitic phase transitions in Ti and Ni-Ti alloys in addition to a relative accurate description of Ti properties. However, besides α-Ti and β-Ti phases, the phase diagram of Ti includes a high pressure ω-Ti (hexagonal) phase [261], and KGN potential is unable to properly reproduce ω-Ti phase and martensitic phase transitions that includes this phase. Finally, HLTRW MEAM potential [261] is fitted to completely reproduce Ti phase diagram including α-Ti, β-Ti, and ω-Ti phases as well as martensitic phase transitions between them. However, reproduction of stacking faults and free surface energies is worse compared with other listed MEAM potentials.

Beside accuracy of representation of material properties, selection of interatomic potential is also dictated by the computational cost, which is summarized in Table 5. The computational cost of EAM potentials, if they are tabulated, is dictated by a number of neighbors to be processed during force calculation, which is proportional to the number of atoms inside a sphere of radius R_{cut} (a cutoff distance of a particular potential). The expected value of computational cost, estimated as the volume of a sphere of radius R_{cut}, is in a good agreement with the computational cost obtained from test simulations. The computational cost of MEAM potentials is more difficult to estimate, and we list only the value obtained from a test simulation with HLTRW potential.

Table 5. Computational cost. The time per iteration is normalized based on MUA1 potential.

	R_{cut} [Å]	time per iteration (expected)	time per iteration (test)
MUA1 [164]	6.9	1.0	1.0
MUA2 [164]	6.9	1.0	1.0
MUA3 [164]	6.9	1.0	1.0
Mishin [256]	5.19	0.43	0.44
Ackland [257]	5.09	0.40	0.39
Johnson [81]	6.16	0.71	0.74
Johnson1 [258]	3.95	0.19	0.21
Johnson2 [258]	3.95	0.19	0.21
HLTRW [261]	5.5		2.0

Based on the Table 5, from the MD code efficiency point of view EAM potentials are more preferable than MEAM, since HLTRW potential is twice slower than MUA1 and approximately 4 times slower than an EAM potential with the same cutoff distance. Thus, MEAM are feasible for using mostly in study of martensitic phase transformations and in cases where reproduction of Ti phase diagram is crucial. MUA potentials, based on the Table 4, can accurately reproduce plasticity and point defect generation with lower computational cost than more accurate MEAM potentials. Meanwhile, Mishin potential is about twice computationally cheaper than MUA potentials and thus is feasible for using in simulations where computational cost is the limiting factor or reproduction of microstructure is not the main focus.

Melting properties of EAM Ti

The following subsection presents results of melting temperature, heat of fusion, and volume change of melting calculations performed for a number of Ti interatomic potentials. In contrast to properties discussed in the previous sections and calculated at zero temperature, computing of high temperature material properties is more complicated task, and thus these properties are not often provided and even more infrequently are considered in fitting of interatomic potentials. Meanwhile, knowledge of the melting point may be essential in analysis of computational results, for example, understanding kinetics of homogeneous melting or investigation of microstructure generated in resolidification. Thus, we have performed calculation of melting properties, which are computed for the first time for Ti potentials listed in Table 6 besides MUA potentials. The details of the method used for computing the melting point are summarized in Section 2.4.

Table 6. Melting properties (melting temperature, heat of fusion, and volume change of melting) calculated for BCC (β-Ti) and HCP (α-Ti) phases.

	$T_{m,\mathrm{hcp}}$ [K]	$\Delta H_{m,\mathrm{hcp}}$ [eV/atom]	$\Delta V_{m,\mathrm{hcp}}$ [nm^3/atom]	$T_{m,\mathrm{bcc}}$ [K]	$\Delta H_{m,\mathrm{bcc}}$ [eV/atom]	$\Delta V_{m,\mathrm{bcc}}$ [nm^3/atom]
MUA1 [164]	1766.2 1765±1 [164]	0.143	3.64×10^{-4}	1917.8 1918±1 [164]	0.130	4.16×10^{-4}
MUA2 [164]	1277±1 [164]	0.124	4.46×10^{-4}	1322±1 [164]	0.097	4.08×10^{-4}
MUA3 [164]	1189±1 [164]	0.122	5.39×10^{-4}	1210±1 [164]	0.083	3.96×10^{-4}
Mishin [256]	1533.5	0.153	7.01×10^{-4}	1438.9	0.108	6.53×10^{-4}
Ackland [257]	1347.3	0.141	9.44×10^{-4}	1238.2	0.108	7.54×10^{-4}
Johnson [81]	1580.6	0.144	8.75×10^{-4}	1537.7	0.118	8.01×10^{-4}
HLTRW [261]	1830.5	0.122	9.39×10^{-5}	1875.9	0.094	1.33×10^{-4}
experiment [107]				1941	0.1467	

The calculated values are summarized in Table 6. We calculate the melting properties for both BCC (β-Ti) and HCP (α-Ti) phases since the equilibrium phase of real Ti at the malting point is β-Ti, but only minority of the listed potentials can reproduce the equilibrium phase, predicting α-Ti instead. The table shows that only MUA1 and HLTRW potentials can reproduce both presence of high temperature β-Ti and relatively accurate value of the melting temperature. MUA2 and MUA3 potentials also reproduce higher melting temperature of β-Ti compared with α-Ti; however, the melting temperature is much lower that the experimental value since these potentials are fitted to accurately describe point defects and plasticity [272]. Other potentials predict α-Ti as the stable phase at the melting point, and the melting temperature is 400-600 K below the experimental value. The heat of β-Ti to liquid phase transition is underestimated for both MUA1 and especially for HLTRW potentials; meanwhile, it is noticeable that the heat of fusion of α-Ti to liquid transition (at $T_{m,\mathrm{hcp}}$) is approximately equal to the experimental heat of fusion.

Surface tension of EAM Ti

This subsection is focused on the investigation of the temperature dependence of the surface tension in liquid state calculated for a number of Ti EAM potentials. Despite several methods of surface tension calculation have been proposed [162,273], this property is evaluated very infrequently, and very often only for one particular temperature. A systematic study of the temperature dependence of interface tension of liquid-gas mostly is focused only on Lennard-Jones (LJ) fluid [274], and no studies are performed for EAM potentials. Meanwhile, there is a number of applications where EAM potentials are utilized to model flow and decomposition of melt material, and values of the surface tension may be vital for interpretation of the computational predictions and following mapping the results to the experimental conditions, as discussed in subsections below.

In our study, Test Area Method (TA) [162] is utilized to compute surface tension, which is based on a NVT liquid-vapor coexistence simulations performed to compute the free energy difference between the primary state and perturbed states, which have smaller and larger surface area. The details of these methods and parameters used in our simulations are summarized in Section 2.4.2. Values of surface tension are calculated in a range of temperature from 1500 K to ~0.9 T_c and fitted with utilization of the following dependence:

$$\sigma(T) = \sigma_0(1 - T/T_c^*)^\mu \quad (3.19),$$

which is suggested by the mean-field theory in the vicinity of the critical point [275]. T_c^* is an estimation of critical temperature of critical temperature T_c based on the surface tension calculations. The asterisk is added to distinguish this estimation from one obtained based on fitting the binodal line in the next subsection.

The results of fitting are summarized in Table 7 and plot in Figure 56. Even if Eq. 3.19 is proposed for description of temperature dependence in the vicinity of critical point, it provides a relatively accurate description even at low temperature, as shown in Figure 56. Only HLTRW potential requires splitting the dataset into two intervals for fitting, as listed in Table 7. Apart from MUA2 and MUA3, which have very low melting temperature, all listed potentials underestimate the surface tension at the melting point as well as the slop of the surface tension.

Table 7. Surface tension (fitting parameters in Eq. 3.19 and the values at the melting point).

	γ_0 [J/m^2]	T_c* [K]	μ	$\gamma(T_m)$ [J/m^2]	-dγ/dT(T_m) [mJ/m^{2}K]
MUA1 [164]	1.329±0.005	8070±20	0.98±0.01	1.02	0.16
MUA2 [164]	1.895±0.004	10300±40	0.91±0.01	1.67	0.17
MUA3 [164]	2.240±0.006	11690±30	0.96±0.01	2.02	0.18
Mishin [256]	1.169±0.003	10340±40	1.07±0.01	0.98	0.12
Ackland [257]	0.949±0.003	7130±30	1.07±0.01	0.76	0.14
Johnson [81]	1.224±0.002	10440±10	1.03±0.04	1.03	0.12
Johnson1 [258]	0.75±0.02	3790±70	1.05±0.06		
Johnson2 [258]	0.72±0.02	3760±60	1.12±0.07		
HLTRW (T < 9000 K) [261]	1.393±0.004	10600±100	0.50±0.01	1.26	0.072
HLTRW (T > 7000 K) [261]	1.65±0.02	12320±80	0.84±0.02		
experiment [60]				1.500 – 1.525	0.2 – 0.26

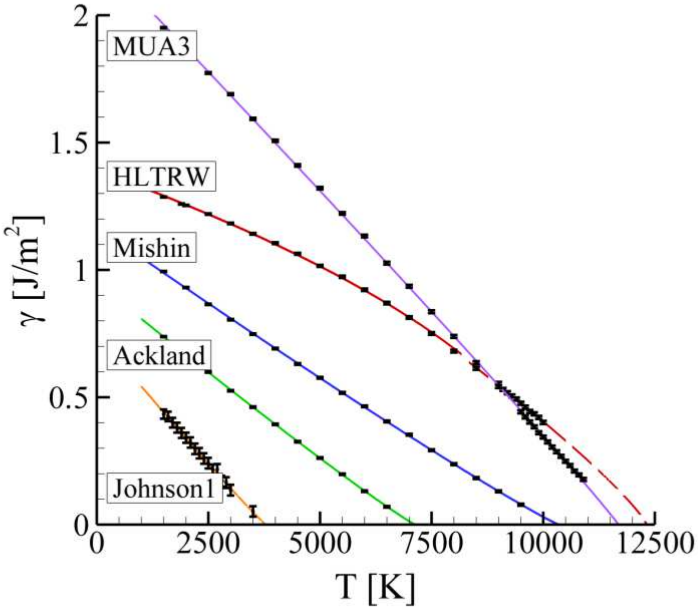

Figure 56. Dependence of surface tension on temperature for several representative Ti potentials from Table 7. Solid lines depict fitted curves according to Eq. 3.19. Dashed curve for HLTRW Ti potential [261] depicts fitting according to parameters fitted for T > 7000 K.

The expected value of the critical exponent μ obtained from the renormalization group technique with applying hyperscaling relation is 1.26 [276] that is later confirmed computationally [277,278]. The values of μ in Table 7, however, are lower than expected 1.26 that may be explained by the fact that the Eq. 3.19 accurately describes the behavior of matter only near the critical point, and the low temperature behavior may alter from this dependence. As demonstrated by the example of HLTRW potential, the values of μ for low and high temperature regions are different. For other considered potentials, however, this change μ of is not strongly pronounced, and the data points can be accurately fitted with using only one set of parameters. More careful investigation of the behavior of μ in the vicinity of the critical point would require calculation of the liquid-vapor interface tension at temperatures T > 0.9 T_c, which is more challenging due to the difficulty of stabilizing the interface, and may be a subject of a separate study. Also, the alternation from Eq. 3.19 may explain that the values of T_c*, critical temperature expected from the surface tension fitting, are lower compared with critical point calculations performed in the next subsection based on the binodal line reconstruction (Table 8). This discrepancy is relatively small for the most considered potentials and lies almost within the error bar. However, for HLTRW potential the difference is more distinct and resulted by a stronger deviation of surface tension in low temperature region from the dependence described by Eq. 3.19.

Critical point of EAM Ti

A critical point of a material is a crucial parameter for description of the material behavior under conditions where formation of a supercritical fluid takes place. Particularly, critical pressure defines the onset and dynamics of the material decomposition, as discussed in the following section. However, calculation of critical point in MD is not a straightforward task and requires reconstruction of a liquid-vapor coexistence curve (binodal line). Thus, only a limited number of studies is focused on the critical point calculation, and their major part are performed for LJ potential [165,166,274,278,279]. Only several publications report result for EAM potentials [272,280].

Critical parameters of considered Ti potentials are computed with using the method described in in Section 2.4.3 and are summarized in Table 8. The values of critical temperature for listed potentials are broadly scattered in the range from 4030 to 13100 K. This range, in general, is in agreement with the available experimental estimations giving 5850 and 11790 K. Difficulties in experimental evaluation of a critical point of metals lead to the significant uncertainty. Using Eq. 3.19 with the experimental value of the surface tension and its slop at the melting point (Table 7) and μ = 1.26 suggests a comparable temperature range from 9000 to 11000 K.

Table 8. Critical point for Ti EAM potentials.

	T_c [K]	ρ_c [nm^{-3}]	P_c [MPa]
MUA1 [164]	8160±20	15.5±0.1	101
MUA2 [164]	10900±40	16.0±0.3	297
MUA3 [164]	12050±40	15.7±0.1	359
Mishin [256]	10580±40	12.3±0.4	200
Ackland [257]	7210±30	12.5±0.9	72.3
Johnson [81]	10540±20	12.3±0.3	199
Johnson1 [258]	4050±20	12.5±0.3	46
Johnson2 [258]	4030±20	11.7±0.3	46
HLTRW [261]	13100±100	19.1±0.2	635
experiment	11790 [281] 5850 [282]	16.5 [281]	763 [281]

The computed critical density for most of the potentials does not strongly deviate from the suggested value of real Ti. However, the critical pressure for all EAM potentials is substantially lower than the suggested experimental estimation, and only MEAM HLTRW potential reproduces a comparable value. This result may suggest that EAM potentials have a difficulty in reproduction of high critical pressure, and explicit consideration of angular dependence of bonding may be essential for accurate reproduction of critical material behavior.

Implications for high-temperature material behavior

This subsection provides examples how high temperature properties reproduced by interatomic potentials affect results of atomistic simulations and explains implications of choice of the potential on high temperature material behavior. We focus on applications involving MD simulations of laser-material interactions; however, the reported conclusions are rather general and can be imposed to interpret results of other applications involving high temperature material behavior. We consider two regimes: (1) laser-induced melting and resolidification and (2) laser ablation accompanied by disintegration of the irradiated material. Mishin [256], Ackland [257], MUA1 [164], and HLTW [261] potentials are picked as representative examples since they provide a broad range of high temperature properties, including surface tension and the critical point, and demonstrate a different level of accuracy in microstructure reproduction.

Computational model for simulation of laser-interactions with Ti: The laser interaction with mater is described in a framework of a hybrid atomistic – continuum model [102] that combines the classical molecular dynamics (MD) method with the continuum-level two-temperature model (TTM) [9]. A complete description of the TTM-MD model is provided elsewhere [39,102], and below we only outline the computational setup used in the simulations reported in this subsection

The simulations are performed for single crystal Ti targets having (0001) surface orientation. The dimensions of the MD domain are approximately 4.1 nm × 4.1 nm × 135 nm that corresponds to 129 thousand atoms, and periodic boundaries are applied in lateral (x and y) directions. At the bottom of the atomistic part of the model, a pressure-transmitting [106], heat-conducting boundary condition is applied to ensure non-reflecting propagation of the laser-induced stress wave and heat transfer from the atomistic part of the computational system into the bulk of the target. The irradiation of target by 100 fs laser pulse is represented through a source term added to the TTM equation for the electron temperature [102]. The source term simulates the excitation of the conduction band electrons by a laser pulse with a Gaussian temporal profile and reproduces the exponential attenuation of laser intensity with depth under the surface according to Beer–Lambert law, with the optical absorption depth of 19.1 nm assumed for Ti at the laser wavelength of 800 nm [181].

The electron temperature dependences of the electron-phonon coupling factor and the electron heat capacity used in the TTM equation for the electron temperature are taken in the forms that account for the contribution from the thermal excitation from the electron states below the Fermi level [101]. Similar to Ref. [32], the temperature dependence of the electron thermal conductivity is described by the Drude model relationship, $K_e(T_e,T_l) = v^2 C_e(T_e)\tau_e(T_e,T_l)/3$, where $C_e(T_e)$ is the electron heat capacity, v^2 is the mean square velocity of the electrons contributing to the electron heat conductivity, approximated in this work as the Fermi velocity squared, ${v_F}^2$, and $\tau_e(T_e,T_l)$ is the total electron scattering time, $1/\tau_e = A{T_e}^2 + BT_l$. The value of the coefficient A (3.0×10^6 $K^{-2}s^{-1}$) is estimated within the free electron model. The coefficient B is described as a function of the lattice temperature, so that the experimental temperature dependences of thermal conductivity of Ti [283] under conditions of electron-phonon equilibrium are reproduced in the simulations. The analyses of microstructure structure and cluster size distribution are performed with utilization of OVITO tool [180,284]. The tables for Mishin, MUA1, and Ackland potentials are provided in Ref. [285].

Laser melting and resolidification: First, we will focus on a low laser fluence regime, which causes melting of the top part of the irradiated surface followed by resolidification, to expose the effect of Ti interatomic potentials on description of microstructure evolution. Figure 57 depicts the evolution of the fraction of melt in Ti targets irradiated at the absorbed laser fluence 400 J/m^2. The features of the generated microstructure are labeled in Figure 57 and exposed in more details in Figure 58 as atomic snapshots colored based on the local crystal structure environment.

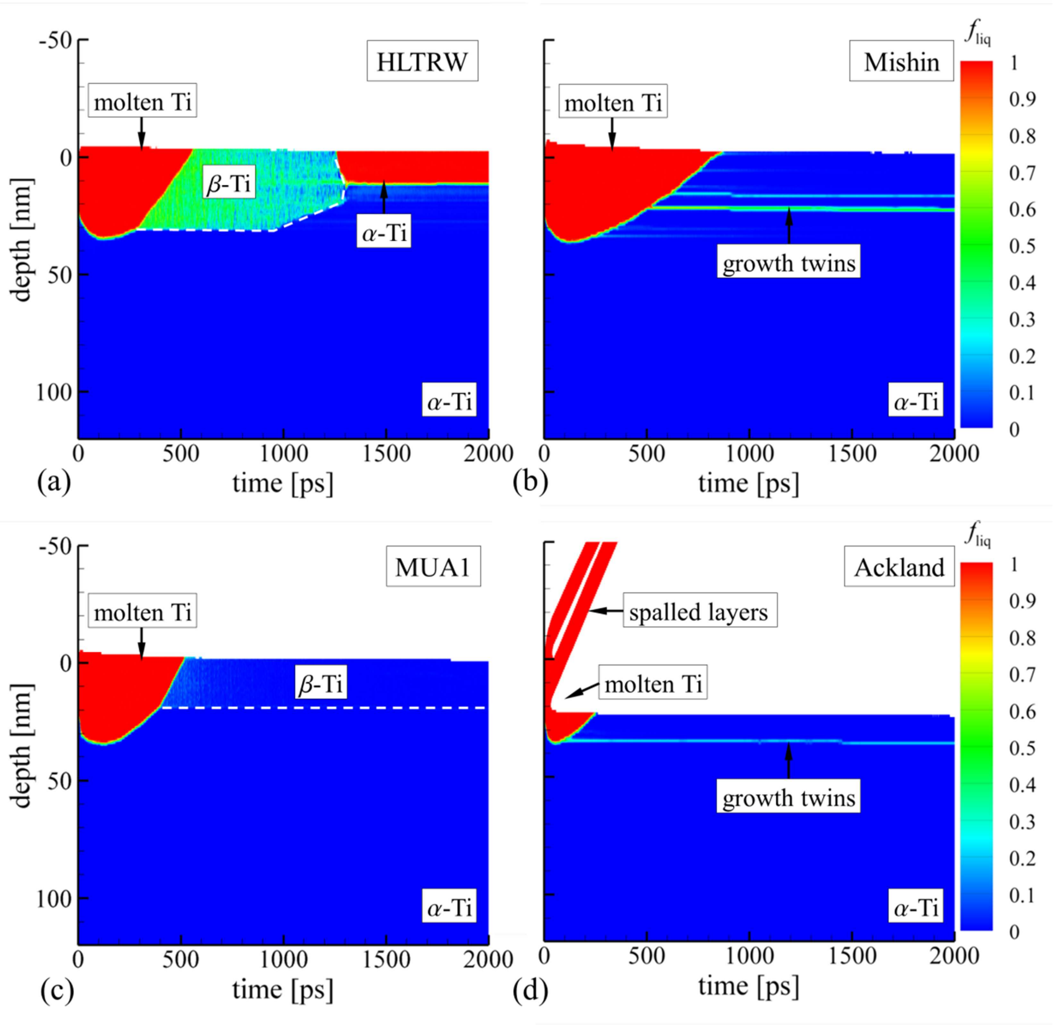

Figure 57. The evolution of the fraction of molten material in Ti targets irradiated at the laser fluence 400 J/m^2. The laser irradiation is directed from the top, and the initial surface position is set to zero. White dashed line outlines the region with β-Ti phase. Since the fraction of melt is calculated based on the value of the local order parameter, atoms not corresponding to α-Ti phase with (0001) surface orientation may be recognized as liquid. Thus, these regions may have greenish or red color, and to avoid confusion we marked them explicitly.

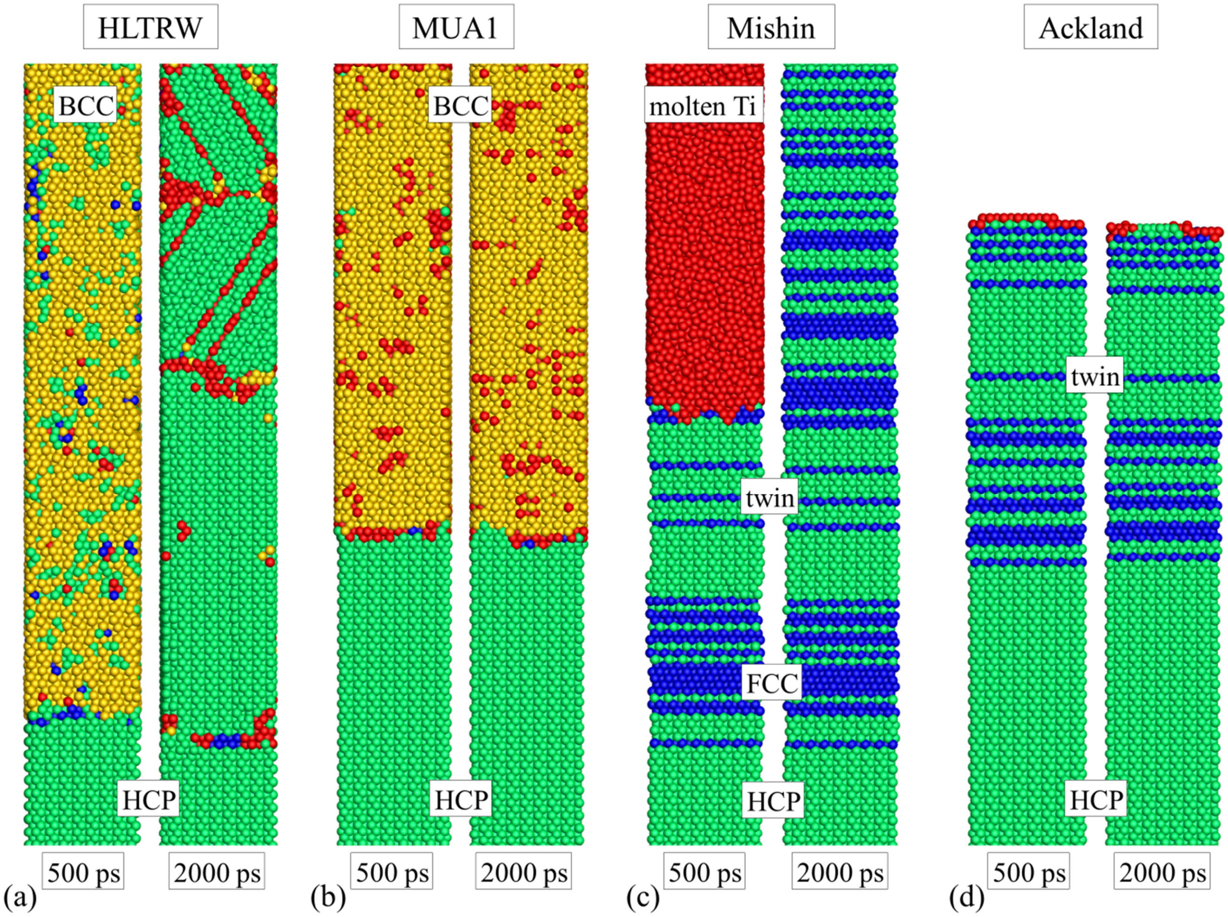

Figure 58. Microstructure of Ti targets produced at 0.5 and 2 ns after laser irradiation. 29 nm long part of each target is cut to expose the variety structures labeled in Figure 57. Atoms are colored based on the local crystal structure environment: green – HCP, blue – FCC, yellow – BCC, red – unidentified.

The predicted melting depth is almost the same for all considered potentials; however, the produced microstructure is very different. In the case of Mishin potential, melting follows by epitaxial regrowth and formation of numerous growth twins, stacking faults, and FCC layers when the temperature drops below $0.92T_{m,\mathrm{hcp}}$. The mechanism of growth twinning is the same as in the case of resolidification of FCC (111) targets, described in more details in Ref. [76] and Sections 3.2 and 3.3. Resolidification proceeds through subsequent nucleation and growth of close packed layers on HCP (0001) facet. Formation of a new layer can either produce a regular HCP arrangement of close packed planes or a sequence typical for FCC producing twins, stacking faults, or even an FCC (111) layers when undercooling is sufficiently strong. At very strong undercooling these two cases are almost equiprobable, and, thus, the upper part of the target is composed by randomly arranged closed packed planes. If the lateral size of the system is larger than the typical size of two dimensional nuclei formed on HCP (0001) facet, generated twins will rapidly shrink in de-twinning process [218], and the final structure will be composed of several nanometer thick twinned domains, similar to Ref. [32]. If the target does not have any close packed plane parallel to the solid-liquid interface, resolidification will proceed through epitaxial regrowth of α-Ti phase. The above described picture of microstructure evolution is reasonable for materials that do not have additional phases in the phase diagram apart from HCP and liquid. However, as shown below, the presence of high temperature β-Ti phase in the phase diagram completely changes the generated microstructure.

In the case of Ackland potential, similar to results predicted by Mishin potential, numerous growth twins and stacking faults are formed when the temperature drops below $0.86T_{m,\mathrm{hcp}}$. However, since Ackland potential predicts lower value of the surface tension of melt than Mishin potential (Figure 56,Table 7), the spallation (or cavitation) threshold is lower, and the top part of the target is spalled. As discussed in Section 4.1, the cavitation threshold can be estimated from the classical nucleation theory and exhibits a strong dependence on the surface tension:

$$P_{cav}(T) \sim \sqrt{\sigma(T)^3 / k_B T} \qquad (3.20).$$

This fact has to be considered during comparison of MD predictions with experimental results if the interatomic potential cannot reproduce the experimental value of the surface tension of melt.

MUA1 potential makes one more step toward reproduction of a realistic microstructure due to the capability to describe formation of high temperature β-Ti phase. As shown in Figure 57, initially resolidification proceeds through an epitaxial regrowth followed by cross-nucleation of β-Ti phase, when the temperature drops down to $0.85T_{m,\mathrm{hcp}}$, and formation of a 20 nm BCC layer (Figure 58). However, even after quenching the produced structure to 300 K, the metastable β-Ti phase does not transform into α-Ti.

HLTRW potential is also capable to reproduce cross-nucleation of β-Ti phase when the temperature drops down to $0.87T_{m,\mathrm{hcp}}$ followed by generation of 34 nm thick β-Ti layer. At the temperature ~$0.60T_{m,\mathrm{hcp}}$ the β-Ti region starts shrinking, and at ~$0.55T_{m,\mathrm{hcp}}$ the metastable β-Ti region experiences a martensitic phase transformation into α-Ti, forming several grains (Figure 58). Small lateral size does not allow investigation of this martensitic transformation in details, but the reported simulation provides evidence that HLTRW potential is capable to provide a realistic description of microstructure modification in laser irradiation of Ti targets. The microstructure generated in laser processing of Ti produced in a large scale atomistic simulation is discussed in the next subsection. From the list of considered Ti potentials only MUA1 and HLTRW potentials can reproduce formation of high temperature β-Ti phase, and only HLTRW potential is capable to reproduce the β-α martensitic phase transformation and, thus, have to be considered if martensitic phase transformations are crustal for simulated microstructure modification.

Laser ablation: The next regime corresponds to much higher absorbed laser fluence, 1400 J/m^2, leading to decomposition of the top part of the target. The evolution of temperature in the irradiated targets is illustrated in Figure 59. The maximum temperature is 1.4×10^4, 1.34×10^4, 1.3×10^4, and 1.33×10^4 K for simulations with HLTRW, Mishin, MUA1, and Ackland potentials, respectively. According to Table 8, the listed temperature is above the critical point found for these potentials, and thus the top part of the target is decomposed into vapor and small clusters. Meanwhile, deeper parts of the target are spalled in regions where the generated tensile stresses reach the spallation threshold, which can be approximated with using Eq. 4.1.

According to Figure 56, HLTRW potential shows a high surface tension of melt, which decreases slower with temperature compared to other potentials. Thus, the total ablation yield predicted by this potential is relatively low, and a substantial part of the material is ejected as vapor, as illustrated in Figure 60a. Mishin potential exhibits lower surface tension, which drops almost to zero at 10000 K. Therefore, in simulation with this potential spallation is more feasible, and the ablation yield is higher. The critical temperature of MUA1 and Ackland Ti is equal to approximately 8000 and 7000 K (Table 8), respectively, and thus surface tension of these materials drops to zero at lower temperature compered to Mishin Ti. Thereby, in simulations with MUA1 and Ackland potentials spallation is more pronounced that is in agreement with further increase of the ablation yield and formation of thick spalled layers in Figure 59c and Figure 59d.

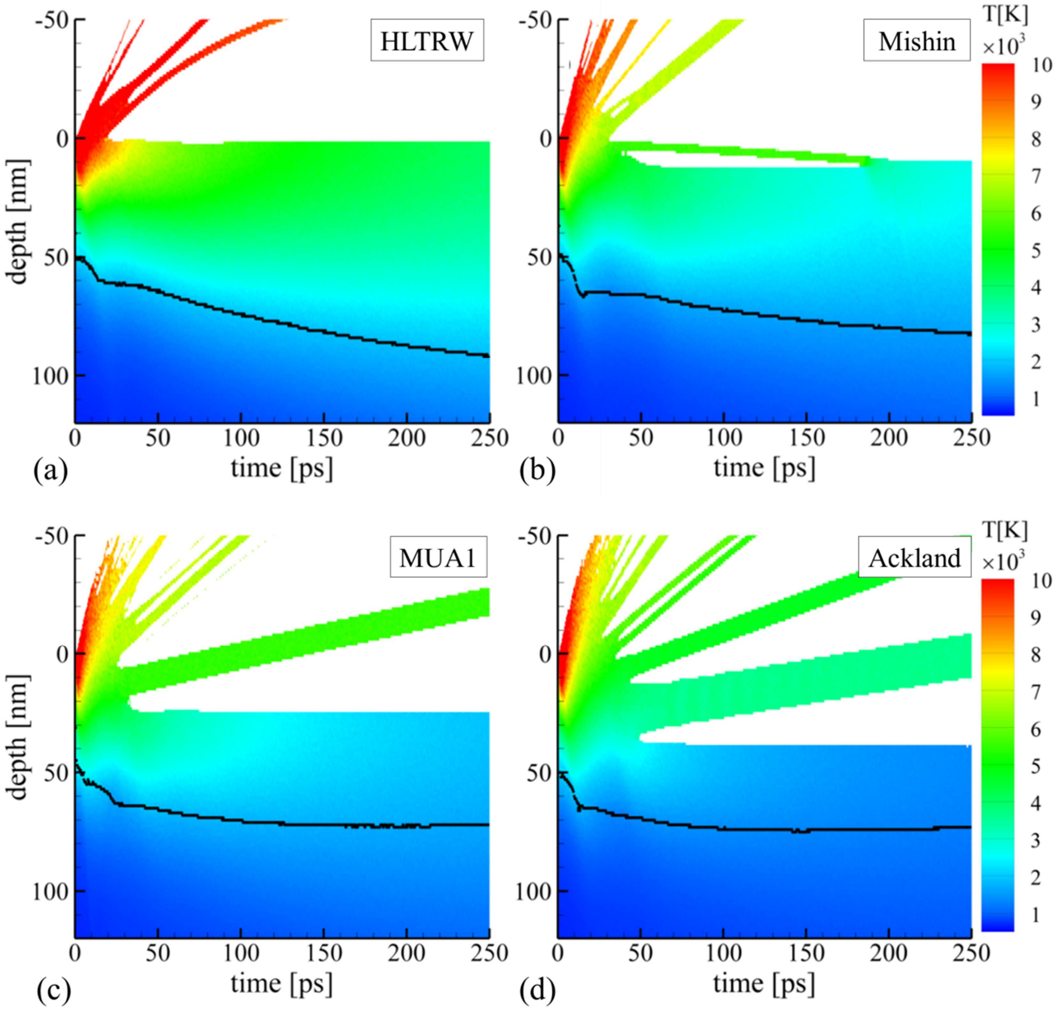

Figure 59. The evolution of the temperature in Ti targets irradiated at the laser fluence 1400 J/m^2. The laser irradiation is directed from the top, and the initial surface position is set to zero. The black line shows the position of the solid-liquid interface.

Figure 60b illustrates the number of atoms in the ablation plume corresponding to clusters of different size. The plot demonstrates a clear correlation between the critical temperature (Table 8) and the cluster size distribution. For HLTRW and Mishin Ti, having a high value of critical temperature, the number of individual atoms in the ablation plume is high, and abundance of clusters is low compared with other considered potentials. While, in the simulations with MUA1 and especially with Ackland potentials, which have a lower value of critical temperature, the abundance of clusters is higher.

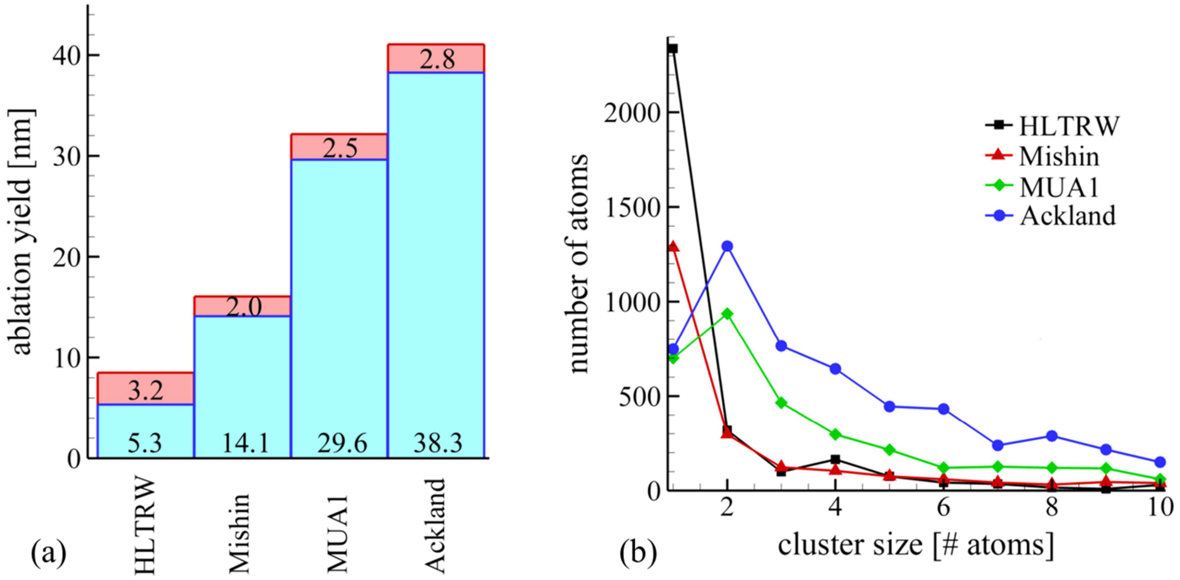

Figure 60. (a) Ablation yield of vapor, identified as atoms having less than six neighbors within the cutoff radius of the interatomic potential, (red) and residual species (blue). (b) The total number of atoms corresponding to clusters of different size. The cutoff distance used in the cluster analysis is 3.6 Å.

Microstructure modification in Ti

The analysis performed in the previous subsection has demonstrated that choice of the interatomic potential can adversely change the microstructure predicted in atomistic simulations. In particular, formation of high temperature BCC β-Ti phase is observed only in simulations with MUA1 and HLTRW potentials, and only the second potential can reproduce transformation of high temperature β-Ti phase into α-Ti phase when the temperature of the sample drops down. Small lateral system size of simulations reported above limits the ability of the model in predicting the final microstructure. Therefore, we ran an additional simulation with large system size of 103 nm × 102 nm × 70 nm and interatomic interactions described by HLTRW [261] potential. The absorbed laser fluence is 500 J/m^2, and pulse duration is 200 fs. Other parameters of the computational setup are identical to simulations described in the previous subsection.

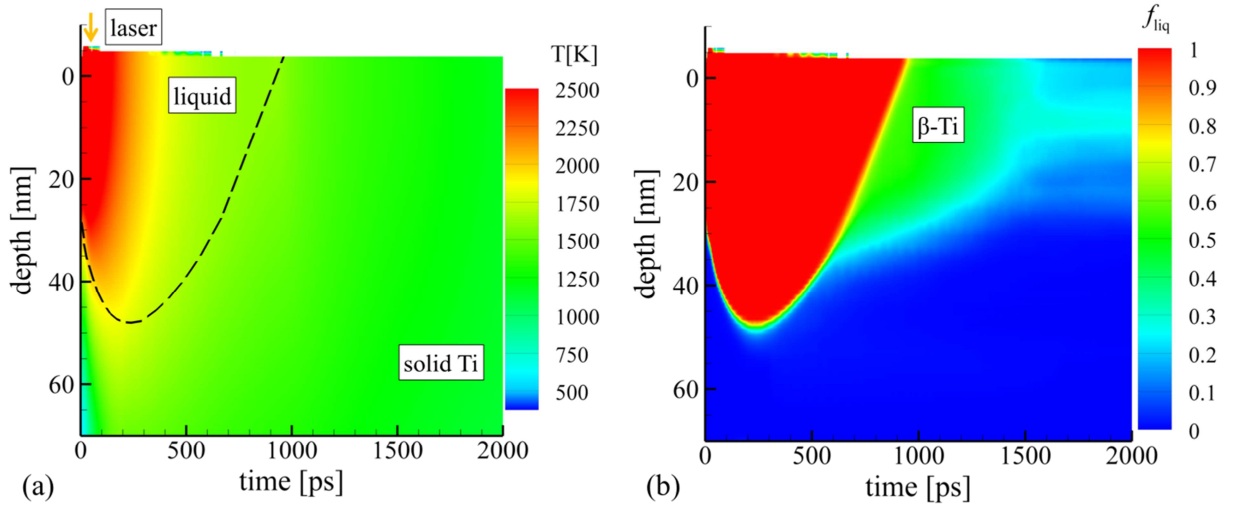

Figure 61. The evolution of temperature (a) and fraction of liquid (b) in Ti target irradiated at 500 J/m^2 absorbed fluence by 200 fs laser pulse. The laser irradiation is directed from the top, and the initial surface position is set to zero. In (a) molten part of the target is outlined by black dashed line. Since the fraction of melt is calculated based on the value of the local order parameter, atoms not corresponding to α-Ti phase with (0001) surface orientation may be recognized as liquid. Thus, these regions have greenish color.

After laser irradiation, approximately 48 nm of material is molten to the moment of 200 ps followed by solidification, Figure 61. Similar to irradiation of Ni (001) target discussed is Section 3.1, no dislocations are emitted initially during propagation of the tensile component of the laser-induced wave. Meanwhile, when solidification starts, several dislocations are generated during crystal growth. Their presence is demonstrated in Figure 62 in the bottom part of the system. Initially, solidification occurs through epitaxial regrowth of α-Ti. However, it is followed by cross-nucleation of β-Ti BCC high temperature phase at approximately 600 ps, when the temperature drops to ~0.89 $T_{\mathrm{m,hcp}}$. Cross-nucleation of several β-Ti nuclei results in growth of independent columnar grains elongated along z-direction during crystal growth. Formation of grains of similar shape is demonstrated in Ref. [286]. The characteristic size of grains in lateral directions is approximately 20 nm, and length is 35 nm. The solidification is complete to the time 1000 ps, and during the following 700 ps α-Ti appears inside the grains and coexists with β-Ti, as demonstrated in Figure 62a. In contrast to small scales simulations, periodic boundary conditions do not limit emergence and growth of α-Ti, therefore the transformation occurs more gradually at higher temperature 0.69-0.81 $T_{\mathrm{m,hcp}}$.

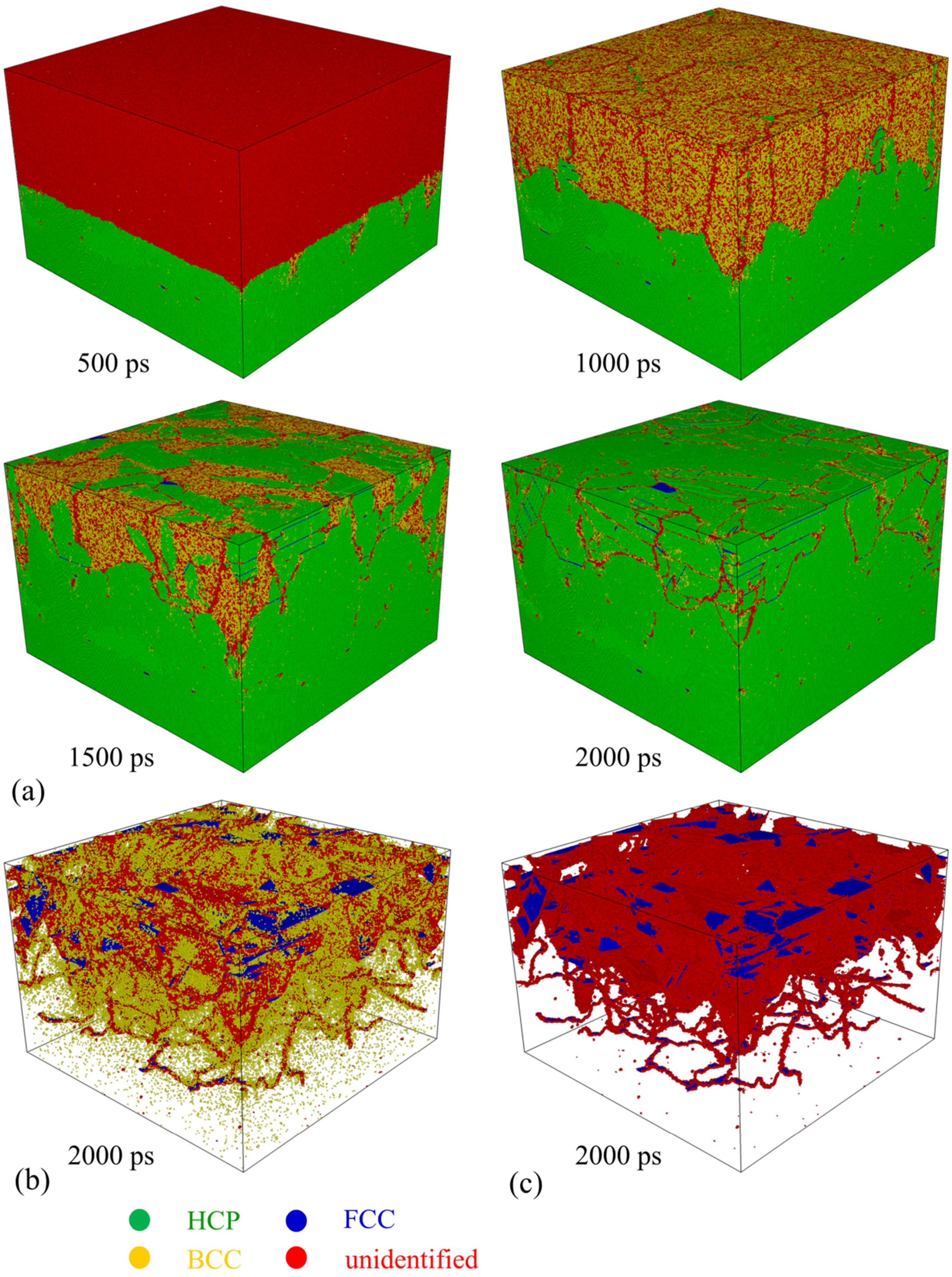

Figure 62. The microstructure produced by laser irradiation of Ti {0001} at 500 J/m^2 absorbed fluence and 200 fs pulse duration. Atoms are colored according to the local crystal structure environment. To illustrate the final microstructure, atoms having HCP (b) and both HCP and BCC (c) local structure environment are blanked to expose the final microstructure produced at 2000 ps. Approximately 2 nm surface layer is cut to expose the defect configuration.

To the time 2000 ps after laser irradiation, the high temperature β-Ti phase is transformed to α-Ti HCP phase, as illustrated in Figure 62a. During this process grains, formed initially, slightly shrink. Moreover, since α-Ti phase can form in several places within each β-Ti grain, additional grain boundaries are formed when these α-Ti parts meat each other. The resulting microstructure formed at the end of the simulation is illustrated in Figure 62. To depict the defect configuration, atoms with HCP and both HCP and BCC local crystal structure environment are blanked in Figure 62b and Figure 62c, respectively. Since HLTRW potential is capable to reproduce martensitic α-β phase transformation, a number of atoms and even atomic clusters have local BCC local crystal structure environment, shown by yellow, even at the time 2000 ps. Numerous grain boundaries generated after laser processing are depicted by red in Figure 62c. In addition, during recrystallization a number of coherent tween boundaries shown by blue are generated.

Summary

The aim of the work done in this subsection is drawing attention to the effect of high temperature material properties, which are usually ignored, on results of atomistic simulations. First, we have provided an overview of low temperature properties of a number of Ti EAM potentials and discussed their main advantages and drawbacks. Particularly, classical EAM potentials have a difficulty in reproduction of high stacking fault energy and solid-solid phase transitions. These difficulties are partially overcome in a newly developed MUA potentials [164]; however, description of martensitic phase transformations in Ti is still beyond capabilities of EAM potentials. Explicit consideration of an angular dependence of bonding in MEAM potentials drastically enhances the accuracy of material properties reproduction and allows description of martensitic phase transformations or even reproduction of full Ti phase diagram [261,262], including not only α-Ti and high temperature β-Ti but also high pressure ω-Ti phase. However, the computational cost of MEAM potentials is several times higher than for classical EAM potentials, and thus they are feasible for usage in cases where martensitic phase transformations are playing the major role.

Next, we focus on evaluation of high temperature material properties for a number of EAM Ti potentials. We have computed melting temperature, heat of fusion, and volume change of melting for both α-Ti and β-Ti phases in the first time. The procedure designed in our works provides a simple, accurate, and robust method of melting temperature evaluation: only several simulations are required to achieve accuracy on the order of 0.1 K. Based on our results, among considered interatomic potentials only MUA EAM [164] and HLTRW MEAM [261] potentials are capable to reproduce presence of high temperature β-Ti phase in the phase diagram.

Test area method has been applied to compute the surface tension of melt in the range of temperatures from 1500 K to ~$0.9T_c$. The calculated values are fitted based on the analytical dependence of surface tension on temperature predicted by mean field theory in a vicinity of the critical point. Our results demonstrate that for considered EAM potentials surface tension can be accurately approximated by this analytical dependence even at temperatures significantly below the critical point, and only HLTRW potential requires splitting the dataset into two intervals for fitting. However, the value of the critical exponent μ deviates from the analytical prediction since the considered temperature range is far from the critical temperature.

Critical point is evaluated for a number of Ti potentials based on results of coexistence simulations targeted on the reconstruction of the binodale line. The found in MD values of critical temperature and density are in a relatively good agreement with the experimental estimation of the critical point. However, the critical pressure for the most of Ti EAM potentials is strongly underestimated, and only HLTRW MEAM potential, which includes explicit angular dependence of the interatomic bonding, reproduces a comparable value.

Finally, we provide several examples of the effect of high temperature material properties on the microstructure and surface morphology modification predicted in atomistic simulations. We focus on applications involving MD simulations of laser-material interactions; however, the reported conclusions are rather general and can be imposed to interpret results of other applications involving high temperature material behavior. We have demonstrated how reproduction of the particular features of Ti phase diagram by interatomic potentials affects the microstructure modification in course of rapid melting and resolidification. Particularly, Mishin and Ackland potentials being unable to reproduce presence of high temperature β-Ti phase predict epitaxial regrowth accompanied by generation of growth twins. MUA1 potential predicts cross-nucleation of β-Ti phase and formation of a β-Ti layer, and only HLTRW potential is capable to reproduce the martensitic phase transformation of this layer into a polycrystalline α-Ti, when the temperature decreases.

We have also assessed the effect of high temperature material properties predicted by Ti interatomic potentials on simulation of laser ablation. Surface tension of melt and the critical temperature strongly affect the predicted ablation yield, which varies by more than 4 times for considered potentials. In addition, we have demonstrated that chose of the interatomic potentials strongly affects the cluster size distribution in the ablation plume.

When MD technique is utilized, it is always important to keep in mind that it is not an omnipotent tool, but only a technique that has its limitations. Results of atomistic simulations are not the inexorable truth but only a suggestion to a researcher who have to interpret them by answering the questions: what are the most important material properties determining the investigated process, how accurate interatomic potential reproduce those properties, and what is the effect of this inaccuracy on the predictions of atomistic simulations.

Generation of Frank Kasper σ-phase in Ni

Despite EAM potentials are suitable for description of materials with metallic bonding, a substantial covalent contribution in transitional metals makes it difficult to reproduce certain properties and requires accounting for directional nature of bonds. In particular, since ideal HCP and FCC have the same number of neighbors in the 1-st and 2-nd nearest neighbor shell and the same distance to the shells, the interaction with the 3-rd nearest neighbors should be sufficiently strong to distinguish HCP and FCC structures without introducing angular dependent components, which complicates the potential and increase the computational cost of the simulation. The ability to distinguish the contribution from the 3-rd nearest neighbor is not only important to reproduce the equilibrium FCC vs. HCP phase but also to accurately describe stacking fault and coherent tween boundary energies, one of the key parameters responsible for microstructure modification. One of the way to address this problem proposed by Mishin and used by him in fitting several interatomic potentials for Ni, Al, Ti, Ag, Cu [130,256,287] is adding an oscillating component to the interatomic potential to amplify the contribution of the 3-d and decrease the contribution of the 2-nd nearest neighbor shells, Figure 63e.

Oscillating shape of the pair interaction function allows reproducing the nearly exact experimental values of stacking fault and twin boundary energies within EAM framework. However, this approach is shown to have an unexpected drawback. In our study of the behavior of Mishin EAM Ni potential [130] under condition of deep undercooling we have identified a liquid-solid phase transition in systems cooled to $0.6T_m$ and below. As demonstrated in Figure 63a, in the temperature range $0.65\text{-}1.0T_m$ the self-diffusion in liquid is described with an Arrhenius dependence with activation energy E_b = 0.683 eV. However, self-diffusion experiences a noticeable drop at $0.6T_m$, and the diffusion barrier changes to 0.30 eV. This observation suggests a change of the structure. A visual analysis of the system (Figure 63c left) also suggests presence of an ordered structure; however, a crystal analysis tools such as OVITO [284] or DXA [179,180] are unable to recognize generation of any crystal structure.

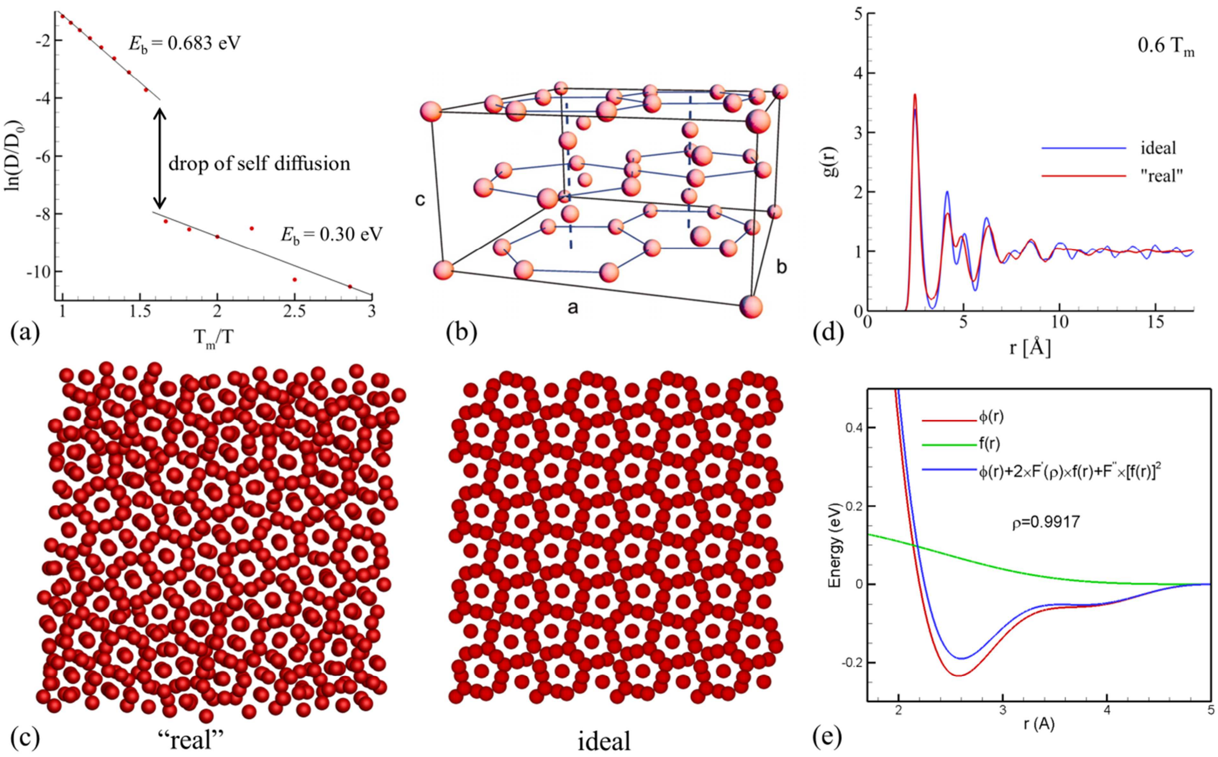

Figure 63. Temperature dependence of self-diffusion coefficient (a). Unit cell of Frank Kasper σ-phase adapted from Ref. [288] (b). Top view on a system generated in undercooled Ni (left) and Frank Kasper σ-phase (right) parallel to *c*-axis (c). The radial distribution function calculated for a system generated in undercooled Ni (red) and Frank Kasper σ-phase (blue) computed at $0.6T_m$ (d). The dependence of a pair component of EAM potential (red), electron density (green), and effective pair potential [289] (blue) computed by C. Wu for Mishin EAM Ni potential [130] (e).

The noticeable thing apparent from the radial distribution function depicted in Figure 63d by red is that the second peak is located at the distance more than 4 Å. Given the first peak at ~2.5 Å, the second peak in FCC and HCP is located at 3.5 Å and 2.9 Å for BCC, respectively. Therefore, the generated structure has icosahedral ordering. The most similar structure to one generated in the modeling is Frank Kasper (FK) σ-phase as demonstrated by the top view in Figure 63c and by radial distribution function in Figure 63d.

With using an approach suggested in Ref. [289], C. Wu have computed the effective pair potential under condition of constant average electron density Figure 63e that clearly demonstrates presence of oscillations. A recent study [290] demonstrates formation of different quasicrystal configurations for a one component system with particles interacting based on an oscillating pair potential, Table 9. Therefore, presence of oscillations can explain lower cohesive energy of the FK σ-phase for Mishin interatomic potential compared with other Ni potentials. However, the cohesive energy of FCC is still lower than for FK σ-phase, and, thus, generation of the icosahedral FK σ-phase structure is largely defined by kinetic factors.

Table 9. The cohesive energy and atomic volume of Frank Kasper σ, FCC, and HCP phases.

	Frank Kasper σ-phase		FCC		HCP	
	E_0 (eV)	V_0 (Å^3)	E_0 (eV)	V_0 (Å^3)	E_0 (eV)	V_0 (Å^3)
Mishin Ni [130]	-4.4176	10.92	-4.4500	10.90	-4.4279	10.95
FBD Ni [291]	-4.3565	11.15	-4.4500	10.90	-4.4506	10.90
Johnson Ni [81]	-4.3666	11.21	-4.4500	10.90	-4.4307	10.99

To sum up, an oscillating component of Mishin EAM Ni potential [130] introduced to provide an accurate description of stacking fault and twin boundary energies also stabilizes Frank Kasper σ-phase. As a result, under conditions of deep undercooling the model material experiences not classical nucleation and growth of FCC phase observed for other EAM potentials [81,291] in the previous study [292] but formation of FK σ-phase. Since presence of neither FK phases nor other quasicrystal phases is observed experimentally for single component metals, we conclude that this effect is artificial and resulted by oscillating component of the EAM potential introduced instead of angular dependent interaction.

3.5. Atomistic simulation study of short pulse laser interactions with a metal target under conditions of spatial confinement by a transparent overlayer[2]

Abstract: The distinct characteristics of short pulse laser interactions with a metal target under conditions of spatial confinement by a solid transparent overlayer are investigated in a series of atomistic simulations. The simulations are performed with a computational model

---

[2] Work reported in this section is done in collaboration with E.T. Karim. The results of the work are reported in Ref. [108].

combining classical molecular dynamics (MD) technique with a continuum description of the laser excitation, electron-phonon equilibration, and electronic heat transfer based on two-temperature model (TTM). The material response to the laser energy deposition is studied for a range of laser fluences that, in the absence of the transparent overlayer, covers the regimes of melting and resolidification, photomechanical spallation, and phase explosion of the overheated surface region. In contrast to the irradiation in vacuum, the spatial confinement by the overlayer facilitates generation of sustained high-temperature and high-pressure conditions near the metal-overlayer interface, suppresses the generation of unloading tensile wave, decreases the maximum depth of melting, and prevents the spallation and explosive disintegration of the surface region of the metal target. At high laser fluences, when the laser excitation brings the surface region of the metal target to supercritical conditions, the confinement prevents the expansion and phase decomposition characteristic for the vacuum conditions leading to a gradual cooling of the hot compressed supercritical fluid down to the liquid phase and eventual solidification. The target modification in this case is limited to the generation of crystal defects and the detachment of the metal target from the overlayer.

Introduction

While the general mechanisms of short pulse laser melting, spallation, and ablation of metals in vacuum and in a background gas have been extensively studied experimentally, theoretically, and computationally, the effect of strong spatial confinement of the laser-induced processes by a solid transparent overlayer remains largely unexplored. The spatial confinement is realized when a metal target (a film or a bulk substrate) is covered by a transparent overlayer, and the laser irradiation is focused on the metal surface through the overlayer. This setup has been shown to be advantageous for a number of practical applications, from laser shock peening [293-296] to laser-induced forward transfer [297-299] and thin film patterning/scribing [300,301], and to the generation of high-quality surface nanostructures [302]. In particular, a substantial increase in pressure generated in laser ablation confined by a glass overlayer [293,294,303] has been utilized in material processing by laser-induced shock waves [293-296] and has enabled design of “exotic targets” with enhanced momentum transfer for laser propulsion applications [304]. Recently, the generation of periodic nanostructures by multiple beam interference has been reported for Ni and Si surfaces covered by optically transparent 400 nm thick polymer layers [302]. A significant improvement in the quality of the nanostructured surfaces, as compared to processing of bare surfaces, is observed and attributed to the suppression of the expansion and breakup of molten material as well as trapping of the ejected droplets by the overlayer.

The analytical description and computer modeling of laser-induced processes under conditions of spatial confinement have been largely focused on thermodynamic analysis of the evolution of pressure exerted on the metal target by the vapor/plasma plume expansion and evaluation of the momentum transfer to the irradiated target [294,301,303,304]. In several recent numerical simulations of thin film removal by backside femtosecond pulse irradiation through a transparent substrate, the dynamics of the relaxation of thermo-elastic stresses and the mechanical deformation of the metal film are considered [141,296,305] and found to play the dominant role in the separation and ejection of the film fragments at laser fluences close to the ablation threshold [306]. The analysis of the effect of the spatial confinement on the kinetics and mechanisms of laser-induced phase transformation, as well as the structural modification of the metal target, however, is beyond the capabilities of the continuum-level finite difference [141] or finite element method [296,305] calculations. On the other hand, the atomistic molecular dynamics (MD) simulations, while more computationally expensive, have been shown to be capable of providing detailed information on the fast nonequilibrium structural and phase transformations induced by short pulse laser irradiation of thin films [11,28,183,307-310] and bulk targets [28,39,81,104,134,311-314] under vacuum conditions or in the presence of background gas [315].

Computational setup

The laser interaction with the bulk Ag target is simulated with a model that combines the classical MD method with the two-temperature model (TTM) [9] that describes the evolution of lattice and electron temperatures by two coupled nonlinear differential equations and accounts for the laser excitation of the conduction band electrons, electron-phonon energy exchange, and electron heat conduction. A complete description of the TTM-MD model is given in Ref. [102] and Section 2.1.1, and below we only delineate the computational setup and provide the parameters of the model used in the simulations reported in this subsection.

The interatomic interactions in the Ag target are described by the embedded atom method (EAM) potential in the form proposed by Foiles, Baskes, and Daw (FBD) [291]. A cut-off function [316] is added to the potential to smoothly bring the interaction energies and forces to zero at interatomic distance of 5.5Å. Although the FBD EAM potential is fitted to low-temperature values of the equilibrium lattice constant, sublimation energy, bulk modulus, elastic constants, and vacancy formation energy, it also provides a good description of high-temperature thermodynamic properties of Ag relevant to the conditions of laser-induced melting and ablation. In particular, the equilibrium melting temperature, T_m, determined in liquid-crystal coexistence MD simulations is 1139 K [317], about 8% below the experimental value of 1235 K [107]. Details on calculation of the spinodal line are provided in Section 4.1.

The choice of the parameters of the TTM equation for the electron temperature of Ag is the same as in Ref. [317], where a more detailed explanation of the parameters is provided. The electron temperature dependences of the electron-phonon coupling factor and electron heat capacity are taken in the forms that account for the thermal excitation from the electron states below the Fermi level [101]. The temperature dependence of the electron thermal conductivity is described by the Drude model relationship, with parameters evaluated based on the free electron model and the experimental value of the thermal conductivity of Ag [317].

The irradiation of the target with a 10 ps laser pulse is represented through a source term added to the TTM equation for the electron temperature [102]. The source term simulates excitation of the conduction band electrons by a laser pulse with a Gaussian temporal profile and reproduces the exponential attenuation of laser intensity with depth under the surface. To account for the energy transport occurring before the thermalization of the excited electrons, the optical absorption depth, L_p = 12 nm at laser wavelength of 1 μm, is combined with the effective depth of the "ballistic" energy transport, L_p = 56 nm, roughly estimated here as a product of the Fermi velocity and the Drude relaxation time [318]. To ensure complete deposition of the energy of the 10 ps laser pulses, the peak intensity of the Gaussian laser pulse is shifted to 25 ps from the beginning of the simulations. The absorbed laser fluence, F_{abs}, rather than the incident fluence is used in the discussion of the simulation results.

As illustrated in Figure 7 and Figure 64, the atomic-level TTM-MD representation is used only for the top part of the Ag target, where the laser-induced structural modifications take place. The systems with different depth of the TTM-MD region, $L_{TTM\text{-}MD}$, are used at different laser fluences, namely, $L_{TTM\text{-}MD}$ = 209 nm for F_{abs} = 900 J/m^2 and F_{abs} = 1000 J/m^2, $L_{TTM\text{-}MD}$ = 209 nm for F_{abs} = 3000 J/m^2, and $L_{TTM\text{-}MD}$ = 699 nm for F_{abs} = 6000 J/m^2. The heat transfer in the deeper part of the target is described by the TTM equations for lattice and electron temperatures solved down to the depth of $L_{TTM\text{-}MD} + L_{TTM}$, with L_{TTM} = 2.5 μm chosen to ensure the absence of any significant increase in the electron or lattice temperatures at the bottom of the computational domain by the end of the simulation.

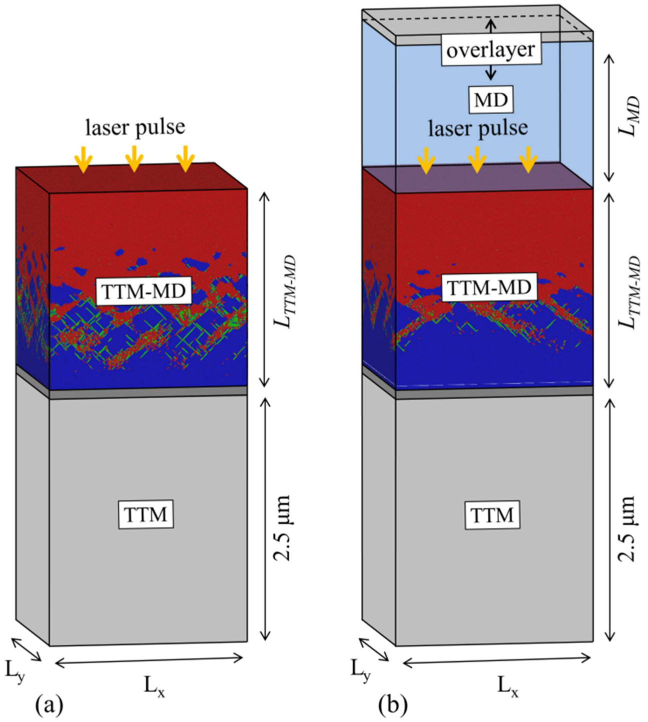

Figure 64. Schematic sketches of the computational setups used in MD simulations of laser interaction with metal targets in vacuum (a) and in the presence of an optically transparent solid (or liquid, as discussed in Section 3.6) overlayer (b). The top part of the target is represented by TTM-MD model, whereas the temperature evolution in the deeper part is described by TTM equations. Molecular dynamics representation is used for parts of the overlayers adjacent to the target, as shown by the blue rectangular parallelepiped in (b). At the bottom of the TTM-MD and on the top of the MD regions the pressure wave transmitting boundary conditions are imposed. The boundary conditions mimic the non-reflective propagation of laser-induced pressure waves in the Ag target and the overlayer, which are assumed to be sufficiently thick to ensure that any effects caused by the reflection of the waves from the outer surfaces of the target and overlayer can be neglected. Periodic boundary conditions are applied in the lateral directions, parallel to the surface of the target. The MD part is represented by atomistic snapshots reported in Section 3.6. Adapted from Ref. [319]

The lateral (parallel to the surface of the Ag target or the interface with the overlayer) dimensions of the computational systems are 4.1 × 4.1 nm^2, and the number of Ag atoms in the TTM-MD parts of the systems is 203 600 for $L_{TTM\text{-}MD}$ = 209 nm, 399 600 for $L_{TTM\text{-}MD}$ = 411 nm, and 680 000 for $L_{\text{TTM-MD}}$ = 699 nm. The periodic boundary conditions are imposed in the lateral directions to reproduce the interaction of the atoms with the surrounding material. This approach is appropriate when the laser spot diameter is much larger than the depth of the laser energy deposition, so that any effects related to the lateral variations of the irradiation and thermal conditions can be neglected, and the simulated part of the system remains laterally confined by the surrounding material during the time of the simulation. At the bottom of the TTM-MD part of the model, a special pressure-transmitting [105,106], heat-conducting boundary condition is applied in order to avoid an artificial reflection of the laser-induced pressure wave and to account for the heat transfer from the surface region of the metal target, represented with atomic-level resolution, to the deeper part of the target, represented at the continuum level. The simulations are performed for systems with free metal surfaces exposed to the laser irradiation as well as for metal targets covered by thick transparent overlayers. The computational representation of the overlayer is described in Section 2.1.1. Before applying the laser irradiation, all systems are equilibrated at 300K for 200 ps.

Thermal, stress, and spatial confinement in laser-materials interactions

To reveal the effect of the transparent overlayer on laser-induced processes, two series of simulations, with and without the overlayer, are performed for a range of laser fluences that covers the regimes of surface melting, photomechanical spallation, and phase explosion in the absence of the overlayer. The presentation of the results of the simulations is preceded by a brief discussion of the concepts of thermal, stress, and spatial confinement.

Before discussing the effect of the spatial confinement on the material response to the laser excitation, we would like to distinguish it from the thermal and stress confinement realized when the characteristic times of the redistribution of the absorbed laser energy by thermal conduction or stress waves are longer than the time of the temperature increase due to the laser energy deposition [27,28,104,134,320,321]. The condition for the thermal confinement, in particular, can be expressed as $max(\tau_p, \tau_{e-ph}) \leq L_c^2/2D_T$, where τ_p is the laser pulse duration, τ_{e-ph} is the characteristic time of the electron-phonon equilibration, L_c is the diffusive/ballistic penetration depth of the excited electrons before the electron-electron and the electron-phonon equilibration, and D_T is the thermal diffusivity of the target material. The condition for the stress confinement can be expressed as $max(\tau_p, \tau_{e-ph}) \leq L_c/C_s$, where C_s is the speed of sound in the target material.

In the simulations of Ag targets irradiated by 10 ps laser pulses, τ_p = 10 ps, τ_{e-ph} = 8 ps (defined as the timescale of the exponential decay of the energy of the excited electrons due to the electron-phonon coupling), L_c = 140 nm (defined as the depth where 63% of the total excitation energy is deposited by the time τ_{e-ph}), D_T = 1.47×10^{-4} m^2/s (in the solid state near the melting temperature), and C_s = 3650 m/s, Ref. [107]), the conditions for both thermal and stress confinement are satisfied, and a buildup of both thermal energy and the thermoelastic compressive stresses can be expected in the regions of the laser energy thermalization during the laser pulse [28,39,81,104,134,314]. The conditions of the thermal and stress confinement have similar effect on targets with and without the transparent overlayer, thus suggesting that the initial levels of temperature and pressure generated in both cases are likely to be similar.

In contrast to the thermal and stress confinement that define the initial temperature raise and pressure build up in the surface region of the irradiated target, the spatial confinement by the transparent overlayer is affecting the longer-term material response to the laser energy deposition and can have a significant effect on the laser-induced phase transformations, generation of crystal defects, surface damage, and material removal (ablation). The results of the atomistic simulations reported below are providing first detailed insights into the kinetics and mechanisms of the structural and phase transformations occurring under conditions of spatial confinement by a transparent overlayer.

Melting and resolidifications under conditions of spatial confinement

The effect of the spatial confinement on the processes of melting and resolidification induced by the laser energy deposition is illustrated in Figure 65, where the temperature and pressure evolution are shown for three simulations performed at the same absorbed laser fluence of 900 J/m^2. For a bulk Ag target with a free surface, in the absence of the overlayer, this fluence is about 10% above the threshold for surface melting. The energy transfer from the excited electrons to the lattice leads to a rapid temperature increase in a surface region of the target, Figure 65a. The temperature exceeds the equilibrium meting temperature of the EAM Ag, T_m = 1139 K at zero pressure, causing a rapid homogeneous melting of ~35 nm thick surface layer between 40 and 70 ps of the simulation time (15 and 45 ps after the time of the laser peak intensity). The steep temperature gradient established in the surface region by the end of the electron-phonon equilibration leads to the cooling of the melted region and causes epitaxial resolidification. The velocity of the solidification front increases with increasing degree of undercooling below the melting temperature, and the front reaches the surface of the target by the time of ~1.1 ns.

In the simulations performed for targets covered by an overlayer, Figure 65b and Figure 65c, the melting is limited to a few small regions transiently appearing in the vicinity of the interface with the overlayer and disappearing by the time of 400 ps. In the simulation where the overlayer is represented by an imaginary plane, Figure 65b, the melting affects a thin (<4nm) layer adjacent to the interface with the overlayer and another region that appears through homogeneous nucleation at a depth of about 10 nm below the interface. A very similar transient melting is observed in the simulation with the atomistic representation of the overlayer, Figure 65c, where two small melting regions transiently appear within 20 nm from the interface with the overlayer. The difference of these results from the much more extensive melting observed in the absence of the overlayer, Figure 65a, is surprising from the first sight, as the same initial temperature increase is caused by the laser energy deposition, and the temperature decrease is even faster in the case of free surface due to the rapid expansion of the surface region. To explain this difference, the evolution of the laser-induced pressure is considered below.

As discussed above, the rapid increase of the lattice temperature in the simulations takes place under conditions of the stress confinement, and results in the buildup of strong compressive stresses in the surface region of the irradiated target. The generation of compressive stresses of similar strength can be seen in all pressure plots shown in Figure 65. The relaxation of the compressive stresses, however, proceeds differently with and without the confining overlayer. Without the overlayer, the expansion of the compressed material results in the generation of a strong tensile component of the stress wave that follows the compressive component in its propagation into the bulk of the target, Figure 65a. In the presence of the overlayer, however, the tensile component of the stress wave is largely suppressed, Figure 65b and Figure 65c. Since the acoustic impedance of the overlayer material is more than twice smaller than one of Ag, the relaxation of the initial laser-induced compressive stresses results the generation of both a compressive wave in the overlayer and a relatively weak unloading wave in the Ag target.

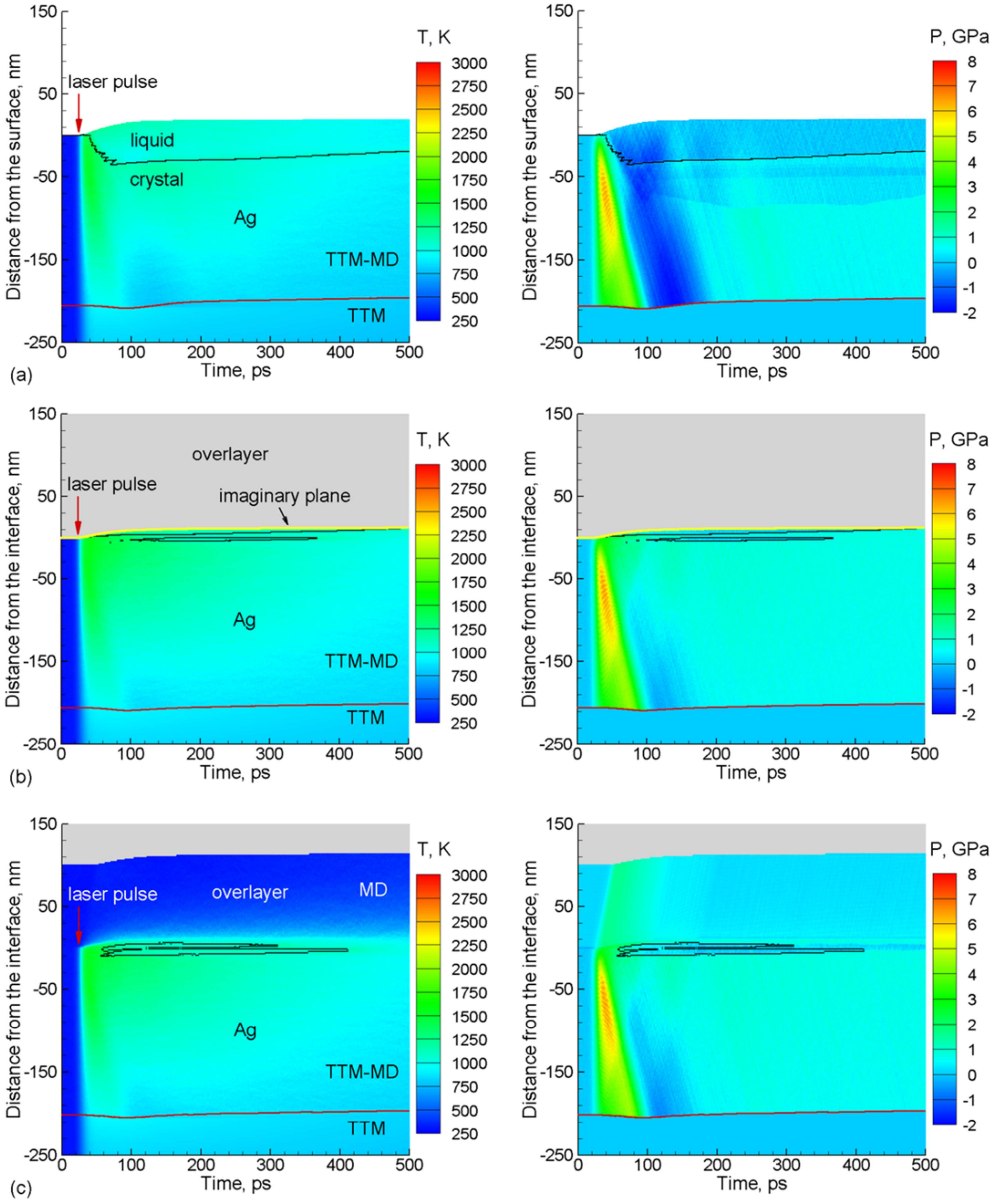

Figure 65. Temperature (left) and pressure (right) contour plots in simulations of a bulk Ag target irradiated by a 10 ps laser pulse at an absorbed fluence of 900 J/m^2. The irradiated surface is free of confinement in (a) and is covered by a transparent overlayer in (b,c). The overlayer is represented by a dynamic imaginary plane in (b) and by an atomistic MD description of a part of the overlayer adjacent to the Ag target combined with a pressure-transmitting boundary condition in (b). The laser pulse has a Gaussian profile with the peak intensity reached at 25 ps from the beginning of the simulations and is directed along the *y*-axis, as shown by the red arrows in the left panels. The black curves separate the melted regions from crystalline parts of the Ag target. The red curves separate the atomistic (TTM-MD) and continuum (TTM) parts of the model representing the Ag targets. The yellow curves in (b) show the position of the Ag-overlayer interface represented by the dynamic imaginary overlayer. Adapted from Ref. [108].

The suppression of the tensile component of the pressure wave by the overlayer has direct implications for the melting process. In the absence of the overlayer, the expansion of the surface region results in the tensile stresses and, concurrently, a transient temperature drop that can be estimated by considering the expansion as an isentropic process for which $(\partial P/\partial T)_S = T\alpha/c_p$ [11,102], where c_p is the specific heat capacity per unit volume, and α is the volume coefficient of thermal expansion. At the same time, the equilibrium melting temperature is also affected by the negative stresses, with the variation of the melting temperature described by the Clapeyron equation, $(\partial T/\partial P)_m \approx \Delta V_m/\Delta S_m$, where ΔV_m and ΔS_m are the volume change upon melting and the entropy of melting, respectively. Following an approach described in Ref. [102], the thermodynamic parameters of the FBD EAM Ag, $\Delta V_m = 0.81$ cm^3/mol, $\Delta H_m =$12350 J/mol, $\Delta H_m/T_m = 10.84$ J/(mol K), as well as $\alpha = 1.02\times10^{-4}$ K^{-1} and $c_p = 31.8$ J/(mol K) = 2.85 J/(cm^3 K) for the solid phase at $T \approx T_m$ and zero pressure have been evaluated based on the temperature dependences of volume and internal energy of liquid and solid phases at constant pressure. With these thermodynamic parameters, $(\partial T/\partial P)_m = 74$ K/GPa and $(\partial T/\partial P)_S = 41$ K/GPa for the solid phase close to the melting temperature and zero pressure. The steeper slope of the liquid-crystal coexistence line compared to the isentrope for the solid phase, $(\partial T/\partial P)_m > (\partial T/\partial P)_S$, typical for metals, suggests that the expansion of the target by the unloading wave facilitates melting despite simultaneously causing a transient cooling of the material. This explains why the partial suppression of the generation of the unloading wave also suppresses melting in the simulations of Ag targets covered by overlayers.

An examination of the pressure contour plots in Figure 65 also reveals that, in all simulations, the propagation of the unloading wave takes place on a background of quasi-static compressive stresses related to the inability of the crystalline part of the target to completely relax the thermoelastic stresses through uniaxial expansion in the direction normal to the irradiated surface or metal-overlayer interface [28,81,104]. The compressive stresses are partially relaxed by the emission of dislocations from the melting front in the simulation with free surface, Figure 65a, where the depth of the dislocation propagation can be seen from the reduction of the compressive stresses in a region extending down to ~45nm below the melting front. The emission of the dislocations coincides with the propagation of the unloading wave through the melting front and is triggered by the shear stresses transiently created by the unloading wave in the four different active $\{111\}$ slip planes of the single crystal fcc target oriented along $\langle 100 \rangle$ direction [76]. Interactions between the Shockley partial dislocations propagating on different slip planes result in the generation of immobile dislocation segments and formation of stable dislocation configurations in the sub-surface region of the target. The much weaker unloading wave generated in the presence of the overlayer is incapable of inducing the dislocation emission, and no dislocations are observed in simulations illustrated in Figure 65b and Figure 65c.

The results obtained with two different representations of the overlayer, Figure 65b and Figure 65c, are very similar to each other. This similarity suggests that both approaches provide an adequate description of the effect of the overlayer on the target response to the laser excitation under irradiation conditions that leave the overlayer intact. At higher laser fluences, however, a part of the overlayer adjacent to the metal target can be expected to undergo transient melting and possible mixing with the melted metal. To provide a semiquantitative description of these processes, the atomistic representation of a part of the overlayer adjacent to the metal target Figure 65b is used in the higher-fluence simulations presented below.

Suppression of laser spallation by the overlayer

A moderate increase in the absorbed laser fluence from 900 J/m^2 to 1000 J/m^2 leads, in the absence of overlayer, to the transition from the regime of melting and resolidification of a surface region of the target to a separation of a melted layer from the bulk of the target, Figure 66a. As discussed in a number of earlier papers, e.g., Refs. [28,39,104,134,314], the separation and ejection of the liquid layer (commonly referred to as spallation) is driven by the relaxation of the laser-induced stresses generated in the surface region of the target under conditions of stress confinement. The magnitude of both the compressive and tensile stresses increases with increasing fluence up to the spallation threshold, when the tensile stress exceeds the dynamic strength of the melted material leading to the nucleation, growth, and coalescence of multiple voids that eventually cause spallation of a liquid layer from the target. The spallation interrupts the heat flow from the hot surface layer to the bulk of the target and results in a rapid resolidification of the liquid part of the target left behind after the separation of the spalled layer. In the simulation illustrated in Figure 66a, the resolidification process is completed at ~550 ps after the laser pulse. Similarly to the lower fluence simulation discussed in the previous subsection, the emission of dislocations from the melting front takes place at the time when the tensile component of the stress wave crosses the melting front. The plastic deformation partially relaxes the residual compressive stresses in ~40 nm surface region of the resolidified target.

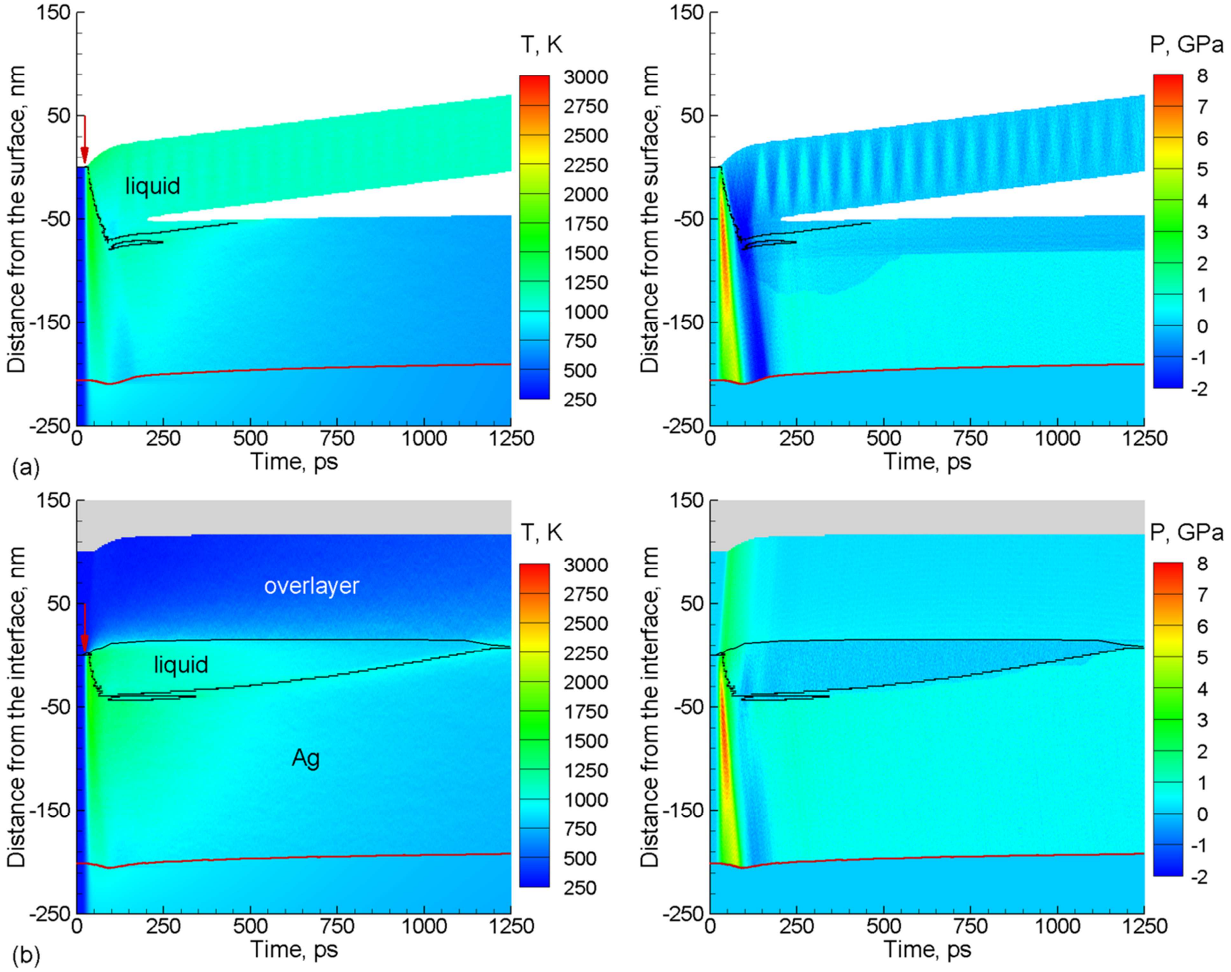

Figure 66. Temperature (left) and pressure (right) contour plots in simulations of a bulk Ag target irradiated by a 10 ps laser pulse at an absorbed fluence of 1000 J/m^2. The irradiated surface is free of confinement in (a) and is covered by a transparent overlayer in (b). The laser pulse has a Gaussian profile with the peak intensity reached at 25 ps from the beginning of the simulations and is directed along the Y-axis, as shown by the red arrows in the left panels. The black curves separate the melted regions from crystalline parts of the Ag target. The red curves separate the atomistic (TTM-MD) and continuum (TTM) parts of the model representing the Ag targets. Areas where the density of the material drops below 10% of the initial density of the solid Ag target are blanked in the plots. Adapted from Ref. [108].

Turning to the simulation of a Ag target covered by an overlayer, Figure 66b, the following effects of the spatial confinement can be observed: (1) the depth of the region affected by melting decreases from ~70 nm in Figure 66a to ~40 nm in Figure 66b as discussed in the previous subsection, (2) no dislocation emission from the melting front takes place, and (3) no voids nucleate in the melted region and no spallation occurs. All of these effects can be attributed to the containment of the free expansion of the surface region of the target and the corresponding suppression of the tensile component of the stress wave.

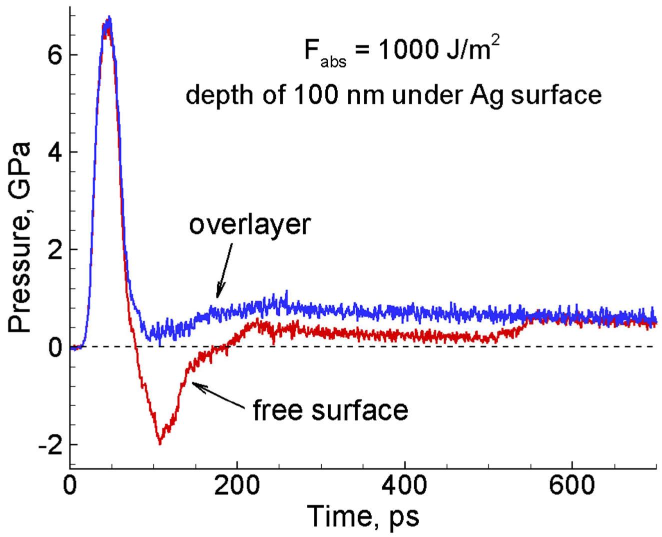

Figure 67. Pressure profiles at a depth of 100 nm below the surface of Ag targets in simulations performed with and without the transparent overlayer and illustrated by contour plots in Figure 66. Adapted from Ref. [108].

The suppression of the tensile stresses is illustrated in Figure 67, where the evolution of pressure at a depth of 100 nm below the irradiated Ag surface is shown in the form of pressure profiles. Although the initial peaks of the compressive pressure are almost identical in the two simulations, with the maximum pressure reaching ~6.7 GPa at ~45 ps after the laser pulse, the pressure profiles diverge after ~70 ps. In the case of free surface, the unloading tensile component of the pressure wave, while weakened by the void nucleation and spallation in the region closer to the surface, is still clearly pronounced and reaches the maximum value of ~2 GPa. In the presence of the overlayer, however, the pressure at this depth remains positive at all times. Following the initial dynamic relaxation of the laser-induced stresses, after ~250 ps, the level of pressure stays at an almost constant level that is slowly drifting from ~0.8 to 0.6 GPa during the time from 250 to 700 ps. As discussed in the previous subsection, this compressive pressure corresponds to the residual thermoelastic stresses that cannot relax by the uniaxial expansion of the crystal in the direction normal to the surface and are slowly decreasing due to the cooling by thermal conduction to the bulk of the target.

Note that the level of the residual stresses in the simulation with free surface stays at a lower level of ~0.2-0.3 GPa until the time of ~530 ps, when it increases to the level similar to the one observed in the presence of the overlayer. The reduction of the compressive stresses can be attributed to dislocations that propagate deeper than 100 nm during the initial relaxation of laser-induced stresses and bring the stress state of the crystal closer to hydrostatic one. The partial dislocations retreat up to the depth of ~80 nm below the original surface during the time of 400-600 ps, and the increase of the level of pressure at around 530 ps corresponds to the time when they cross the depth of 100 nm.

In the absence of spallation, the resolidification process in the target covered by an overlayer takes about 1.25 ns, Figure 66b, the time comparable to that in the simulation of a target with free surface performed at a lower fluence of 900 J/m^2, below the spallation threshold, Figure 65a. The melting turns into resolidification when the temperature of the liquid-solid interface drops below the melting temperature at ~150 ps, the solidification front accelerates with increasing supercooling and reaches its maximum velocity of ~65 m/s by the time of 1.1 ns. By this time, however, the temperature of Ag near the interface with the overlayer drops down to ~0.7 T_m, triggering nucleation of new crystallites near the interface and leading to the rapid solidification of the strongly supercooled layer of Ag adjacent to the interface. The relatively small lateral size of the computational cell used in the simulations, however, does not allow for a reliable investigation of the nucleation and growth of new crystallites in the supercooled interfacial region of the target, and additional larger scale simulations targeted at analysis of this phenomenon are reported in the Section 3.6.

Suppression of phase explosion by the overlayer

Further increase of the laser fluence above the spallation thresholds leads to explosive decomposition of the surface region of the target into vapor, clusters, and small droplets, which correspond to the transition from spallation to the phase explosion regime. The contour plots shown in Figure 68a depict dynamics of material decomposition in a simulation performed at a fluence of 3000 J/m^2, slightly above the threshold for this transition. The temperature plot exhibits a momentary (between 30 to 60 ps of the simulation, or 5 to 35 ps after the peak intensity of the 10 ps laser pulse) spike to the values exceeding the temperature of onset of explosive decomposition at zero pressure, ~3100 K, in the surface region with a depth of ~115 nm, close to the depth of the initial laser energy deposition.

The rapid cooling of this region proceeds through the expansion and decomposition of the material overheated above the limit of its thermodynamic stability into a mixture of liquid droplets, atomic clusters, and vapor. The unloading wave, while partially suppressed by the compressive pressure generated by the explosive decomposition and expansion of the top layer of the target, still generates tensile stresses that exceed -1 GPa below the depth of ~140 nm. These tensile stresses induce cavitation of the superheated liquid deeper into the target and, similarly to the spallation discussed above, lead to the ejection of additional large droplets.

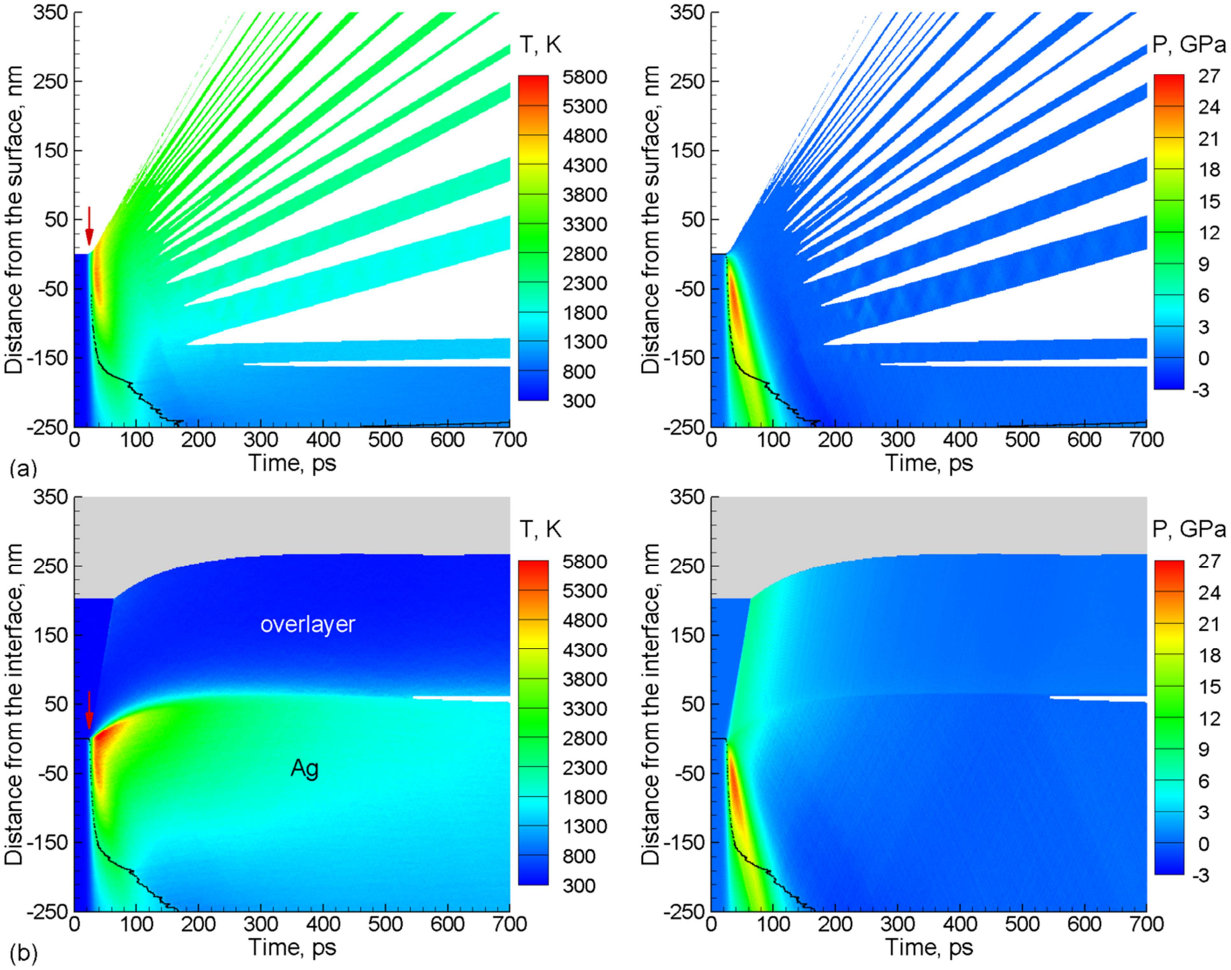

Figure 68. Temperature (left) and pressure (right) contour plots in simulations of a bulk Ag target irradiated by a 10 ps laser pulse at an absorbed fluence of 3000 J/m^2. The irradiated surface is free of confinement in (a) and is covered by a transparent overlayer in (b). The laser pulse has a Gaussian profile with the peak intensity reached at 25 ps from the beginning of the simulations and is directed along the *y*-axis, as shown by the red arrows in the left panels. The black curves separate the melted regions from crystalline parts of the Ag target. Areas where the density of the material drops below 10% of the initial density of the solid Ag target are blanked in the plots. Adapted from Ref. [108].

In contrast to the explosive decomposition of a surface region discussed above, no phase separation is observed in a simulation performed at the same laser fluence for a target covered by an overlayer, Figure 68b. The initial temperature increase is similar to the one in a target with free surface and brings the surface region to a supercritical state. Although the pressure from the hot metal pushes the overlayer up by 65 nm, the supercritical fluid remains confined by the overlayer. This confinement prevents the phase decomposition and fast cooling observed for a target with free surface and keeps the temperature and pressure of the surface region at high levels for a much longer time. Only by the time of 350 ps, the pressure in the interfacial region drops down to zero, and the expansion of the metal target turns into contraction as the interfacial region continues to cool down by thermal conduction to the bulk of the target. The contraction results in the formation of voids near the interface and eventual detachment of the metal target from the overlayer. In the absence of the phase explosion, which provides an efficient channel of fast cooling of the hot surface region of the target with free surface, the maximum melting depth is larger (270 nm vs 250 nm in the simulation with free surface), and the time needed for resolidification of the metal target is much longer. The emission of partial dislocations, though, is observed at this fluence both with and without overlayer.

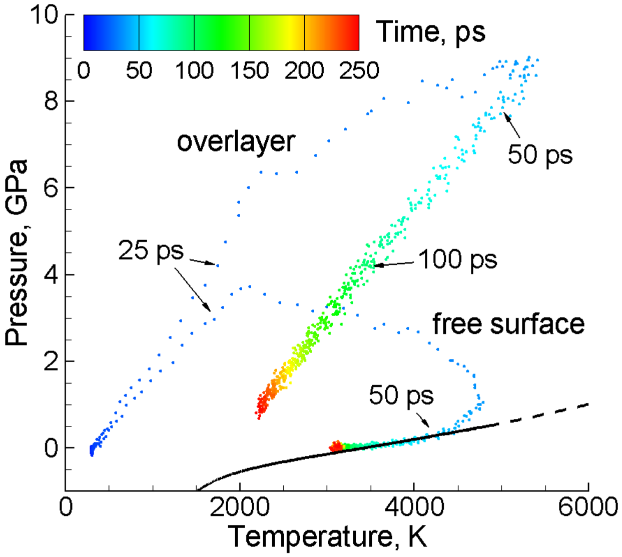

Figure 69. The evolution of temperature and pressure averaged over atoms that are initially located in the top 5 nm thick layer of the Ag target irradiated by 10 ps laser pulses at a fluence of 3000 J/m^2 with and without the presence of a transparent overlayer. The black curve shows the temperature–pressure conditions (T^*, P^*) for the onset of the cavitation or phase explosion in the metastable liquid, calculated for the EAM Ag material as explained in Section 4.1. Adapted from Ref. [108].

An additional illustration of the effect of spatial confinement by the overlayer on the conditions experienced by the top layer of the metal target is provided in Figure 69, where the temperature-pressure trajectories are shown for material initially located within the top 5 nm layer of the target. In the simulation with free surface, the initial linear pressure temperature dependence characteristic of almost constant volume heating of the layer (stress confinement) gives a way to the pressure drop associated with the onset of free expansion of the top layer at

~25 ps. The relaxation of the laser-induced pressure and continued temperature increase makes the trajectory cross the solid curve that marks the temperature and pressure conditions for the onset of the explosive phase separation into liquid and vapor, T* and P*, determined as explained in Section 4.1. In the presence of overlayer, however, the expansion of the hot metal layer is limited and the pressure builds up to much higher levels. The expansion of the surface allowed by up to 65 nm upward displacement of the overlayer results in a pressure plateau at the end of the electron-phonon energy equilibration and leads to a hysteresis in the pressure-temperature dependence, when the pressure decreases during the cooling of the interfacial region along the path that is almost parallel to the one of the heating stage but shifted to lower values of pressure for the same temperature. This hysteresis eventually leads to the detachment of the metal target from the overlayer when the pressure near the interface becomes negative after about 400 ps, when the temperature drops below 1800 K.

The overall picture of the material response to the laser energy deposition with and without the overlayer does not change even when the laser fluence is doubled from 3000 J/m^2 to 6000 J/m^2, Figure 70 and Figure 71. The much stronger laser excitation leads to higher maximum temperature and pressure, larger displacement of the overlayer, and higher melting depths of 455 and 415 nm with and without overlayer, respectively. The combination of the phase explosion and material expulsion due to the unloading wave leads to almost complete ejection of melted part of the target down to the depth of 385 nm in the case of the target with a free surface, Figure 70a. In the presence of the overlayer, the expansion of the metal brought to the supercritical state by the fast laser energy deposition is limited by the overlayer that maintains the high density and pressure of the supercritical fluid for hundreds of ps and prevents its decomposition into vapor and liquid droplets. The pressure exerted by the supercritical Ag pushes the overlayer by up to 137 nm by the time of 600 ps, when the pressure approaches zero level, Figure 70b. Similarly to the lower fluence simulation illustrated in Figure 68b, the cooling and contraction of the metal target lead to its detachment from the overlayer at around 800 ps, Figure 70b. The temperature of the metal near the interface is about 2500 K, more than twice above the melting temperature but below the stability limit for phase explosion. Due to the high temperature of the interfacial region, the detachment takes place at a relatively low negative pressure of about -0.11 GPa (this value is obtained by averaging from 700 to 800 ps over the top 50 nm part of the metal target).

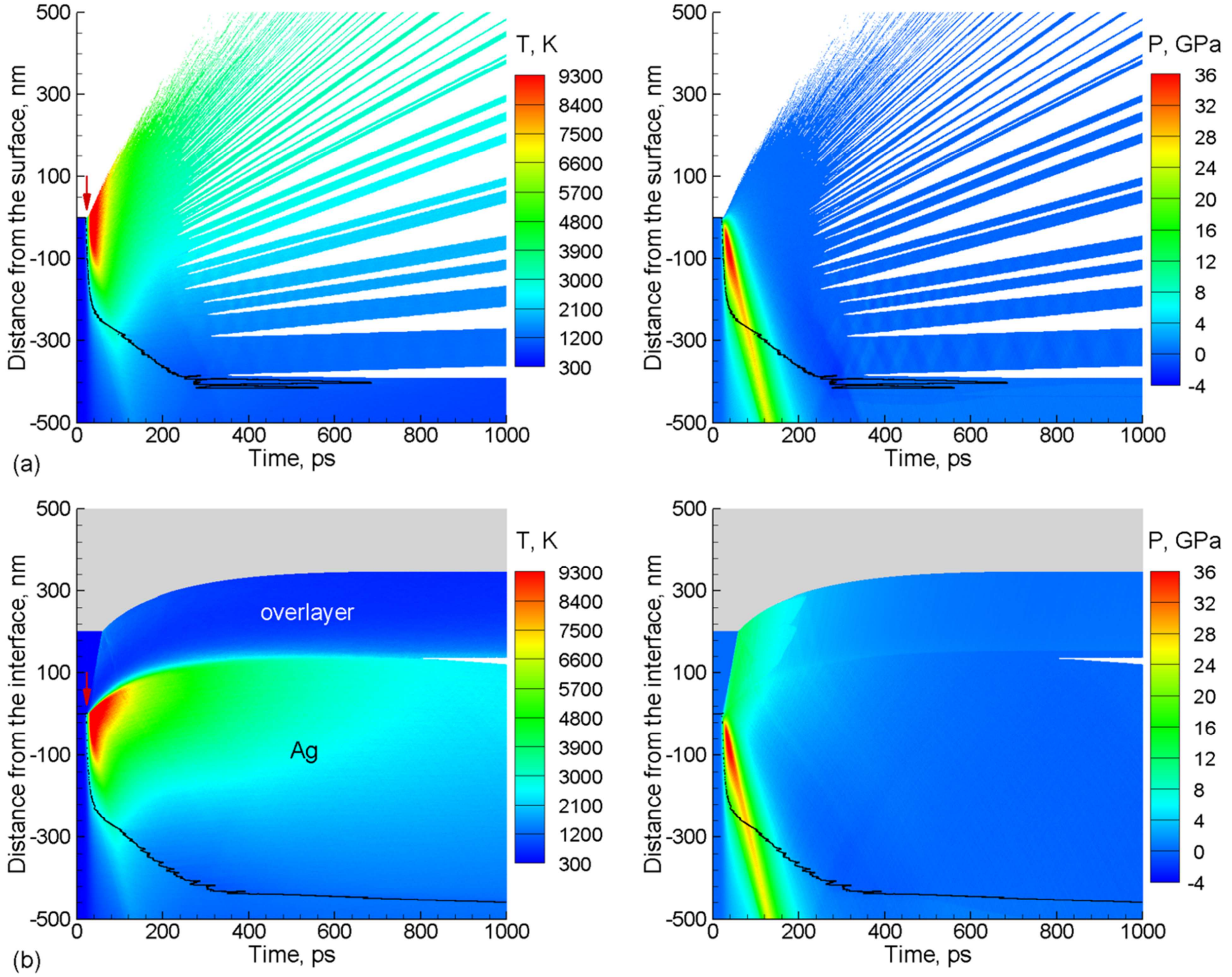

Figure 70. Temperature (left) and pressure (right) contour plots in simulations of a bulk Ag target irradiated by a 10 ps laser pulse at a fluence of 6000 J/m^2. The irradiated surface is free of confinement in (a) and is covered by a transparent overlayer in (b). The laser pulse has a Gaussian profile with the peak intensity reached at 25 ps from the beginning of the simulations and is directed along the *y*-axis, as shown by the red arrows in the left panels. The black curves separate the melted regions from crystalline parts of the Ag target. Areas where the density of the material drops below 10% of the initial density of the solid Ag target are blanked in the plots. Adapted from Ref. [108].

The temperature-pressure trajectories shown in Figure 71 further illustrate the difference in thermodynamic conditions experienced by the material in the top surface layers of the two targets. While in both simulations, the strong laser excitation brings the layers into supercritical state, the evolution of the supercritical fluid is very different in the two cases. In the absence of overlayer, free expansion of the supercritical fluid releases the pressure and results in complete vaporization of the material. The supercritical fluid confined by the overlayer, on the other hand, slowly cools down from the supercritical to the liquid state without crossing the line that corresponds to the explosive phase separation.

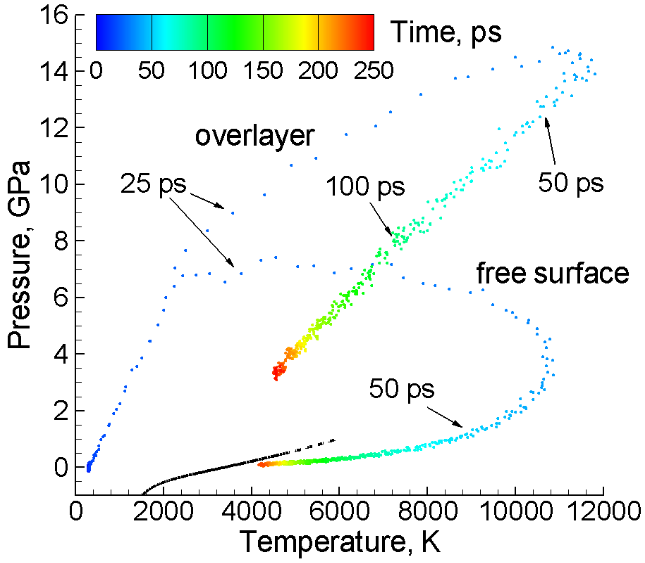

Figure 71. The evolution of temperature and pressure averaged over atoms that are initially located in the top 5 nm thick layer of the Ag target irradiated by 10 ps laser pulses at a fluence of 6000 J/m^2 with and without the presence of a transparent overlayer. The black curve shows the temperature–pressure conditions (T^*, P^*) for the onset of the cavitation or phase explosion in the metastable liquid, calculated for the EAM Ag material as explained in Section 4.1. Adapted from Ref. [108].

The observation that the maximum temperature of the top region reaches ~12 000K in the simulation with overlayer and ~11 000K without overlayer by the time of ~40 ps suggests the possibility of ionization of a fraction of Ag atoms. Indeed, estimations based on the Saha equation yields ionization fraction of about 1% at densities realized during the peak temperatures. The short time of the temperature spike (the temperature drops down to 9000K by 80 ps and down to 6000K by 170 ps in the simulation with overlayer, where the cooling is slower) and the high density of the supercritical fluid indicate, however, that any effects related to the ionization and charge fluctuations [20] in the supercritical fluid are likely to have negligible effect on the material expansion and interaction with the overlayer under conditions considered in the simulations.

The mechanisms responsible for the appearance, growth, and percolation of the interfacial voids leading to the detachment of the overlayer from the metal substrate are investigated in a large-scale atomistic simulation reported in Ref. [80]. The growth and coalescence of the interfacial voids results in the formation of liquid bridges connecting the overlayer and the metal substrate, whereas solidification of the transient liquid structures produced by the breakup of the liquid bridges may be responsible for the formation of the nanoscale roughness of the interfacial voids observed in experiments [80].

The effect of preexisting interfacial voids

In contrast to the perfect metal–overlayer interface considered in the previous section, real experimental samples may contain small interfacial gaps or voids formed in the process of sample preparation. Moreover, the voids generated by prior laser pulses may affect the response of the target to irradiation by subsequent laser pulses in the multi-pulse irradiation regime. To investigate the effect of preexisting interfacial voids on the laser-induced processes, a simulation of a system with a 50-nm gap between the transparent overlayer and Ag substrate has been performed for a system irradiated at 4000 J/m^2.

The evolution of temperature, pressure and density in the irradiated system is presented in Figure 72. The presence of the void makes it possible for the hot metal region to expand and generate an unloading wave propagating from the interfacial region and initiating the material decomposition down to the depth ~180 nm. As a result, the initial stage of the material response to the laser excitation is similar to the one of a target with a free surface, when the top surface region undergoes an explosive decomposition into a mixture of vapor and small droplets while the generation of voids in a deeper and colder melted region is driven by the tensile stresses associated with the unloading wave [39,104,134]. In the present simulation, however, the collision of the ejected material with the overlayer interrupts the expansion of the ablation plume, converts the kinetic energy of directed motion of the plume into thermal energy, and creates highly energetic supercritical fluid with the maximum temperature and pressure values reaching 10 000 K and 8 GPa by the time of 70 ps.

The pressure exerted by the hot supercritical metal pushes the overlayer up by ~100 nm and launches a compaction wave that stops the material decomposition initiated by the unloading wave and leads to the collapse of all but the deepest subsurface voids generated in the course of the initial material expansion. Each of the collapsing voids generates a pressure pulse consisting of compressive and unloading/tensile components that can be seen in the pressure contour plot in Figure 72. The initial electronic heat transfer to deeper regions of the metal substrate combined with the fluid expansion and the energy loss on the mechanical work spent on displacing the overlayer (the latter can be estimated to be on the order of 400 J/m^2,which roughly corresponds to the thermal energy change upon cooling of a 50 nm Ag layer by ~2500 K) leads to a rapid cooling of the interfacial part of the metal substrate from the supercritical state with temperature of ~10^4 K down to the regular liquid with a temperature of 2700 K by the time of 900 ps.

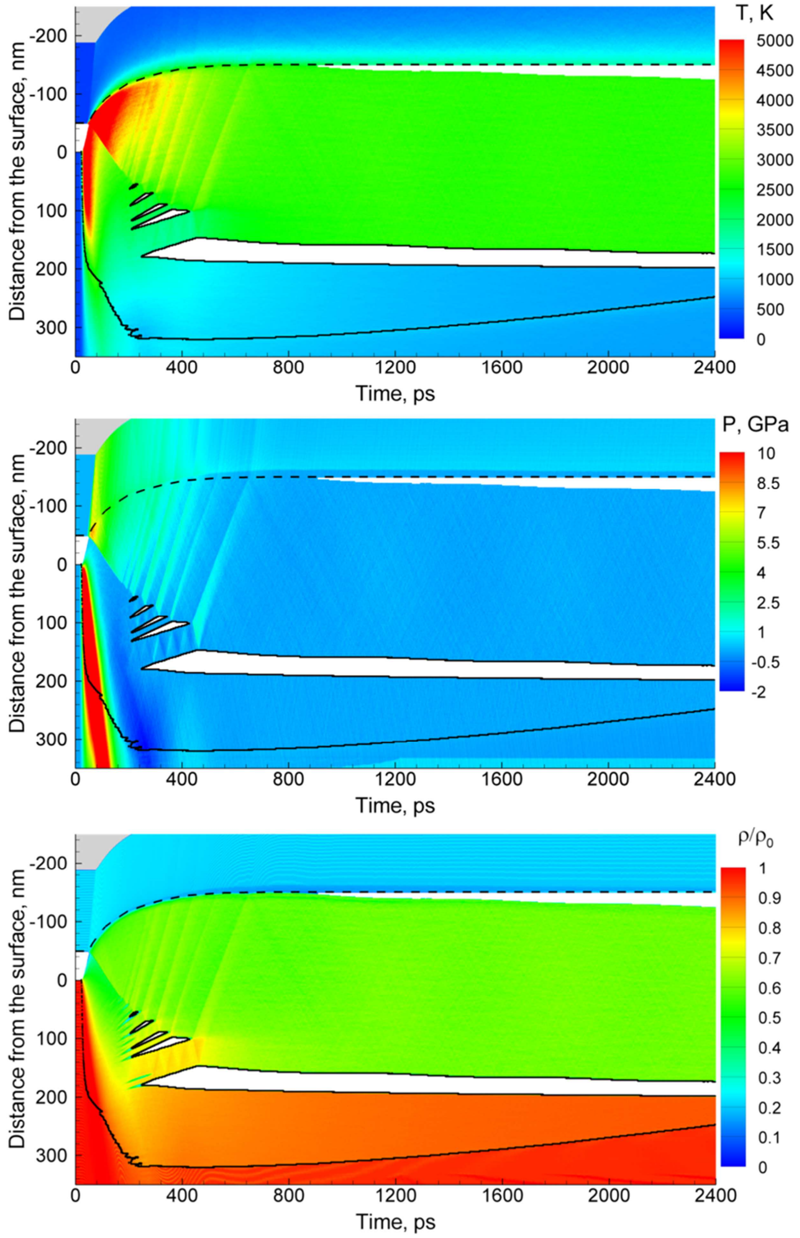

Figure 72. Temperature, pressure and density contour plots obtained in a simulation of bulk Ag substrate covered by a transparent overlayer with an initial 50 nm thick gap between the overlayer and the Ag substrate. The Ag-overlayer target is irradiated by a 10 ps laser pulse at an absorbed laser fluence of 0.4 J/cm^2. Areas where the density of the material drops below 10 % of the initial density of the solid Ag target are blanked in the plots. The black curves outline voids inside the material and separate the melted region from the crystalline part of the Ag target. The black dashed line shows the position of the Ag-overlayer interface. Adapted from Ref. [80].

At 900 ps, the combined effect of the contraction of the rapidly cooled liquid Ag and an arrival of a weak tensile stress wave generated at the onset of the collapse of the last void (the maximum tensile stresses at the interface reach the level of about -50 MPa at 850 ps) results in the detachment of the metal substrate from the overlayer at the interface. Given the slower (~11 m/s) downward motion of the detached liquid layer as compared to the faster (~56 m/s) advancement of the solidification front, one can expect the solidification front to reach the location of the void ~1.5 ns earlier. While the small lateral size of the computational system used in this simulation does not allow us to simulate the void capture and stabilization by the solidification front, such process has been observed in larger-scale simulations of laser interaction with an Ag target in vacuum [17]. Thus, the results of the simulation discussed above indicate that the presence of preexisting interfacial voids may facilitate generation of voids at some depth below the interface, as observed in experimental images in Ref. [80].

Summary

The effect of spatial confinement on laser-induced structural and phase transformation in a metal target is investigated by contrasting the results of two series of simulations of short pulse laser interactions with a bulk Ag target. The metal target is covered by a thick transparent overlayer in one series of simulations and has a free surface in the other series. The simulations are performed with a combined atomistic-continuum TTM-MD model accounting for the laser excitation of conduction band electrons, electron-phonon equilibration, as well as electronic and phononic heat transfer in the metal target and the overlayer. The model is extended by incorporation of two alternative computational methods for representations of the transparent overlayer. In one method, the layer is represented by a dynamic acoustic impedance matching boundary condition designed to represent the partial propagation of the laser-induced pressure wave into the overlayer, as well as the work of adhesion between the metal and the overlayer. In the second method, a part of the overlayer is represented with atomic resolution, allowing not only to account for the elastic response of the overlayer but also to reproduce the plastic deformation, melting, and atomic mixing in the region of the overlayer adjacent to the hot metal target. Both methods are parameterized for Ag-silica system and show similar performance at low fluences, when no melting of the overlayer takes place. The second (atomistic) representation of the metal overlayer interface is used in the simulations performed at high fluences, when melting and atomic mixing take place on both sides of the interface.

The simulations are performed for a broad range of laser fluences that, in the absence of overlayer, covers the regimes of melting and resolidification, photomechanical spallation, and phase explosion of the surface region of the metal target. At low fluences that correspond to melting and spallation of targets with free surfaces, the spatial confinement by the overlayer is found to suppress the generation of the unloading tensile wave, decrease the maximum depth of melting, reduce or eliminate the emission of dislocations from the melting front, and prevent the cavitation and spallation in the surface region of the metal target.

At higher fluences that bring the surface region of the metal target to the supercritical state, the confinement prevents the expansion and explosive phase decomposition of the surface region and leads to a gradual cooling of the hot and compressed supercritical fluid down to the liquid phase. This is in a sharp contrast with the material response to the same laser energy deposition under the vacuum conditions (free surface of the target), when the free expansion of the supercritical fluid results in a rapid cooling and phase decomposition into liquid droplets and vapor or complete vaporization of the top surface layer at higher fluences. The confinement of the superheated metal by the overlayer increases the maximum depth of melting and the time required for resolidification after the laser pulse. Moreover, the relatively long lifetime of the supercritical state sustained under conditions of spatial confinement results in a transient melting of a part of the overlayer exposed to the hot metal and atomic mixing between the overlayer material and metal within tens of nanometers from the interface. The simulations also suggest the possibility of detachment of the metal target from the overlayer during the rapid cooling and contraction of the surface region of the metal target.

3.6. Generation of nanocrystalline surface layer in short pulse laser processing of metal targets under conditions of spatial confinement by solid or liquid overlayer[3]

Abstract: The effect of spatial confinement by a solid or liquid overlayer on short pulse laser-induced modification of subsurface microstructure is investigated in a series of large-scale atomistic simulations performed for Ag targets irradiated in the regime of melting and resolidification, below the thresholds for laser spallation and ablation. For Ag targets with free surfaces, the formation of a nanocrystalline region with random crystallographic grain orientation is observed under irradiation conditions leading to the generation of numerous sub-surface voids that slow down the solidification process. When no voids are generated, the resolidification produces grains misoriented with respect to the bulk of the target by just several

---

[3] Work reported in this section is done in collaboration with C. Shih and C. Wu. Results of this work are reported in Ref. [319].

degrees and separated from each other by low angle grain boundaries or dislocation walls. The presence of a liquid or solid overlayer suppresses nucleation of sub-surface voids, provides an additional pathway for cooling through the heat conduction to the overlayer, and facilitates the formation of nanocrystalline structure in a region of the metal target adjacent to the overlayer. Moreover, the stabilizing effect of the solid overlayer may result in an incomplete melting of metal in the vicinity of the interface, making it possible for grains growing from the interface to retain "memory" of the target orientation and to produce nanocrystalline interfacial region with small misorientation of grains with respect to the bulk of the target. In all simulations, the nanocrystalline layers generated by laser processing of single crystal Ag targets are characterized by a high density of stacking faults, twin boundaries, and point defects produced in the course of the rapid resolidification.

Introduction

Laser processing of metal surfaces in liquid environment and in the presence of a solid overlayer has a number of distinct characteristics that may be beneficial for practical applications. The confining effect of optically transparent solid or liquid layers covering irradiated targets can alter the dynamics of material decomposition and ejection in the ablation regime [264,322-325], thus directly affecting the surface morphology of laser-modified targets. Moreover, the interaction of melted metal with an overlayer can contribute to cooling of the molten layer, thus creating conditions for stronger, as compared to laser processing in air or vacuum, undercooling and formation of highly nonequilibrium subsurface microstructure. Indeed, a number of experimental studies have demonstrated that the presence of liquid environment [326-334] or a solid overlayer [80,302,335] can have major impact on the morphology of laser-processed surfaces. The effect of the spatial confinement on the microstructure of the irradiated targets has also been demonstrated in laser shock peening experiments performed in the ablation regime [293,294,296].

More "gentle" microstructure modification at lower laser fluences, in the regime of melting and resolidification, however, has not been investigated in the presence of liquid or solid over-layers so far. For irradiation in vacuum or in air, the utility of short laser pulses for selective nanoscale engineering of subsurface microstructure has been demonstrated for various material systems. In particular, the formation of nanoscale twinned domains has recently been observed in femtosecond laser processing of Ni and explained by the onset of growth twinning under conditions of strong undercooling realized in the course of the rapid resolidification of a transiently melted surface region [32] (Section 3.2). Even stronger undercooling of the melted region, sufficient to trigger massive nucleation of new crystallites and generation of nanocrystalline surface layer with high density of twin boundaries and stacking faults present in the nanograins, has been predicted in recent atomistic simulations of laser processing of Ag targets [17].The possibility of the generation of thin nanocrystalline layers with high density of twins is highly attractive, as such layers can exhibit an unusual combination of high strength and ductility [336-339], as well as enhanced catalytic activity [36,37] and tunable surface reflectance spectra [38]. The results of the simulations, however, suggest that the laser-induced generation of nanocrystalline layer on the surface of a pure Ag target is only possible in a narrow range of laser fluences close to the spallation threshold, when the generation sub-surface voids slows down the propagation of the resolidification front from the bulk of the target [17]. This leads to an intriguing question on whether the presence of liquid or solid overlayer could broaden the range of irradiation conditions that yield surface nanocrystallization and result in the formation of a nanocrystalline surface layer without the generation of sub-surface voids.

In this section we investigate the specific mechanisms of overlayer-assisted surface nanostructuring by performing a series of large-scale atomistic simulations of short pulse laser irradiation of Ag targets in water environment and under confinement by a silica glass overlayer, and contrasting the results of these simulations to the ones obtained for similar irradiation conditions in vacuum. The main focus of the analysis of the simulation results is on revealing the irradiation conditions and mechanisms responsible for the generation of nanocrystalline surface layer and establishing the processes that control the structural characteristics of the nanocrystalline layer.

Computational model

The computational setups used in the simulations of laser interactions with bulk Ag targets in vacuum and in the presence of liquid or solid overlayer are discussed in Section 2.1.1 schematically illustrated in Figure 64. In all simulations, the top part of the Ag target is simulated with a hybrid atomistic–continuum model [102] that combines the classical molecular dynamics (MD) method [85] with the continuum-level two-temperature model (TTM) [9]. The detailed description of the model is provided in Section 2.1.1 and Section 3.5, and below we outline only the key parameters relevant to the simulations reported in this section.

The system used in the simulation is schematically outlined in Figure 64. Since the goal of this study is to explore the possibility of laser-induced surface nanocrystallization, the irradiation conditions in all simulations are chosen to produce transient melting and resolidification of a surface region of the target. The simulations of laser interaction with Ag targets in vacuum are performed for two sets of irradiation parameters (laser pulse duration τ_p and absorbed laser fluence F_{abs}). The first set, τ_p = 100 fs and F_{abs} = 850 J/m^2, corresponds to the formation of a porous sub-surface region covered by a nanocrystalline surface layer, as discussed in detail in Ref. [17]. The second set is performed with τ_p = 10 ps and F_{abs} = 900 J/m^2 and results in the melting and resolidification of ~60 nm surface layer without nucleation of sub-surface voids. Dimensions of the computational systems in lateral directions are about 100 nm × 100 nm. The depth of the surface part of the Ag target represented with atomistic resolution, $L_{\text{TTM−MD}}$ in Figure 64, is 150 nm for the first set and 103 nm for the second set of irradiation parameters, which corresponds to 84.2 and 62.5 million Ag atoms, respectively (the lateral size of the computational cell used in the second simulation is slightly larger, 103 nm × 103 nm). The interatomic interactions are described by the embedded atom method (EAM) potential parametrized for Ag [291].

The simulation of laser melting and resolidification in liquid environment is performed for irradiation parameters of τ_p = 100 fs and F_{abs} = 850 J/m^2. These parameters are the same as in the first simulation in vacuum, making it possible to directly compare the results and elucidate the effect of the liquid environment on the material response to the laser excitation. The TTM-MD part of the model has a depth of $L_{\text{TTM-MD}}$= 200 nm and consist of about 114.8 million Ag atoms. The liquid environment above the Ag target is described by a combination of a coarse-grained MD model parametrized for water [264,340,341] and a dynamic acoustic impedance matching boundary condition [108]. The coarse-grained MD model represents several water molecules by a single particle, which drastically increases the computational efficiency of the model. Despite the reduced, as compared to real water, number of dynamic degrees of freedom, the coarse-grained MD model enhanced by an advanced local heat bath approach [264,340,341] is capable of reproducing, at a semi-quantitative level, many of the relevant experimental properties of real water. In particular, the density and heat capacity are directly fitted to the experimental values, while the speed of sound, bulk modulus, viscosity, surface energy, melting temperature, critical temperature, and critical density do not deviate from the experimental values by more than 25% [264]. The thickness of a part of water overlayer represented by the coarse-grained MD model is L_{MD} = 300 nm, and the corresponding number of coarse-grained particles is 36.1 million. The dynamic impedance matching boundary condition based on an imaginary plane approach [108] is applied at the top of the coarse-grained MD region to ensure nonreflecting propagation of the pressure wave generated at the metal-water interface into the bulk of the water environment. This boundary condition mimics the response of an infinitely thick overlayer and is suitable for simulation of experimental conditions, where the reflection of the pressure wave from the outer surface of the water overlayer does not have any significant effect on processes occurring in the vicinity of the irradiated metal surface.

The effect of the solid transparent overlayer on the microstructure modification is studied for irradiation parameters of τ_p = 10 ps and F_{abs} = 1000 J/m^2. These irradiation conditions result in approximately the same melting depth as in the second simulation performed in vacuum, where the same pulse duration but a lower laser fluence of 900 J/m^2 is used. The overlayer is represented by MD model with particles interacting with each other through Lennard-Jones potential fitted to approximately reproduce the elastic properties and melting temperature of fused silica glass. Similar to the liquid overlayer, the dynamic impedance matching boundary condition is applied at the top of the MD region to simulate nonreflecting propagation of the laser-induced pressure wave into the bulk part of a thick overlayer. Details of the implementation and parametrization of the computational description of the silica overlayer are providers in Ref. [108]. The initial sizes of the TTM-MD and MD computational domains are $L_{\mathrm{TTM\text{-}MD}}$ = 103 nm and L_{MD}= 103 nm, which corresponds to 62.5 million Ag atoms and 13.5 million "silica" particles, respectively.

Generation of nanocrystalline surface layer by laser irradiation in vacuum

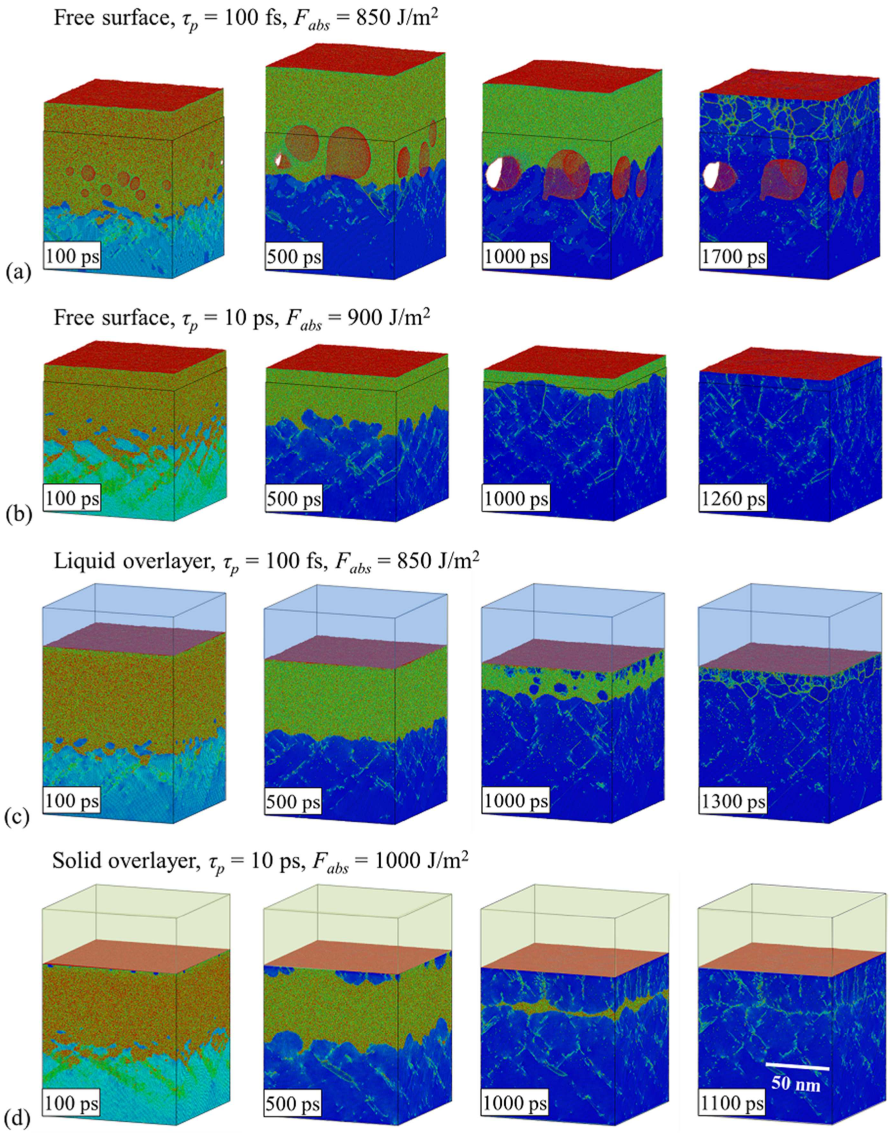

Figure 73. Snapshots of atomic configurations generated in TTM-MD simulations of laser irradiation of Ag targets in vacuum (a,b), in water environment (c), and in the presence of a solid silica overlayer (d). The laser pulse durations τ_p and absorbed laser fluences F_{abs} are indicated on the corresponding panels. Only the regions that correspond to the top 100 nm parts of the targets before the irradiation are shown in the snapshots. The boxes in (a) and (b) outline the initial position of the target before the irradiation, while boxes in (c) and (d) also include parts of the overlayers extending up to 50 nm from the original surface. The atoms are colored by their potential energies, with the scale from -2.84 eV (blue) to -2.64 eV (red) chosen to ensure that the crystalline parts of the targets are blue, the melted regions are green, and the free surfaces are red. Crystal defects, such as vacancies, dislocations, stacking faults, and grain boundaries, can also be distinguished as regions with elevated potential energy. To reduce thermal noise in potential energies, the atomic configurations are quenched for 1-2 ps using the velocity-dampening technique. Adapted from Ref. [319].

The effect of the liquid and solid overlayers on the ability of short pulse laser irradiation of metal targets to produce nanocrystalline surface layers is investigated by comparing results of the simulations performed in vacuum and in the presence of the overlayers. Computational predictions for irradiation in vacuum are described first and are followed by the results for laser processing in liquid environment and in the presence of a solid overlayer.

The first simulation of laser-induced melting and resolidification of Ag target in vacuum, performed at τ_p = 100 fs and F_{abs} = 850 J/m^2, has already been described in Ref. [17], and only a brief summary of the results is provided here. The snapshots from the simulation are shown in Figure 73a, where the atoms are colored by their potential energy, so that the melted and solid parts of the target can be easily distinguished. Laser excitation of the conduction band electrons followed by the rapid energy transfer from the hot electrons to the lattice through electron-phonon coupling leads to the superheating and melting of an about 70-nm-deep surface region of the target within the first tens of picoseconds after the laser pulse. Due to the fast heat conduction to the bulk of the target, the temperature of the liquid-solid interface drops below the equilibrium melting temperature of the EAM Ag material, T_m= 1139 K, and the melting gives way to resolidification by ~75 ps.

The melting and resolidification are occurring simultaneously with the generation and dynamic relaxation of laser-induced stresses that are illustrated in Figure 74a. The rapid temperature increase in the surface region of the target takes place under conditions of stress confinement [27,28,104,134] and results in a build-up of strong compressive stresses, as can be seen from Figure 74a. The relaxation of the compressive stresses in the presence of the free surface of the target results in the generation of an unloading tensile wave marked by dashed arrows in Figure 74a. The tensile stresses, shown by blue color in Figure 74, are sufficiently strong to induce cavitation in the lower part of the melted region, with the appearance of small cavities already apparent in the snapshot shown for 100 ps in Figure 73a. The cavities grow, coalesce, and are eventually trapped by the solidification front advancing from the crystalline part of the target. The movement of the front of the epitaxial solidification can be followed in Figure 75a, where the location of the front is shown by a black line. The presence of voids impedes the solidification front propagation, extends the time that the top surface layer of the target remains in the molten state, and contributes to the generation of increasingly deep undercooling in the melted surface region. At about 1300 ps, when the surface temperature drops down to ~0.69 T_m, a massive nucleation of small crystallites is initiated throughout the deeply undercooled liquid region and results in the formation, within the next 400 ps, of a nanocrystalline layer with ultrafine grains featuring random crystallographic orientation and a high density of stacking faults and twin boundaries [17]. Similar to the solidification front propagation, the homogeneous nucleation of new crystallites leads to the release of the latent heat of melting and is reflected in a noticeable temperature increase in the surface region of the target, Figure 75a.

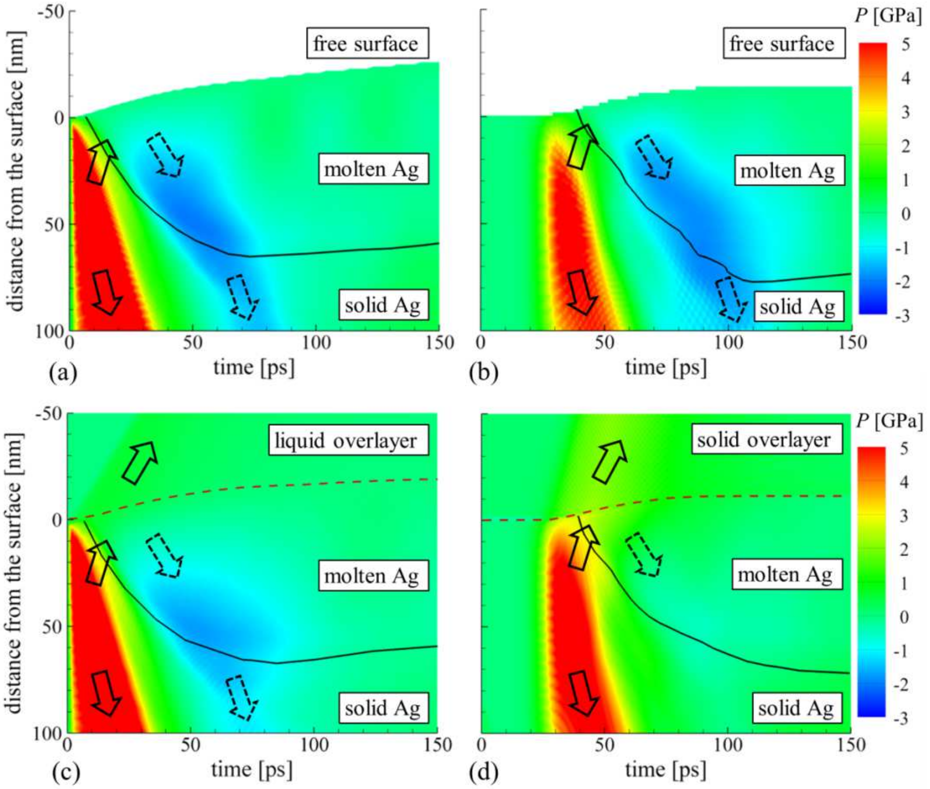

Figure 74. Contour plots of the spatial and time evolution of pressure in TTM-MD simulations of laser irradiation of Ag targets in vacuum (a,b), in water environment (b), and in the presence of a solid silica overlayer (c). The targets are irradiated by 100 fs laser pulse at 850 J/m^2 in (a) and (c), by 10 ps pulse at 900 J/m^2 in (b), and by 10 ps pulse at 1000 J/m^2 in (d). The laser pulse is directed along the *y* axis from the top of the contour plots. The black curves separate melted and solid parts of the Ag targets. The dashed red curves in (b,c) show the position of the Ag-overlayer interface. The arrows schematically show the directions of the propagation of laser-induced pressure waves. The compressive waves, shown by the solid arrows, are generated by the fast laser heating of the surface regions of the targets and can partially propagate into the overlayers in (c) and (d), thus decreasing the amplitude of the unloading tensile waves shown by dashed arrows. In (b) and (d), the maximum intensity of the 10 ps laser pulse is reached at 25 ps. The snapshots from the simulations are shown in Figure 73. Adapted from Ref. [319].

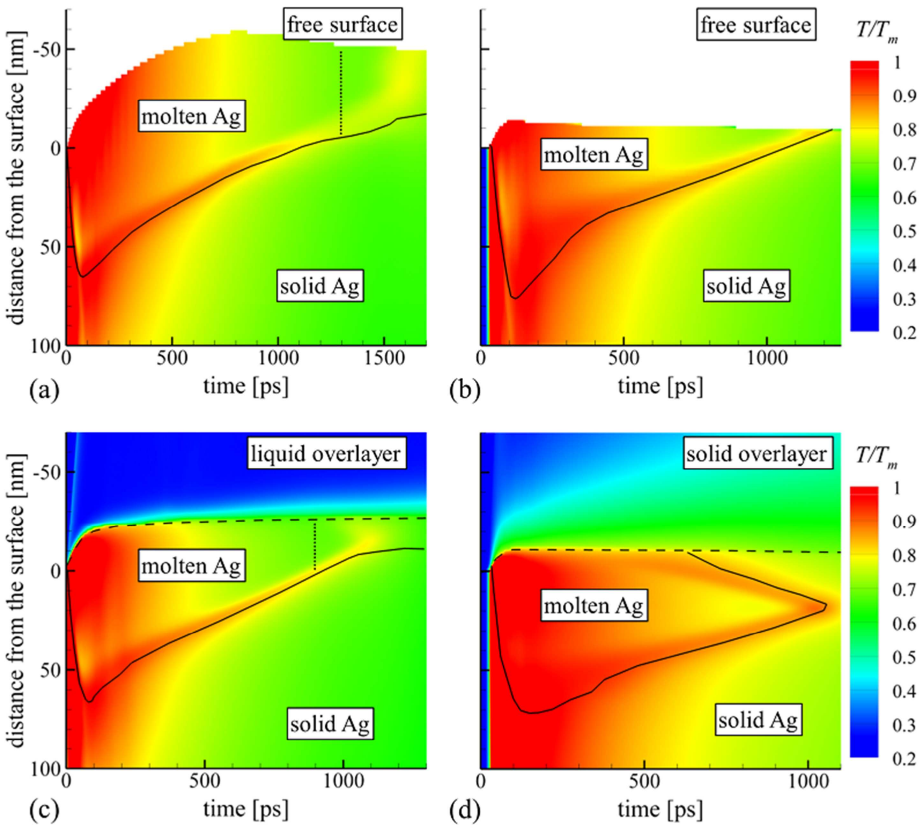

Figure 75. Contour plots of the long-term spatial and time evolution of temperature in TTM-MD simulations of laser irradiation of Ag targets in vacuum (a,b), in water environment (b), and in the presence of a solid silica overlayer (c). The targets are irradiated by 100 fs laser pulse at 850 J/m^2 in (a) and (c), by 10 ps pulse at 900 J/m^2 in (b), and by 10 ps pulse at 1000 J/m^2 in (d). The laser pulse is directed along the *y* axis from the top of the contour plots. The temperature scale is normalized by the melting temperature of EAM Ag, T_m. The maximum temperature reached in the Ag target is 1.60 T_m in (a), 1.33 T_m in (b), 1.63 T_m in (c) and 1.49 T_m in (d). The black curves separate melted and solid parts of the Ag targets. The dashed red curves in (b,c) show the position of the Ag-overlayer interface. The vertical dashed lines in (a) and (c) mark the times when the nucleation of the first crystallites is detected in the undercooled surface regions of the Ag targets. The snapshots from the simulations are shown in Figure 73. Adapted from Ref. [319].

The observation of the formation of the nanocrystalline layer covering the porous subsurface region leads to a question on whether it is possible to induce surface nanocrystallization of the Ag target without the generation of sub-surface voids. To address this question, another simulation is performed with τ_p = 10 ps and F_{abs} = 900 J/m^2. The absorbed fluence of 900 J/m^2 is above the spallation threshold for τ_p = 100 fs, as has been demonstrated in Ref. [31], where the separation and ejected of a molten layer is observed. The use of a longer 10 ps laser pulse, however, allows for a partial relaxation of thermoelastic stresses during the laser-induced heating and prevents the generation of voids. As can be seen from the snapshots shown in Figure 73b and the solidification curve shown in Figure 75b, the epitaxial solidification front proceeds all the way to the surface, and no nucleation of new crystallites is observed in the surface region. In the absence of voids impeding the propagation of the solidification front, the front reaches the surface faster, before the critical undercooling of 0.69 T_m required for the onset of massive homogeneous crystallization is achieved in the melted part of the target.

Despite the absence of the nucleation of new crystallites, the microstructure of the resolidified surface region features a high density of the stacking faults and twin boundaries, which can be attributed to the highly nonequilibrium conditions of the rapid solidification, as well as the small energy of these defects in the EAM Ag material [342]. Moreover, several distinct surface domains misoriented with respect to each other by several degrees and separated by low-angle grain boundaries (dislocation walls) are also identified in the surface region, Figure 76a. The formation of these domains can be explained by the rough morphology of the liquid-crystal interface formed by the end of the rapid melting process. The melting proceeds on the same timescale the unloading wave develops and propagates through the melting front, leading to the emission of numerous partial dislocations from the melting front. The stacking faults left behind by the partial dislocations can be seen as green stripes appearing below the melting region in Figure 77a.The dislocation emission into the superheated part of the crystal facilitates nucleation of liquid regions at the defect sites and produces a mixed molten-crystalline structure at the melting front. Some of the crystalline regions in this mixed region are fully or partially surrounded by liquid and may undergo small stochastic rotations prior to merging into the continuous solidification front that can be seen at a later time in Figure 73b. The growth of the crystallites that are tilted with respect to the original crystallographic orientation of the target is responsible for the generation of the slightly misoriented domains/grains in the surface region of the target, Figure 76a.

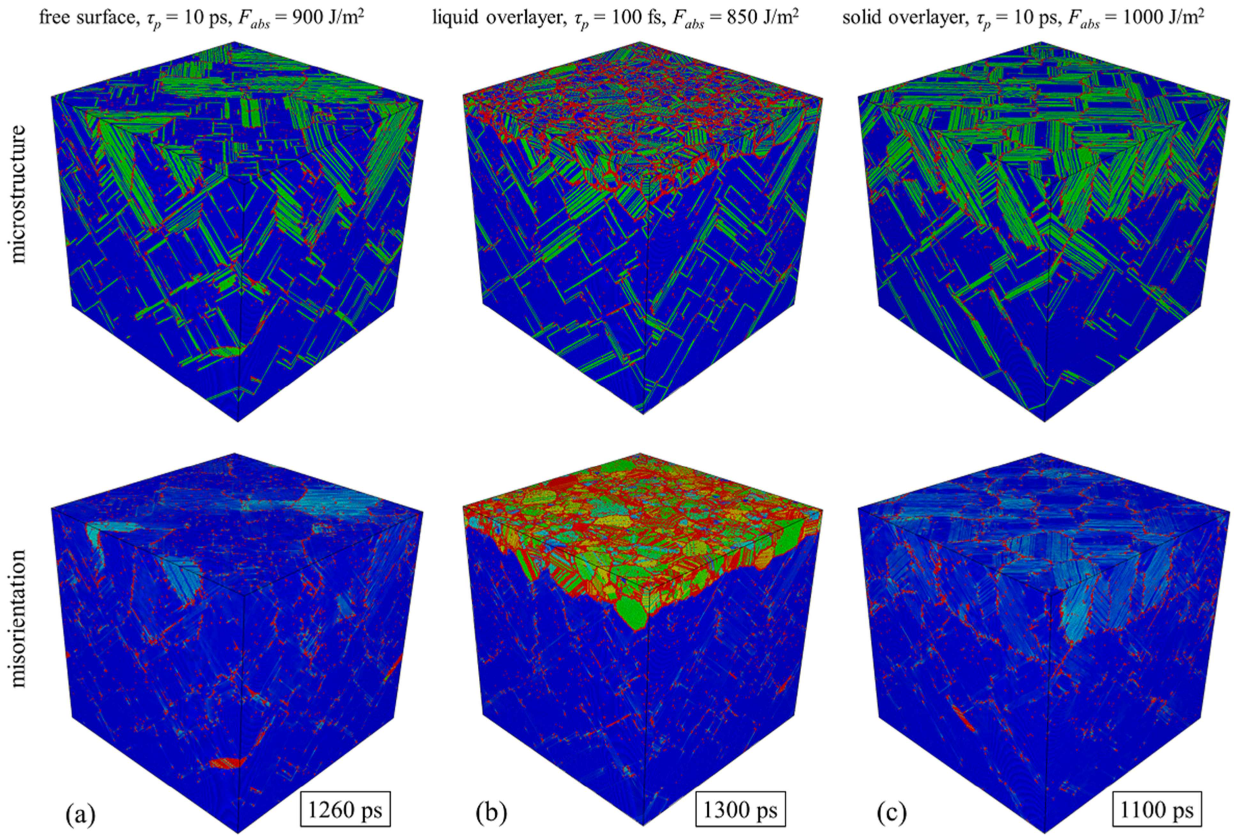

Figure 76. Snapshots of atomic configurations generated at the end of resolidification process in TTM-MD simulations of laser irradiation of Ag targets in vacuum (a), in water environment (b), and in the presence of a solid silica overlayer (c). The laser pulse durations τ_p and absorbed laser fluences F_{abs} are indicated on the corresponding panels. The top 1 nm layers of the targets are blanked to expose the underlying defect structures. *In the upper panels*, the atoms are colored by their local structural environment, so that the fcc and hcp atoms are blue and green, respectively, and the red atoms have unidentified local crystal structure environment. With this coloring scheme, the single and double green layers on a blue background correspond to twin boundaries and stacking faults in the fcc structure, respectively. Unidentified atoms belong to grain boundaries, dislocation cores, and point defects. *In the lower panels*, the atoms are colored by the smallest angle between one of the $\langle 111 \rangle$ directions of the original fcc lattice and a $\langle 111 \rangle$ direction in the corresponding grain. The blue to red color scale corresponds to misorientation angles ranging from 0° to 30°. Adapted from Ref. [319].

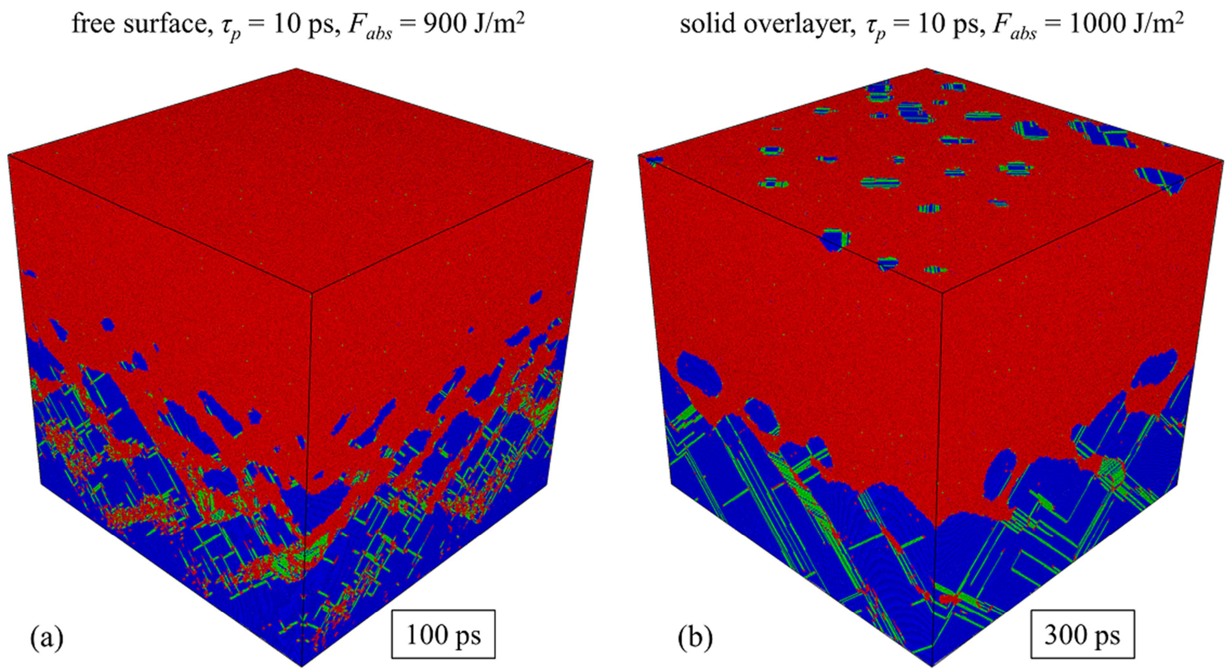

Figure 77. The snapshot of atomic configurations of Ag target with free surface (a) and covered by a silica glass overlayer (b) taken at 100 and 300 ps after laser irradiation. The laser pulse durations τ_p and absorbed laser fluences F_{abs} are indicated on the corresponding panels. The coloring scheme is the same as in upper panels of Figure 76, but the red color is also used for molten Ag. The snapshots illustrate the presence of crystalline regions surrounded by liquid within the melting front in (a) and crystalline regions stabilized by the overlayer in (b). Adapted from Ref. [319].

Effect of liquid environment on surface nanocrystallization

The results of the simulations performed for targets with free surfaces suggest that it is difficult to expect generation of a nanocrystalline surface layer on a (001) Ag target without the con-current formation of a sub-surface porous region that corresponds to an incomplete spallation conditions. This leads to the question on the possibility of using a liquid or solid overlayer that could suppress the generation of sub-surface voids, contribute to the cooling of the metal target, and facilitate the surface nanocrystallization. This possibility is explored in this section for a liquid overlayer parametrized for water.

The large-scale simulation of laser interaction with a Ag target in liquid environment is performed with the same irradiation conditions as the first simulation in vacuum discussed above, where the generation of a nanocrystalline layer covering a porous sub-surface layer (Figure 73a) is observed. The snapshots from the simulation are presented in Figure 73c, while the pressure and temperature contour plots are shown in Figure 74c and Figure 75c, respectively.

Two notable effects, apparent from the visual inspection of the snapshots, are (1) the absence of the sub-surface voids in the molten part of the target and (2) the onset of the nucleation of new crystallites near the surface of the target at the final stage of the solidification process. These two effects are discussed next.

The absence of the sub-surface voids can be explained based on the evolution of the laser-induced pressure illustrated in Figure 74c.The generation of the initial compressive pressure is defined by the electron-phonon equilibration and rapid heating of the surface region occurring under conditions of the thermal and stress confinement [27,28,104,134], and is largely unaffected by the presence of the liquid environment. This is reflected in almost identical compressive parts of the pressure contour plots in Figure 74a and Figure 74c. The formation of the unloading tensile component of the pressure wave, however, is significantly affected by the liquid environment. Since the acoustic impedance of water is much lower than that of Ag, the relaxation of the compressive pressure results in the generation of both a compressive wave emitted into the water and a weaker, as compared to the simulation with free surface (Figure 74a), tensile wave propagating into the bulk of the Ag target, as schematically shown by solid and dashed arrows in Figure 74c. The reduced amplitude of the unloading tensile wave is not sufficient for the initiation of cavitation, which explains the absence of voids in the melted part of the target in Figure 73c. Note that the suppression of the nucleation of subsurface voids has also been observed in earlier MD simulations of short pulse laser interactions with Ag targets performed under stronger spatial confinement by a solid silica overlayer [108] (Section 3.5), while the reduction in the number of spalled layers was reported in hydrodynamic modeling of laser ablation of Al in water [325].

The suppression of the void nucleation has important consequences for the kinetics of resolidification of the melted region. While the melting time and the maximum melting depth are very similar in the simulations performed in vacuum and in water environment, as can be seen from the similarity of the black curves showing the location of the liquid-crystal interface in Figure 74a,c, the same black curves shown for a longer time in Figure 75a,c clearly demonstrate the diverging resolidification behavior. The appearance of sub-surface voids not only increases the effective path the solidification front has to cover before it reaches the surface but also decreases the velocity of solidification front [17] when it passes through the region with voids. In the simulation with water overlayer, Figure 75c, after the initial rapid apparent advancement due to the solidification of a liquid-crystalline mixture formed by the end of the melting process (similar to those shown in Figure 77), the velocity of the resolidification front reaches a steady level of ~63 m/s. In contrast, in the simulation with free surface, Figure 75a, the velocity ofthe solidification front drops below 45 m/s when the front passesthrough the region with voids.

The slowdown of the epitaxial solidification front by the subsurface voids extends the time that the top surface layer of the target remains in the molten state and allows it to reach a deeper undercooling. On the other hand, the reduced effective thermal conductivity of the porous sub-surface region slows down the cooling of the top layer. As a result, it takes about 1.3 ns for the top molten layer to cool down to 0.69 T_{m}, when a massive homogeneous nucleation of new crystalline Ag grains is observed, Figure 75a.In the presence of liquid environment, the surface cooling and the solidification front propagation proceed without the impediment from the voids, and the rapid nanocrystallization is initiated much earlier, at ~900 ps, Figure 75c. The nucleation and fast growth of multiple crystallites in the undercooled liquid region result in the formation of an about 18-nm-thick nanocrystalline surface layer with grains randomly oriented with respect to the crystallographic orientation of the Ag target. Similar to the targets with free surfaces discussed above, the rapid solidification under conditions of strong undercooling produces complex internal structure of individual grains characterized by a high density of stacking faults and twin boundaries, Figure 76b.

In addition to the thermal conduction to the bulk of the Ag target, the interaction with water provides an additional pathway for cooling of the Ag surface region. The efficiency of this channel is limited by the rapid superheating of water adjacent to the hot surface of the metal target and the formation of a low-density supercritical water layer with poor thermal conductivity. As a result, the total amount of the thermal energy transferred to the water overlayer by the end of the simulation is only ~2% of the energy deposited by the laser pulse. Nevertheless, this channel of cooling of the metal surface may play an important role defining the microstructure of resolidified surface, as discussed for the case of solid overlayer in the next section.

Effect of a solid overlayer on surface nanocrystallization

The characteristic features of laser-induced modification of subsurface microstructure under conditions of spatial confinement by a solid transparent overlayer have both similarities to and clear distinctions from the processing in a liquid environment discussed above. Similar to liquids, the presence of a solid overlayer can suppress the generation of tensile waves and contribute to the cooling of the transiently melted region of the metal target. Both of these effects can be stronger with a solid overlayer. The acoustic impedance (product of material density and speed of sound) of the overlayer can be much closer to the one of the metal target (e.g., it is only about twice lower for silica glass as compared to Ag), leading to an effective propagation of the compressive pressure wave into the overlayer and a weaker unloading wave generated in the metal target [80,108]. The higher thermodynamic stability of solid overlayers can be expected to keep the heat transfer from a hot metal surface to an overlayer uninterrupted by the formation of a layer of low-density vapor or supercritical fluid observed at the metal-liquid interface.

Moreover, in contrast to a free surface or a surface covered by a liquid, which typically do not allow for heterogeneous nucleation of new crystallites, the interface between molten metal and over-layer can facilitate the heterogeneous nucleation if the condition of $\gamma_{so} < \gamma_{lo} + \gamma_{sl}$ is satisfied (γ_{so}, γ_{lo}, γ_{sl} are the interface free energies for solid metal – overlayer, liquid metal – overlayer, and liquid metal – solid metal interfaces, respectively). Depending on the interface free energies, an overlayer may even facilitate preferable nucleation and stabilization of metastable solid phases, as exemplified by the generation of a layer of metastable bcc Cu in MD simulations of laser melting and resolidification of Cu-Ag interface [317]. Moreover, an additional cooling due the heat transfer to the overlayer combined with the stabilizing effect of the low interfacial energy may result in an incomplete melting near the interface and regrowth of the melted part of the target from both the crystalline bulk and the crystalline metal layer or islands "survived" on the overlayer. The latter effect is observed in the simulation discussed below.

The effect of a solid overlayer on the microstructure modifica-tion is illustrated by a simulation performed with τ_p = 10 ps and F_{abs} = 1000 J/m^2. These irradiation conditions are chosen to ensure that the maximum melting depth in this simulation is similar to the one in the second simulation with free surface, where a lower absorbed fluence of 900 J/m^2 is used. The need for the higher fluence was defined by the inhibiting effect the overlayer has on the melting process [108] (Section 3.5). For a target with free surface, the tensile stresses associated with the unloading wave reduce the crystal stability against melting [11] and assist in the propagation of the melting front at the final stage of the melting process, Figure 74b. The unloading wave is significantly reduced in the presence of the overlayer, Figure 74d, and the maximum melting depth is approximately the same in the two simulations. Despite the similarity of the melting curves in Figure 74b and Figure 74d, the solidification process proceeds very differently in the two simulations. In the case of the free surface, a single solidification front propagates from the solid part of the target and sweeps the entire melted region, as can be seen from Figure 73b and Figure 75b. In the simulation with the solid overlayer, however, the solidification also proceeds from several areas adjacent to the overlayer, and the growing crystalline islands merge into the second solidification front that meets the one advancing from the bulk of the target at a depth of about 25 nm below the interface, Figure 73d and Figure 75d.

The reason for the appearance of the second solidification front in this simulation is apparent from the inspection of a snapshot of an atomic configuration shown in Figure 77b for a time of 300 ps. The stabilizing effect of the overlayer makes it possible for several small islands of the original crystal to survive the thermal spike induced by the laser irradiation. These islands start growing immediately after the temperature of the molten Ag drops below Tm, without the need for any undercooling. As illustrated in Figure 76c, the final microstructure of the resolidified layer consists of nanograins with sizes in the range of 20–30 nm. The nanograins are slightly misoriented with respect to each other and the bulk of the target. The interfacial islands from which the nanograins grow largely retain the “memory” of the original crystallographic orientation of the tar-get and, similarly to the crystalline islands generated at the melting front (Figure 77a), are slightly misoriented due to the random statistical fluctuations during the melting and resolidification process.

The temperature distributions shown in Figure 78 for a time of 100 ps further illustrate the reason for the survival of the crystalline islands near the overlayer. While cooling due to the heat transfer to the cold overlayer only affects an about 10-nm-thick layer of the metal target, Figure 78b, it is sufficient to prevent the complete melting of the layer. In the absence of the overlayer, Figure 78a, the temperature of the surface is the highest at the surface, as expected. The electron temperature shown in Figure 78 by blue lines deviates from the vibrational temperature (also called “lattice” temperature in TTM) due to the relatively weak electron-phonon coupling in Ag [101]. In particular, the temperature drop by ~$0.3T_m$ within 5-10 nm from the Ag-silica interface is mainly defined by the phonon thermal conductivity. The spatial scale of a region affected by the phononic heat transfer can be estimated as $l_{ph} \sim \sqrt{k_{ph}/g}$, where k_{ph} is the phonon thermal conductivity and g is the electron-phonon coupling factor. Within this region, the heat transfer by the phonon thermal conductivity is counterbalancing the energy transfer due to the electron-phonon coupling, thus creating a quasi-steady-state gap between the electron and phonon temperatures. The temperature gap and the spatial scale of the phononically-cooled region are particularly large for metals with weak electron-phonon coupling. Note that a similar state of quasi-steady electron-phonon nonequilibrium can also be created at a rapidly advancing melting [184] or solidification [215] front, where the release or absorption of the latent heat of melting can produce a local temperature drop or spike that cannot be eliminated by the energy transfer from electrons due to the finite time of electron-phonon equilibration.

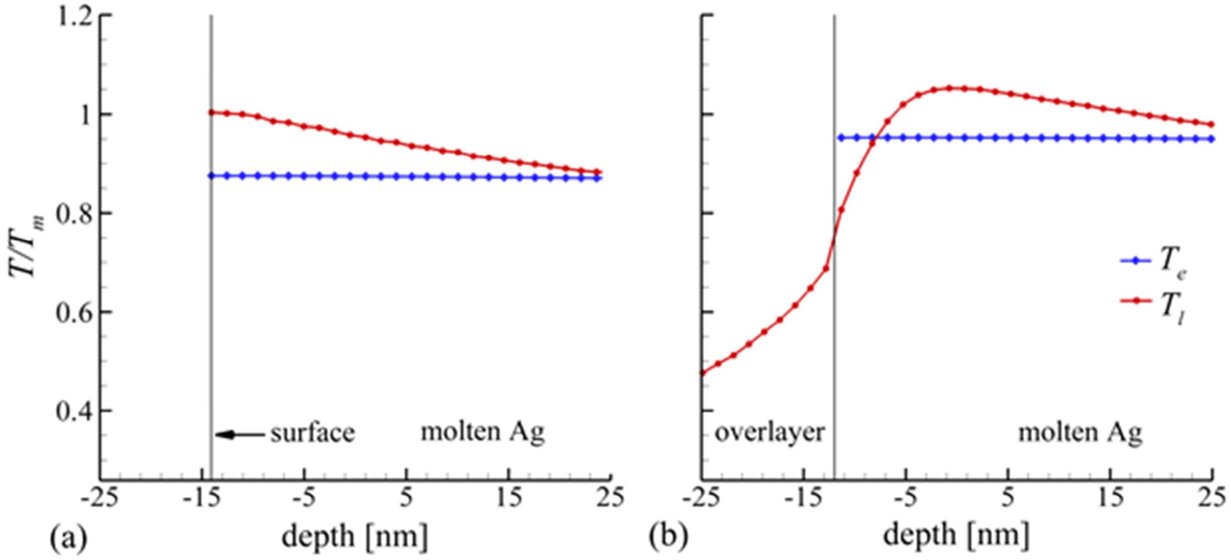

Figure 78. The temperature distributions with depth at 100 ps after irradiation of a Ag target with free surface (a) and surface covered by a silica overlayer (b). The lattice and electron temperatures are shown by red lines/circles and blue lines/diamonds, respectively. The targets are irradiated by 10 ps pulses at absorbed fluences of 900 J/m^2 in (a) and 1000 J/m^2 in (d). The sharp temperature drop near the interface in (b) demonstrates the effect of the heat diffusion into the overlayer. Adapted from Ref. [319].

Finally, we would like to note that, although the temperature of the melted Ag stayed above the critical undercooling of 0.69 T_{m} required for the onset of massive homogeneous nucleation of new crystallites during the resolidification process, this does not mean that the homogeneous nucleation is not possible in short pulse laser processing of metal targets covered by a solid overlayer. On the contrary, when slightly higher laser fluence is applied in smaller-scale simulations performed with the solid overlayer, the top part of the target is completely melted, the second solidification front is not created, and the region of the target adjacent to the over-layer is readily undercooled down to the temperature required for the rapid homogeneous nucleation of new crystallites. Moreover, the cooling due to the heat conduction to the overlayer and the reduced free energy barrier for heterogeneous nucleation of new crystallites at the metal-overlayer interface are the factors facilitating the nanocrystallization in the presence of the overlayer. The final microstructure in this case is expected to be similar to that observed in the simulation with a water overlayer, Figure 76b, i.e., instead of slightly misoriented grains, a layer of randomly oriented grains is likely to be formed.

Summary

The mechanisms responsible for modification of subsurface microstructure in short pulse laser processing of metal targets in vacuum, in liquid environment, and under spatial confinement by a solid overlayer are investigated in large-scale atomistic simulations. The simulations are performed in the regime of melting and resolidification, below the thresholds for laser spallation or ablation.

For single crystal (001) Ag targets with free surfaces, the formation of a nanocrystalline region with random crystallographic orientation of nanograins is only observed under irradiation conditions leading to the generation of sub-surface voids in the transiently melted surface region of the target. The presence of voids slows down the propagation of the epitaxial resolidification front and creates the conditions for reaching the critical level of undercooling required for the onset of a massive homogeneous nanocrystallization. The generation of sub-surface voids can be avoided by reducing the laser fluence or increasing the laser pulse duration. When no voids are generated, however, the resolidification proceeds through the solidification front propagation from the bulk of the target, and the maximum undercooling of the melted surface is not sufficient for the activation of homogeneous surface nanocrystallization. Due to the rough morphology of the liquid-solid interface created by the rapid laser-induced melting, the resolidification in this case produces subsurface microstructure featuring grains that are slightly misoriented with respect to each other and are separated by low angle grain boundaries or dislocation walls.

The presence of a liquid or solid overlayer suppresses the generation of strong tensile stresses responsible for the formation of sub-surface voids, provides an additional pathway for cooling through the heat conduction to the overlayer, and facilitates the formation of nanocrystalline structure in a region of the metal tar-get adjacent to the overlayer. The higher acoustic impedance of the solid silica overlayer makes it more efficient, as compared to the water environment, in reducing the tensile stresses and extending the range of fluences that do not produce sub-surface voids or spallation. It is also found that the stabilizing effect of the solid overlayer may result in an incomplete melting of metal in the vicinity of the overlayer. In this case, the growth of the surviving crystallites from the metal-overlayer interface prevents the homogeneous nucleation of randomly-oriented crystallites and results in the formation of a nanocrystalline interfacial region with small grain misorientation. In all simulations, the nanocrystalline layers generated by laser processing of single-crystal Ag targets are characterized by a high density of stacking faults, twin boundaries, and point defects produced in the course of the rapid resolidification. The strong effect of the solid and liquid overlayers on laser-generated subsurface microstructure suggests a potential use of the overlayers in laser processing aimed at inducing surface nanocrystallization and achieving desired optical and mechanical properties of the surface.

The general conclusions derived in this study from the simulations of laser interactions with Ag targets are also applicable to other metals and alloys, although quantitative aspects may be sensitive to specific properties of target materials. In particular, while the presence of liquid or solid overlayers can be expected to facilitate the formation of nanocrystalline surface structure in short pulse laser processing of various systems, the conclusion that nanocrystallization is not possible for targets with free surfaces without the formation of sub-surface voids is specific to the (001) Ag target and may not hold for a different material system or even different crystallographic surface orientations of the same target.

Finally, we note that the nanocrystalline surface structures generated by short pulse melting and resolidification of one-component metal targets will have limited thermal stability and are likely to undergo grain coarsening beyond the timescale of simulations. In order to mitigate the grain coarsening and stabilize the nanocrystalline surface structures, the addition of appropriate alloying elements (solute) [343-345] during the laser synthesis can be a viable strategy from kinetic and thermodynamic perspectives. The solute atoms can preferably segregate to grain boundaries, thus reducing the free energy of nanocrystalline structures [346-348] and acting as obstacles for grain boundary migration [349,350].

4. Laser-induced modification of surface morphology

Abstract: The process of laser-induced removal of material from an irradiated target, commonly called laser ablation, is at the core of many practical laser-enabled applications, including high-precision cutting and drilling, surface nanostructuring, pulsed laser deposition of films and coatings, and generation of nanoparticles with narrow size distributions and well controlled compositions. In particular, a complex multiscale surface morphology created in short pulse laser processing is demonstrated to turn the surface wetting properties from superhydrophilic [40] to superhydrophobic [41] (and even superwicking, making water and other liquids to move uphill, against the gravity forces [42]), to fabricate black (strongly enhanced broadband absorption) or colored (wavelength-selective reflection) metals [44], and to enhance of photoelectron and thermal emission from surfaces nanostructured by femtosecond laser irradiation [45].

The ultrafast laser energy deposition in short pulse laser processing can result in a rapid melting and resolidification of a surface region of the irradiated target, as well as the generation of high transient thermal stresses. The stresses relax by driving expansion of the material toward the free surface and create an unloading tensile wave, which propagating through the melted surface region results in the nucleation, growth, and coalescence of multiple voids, and eventually leads to the so-called photomechanical spallation, *i.e.*, complete separation and ejection of a molten layer. Numerous liquid bridges created on the surface during this process can be frozen by rapid resolidification and produce complex surface morphology.

Further increase in the laser fluence above the spallation threshold results in the separation and ejection of thinner layers and/or multiple droplets from the target, and, at a sufficiently high laser fluence, induces a transition to a different ablation regime commonly referred to as “phase explosion” or “explosive boiling.” In this regime, the melted surface region of the irradiated target is overheated above the limit of thermodynamic stability of the liquid phase [18-20], leading to a rapid decomposition of the overheated melted material into a mixture of vapor and liquid droplets. An explosive release of vapor, rather than the relaxation of photomechanical stresses, provides the main driving force for the collective ejection of the overheated surface region of the target in the regime of phase explosion.

This section discusses two topics: fundamentals of photomechanical spallation and mechanism of generation of Laser-Induced Periodic Surface Structure (LIPSS) in the phase explosion regime. Consideration of spatial and temporal evolution of the free energy barrier for cavitation in starched liquid has allowed to define the region affected by nucleation and growth of voids. The developed criterion is verified against several large-scale simulations to provide an adequate description of the onset of cavitation in both the spallation and phase explosion regimes. In the second part, a large-scale simulation of LIPSS formation has revealed an interplay of material removal and redistribution in the course of spatially modulated ablation leading to generation of a ∼100-nm-tall frozen surface protrusion, which is shown to be in a good quantitative agreement with the surface morphology observed in experimental study by our collaborator. In addition, the atomistic picture of the final configuration has allowed to look in details into microstructure of the surface region.

4.1. Microscopic mechanisms of photomechanical spallation

Abstract: The thermodynamic conditions defining the spatial extent of a subsurface region affected by the nucleation and growth of voids in photomechanical spallation of metals is investigated theoretically and in atomistic simulations. A theoretical analysis of cavitation in a surface region of a target melted by laser irradiation suggests a functional form for the temperature dependence of the cavitation threshold. A series of small-scale molecular dynamics simulations performed for Al, Ag, Cr, and Ni has revealed the minimum value of the free energy barrier that results in the onset of cavitation on the timescale of 10s of ps, which is a typical duration of transient tensile stresses produced by the unloading wave generated in the spallation regime. The predictive ability of the theoretical description is verified in a large-scale simulation of photomechanical spallation of a Ni target. The temporal and spatial evolution of the free energy barrier for the onset of cavitation under conditions of short pulse laser processing is shown to univocally describe the region where the nucleation of voids takes place.

Introduction

Short (femtosecond and picosecond) pulse laser processing and ablation of metal targets is widely used in modern applications ranging from high precision cutting and drilling [1,173] to surface nanostructuring [25,351,352] and generation of nanoparticles with narrow size distribution and well-controlled compositions [353-355]. In particular, highly non-equilibrium conditions created by laser irradiation are capable of generation of complex multiscale surface morphology [24-26,352], unusual metastable phases [21,317,356], and microstructure [17,32,319] that cannot be produced by any other means. The surface modification by short laser pulses is often defined by processes induced by dynamic relaxation of laser-induced compressive stresses. The laser-generated stresses are particularly high in the regime of stress confinement [27,28,134], when the time of the laser heating is shorter than the time required for the mechanical relaxation (expansion) of the heated volume. The relaxation of the laser-induced compressive stresses near the free surface of an irradiated target results in the generation of an unloading tensile component of the stress wave propagating into the bulk of the target. The tensile stresses can cause nucleation of voids in the molten surface region of the target. The voids can subsequently collapse, be trapped by the resolidification process leading to surface swelling [17,135,357], or grow and coalesce leading to photomechanical spallation, *i.e.*, complete separation and removal of the liquid layer [27,28,134]. Although these processes have been extensively studied in large-scale atomistic simulations [17,28,31,39,102,104,134,138,358-360], realistic description of the spallation process in continuum-level models remains challenging and requires special consideration. The onset of sub-surface cavitation in one-dimensional (1D) hydrodynamics simulations of laser spallation has been treated using the classical nucleation theory [361], as well as with Grady's criterion [362] for spallation threshold based on the energy cost of void growth during the time of tensile loading [357]. The 1D nature of the models, however, makes it difficult to provide an adequate description of the initial stage of void nucleation and growth.

Theoretical analysis based on the classical nucleation theory and atomistic modeling have provided important insights into conditions leading to the onset of the cavitation in an overstretched liquid and enabled estimations of the cavitation threshold and void nucleation rate [363-370]. Most of the atomistic simulations, however, are performed for systems described by Lennard-Jones interatomic potential, which is unable to accurately describe the behavior and properties of molten metals. Moreover, the temperature dependence of the cavitation threshold is neglected in most these studies, which are performed under conditions of constant temperature and constant total volume. Meanwhile, short pulse laser irradiation produces strong temperature and pressure gradients and rapidly changing thermo-mechanical conditions in the surface region of the irradiated target [39], which cannot be approximated without considering the temperature dependence of the cavitation threshold. In this letter, we suggest a criterion for the onset of cavitation in a molten metal that accounts for the temperature dependence of relevant thermodynamic parameters. The criterion is suitable for predicting the location and size of the subsurface region affected by laser-induced cavitation and the amount of spalled material. The analytical description is parametrized based on the results of atomistic simulations and verified against the predictions of a large-scale molecular dynamics (MD) simulation of laser spallation.

Theoretical derivation of cavitation threshold

The free energy change due to appearance of a cavity of radius R in a system under tension can be expressed as $\Delta G = PV + \sigma A$, where P and σ are the pressure in the system and the surface tension of liquid-vapor interface, $V = 4\pi R^3/3$ and $A = 4\pi R^2$ are the volume and surface area of the cavity, respectively. Since the magnitude of pressure variations in a target irradiated under conditions of stress confinement is usually much larger than the saturated vapor pressure, P_v, in a wide range of temperatures above the melting point of a target material, the contribution of the vapor pressure is neglected here to simplify the analysis. Thus, we consider the regime of photomechanical spallation, when the dominant driving force responsible for the appearance of the voids or cavities is the dynamic relaxation of the laser-induced stresses (see Ref. [28] for the discussion of the terminology used for the description of this process). As the temperature approaches the critical point, however, $P - P_v$ should be used in the free energy equation instead of P, and the release of the vapor phase can drive the massive nucleation and growth of the vapor bubbles even in the absence of any negative/tensile pressure. The conditions when the release of the vapor phase starts to make dominant contribution to the material decomposition and ejection correspond to the transition from spallation to phase explosion or explosive boiling.

For a spherical cavity generated in the regime of photomechanical spallation, the critical radius and free energy barrier for the onset of the cavitation can be obtained from a condition of $d(\Delta G)/dR|_{R_c} = 0$, yielding $R_c = -2\sigma/P$ and $G_0 = \Delta G(R_c) = 16\pi\sigma^3/3P^2$ [363-370]. For a system under tension ($P < 0$), the rate of void nucleation can then be written as $R = R_0 \times exp(-16\pi\sigma^3/3P^2 k_B T)$, where k_B and T are Boltzmann constant and temperature. The prefactor R_0 is a expressed in units of nuclei per second per cubic meter, and can be estimated as $R_0 \approx k_B T/hV_a$ [367], where V_a is the atomic volume, and h is Planck's constant.

For a typical metal, R_0 is on the order 10^{42} [s^{-1}m^{-3}], and a more accurate consideration of the prefactor accounting for the number of surface atoms in the critical nucleus [367] increases R_0 up to $10^{43} - 10^{44}$ [s^{-1}m^{-3}]. According to a large-scale atomistic simulations of laser-induced spallation of Ag and Al targets [17,39], the propagation of the unloading tensile wave through a molten parts of the targets generates approximately 100 voids within a volume of about 100 × 100 × 50 nm^3 during 20 ps, which suggests a nucleation rate of $R{\sim}10^{34}$ [s^{-1}m^{-3}]. To match this rate, the nucleation free energy barrier should reach the value of $G_0^{th}{\sim}23\ k_BT$, which gives the criterion for evaluation of the temperature dependence of the threshold tensile pressure for the onset of cavitation in short pulse laser spallation:

$$P_{th}^2 = \alpha\sigma(T)^3/k_BT \tag{4.1}$$,

where $\alpha \approx 0.7$ is estimated based on the nucleation rate in the photomechanical spallation regime observed in the atomistic simulations. The temperature dependence of surface tension of a liquid-vapor interface can be approximated as:

$$\sigma(T) = \sigma_0(1 - T/T_c)^{\mu} \tag{4.2}$$,

where σ_0 is a material dependent parameter, T_c is the critical temperature, and μ can be approximated as 1.26 based on the value of surface tension critical exponent obtained using the renormalization group technique [371]. The experimental values of the surface tension at the melting point and the corresponding temperature slops are available for a wide range of materials [372,373]. In the following analysis, the values of T_c, σ_0, and μ are directly calculated in atomistic MD simulations performed with Embedded Atom Method (EAM) potential parametrized for Al [130], Ni [130], Ag [291], and Cr [81] using the test area method [162] and are summarized in Table 10. The corresponding temperature dependencies of surface tension are plotted in Figure 79. It should be noted that the obtained values of μ are lower than the theoretical prediction and depend on the interatomic potential, which can be attributed to the fact that the dependence given by Eq. 4.2 is derived for temperatures in the vicinity of the critical point [371], whereas the data provided in Figure 79 is fitted for a broader temperature range.

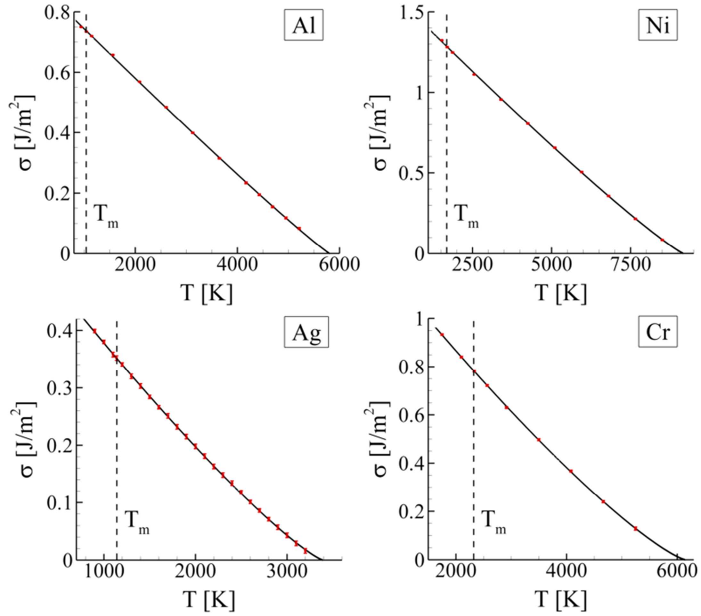

Figure 79. Temperature dependence of surface tension calculated for Al, Ni, Ag, and Cr in a series of MD simulations (red symbols), and fitted to Eq. 4.2 (solid lines). The parameters of Eq. 4.2 obtained by the fitting are provided in Table 10. The error bars show standard deviation of the mean and are comparable with the size of the symbols. The values of equilibrium melting temperature calculated for the model materials described by EAM potentials are marked by vertical dashed lines.

Table 10. Parameters of Eq. 4.2 calculated for Al, Ni, Ag, and Cr described by EAM potentials.

	T_c [K]	σ_0 [J/m^2]	μ
Al	5800	0.910	1.07
Ni	9170	1.61	1.11
Ag	3380	0.573	1.19
Cr	6140	1.41	1.24

Cavitation threshold in MD

The analytically derived criterion for the onset of cavitation, Eq. 4.1, is tested in a series of small-scale atomistic simulations performed for several cubic systems consisting of 4000 atoms and described by different interatomic potentials. In each simulation, the tensile pressure is kept at a constant level and the temperature is gradually increased with a heating rate of 1 K/ps. The onset of cavitation is identified by a rapid increase of the system volume. Figure 80 illustrates the dependence of the cavitation threshold on temperature for Al, Ni, Ag, and Cr described by EAM potentials. The functional dependence given by Eq. 4.1 is able to describe the simulation results quite well with the proportionality coefficients α equal to 0.61, 0.66, 0.85, and 1.00 for Al, Ni, Ag, and Cr, respectively, which is close to the value of 0.7 obtained based on the theoretical consideration and the number of voids generated in large-scale atomistic simulations of spallation. The corresponding minimum free energy barriers for the onset of cavitation are 27.7, 25.5, 19.7, and 16.8 k_BT, for Al, Ni, Ag, and Cr model systems, respectively. These values of the free energy barrier are distributed around the value of 23 k_BT obtained through the order of magnitude estimation discussed above, and the deviation from the estimated value does not exceed 20% for all considered materials. The nonsphericity of voids was checked in an attempt to explain the variability of α. Analysis of the results of a series of atomistic simulations has suggested that the surface area of voids exceeds the area of the corresponding spherical voids by 1.47, 1.70, 1.85, and 2.50 times for Al, Ag, Cr, and Ni, respectively. These values do not show direct correlation with the material dependence of the coefficient α, thus suggesting that this dependence cannot be explained by the difference in shapes of the voids alone.

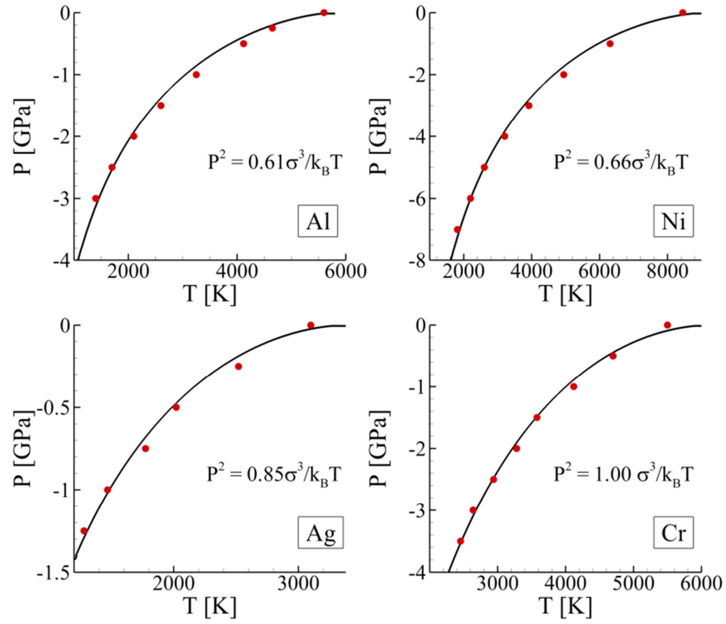

Figure 80. Temperature and pressure dependence of the cavitation threshold predicted for Al, Ni, Ag, and Cr in a series of MD simulations and fitted to an analytical function, Eq. 4.1, also provided in the plot.

Photomechanical spallation

To verify the applicability of the theoretical analysis discussed above, we perform a large-scale atomistic simulation of laser spallation of Ni target. The simulation is performed with a model combining the classical MD method with the two temperature model (TTM) [39,102]. This hybrid TTM-MD model is capable of describing the absorption of laser energy by conduction band electrons, electron-phonon equilibration, rapid non-equilibrium melting, cavitation in liquid, and spallation. The computational setup and parameters of the model are similar to those used in the simulations of laser-induced melting and resolidification reported in Ref. [32] and Section 2.1.1. Briefly, the atomistic part of the TTM-MD model consists of 162 million atoms and represents the top 150 nm surface region of the target. In the lateral directions, parallel to the surface of the target, the dimensions of the computational systems are about 100 nm × 100 nm, and the periodic boundary conditions are applied. In the continuum part of the model, beyond the surface region represented with atomic resolution, conventional TTM equations [9], accounting for the electronic heat conduction and the energy exchange between the electrons and the lattice, are solved down to 2.5 μm to ensure negligible temperature changes at the bottom of the computational domain during the time of the simulations. At the bottom of the atomistic part of the model, a pressure-transmitting, heat-conducting boundary condition is applied to ensure nonreflecting propagation of the laser-induced stress wave and heat transfer from the atomistic part of the computational system into the bulk of the target. The interatomic interactions between Ni atoms in the atomistic part of the model are described by the EAM potential [130]. The Ni target is irradiated by a 50 fs laser pulse at 1500 J/m^2, which is above the threshold for photomechanical spallation.

The temporal evolution of temperature and pressure in the irradiated target is illustrated in Figure 81a and Figure 81b. The fast laser energy deposition results in the generation of a strong pressure wave propagating from the surface to the bulk of the target, Figure 81b. When the tensile component of the pressure wave passes through the molten part of the target, the free energy barrier for cavitation drops down to a minimum value of $\sim 24.8\, k_B T$ (Figure 81d), which is below the cavitation threshold value of $25.5\, k_B T$ identified in a series of small scale simulations for Ni under well-controlled pressure and temperature conditions. This drop is sufficient to induce nucleation of multiple voids in the subsurface region of the target, at depth between 15 and 35 nm below the initial surface (see density contour plot in Figure 3c and an atomic snapshot shown for a time of 100 ps in Figure 81e). Both the time of the void nucleation and the spatial extent of the cavitation region are in a good quantitative agreement with the prediction of the theoretical model. In particular, the region where the voids nucleate is the one where the temperature dependent threshold tensile pressure is exceeded and the free energy barrier for the cavitation drops below the threshold value (outlined by the purple dashed line in Figure 81a-c).

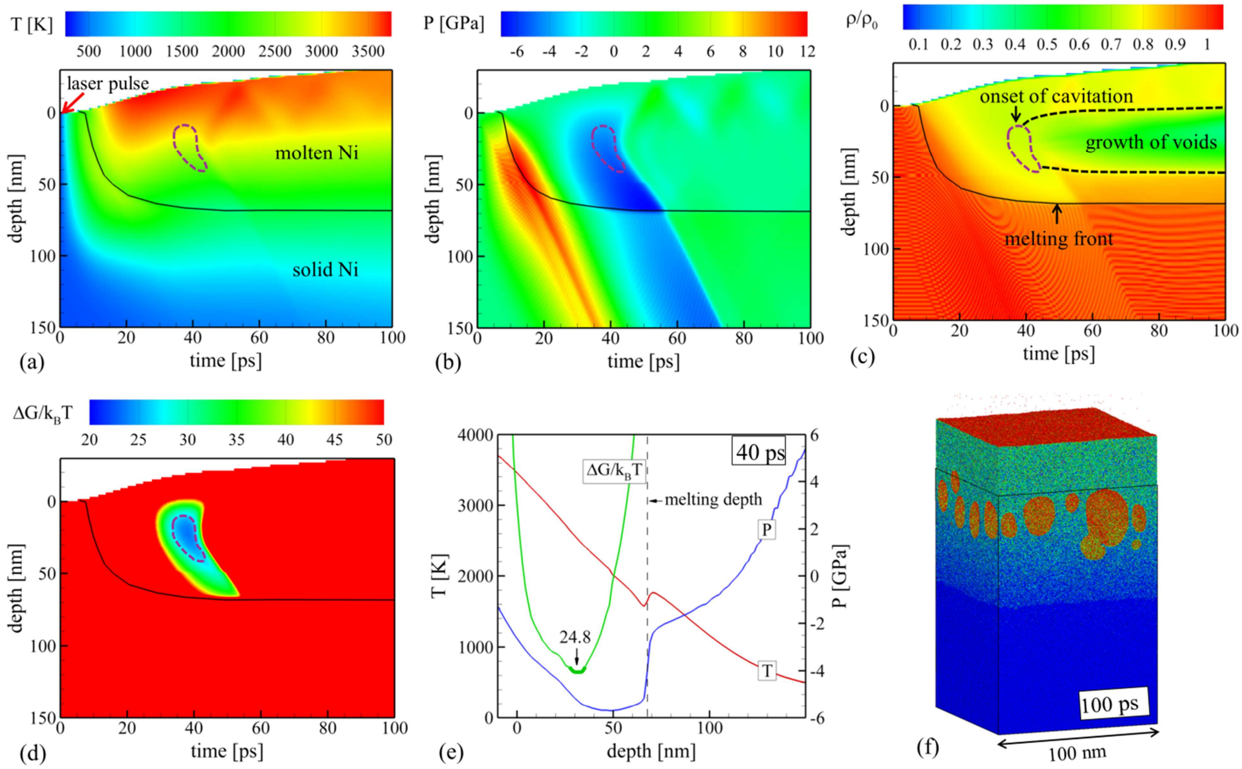

Figure 81. (a-d) Contour plots of temporal and spatial evolution of temperature (a), pressure (b), density (c), and free energy barrier for the onset of cavitation (d) in a bulk Ni target irradiated by a 50 fs laser pulse at an absorbed laser fluence of 1500 J/m^2, which is just above the spallation threshold. The black lines show the location of the solid-liquid interface. Purple dashed lines outline the region with free energy barrier below 25.5 k_BT, where nucleation of voids is predicted theoretically and observed in the simulation. The region of void growth is outlined by black dashed lines in (c). (e) The spatial profile of lattice temperature (red), pressure (blue), and the free energy barrier (green) at the moment when the barrier reaches its minimum level. The scale of the free energy is from 20 to 50 k_BT, and a part of the curve for the free energy barrier below the threshold of $25.5\ k_BT$ is shown by a thicker line. (f) An atomic configuration at a time of 100 ps, when the cavitation voids are clearly seen. The atoms are colored based on their potential energy, with blue color corresponding to solid, atoms colored light blue to green are in the liquid phase, and atoms colored orange and red are on the free surfaces.

Following the nucleation, the voids grow, coalesce, and eventually percolate, leading to the separation/spallation of the top liquid layer from the bulk of the target. It is interesting to note that the depth where the free energy barrier reaches its minimum value, Figure 81d, and the voids nucleate, Figure 81c, does not coincide with the depth of the maximum tensile stresses are generated, Figure 81b,e. In fact, the depth where the maximum tensile stresses are observed is below the region where the theoretical cavitation threshold is reached, and no void formation is observed at this depth. While the tensile stresses are increasing with depth and reach their maximum value close to the liquid-solid interface, the temperature decreases with the depth, leading to an increased ability of the material to support transient tensile stresses. The theoretical equation, Eq. 4.1, accounts for the interplay of these two factors and predicts the onset of the cavitation at an intermediate depth, where the free energy barrier reaches the sufficiently low values. This observation is consistent with the results of earlier MD simulations of photomechanical spallation of molecular targets [134,374], Ni [28,104], Cr [314,360], Al [39], and Ag [17,31].

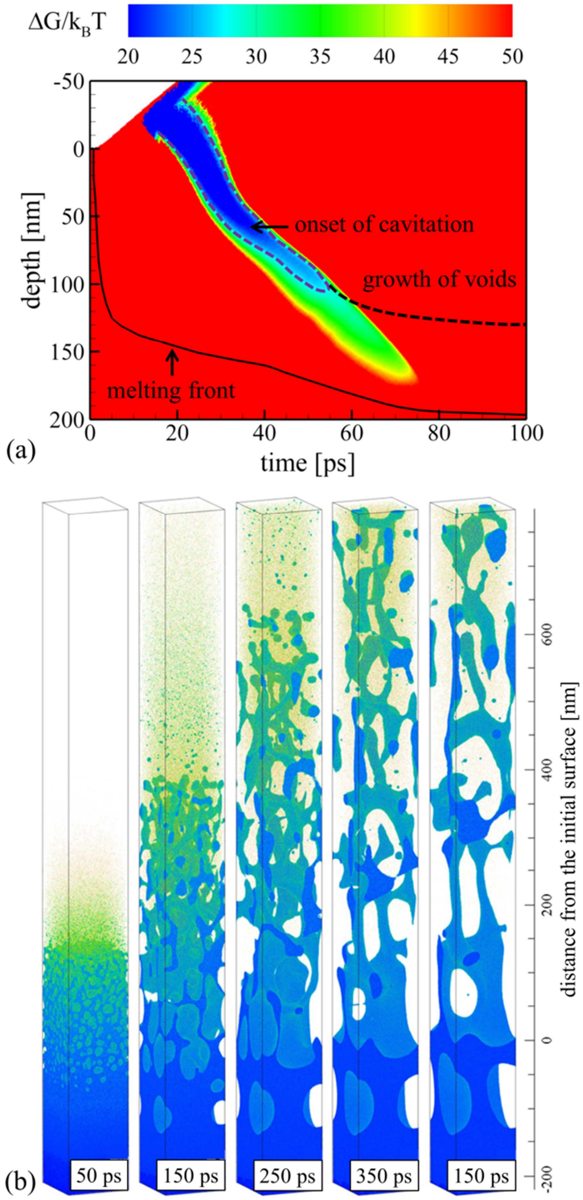

Figure 82. (a) Contour plot of temporal and spatial evolution of free energy barrier for the onset of cavitation in an Al target irradiated by a 100 fs laser pulse at an absorbed laser fluence of 2000 J/m^2, which corresponds to phase explosion regime. The black line shows the location of the solid-liquid interface. Purple dashed line outlines the region with free energy barrier below 27.7 k_BT, where nucleation of voids is predicted theoretically and observed in the simulation. The region of void growth is outlined by black dashed line. (b) Atomic snapshots demonstrating nucleation and growth of voids. The atoms are colored based on their potential energy, with blue color corresponding to solid and liquid, and green to vapor. Figure 82b is adapted from Ref. [39].

Note that the simple criterion defining the size of the cavitation region in laser spallation can also be used for evaluation of the maximum depth affected by cavitation at higher fluences, in the regime where the top layer of the target undergoes an explosive decomposition into vapor and small liquid droplets. While the magnitude of the tensile component of the laser-induced stress wave is reduced in this case by superposition with the compressive pressure wave generated by the phase explosion and ejection of material from the top layer [39,134], the tensile wave can still induce cavitation in a broad subsurface region. To illustrate the applicability of the cavitation criterion to this regime, we consider the results of an atomistic simulation reported in Ref. [39] for Al target irradiated by 100 fs laser pulse at 2000 J/m^2, above the threshold for the phase explosion. The evolution of free energy barrier for the onset of cavitation and the propagation of the melting front in this simulation can be seen from Figure 82a. Following the laser excitation, the surface part of the target is rapidly heated and melted down to a depth of ~200 nm. Propagation of a tensile wave through the molten material creates conditions for void nucleation in a region extended down to a depth of ~110 nm. The appearance of voids is confirmed by visual analysis of a sequence of atomistic snapshots adapted from Ref. [39] and provided in Figure 82b. In the snapshot shown for 50 ps, the voids are visible down to the depth of ~70 nm and are just starting to emerge in the underlying ~40 nm thick layer. This observation is consistent with application of the theoretical criterion for the onset of cavitation shown by the dashed line in Figure 82a. During the following evolution, the voids grow and coalesce, leading to a gradual decomposition of the foamy liquid structure into individual liquid droplets. The proposed cavitation criterion depends of the temperature dependence of the surface tension rather than on the material, therefore it is applicable not only for pure metals but also for alloys.

Summary

In summary, a criterion for the onset of cavitation in a molten metal is revisited, and a theoretical description of spallation is developed in terms of free energy barrier and void nucleation rate. The comparison of the number of voids generated in large scale atomistic simulations of short pulse laser ablation and the analytically evaluated nucleation rate has enabled formulation of the temperature-pressure conditions in a region of an irradiated target affected by the cavitation, $P_{th}^2 = \alpha\sigma(T)^3/k_BT$. The analytical description is parametrized based on the results of atomistic simulations performed for Ni, Cr, Al, and Ag, and is shown to be applicable for a wide range of temperature and pressure conditions. While the value of parameter

α exhibits some material dependence, its variation is found to be less than 20% for all considered metals, and the value of 0.7 obtained analytically can be used for a reasonably accurate estimation of the spatial extent of the cavitation region. The results of large-scale atomistic simulations demonstrate the ability of the theoretical treatment to provide an adequate description of the onset of cavitation in both the spallation and phase explosion regimes. The cavitation criterion can be used to predict the onset of spallation in continuum-level models of laser-materials interaction.

4.2. Mechanism of single-pulse ablative generation of laser-induced periodic surface structures (LIPSS)[4]

Abstract: One of the remarkable capabilities of ultrashort polarized laser pulses is the generation of laser-induced periodic surface structures (LIPSS). The origin of this phenomenon is largely attributed to the interference of the incident laser wave and surface electromagnetic wave that creates a periodic absorption pattern. Although, commonly, LIPSS are produced by repetitive irradiation of the same area by multiple laser pulses in the regime of surface melting and resolidification, recent reports demonstrate the formation of LIPSS in the single-pulse irradiation regime at laser fluences well above the ablation threshold. In this section, we report results of a large-scale molecular dynamics simulation aimed at providing insights into the mechanisms of single-pulse ablative LIPSS formation. The simulation performed for a Cr target reveals an interplay of material removal and redistribution in the course of spatially modulated ablation, leading to the transient formation of an elongated liquid wall extending up to ~600 nm above the surface of the target at the locations of the minima of the laser energy deposition. The upper part of the liquid wall disintegrates into droplets while the base of the wall solidifies on the time scale of ~2 ns, producing a ~100-nm-tall frozen surface feature extending above the level of the initial surface of the target. The properties of the surface region of the target are modified by the presence of high densities of dislocations and vacancies generated due to the rapid and highly nonequilibrium nature of the melting and resolidification processes. The insights into the LIPSS formation mechanisms may help in designing approaches for increasing the processing speed and improving the quality of the laser-patterned periodic surface structures.

---

[4] Results of this work are reported in Ref. [149].

Introduction

One of the remarkable capabilities of ultrashort (femto- and picosecond) polarized laser pulses is imprinting of light polarization direction on a material surface in the form of laser-induced periodic surface structures known as LIPSS (see Refs. [375-377] and references therein). These structures are already used and have a potential to be applied in various fields, including control over surface wettability [378,379], enhancing light absorption [379], improving adhesive [380] and tribological [381] properties of surfaces, surface marking [382], controlled growth and migration of cells [383], etc. The origin of the universal phenomenon of LIPSS formation, observed on metals, semiconductors, dielectrics, and polymers irradiated at a broad range of laser wavelengths and pulse durations, is largely attributed to the interference of the incident laser wave and a surface scattered electromagnetic wave, thus creating a periodic pattern of the absorbed laser energy along the irradiated surface, as established by Sipe *et al.* for metals [203] and generalized to other materials by Bonse *et al.* [384]. The spatial period of this interference pattern defines the period of the produced surface structures, which for a free surface is approximately equal to the laser wavelength. A periodic (modulated) absorption of laser energy by electrons during the laser pulse is only the first stage of the LIPSS formation. This stage results in a modulation of the lattice temperature along the surface, which has been shown to preserve up to tens of picoseconds even on surfaces of metals with high thermal conductivity [385]. While such time scale is sufficient for triggering the material melting and ablation [104], the longer-term post-irradiation processes leading to the material redistribution and/or removal within/from the surface layer of the target must play a paramount role in the final imprinting of the LIPSS on the surface.

Usually, LIPSS imprinting on material surfaces is performed by laser pulses with relatively low laser fluences, near or only slightly above the ablation threshold [375,376,382,384,386]. This requires dozens or even hundreds of laser pulses coupled to the same irradiation spot on the surface to produce the periodic surface relief. It was believed that an increase of the laser fluence well above the ablation threshold would result in disordering or even complete erasure of the periodic structures by the recoil pressure of the ablation plume. It was recently shown, however, that a well-pronounced LIPSS pattern can be imprinted with a single or very few laser pulses coupled to the same irradiated area at fluences well above the ablation threshold [387-389]. In particular, in Ref. [389] the high-quality LIPSS were generated on a silicon surface by fast laser scanning with overlap of only 2–3 pulses per irradiation spot. The mechanisms of LIPSS formation in the regimes of developed ablation are not established yet. It was speculated [389] that periodic ablation, which replicates the laser energy absorption pattern, and material relocation due to recoil pressure of the ablation products could cause the periodic surface rippling. In this section, we report the results of a large-scale molecular dynamics simulation that suggest an alternative mechanism of the single-pulse ablative LIPSS formation, where the material redistribution in the lower part of the ablation plume plays an essential role in the formation of frozen surface protrusions in the regions of reduced laser energy deposition. Detailed structural analysis of the frozen protrusions reveals a high concentration of crystal defects that are likely to have important implications on the mechanical and chemical properties of the nanostructured surfaces.

Computational setup

The simulation reported in this section is performed with a hybrid computational model combining a continuum level description of laser excitation of conduction band electrons and following electron-phonon equilibration based on two temperature model (TTM) [9] with a classical molecular dynamics (MD) representation of the nonequilibrium dynamics of laser-induced phase transformations and material decomposition. A complete description of the computational model is provided in Section 2.1.1 and elsewhere [39,102]. Below we only delineate parameters of the computational setup specific for the simulation reported in this section.

A schematic representation of the computational system is illustrated in Figure 83. The initial dimensions of the TTM-MD domain are 260 nm × 43 nm × 87 nm, which corresponds to 81 million atoms. The length of the system corresponds to the laser wavelength and is taken to be equal to the 4-th harmonic of the wavelength typically used in experiments since the computational cost of the atomistic simulation is high. The interatomic interactions are described by the embedded atom method (EAM) potential parametrized for Cr [81]. The potential provides a relatively accurate and computationally inexpensive description of Cr experimental properties, including lattice parameter, cohesive energy, elastic constants and their temperature dependence, melting temperature, and vacancy formation energy. The electronic heat transfer in the deeper part of the target, where no structural changes take place in response to the laser irradiation, is described by the conventional TTM. The depth covered by the TTM is chosen to be 1 μm to ensure a negligible temperature change at the bottom of the computational system by the end of the simulation. Periodic boundary conditions are applied along *x* and *y* directions (parallel to the irradiated (001) surface of the target), a free boundary is used at the top surface of the target, and a novel Langevin Non-Reflecting Boundary (LNRB) condition, developed in this study and described in Section 2.3.1, is imposed at the bottom of the TTM-MD part. The LNRB condition ensures nonreflecting propagation of laser-induced non-planar pressure wave into the bulk of the target, mimicking the elastic response of an infinitely thick target. This approach is suitable for simulation of experimental conditions where the reflection of the pressure waves from the back surface of the irradiated target does not have any significant effect on processes occurring in the vicinity of the irradiated surface. After 250 ps, the dynamic relaxation of laser-induced stresses in the TTM-MD part of the system is completed, and the LNRB is replaced with a rigid boundary condition. Before laser irradiation, the system is thermalized at 300 K for 50 ps.

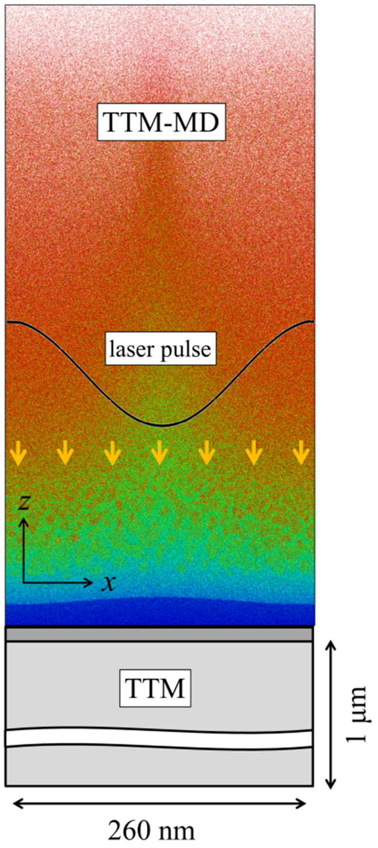

Figure 83. Schematic representation of the computational setup used in the simulation of single-pulse ablative LIPSS formation. A snapshot from a simulation taken at 80 ps after the laser pulse is used as a background in the representation of the atomistic (TTM-MD) part of the model. The atoms in the snapshot are colored by their potential energies with the color scale explained in the caption for Figure 85. The black curve shows schematically the modulation of the laser energy deposition along the x direction, with the minimum at the center of the computational domain. The dark gray layer between the TTM-MD and TTM parts of the model represents the Langevin nonreflecting boundary described in Section 2.3.1. Adapted from Ref. [149].

The thermophysical properties of Cr entering the TTM equations are as follows. The electron heat capacity of Cr is approximated as $C_e(T_e) = \gamma T_e$ with γ = 194 Jm^{-3}K^{-2} [141,265].

Constant values of the electron-phonon coupling factor, g = 4.2×10^{17} $\mathrm{Wm^{-3}K^{-1}}$ [390], and the lattice heat capacity in the TTM part of the model, C_l = 3.23×10^{6} $\mathrm{Jm^{-3}K^{-1}}$ [242], are assumed in the calculations. The temperature dependence of the electron thermal conductivity is approximated by the Drude model relationship, $K_e(T_e, T_l) = v^2 C_e(T_e) \cdot \tau_e(T_e, T_l)\,/3$, where v^2 is the mean square velocity of the electrons contributing to the electron heat conductivity, approximated in this work as the Fermi velocity squared, v_F^2, and $\tau_e(T_e, T_l)$ is the total electron scattering time. The latter is defined by the electron-electron scattering rate, $1/\tau_{e-e} = AT_e^2$, and the electron-phonon scattering rate, $1/\tau_{e-ph} = BT_l$, so that $1/\tau_e = AT_e^2 + BT_l$. The value of the coefficient A = 2.66×10^{6} $\mathrm{K^{-2}s^{-1}}$ is estimated within the free electron model [103]. Similar to Ref. [32], the coefficient B is described as a function of the lattice temperature and the phase state of the material, so that the experimental temperature dependences of thermal conductivity of Cr under conditions of electron-phonon equilibrium [283] are reproduced for both solid and liquid states. In particular, this description accounts for the two-fold drop of thermal conductivity as the temperature increases from 300 K to the melting point.

The absorption of laser energy is represented through a source term added to the TTM equation for the electron temperature [102]. The source term has a temporal Gaussian profile corresponding to 200 fs pulse and accounts for the exponential attenuation of the deposited laser energy with depth. The optical absorption depth of Cr is equal to 9.6 nm at a wavelength of 258 nm [181]. Similar to Ref. [385], the absorbed laser fluence is spatially modulated along the *x* direction to represent the periodic absorption pattern generated by the interference of the incident laser wave and surface electromagnetic wave. The period of the sinusoidal modulation is taken to be 260 nm, which matches the size of the computational domain in *x* direction. The maximum and minimum of absorbed fluences (at the boundaries and in the middle of the computational domain shown in Figure 83, respectively) are 2000 to 3000 $\mathrm{J/m^2}$, which corresponds to 20% modulation of the laser energy deposition with respect to the average level of 2500 $\mathrm{J/m^2}$. Such level of modulation of the absorbed laser energy is predicted to result from periodic generation of free carriers [391] in silicon, and is also expected for metals exhibiting a pronounced decrease of reflectivity with heating of the electron subsystem [392].

Results and discussion

The mechanisms of the single-pulse LIPSS formation in the regime of laser ablation is investigated in a large-scale TTM-MD simulation performed for a Cr target irradiated by a 200 fs laser pulse. The irradiation is assumed to produce a spatially modulated energy deposition with the average absorbed fluence of 2500 J/m^2, which is approximately 70% above the phase explosion threshold for Cr target.

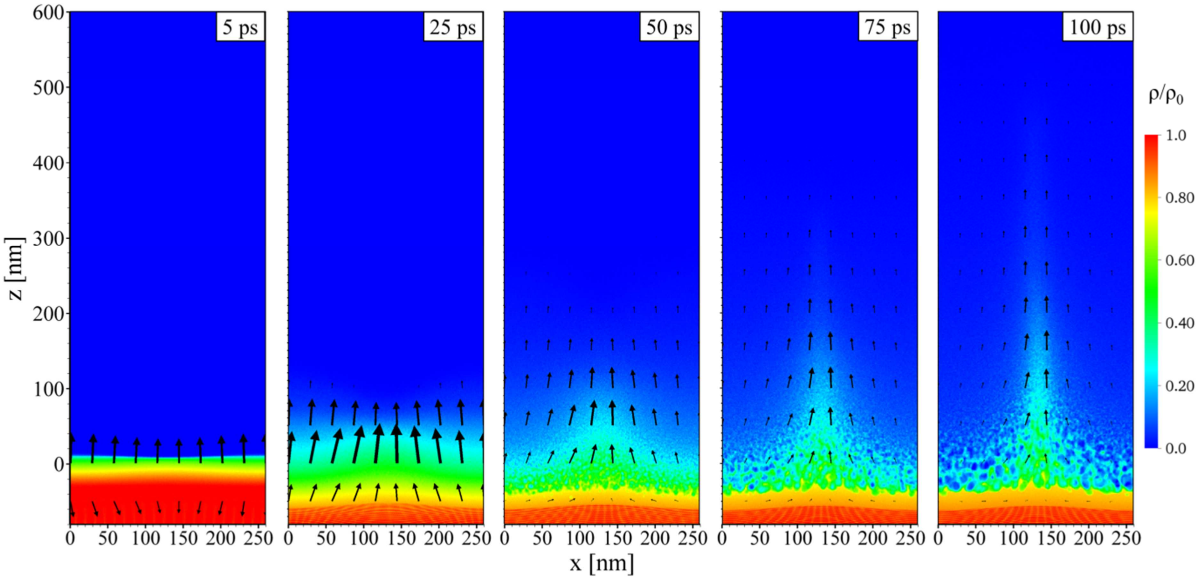

Figure 84. The dynamics of material redistribution at the initial stage of the ablation process. Plots are colored based on the instantaneous density distribution, and arrows depict the relative magnitude of material flow (length/thickness of the arrows are scaled by the product of local density and velocity). Red color corresponds to solid, while orange, yellow, and green depict molten material. Adapted from Ref. [149].

The initial response of the Cr target to the modulated laser energy deposition is illustrated in Figure 84, where the evolution of density distribution and material flow are shown for the initial 100 ps after the laser pulse. Laser excitation and rapid electron-phonon equilibration lead to the heating of the top region of the target and induce an upward material expansion as early as 5 ps. Since the absorbed laser fluence is lowest in the middle of the computational system and highest on the sides, the temperature and pressure gradients have lateral components and drive material rearrangement towards the center, as demonstrated by the deviation of the arrows showing the material outflow from the vertical direction. Meanwhile, at the bottom part of the system, smaller downward-pointing arrows are also inclined toward the center, signifying the nonplanar nature of the pressure wave propagating into the bulk of the target and highlighting the need for the modified nonreflecting boundary condition applied at the bottom of the TTM-MD domain, Section 2.3.1. The successive density snapshots in Figure 84 illustrate the rapid expansion and decomposition of the material overheated above the limit of its thermodynamic stability. The higher vapor pressure generated at the periphery of the computational cell (the area of the higher energy deposition) drives the vapor and liquid droplets to the central part of the system, where a high-density region evolving into a liquid wall is generated.

The formation of the liquid wall can be clearly seen in the snapshots of atomic configurations shown in Figure 85 for a longer time up to 2100 ps. The base of the liquid wall emerges from the foamy structure of interconnected liquid regions generated in the lower part of the ablation plume, while the upper part forms through the coalescence of small liquid droplets pushed toward the center by the lateral component of the vapor pressure gradient. Moving by inertia upward, the liquid wall elongates and becomes thinner. The wall reaches its maximum length of ~600 nm by ~1300 ps, when it starts to decompose into separate liquid droplets. Meanwhile, the rapid electron heat conduction to the bulk of the target undercools the molten surface region and causes the upward motion of the solid-liquid interface. The solidification front reaches the base of the liquid wall by ~500 ps, and the surface region of the target completely solidifies at 2100 ps, shortly after the last group of liquid droplets separates from the wall. As can be seen from Figure 85, the solidification of the lower part of the transient liquid wall leads to the formation of an elongated protrusion with the height of approximately 100 nm. Note that the amount of material removed from the trough area of the modified surface corresponds to the ablation depth of ~40 nm, and the frozen protrusion extends above the level of the original surface of the target. The latter computational prediction is consistent with experimental observations of Refs. [388,392], where the LIPSS pattern generated by single femtosecond pulse irradiation of Au has a characteristic shape of frozen wall-like structures similar to the ones in Figure 85. The simulation results demonstrate that the height and shape of the protrusion are defined by the competition between the disintegration of the liquid wall into droplets and the propagation of the solidification front. The latter accelerates with increasing undercooling of the crystal-liquid interface, reaches its maximum velocity of ~65 m/s when the temperature of the interface drops down to ~0.92 T_m by 300 ps, and stays close to this level until the end of the solidification process.

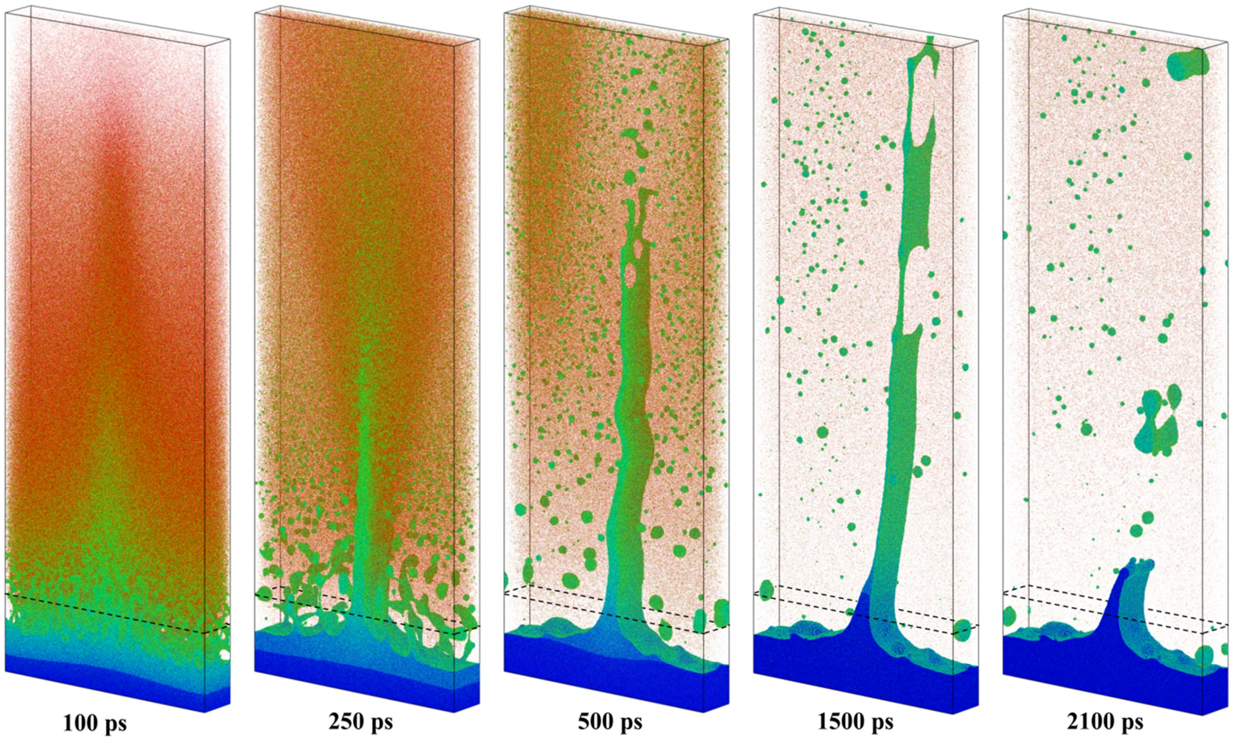

Figure 85. A sequence of atomistic snapshots demonstrating formation of a liquid wall in the ablation process followed by rapture of the wall and generation of a solidified protrusion. The snapshots show a part of the system with z coordinate ranging from -80 nm to 600 nm with respect to the location of the original surface marked by the dashed lines. The atoms in the snapshots are colored by their potential energy, with color scale ranging from -3.8 eV (blue) to -1.4 eV (red). With this coloring scheme, dark-blue regions correspond to the solid phase, light-blue and green represent liquid phase and free surfaces, and red atoms belong to the vapor phase. The dashed line outlines the initial position of the surface. Adapted from Ref. [149].

The computational prediction that the material redistribution in the lower part of the ablation plume is largely responsible for the generation of the frozen surface protrusions does not support the scenario of the LIPSS formation suggested in Ref. [389], where a combination of ablative material removal and redistribution of the molten material driven by the gradient of the ablation recoil pressure is suggested to be responsible for the formation of the periodic surface relief. The latter mechanism, i.e., the liquid flow along the surface of the target induced by the pressure gradient, is indeed observed in the simulation, as evidenced by small arrows in the molten (yellow/orange) part of the target in the snapshots shown for 25-100 ps in Figure 84. The contribution of this mechanism of material redistribution to the formation of the final frozen protrusion, however, is relatively small. To quantify this contribution, we calculated the total amount of liquid passed towards the central part of the system through vertical planes located at positions of 80 and 180 nm along the x axis and at any depth larger than 40 nm, i.e., z -40 nm in Figure 84. This depth of 40 nm roughly corresponds to the ablation depth in the region of the maximum energy deposition. The total amount of the material redistributed through the liquid flow generated within the molten surface layer of the target is found to only account for about 10% of the material in the protrusion ($z > -35$ nm) after complete solidification of the target. Decreasing the cutoff depth in the analysis of the liquid flow to 35 nm ($z \leq 35$ nm) yields a larger contribution of 17% to the protrusion. However, this increase is largely attributed to the displacement of liquid droplets partially attached to the surface and moving with a considerable speed towards the center of the computational system.

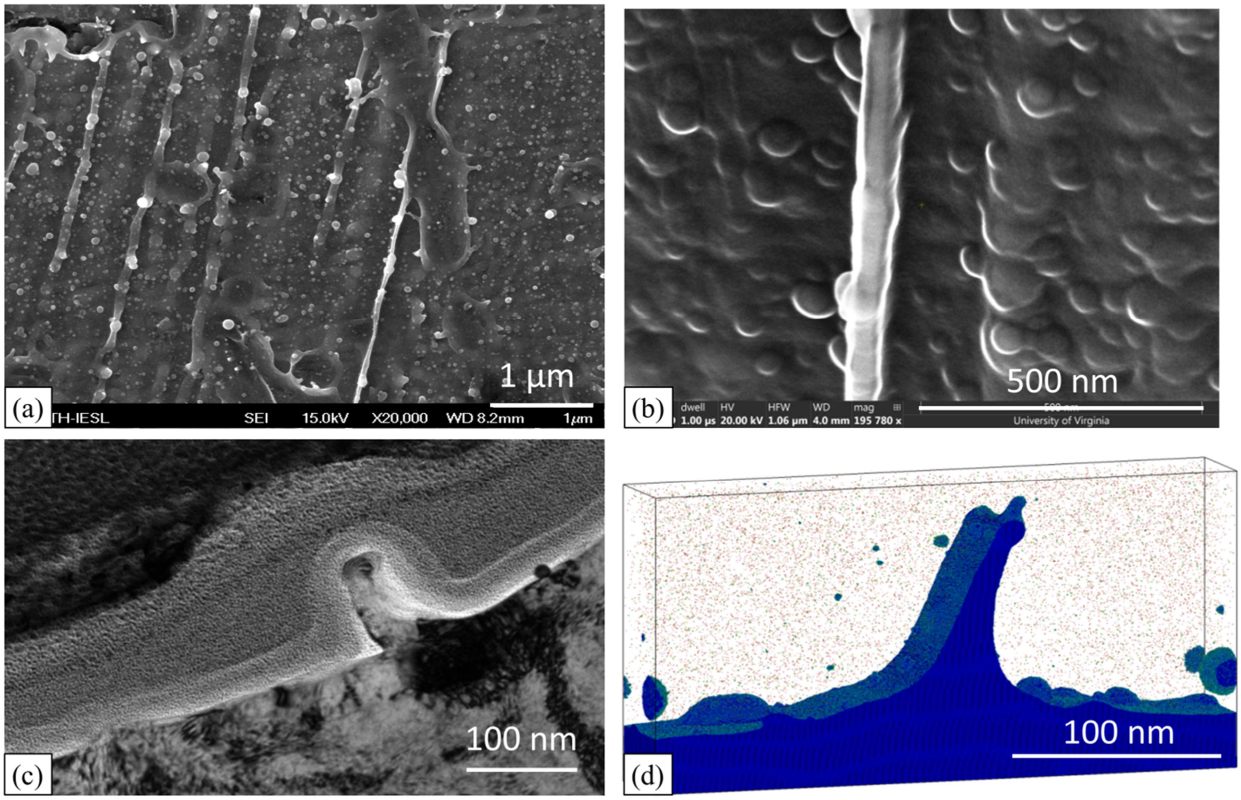

Figure 86. SEM images of Cr (001) surface irradiated at 6000 J/m^2 incident laser fluence (a,b), TEM of a cross-section demonstrating the shape of the produced surface protrusion (c), and the surface morphology predicted in atomistic simulation (d). The experimental portion of the work is done by I. Gnilitskyi.

In Figure 86, the predicted surface morphology is compared with results of experimental study performed by I. Gnilitskyi. The target is irradiated by 200 fs laser pulse with 1030 nm wavelength at the 6000 J/m^2 incident fluence averaged over the laser spot. With assuming constant reflectivity 0.63 [181], the absorbed laser fluence is 2200 J/m^2, which is 50% above the phase explosion threshold. Laser irradiation produces a sequence of parallel lines with noticeable periodicity. It should be pointed out that the spot is irradiated only by a single laser pulse, and spots do not overlap. Therefore, the produced absorption pattern is defined only by pretense of initial surface defects and roughness rather than by preexisting periodic motif. Meanwhile, the experiment clearly demonstrates of generation of LIPSS like structures in a single pulse irradiation regime. According to a TEM image in Figure 86c of a cross-section of surface feature depicted in the enlarged view in Figure 86b, the height and thickness of a produced surface protrusion in a very good agreement with the surface morphology predicted in the atomistic simulation.

The predicted shape of the frozen protrusion is also similar to the shapes of LIPSS generated on Au surface by single femtosecond pulse irradiation [388,392] but is clearly distinct from the highly regular LIPSS produced by scanning Si surface by high repetition rate femtosecond laser pulses [389], where broad hills separated by narrow troughs are generated. In addition to the differences stemming from material-specific response to the laser excitation, the larger spatial modulation of the absorbed fluence may cause generation of a thicker liquid wall that could exhibit slower decomposition and more substantial flattening of the protrusion prior to the solidification. The partial overlap of the laser pulses, leading to the effective irradiation by several shots per spot, may also smooth the surface topology via re-melting the walls and relocation of the material driven by surface tension. Finally, the nonlinear nature of the laser energy absorption, particularly a drop of reflectivity at high electron temperatures, could also play a role by further sharpening the contrast between regions of higher and lower energy density deposition. As a result, instead of the sinusoidal modulation assumed in the simulation, the deposited laser energy may exhibit narrow spikes that could produce deep troughs in the resolidified surface.

It is notable that the patterning associated with the material redistribution toward the regions of the minimum laser energy deposition is in contrast with the results of simulations and experiments where the protrusions induced by interference of two laser beams at lower fluences appear in the regions of the maximum laser energy deposition [393]. The interference technique implies much higher modulation amplitude of laser intensity along the material surface than in the present study, up to 50%. Although the electronic heat conduction should somewhat smooth the temperature profile on the temporal scale of the protrusion formation, in the irradiation regime investigated in Ref. [393] the extended regions between the absorption maxima remain solid, thus confining the molten material. As a result, the lower-energy patterning is produced through melting and expansion of regions of the maximum energy deposition, where the generation of subsurface voids captured by rapid solidification [17] is responsible for surface swelling or formation of frozen surface features. In contrast, the material redistribution in the ablative surface patterning is driven by the pressure gradients in the initial ablation plume and results in a rapid density "inversion" in the ablation plume from the initial maxima above the higher energy deposition regions of the target to the material concentration and formation of the liquid wall in the regions above the minima of the energy deposition.

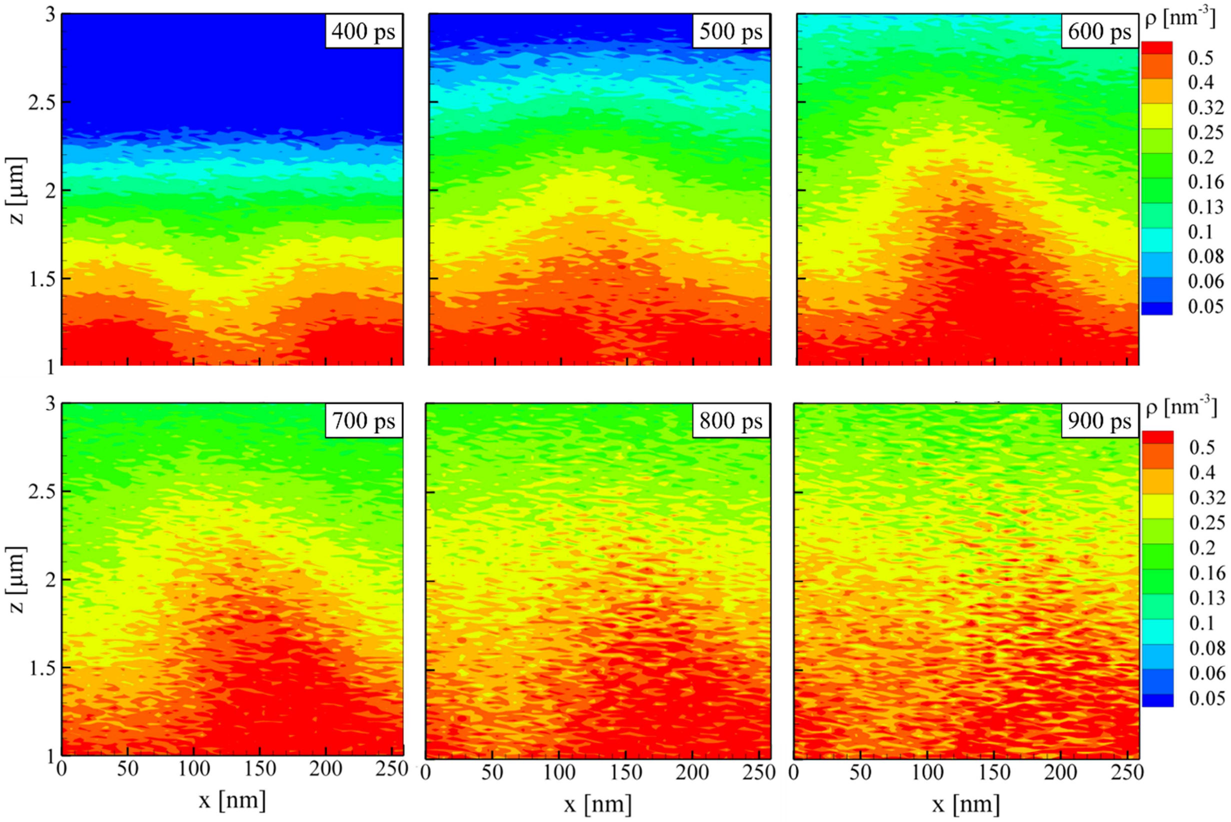

Figure 87. Density evolution in the ablation plume generated in a simulation of spatially modulated ablation illustrated by Figure 84 and Figure 85. The plume density is expressed in units of number of Cr atoms per nm^3 and is shown for a region extending from 1 to 3 μm above the irradiated surface.

While the density inversion happens within a few tens of picoseconds in the immediate vicinity of the surface and may be difficult to see from Figure 84, it is more apparent in the higher part of the ablation plume, where the density inversion from the regions above the maxima of the energy deposition to the ones above the minima is observed at a longer time scale of 400-500 ps. The material redistribution reflected in the modulation of density in the ablation plume is illustrated in Figure 87, where the plume density is shown for a region extending from 1 to 3 μm above the irradiated surface. Initially, the plume density is higher in the regions located above the maxima of the laser energy deposition, while later the lateral vapor pressure gradient drives the material redistribution to the central part of the system, leading to the density inversion occurring between 400 and 500 ps. The maximum observed density contrast at a height of 1-1.5 μm above the target is approximately half of the maximum value that reaches 0.5% of the original density of solid Cr target. As time progresses, the plume becomes uniform and, by the time of 1 ns, any lateral density contrast disappears.

Turning the attention to the internal structure of the frozen surface protrusion and the surrounding subsurface region, we note a high density of crystal defects generated in the course of laser-induced melting and resolidification. The distribution of crystal defects is visualized in three complementary images shown in Figure 88. The dislocation configurations can be seen in Figure 88a, where the atoms with elevated potential energy are shown, and the chains of such atoms correspond to dislocation cores. The dislocation types are identified with the dislocation extraction algorithm described in Ref. [180] and are shown in Figure 88b. Analysis of the dynamics of the dislocation generation reveals that they are not produced during the initial dynamic relaxation of laser-induced stresses, when the stresses partially relax due to the transient appearance of a high density of stacking faults along the $\{110\}$ planes [81]. The stacking faults are unstable and quickly disappear when the tensile stress wave leaves the surface region. The emission of the dislocations is then initiated at approximately 500 ps, when the solidification front reaches the base of the liquid wall, and the resolidified material gets an opportunity to expand laterally and generate shear stresses sufficiently strong for the emission of dislocations. The majority of dislocations have a Burgers vector $1/2\langle 111\rangle$, although several segments of $\langle 111\rangle$ dislocations, produced by dislocation reactions, are also observed. The average density of dislocations in the subsurface region of the target included in the MD part of the computational cell is approximately 10^{15} m^{-2}.

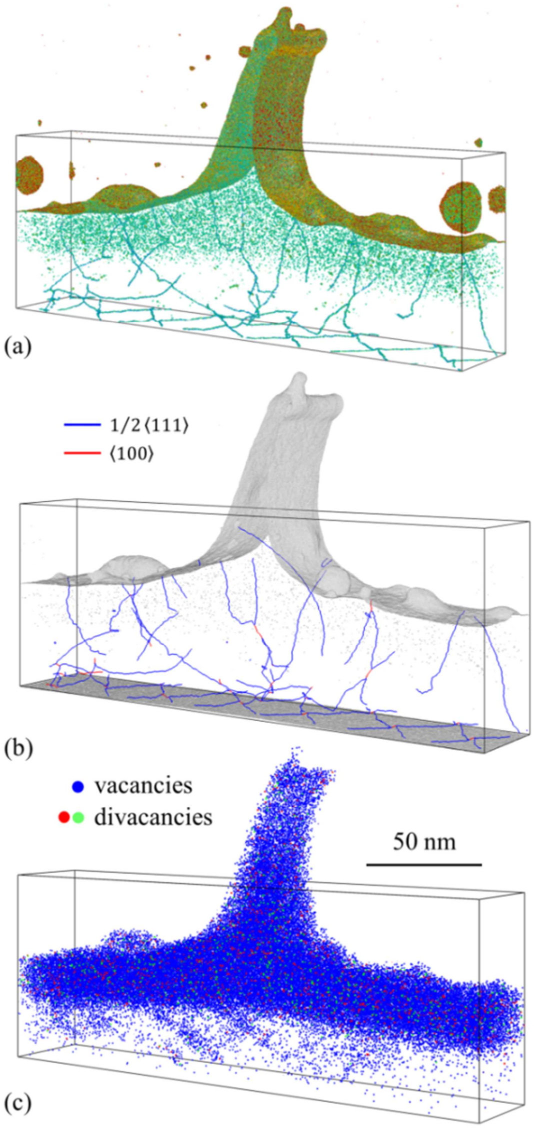

Figure 88. Three representations of the microstructure of the surface region of the irradiated Cr target at 2100 ps, after complete resolidification of the target. In (a), dislocations and vacancy clusters present in and below the frozen protrusion are exposed by blanking the atoms with the potential energy below -3.94 eV (correspond to atoms with BCC local coordination and atoms surrounding single vacancies) and the remaining atoms are colored by their potential energy, with color scale ranging from -4.0 eV (blue) to -3.4 eV (red). In (b), dislocations identified with the algorithm of Ref. [180] are shown and colored by dislocation type. In (c), the distribution of vacancies and vacancy clusters is shown, with single vacancies marked by blue color while divacancies with two vacancies on the first and second nearest neighbor lattice sites with respect to each other marked green and red, respectively. The box outlines the shape of the original target before the laser irradiation. Before analysis, the system is quenched for 1 ps using the velocity-dampening technique.

In addition to the dislocations, a very high concentration of vacancies and vacancy clusters is observed inside the frozen protrusion and in a subsurface region of the target, as shown in Figure 88c. The concentrations of vacancies and divacancies in the part of the target that experienced the laser-induced melting and rapid resolidification are calculated to be approximately 0.21% and 0.017% of lattice sites, respectively. The high vacancy concentration is consistent with values of the vacancy concentration observed in earlier simulations of laser processing of Cr targets [81], and largely exceeds the equilibrium vacancy concentration at the melting point, which can be estimated to be approximately 10^{-4} of lattice sites. The rapid solidification proceeding under conditions of strong undercooling results in the generation of strong vacancy supersaturation, while the rapid (up to $\sim 10^{12}$ K/s [17,81]) cooling of the resolidified target does not leave time for equilibration of the vacancy concentration. The estimated vacancy diffusion path is on the order of several nanometers during the rapid quenching of the resolidified surface region, and even the vacancies located close to the free surface can be "frozen" in the target. In addition to the vacancies generated in the course of the rapid solidification, in this region due to motion of dislocations is approximately 0.012% of lattice sites.

Summary

A large-scale molecular dynamics simulation is employed to study the mechanism of single-pulse LIPSS formation in the regime of strong ablation. The simulation of spatially modulated ablation induced by irradiation at an average laser fluence well above the threshold for the phase explosion reveals a complex interplay of material removal and redistribution leading to the formation of prominent surface features extending above the level of original surface of the target. The fast heating of Cr target by the laser pulse leads to an explosive decomposition of about 30-40 nm deep surface layer into a mixture of vapor and liquid droplets. Lateral pressure gradients in the plume generated by the spatially modulated laser ablation drive the vapor and liquid droplets to the regions located above the minima of the laser energy deposition at the target surface. The material redistribution leads to formation of a high-density region evolving into an elongated liquid wall extending up to ~600 nm above the surface of the target. The upper part of the liquid wall disintegrates into droplets, while the base of the wall solidifies on the time scale of ~2 ns, producing a ~100-nm-tall frozen surface feature. The shape and size of the produced surface protrusion is in a good quantitative agreement with results of experimental study.

In contrast to earlier simulations of low-fluence laser processing through spatially modulated energy deposition by two interfering laser beams, where the frozen surface protrusions are generated in regions of the maximum energy deposition, the ablative laser patterning investigated in this work reveals a density "inversion" in the ablation plume, where the maximum plume density rapidly switches from the regions above the maxima to the ones of minima of the energy deposition due to an active lateral motion of the material. The results of the simulation also suggest that the material redistribution in the lower part of the ablation plume is playing the major role in the formation of the frozen protrusions, while the liquid flow in the molten part of the target driven by the gradient of the recoil pressure makes a relatively small contribution to the LIPSS formation.

The properties of the solid protrusions and adjacent regions of the target can be expected to be strongly affected by a high vacancy concentration produced through the rapid solidification under conditions of deep undercooling and predicted to exceed 10^{-3} of lattice sites. Moreover, the simulation demonstrates generation of a high density of dislocations, 10^{15} m^{-2}, that can further modify the mechanical and chemical properties of the laser-processed surface. The insights into the LIPSS formation mechanisms may help in designing approaches for increasing the processing speed and improving the quality of the laser-generated surface structures.

5. Acoustic activation of surface processes

Abstract: The relaxation of laser-induced thermal stresses, in addition to affecting surface morphology and microstructure, generates intense bulk and surface acoustic waves (SAWs), which are capable to influence processes on substantial distance from the laser spot. Apart from modifications at macroscopic scale, such as back spallation [394] or delamination of material at the rear side of the target due to reflection of a compressive wave, SAWs and bulk waves have been shown to affect surface processes at atomic/molecular level. In particular, experimental studies demonstrate acoustically activated desorption of molecules, atoms, and ions from surfaces [65-72], enhancement of surface diffusion of small atomic clusters [73,74], and increase of the rates and selectivity of heterogeneous catalytic reactions [57-65]. These observations are unexpected and surprising as there is a large mismatch between the relatively low frequencies of SAWs, typically less than 100 MHz, and the vibration frequencies characteristic for individual atoms and molecules on the surface, on the order of 1 THz.

The work reported in this section is focused on resolving the long-standing question on the mechanisms responsible for the acoustic activation of surface processes and providing a guideline for developing techniques that fully utilize the benefits of the acoustic stimulus. Section 5.1 reports results of a series of continuum-level simulations targeted at the revealing the parameters of SAWs generated in nonablative laser irradiation regime. In Section 5.2 an atomistic approach designed for modeling of free propagation of SAWs is described, and the results of a detailed analysis of intrinsic features of linear and nonlinear evolution of SAW are presented. Before our study, MD method has never been applied for description of free propagation of SAWs. Next, the phenomenon of acoustic activation of surface diffusion of small clusters on a surface is investigated in a series of large-scale atomistic simulations (Section 5.3). Nonlinear sharpening of SAWs and the corresponding enrichment of the SAW spectra by high frequency harmonics, which are capable of reaching the cluster resonance frequencies and enabling an effective dynamic coupling between the SAW and the cluster vibrational modes, are found to be responsible for the efficient acoustic activation of surface mobility. In our further study, the direct coupling of high frequency harmonics of bulk waves is demonstrated to result in acoustic desorption of small clusters and graphene sheets (Section 5.4). Moreover, analysis of the interaction of SAWs with graphene sheets on Cu substrate has suggested the possibility of

acoustic activation of surface motion of large sheets of graphene (Section 5.5). The observation of importance of dynamic coupling for both acoustically activated diffusion and desorption suggests that the generation of high frequency harmonics in nonlinear wave propagation may be relevant to a variety of surface processes.

5.1. Continuum level modeling of laser-induced generation of surface acoustic waves

Laser irradiation is a common noncontact method for generating elastic waves in solids, which is capable of producing very strong SAWs with strain amplitude on the order of 10^{-2} [53]. Such strong waves, however, can be generated only at sufficiently high laser fluences, in the ablation regime. The efficiency of SAW generation in thermoelastic and non-ablative regimes is typically considered to be low [120]. However, the regimes below the damage threshold are attractive for practical applications since the target can be irradiated repeatedly to generate not only one SAW pulse, but a sequence of pulses, which can be used for activation of surface processes. In particular, as discussed in Section 5.3, the magnitude of surface diffusion enhancement is proportional to the number of acoustic pulses passing through the region of interest. The experimental study performed by our collaborator from the group of Dr. Helvajian suggests 19-fold enhancement for 100 Hz laser repetition rate. Moreover, estimations suggest that application of lasers with kHz repetition rate combined with circular movement of the laser spot around the observation region to avoid accumulation of heat may create an equivalent of 10^3 K for surface diffusion under room temperature conditions. In addition, irradiation in the nonablative regime allows avoiding pollution of the surface by ablation products.

As discussed in Section 5.3, nonlinear effects in the SAW-induced activation of surface processes are essential, and the SAWs should be sufficiently strong to form a shock front. Since shock front formation distance is inversely proportional to strain amplitude and the wave vector, $L_{shock} \sim \lambda/e$, for a typical laser spot with size on the order of 10 microns the required maximum strain should be approximately 10^{-4} to have a shock front formation on the length scale of 10 centimeters. The absence of accurate experimental and computational data regarding the SAW amplitude generated in non-ablative regimes complicates interpretation of experimental results [73,74]. In addition, a study of the optimal parameters of laser-induced generation of SAWs can improve the efficiency and enable generation of stronger waves.

The temporal evolution of temperature and stress in the irradiated target is investigated with a thermoelasticity model discussed in details in Section 2.2.2. The problem is solved in 2D Cartesian coordinate setup with uniform temperature and zero strain assumed along the third direction. This setup is motivated by the use of rectangular laser spots produced by cylindrical lenses in experimental studies utilizing the laser-induced generation of SAWs [73,74,125,140,395,396]. Si (100) substrate is considered in the modeling, and the following parameters are assumed: elastic moduli C_{11} = 165.78 GPa, C_{12} = 63.94 GPa, C_{44} = 79.62 GPa; density ρ = 2328 kg/m^3; thermal conductivity k = 124 Wm^{-1}K^{-1}; heat capacity C_p = 702 Jkg^{-1}K^{-1}; linear thermal expansion coefficient α_L = 2.49×10^{-6} K^{-1} [220]. High anisotropy of silicon makes isotropic approximation, commonly used in studies of laser-induced generation of stress waves [143,145], unrealistic. Therefore, we have developed a model that accounts for the strong dependence of the wave velocity on the propagation direction. The computational setup is schematically illustrated in Figure 89. Heat insulating boundary conditions are applied in all four directions, rigid boundaries are applied at the bottom, left, and right sides of the system, and free boundary is imposed at the top surface. The system size is selected so that the stress waves do not reach the rigid boundaries. The number of cells in x direction is 10000, and 5000 or 6000 cells in y direction. The spatial resolution of the mesh is defined based on the size of the laser spot to ensure accurate description of the acoustic wave generation. The time step is set according to the procedure described in Section 2.2.2.

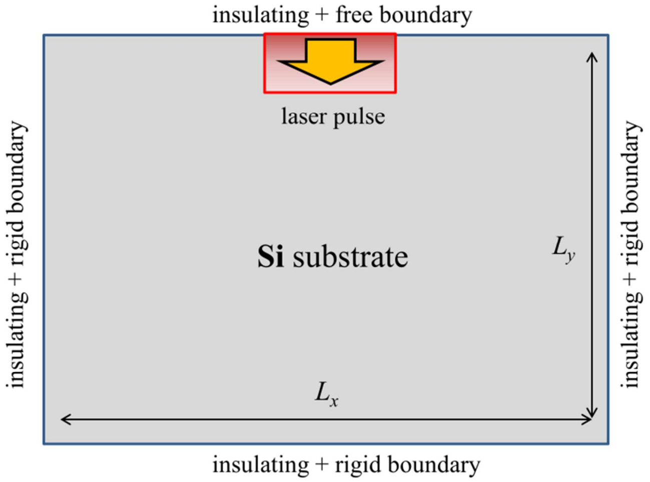

Figure 89. Schematic illustration of the computational system used in 2D thermoelasticity modeling of laser irradiation of Si substrate.

First, we consider generation of surface waves under the experimental setup used to study activation of surface diffusion in Ref. [73], also discussed in Section 5.3. In particular, 6 ns laser pulse at 355 nm wavelength is focused into a rectangular laser spot of size 16 μm (FWHM for Gaussian profile) along *x* direction and 5 mm in the direction perpendicular to the plain of the plot in Figure 89. The absorption depth and reflectivity at this wavelength are 9 nm and 0.58, respectively [181]. The spatial resolution of the mesh is 0.2 μm, the time step is 18.4 ps, and the system size is 2 mm × 1.2 mm. The target is irradiated at 0.5 J/m^2 absorbed laser fluence, and the maximum temperature reached in the target is 3000 K.

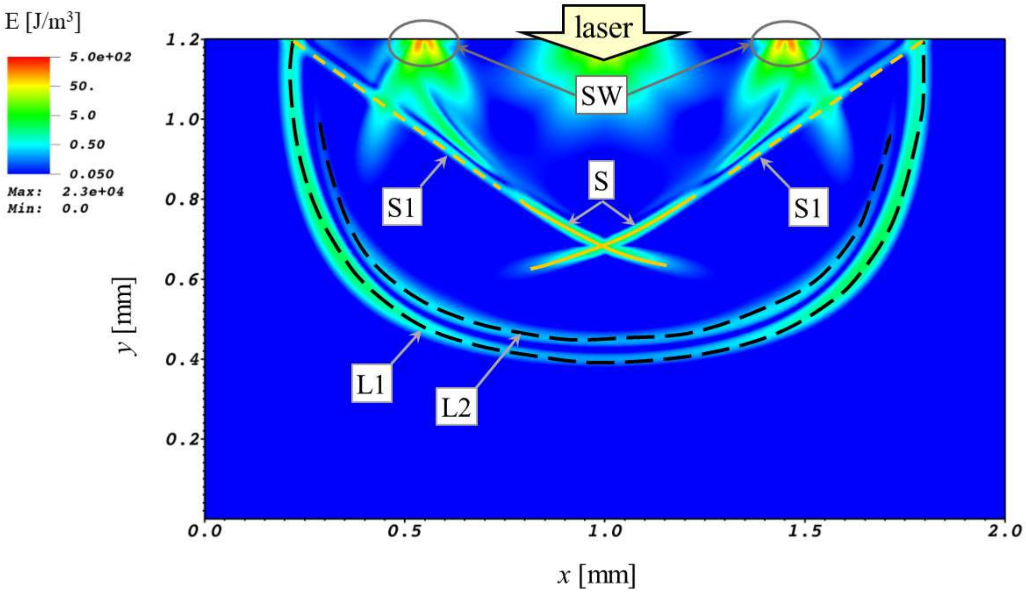

Figure 90. An illustration of thermoelastic wave generation in laser irradiation of silicon under conditions described in Ref. [73]. The plot shows the energy density at 100 ns after pulse, and the longitudinal and shear waves are schematically outlined by black and yellow lines, respectively. Rayleigh waves (a type of SAW), longitudinal compressive, longitudinal tensile, and shear waves generated by rapid laser heating are marked as RW, L1, L2, S, respectively. Shear waves emitted due to interaction of L1 waves with the free surface are marked as S1. The thermal stresses generated by laser heating cannot be completely relaxed by the material expansion towards the free surface and, therefore, are still present in the vicinity of the irradiated area.

The density of acoustic energy in Si target at 100 ns after laser irradiation is shown in Figure 90. Laser irradiation leads to generation of a variety of bulk and surface waves. Since for typical setups applied for laser-induced generation of SAWs [73,74,125,140,395,396] a cylindrical lens is used, the length of the laser spot in one direction is much longer than in another one. This feature explains applicability of 2D approach in our study and suggests that only Rayleigh mode of SAWs is generated, while generation of other modes with nonzero displacement components parallel to the surface and perpendicular to the wave propagation, such as Love waves, is suppressed. Strains in the predicted SAWs lay in the range from -4.9×10^{-5} to 1.9×10^{-5} for e_{xx} and from -1.5×10^{-5} to 2.0×10^{-5} for e_{yy} components. The SAW amplitude of 4.9×10^{-5} results in formation of a shock front on the length scale of ~10 cm and supports the explanation of SAW activation of surface diffusion based on generation of high frequency SAWs harmonics provided in Ref. [73] and Section 5.3. However, under these irradiation conditions only about 10^{-5} of the deposited energy goes into the generation of acoustic waves, and about 0.77 of this energy corresponds to SAWs. In our study, we also examined the effect of the shape of the laser beam profile on the SAW generation. We found that a rectangular laser energy distribution profile along *x* axis (flat top laser beam) instead of a Gaussian one produces a higher 6×10^{-5} amplitude of the generated wave. Thus, we can make a conclusion that the sharpness of the energy distribution within the laser spot may affect the efficiency of the wave generation.

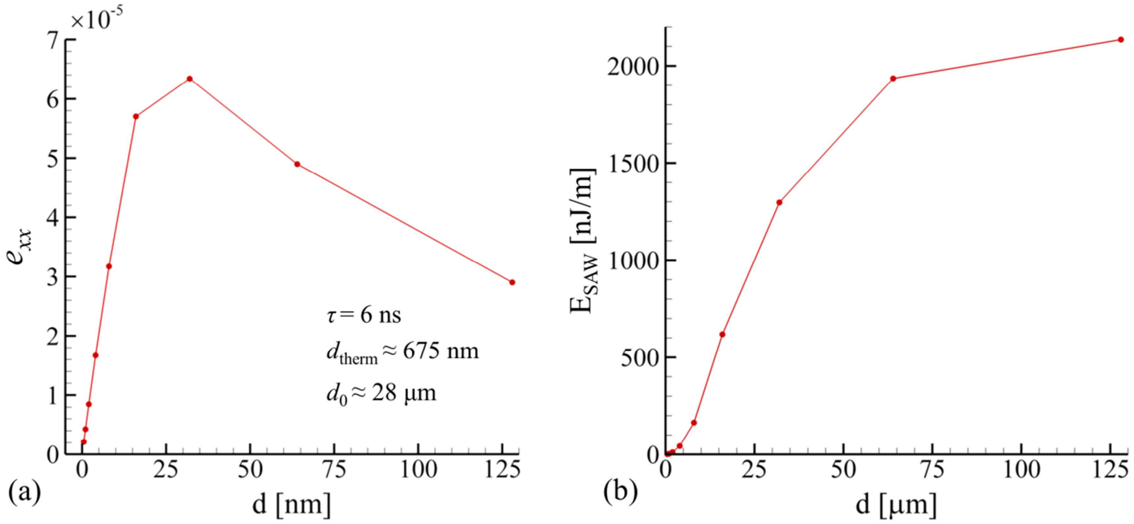

Figure 91. The laser spot size dependence of the maximum amplitude (a) and the energy of the SAW per unit length of the wave front (b) of SAWs generated in simulations of laser irradiation of Si. The laser pulse duration 6 ns corresponds to the thermal diffusion length of 675 nm and wave propagation distance of 28 μm during the laser irradiation.

To find the optimal set of laser parameters and absorption depth, laser-induced generation of SAW is explored under different conditions. Figure 91 depicts the dependence of wave amplitude and the wave energy on the laser spot size. According the study reported in Ref. [397], for a circular laser spot $E_{SAW}{\sim}d^2$ for small and $E_{SAW}{\sim}d$ for large diameter of the laser spot d

relative to the characteristic length of the SAW propagation during the time of the laser irradiation, *d₀*. Similar analysis for a rectangular laser spot gives $E_{SAW} \sim d^2$ for small and $E_{SAW} \sim const$ for large laser spot size. At the distance smaller than the wavelength interference of a set of coherent point sources leads to square increase of the total intensity, while if the sources are separated by a distance comparable to (or larger than) the wavelength, the interference gives a constant value. At $d < d_0$ SAW wavelength λ is mostly dictated by the pulse duration and does not depend on the spot diameter. Meanwhile, at $d > d_0$ SAW wavelength is proportional to the spot size, $\lambda \sim d$. Since $E_{SAW} \sim e_{xx}^2 \lambda^2$ for SAWs, one can derive the following dependence of the wave strain amplitude on the spot size:

$$\begin{cases} e_{xx} \sim d, E_{SAW} \sim d^2 & at\ d < d_0 \\ e_{xx} \sim d^{-1}, E_{SAW} \sim const & at\ d \gg d_0 \end{cases} \tag{5.1}$$

The above dependence is in a good agreement with dependencies depicted in Figure 91. The maximum wave amplitude is reached at $d \approx d_0$ and is equal to ~6.4×10^{-5}. The profile of SAW pulse generated in laser irradiation is illustrated in Figure 92.

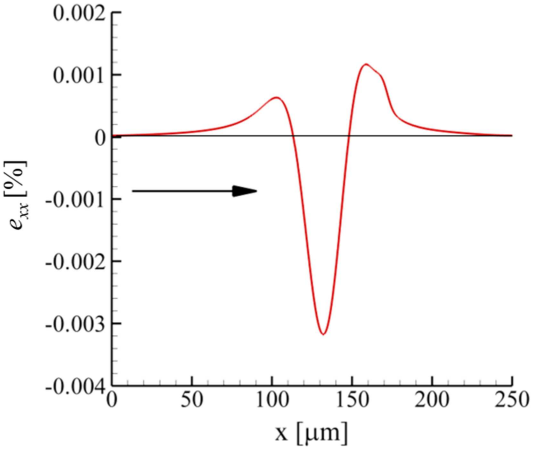

Figure 92. The profile of e_{xx} strain of laser generated SAW pulse at free surface. The spot size is 8 μm.

The effect of pulse duration is studied in another series of simulations performed for pulse duration of 10 ps. We select this pulse duration for illustrative purposes, to demonstrate how three orders of magnitude reduction of the pulse duration affects the generation of SAWs. Though, the change of the concentration of conduction band electrons capable to affect the initial dynamics of energy redistribution for so short pulses is not accounted for [398]. The laser fluence is selected to be 0.02 J/cm^2 that gives approximately the same maximum temperature in the target during laser irradiation as for previously considered case of a longer 6 ns pulse. A representative example of the energy density distribution in a target after laser irradiation is shown in Figure 93 for a laser spot size of 400 nm at 191 ps after the laser irradiation. The values of strain in the SAWs lay in the range of -3.6×10^{-4} – 8.8×10^{-5} for e_{xx} and -1.3×10^{-4} – 1.4×10^{-4} for e_{yy} components. The fraction of the total energy that goes into the generation of acoustic waves is about 2.3×10^{-4} in this case, and approximately 11% of the total acoustic energy is carried by SAWs. The generated acoustic pattern is very similar to the one shown in Figure 90 for longer laser pulse; however, irradiation under conditions close to the stress confinement along vertical direction results in emission of more intense longitudinal waves propagating downwards. The application of a rectangular laser energy distribution profile along x axis leads to generation of more intense SAWs reaching 7.6×10^{-4} e_{xx} strain amplitude.

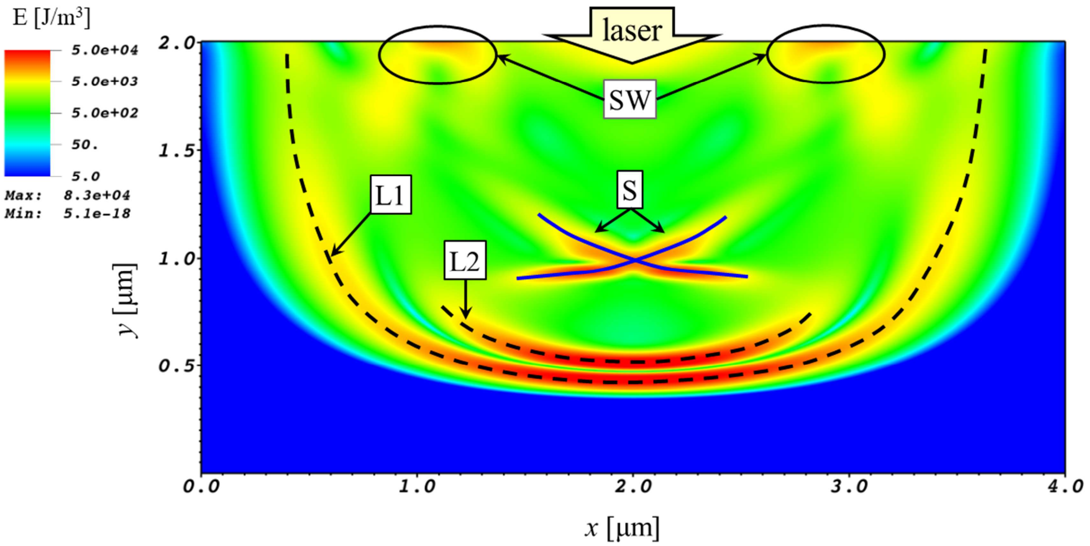

Figure 93. An illustration of wave generation in laser irradiation of silicon with 10 ps laser pulse at 0.02 J/cm^2 absorbed laser fluence. The laser spot size is set to 400 nm and has a Gaussian spatial profile along the x-axis. The plot shows the energy density at 191 ps after the laser irradiation, and the longitudinal and shear waves are schematically marked by black and blue lines, respectively. Rayleigh waves (a type of SAW), longitudinal compressive, longitudinal tensile, and shear waves generated by the rapid laser heating are marked as RW, L1, L2, S, respectively.

The dependence of the SAW energy and amplitude on the laser spot size is depicted in Figure 94. Similar to the long laser pulse case considered above, two distinct regimes for small, $d < d_0$, and large, $d > d_0$, laser spots are present. In the first case, the SAW energy is proportional to the square of the laser spot size, and the maximum strain increases linearly with increase of the laser spot size. The maximum strain of 9.2×10^{-4} is reached for a laser spot size equal to $1.3d_0$, characteristic length of wave propagation during the laser pulse. Additional increase of the laser spot size is accompanied by slow decrease of the wave energy and decrease of the maximum strain according to $e_{xx} \sim d^{-0.9}$. This dependence slightly deviates from Eq. 5.1 that predicts $e_{xx} \sim d^{-1}$, which may be a result of a substantial depth of heating with respect to d_0. Thus, the integral source cannot be considered as an infinitely thin plain of point sources, and three-dimensional distribution of point sources must be considered.

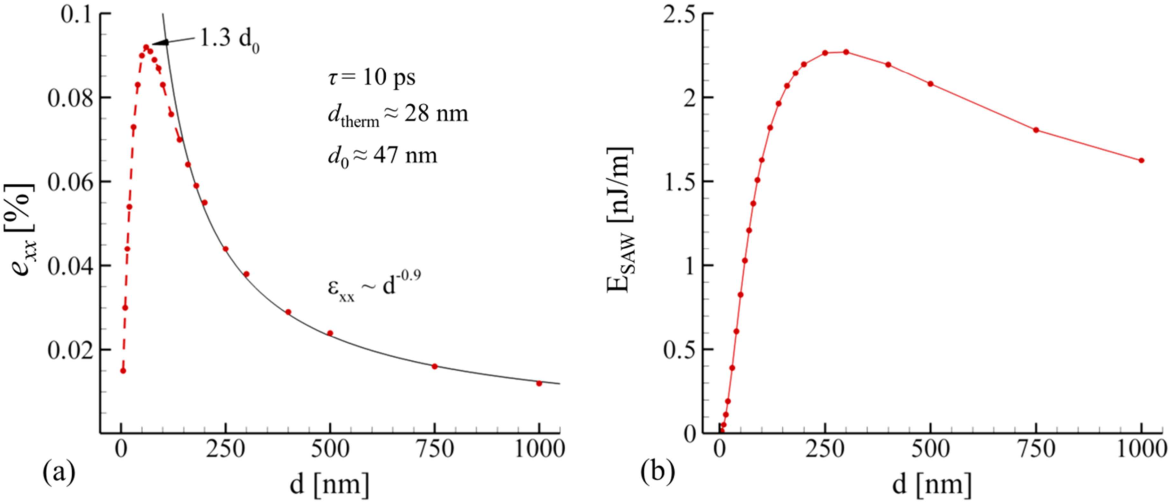

Figure 94. The maximum amplitude of SAWs generated in laser irradiation of Si (a) and the energy of the SAW front per unit length (b) depending on the spot size. The laser pulse duration of 10 ps corresponds to the thermal diffusion length of 28 nm and SAW propagation distance of 47 nm during the time of the laser irradiation.

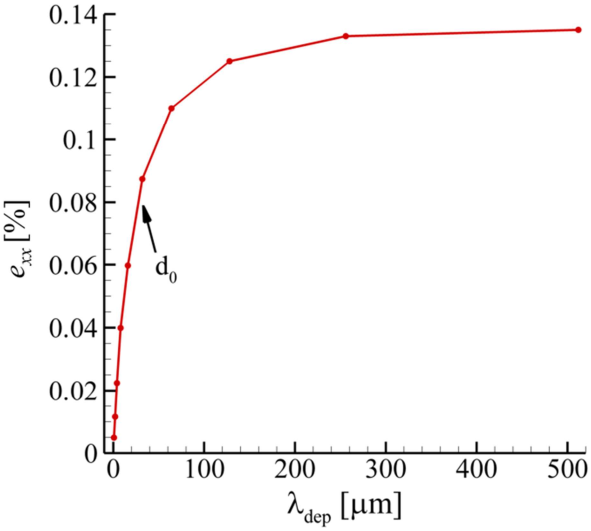

Figure 95. The dependence of the SAW amplitude on the characteristic depth of laser energy deposition for irradiation by 8 ns laser pulse with laser spot size of 32 μm. d_0 = 28 μm is the length of SAW propagation during the laser pulse.

To reveal the origin of an order of magnitude difference in the SAW amplitude generated in picosecond and nanosecond pulse irradiation, the effect of the energy absorption depth is assessed in a series of simulations performed for 8 ns laser pulse and a width of a Gaussian laser pulse profile of 32 μm. The laser fluence in each simulation is selected to ensure that the maximum temperature is the same as in our earlier simulations. For small depth of laser energy deposition relative to d_0, the energy of the generated SAWs is proportional to λ_{dep}^2, which leads to $e_{xx} \sim \lambda_{dep}^2$. At large energy deposition depth, the energy of the emitted waves approaches a constant value that also suggests constant e_{xx} since $E_{SAW} \sim e_{xx}^2 \lambda^2$. This prediction is in a good agreement with the dependence obtained in simulations and shown in Figure 95. In the above-reported simulation for the short laser pulse setup, effective heat deposition depth is $\lambda_{dep} \approx 0.8d_0$ that gives the maximum strain ~0.09%. For a longer laser pulse and 32 μm laser spot, $\lambda_{dep} \approx 0.8d_0$ gives the maximum SAW strain ~0.07%, which is close to the result obtained for three order of magnitude shorter laser pulse. The slight difference may be attributed to the temperature distribution: in one case the temperature profile is mostly generated by heat diffusion, while in another case the profile is produced by Beer-Lambert law assumed in the simulation of laser energy absorption.

Based on the series of simulations performed in this section, we formulate the following conclusions on the optimal set of laser parameters (pulse duration, spot size, and absorption depth) for laser-induced generation of strong SAWs:

1) The maximum amplitude of laser generated SAW can be achieved for the laser spot size comparable to the characteristic SAW propagation length during the laser irradiation, which is equal to the pulse duration multiplied by the SAW speed: $d_{optimal} \sim 1.3 d_0$ for $d_0 = v_{SAW} \tau$.
2) The amplitude of SAW increases with increase of characteristic laser energy deposition depth and saturates at $\lambda_{dep} \sim 2 - 4\ d_0$.
3) If absorption depth is large, laser pulses with sharp spatial energy deposition profile (flat top laser beam) produces stronger SAWs.

The first two rules can be explained based on the coherence of wave point sources as discussed in Ref. [397]. If the laser parameters are optimized, the maximum SAW strain amplitude in Si generated in the nonablative regime can reach ~0.1%, which is almost 20 times higher compared to the amplitude of waves generated with the setup used in the experimental study of SAW-activated surface diffusion [73,74]. Meanwhile, the performed simulations have confirmed that SAWs generated under the experimental conditions are able to form a shock front at a distance of

~10 cm from the laser spot, which supports the explanation of SAW activation of surface diffusion based on the generation of high frequency SAW harmonics provided in Ref. [73] and Section 5.3.

5.2. Molecular dynamics modeling of nonlinear propagation of surface acoustic waves

Abstract: Results of molecular-dynamics (MD) simulation of nonlinear propagation of surface acoustic waves (SAW) are reported. The possibility of accounting for both linear and fully nonlinear (up to material damage) evolution of SAW field is an essential intrinsic advantage of the MD approach. Here, we describe the designed computational setup with justification of the choice of key parameters and present the obtained simulation results illustrating main features of the linear and nonlinear effects accompanying propagation of SAWs. In particular, the unusual character of spatial dispersion of SAWs and a number of specific features of nonlinear SAW evolution that are strongly distinct from their counterparts in bulk-wave propagation are pointed out. Good agreement of the MD data with some important features that have been predicted by the earlier known analytical models confirms reliability of the implemented MD approach. Compared with alternative methods of SAW description (analytical, finite-difference and other similar numerical methods), the developed MD approach opens unprecedented possibilities for investigation of influence of intense SAWs on diffusion of surface species (from individual atoms to clusters), interaction of SAWs with subsurface structural defects (dislocations, impurities and vacancies), as well as for detailed studies of interaction of SAWs with the substrate for material-characterization purposes.

Introduction

Surface acoustic waves (SAWs) are elastic waves that propagate along free surfaces of solid materials and are characterized by strain profiles exponentially decaying with depth under the surface. The research interest in SAWs is defined by their relevance to various natural phenomena, such as propagation of seismic waves generated by earthquakes in the Earth's crust [399] or long-range communication among elephants [400], as well as by the rapid expansion of the area of practical applications of SAWs, currently encompassing nondestructive probing of mechanical properties and surface defects [53,125,139,140,401,402], signal-processing [50,403,404] and acousto-optical [405] devices, chemical sensing [51,52,406], micro-scale manipulation of fluid flow, biomolecules, and nanoparticles in microfluidics devices [55,56,407,408], and "atomization" of liquid samples for mass spectrometry analysis [409-411].

Some of the applications, such as the analysis of the crack nucleation and evaluation of fracture strength of brittle materials [53,125,140,401] are relying on nonlinear evolution of SAW profiles leading to the formation of shock fronts and associated increase in the peak stress values. The nonlinear transformation of laser-generated SAW pulses has been shown to facilitate the removal of sub-micron particles in surface cleaning [412], whereas the enrichment of the SAW spectra by high frequency harmonics due to the nonlinear acoustic effects has recently been shown to enable dynamic coupling and acoustic activation of molecular level processes, such as surface diffusion of small atomic clusters [73].

In general, the nonlinear sharpening of the SAW profiles and shock formation are proceeding through up-conversion of the initially excited frequency components, which has much in common with similar nonlinear effects observed for bulk waves. The nonlinear transformation of SAWs, however, has certain features that are unique and are not typical of bulk waves. In particular, due to the direct relation between the SAW wavelength and the characteristic depth of the strain field localization, the nonlinear frequency up-conversion results in increasing strain energy concentration near the surface. This, in turn, can produce a noticeable raise in the strain magnitude in the vicinity of the developing shock fronts [110,111,396,413-415], which is not observed in nonlinear propagation of bulk elastic waves. Therefore, the propagation of strong SAWs exhibits a number of physical features that cannot be elucidated based on straightforward analogies with well-developed theoretical descriptions of nonlinear propagation of bulk waves.

In view of the specific features of SAWs, a number of continuum-level theoretical and numerical approaches have been developed for treating the nonlinear effects in SAW propagation. In particular, the approaches based on multiple scale perturbation method [416-424], solution of the evolution equation with slowly varying wave profile method [425,426], and Hamiltonian formalism [110,111,396,413-415,427] applied either in the frequency domain using a system of equations for interacting harmonics [110] or in the form of an evolution equation for the SAW profile in time domain [111,415] have been developed to describe the variation of different harmonic constituents and the overall evolution of SAW profiles in isotropic [111,396,413,415-421,426,427] and anisotropic elastic solids [414,422-425].

The continuum-level numerical and theoretical investigations have significantly advanced the understanding of the nonlinear evolution of SAWs. It has been demonstrated, in particular, how the variation of different harmonic constituents leads to the distortion of the wave profile and formation of a shock front in the lateral (parallel to the surface) component of the velocity and, correspondingly, lateral strain. A number of peculiarities of the nonlinear sharpening of SAWs have been revealed, including a significant difference between the profiles for the lateral velocity (exhibiting shocks) and vertical velocity (that forms spikes rather than shocks) [110], as well as cusping of the wave profile near the shock front, with the peak values of the lateral velocity/strain exceeding those of the initial wave before shock formation [110,111,396,413-415]. The latter effect has been attributed to the increasing localization of the strain energy of the wave in the surface region as the wave profile sharpens and the energy is transferred from the fundamental to higher-harmonic components of the wave. The effective nonlinearity in this case becomes nonlocal even for a homogeneous material, *i.e.*, in contrast to bulk waves in a homogeneous media, the nonlinear distortion of a particular part of the SAW profile is defined by processes occurring in other parts of the wave [110,111].

Despite the demonstrated ability of the continuum models to provide important insights into the evolution of the wave profiles during the propagation in a nonlinear medium, the limitations of these models with respect to the analysis of the interaction of surface and bulk acoustic waves with any material heterogeneities (crystal defects, precipitates, surface roughness and adsorbates) are quite evident and difficult to overcome through straightforward extension of the existing theoretical approaches. In particular, the wave dissipation due to the thermal conduction and internal friction is often introduced in the equations on an *ad hoc* basis, to ensure numerical stability of the solution after the shock front formation [110,396,413-415]. The absorption of the acoustic energy in real materials, however, may be sensitive to the microstructure, leading to deviations from the typically assumed square dependence of the attenuation coefficients on the frequency of the wave harmonics [110,396,413-415,420] characteristic for viscous dissipation in fluids [428]. Moreover, while the quadratic in strain approximation of the stress-strain relation (*i.e.*, cubic in strain approximation of the elastic energy) is used in the continuum models to account for the nonlinear elastic properties of the material, the higher order nonlinearities may become important at large strains, close to the levels that cause damage or produce modification of material microstructure. Finally, the representation of the material modification itself, as well as the acoustic activation of various surface processes, such as diffusion [73,74,78] desorption [66,67,429,430], and heterogeneous catalysis [57,59,64,424], requires *a prior* knowledge of the acoustic coupling to different elements of material microstructure or surface species and is far beyond the current capabilities of continuum modeling.

Given the limitations of the continuum approaches discussed above, the classical atomistic molecular dynamics (MD) technique based on the numerical integration of the equations of motion for all atoms in the system [76,85,86] presents an attractive alternative for investigation of free nonlinear SAW propagation, dissipation and coupling to surface defects, heterogeneities, and adsorbates. The main strength of the MD method is that it does not require any assumptions about the processes taking place in the systems that are investigated. The only input into the model is the interatomic potential that defines all the thermodynamic, structural and mechanical properties of the material. This characteristic of the MD technique presents a significant advantage over the continuum-level methods where all relevant processes have to be known (and described mathematically) before the simulations can be performed.

The MD simulations of bulk shock waves have indeed been instrumental in providing valuable information on the shock front structure [116,431], shock-induced plasticity and phase transformations [117,432-434], and interaction of strong shock waves with voids and crystal defects [435-437]. Beyond the analysis of the steady-state properties of the shock front and fast dynamic material response to the strong shock loading, however, there has been little progress in extending the MD simulations to the investigation of the nonlinear sharpening and dissipation of the bulk stress waves during their long-term propagation and interaction with material microstructure. Similarly, while the dynamic fracture (spallation) caused by the reflection of a strong pressure pulse from a free surface of a sample has been investigated in a number of studies [115,438,439], more "gentle" interactions of the bulk acoustic waves with surfaces causing atomic-level structural rearrangements, diffusion enhancement, or desorption have not yet been systematically explored. The main factors that have been limiting the application of the atomistic modeling in this area are the severe limitations on the time- and length-scales accessible for MD simulations that typically do not exceed several nanoseconds and a hundred of nanometers. These limitations are further amplified in the case of SAWs, where a realistic simulation of free nonlinear propagation of a SAW requires the dynamic representation of a several-wavelength-deep surface region of the substrate, while the size of the computational system along the direction of the SAW propagation should increase with increasing distance covered by the wave.

In this section we alleviate some of the limitations of the MD technique through the design of computational methodology suitable for the exploration of the nonlinear effects in the propagation and dissipation of SAWs. The subsections below summarize the computational setup and discuss the conditions for the breakdown of the continuum description of weak (linear regime) SAWs and the effects related to the discrete atomic nature of the material structure; the nonlinear transformations of wave profiles, formation of shocks, localization of the acoustic energy near the surface, and rapid dissipation of high-frequency harmonics generated via nonlinear frequency up-conversion for strong (nonlinear regime) SAWs; and the ability of a strong SAW to produce quasi-periodic structural modification or “damage” in the surface region of the substrate along the path of its propagation. The results of this section provide an opportunity for atomistic modeling to explore new applications of SAWs for surface characterization, modification, and acoustic processing.

Computational model

Details of the computational setup are provided in Section 2.2.2, and below we only outline the key parameters. The size of the computational box is chosen to be equal to the wavelength along x, the direction of wave propagation, 5 fcc unit cells (7.8σ) along y, and 3 wavelengths along z. The wavelength in the simulations is varied in the range from 12 to 1200 unit cells, so the largest system simulated in this work has dimensions of $L_x \times L_y \times L_z = 1860\sigma \times 7.8\sigma \times 5580\sigma$ (1200 × 5 × 3600 fcc unit cells) and consists of 86.4 million atoms. Periodic boundary conditions are applied along x and y directions, rigid boundary is imposed at the bottom, and the top part of the system remains free. After thermalizing each system, SAWs are added to the system according to the analytical solution, as discussed in Section 2.2.2. The temperature of the system is set zero if another value is not specified in text. At nonzero temperature, the necessary values of the elastic moduli of the LJ material were calculated based on statistical fluctuation method [440].

Linear regime of SAW propagation: spatial dispersion

The developed implementation of MD model of SAW made it possible to rather clearly illustrate some properties of surface acoustic waves that are difficult to study analytically, for example, manifestations of spatial dispersion of high-frequency SAWs, for which the wavelength is only 1-2 orders greater that the lattice period of the material. Manifestation of such effects can readily be observed in test simulations of relatively small-amplitude SAWs, for which nonlinear distortions are not very strong.

It is well known that in a non-dispersive case, initially the amplitude of the second harmonic of a plane sinusoidal wave is proportional to the propagation distance. However, in the presence of dispersion that introduces phase mismatch between the interacting fundamental and higher harmonics, peculiar periodic beatings of the wave amplitudes should be observed. For example, for the fundamental and second harmonics, the spatial period L_{1-2}^{b} of the beats is determined by the difference of the wavevectors for the fundamental and second harmonics,

$$L_{1-2}^{b} = 2\pi/|2k_1 - k_2| \tag{5.2}$$

corresponding to the fact that, after each portion of the propagation path with the length $L_{1-2}^{b}/2$, the nonlinear double-frequency sources (propagating with the phase velocity of the fundamental harmonic $c_1 = \omega_1/k_1$) and the second harmonic with the phase velocity $c_2 = 2\omega_1/k_2$ acquire relative phase mismatch equal to π. Figure 96 shows examples of the distance-dependence for the second-harmonic amplitudes obtained from the MD simulations of free evolution of initial sinusoidal SAWs with different wavelengths. In these computations, the initial displacement amplitude is chosen approximately the same for different wavelengths, and sufficiently small to ensure that during the simulation time the shock front is not formed. The appearance of the latter results in drastic increase of the wave dissipation. The strong decrease in the beating period for shorter wavelengths visible in Figure 96 is related to more pronounced spatial dispersion induced by the discrete structure of the material.

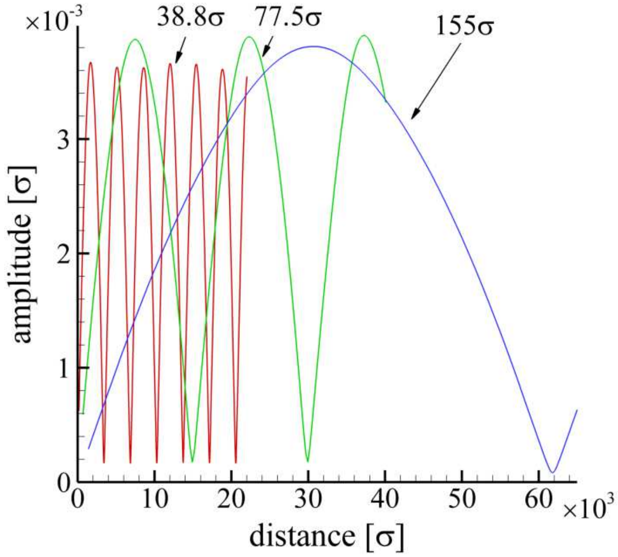

Figure 96. The evolution of the amplitudes of the second harmonic as functions of the propagation distance for the initially sinusoidal SAWs with approximately the same initial displacement amplitude $d_0 = 0.019\sigma$ of the fundamental harmonic having different wavelengths $\lambda = 155\sigma, 77.5\sigma$, and 38.8σ (the respective curves are marked in the plot). The spatial period of the beatings becomes pronouncedly smaller for smaller wavelength due to faster accumulation of the phase mismatch related to the spatial dispersion. The initial temperature of the system is equal to zero.

Table 11. The distance d_{beat} needed for the double-frequency wave with wavevector k_2 to accumulate the phase mismatch $|2k_1 - k_2|d_{beat} = 2\pi$ with the fundamental harmonic for different wavevectors k_1.

Wavelength [σ] (unit cells)		19.4 (12)	38.8 (25)	77.5 (50)	155 (100)
Distance [σ]	Surface waves	620	3440	15000	61800
	Longitudinal waves	3070	35200	301000	
	Shear waves	1030	9380	74300	

For generation of the second harmonic in structures with spatial dispersion related to the material discrete structure, known solutions are based on the approximation that the lowest dispersion correction to the dispersionless dependence $\omega = ck$ should be cubic in k, namely $\omega \approx ck - \alpha k^3$, where normally α is positive. Quadratic in k dispersional correction is absent, because quadratic and other even-order terms correspond to the influence of dissipation rather than dispersion. In particular, a cubic in k dispersion term naturally appears for smaller wavelengths in the case of periodic chains of masses interacting via elastic springs. By additionally taking into account the lowest (quadratic in amplitude) nonlinear term, the wave evolution in this system is described by the Korteveg-de Vries equation [441]. Its solution (see e.g. [442]) predicts that in the neglection of dissipation the maximum displacement amplitudes of second harmonics should be the same for fundamental harmonics with different k_1 and the same initial displacement amplitude. This prediction fairly well agrees with the results shown in Figure 96.

Next, in view of the usually cubic in k dispersional correction to $\omega(k)$ (which is equivalent to the cubic in $\omega \approx ck$ correction to the wave vector $k(\omega)$ for the initial deviation from the non-dispersive propagation), the spatial frequency $2\pi/L_{1-2}^{b} = |2k_1 - k_2|$ of the second-harmonic beatings should be cubic in k_1. This cubic dependence is indeed found for bulk longitudinal (compressive) and shear waves in the MD simulations of the beatings between the fundamental and double-frequency harmonics as shown in Table 11. In contrast, the results of SAWs presented in Figure 96 and summarized in Table 11 demonstrate strongly different behavior. For example, comparing the beating period for the fundamental-harmonic wavelength $\lambda = 155\sigma$ and twice smaller $\lambda = 77.5\sigma$, instead of the expected for the cubic dispersion difference $2^3 = 8$ times one can see the $2^2 = 4$ times (i.e. rather quadratic) difference of the beating periods. At first glance, this result looks counter-intuitive, because as mentioned above, the quadratic correction to the relationship between the frequency and wavenumber normally corresponds to dissipation terms rather than dispersion. However, such a distinction from the bulk waves can be attributed to the difference of SAW propagation from 1D propagation of a wave in a periodic chain. Indeed, the SAW field penetrates in the material to the depth on the order of λ. Thus for SAWs, the dispersion arises due to scattering not only from the atoms localized in the upper atomic layer, but from periodically spaced vertical "screens" with the effective vertical size determined by the depth of the SAW penetration along the vertical z-coordinate as shown schematically in Figure 97.

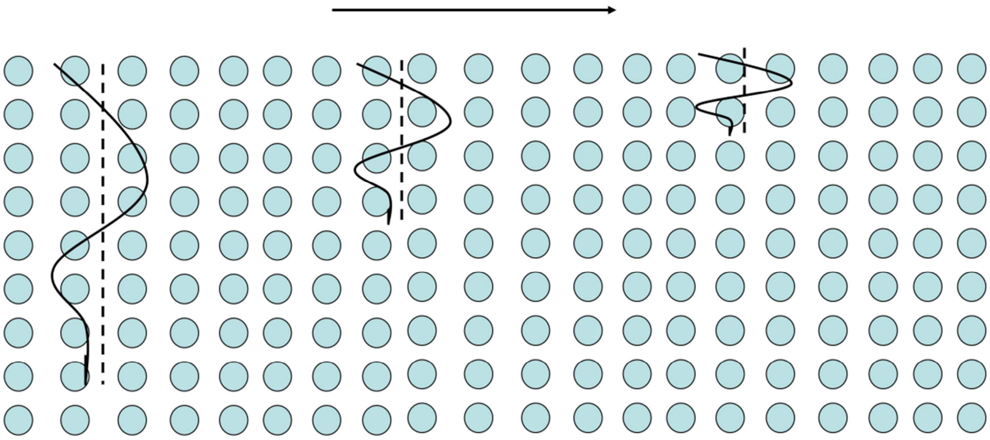

Figure 97. Schematic elucidation of the nature of the $\sim k^2$ correction to the dispersion law for SAW waves in contrast to $\sim k^3$ correction typical for bulk waves and 1D waves in chains of masses and springs. The effective "apertures" of the scattering periodic structure for SAWs with different wavelengths are shown by dashed lines. The vertical size of these effective apertures is proportional to k^{-1}.

Although the scattering "screens" along the *x*-direction are spaced like for one-dimensional propagation, the effective number of scattering elements (atoms) in each screen is proportional to k^{-1}, considering the k^{-1} dependence of in-depth SAW penetration. Thus, the conventional $\sim k^3$ effect of scattering by periodically spaced "screens" should be multiplied by a factor of k^{-1} reflecting the decrease in the effective number of scattering atoms with increasing k. Consequently, for SAWs, the resultant dispersion law becomes quadratic, $\sim k^{-1}k^3 = k^2$ unless the SAW wavelength becomes extremely small (only a few times larger than the interatomic distance. This expectation perfectly agrees with the obtained computational results. For very large k (when λ decreases down to several atomic cell-sizes), the role of the very upper atomic layers becomes strongly dominant (closer to 1D case), so that effective vertical aperture of the "screens" does not continue to decrease as k^{-1}. Consequently, for such extremely short SAWs, the initial $\sim k^2$ dependence of the dispersion correction gradually becomes steeper, with a law intermediate between the initial quadratic behavior $\sim k^2$ and the cubic $\sim k^3$ limit corresponding to 1D chains or bulk waves in 3D atomic lattices. This difference in the linear dispersion is a bright example demonstrating significant difference between bulk waves and SAWs, for which strong frequency-dependent localization near the surface is intrinsic. In the next section we will discuss some other localization-dependent features that manifest themselves in rather specific features of nonlinear distortions of SAW shapes.

Nonlinear localization of SAW energy and coupling with thermal phonons

The developed computational setup readily makes it possible to simulate nonlinear propagation of SAWs, including ultimately strong SAW amplitudes, for which material damage already becomes noticeable. As mentioned above, one of the most distinct features of nonlinear propagation of SAWs is related to the fact of strong frequency dependence of the elastic-energy localization. Consequently, with gradual generation of higher harmonics during the propagation of initially sinusoidal wave, the phenomenon of pronounced localization of the wave energy closer to the surface is observed in the MD simulation. This effect is illustrated in Figure 98, where the initial sinusoidal wave has the wavelength of 930σ and the strain amplitude of 2%. The image shows the change of the kinetic energy distribution along in-depth direction over time (averaged over the wave period), from which the gradual localization of the SAW energy closer to the surface with increasing propagation distance is clearly seen. For clarity, the MD simulation corresponding to Figure 98 is performed for a cold sample (with zero temperature) to exclude procedures of filtering the thermal noise and averaging the collective motion of the atoms in order to single out the wave-induced contribution against the background of thermal oscillations of the atoms. At room temperatures, even for rather strong SAWs with characteristic strains on the order 10^{-3}-10^{-2} and wavelength 930σ, velocities of the regular atom motion in the acoustic wave are significantly masked by the background thermal fluctuations. Consequently, only time and space averaging, which is naturally performed by macroscopic acoustic probes in real physical experiments, makes it possible to easily capture acoustic waves with frequencies much smaller than that of thermal phonons even if the acoustic strains are orders of magnitude smaller.

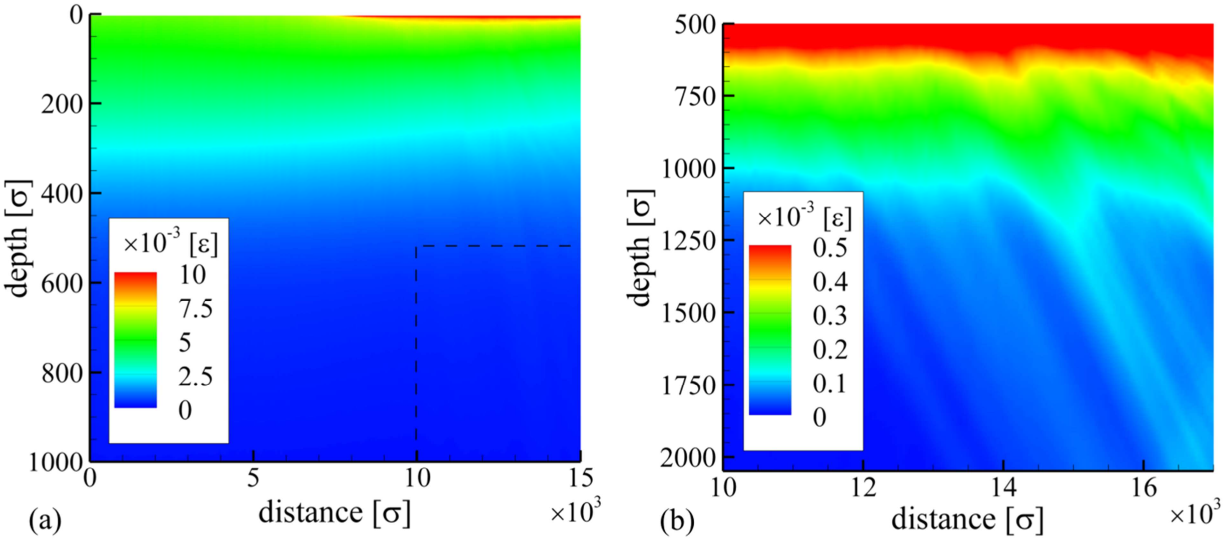

Figure 98. The evolution of kinetic energy distribution along in-depth direction demonstrating gradual localization of the elastic-wave energy during nonlinear SAW propagation. Coloring corresponds to the kinetic energy per atom averaged over the atoms in the one-wavelength long thin layer. In this example, the fundamental wave length is 930σ, and the evolution in panel (a) is shown up to a propagation distance of 15000σ, where the shock front is formed and intense dissipation of the SAW energy occurs due to effective coupling of the high-frequency harmonics and thermal phonons. Panel (b) zooms in the spatial-temporal region marked by the dashed rectangle in the panel (a). At this distance, the shock from is already well developed and intense dissipation of the SAW energy occurs due to effective coupling of the high-frequency harmonics and thermal phonon modes. Propagation of the thermal phonons carrying the energy into material bulk is clearly seen in the right-hand part of panel (b)

The simulations described here are performed for SAWs of significantly shorter wavelengths (19.4σ – 1860σ) than that typical of usual experimental conditions. For such short waves, manifestations of the atomic-scale discreetness of the material can be especially easily visible. The nonlinearly generated harmonics become comparable with the Debye frequency after merely several stages of nonlinear transformation of the SAW components. In other words, the newly generated harmonics become close to the range of thermal phonons, so that transformation into even higher-order acoustic phonons becomes impossible because their propagation in the atomistically discrete material is forbidden (or maybe corresponds to the optical phonon branch).

Figure 98 corresponding to the evolution of such a fairly short wave shows that the nonlinear transformation evolves like in a continuum case at the initial stage: the wave spectrum is enriched by higher harmonics and the characteristic depth of the energy localization gradually decreases. However, after a propagation a distance of about $8 \times 10^3 - 10^4\sigma$, the energy-localization depth practically reaches saturation. Further nonlinear transformation results in the generation of extremely high-frequency components that correspond to thermal phonons of various types. Those thermal phonons carry the energy into the material bulk, so that the coherent components of the elastic wave begin to efficiently dissipate their energy. The appearance of pronounced energy transport by bulk phonons is clearly visible in Figure 98b and is shown in more detail in Figure 99 for the propagation distance larger than $10^4\sigma$. Wave packets with very high frequencies corresponding to wavelengths ranged from 2 atomic-cell sizes to 5-7 cell sizes are clearly seen in Figure 99. Taking into account that the minimum wavelength of the propagating acoustic phonons is 2 atomic-cell size, the shortest visible packets (phonons) evidently correspond to the smallest wavelength of elastic perturbations with the maximal Debye frequency. As expected, comparison between the snapshots similar to those shown in Figure 100 demonstrates that the group velocities of such high-frequency wave packets are much smaller than that of the SAW. These interesting details of the wave energy dissipation in the form of clouds of phonons gradually expanding in the material bulk from the shock front cannot be described by alternative approaches (either analytical or numerical ones based on continuous-medium approximation), but are readily observed in MD simulations of the described type.

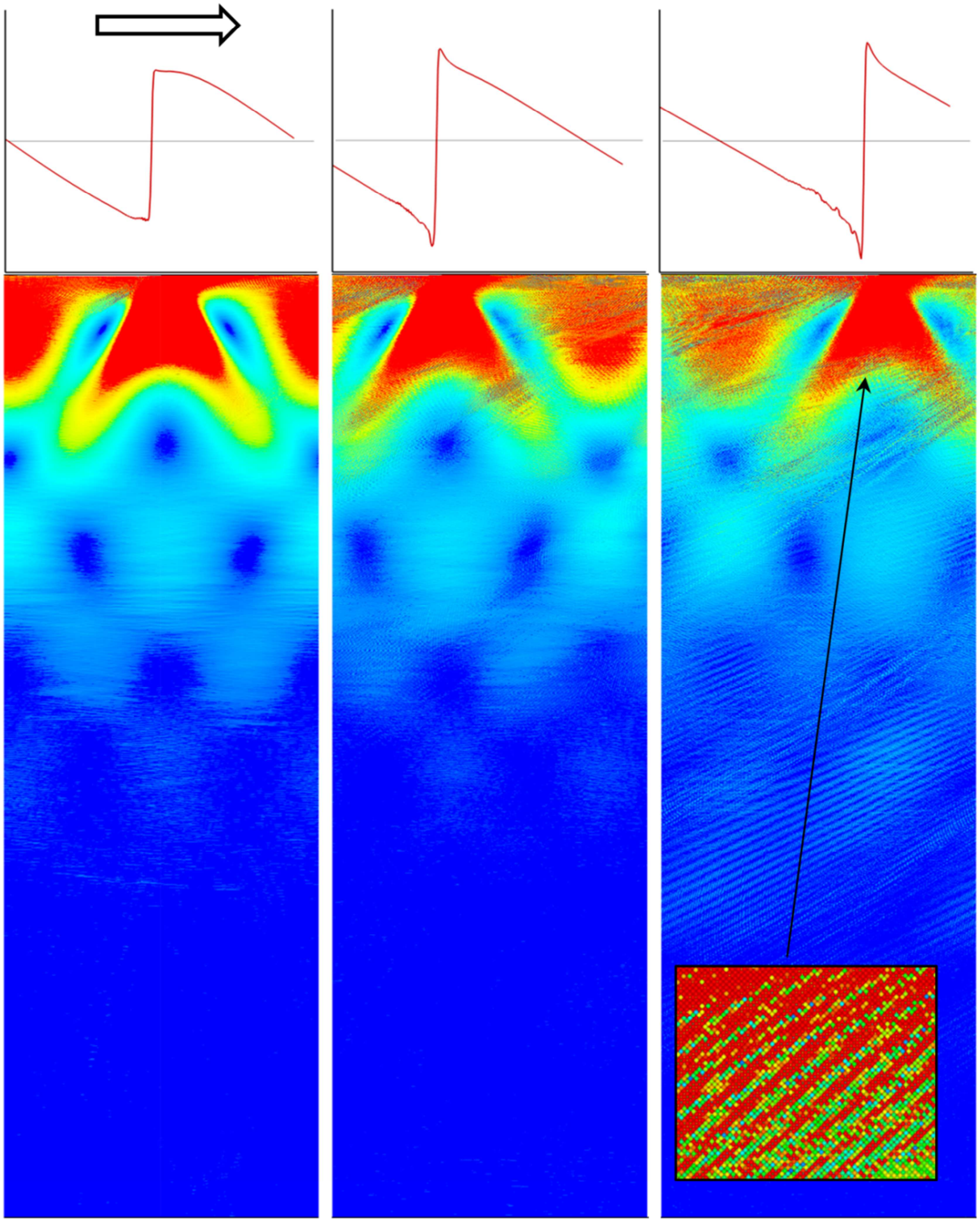

Figure 99. The sequence of snapshots demonstrating instantaneous distribution of the kinetic energy in the substrate at the stage of well-developed shock corresponding to the propagation distances 9×10^3, 11×10^3 and 13×10^3 in Figure 98. Wave packets corresponding to thermal phonons with the wavelengths of 2-4 atomic cells are clearly visible (zoomed on the right plot). Gradual propagation of the dissipated energy in the form of cloud of phonons descending into the material bulk can be readily seen in the sequence of these snapshots.

It should be emphasized that shock front formation is also observed [125,443] in real experiments with intense SAWs characterized by much larger initial wavelengths. In the vicinity of such well-developed shocks the values of strain and characteristic spatial scales of its variation become comparable with those in the above presented MD results, so that the dissipation of coherent wave energy into thermal phonons should also have a rather similar character.

Nonlinear transformation of the SAW profile and shock-front formation

In this section we consider the main features of SAW-profile evolution during the nonlinear transformation. Figure 100 shows several instantaneous SAW profiles for the lateral strains e_{xx} (positive for tensile and negative for compression) obtained in MD simulations of a right-running SAW with a fundamental wavelength of 930σ, for which the velocity dispersion related to the material atomic structure is yet fairly weak. For the material with LJ-type interaction, tension leads to softening (i.e. decrease in the elastic modulus). Correspondingly, the compressional phase of the wave propagates faster that the tensile phase, which results in formation of the shock front at the ascending branch of the initially sinusoidal wave profile as illustrated in Figure 100.

The above-mentioned features are also well-known for nonlinear transformation of bulk waves. However, nonlinear transformation of SAWs demonstrates some peculiarities which are related to the above-mentioned fact of gradual concentration of elastic energy closer to the surface. Especially pronounced are manifestations of this SAW feature for larger strains resulting in more efficient generation of higher harmonics. Strong localization of energy of these harmonics near the surface leads to formation of peculiar asymmetrical (between minimums and maximums) sharpening of the wave with pronounced enhancement of strains near the developed sharp cusps in the SAW profile (this feature is known as nonlocal nonlinearity of Rayleigh waves [110-112]).

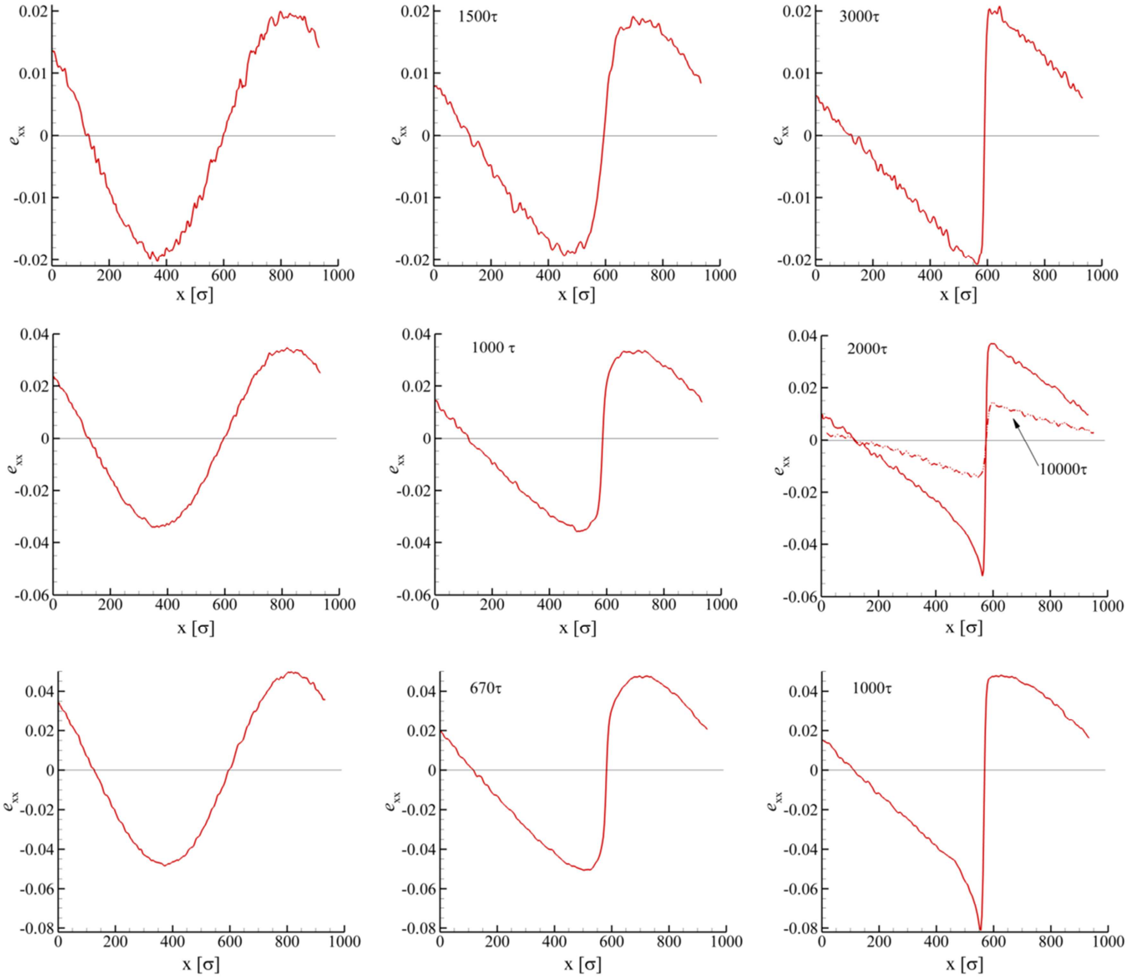

Figure 100. Examples of nonlinear distortion of SAW profile for the lateral strain e_{xx} for a SAW propagating to the right. Rows (a), (b), and (c) are for the initial strain amplitudes 2, 3.4, and 4.7%. The first column corresponds to the initial sinusoidal wave; the next one represents formation of shock front. The last column demonstrates later stage of the wave profile evolution. The temperature of the sample in reduced units is 0.15ε. For these examples, the fundamental wavelength is 930σ and the propagation distance is up to 50 wavelengths (the wave propagation velocity at the temperature 0.15ε is approximately 4.87σ/τ). Gradual steeping of the SAW profile leads to formation of shocks exhibiting peculiar cusps. Pronounced asymmetrical increase in the strain magnitude for larger propagation distances (large evolution time) is also well visible for rows (b) and (c). The shock is formed at the SAW-profile branch with positive slope, which agrees with the expectation for the "soft" nonlinearity intrinsic to LJ potential.

In the bulk non-dispersive waves (e.g., classical nonlinear Riemann wave) the points of the wave profile are merely displaced horizontally with different velocities, so that the amplitude of the developed shock is not higher than in the initial sinusoidal wave and only the gradient of stress (or pressure) becomes much higher compared with the initial values. In contrast to this, strong redistribution of the elastic-wave energy over the depth due to stronger sub-surface localization of nonlinearly-generated higher harmonics in addition to the wave-form sharpening leads to pronounced increase in the elastic strain itself in the vicinity of the shock front (over 1.5 times as shown in the right column in Figure 100). This is a very distinctive feature of nonlinearly propagating SAWs. Even if the initial strain in a SAW is lower than the material-damage threshold, after some distance, the gradually increasing near-shock strains may reach the damage threshold and lead to either plastic deformation or fracture of the material depending on its brittleness. We discuss such effects in more detail later in this section.

In addition to the above-mentioned absolute increase of local strains near the shock front, another important feature of the shocks formed by sufficiently large-amplitude SAWs is their pronounced asymmetry with respect to tension/compression. Indeed, in contrast to linearly propagating SAWs, for which in the first approximation the material reaction to tensile and compressing phases of the SAW is symmetrical (resulting in a symmetric shape for small-amplitude sinusoidal waves), for stronger strains, the asymmetric nonlinearity of the interaction potential may become pronounced. In the example shown in Figure 100a, the strain is fairly weak for pronounced manifestation of this asymmetry. Consequently, even if the shock is already formed, the difference between the tensile and compressive deformations still is insignificant, and the upper and bottom parts of the shock profile remain fairly symmetrical. However, for larger strains as in rows (b) and (c), the shock front becomes noticeably asymmetrical due to the well-known asymmetry of the atom interaction with respect to compression and tension phases of the SAW.

It is essential to point out that the shock-front asymmetry shown in rows (b) and (c) in Figure 100 corresponds to the "soft" nonlinearity of the LJ material, in which tensile strains cause material softening. It can be thus expected that if the stress-strain relationship for a material has the quadratic nonlinear correction of the opposite sign ("rigid-type" nonlinearity), then the sharp cusp should appear not at the bottom part of the shock front as in Figure 100, but at the upper part. Besides, in contrast to Figure 100, the shock front itself should form not at the ascending branch of the wave period, but at the descending branch. To verify this, we have performed an MD simulation on a system with the parabolic potential (include only first nearest neighbors), where the physical nonlinearity (due to the form of the potential itself) is absent in contrast to LJ potential, but the residual material nonlinearity of geometrical origin has the opposite sign (i.e. the tensile strain leads to the material stiffening) from the LJ system, see Section 2.1.2. The simulation result in terms of the surface strain profile after shock formation is shown in Figure 101. In this case indeed formation of the sharp cusp occurs in the upper part of the shock front and the shock front itself has the opposite orientation and is located at the descending branch.

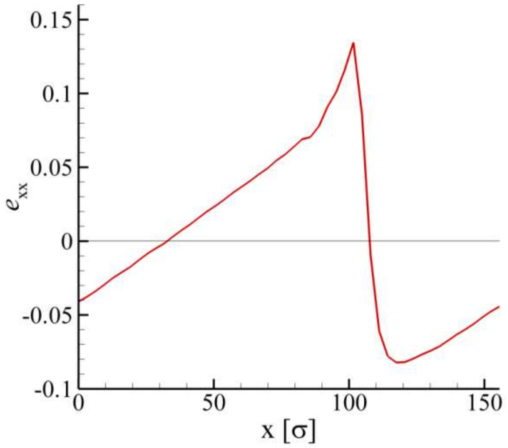

Figure 101. The SAW profile for the lateral strain e_{xx} after shock formation in the material with parabolic interaction potential exhibiting "rigid-type" nonlinearity. This result is obtained at zero initial temperature for the SAW with wavelength 155σ and the initial strain 8.5%. Pronounced asymmetrical increase in the strain magnitude for larger distances is well visible, but in contrast to the "soft" nonlinearity of the LJ potential the stronger cusp is formed at the upper part of the shock, and the shock itself appears at the descending branch in the SAW profile.

In agreement with the analytical results reported in Refs. [110,414], our MD simulations also well reproduce the difference in the behavior of the profiles for the horizontal velocity V_x of the particles (for which shock front formation is observed) and the profile of the vertical-velocity V_z (for which a narrow spike develops instead of shock front). Figure 102 shows in more detail the corresponding examples for the profiles of the horizontal velocity and the vertical velocity for two SAWs of different initial strains (compare with Figure 1 and Figure 3 from paper [415]). It should be noted, however, that in paper [415] the velocity is recorded as a function of time at a particular position, whereas Figure 102 shows the profile as a function of position at a fixed moment, so that for correct comparison, the wave profile should be flipped in the horizontal direction. Taking into account the proportionality $V_x \sim e_{xx}$, the examples shown in Figure 102 once again illustrate the fact mentioned in the discussion of Figure 100. Namely, for smaller strains, quite well visible shock can be formed with fair symmetry with respect to compression/tension (upper panel in Figure 102a). However, for more than twice greater initial strain amplitude, the front shape becomes pronouncedly asymmetrical and maximum absolute strain developed at the shock can over 1.5 times exceed the initial value [upper panel in Figure 102b]. Another interesting point is that in paper [415], Figures 1 and 3 demonstrate the opposite sign of the vertical-velocity cusp, the position of which either in compression or tension phases is determined by the sign of the effective nonlinearity parameter. This sign can be changed in the analytical description like [415] based on the material properties or can be set by using an appropriate interaction potential as we used for the solutions shown in Figures Figure 100 and Figure 101.

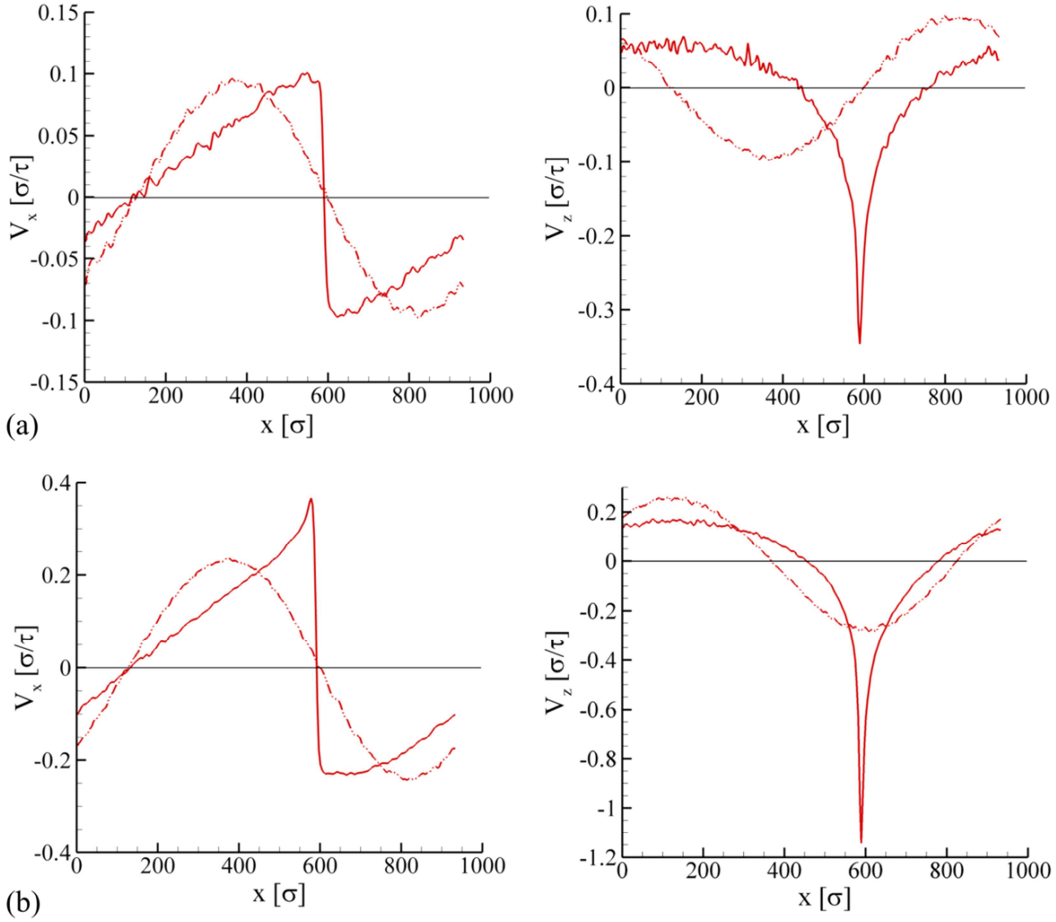

Figure 102. Examples illustrating the difference in the profiles for the horizontal velocity (exhibiting shock fronts like for the lateral strain $V_x \sim e_{xx}$) and vertical velocity (exhibiting spikes) for the initial lateral-strain amplitude 2% (a) and panel is for 4.7% (b). The temperature of the sample is 0.15ε and the fundamental wavelength is 930σ.

The performed simulations also made it possible to investigate the dependences of the distance of shock front formation on the initial wave amplitude and the wavelength. In fact, for initially sinusoidal profile, this dependence for SAWs is theoretically predicted to be functionally the same as for compressional bulk waves [112,444,445]:

$$x_{sh} \sim 1/\beta e_0 k \tag{5.3}$$,

i.e., the shock front formation distance x_{sh} is inversely proportional to the initial strain amplitude e_0, effective nonlinearity parameter β, and wave vector k.

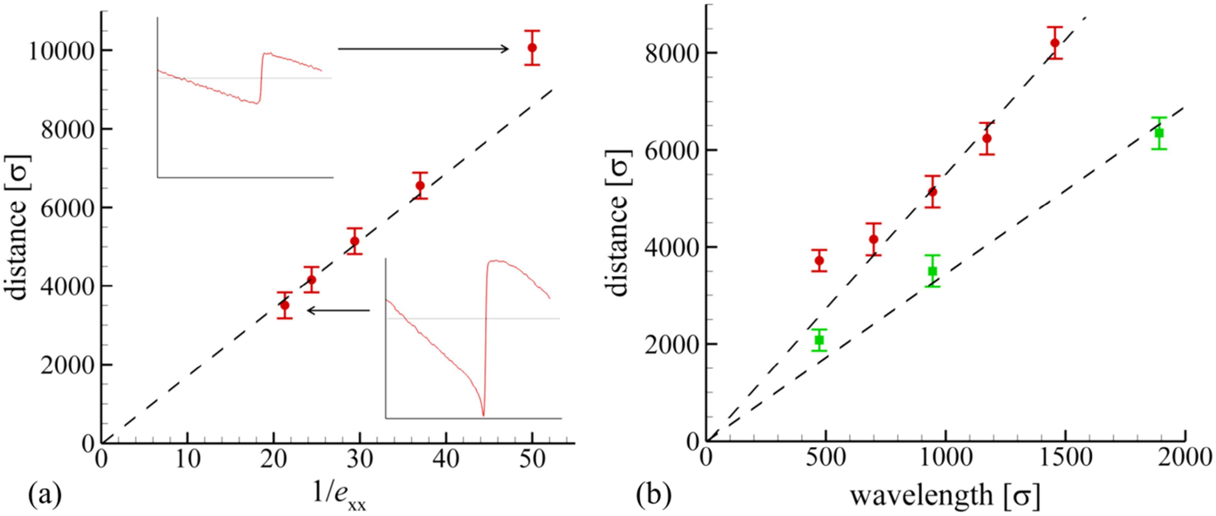

Figure 103. Dependencies of the shock-formation distance on the initial strain (a) and wavelength (b) calculated for the LJ material with temperature 0.15ε. The strain-dependence on the plot (a) corresponds to the wavelength 930σ and the dependences on the wavelengths are found for the initial strain amplitudes e_{xx} = 3.4% (steeper line) and e_{xx} = 4.7%.

Figure 103 shows the shock front formation distance x_{sh} as functions of the inverse strain e_0^{-1} and the wavelength $\lambda = 2\pi k^{-1}$, obtained from MD simulations performed on a system at temperature 0.15ε. The estimated value of the nonlinearity parameter β by fitting these results to Eq. 5.3 is about unity. The typical value of the effective nonlinearity parameter β in the case of compressional bulk waves for many crystals and amorphous materials is several times greater, in the range 4-8 [446]. The observed smaller effective value of β is attributed to the SAW-intrinsic feature of frequency dependent localization: strain is localized within the depth of around one wavelength for each harmonic component of SAW. Therefore, the fields of different-order harmonics are significantly separated in depth, which results in a weaker coupling between the harmonics than in the case of the bulk waves, which consequently reduces the effective nonlinearity parameter for SAWs.

The error bars in Figure 103 show the uncertainty of the measured distances x_{sh}, because by analogy with real experimental measurements the calculated wave shapes were distorted by the thermal noise and the slope of the shock front was not an ideal vertical line with 90^0 slope due to the influence of wave dissipation, so that the slope of the developed fronts varied in the range 86^0 – 88^0. Theoretical expectation given by Eq. 5.3 corresponds to straight lines coming from the coordinate origin. The corresponding linear fits are shown in Figure 103 by dashed lines which fairly well reproduce the computational results. The deviation of the most-right point for small strain in Figure 103a toward larger x_{sh} is physically meaningful, because for smaller strain, the influence of linear losses that counteract shock-front front formation becomes more pronounced. We can expect that for even smaller strains, the shock front does not form at all, and the wave decays due to linear dissipation. Similarly the deviation of the most left points for shorter wavelengths in Figure 103b is also meaningful and related to both stronger dissipation and dispersion for SAWs with smaller wavelengths. It has been verified that for very short waves ($\lambda = 39\sigma$), the dispersion influence is so strong that the shock cannot be formed at all and the nonlinear evolution of the SAW results in formation of a train of soliton-like pulses.

Strongly nonlinear regime: formation of shock fronts with strains exceeding the damage threshold

In the previous sections the simulated examples correspond to the manifestations of relatively weak or moderate nonlinearity, for which retaining only the lowest quadratic corrections to the stress-strain relationship can be fairly sufficient. However, as mentioned above, one of the most attractive advantages of MD simulations is the possibility to naturally incorporate ultimately strong nonlinearity, including SAW-produced damage of the material. The corresponding experimental observations of such acoustically-induced surface cracks, in particular in such a practically important material as Si, are well known for intense laser-generated SAWs [125,443].

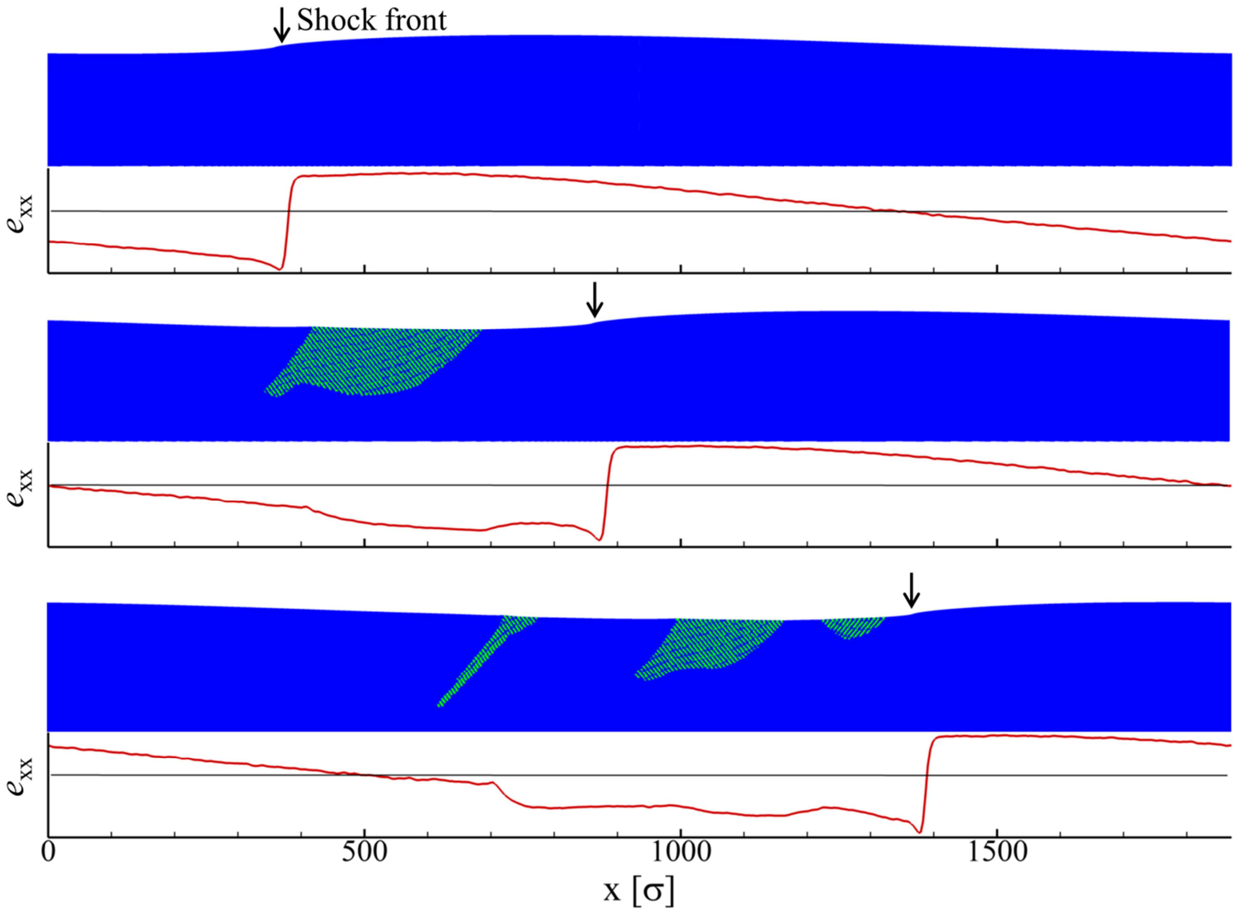

Figure 104. Illustration of the simulated SAW sharpening accompanied by material damage (in the form of localized zone of plastics deformation. The first plot corresponds to the distance 7700σ passed by the wave; for each next plot the wave passes extra 510σ. The initial strain is 4.7 %, the temperature of the sample is 0.15ε, and the fundamental wavelength is 1900σ. The darker (blue online) color corresponds to intact fcc packing of the substrate atoms, and lighter dashed zones correspond to regions affected by plastic deformations (green color depicts stacking faults). The snapshots depict only top ~ 200σ of the atomistic system and corresponding profiles of the SAW strain are shown below. The position of the shock front is outline by black arrows.

The MD simulations of LJ system do not directly allow to imitate brittle materials with developing cracks, but the material damage in the form of plastically-deformed zones can be readily simulated. In Figure 104 the corresponding examples are shown for the development of localized zones of plastic deformation induced by sufficiently intense SAWs in which the nonlinear wave transformation results in formation of shock fronts with cusps as in Figure 102b. Although the initial strain magnitude is smaller than the damage threshold for the material, the strain significantly exceeds the initial value near the formed cusps, reaching the threshold of partial dislocation emission and producing damage in the form of well-localized plastic deformation. The damage process partially adsorbs the SAW energy and reduces its strain (Figure 105), so that afterwards the wave propagates for a while in elastic regime. However, continuing wave sharpening results in formation of a new intense cusp at the shock front, which again produces material damage. This repeated damaging is clearly seen in Figure 104. This process could be repeated several times resulting in formation of a series of damaged zones having striking resemblance with the experimental observations of quasi-periodic arrays of SAW-induced cracks presented in Ref. [125].

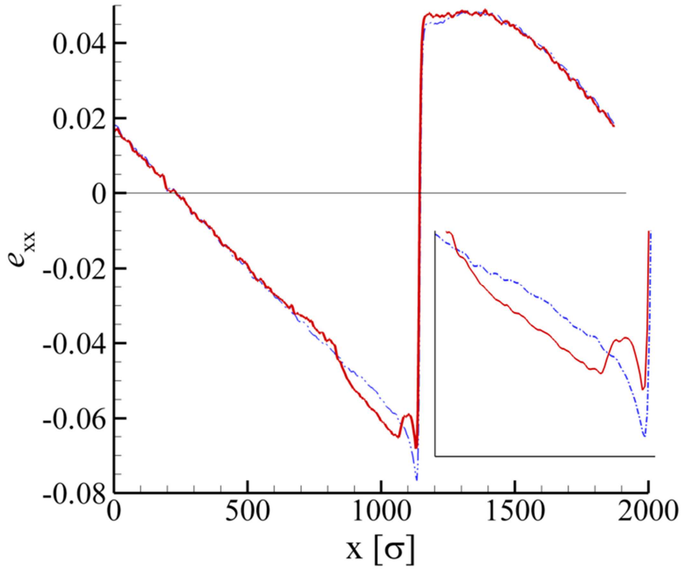

Figure 105. The reduction of the wave amplitude due to plastic deformation of the substrate. This plot is presented for the same conditions as Figure 104. The blue dashed line corresponds to the moment of time just before plastic deformation appearance. The red line corresponds to the damaged material. This plot is presented in the reference system moving with the wave.

When the shock front leaves the plastically deformed region, the generated partial dislocations can start retreating back as shown in Figure 104. Small system size in *y* direction limits accuracy of dislocation evolution description, in the current setup only one partial dislocation is emitted and replicated by the periodical boundary condition. However, in a laterally larger system emission of numerous partial dislocations can be expected, and during following propagation they can form dislocation locks, for example Lomer-Cottrell locks, which will prevent complete retreatment of the deformed material. Although, the results presented here are obtained for LJ potential, the very similar methodology of SAW creation and simulation of its evolution can be implemented with other types of interaction potential. In particular, Tersoff and Stillinger-Weber potentials [447,448] can be used for simulation of brittle materials with insignificant increase of computational costs.

Summary

The above presented results demonstrate that modern computational possibilities open interesting prospects for molecular-dynamics simulations of quite macroscopic wave-transformation phenomena that are traditionally studied using finite-element numerical methods and analytical approaches (combined with numerical analysis of rather nontrivial systems of equations even for weakly nonlinear waves). Such methods have their own advantages, although for realization of certain very important features (e.g. the possibility of unified description of weakly nonlinear transformations and ultimate manifestations of the material nonlinearity in the form of material damage) these conventional approaches are either not suitable or have to be artificially modified to comprise the corresponding phenomena. In contrast, in MD simulations, all orders of nonlinearity are naturally incorporated in the computational setup together with the dissipation, which is also very important for the adequate description of SAW propagation.

The above presented data demonstrate wide possibilities of the MD-approach for modeling linear and nonlinear phenomena accompanying propagation of SAWs. Even in the linear approximation the described MD simulations made it possible to reveal at the first glance surprising (in comparison with 1D and bulk waves) features of spatial dispersion of SAWs. To explain the numerically revealed differences, a natural physical interpretation was proposed based on specific for SAWs character of wave-energy localization. This difference in the linear dispersion properties has much in common with the peculiar features of nonlinear transformation of SAW. This transformation is also strongly affected by the differences in the wave-energy localization for SAWs with different frequencies, which result~~s~~ in appearance of nonlocal nonlinearity in equations describing nonlinear transformation of SAWs [110-112]. Overall, those features, for which analytical predictions are known, demonstrate good agreement with the obtained MD data, which confirms the validity of the computational model.

Although, because of rather significant limitations on the size of modeled systems in MD computations, some the results have been obtained for SAWs with very high-frequencies that does not look realistic for conventional experimental techniques, recent experimental works demonstrate possibilities to generate SAWs with frequencies up to several hundred GHz [449-451] which seemed unattainable in quite recent past. Furthermore, from the practical point of view it is important to emphasize the following. Nonlinear transformations of even initially relatively low-frequency SAWs (compared with the presently acceptable frequencies in MD simulations), during the shock-front formation naturally generate a cascade of extremely high-frequency harmonics up to the frequencies typical of thermal phonons. Just these very high-frequency harmonics exhibit very efficient coupling with thermal phonons resulting in drastic increase of SAW-energy dissipation after formation of the shock front. This intense generation of thermal phonons at the shock front is directly visualized in the results of the performed MD simulations as demonstrated in Figure 99. Processes of the same type occur in the vicinity of shock fronts formed by intense laser-generated pulses such as in experiments [125,443]. Although, for clarity of interpretations in the present study we used initially sinusoidal waves and periodic boundary conditions in the direction of wave propagation, the application of the moving window variant of MD simulations [117] should readily allow for description of propagation of pulse-type shock waves. This should make it possible to apply the MD-technique for description of near-shock region even for perturbations readily attainable by modern experimental techniques with initial frequencies that are too low for MD simulations from the initial stage.

Concerning practical implications of such studies, it can be pointed out that application of intense SAWs may open interesting prospects for enhancement of surface-adatom diffusion in situations, for which straightforward increase in temperature is undesirable or even impossible [78]. Besides, possibilities of SAW application for spatial structuring of diffusing adatoms also recently attracted attention [77,452]. Analysis and simulations performed in work [73,78] and Section 5.3 demonstrate that not only straightforward increase in SAW strain is favorable, but also exploitation of SAWs with ultimately high frequencies can be even more important for diffusion enhancement, because the high-frequency wave components can ensure direct dynamic (quasi-resonant) coupling with the surface species. As is clear from the results of presented above and other supporting data, the nonlinear transformation of SAWs suggests a natural way to simultaneously drastically shift the SAW spectrum towards very high frequencies (which is typical of shock formation) and at the same time significantly increase the maximum strain (which is a specific feature of SAWs and is not typical of bulk waves). Such dynamic coupling can be easier obtained for massive and/or relatively weakly bonded surface species like heavy atoms (as demonstrate simulations in Ref. [73,78] and Section 5.3) and seems to be especially promising for atomic clusters. The above described MD technique is applied in the next section to detailed studies of such acoustically-stimulated diffusion processes.

5.3. Enhancement of surface diffusion by nonlinear surface acoustic waves[5]

Abstract: The phenomenon of acoustic activation of surface diffusion is investigated in computational studies. The ability of laser-generated surface acoustic waves (SAWs) to enhance the mobility of small atomic clusters is demonstrated by large-scale molecular dynamics simulations and confirmed by our collaborator in an experimental study. The analysis of the computational results demonstrates that the nonlinear sharpening of SAWs and the corresponding enrichment of the SAW spectra by high frequency harmonics, which are capable of dynamic coupling to the cluster vibrations, are responsible for the efficient acoustic activation of surface mobility in the simulations. It suggests a novel mechanism for acoustic activation of surface processes on atomic and molecular level.

The increase in the effective diffusion coefficient is proportional to the number of the SAW pulses passing through the diffusion region per unit time, and a dramatic 4500-fold diffusion enhancement (corresponds to an equivalent temperature increase by $\sim 10^3$ K) is predicted in the simulations for 15 GHz SAWs. Rescaling the computational prediction to the experimental conditions suggests 22-fold enhancement that is in a good agreement with 19-fold increase in the effective diffusion coefficient measured by our collaborator in room temperature experiments in the presence of SAWs generated by nanosecond pulse laser irradiation at a 100 Hz repetition rate. The ability of SAWs to affect atomic-level surface processes has far-reaching implications for the design of new techniques where the acoustic energy serves as an effective substitution for thermal activation in applications where heating must be avoided or rapid switching of surface conditions is required.

Introduction

Surface acoustic waves (SAWs) are actively used in many practical applications, including signal processing [50], chemical sensing [51,52], nondestructive evaluation of mechanical properties [53,54], and microscale manipulation of fluid flow in microfluidics devices [55,56]. Moreover, there is growing experimental evidence of the ability of SAWs to affect surface processes at the atomic/molecular level. In particular, SAWs and bulk acoustic waves interacting with surfaces have been shown to be able to substantially enhance the rates

---

[5] Results of this work are reported in Ref. [73], the experimental portion of the work is performed by a group of H. Helvajian.

and selectivity of heterogeneous catalytic reactions [57-65], desorb molecules, atoms, and ions from surfaces [65-72], and facilitate surface diffusion of small atomic clusters [73,74]. These observations are surprising as there is a large mismatch between the relatively low frequencies of the acoustic waves, typically less than 100 MHz, and the vibrational frequencies characteristic of atoms and molecules on the surface, on the order of terahertz. This frequency mismatch calls into question the contribution of the dynamic resonant coupling of the acoustic wave to surface vibrational states [69,70,453,454] and gives rise to hypotheses based on the presumed presence of mesoscopic-scale substructures/domains [59,60] that can effectively couple to a long-wavelength acoustic excitation, nanoscale stressed surface features that can release the stored strain energy in response to an acoustic activation, thus providing the needed extra energy for the desorption of molecules [71], or acoustically induced variation of the spatial distribution of adsorbates to affect the surface reaction rates [63].

Modification of the binding energies and diffusion barriers of adsorbed species induced by the surface strain [455-458] has also been considered as a mechanism responsible for the acoustic activation of surface processes [64,78,306]. Indeed, a recent theoretical and computational analysis performed for linear (sinusoidal) elastic SAWs [78] suggests that a combined effect of the transient modification of the diffusion barriers and adiabatic temperature variation due to the periodic oscillations of the acoustic strain can lead to a noticeable enhancement of surface diffusion for large strain magnitudes and systems that exhibit strong strain dependence of the diffusion barriers [455-461]. The large surface strains ($\sim 10^{-2}$) required for reaching practically relevant levels of the diffusion enhancement and the strong quadratic scaling of the diffusion enhancement with the strain amplitude in the absence of nonlinear enrichment of SAW spectrum by higher harmonics [78], however, make the assumption of the linear SAW propagation questionable and suggest that nonlinear effects should be considered.

In this section, we report the results of a combined computational and experimental study targeted at resolving the longstanding question on the mechanism of the acoustic activation of surface processes. A simple model system consisting of small atomic clusters moving on a substrate exposed to SAWs is considered. The experimental results, obtained by our experimental collaborators from the group of Dr. Helvajian [73], provide direct evidence of strong acoustic enhancement of surface mobility of atomic clusters. The simulations also predict a dramatic diffusion enhancement by SAWs and link it to the nonlinear wave profile sharpening accompanied by the generation of high frequency harmonics that effectively couple to the vibrational modes of the clusters. The mechanistic insights into the key role of the nonlinear effects in the SAW-induced activation of surface processes provide guidelines for the design and optimization of a new class of applications in the areas of chemical catalysis, low temperature thin film growth, and mass spectrometry of heat sensitive molecules.

Computational model

In order to reveal the atomic-level mechanisms responsible for the pronounced acoustic enhancement of the surface mobility, we perform a series of large-scale molecular dynamics (MD) simulations of surface diffusion of small atomic clusters in the presence of SAWs. In contrast to earlier MD simulations of SAWs [77,78], where the close-to-sinusoidal wave profiles are generated and maintained through dynamic boundary conditions, the simulations of free nonlinear wave propagation require much larger computational systems and a careful choice of the initial and boundary conditions. These technical difficulties have prevented the application of atomistic simulations for the investigation of nonlinear SAWs so far. At the same time, the ability of MD simulations with anharmonic interatomic potentials to naturally reproduce the nonlinear sharpening of SAWs, their dissipation and interaction with surface adsorbates presents a clear advantage over continuum modeling, as the latter involves a number of assumptions and approximations [53,54,110], as discussed in Section 5.2.

Given the uncertainties as to the exact structure of the cluster, its interaction with the substrate, the effect of the exposure to ambient atmosphere and presence of surface defects, as well as the length- and timescale limitations inherent to the MD simulations, we do not attempt to quantitatively mimic the experimental conditions in the simulations. Rather, we choose the parameters of the model so that the key physical features of the experimental system are reproduced. Namely, (1) on the short timescale of the MD simulations, the clusters remain motionless at the surface in the absence of SAWs, (2) the acoustic activation of cluster mobility does not lead to cluster decomposition or any significant changes in the shape of the clusters, and (3) there is no surface modification or any structural damage to the substrate under conditions of the simulations.

The system used for the MD simulations consists of a substrate with face centered cubic (fcc) structure and several clusters composed of 10 atoms each placed on the (001) surface of the substrate, as schematically shown in Figure 106a. The minimum distance between the clusters is chosen so that they do not have any chance to meet each other during their diffusional motion on the surface in any of the simulations. The computational system has dimensions of $Lx \times Ly \times Lz = 600 \times 5 \times 1800$ fcc unit cells and consists of 21.6M atoms. The periodic boundary conditions are applied along x and y directions that are parallel to the free surface of the substrate, and a rigid boundary condition is applied at the bottom of the substrate.

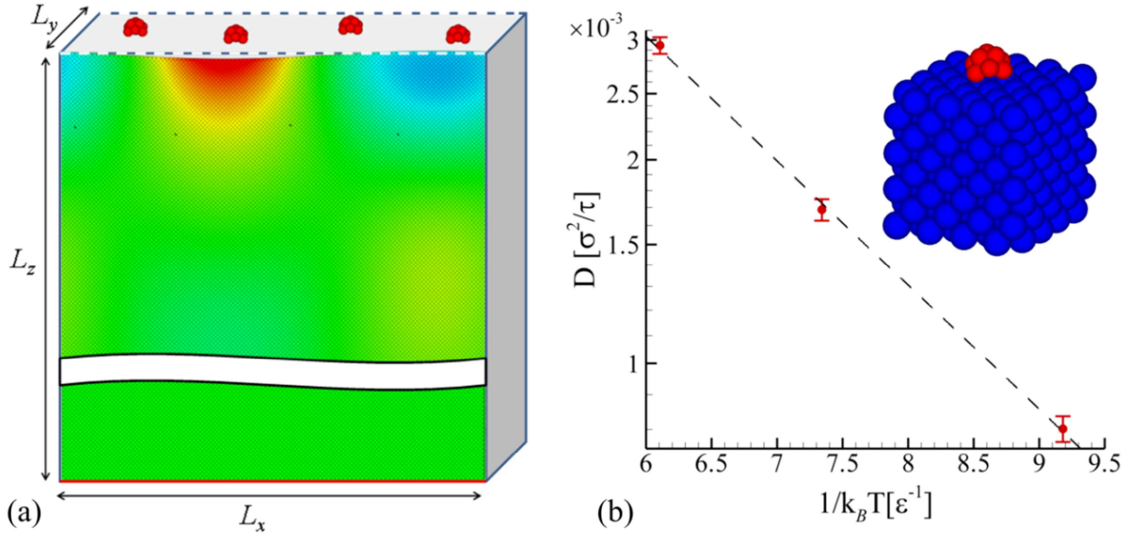

Figure 106. A schematic representation of the MD computational system used in the simulations of free propagation of SAWs (a) and the Arrhenius plot of the diffusion coefficient for thermally-activated surface diffusion of a small atomic cluster in the absence of SAWs (b). In (a), the SAW propagates along x direction and the color shows an instantaneous pressure distribution for an initial sinusoidal SAW. In (b), the error bars correspond to the estimated standard error of the mean and the fitting of the data to the Arrhenius equation yields the diffusion barrier of 0.421ε. The inset in (b) shows a fragment of the computational system with an atomic cluster (colored red) located on the surface of the substrate (colored blue). Adapted from Ref. [73].

The interatomic interactions in the computational system are described by the Lennard-Jones (LJ) potential with parameters σ and ε defining the length and energy scales of the substrate. A cutoff function [121] is used to ensure that the interactions vanish at a cutoff distance of 3σ. The LJ parameters for the interactions between the atoms in the clusters are $\sigma_{cc} = 0.60\sigma$ and $\varepsilon_{cc} = 3.72\varepsilon$, whereas the parameters for cluster-substrate cross-interactions are $\sigma_{cs} = \sigma$ and $\varepsilon_{cs} = 0.5\varepsilon$. The mass of an atom in a cluster is $m_c = 1.74m$, where m is the mass of an atom in the substrate. All the physical quantities obtained in the simulations are expressed in reduced units scaled by the LJ length and energy parameters, σ and ε, and atomic mass m used for the substrate.

The SAWs are generated on thermally equilibrated substrates by assigning instantaneous displacements and additional velocities to all atoms in the systems according to the analytical expressions for the continuous periodic unidirectional Rayleigh wave propagating along [100] direction on (001) surface in a cubic crystal [79]. The velocities due to the wave are added to the thermal velocities of the atoms. Following the initialization, the waves are allowed to evolve freely in dynamic simulations. The SAW propagates along the *x* direction, and the choice of *Lx* thus defines the spatial periodicity of the simulated nonlinear SAW. Additional details on system preparation are provided in Section 2.1.2.

The strain magnitude of the initial sinusoidal SAWs is chosen to be 0.02, which is more than 30% below the threshold for the onset of damage (plastic deformation) to the substrate. At the same time, the initial wave magnitude is sufficiently large to enable computationally efficient exploration of the effect of the acoustic activation of surface diffusion within the relatively short timescale accessible to MD simulations. In particular, the time (or distance traveled by the wave) needed for the nonlinear sharpening of the wave scales inversely with the initial strain magnitude [112], and the relatively high strength of the wave makes it possible to explore the effect of the shock front formation of the diffusion enhancement in the atomistic simulations.

The thermally and acoustically activated surface mobility of the clusters is characterized by the diffusion coefficient *D* calculated from the time dependence of the MSD of the cluster center of mass:

$$4Dt = \frac{1}{N_i N_j} \sum_1^{N_i} \sum_1^{N_j} \left[\vec{r_i}(t + t_j) - \vec{r_i}(t_j)\right]^2 \qquad (5.4),$$

where $\vec{r_i}(t_j)$ is the true “unfolded” (unaffected by the periodic boundary conditions) position of the center of mass of cluster *i* at time t_j, N_j is the number of data points collected for a particular trajectory, and N_i is the number of independent cluster trajectories obtained in the simulations. To collect statistically reliable information on the diffusion in the presence of SAWs, 10 simulations yielding a total of N_i = 835 independent trajectories of atomic clusters are performed. The duration of each simulation is 6720τ, where $\tau = (m\sigma^2/\varepsilon)^{1/2}$. Since the wave shape changes during the nonlinear propagation and dissipation, the total simulation time is divided into sixteen 420τ -long intervals, and the values of D are evaluated for each time interval.

The diffusion barrier for thermally activated diffusion, without SAWs, is calculated to be equal to 0.421ε by performing three series of simulations at different temperatures and fitting the corresponding values of D to the Arrhenius equation, Figure 106b. An extrapolation of the Arrhenius dependence to a lower temperature of $0.036\varepsilon/k_B$, at which all simulations with SAWs are performed, yields $D = 3.5 \times 10^{-7}\ \sigma^2/\tau$ that corresponds to about one jump per 10^6 τ. This estimation confirms that, within the simulation time of 6720τ, the probability of thermally activated jumps is virtually zero.

The spectrum of the SAW is analyzed by applying spatial fast Fourier transform (FFT) with the Hanning window function to the instantaneous displacements of the surface in the x direction caused by the SAW. The instantaneous displacements of the substrate atoms with respect to their positions in an ideal crystal are averaged over surface subdomains with sizes of one unit cell in x direction and 4 unit cells in z direction. The pattern of the subdomain displacements obtained for one wave period is replicated to produce 2^{14} data points for the FFT. To further suppress thermal noise, the final spectrum is additionally averaged over 10 independent MD simulations, and an exponentially weighed moving average filter with an effective window size of 200τ is applied in the time domain.

Atomistic simulations of the effect of nonlinear SAWs on surface diffusion

Acoustic activation of surface diffusion is confirmed by our collaborator in an experimental study [73,74]. Figure 107a presents the MSD of the tracked Au_8 clusters on a (111) silicon substrate plotted as a function of time for three independent experiments in which the clusters are monitored at 12 mm from the SAW source, 6 mm from the source, and with no SAW excitation. The slopes of the lines representing the best linear fits to the data points can be related to the diffusion coefficient, $D = MSD/4\Delta t$, where MSD is mean square displacement evaluated for the time interval Δt. In the absence of SAWs, the thermally mediated diffusion is characterized by $D = 8.56\times10^{-17}$ cm^2/s, whereas the effective diffusion coefficients in the presence of acoustic activation are $D = 1.64\times10^{-15}$ cm^2/s at 6 mm from the source and $D = 1.46\times10^{-15}$ cm^2/s at 12 mm from the source.

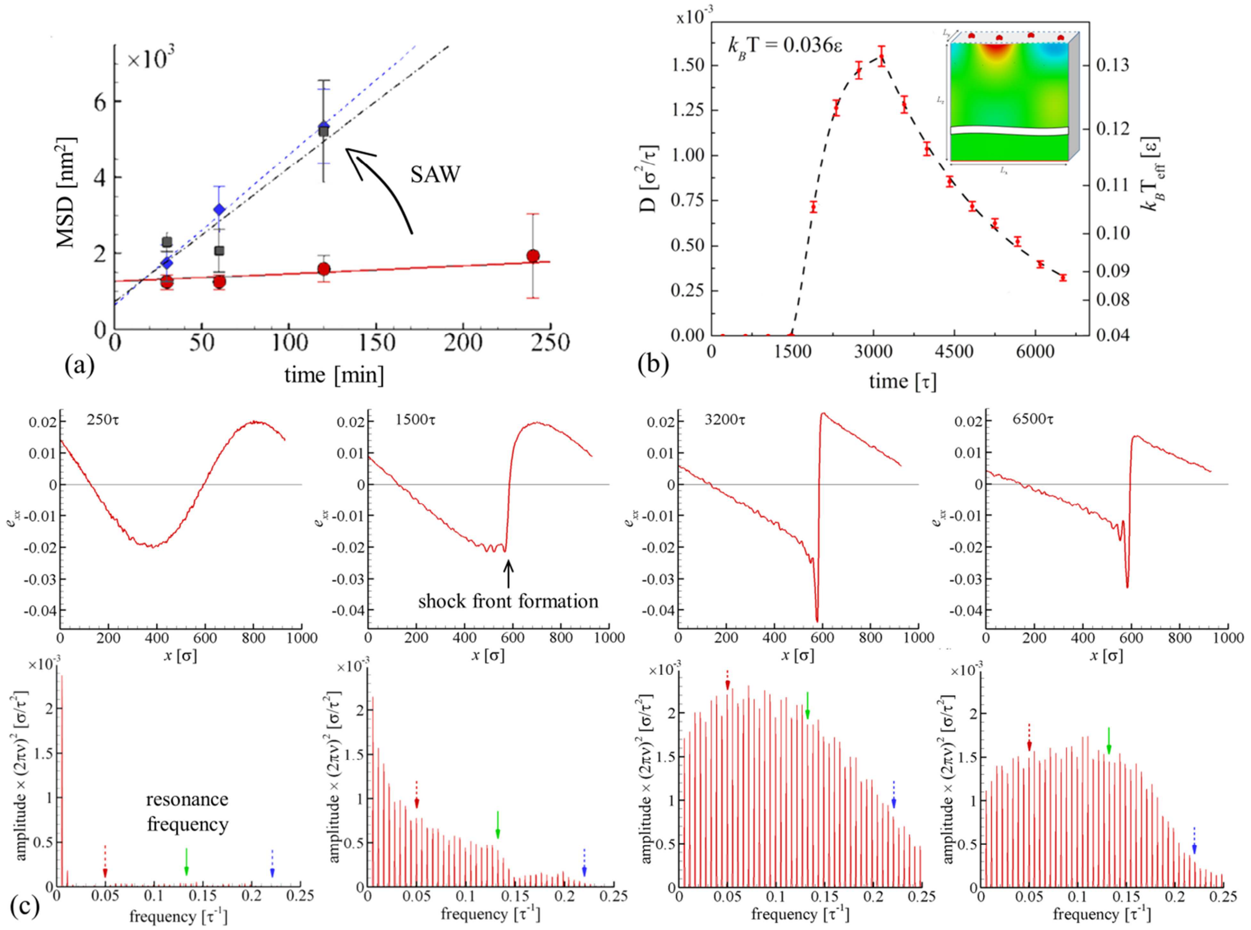

Figure 107. Acoustic activation of surface diffusion of small atomic clusters by SAWs confirmed experimentally (a) and predicted in a series of large-scale MD simulations (b). The explanation of the mechanism of acoustic activation of surface diffusion based on the formation of a shock front and generation of high frequency harmonics capable of direct energy transfer to the clusters adsorbed on the surface (c). The plot in (a) shows the evolution of the cluster diffusion coefficient with time of SAW propagation. The insert depicts a schematic representation of the computational system. The plot in (b) shows the evolution of mean square displacement (MSD) of individual Au_8 clusters moving on a (111) silicon substrate with and without SAWs. In (c), the temporal evolution of the SAW profile and corresponding harmonics in the wave spectrum predicted in the simulations are shown. Lennard-Jones reduced units are used in (b) and (c). The figure is adapted from Ref. [73].

Two startling conclusions arise from the experimental measurement of the diffusion coefficients. First, laser excitation of SAWs leads to a pronounced 19-fold increase in the diffusion coefficient with respect to the thermal diffusion. Second, the measured diffusion coefficient at 12 mm is nearly that as measured at 6 mm from the source, which would argue a small attenuation coefficient of the relevant SAWs. Unlike for continuous thermal activation, for SAWs the diffusion is only affected during the passage of the waves through the probe area. Given a 100 Hz laser repetition rate and a pulse duration of 6 ns, over the course of the 30–780 min exposures used in the experiment, the acoustic source is active for mere milliseconds. This observation, combined with the relatively low frequencies of initially excited SAWs, less than 166 MHz, makes it impossible to explain the strong enhancement of surface mobility with existing physical models that only consider the effect of linear SAWs [78]. The experimental data, therefore, motivate the computational effort reported below, where nonlinear acoustic effects are fully accounted for.

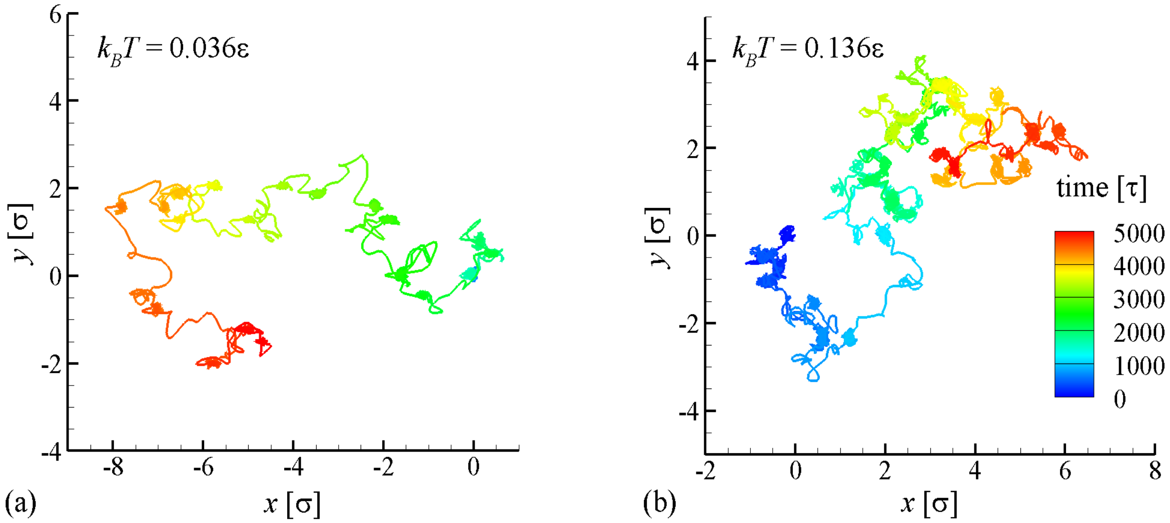

Figure 108. The representative trajectories of the cluster center of mass recorded in simulations of SAW-induced diffusion at a temperature of 0.036ε/k_B (a) and thermal diffusion at a temperature of 0.136ε/k_B (b). The scale is the same in both plots, the initial location of the clusters is at the origin of the coordinate system, and the trajectories are colored by time. The local displacement of the surface due to the SAW is subtracted from the instantaneous position of the cluster in (a). The temperature of 0.036ε is too low to induce any thermally activated diffusion of the cluster on the timescale of the simulation. Note that in (a) no jumps of the cluster take place before ~1500τ, which is the approximate time of the shock front formation. The SAW-induced cluster mobility after 2000τ is similar to that in the thermally activated diffusion at $k_BT = 0.136\varepsilon$. Adapted from Ref. [73].

The mechanisms of acoustic activation of surface diffusion are investigated in a series of MD simulations of SAWs propagating on a substrate equilibrated at a temperature of 0.036ε/k_B. In Figure 108a, a representative trajectory is shown for a cluster located on a substrate exposed to SAW. The cluster exhibits an active motion despite the negligible contribution of thermal diffusion expected at the temperature of 0.036ε/k_B. Actually, the diffusion length in the acoustically activated diffusion is comparable to that of thermal diffusion but at almost four times higher temperature, 0.136ε/k_B, Figure 108b. A notable difference between the two trajectories, however, is that the acoustically activated motion of the cluster in Figure 108a starts not from the beginning of the simulation, but at a time of around 2000τ. Note that since periodic boundary conditions are applied along the direction of SAW propagation, the increasing time in the simulations corresponds to the linearly increasing distance from the source of the wave in the experiments.

The changes in the cluster mobility in the course of the nonlinear SAW propagation are revealed in Figure 107b, where the effective diffusion coefficients calculated for the 16 time intervals during the simulations are plotted. The distinct stages of the time dependence of the diffusion coefficient can be correlated with the evolution of the SAW profile illustrated in Figure 107c (top row). During the first 1500τ , the diffusion coefficient remains below the level that can be resolved in the MD simulations while the wave profile gradually evolves from the initial sinusoidal shape generated at the beginning of the simulations, Figure 107c, to a shape with an increasingly steep front. Starting from around 1500τ, the diffusion coefficient rapidly goes up and reaches its peak value at around 3200τ (Figure 107b). The maximum value of the diffusion coefficient is about $1.6\times10^{-3}\ \sigma^2/\tau$ that signifies more than 4500-fold increase with respect to the thermal diffusion at the substrate temperature of $0.036\varepsilon/k_B$. The temperature required to induce an equivalent diffusion by thermal activation is $0.132\varepsilon/k_B$, which is about 3.7 times higher than the actual substrate temperature maintained in the simulation. The plots of the wave profiles shown in Figure 107c demonstrate that the onset of the cluster motion coincides with sharpening of the SAW and generation of a shock front. The pronounced cusp formed on the compressive side of the wave profile at 3200τ is related to the nonlocal nonlinearity of SAWs [110-112]. The increase of the strain magnitude above the initial level in the course of the shock front formation is a distinct feature of SAWs that is not observed for bulk waves, whereas the appearance of small oscillations near the shock front is typical for a medium with dispersion (see discussion in Section 5.2).

During the next stage of the SAW profile evolution, after 3200τ, the wave amplitude and the shock front sharpness are decreasing due to the strong dissipation near the wave front, Figure 107c. The dissipation results in the exponential decrease of the cluster mobility, Figure 107b. However, despite the substantial attenuation of the wave by the time of 6500τ, the diffusion coefficient at this time still remains almost 1000 times higher than the one for thermally activated diffusion. By extrapolating the exponential decay of *D* beyond the time of the simulation, it can be estimated that the cluster mobility becomes comparable to the one characteristic of thermal diffusion only at around 20 000τ.

To explain the connection between the SAW shock front formation and the sharp rise in the surface mobility, a detailed analysis of the cluster vibrations and the evolution of SAW spectrum are undertaken. The spectrum of thermal vibrations of the cluster on the surface reveals two main resonance peaks at about 0.13 and $0.24\tau^{-1}$ for horizontal (parallel to the surface) vibrations and higher frequencies for oscillations in the vertical direction. Therefore, harmonics with a minimum frequency of about $0.13\tau^{-1}$ must be generated for the direct resonant excitation of cluster vibrations.

The generation of high frequency harmonics in the process of SAW front sharpening can be tracked in the frequency domain by applying Fourier transform to the instantaneous displacements of the surface in *x* direction caused by the SAW. The four representative spectra shown in Figure 107c demonstrate that the nonlinear propagation of a SAW with an initial frequency of $0.0055\tau^{-1}$ can result in dramatic changes in the spectral composition of the wave. The spectra are shown in units of the maximum acceleration for each frequency harmonic to reflect the corresponding forces acting on the adsorbed cluster. The generation of high frequency harmonics due to the wave front sharpening causes excitation forces acting at high frequencies, including the cluster resonance frequency marked by green arrow. These forces are rather strong, i.e., comparable to the force acting at the fundamental frequency of the initial wave. When the shock front is fully developed, the harmonics with frequencies as high as $0.5\tau^{-1}$ (corresponds to 1.4 THz with the scaling discussed below) can be generated.

The three curves in Figure 109 show the evolution of the amplitudes of three harmonics marked by arrows in both Figure 107c and the inset in Figure 109. The green solid line is for the harmonic that corresponds to the resonance frequency of the cluster, $0.132\tau^{-1}$, whereas the red and blue dashed lines are for the harmonics with lower and higher frequencies, 0.05 and $0.22\tau^{-1}$, respectively. It is remarkable that the amplitude of the resonance harmonic starts to rise at around 1500τ, which is exactly the time when the cluster diffusion coefficient exhibits the sharp increase in Figure 107b. The amplitude of the resonant harmonic reaches its maximum value at around 3000-3200τ, when the cluster mobility is at its maximum. The following decrease of the amplitude correlates with the decrease of the cluster mobility after 3200τ. This direct correlation between the evolution of the high frequency components of the wave spectrum and the diffusion enhancement strongly suggests that the latter can be attributed to the dynamic coupling of high frequency harmonics with the cluster vibrational modes. The dynamic coupling has also been identified as a mechanism responsible for strong, 1-2 orders of magnitude, enhancement of surface mobility of an individual adatom by linear (sinusoidal) SAWs at frequencies that are 3-4 times away from the direct resonance with the adatom vibrations [35]. This observation suggests that the phenomenon of the diffusion enhancement due to the generation of high frequency harmonics in nonlinear propagation of SAWs is not specific to the diffusion of atomic clusters but is likely to be relevant to a variety of surface processes. In particular, results of computations studies reported in Section 5.4 have demonstrated the formation of high frequency harmonics of bulk waves to be responsible for acoustically activated desorption of surface species. It is important to clarify that in the proposed mechanism the capability to activate surface processes by a nonlinear wave is dictated by the sharpness of the wave front rather than compressive/tensile components of the wave.

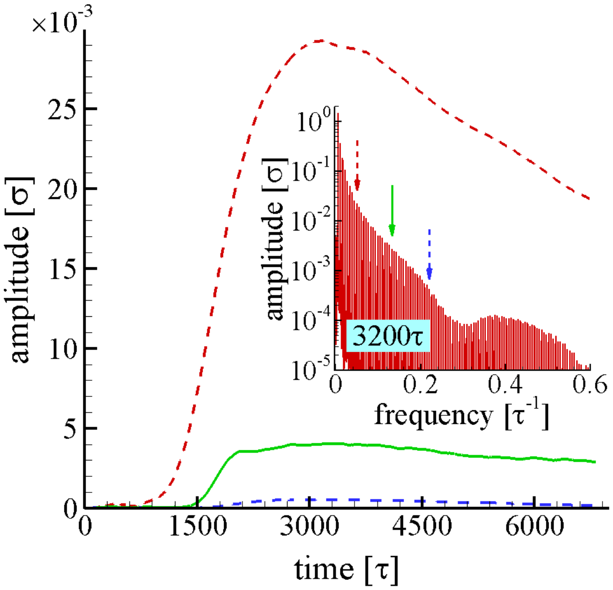

Figure 109. The evolution of the amplitudes of three high frequency harmonics during the nonlinear SAW propagation. The inset in shows a representative frequency spectrum of a SAW for a time of 3200τ. The dashed red, solid green, and dashed blue curves correspond to harmonics with frequencies of $0.05\tau^{-1}$, $0.132\tau^{-1}$, and $0.22\tau^{-1}$, respectively. These frequencies are also marked by arrows in Figure 107c and in the insert. The simulations are performed at a temperature of $0.036\varepsilon/k_B$, and the contribution of the thermal atomic vibrations to the spectrum shown in the inset is below $10^{-5}\sigma$ for all harmonics. Adapted from Ref. [73].

Mapping computational predictions to experiment

The connection between the computational results and experimental observations can be established by converting the computational predictions from reduced to real physical units, using the LJ parameters of σ = 3.50 A, ε = 0.534 eV, and m = 56.2 Da. These parameters are fitted to the density of Si, 2.33 g/cm^3 [462], and the velocity of a Raleigh wave on {001} Si surface along ⟨100⟩ direction, 4920 m/s [463], assuming that each atom in the fcc LJ crystal with a lattice parameter of 5.43 A represents two Si atoms. The time parameter and the SAW velocity are then $\tau = (m\sigma^2/\varepsilon)^{1/2} \approx 0.366$ ps and $\upsilon = 5.14\ \sigma/\tau \approx 4920$m/s, respectively. With these parameters, the SAW generated in the simulations have the initial wavelength $\lambda = 600 \times 5.43$ A = 326 nm and frequency $\nu = \upsilon/\lambda = 15$ GHz. During the time of a simulation, the SAW covers a distance of $6720\tau \times \upsilon = 12$ μm, and the estimated maximum range of the acoustic activation of surface diffusion is $20\,000\tau\times\upsilon = 36$ μm.

For the strongly nonlinear evolution of elastic waves, when the energy dissipation mostly occurs after the formation of a shock front, the characteristic time and, correspondingly, length scale of the decay of a wave increase linearly with the increasing wave period (or corresponding wavelength) [464]. Applying this reasoning for mapping the SAW dissipation observed in the simulations to the experimental conditions, the range of the acoustically affected diffusion can be expected to be on the order of 10 mm for the experimental values of $\nu \approx$ 10-100MHz [395] and $\lambda \approx$ 50-500 μm. Moreover, the inverse scaling of the shock formation distance with the initial acoustic strain [112] may further increase this range for the experimental conditions, where the strain amplitudes are likely to be much smaller than 1-2% recorded for SAWs generated in Si substrates with an assistance of ablative layers [53,54,443]. Indeed, similar scaling arguments suggest that the initial strain of the order of or even smaller than 10^{-3} would be sufficient to produce the SAW front sharpening and shock front formation at the experimental length scale of several millimeters and, consequently, to yield the diffusion enhancement through the mechanism predicted in the simulations. The higher strain magnitude of the simulated waves is mainly needed to ensure that the wave front sharpening takes place at a much shorter time/length scales accessible to the atomistic simulations.

The computational prediction that the physical origin of the diffusion enhancement is the interaction of the diffusing species with the steep front of the nonlinear SAW can be used to relate the striking (more than 4500-fold) increase of the cluster diffusion coefficient in the simulations to a more moderate 19-fold increase observed in experiments. The number of wave fronts passing through the diffusion region per unit time is defined by the frequency of the continuous wave generated in the simulations, 15 GHz, and by the laser repetition rate, 100 Hz, in the experiments. The increase predicted in the simulations is from $D_{\mathrm{th}} = 3.5\times10^{-7}\ \sigma^2/\tau$ for thermal diffusion without SAWs to $D_{\max} = 1.6\times10^{-3}\ \sigma^2/\tau$ at the maximum enhancement (Figure 107b). Using the scaling to Si substrate discussed above, this increase is from $D_{\text{th}} = 1.2\times10^{-9}$ cm^2/s to $D_{\max} = 5.4\times10^{-6}$ cm^2/s. Since $D_{\text{th}} \ll D_{\max}$, it is reasonable to assume that the thermal contribution to $D_{\max}$ is negligible and the acoustic activation is solely responsible for the high cluster mobility observed in the simulations. Scaling the value of $D_{\max}$ to the experimental repetition rate yields $D_{\max}\times100$ Hz/15 GHz = 3.6×10^{-14} cm^2/s or 22 times larger than the maximum value of the acoustically enhanced diffusion coefficient evaluated from the experimental data for 6 mm from the source, 1.64×10^{-15} cm^2/s. Given the approximate semiquantitative nature of the model and the lack of precise information on the strength of the SAWs generated in the experiments, the comparable orders of magnitude of the diffusion enhancements provide an additional support for the hypothesis that the same physical mechanism of the diffusion enhancement revealed in the simulations is also responsible for the experimental observations shown in Figure 107a. Moreover, the linear scaling of the acoustically activated diffusion enhancement with the number of the SAW fronts passing the region of interest per unit time suggests that the existing sources of SAWs with frequencies on the order of tens of gigahertz [449-451] may create an equivalent of 10^3 K for surface diffusion under room temperature conditions. It is also apparent from the experimental results that an area on the order of 1 cm can be affected, thus increasing the practical use of the energy source.

Summary

A combined computational and experimental study of surface diffusion of small atomic clusters has revealed an enhancement of surface mobility under the action of SAWs. The direct tracking of individual gold clusters on a Si substrate by fluorescence microscopy demonstrates that the clusters can be moved by laser-generated SAWs under conditions when thermally activated diffusion is negligible. A plausible explanation of these observations is suggested based on the results of large-scale MD simulations performed for a model system that mimics the key physical characteristics of the experimental material system. The analysis of the evolution of the SAW frequency spectrum reveals a direct connection between the diffusion enhancement and the generation of high frequency harmonics associated with the nonlinear wave sharpening and shock front formation. The high harmonics reach frequencies typical of natural cluster vibrations and lead to an effective dynamic coupling between the acoustic wave and the cluster vibrational modes. Extrapolation of the experimentally observed 19-fold diffusion enhancement from the

100 Hz pulse repetition rate to higher rates (e.g., by circularly moving the laser spot around the observation region to avoid accumulation of heat) suggests that the SAW-induced athermal increase of the diffusion coefficient by a factor of 10^2-10^3 is feasible even for the experimental conditions used, although they were not specially optimized. Given the computational prediction of the key role that the nonlinear sharpening of the wave profile plays in the activation of surface diffusion, the direction of the SAW may also be optimized to ensure the strongest nonlinear effects in the wave propagation on anisotropic substrates [465].

Other surface processes, such as desorption and chemical bond rearrangements, may exhibit a similar sensitivity to the generation of high frequency harmonics in the nonlinear propagation of SAWs. The phenomenon of the acoustic activation of surface processes, therefore, can be utilized in a range of practical applications where the thermal activation should be avoided. In particular, the acoustic energy may serve as an effective substitution for heat in thin film growth on heat-sensitive substrates, cold desorption of fragile molecules for mass spectrometry analysis, or rapid switching of surface catalytic activity.

5.4. Mechanism of acoustically activated desorption

Abstract: The phenomenon of acoustic activation of desorption is studied in a series of atomistic simulations. Nonlinear wave propagation, formation of a shock front, and its interaction with surface species are analyzed. Reflection of a sinusoidal wave from the free surface does not exhibit any substantial effect on the surface species. However, nonlinear propagation of the wave prior interaction with the surface leads to an effect clearly distinguishable from thermal desorption at studied temperature. In particular, in the simulations we have observed an acoustically activated desorption that corresponds to thermally activated desorption at more than 10 folds higher temperature. The mechanism of acoustically activated desorption is explained by coupling of high frequency harmonics of the wave with vibrational modes of clusters that facilitates effective transfer of the acoustic energy into cluster desorption. Simulations performed for clusters of different mass have further confirmed the proposed mechanism. A series of atomistic simulations has allowed us to derive an expression for the dependence of the wave amplitude required for acoustic desorption of clusters on bonding energy and cluster mass. According to our estimation the wave strain amplitude of 10^{-3}-10^{-2} is sufficient for acoustic desorption of the most clusters under experimental conditions. The study

is extended to a realistic system of graphene on Cu substrate with {111} orientation, which is commonly used to grow large area graphene. Interaction of the acoustic waves with single- and double-layer graphene has not result in acoustic desorption, which is in agreement with the estimation derived for desorption of clusters. However, simulations have demonstrated an acoustically activated desorption of 4-layer graphene resulted in removal of 3 layers with keeping a single layer on Cu substrate. This method therefore can be used to remove multilayer parts formed during growth with keeping large area single layer graphene. For larger number of graphene layers, we have suggested a continuum level description of the desorption process. Formation of a tensile wave and interaction with copper-graphite interface leads to desorption of graphite with keeping a single graphene layer on the copper substrate.

Introduction

Bulk and surface waves are actively used to affect processes on atomic/molecular level. In particular, SAWs and bulk acoustic waves interacting with surfaces have been shown to be able to substantially enhance the rates and selectivity of heterogeneous catalytic reactions [57-65], desorb molecules, atoms, and ions from surfaces [65-72,466-468], and facilitate surface diffusion of small atomic clusters [73,74]. One of the most successful applications of this effect is laser-induced acoustic desorption (LIAD) [68-72,466,467] allowing transfer of neutral and low charge volatile molecules into a gas phase without using a carrier gas or matrix that prevents contamination and allows effective detection of rare samples with mass spectrometry.

Variety of experimental conditions in LIAD studies [68-72,466-468] have facilitated suggestion of a range of explanations for the desorption mechanism ranged from purely acoustic and thermal to more exotic ones based on the hypothesis that structures with excess energy are present on the surface and release their energy upon acoustic or thermal impact. In particular, Ref. [69] shows that the increase of the thickness of the substrate, irradiated by laser from the opposite side, from 1 to 20 μm substantially reduces the fragmentation of desorbed molecules and suggests transition from thermal to shock wave driven desorption. Refs. [68,70] report results obtained for an acoustic cell formed by two sapphire plates each of 2 mm thickness separated by a 0.75 mm absorbing layer of liquid mercury that suggests acoustic mechanism of desorption. The majority of the studies are performed for nanosecond laser pulses that limits the amplitude of generated acoustic waves. Though, using an experimental setup with confinement of the irradiated material by a transparent overlayer or using sufficiently high laser fluence capable to result in explosive phase separation in the irradiated material [18-20] can produce nanosecond acoustic pulses with strain up to ~0.01 [53]. Moreover, irradiation by femtosecond and picosecond laser pulses is capable to produce intense (0.01-0.1 strain) compressive bulk waves in the non-ablative regimes [108,319] that allows repetitive irradiation of the same spot.

The observations of the acoustic activation of atomic/molecular-level processes are surprising, as there is a large mismatch between the relatively low frequencies of the acoustic waves used in experiments, typically less than 100 MHz, and the vibrational frequencies characteristic of atoms and molecules on the surface, on the order of terahertz. This frequency mismatch calls into question the contribution of the dynamic resonant coupling of the acoustic wave to surface vibrational states [69,70,453,454] and gives rise to hypotheses based on the presumed presence of mesoscopic-scale substructures/domains [59,60] that can effectively couple to a long-wavelength acoustic excitation, nanoscale stressed surface features that can release the stored strain energy in response to an acoustic activation, thus providing the needed extra energy for the desorption of molecules [71], or acoustically induced variation of the spatial distribution of adsorbates to affect the surface reaction rates [63].

The results of large scale atomistic simulations of surface diffusion of atomic clusters in the presence of nonlinear SAWs reported in Section 5.3 and in Ref. [73] have suggested an alternative mechanism of the acoustic activation of surface processes. The nonlinear sharpening of the wave front is associated with the generation of high frequency harmonics that can reach the cluster resonance frequency and lead to an effective dynamic coupling between the SAW and the cluster vibrational modes. This coupling facilitates an effective transfer of the acoustic energy to the cluster motion. Following the explanation suggested in Section 5.3 and in Ref. [73], in this section we report results of computational study of the effect of nonlinear bulk waves on desorption of small clusters and graphene layers.

Computational setup

Acoustically activated desorption of surface species by bulk waves have been studied in a series of atomistic simulations. The mechanisms of acoustic activation have been elucidated with using a model system with interatomic interaction described with Lennard-Jones potential. In this study we do not try to quantitatively mimic any particular system but use a general model capable of reproducing the key features of the desorption process such as nonlinear wave sharpening and reflection from the free surface followed by energy transfer to clusters. It allows us to analyze the effect of the cluster bonding energy and wave nonlinearity on the desorption process. Lennard-Jones units (σ, ε, m, τ) are used to describe the system setup and computational results. The system size is 78 σ × 78 σ × 935 σ (50×50×600 Face Centered Cubic unit cells), which corresponds to 6M atoms.

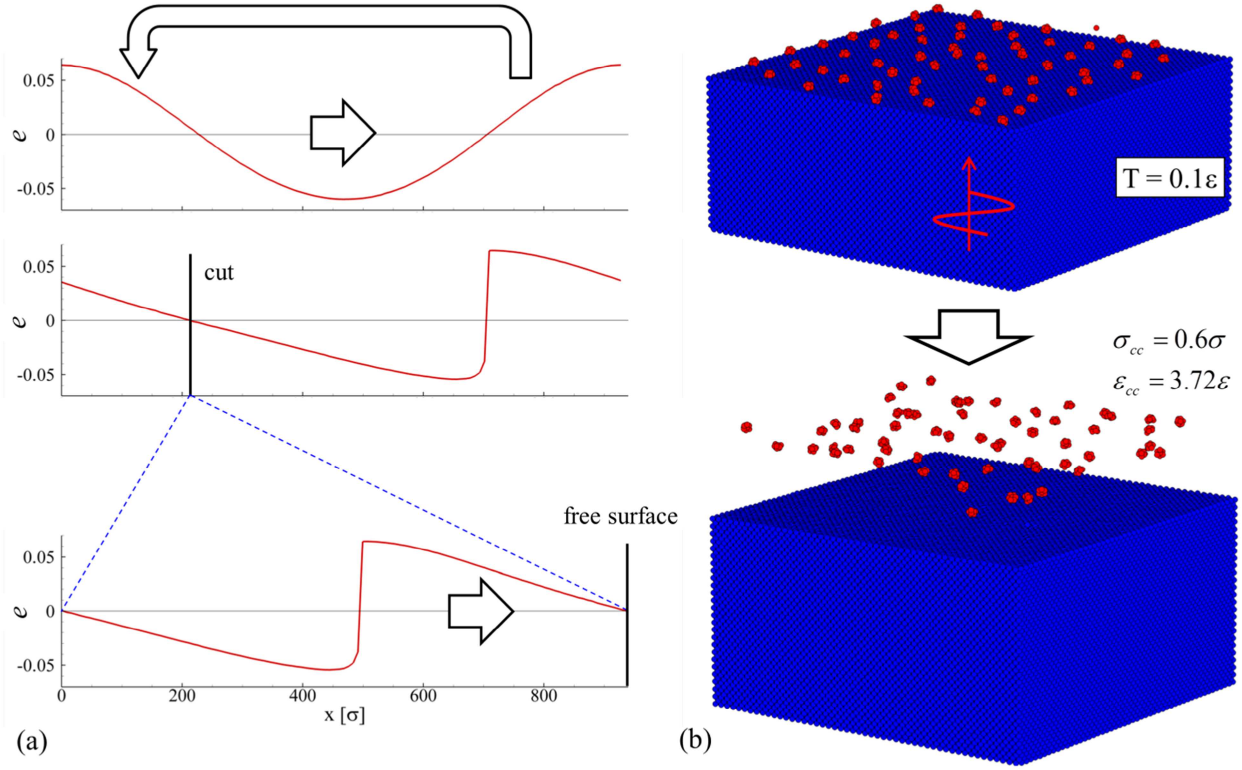

Figure 110. (a) Schematic illustration of system preparation for modeling of acoustically activated desorption. First, a system with periodic boundary conditions is used to simulate nonlinear propagation of a wave. After shock front is formed, the system is split at a position of zero strain and atomic clusters are put on the surface. (b) Illustration of clusters and their desorption, only the top part of the target is plot.

The atomistic system for modeling of acoustic desorption is prepared in the following sequence of steps. After generation of the initial atomic configuration, it is equilibrated at the temperature 0.1ε with periodic boundary conditions applied in all three directions. The longitudinal wave is incorporated into a system by adding extra displacement and velocities to atoms in the system according to $dz = A \cdot \sin(kz_0)$, $dv_z = Akc \cdot \cos(kz_0)$, where k is the spatial angular frequency calculated as $2\pi/L_z$, L_z is the system length along z axis, c is the speed of the wave equal to 8.687 σ/τ at the studied temperature, z_0 is the z coordinate of a particular atom in the ideal crystal, A is the wave amplitude set to reproduce a particular initial strain amplitude that is calculated as $e_{init} = Ak$. The wave is allowed to propagate in the system to allow nonlinear sharpening and formation of a shock front, as illustrated in Figure 110a. At a particular moment of time, defined individually for a particular setup, the system is cut at the position having zero strain to form free surfaces, and 10-atomic-clusters are added to the surface and quenched to ensure that clusters do not have excess energy that may cause desorption. The clusters are placed on the surface at a sufficient distance to ensure that clusters do not interact with each other. The parameters of the clusters are chosen to be the same as in Section 5.3 and Ref. [73]. The interaction potential for atoms within clusters has $\sigma_{cc} = 0.6\,\sigma$ and $\varepsilon_{cc} = 3.72\,\varepsilon$, for interaction with substrate $\sigma_{cs} = \sigma$ and ε_{cs} is varied to identify the desorption threshold. The mass of atoms in the cluster is set to be equal to 1.74 mass of atoms of the substrate m, until a different value is specified in the text. After clusters are added, the simulations are continued, and clusters can be desorbed when the wave shock front approaches the surface, as shown in Figure 110b.

In the second part of this study, acoustically activated desorption of graphene is checked. A system with {111} surface orientation of size 2.2 nm × 2.1 nm × 207 nm, which corresponds to 80000 atoms, is utilized. With using the above described procedure, bulk waves are incorporated into the system, and single or multilayer graphene is added to the surface. The interactions between atoms in the substrate is described by EAM potential parametrized for Cu by Mishin [287], the graphene is described with AIREBO potential [469], and the weak Van der Waals interaction of graphene and substrate is described with Lennard-Jones potential with σ = 3 Å and ε = 0.016 eV fitted in ref. [470]. The desorption energy of graphene calculated for this setup equal to 75.1 meV/atom is close to the *ab initio* results 70.9 meV/atom [471]. The simulations for the second part of the section are performed with using LAMMPS package [472].

Mechanism of acoustically activated desorption of small clusters

We investigate the effect of a nonlinear longitudinal wave on desorption of small 10 atomic clusters. A model system described by Lennard-Jones potential is used to study fundamental mechanisms of acoustic desorption. This general model is capable of reproducing the key features of the desorption process such as nonlinear wave sharpening and reflection from the free surface followed by energy transfer to clusters. The application of the model to a realistic system of graphene from copper substrate is studied in the next section. Figure 111 shows results obtained for a wave with the initial amplitude 0.0628. Reflection of a sinusoidal wave from the free surface does not exhibit any substantial effect on the surface species. Propagation of the wave for 50 τ in a system with periodic boundary condition along *z* results in nonlinear distortion, as shown in Figure 2a. Interaction of such wave with free surface results in desorption of clusters clearly distinguishable from purely thermal mechanism, as shown in the plot of the desorption probability vs. cluster bonding energy in Figure 111a. The typical range of bounding energy of absorbed molecules in a surface is 0.05-0.5 eV [71] that corresponds to approximately 0.1-1ε if ε is assumed to be 0.410 eV as for Cu substrate [473]. According to a series of simulations, clusters with bonding energy 0.76ε are desorbed with 0.5 probability. The effect of the acoustic wave on surface species is considerably stronger if the wave propagates for longer, 150τ, and a shock front is formed (Figure 111b). In this case clusters with bounding energy as high as 6.1 ε are desorbed with 0.5 probability.

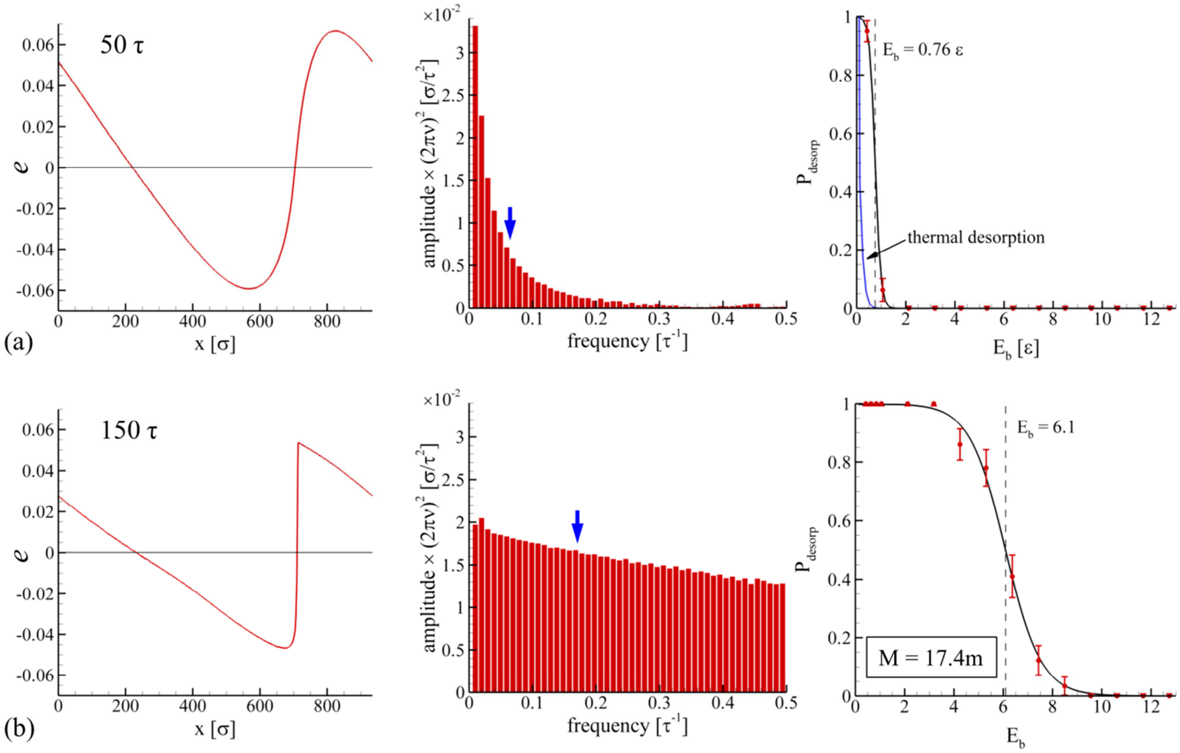

Figure 111. From left to right: the wave profile, the spectrum of the wave, and the dependence of desorption probability on the cluster binding energy for waves propagating for 50 and 150 τ before reaching the surface. The wave profile and the corresponding spectra are obtained in a simulation with periodic boundary condition and indicate the sharpness of the wave front expected at the moment of reflection from the surface. The initial wave strain amplitude is 0.0628. Blue arrows indicate the resonance frequency of a cluster on the surface that has binding energy E_b leading to 0.5 probability of desorption for a particular wave.

To reproduce the same desorption probability on the simulation timescale but by thermal desorption, the temperature of the substrate should be 1.9ε, which is more than 10 times higher than the real temperature. This effect is explained by coupling of high frequency harmonics of the wave with vibrational modes of clusters. Spectrums in Figure 111 illustrate increase of the energy of high frequency harmonics as the wave propagates and becomes sharper that, as a result, allows desorption of clusters with higher bonding energies, which have higher frequencies of vibrational modes. The energy transferred from the wave to a cluster is estimated as:

$$E = \left|\int_{-\infty}^{\infty} F(t) \cdot e^{-i\omega t} dt\right|^2 / 2M = MA_{\omega}^2 L^2 / 2C_s^2 \qquad (5.5),$$

where $F(t)$ is the force acting on the cluster, ω and A_{ω}^2 are the cluster vibration frequency and the Fourier transform of the surface acceleration corresponding to this frequency (Fourier transform of surface displacement multiplied by the square frequency), M, L, and C_s are the mass of the cluster, wavelength of the incoming wave, and the wave velocity. The prediction provides a correct functional dependence but overestimates the bonding energy of desorbed clusters by 2-4 times that can be attributed to the assumption that the cluster is a single particle rather than an agglomeration of atoms, and part of the energy is transferred in internal vibration of clusters. In particular, the average internal temperature of desorbed clusters is 0.21-0.25 ε.

After formation of a shock front at 60 τ (0.6 of the wave period), active dissipation of the wave starts. The dissipation rate increases with frequency [428,474], and after the generated harmonics reach high enough frequency, the dissipation rates reaches the generation rate suppressing further increase of the frequency. Propagation of the wave with a developed shock front results in heating of the material. In addition, the material is heated due to adiabatic heating under propagation of the compressive part of the wave. This heating could be responsible for desorption lasted for 10s of μs in several experimental studies [71,466]. In the simulations, at the moment of reflection of the shock wave from the free surface the surface temperature reaches 0.16ε that can contribute to the mechanism of desorption.

To further support the proposed mechanism of acoustically activated desorption we have performed a series of simulations for different masses of atoms in the clusters (1,2, and 4 m), as shown in Figure 112. The initial amplitude of the wave is selected to be twice smaller than in the previous simulations to suppress the effects of surface heating due to adiabatic compression and wave dissipation. According to Eq. 5.5, the energy transferred to the cluster, and therefore the maximum bonding energy of desorbed clusters, is proportional to the cluster mass that is namely observed in Figure 112. In particular, the increase of the cluster mass from 17.4m to 34.8m and 69.6m, leads to nearly linear increase of the maximum cluster bounding energy from 1.51 to 2.66 and 5.28ε. The deviation is explained by decrease of the amplitude, A_ω^2, of high frequency harmonics with frequency, as illustrated in Figure 111. Meanwhile, since thermally activated desorption does not have a dependence of the maximum bonding energy for desorbed species on their mass, this series of simulations univocally confirms the acoustic activation mechanism. Suppression of the thermal effects also allows to obtain a sharp threshold of desorption that can have a practical use for selective desorption of particular species.

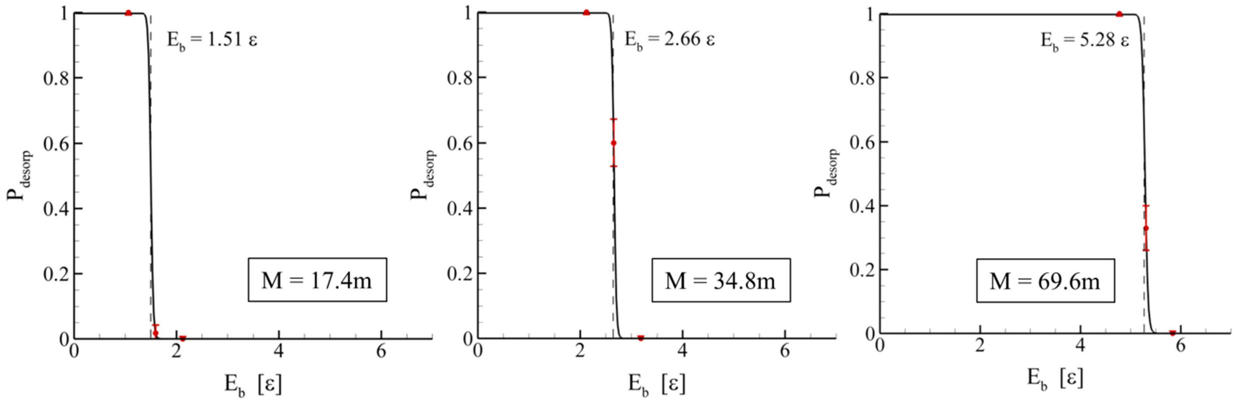

Figure 112. The probability of cluster desorption on the bonding energy of cluster for 10 atomic clusters having 17.4m, 34.8m, and 69.6m mass. The initial wave strain amplitude is 0.0314, wave propagates for 190τ before interacting with free surface.

Table 12. The maximum bonding energy and α parameter (Eq. 5.6) computed in a series of atomistic simulations.

e	M	E_b	α
0.0628	17.4	6.1	0.106
0.0314	17.4	1.51	0.107
0.0314	34.8	2.66	0.114
0.0314	69.6	5.28	0.114

Since the maximum amplitude of higher harmonics is approximately proportional to the initial wave amplitude, the wave amplitude required for desorption of species with bonding energy E_b can be roughly estimated as:

$$e = \alpha\sqrt{E_b/M} \qquad (5.6),$$

where α is an empirical coefficient equal to 0.107-0.114 according to a series of atomistic simulations. The summary of performed series of simulations, computed bonding energy, E_b, and the parameter α are provided in Table 12. Mapping this estimation on a real substrate material and real surface species with bonding energy E_b equal to 0.05-0.5 eV [71] and M = 1000-10000 Da suggests that the wave strain amplitude 10^{-3}-10^{-2} is sufficient for acoustic desorption.

Acoustically activated desorption of graphene

Further studies of the mechanisms of acoustic desorption are perform for a realistic system: graphene on Cu substrate with $\{111\}$ orientation. This setup is commonly used to grow large-area graphene [475], which is formed on the catalytic substrate. However, one of the challenges is transfer of the graphene form the substrate to an acceptor that requires chemical etching of Cu prohibiting its reuse. One of the promising approaches to remove the layer is direct coupling of high frequency bulk waves with vibrational modes of graphene, which can transfer the energy to the graphene layer and lead to detachment from the substrate.

Estimation based on Eq. 5.6 for a single layer graphene on Cu suggests that the wave strain amplitude required for desorption is ~0.11 (E_b = 75.1 meV/atom, ε = 0.410 eV, M = 12.0 Da, m = 63.5 Da). Therefore, we have performed a series of simulations of desorption of single, double, 4-layer graphene, and 25-layer graphite by bulk waves of the strain amplitude 0.04 and 0.06, which are shown to cause no damage to the substrate in the simulations during wave propagation. It should be noted that the above estimation provides only an approximate value since it does not account for nonlinear properties of a particular substrate as well as the direction of wave propagation that affects nonlinear propagation of the wave and generation of high frequency harmonics. In addition, part of the energy, especially for multilayer graphene (graphite), is transferred into internal vibrational modes rather into overcoming the desorption barrier.

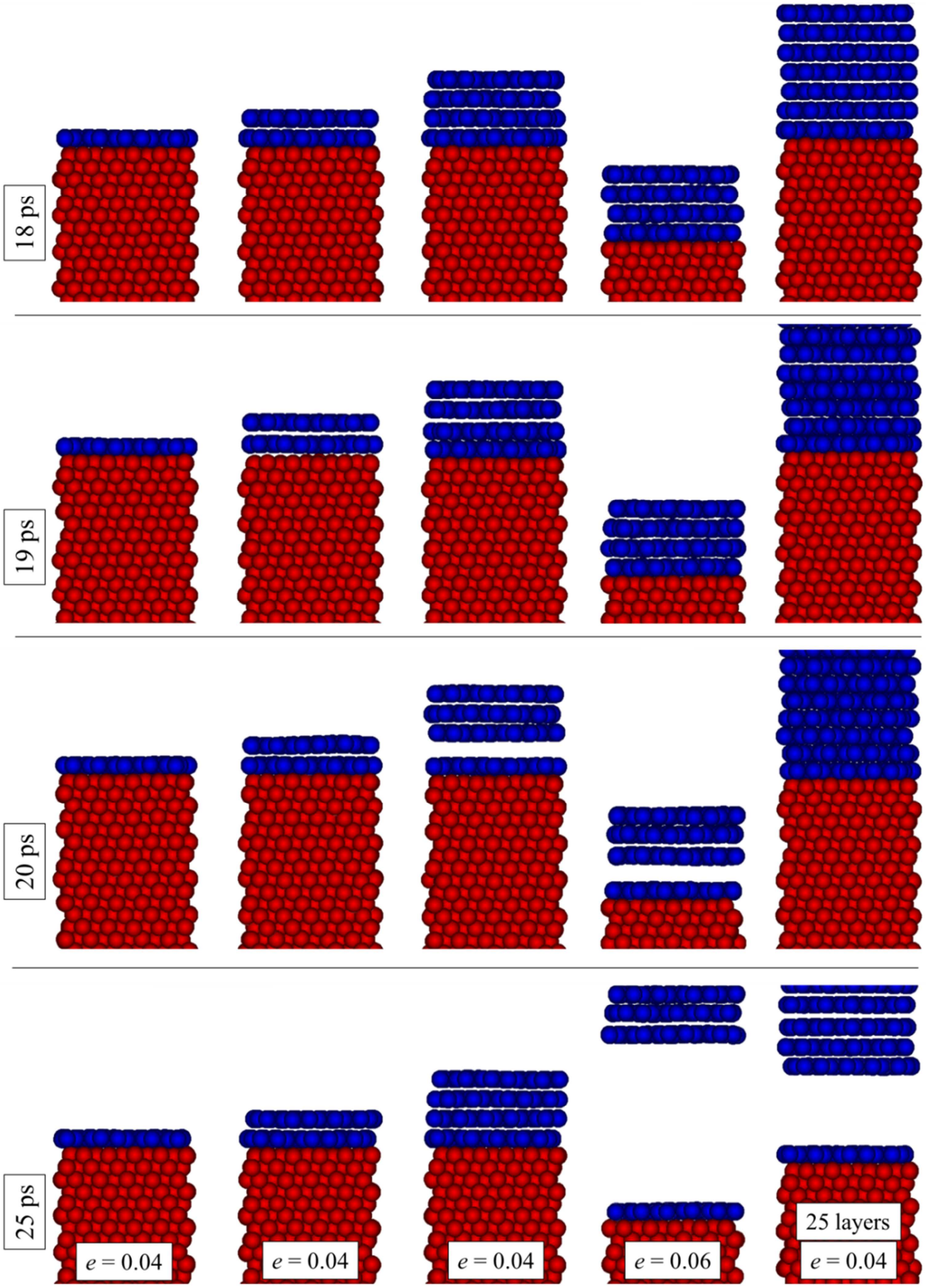

Figure 113. A series of atomic snapshots demonstrating acoustically activate desorption of single, double, 4-layer, and 25-layer graphene from {111} Cu surface. The initial wave strain amplitude is 0.04 and 0.06. The time in left is measured after cutting the system that corresponds to 70 ps and 40 ps for waves with 0.04 and 0.06 initial strains, respectively. Only the top part of the system is shown, red color depicts Cu, and C atoms are shown by blue color.

Atomistic snapshots demonstrating the interaction of a bulk shock wave with the surface are summarized in Figure 113. Only the top part of the system selected to include 4 layers for 4-

layers graphene is depicted in the figure. Interaction of a wave with the strain amplitude 0.04 with a surface does not lead to any noticeable effect. For two-layer graphene, at the moment of shock wave approaching the surface, 19 ps, slight change of the distance between substrate and graphene is visible. For 4-layer graphene, top three layers are detached; however, the speed of the desorbed graphene is not sufficient, and upward motion of the substrate followed by approaching the compressive component of the wave leads to reattachment. Increase of the wave strain amplitude to 0.06 leads to detachment and desorption of the top three layers. The detachment of only three layers is explained by lower graphene-graphene interlayer interaction than graphene-Cu. In particular, for our atomistic setup we have computed graphene-Cu energy of interaction to be 75.1 meV/atom, while graphene-graphene interlayer interaction is only 40.6 meV/atom if recomputed per atom in one of the graphene planes.

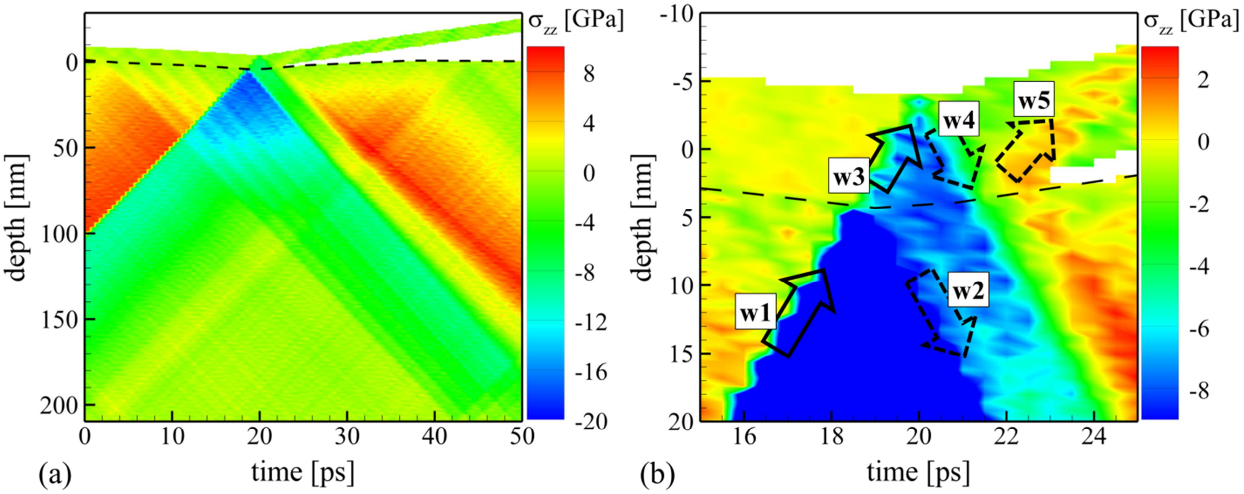

Figure 114. A contour plot illustrating the propagation and reflection of a nonlinear wave leading to desorption of graphene. The zoomed image (b) illustrates the wave propagation in the 25 layer graphene. Black dashed line outlines the Cu surface. Solid and dashed arrows in Figure 5b illustrate the direction of propagation for compressive and tensile waves.

Interaction of bulk waves with 25-layer graphite can be considered in a continuum approximation. The temporal evolution of the stress, σ_{zz}, in the target and in the graphite is depicted in Figure 114. A compressive wave (w1) approaches graphite-Cu interface at about 19 ps and reflects backwards (w2). Meanwhile, the incident wave (w1) partially propagates into graphite (w3), reflects from free surface as a tensile wave (w4) and interacting with graphite-Cu interface leads to detachment of graphite. The acoustic impedance of $\{111\}$ Cu can be calculated as $Z_{111} = \sqrt{(C_{11} + 2C_{12} + 4C_{44})\rho/3}$. At 300 K the EAM potential [287] used in this study gives C_{11} = 163.52 GPa, C_{12} = 120.06 GPa, C_{44} = 71.44 GPa, ρ = 8811 kg/m^3 that results Z_{Cu}= 3.90×10^7 Pa·s/m. The acoustic impedance of graphite is computed as $Z_C = \sqrt{C_{33}\rho}$ = 0.94×10^7 Pa·s/m for C_{33} = 38.7 GPa and ρ = 2261 kg/m^3 [476]. The reflection and transmission of waves for propagation of waves through an interface can be computed as:

$$R = (Z_1 - Z_2)/(Z_1 + Z_2) \quad (5.7),$$

$$T = 2Z_2/(Z_1 + Z_2) \quad (5.8),$$

where Z_1 and Z_2 are acoustic impedances marked according the direction of the wave propagation through the interface. Therefore, $R_{\mathrm{Cu-C}}$ = -0.61, $T_{\mathrm{Cu-C}}$ = 0.39, $R_{\mathrm{C-Cu}}$ = 0.61, $T_{\mathrm{C-Cu}}$ = 1.61. The stress amplitude of the incident compressive wave (w1) is $\sigma_{zz} = (C_{11} + 2C_{12} + 4C_{44}) \cdot e/3$ = -9.2 GPa, and the transmitted wave into graphite (w3) is thus -3.6 GPa. It should be noted that the overlap of the incident reflected waves overshadows the value of stress in Figure 114. Therefore, in Figure 114a at the time ~20 ps the stress near the surface reaches -20 GPa. The wave reflected from the free surface (w4) has amplitude 3.6 GPa that reflects from the graphite-Cu interface producing a tensile wave (w5) of an amplitude 2.2 GPa. Interaction of waves (w4) and (w5) produces strong negative stress at the graphite-Cu and leads to a detachment of graphite. A single layer graphene remains attached to the substrate since it has stronger interaction energy with the substrate than with the second graphene layer.

Summary

A series of atomistic simulations is completed to study mechanisms of acoustically activated desorption. A model system described with Lennard-Jones potential is used to reproduce the key features of the desorption process such as nonlinear wave sharpening and reflection from the free surface followed by energy transfer to small clusters placed of the surface. It has allowed us to analyze the effect of the cluster bonding energy and wave nonlinearity on the desorption process. Reflection of a sinusoidal wave from the free surface does not exhibit any substantial effect on the surface species. However, nonlinear propagation of the wave and formation of the shock front prior interaction with the surface leads to an effect clearly distinguishable from thermal desorption at studied temperature, 0.1 ε. In particular, interaction of a shock bulk wave of the strain amplitude of 0.0628 allows desorption of clusters with 6.1ε bounding energy. To reproduce the same desorption probability on the simulation timescale but by thermal desorption, the temperature of the substrate should be 1.9 ε, which is more than 10 times higher than the real temperature. This effect is explained by coupling of high frequency harmonics of the wave with vibrational modes of clusters that facilitates effective transfer of acoustic energy into cluster desorption, which is confirmed based on the Fourier analysis. A series of simulations performed for different mass of clusters has demonstrated almost linear increase of the maximum bonding energy of desorbed clusters with mass increase, which is predicted by our model and provides further support for the proposed mechanism. Based on a series of atomistic simulation we also have derived an empirical expression for estimation of the wave amplitude required for desorption depending on the mass end bonding energy of clusters. In particular, 10^{-3}-10^{-2} wave strain amplitude is sufficient for acoustic desorption of the most clusters under experimental conditions.

Further studies of the mechanisms of acoustic desorption are perform for a realistic system: graphene on Cu substrate with $\{111\}$ orientation, which is commonly used to grow large area graphene. Since carbon atoms are lighter than clusters considered in the previous part of our study, we have not observed desorption of single- and double-layer graphene, which is consistent with an empirical dependence derived for clusters. However, acoustic wave is shown to be able to desorb 3 layers for 4-layer graphene with keeping only a single layer on the substrate. This method therefore can be used to remove multilayer parts formed during growth with keeping large area single layer graphene. Meanwhile, weaker interaction of graphene with a substrate, for example in the case of silicon carbide [477], could allow usage of acoustically activated desorption to transfer the graphene from the substrate to an acceptor. For thicker graphene (graphite) layer instead of direct coupling of high frequency harmonics with surface species, a continuum level approximation is considered to explain desorption. In particular, formation of a tensile wave and interaction with copper-graphite interface leads to desorption of graphite with keeping a single graphene layer on copper substrate since copper-carbon interaction is stronger than cross-layer interaction between graphene layers.

5.5. Motion of graphene induced by surface acoustic waves

Chemical vapor deposition method is the most promising route for synthesis of large-area graphene [478]. Cu or Ni catalytic substrates are typically used to initiate formation of graphene sheets. As pointed out in the previous section, transfer of graphene from the catalyst substrate to an insulating substrate for device fabrication requires chemical etching of the substrate, and acoustically activated desorption was suggested as an alternative method that allows one to avoid destruction of the substrate. This section reports results of a series of atomistic simulations targeted at the exploration of the effect of nonlinear Surface Acoustic Waves (SAWs) on graphene located on Cu {111} substrate. Although our original goal of SAW-activated desorption of graphene has not been achieved, we observed an intriguing result on motion of graphene sheets induced by SAWs. The capability to move graphene on a substrate, in addition to the desorption, may be useful at the stage of device fabrication, and below we provide an explanation of the mechanism of the acoustically activated motion.

The system used for the MD simulations consists of a substrate with face centered cubic (fcc) structure and a graphene sheet placed on the top surface. The surface has {111} crystallographic orientation, and the top part of the system with graphene is illustrated in Figure 115. The computational system has dimensions of $L_x \times L_y \times L_z$ = 222 nm × 2.1 nm × 2620 nm and consists of about 100 million atoms. An additional set of simulations targeted at revealing the properties of nonlinear SAWs are performed for a smaller system with dimensions of 44.4 nm × 2.1 nm × 524 nm. The *x*-axis corresponds to the direction of the wave propagation, and the system size along this axis is equal to the wavelength. For a substrate with {100} surface orientation described by Lennard-Jones potential, it was established that the minimum system size along *z*-direction (normal to the surface) that is sufficient to ensure no effect on the wave evolution is equal to three wavelengths, *i.e.*, 3λ. As pointed out in Section 2.1.2, SAWs on {111} surface have longer spatial extension of the wave to the depth than SAWs on {100} surface. For elastic moduli of Cu, the minimums system size is identified to be 4λ for {100} and 10λ for {111} surface orientation. Similar to the setup described in Sections 2.1.2, 0, and 5.3, periodic boundary conditions are applied along *x* and *y* directions, rigid boundary is imposed at the bottom of the computational system, and the top of the system corresponds to a free surface. The interatomic interactions in a substrate are described with EAM potential parametrized for Cu by Mishin [287], graphene is described with AIREBO potential [469], and the weak van der Waals interaction of graphene and the substrate is described with Lennard-Jones potential fitted in Ref. [470]. The temperature of the substrate is set to 300 K for simulations with SAW wavelength of 222 nm and to zero for simulations with SAW wavelength of 44.4 nm. The initial displacement and additional velocities are set according to the procedure described in Section 2.1.2. The simulations are performed using LAMMPS package [472].

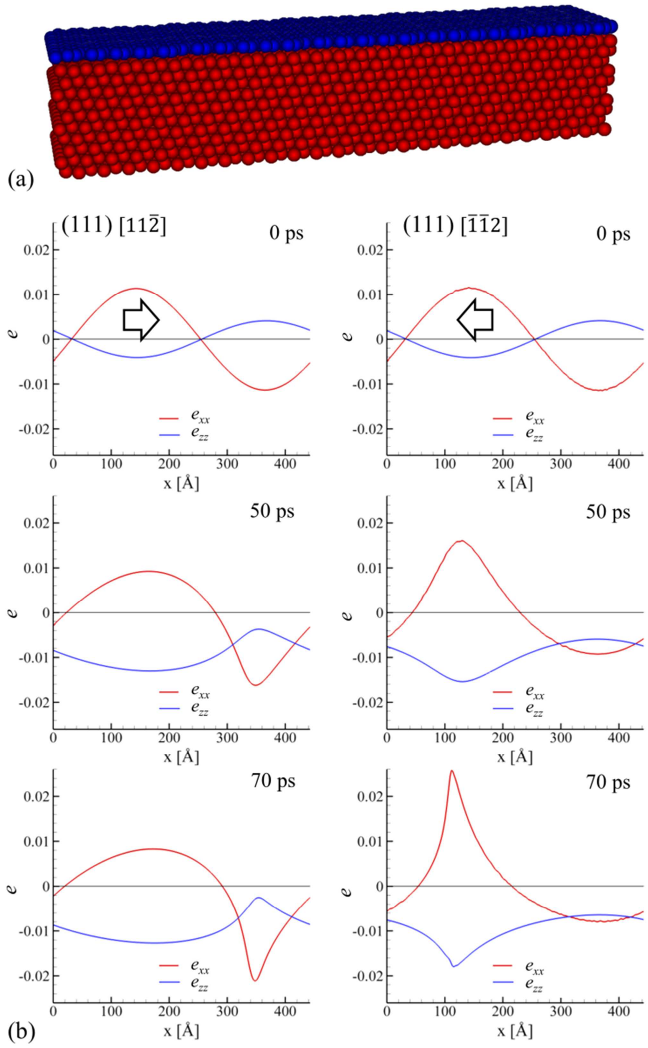

Figure 115. (a) An atomic snapshot of a small part of the computational system illustrating a graphene layer (blue) on a Cu (111) substrate. (b) The evolution of the surface strain profile shown for waves propagating along $[11\bar{2}]$ and $[\bar{1}\bar{1}2]$ directions. The initial amplitude of strain, e, is 0.01%. The initial temperature in the system is set to zero to reduce the thermal noise.

One of the distinct differences of SAWs on $\{111\}$ surface in comparison with earlier considered $\{100\}$ case is the dependence of the wave evolution on the propagation direction. Rayleigh wave solution exists only for propagation in $\langle 112 \rangle$ directions in (111) surface, and $[11\bar{2}]$ and $[\bar{1}\bar{1}2]$ directions are considered in our study. As discussed in Section 2.1.2, rotation of the stiffness tensor to make z-axis perpendicular to (111) surface and x-axis parallel to $[11\bar{2}]$ results in nonzero C'_{15}, C'_{25}, and C'_{46} components and thus absence of mirror symmetry in the wave solution along the direction of wave propagation. Therefore, nonlinear wave propagation, shape evolution, and the shape of the shock front are different for $[11\bar{2}]$ and $[\bar{1}\bar{1}2]$ directions, which is in agreement with experimental studies [125,126]. As shown in Figure 115b, propagation along $[11\bar{2}]$ direction results in the formation of a spike for e_{xx} component of the strain at a compressive part of the wave, while propagation in the opposite direction $[\bar{1}\bar{1}2]$ leads to formation of a spike at the tensile component of the wave. This spike corresponds to a shock front formed in a SAW moving on (111) surface, and its shape is different from the shape observed for waves moving on (100) surface studied in Section 5.2. Due to this drastic difference in the shapes of the wave profiles after shock front, both directions of wave propagation are considered in our study.

The evolution of the strain and displacement in the subsurface layer predicted in large scale atomistic simulations performed for the wavelength of 222 nm and initial e_{xx} strain amplitude of 0.02% is illustrated in Figure 116 for propagation in $[11\bar{2}]$ direction and in Figure 117 for propagation in $[\bar{1}\bar{1}2]$ direction. The shock front is formed at approximately 200 ps. As pointed out in Section 5.2, in contrast to bulk waves, shock front formation for SAWs is accompanied by increase of the strain amplitude due to nonlocal nonlinearity [110-112]. As a result, a pronounced cusp is formed for e_{xx} either on compressive or tensile side of the wave depending on the wave propagation direction.

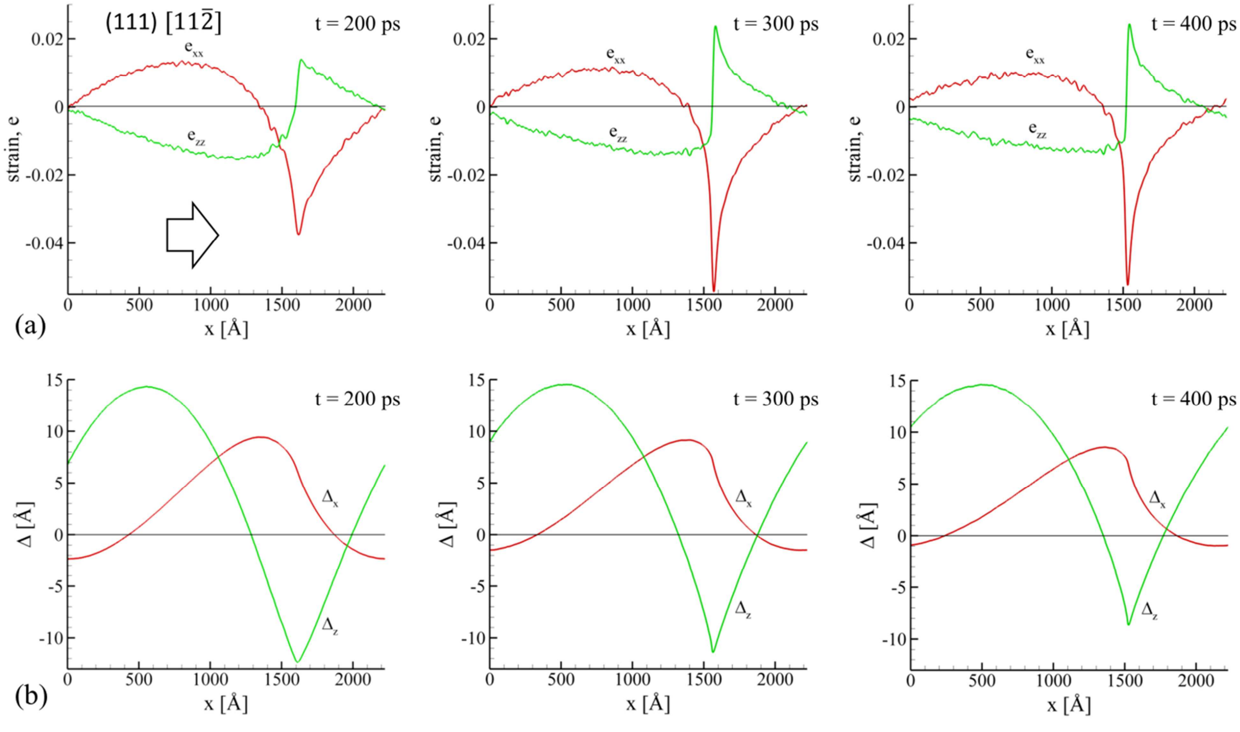

Figure 116. The evolution of SAW strain (a) and displacement (b) in the subsurface layer. The propagation direction is $[11\bar{2}]$, and the initial amplitude of e_{xx} strain is 0.02%.

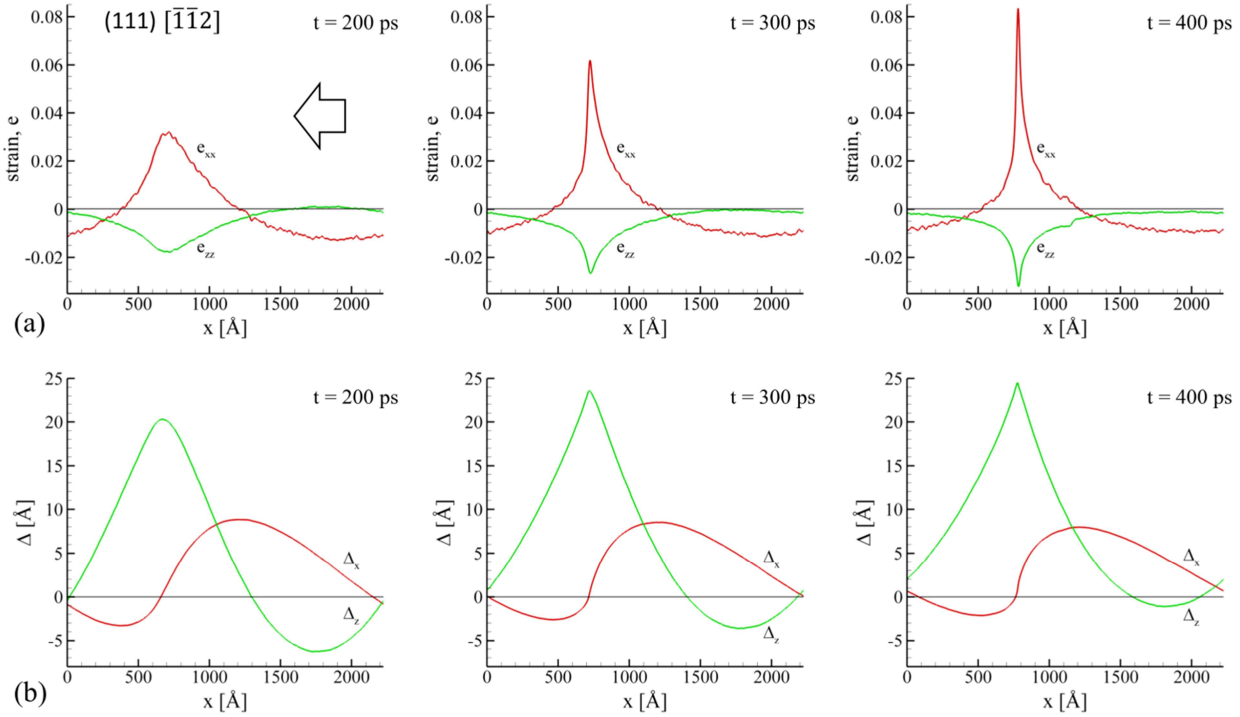

Figure 117. The evolution of SAW strain (a) and displacement (b) in the subsurface layer. The propagation direction is [$\bar{1}\bar{1}2$], and the initial amplitude of e_{xx} strain is 0.02%.

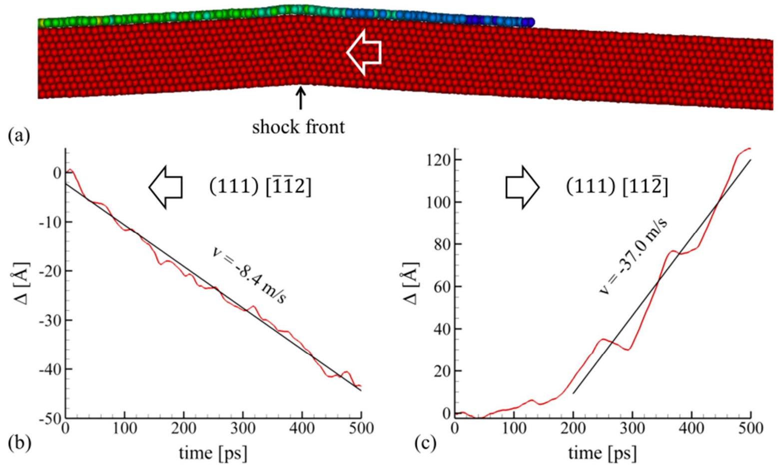

Figure 118. (a) Displacement of a graphene layer with respect to the surface of a Cu substrate caused by SAW propagation. Only a thin subsurface layer of substrate is shown and colored red. The graphene atoms are colored based on their displacement, from blue to red. (b,c)The average displacement of a graphene layer with time for SAWs propagating from right to left and from left to right. At approximately 200 ps, a shock front forms that affects the displacement of the layer in (c).

The interaction of the shock front with a graphene layer on a surface is illustrated in Figure 118a. Propagation of the wave results in displacement of the graphene with respect to the surface, as illustrated by the change of the color within the graphene layer. The total displacement of graphene sheet of the length $\lambda/2$, half of the wavelength, with time for waves moving in $[\bar{1}\bar{1}2]$ and $[11\bar{2}]$ directions is shown in Figure 118b and Figure 118c, respectively. These images clearly demonstrate that SAWs are capable of setting the graphene in motion, and the velocity of graphene is affected by the direction of the wave propagation. In addition, for propagation in $[\bar{1}\bar{1}2]$ direction, nonlinear wave evolution and shock front formation affects the motion of graphene. The effect of the length of graphene sheets is investigated in a series of atomistic simulations, and the measured velocities are summarized in Table 13. For wave propagation in $[11\bar{2}]$ direction, the speed of the graphene sheet is proportional to its length. Meanwhile, for the wave propagating in the opposite direction the dependence is not monotonic. For shot graphene sheets, the velocity is low and increases reaching the maximum value for the length of $\lambda/4$. Further increase of the length leads to decrease of the graphene velocity, reaching -1.9 m/s for continuous graphene layer.

Table 13. The dependence of the velocity of graphene sheets on their length for waves propagating in two opposite directions. Length equal to λ corresponds to a continuous graphene layer.

length	$\lambda/16$	$\lambda/8$	$\lambda/4$	$\lambda/2$	λ
velocity $[11\bar{2}]$, m/s	5.3	12.7	24.5	37.0	86.0
velocity $[\bar{1}\bar{1}2]$, m/s	-0.4	-6.7	-11.4	-8.4	-1.9

In simulations of acoustically activated motion of graphene we do not see strong lateral deformation of graphene, and wave propagation is inducing motion of a graphene sheet as a whole, *i.e.*, the graphene sheet slides with respect to the surface. Therefore, to elucidate the mechanism of acoustically activated motion of graphene, we have measured the dependence of dynamic friction force per carbon atom on the velocity and uniaxial deformation of the substrate in the direction of SAW propagation, Figure 119. In a series of simulations, the graphene is moved with a constant average velocity, and the mean value of force is tracked during the simulation time of 1 ns. For a stretched substrate the dependence of force on velocity can be quite accurately fitted to a combination of linear and square dependencies, and a deviation from these fitted dependences is observed only at velocities larger than 100 m/s. Meanwhile, for a compressed substrate the friction rapidly increases after reaching 90 and 60 m/s for strains of -0.02 and -0.04, respectively. At an even higher strain of -0.06 the friction force is high for all values of considered velocities. The increase of dynamic friction by 1-2 orders of magnitude with compressive deformation of the substrate is attributed to match of the lattice spacing in graphene and Cu (111) substrate. The successful use of Cu (111) for graphene growth is at least partially defined by a very similar lattice parameters of graphene (2.46 Å) and the triangular lattice of the underlying Cu (111) surface (2.56 Å); however, the complete match can be achieved either by stretching the graphene or compressing the substrate. Since stretching of graphene is negligible, the match of the atomic spacing may be achieved with compression of the substrate taking place during the propagation of SAWs.

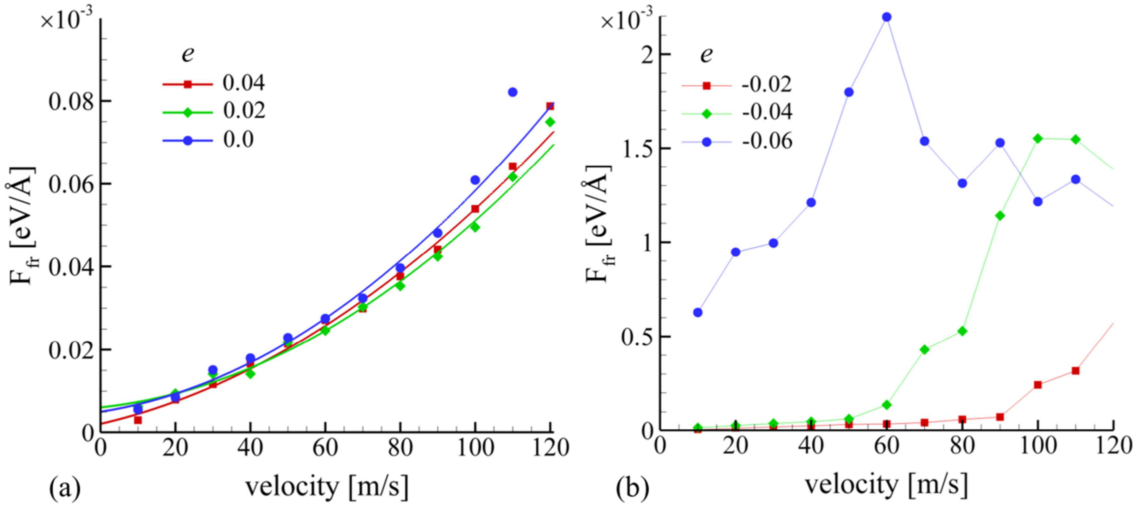

Figure 119. The dependence of friction force per atom of a graphene sheet on the velocity of the graphene on stretched (a) and compressed (b) Cu (111) substrates.

The computed dependence of the friction on the velocity and strain is capable of explaining the acoustic activation of the graphene motion by a SAW propagating in $[11\bar{2}]$ direction. Figure 120 depicts the wave profile at 300 ps and its approximation by a set of step functions. The surface velocity along *x*-direction can be computed as:

$$v_x = \pm c_s e_{xx} \qquad (5.9),$$

where c_s is the speed of SAW, -/+ sign corresponds to propagation of the wave in the same/opposite direction as the *x*-axis. The average force acting on each atom of the graphene sheet is computed as:

$$F_{avr} = \sum_i F_{fr}(v_i) L_i / \lambda \qquad (5.10),$$

where i is the number of a segment used to approximate strain profile, Figure 120b; L_i is the length of the segment, $F_{fr}(v)$ is the friction force at the velocity v approximated based on results in Figure 119, v_i is the velocity of the segment, and λ is the wavelength.

For a continuous graphene layer the speed of the layer identified in the modeling after shock front formation is 86 m/s, Table 13, and the relative speeds of graphene layer with respect to the surface at different parts of the wave are marked in Figure 120b. With these values of the relative velocity the average force acting on each atom of graphene can be estimated based on Eq. 5.10:

$$F_{avr} \approx \left(-0.06\frac{meV}{\text{Å}} \cdot 1500nm + 1\frac{meV}{\text{Å}} \cdot 200nm - 0.04\frac{meV}{\text{Å}} \cdot 500nm\right)/2200nm = 0 \qquad (5.11).$$

Therefore, the graphene moves with a steady rate if the velocity is equal to ~86 m/s, which exactly corresponds to results of large-scale atomistic simulations. Acoustically activated motion of graphene, thus, can be explained by dragging the graphene by a shock front, which reaches -0.055 strain and have more than one order of magnitude higher friction in comparison with other parts of the wave.

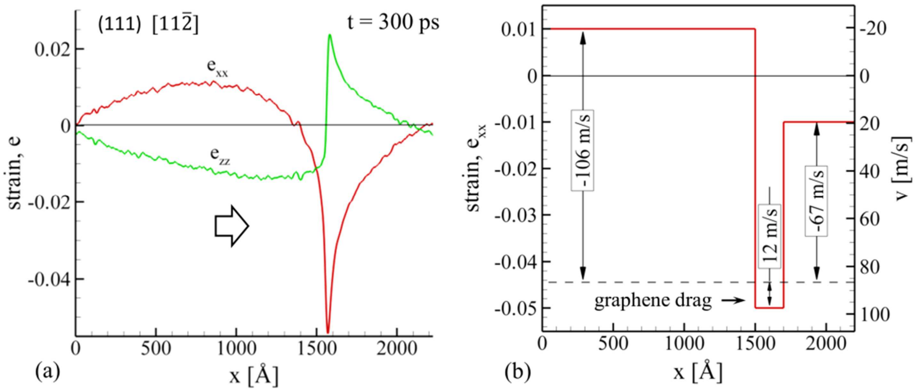

Figure 120. (a) The profile of e_{xx} and e_{zz} stress produced in propagation of SAW in $[11\bar{2}]$ direction for 300 ps. (b) The simplified shape of e_{xx} profile and corresponding relative values of velocities of graphene with respect to the surface. The dashed line outlines -86 m/s, the velocity of a continuous graphene layer.

Since the graphene is dragged by a narrow shock front, noncontinuous graphene sheets move in the same direction as the wave when a shock front is passing through them and in the opposite direction (with lower velocity -20 – 0 m/s) when they do not interact with the shock front. Therefore, as illustrated in Figure 118c, the motion of a graphene consists of periods of moving the graphene sheet in the same and in the opposite direction as the wave propagation, and the average speed is proportional to the length of the sheet relative to the wavelength. Short sheets move along the wave only for a short period of time, while a continuous layer moves constantly. Before the shock front is formed at 200 ps there is no distinct drag of the graphene, but a slightly larger friction coefficient for a compressed substrate leads to motion of the graphene layer with a slow speed in the direction of the wave propagation, which is equal to 16 m/s for a continuous layer.

Similar analysis is performed for waves moving in the opposite direction, $[\bar{1}\bar{1}2]$. For a continuous layer at the velocity 0 m/s (Figure 121b) the total force acting on the graphene can be estimated as:

$$F_{avr} \approx \left(-0.01\frac{meV}{\text{Å}}\cdot 1500nm + 0.05\frac{meV}{\text{Å}}\cdot 200nm + 0.01\frac{meV}{\text{Å}}\cdot 500nm\right)/2200nm = \ 0 \quad (5.12).$$

Therefore, a continuous graphene layer should not move or move with a low velocity, which is beyond the accuracy of the performed estimation. This conclusion is in an agreement with results of large-scale atomistic simulation that strongly suggests the friction to be the major factor defining the motion of graphene. However, a complicated dependence of the velocity of graphene sheets on their length, Table 13, cannot be described in this framework. In particular, for the length $\lambda/2$ the following estimation for the average force can be written (Figure 121c):

$$F_{avr} \approx \left(-0.005\frac{meV}{\text{Å}}\cdot 1500nm + 0.06\frac{meV}{\text{Å}}\cdot 200nm + 0.014\frac{meV}{\text{Å}}\cdot 500nm\right)/2200nm > 0 \quad (5.13).$$

Thus, the graphene sheet cannot move with velocity -8.4 m/s, as observed in the atomistic simulation. If the spike is excluded from computing the total force, meanwhile, the total force can be estimated to be zero:

$$F_{avr} \approx \left(-0.005\frac{meV}{\text{Å}}\cdot 1500nm + 0.014\frac{meV}{\text{Å}}\cdot 500nm\right)/2200nm \approx 0 \quad (5.14).$$

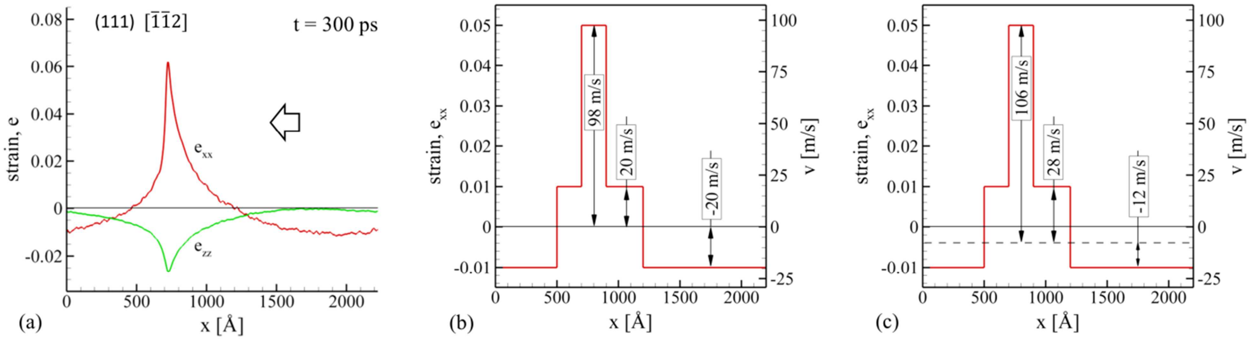

Figure 121. (a) The profile of e_{xx} and e_{zz} stress produced in propagation of SAW in $[\bar{1}\bar{1}2]$ direction for 300 ps. (b,c) The simplified shape of e_{xx} profile and corresponding relative values of velocities of graphene with respect to the surface for motion of graphene with 0 and -8 m/s (dashed line).

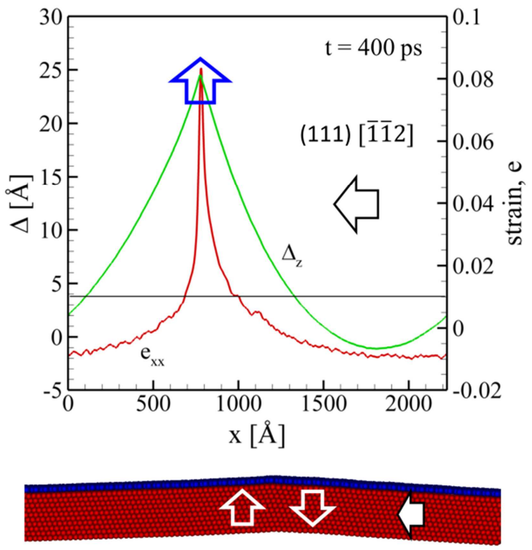

Figure 122. Schematic illustration of the origin of the dynamic effect. The graph on the top shows the wave profile at 400 ps, while the snapshot below depicts the graphene layer and subsurface region of the target in the vicinity of a shock front.

One of the possible explanations of the above-described inconsistency is a dynamic effect resulted by interaction of the wave front with an edge of the graphene sheet. As illustrated in Figure 122, this interaction may result in a lifting the graphene. This effect is not sufficient to completely separate graphene sheet from the substrate, and the detachment is followed by reattachment. However, a wave accompanied by temporal detachment may propagate along with the wave front. This detachment may lead to decrease of the fiction in the vicinity of the shock front, which explains the estimation provided by Eq. 5.14. The above-described hypnosis is also confirmed by additional simulations performed for double layer graphene and a layer with an artificially increased mass of each carbon atom. A layer composed of twice heavier atoms moves with -11.9 m/s velocity, which is faster than -8.4 m/s observed previously for a graphene layer of length $\lambda/2$, Table 13. A double layer graphene also moves faster, with the average velocity -13.1 m/s. As pointed out in Section 5.4, increase of the mass facilitates acoustically activated desorption, and thus may confirm the dynamics effect. In addition, if the detachment wave propagation is limited by the length ~$\lambda/4$, long graphene sheets of length $\lambda/2$ moves slower that $\lambda/4$. The detachment wave vanishes, and the interaction of the graphene sheet with a tensile cusp slows down the overall velocity. A continuous graphene layer, meanwhile, cannot be affected by a detachment wave due to absence of edges where temporal detachment starts. Thus, the estimation given by Eq. 5.12 is valid, and the overall velocity approaches zero. For a wave moving in the opposite direction, [$11\bar{2}$], the appearance of the detachment wave decreases the drag force, which is confirmed in an atomistic simulation performed for $\lambda/2$ sheet suggesting decrease of the graphene velocity from 37 m/s to 32 m/s after two-fold increase of the layer mass.

In summary, a series of large-scale atomistic simulations has been performed to study interaction of SAWs with graphene on catalytic Cu (111) substrate, and acoustically activated motion of graphene is demonstrated. Intrinsic properties of SAWs on (111) substrate result in distinct evolution of the wave profile and shock front formation on compressive and tensile part of the wave for propagation in $[11\bar{2}]$ and $[\bar{1}\bar{1}2]$ directions, respectively. The effect of the length of graphene sheets on their velocity is analyzed. For waves propagating in $[11\bar{2}]$ direction the velocity is found to be proportional to the length of the sheet, while for the wave moving in the opposite direction, $[\bar{1}\bar{1}2]$, the velocity of the sheet first increases with length, reaches its maximum at the length $\lambda/4$, and then decreases again. A significant increase of the friction force for the compressed substrate, resulted by the match of interatomic spacing in the graphene and substrate, is shown to be responsible for acoustically activated motion of graphene by a wave propagation in $[11\bar{2}]$ direction. For a wave moving in the opposite direction the expected graphene speed is close to zero, which is the case for a continuous graphene layer. For graphene sheets of finite length an alternative explanation should be found. The suggested hypothesis is based on a dynamic effect accompanied by temporal detachment of graphene near the wave front. This mechanism is supported by simulations performed for graphene layers with artificially doubled mass and for a double layer graphene.

6. Summary

Rapid expansion of practical applications of ultrashort pulse lasers into new areas where precise nanoscale control of material modification is required can only be sustained with an improved fundamental understanding of laser-materials interactions. The ability to achieve high spatial resolution in material modification and microstructure engineering usually relies on fast and highly localized energy deposition that, unavoidably, creates conditions of strong electronic, thermodynamic, and mechanical nonequilibrium. The intricate connections between the ultrafast material response to laser excitation, generation of crystal defects, phase transformations, and mass transfer occurring under highly nonequilibrium conditions are accounted for in a hybrid TTM-MD model combining the classical molecular dynamics method with a continuum description of the laser interaction with the target. This model is applied in this dissertation to elucidate the processes and mechanisms responsible for modification of subsurface microstructure and morphology as well as the acoustic activation of surface processes. The key results obtained in this study are briefly summarized below.

Subsurface microstructure. The first topic considered in our study is focused at revealing the physical origin of the sensitivity of the laser-induced surface modification to the crystallographic orientation of irradiated surface. A series of large-scale simulations have confirmed the strong effect of the target orientation on the microstructure modification, observed experimentally [177], and provide a detailed description of the defect configuration generated for each surface orientation. The analysis of the resolved shear stress has helped to establish conditions for the dislocation emission during dynamic relaxation of laser-induced stresses. In addition, the results of the simulations have led to the formulation of a novel mechanism of dislocation generation during solidification. Finally, the mechanisms of vacancy generation in the irradiated target are uncovered.

In addition to the generation of dislocations, our simulations have demonstrated generation of a high density of growth twins in a course of solidification of (111) target under conditions of deep undercooling. This observation is confirmed in an experimental study by our collaborators. Both the depth of a surface region affected by growth twinning and the thickness of twinned domains predicted in the simulations are in a good agreement with the experimental observation. Moreover, our combined computational and experimental study has helped to establish a link between generation of high spatial frequency laser-induced periodic surface structures (LIPSS) and surface melting process. The interpretation of the computational predictions is assisted by theoretical analysis of the growth twinning during solidification. A capillarity-based method for calculation of free energy of steps on solid-liquid interface is developed and applied for EAM Ni potential [130]. A series of atomistic simulations has revealed an important role of incoherent twin boundary motion in the generation of the final microstructure.

Next topic related to the microstructure modification is the effect of spatial confinement by a solid overlayer on laser-induced structural and phase transformation. In the low laser fluence regime, the confinement is found to suppress the generation of the unloading tensile wave, which in turn leads to complete suppression of photomechanical spallation and cavitation, decrease of the maximum melting depth, and reduction or elimination of the emission of dislocations from the melting front. At higher fluences that bring the surface region of the metal target to the supercritical state, the confinement prevents the expansion and explosive phase decomposition of the surface region. A series of large-scale atomistic simulations is performed to study the microstructure produced in short pulse laser processing of metal targets under spatial confinement by a solid and liquid overlayer. Solid overlayer is demonstrated to prevent surface swelling and leads to formation of subsurface microstructure featuring grains that are slightly misoriented with respect to each other and are separated by low angle grain boundaries or dislocation walls. The formation of these grains is attributed to the stabilizing effect of the solid overlayer resulting in an incomplete melting of metal in the vicinity of the overlayer. In the case of confinement by a liquid overlayer, a thin nanocrystalline layer with random orientation of grains is formed. In all simulations, the nanocrystalline layers generated by laser processing of single-crystal Ag targets are characterized by a high density of stacking faults, twin boundaries, and point defects produced in the course of the rapid resolidification.

The effect of interatomic potential on results of atomistic simulations of short pulse laser irradiation is illustrated with using Ti as an example. We have designed a procedure that provides a simple, accurate, and robust method of melting temperature evaluation. Other high temperature properties, such as critical point, binodal line, and temperature dependence of surface tension, are also computed for a number of Ti interatomic potentials. Finally, we provide several examples of the effect of high temperature material properties on the laser-induced microstructure and surface morphology modification predicted in atomistic simulations. In particular, a large-scale simulation performed with an EAM Ti potential that accounts for angular dependence of electron density is found to reproduce the expected martensitic phase transformations in Ti. The absence of the angular dependent component in Mishin EAM Ni potential [130], meanwhile, requires introduction of an oscillating component to the potential to accurately reproduce stacking fault and twin boundary energies. However, this component is demonstrated to result in formation of Frank Kasper σ-phase, instead of conventional homogeneous nucleation, under conditions of deep undercooling.

Surface morphology. In the next part of the dissertation, surface morphology modification in short pulse laser processing is considered. A criterion for the onset of cavitation in a molten metal is revisited, and a theoretical description of spallation is developed in terms of free energy barrier and void nucleation rate. The analytical description is parametrized based on the results of atomistic simulations performed for Ni, Cr, Al, and Ag, and is shown to be applicable for a wide range of temperature and pressure conditions. The results of large-scale atomistic simulations demonstrate the ability of the theoretical treatment to provide an adequate description of the onset of cavitation in both the spallation and phase explosion regimes.

A large-scale molecular dynamics simulation is employed to study the mechanism of single-pulse LIPSS formation in the regime of strong ablation. Langevin nonreflecting boundary is developed to describe nonreflecting propagation of pressure waves with nonplanar wave front. The simulation of spatially modulated ablation induced by irradiation at average laser fluence well above the threshold for the phase explosion reveals a complex interplay of material removal and redistribution leading to the formation of prominent surface features. The shape of this feature is demonstrated to be in a good quantitative agreement with results of experimental study performed by our collaborator. The microstructure produced after resolidification is studied in details.

Acoustic activation of surface processes. The relaxation of laser-induced thermal stresses is not only affecting surface morphology and microstructure in the region of the laser energy deposition, but can also generate intense bulk and surface acoustic waves (SAWs) capable triggering surface processes at a substantial distance from the laser spot. A number of recent experimental studies indicate that SAWs and bulk waves may affect surface processes at atomic/molecular level, which is surprising given a large mismatch between the relatively low frequencies of SAWs, typically less than 100 MHz, and the vibration frequencies characteristic for individual atoms and molecules on the surface, on the order of 1 THz. Thus, the third part of the dissertation is focused on providing a physical explanation of the effect of laser-induced acoustic activation of surface processes.

First, we have examined laser induced generation of SAWs in nonablative regime. A 2D thermoelasticity model suitable for description of highly anisotropic materials is developed and applied to assess the parameters of SAWs generated under experimental conditions in Si substrate. The laser-generated waves are demonstrated to be sufficiently strong to be able to form a shock front at the distance ~10 cm, a typical distance considered in experiments [73]. Thorough study of the effect of laser parameters, such as the pulse duration, spot size, and absorption depth, is performed, and the recommendations for maximizing the amplitude of SAWs are formulated. If the laser parameters are optimized, the maximum SAW strain amplitude in Si generated in the nonablative regime can reach ~0.1%.

In the subsequent study we have designed an atomistic approach for modeling of free propagation of SAWs and performed a detailed analysis of intrinsic features of linear and nonlinear evolution of SAW, including the strongly nonlinear regime accompanied by damage to the material. Prior to our study, MD method has never been applied for the description of free propagation of SAWs, with earlier works limited to the analysis of the effect of periodic shaking of surface to produce a wide spectrum of bulk and surface waves [77] or displacing a thin layer of material [78] according to the analytical solution for linear SAWs [79]. The unusual character of spatial dispersion of SAWs and a number of specific features of nonlinear SAW evolution that are distinct from their counterparts in bulk-wave propagation are pointed out. Good agreement of the MD data with some of the important features that have been predicted by analytical models confirms reliability of the implemented MD approach.

The MD model is then applied to study the mechanism of acoustically activated enhancement of surface diffusion of small clusters observed experimentally by our collaborators. The analysis of the evolution of the SAW frequency spectrum reveals a direct connection between the diffusion enhancement and the generation of high frequency harmonics associated with the nonlinear wave sharpening and shock front formation. The high harmonics reach frequencies typical of natural cluster vibrations and lead to an effective dynamic coupling between the acoustic wave and the cluster vibrational modes. Rescaling the computational prediction to the experimental conditions suggests 22-fold enhancement, which is in a good agreement with 19-fold increase in the effective diffusion coefficient measured by our collaborator in room temperature experiments.

The proposed mechanism of acoustic activation is further verified in a series of atomistic simulations of acoustic activation of desorption. Nonlinear wave propagation, formation of a shock front, and its interaction with surface species are analyzed. Reflection of a sinusoidal wave from the free surface does not exhibit any substantial effect on the surface species. However, nonlinear propagation of the wave prior to the interaction with the surface leads to an effect clearly distinguishable from thermal desorption. The performed simulations confirm that coupling of high frequency harmonics of the wave with vibrational modes of adsorbed clusters facilitates effective transfer of the acoustic energy and leads to the cluster desorption. A series of atomistic simulations has allowed us to derive an expression for the dependence of the wave amplitude required for acoustic desorption of clusters on bonding energy and cluster mass. The study is extended to a realistic system of graphene on Cu substrate with $\{111\}$ surface orientation, and desorption of multilayer graphene is demonstrated.

Acoustically activated motion of graphene on Cu (111) substrate is demonstrated in a series of atomistic simulations. We have derived a Rayleigh wave solution for propagation on (111) surface of a cubic crystal and designed a procedure for generation of a SAW in an MD setup. The distinct features of SAWs propagating on (111) surface are analyzed, and the difference in nonlinear shape evolution and shock front formation for wave propagation in opposite, $[11\bar{2}]$ and $[\bar{1}\bar{1}2]$, directions is revealed. The acoustically activated motion by a wave moving in $[11\bar{2}]$ direction is explained based on the dependence of the friction force on the strain induced in the substrate by a SAW. The compressive strain generated at the shock front drags the graphene and produces the motion. Meanwhile, the motion induced by a wave moving in the opposite direction cannot be solely explained based on the transient variation of the friction force, and dynamic effects should be considered. In particular, temporal detachment of graphene near the wave front may affect the friction.

Overall, the results of the reported study of laser-materials interactions expand the limits of the fundamental understanding of material behavior under extreme conditions and provide ideas for the design of new methods of controlled modification of surface morphology and microstructure. Moreover, the insights in the mechanism of acoustic activation of surface processes provide a guideline for developing techniques that fully utilize the benefits of the acoustic stimulus.

Further directions

The topic not included in this dissertation is the effect of material parameters on the surface morphology modification. In our study the process of laser-induced microstructure modification is divided into four stages: (1) Cavitation (described in Section 4.1), (2) Void growth and coalescence, (3) Break of the liquid bridges connecting spalled material and substrate, (4) Rearrangement of material and solidification. At the stage (1) the key parameter found in our study is surface tension. At the next stage the evolution of the system is dictated by the ratio of surface tension to dynamic viscosity characterizing the velocity of the shape relaxation and thus the characteristic spatial scale of produced features. At the stage (3) the break of the liquid bridges is affected by viscosity, surface tension, and density. Finally, the rearrangement of the material prior solidification is affected by the solidification velocity and the rate of cooling in addition to the ratio of surface tension to viscosity. Overall, surface tension and viscosity are found to be the most important parameters, and the spatial scale of surface features predicted in our preliminary analysis based on those two parameters is in agreement with surface morphology observed in experimental studies. Despite this agreement, the results need to be summarized, and additional verification may be required.

Shock front formation in propagation of SAWs is accompanied by increase of the wave amplitude due to nonlocal nonlinearity. Thus, even if a wave of comparatively low amplitude can form sufficiently intense acoustic pulse leading to damage of material, as discussed in Section 5.2. Intense acoustic waves may cause emission of dislocations leading to formation of steps on the surface. Presence of steps on a catalytic substrate affects catalytic activity and may explain acoustically activated change of the catalytic activity reported in a number of experimental studies [57-65].

References

[1] B. N. Chichkov, C. Momma, S. Nolte, F. von Alvensleben, and A. Tünnermann, Femtosecond, picosecond and nanosecond laser ablation of solids, Appl. Phys. A **63**, 109 (1996).

[2] R. R. Gattass and E. Mazur, Femtosecond laser micromachining in transparent materials, Nature Photonics **2**, 219 (2008).

[3] A. Y. Vorobyev and C. Guo, Direct femtosecond laser surface nano/microstructuring and its applications, Laser & Photonics Reviews **7**, 385 (2013).

[4] B. Rethfeld, K. Sokolowski-Tinten, D. von der Linde, and S. I. Anisimov, Timescales in the response of materials to femtosecond laser excitation, Appl. Phys. A **79**, 767 (2004).

[5] M. V. Shugaev *et al.*, Fundamentals of ultrafast laser–material interaction, MRS Bull. **41**, 960 (2016).

[6] A. Rousse *et al.*, Non-thermal melting in semiconductors measured at femtosecond resolution, Nature **410**, 65 (2001).

[7] M. Hase, P. Fons, K. Mitrofanov, A. V. Kolobov, and J. Tominaga, Femtosecond structural transformation of phase-change materials far from equilibrium monitored by coherent phonons, Nature Communications **6**, 8367 (2015).

[8] N. M. Bulgakova, R. Stoian, A. Rosenfeld, I. V. Hertel, and E. E. B. Campbell, Electronic transport and consequences for material removal in ultrafast pulsed laser ablation of materials, Phys. Rev. B **69**, 054102 (2004).

[9] S. I. Anisimov, B. L. Kapeliovich, and T. L. Perel'man, Electron emission from metal surfaces exposed to ultrashort laser pulses, Sov. Phys. JETP **39**, 375 (1974).

[10] B. Rethfeld, K. Sokolowski-Tinten, D. von der Linde, and S. I. Anisimov, Ultrafast thermal melting of laser-excited solids by homogeneous nucleation, Phys. Rev. B **65**, 092103 (2002).

[11] D. S. Ivanov and L. V. Zhigilei, Effect of Pressure Relaxation on the Mechanisms of Short-Pulse Laser Melting, Phys. Rev. Lett. **91**, 105701 (2003).

[12] K. Sokolowski-Tinten, J. Bialkowski, A. Cavalleri, D. von der Linde, A. Oparin, J. Meyer-ter-Vehn, and S. I. Anisimov, Transient States of Matter during Short Pulse Laser Ablation, Phys. Rev. Lett. **81**, 224 (1998).

[13] J. P. Colombier, F. Garrelie, N. Faure, S. Reynaud, M. Bounhalli, E. Audouard, R. Stoian, and F. Pigeon, Effects of electron-phonon coupling and electron diffusion on ripples growth on ultrafast-laser-irradiated metals, J. Appl. Phys. **111**, 024902 (2012).

[14] J. P. Colombier, F. Garrelie, P. Brunet, A. Bruyère, F. Pigeon, R. Stoian, and O. Parriaux, 2012).

[15] G. D. Tsibidis, M. Barberoglou, P. A. Loukakos, E. Stratakis, and C. Fotakis, Dynamics of ripple formation on silicon surfaces by ultrashort laser pulses in subablation conditions, Phys. Rev. B **86**, 115316 (2012).

[16] G. D. Tsibidis, C. Fotakis, and E. Stratakis, From ripples to spikes: A hydrodynamical mechanism to interpret femtosecond laser-induced self-assembled structures, Phys. Rev. B **92**, 041405 (2015).

[17] C. Wu, M. S. Christensen, J.-M. Savolainen, P. Balling, and L. V. Zhigilei, Generation of subsurface voids and a nanocrystalline surface layer in femtosecond laser irradiation of a single-crystal Ag target, Phys. Rev. B **91**, 035413 (2015).

[18] M. M. Martynyuk, Mechanism for metal damage by intense electromagnetic radiation, Sov. Phys. Tech. Phys. **21**, 430 (1976).

[19] R. Kelly and A. Miotello, Does normal boiling exist due to laser-pulse or ion bombardment?, J. Appl. Phys. **87**, 3177 (2000).

[20] N. M. Bulgakova and A. V. Bulgakov, Pulsed laser ablation of solids: transition from normal vaporization to phase explosion, Appl. Phys. A **73**, 199 (2001).

[21] A. Vailionis, E. G. Gamaly, V. Mizeikis, W. Yang, A. V. Rode, and S. Juodkazis, Evidence of superdense aluminium synthesized by ultrafast microexplosion, Nature Communications **2**, 445 (2011).

[22] L. Rapp, B. Haberl, C. J. Pickard, J. E. Bradby, E. G. Gamaly, J. S. Williams, and A. V. Rode, Experimental evidence of new tetragonal polymorphs of silicon formed through ultrafast laser-induced confined microexplosion, Nature Communications **6**, 7555 (2015).

[23] J. Narayan and A. Bhaumik, Novel phase of carbon, ferromagnetism, and conversion into diamond, J. Appl. Phys. **118**, 215303 (2015).

[24] A. Y. Vorobyev and C. Guo, Enhanced absorptance of gold following multipulse femtosecond laser ablation, Phys. Rev. B **72**, 195422 (2005).

[25] Y. Dai, M. He, H. Bian, B. Lu, X. Yan, and G. Ma, Femtosecond laser nanostructuring of silver film, Appl. Phys. A **106**, 567 (2012).

[26] V. J. Oboňa, V. Ocelík, J. C. Rao, J. Z. P. Skolski, G. R. B. E. Römer, A. J. Huis in ‘t Veld, and J. T. M. D. Hosson, Modification of Cu surface with picosecond laser pulses, Applied Surface Science **303**, 118 (2014).

[27] G. Paltauf and P. E. Dyer, Photomechanical Processes and Effects in Ablation, Chem. Rev. **103**, 487 (2003).

[28] E. Leveugle, D. S. Ivanov, and L. V. Zhigilei, Photomechanical spallation of molecular and metal targets: molecular dynamics study, Appl. Phys. A **79**, 1643 (2004).

[29] C.-J. Lin, F. Spaepen, and D. Turnbull, Picosecond Pulsed Laser-Induced Melting and Glass Formation in Metals, J. Non·Cryst. Solids **61-62**, 767 (1984).

[30] J. A. Alonso and J. M. López, Glass-forming ability in binary alloys produced by ion beam mixing and by laser quenching, Materials Letters **4**, 316 (1986).

[31] C. Wu and L. V. Zhigilei, Nanocrystalline and Polyicosahedral Structure of a Nanospike Generated on Metal Surface Irradiated by a Single Femtosecond Laser Pulse, J. Phys. Chem. C **120**, 4438 (2016).

[32] X. Sedao *et al.*, Growth Twinning and Generation of High-Frequency Surface Nanostructures in Ultrafast Laser-Induced Transient Melting and Resolidification, ACS Nano **10**, 6995 (2016).

[33] I. Gnilitskyi, I. Pavlov, F. Rotundo, L. Orazi, C. Martini, and F. Ö. Ilday, in *2015 Conference on Lasers and Electro-Optics (CLEO)*2015), pp. 1.

[34] L. Orazi, E. Liverani, A. Ascari, A. Fortunato, and L. Tomesani, Laser surface hardening of large cylindrical components utilizing ring spot geometry, CIRP Annals **63**, 233 (2014).

[35] S. Hou, Y. Huo, P. Xiong, Y. Zhang, S. Zhang, T. Jia, Z. Sun, J. Qiu, and Z. Xu, Formation of long- and short-periodic nanoripples on stainless steel irradiated by femtosecond laser pulses, J. Phys. D **44**, 505401 (2011).

[36] M. L. Trudeau and J. Y. Ying, Nanocrystalline materials in catalysis and electrocatalysis: Structure tailoring and surface reactivity, Nanostruct. Mater. **7**, 245 (1996).

[37] J. K. Nørskov, T. Bligaard, B. Hvolbæk, F. Abild-Pedersen, I. Chorkendorff, and C. H. Christensen, The nature of the active site in heterogeneous metal catalysis, Chem. Soc. Rev. **37**, 2163 (2008).

[38] Y. Lu, H. Zhang, and F. Liu, UV–visible reflectance spectra of nanocrystalline silver compacted under different pressures, Phys. Lett. A **342**, 351 (2005).

[39] C. Wu and L. V. Zhigilei, Microscopic mechanisms of laser spallation and ablation of metal targets from large-scale molecular dynamics simulations, Appl. Phys. A **114**, 11 (2014).

[40] E. L. Papadopoulou, M. Barberoglou, V. Zorba, A. Manousaki, A. Pagkozidis, E. Stratakis, and C. Fotakis, Reversible Photoinduced Wettability Transition of Hierarchical ZnO Structures, J. Phys. Chem. C **113**, 2891 (2009).

[41] A. Y. Vorobyev and C. Guo, Metal pumps liquid uphill, Appl. Phys. Lett. **94**, 224102 (2009).

[42] A. Y. Vorobyev and C. Guo, Laser turns silicon superwicking, Opt. Express **18**, 6455 (2010).

[43] A. Y. Vorobyev and C. Guo, Femtosecond laser blackening of platinum, J. Appl. Phys. **104**, 053516 (2008).

[44] A. Y. Vorobyev and C. Guo, Colorizing metals with femtosecond laser pulses, Appl. Phys. Lett. **92**, 041914 (2008).

[45] T. Y. Hwang, A. Y. Vorobyev, and C. Guo, Surface-plasmon-enhanced photoelectron emission from nanostructure-covered periodic grooves on metals, Phys. Rev. B **79**, 085425 (2009).

[46] E. S. Massaro, A. H. Hill, and E. M. Grumstrup, Super-Resolution Structured Pump–Probe Microscopy, ACS Photonics **3**, 501 (2016).

[47] A. M. Lindenberg, S. L. Johnson, and D. A. Reis, Visualization of Atomic-Scale Motions in Materials via Femtosecond X-Ray Scattering Techniques, Annual Review of Materials Research **47**, 425 (2017).

[48] A. Barty *et al.*, Ultrafast single-shot diffraction imaging of nanoscale dynamics, Nature Photonics **2**, 415 (2008).

[49] M. V. Shugaev, M. He, S. A. Lizunov, Y. Levy, T. J. Y. Derrien, V. P. Zhukov, N. M. Bulgakova, and L. V. Zhigilei, in *Advances in the Application of Lasers in Materials Science*, edited by P. M. Ossi (Springer International Publishing, Cham, Switzerland, 2018), pp. 107.

[50] K.-y. Hashimoto, *Surface acoustic wave devices in telecommunications: modelling and simulation*, (Springer-Verlag, Berlin, Heidelberg, 2000).

[51] A. Buvailo, Y. Xing, J. Hines, and E. Borguet, Thin polymer film based rapid surface acoustic wave humidity sensors, Sens. Actuators B **156**, 444 (2011).

[52] G. Schmera and L. B. Kish, Surface diffusion enhanced chemical sensing by surface acoustic waves, Sens. Actuators B **93**, 159 (2003).

[53] V. V. Kozhushko, A. M. Lomonosov, and P. Hess, Intrinsic Strength of Silicon Crystals in Pure- and Combined-Mode Fracture without Precrack, Phys. Rev. Lett. **98**, 195505 (2007).

[54] A. Lomonosov, A. P. Mayer, and P. Hess, in *Experimental Methods in the Physical Sciences*, edited by M. Levy, H. E. Bass, and R. Stern (Academic Press, New York, 2001).

[55] M. C. Jo and R. Guldiken, Dual surface acoustic wave-based active mixing in a microfluidic channel, Sens. Actuators B **196**, 1 (2013).

[56] L. Y. Yeo and J. R. Friend, Surface Acoustic Wave Microfluidics, Annu. Rev. Fluid Mech. **46**, 379 (2014).

[57] Y. Inoue, M. Matsukawa, and K. Sato, Effect of surface acoustic wave generated on ferroelectric support upon catalysis, J. Am. Chem. Soc. **111**, 8965 (1989).

[58] Y. Watanabe, Y. Inoue, and K. Sato, Activation of a thin film Pd catalyst for CO and ethanol oxidation by surface acoustic waves, Surf Sci. **357-358**, 769 (1996).

[59] S. Kelling, T. Mitrelias, Y. Matsumoto, V. P. Ostanin, and D. A. King, Acoustic wave enhancement of the catalytic oxidation of carbon monoxide over Pt{110}, J. Chem. Phys. **107**, 5609 (1997).

[60] S. Kelling and D. A. King, Acoustic Wave Enhancement of Catalytic Reaction Rates over Platinum Surfaces, Platinum Met. Rev. **42**, 8 (1998).

[61] S. Kelling, S. Cerasari, H. H. Rotermund, G. Ertl, and D. A. King, A photoemission electron microscopy (PEEM) study of the effect of surface acoustic waves on catalytic CO oxidation over Pt{110}, Chem. Phys. Lett. **293**, 325 (1998).

[62] N. Saito, H. Nishiyama, and Y. Inoue, Acoustic wave effects on catalysis: design of surfaces with artificially controllable functions for chemical reactions, Applied Surface Science **169-170**, 259 (2001).

[63] S. J. Reese, D. H. Hurley, and H. W. Rollins, Effect of surface acoustic waves on the catalytic decomposition of ethanol employing a comb transducer for ultrasonic generation, Ultrason. Sonochem. **13**, 283 (2006).

[64] Y. Inoue, Effects of acoustic waves-induced dynamic lattice distortion on catalytic and adsorptive properties of metal, alloy and metal oxide surfaces, Surf. Sci. Rep. **62**, 305 (2007).

[65] H. Nishiyama, N. Rattana, N. Saito, K. Sato, and Y. Inoue, Effects of Rayleigh Surface Acoustic Wave upon Adsorptive and Surface Properties of a Thin NiO Film, J. Phys. Chem. B **104**, 10602 (2000).

[66] D. R. Denison, Phonic Desorption, J. Vac. Sci. Technol. **6**, 214 (1969).

[67] C. Krischer and D. Lichtman, Observation of desorption from quartz induced by surface acoustic waves, Phys. Lett. A **44**, 99 (1973).

[68] V. V. Golovlev, S. L. Allman, W. R. Garrett, and C. H. Chen, Laser-induced acoustic desorption of electrons and ions, Appl. Phys. Lett. **71**, 852 (1997).

[69] B. Lindner and U. Seydel, Laser desorption mass spectrometry of nonvolatiles under shock wave conditions, Anal. Chem. **57**, 895 (1985).

[70] V. V. Golovlev, S. L. Allman, W. R. Garrett, N. I. Taranenko, and C. H. Chen, Laser-induced acoustic desorption, Int. J. Mass Spectrom. Ion Processes **169-170**, 69 (1997).

[71] A. V. Zinovev, I. V. Veryovkin, J. F. Moore, and M. J. Pellin, Laser-Driven Acoustic Desorption of Organic Molecules from Back-Irradiated Solid Foils, Anal. Chem. **79**, 8232 (2007).

[72] A. R. Dow, A. M. Wittrig, and H. I. Kenttämaa, Laser-Induced Acoustic Desorption Mass Spectrometry, Eur. J. Mass Spectrom. **18**, 77 (2012).

[73] M. V. Shugaev, A. J. Manzo, C. Wu, V. Y. Zaitsev, H. Helvajian, and L. V. Zhigilei, Strong enhancement of surface diffusion by nonlinear surface acoustic waves, Phys. Rev. B **91**, 235450 (2015).

[74] A. J. Manzo and H. Helvajian, Demonstration of enhanced surface mobility of adsorbate cluster species by surface acoustic wave excitation induced by a pulsed laser, Proc. SPIE **8969**, 896908 (2014).

[75] L. V. Zhigilei and H. Helvajian, Acoustic processes in materials, MRS Bull. **44** (2019).

[76] L. V. Zhigilei, Z. Lin, D. S. Ivanov, E. Leveugle, W. H. Duff, D. Thomas, C. Sevilla, and S. J. Guy, in *Laser-Surface Interactions for New Materials Production: Tailoring Structure and Properties*, edited by A. Miotello, and P. M. Ossi (Springer Berlin Heidelberg, Berlin, Heidelberg, 2010), pp. 43.

[77] C. Taillan, N. Combe, and J. Morillo, Nanoscale Self-Organization Using Standing Surface Acoustic Waves, Phys. Rev. Lett. **106**, 076102 (2011).

[78] C. Wu, V. Y. Zaitsev, and L. V. Zhigilei, Acoustic Enhancement of Surface Diffusion, J. Phys. Chem. C **117**, 9252 (2013).

[79] R. Stoneley, The propagation of surface elastic waves in a cubic crystal, Proc. R. Soc. London A **232**, 447 (1955).

[80] E. T. Karim, M. V. Shugaev, C. Wu, Z. Lin, H. Matsumoto, M. Conneran, J. Kleinert, R. F. Hainsey, and L. V. Zhigilei, Experimental characterization and atomistic modeling of interfacial void formation and detachment in short pulse laser processing of metal surfaces covered by solid transparent overlayers, Appl. Phys. A **122**, 407 (2016).

[81] Z. Lin, R. A. Johnson, and L. V. Zhigilei, Computational study of the generation of crystal defects in a bcc metal target irradiated by short laser pulses, Phys. Rev. B **77**, 214108 (2008).

[82] D. S. Ivanov, Z. Lin, B. Rethfeld, G. M. O'Connor, T. J. Glynn, and L. V. Zhigilei, Nanocrystalline structure of nanobump generated by localized photoexcitation of metal film, J. Appl. Phys. **107**, 013519 (2010).

[83] E. T. Karim, C. Wu, and L. V. Zhigilei, in *Fundamentals of Laser-Assisted Micro- and Nanotechnologies*, edited by V. P. Veiko, and V. I. Konov (Springer International Publishing, Cham, 2014), pp. 27.

[84] S. Zhao, E. N. Hahn, B. Kad, B. A. Remington, C. E. Wehrenberg, E. M. Bringa, and M. A. Meyers, Amorphization and nanocrystallization of silicon under shock compression, Acta Mater. **103**, 519 (2016).

[85] M. P. Allen and D. J. Tildesley, *Computer simulation of liquids*, (Clarendon Press, Oxford, 1987).

[86] D. Frenkel and B. Smit, *Understanding molecular simulation: from algorithms to applications*, (Academic Press, San Diego, 1996).

[87] W. C. Gear, *Numerical initial value problems in ordinary different equations*, (Prentice-hall, Inc., Englewood Cliffs, New Jersey, 1971).

[88] L. Verlet, Computer "Experiments" on Classical Fluids. I. Thermodynamical Properties of Lennard-Jones Molecules, Phys. Rev. **159**, 98 (1967).

[89] W. Mattson and B. M. Rice, Near-neighbor calculations using a modified cell-linked list method, Computer Physics Communications **119**, 135 (1999).

[90] M. Tuckerman, B. J. Berne, and G. J. Martyna, Reversible multiple time scale molecular dynamics, J. Chem. Phys. **97**, 1990 (1992).

[91] L. V. Zhigilei, E. Leveugle, D. S. Ivanov, Z. Lin, and A. N. Volkov, in *Nanosized Material Synthesis by Action of High-Power Energy Fluxes on Matter (in Russian)* (Siberian Branch of the Russian Academy of Sciences, Novosibirsk, 2010), pp. 147.

[92] J. Hohlfeld, S. S. Wellershoff, J. Güdde, U. Conrad, V. Jähnke, and E. Matthias, Electron and lattice dynamics following optical excitation of metals, Chem. Phys. **251**, 237 (2000).

[93] M. Bonn, D. N. Denzler, S. Funk, M. Wolf, S. S. Wellershoff, and J. Hohlfeld, Ultrafast electron dynamics at metal surfaces: Competition between electron-phonon coupling and hot-electron transport, Phys. Rev. B **61**, 1101 (2000).

[94] B. Rethfeld, A. Kaiser, M. Vicanek, and G. Simon, Ultrafast dynamics of nonequilibrium electrons in metals under femtosecond laser irradiation, Phys. Rev. B **65**, 214303 (2002).

[95] B. Y. Mueller and B. Rethfeld, Relaxation dynamics in laser-excited metals under nonequilibrium conditions, Phys. Rev. B **87**, 035139 (2013).

[96] M. I. Kaganov, I. M. Lifshitz, and L. V. Tanatarov, Relaxation between Electrons and the Crystalline Lattice, JETP **4**, 173 (1957).

[97] C.-Y. Shih *et al.*, Two mechanisms of nanoparticle generation in picosecond laser ablation in liquids: the origin of the bimodal size distribution, Nanoscale **10**, 6900 (2018).

[98] D. M. Nenno, B. Rethfeld, and H. C. Schneider, Particle-in-cell simulation of ultrafast hot-carrier transport in Fe/Au heterostructures, Phys. Rev. B **98**, 224416 (2018).

[99] S.-S. Wellershoff, J. Hohlfeld, J. Güdde, and E. Matthias, The role of electron–phonon coupling in femtosecond laser damage of metals, Appl. Phys. A **69**, S99 (1999).

[100] N. M. Bulgakova and I. M. Bourakov, Phase explosion under ultrashort pulsed laser ablation: modeling with analysis of metastable state of melt, Applied Surface Science **197-198**, 41 (2002).

[101] Z. Lin, L. V. Zhigilei, and V. Celli, Electron-phonon coupling and electron heat capacity of metals under conditions of strong electron-phonon nonequilibrium, Phys. Rev. B **77**, 075133 (2008).

[102] D. S. Ivanov and L. V. Zhigilei, Combined atomistic-continuum modeling of short-pulse laser melting and disintegration of metal films, Phys. Rev. B **68**, 064114 (2003).

[103] R. H. M. Groeneveld, R. Sprik, and A. Lagendijk, Femtosecond spectroscopy of electron-electron and electron-phonon energy relaxation in Ag and Au, Phys. Rev. B **51**, 11433 (1995).

[104] L. V. Zhigilei, Z. Lin, and D. S. Ivanov, Atomistic Modeling of Short Pulse Laser Ablation of Metals: Connections between Melting, Spallation, and Phase Explosion, J. Phys. Chem. C **113**, 11892 (2009).

[105] V. Zhigilei and B. J. Garrison, Pressure Waves in Microscopic Simulations of Laser Ablation Leonid, MRS Proc. **538**, 491, 491 (1998).

[106] C. Schäfer, H. M. Urbassek, L. V. Zhigilei, and B. J. Garrison, Pressure-transmitting boundary conditions for molecular-dynamics simulations, Comput. Mater. Sci. **24**, 421 (2002).

[107] R. C. Weast (ed.), *Handbook of Chemistry and Physics*, 64 ed., (CRC Press, Boca Raton, 1983).

[108] E. T. Karim, M. Shugaev, C. Wu, Z. Lin, R. F. Hainsey, and L. V. Zhigilei, Atomistic simulation study of short pulse laser interactions with a metal target under conditions of spatial confinement by a transparent overlayer, J. Appl. Phys. **115**, 183501 (2014).

[109] K. S. Gadre and T. L. Alford, Contact angle measurements for adhesion energy evaluation of silver and copper films on parylene-n and SiO2 substrates, J. Appl. Phys. **93**, 919 (2003).

[110] E. A. Zabolotskaya, Nonlinear propagation of plane and circular Rayleigh waves in isotropic solids, J. Acoust. Soc. Am. **91**, 2569 (1992).

[111] M. F. Hamilton, Y. A. Il'insky, and E. A. Zabolotskaya, Local and nonlocal nonlinearity in Rayleigh waves, J. Acoust. Soc. Am. **97**, 882 (1995).

[112] E. Y. Knight, M. F. Hamilton, Y. A. Il'inskii, and E. A. Zabolotskaya, On Rayleigh wave nonlinearity, and analytical approximation of the shock formation distance, J. Acoust. Soc. Am. **102**, 2529 (1997).

[113] V. Y. Klimenko and A. N. Dremin, Structure of a shock-wave front in a solid, Sov. Phys. Dokl. **25**, 288 (1980).

[114] V. V. Zhakhovskii, K. Nishihara, and S. I. Anisimov, Shock wave structure in dense gases, Journal of Experimental and Theoretical Physics Letters **66**, 99 (1997).

[115] S. I. Anisimov, V. V. Zhakhovskii, and V. E. Fortov, Shock wave structure in simple liquids, Journal of Experimental and Theoretical Physics Letters **65**, 755 (1997).

[116] V. V. Zhakhovskiĭ, S. V. Zybin, K. Nishihara, and S. I. Anisimov, Shock Wave Structure in Lennard-Jones Crystal via Molecular Dynamics, Phys. Rev. Lett. **83**, 1175 (1999).

[117] V. V. Zhakhovsky, M. M. Budzevich, N. A. Inogamov, I. I. Oleynik, and C. T. White, Two-Zone Elastic-Plastic Single Shock Waves in Solids, Phys. Rev. Lett. **107**, 135502 (2011).

[118] M. M. Budzevich, V. V. Zhakhovsky, C. T. White, and I. I. Oleynik, Evolution of Shock-Induced Orientation-Dependent Metastable States in Crystalline Aluminum, Phys. Rev. Lett. **109**, 125505 (2012).

[119] V. V. Zhakhovsky, M. M. Budzevich, A. C. Landerville, I. I. Oleynik, and C. T. White, Laminar, cellular, transverse, and multiheaded pulsating detonations in condensed phase energetic materials from molecular dynamics simulations, Phys. Rev. E **90**, 033312 (2014).

[120] A. A. Kolomenskii, V. A. Lioubimov, S. N. Jerebtsov, and H. A. Schuessler, Nonlinear surface acoustic wave pulses in solids: Laser excitation, propagation, interactions (invited), Rev. Sci. Instrum. **74**, 448 (2003).

[121] S. D. Stoddard and J. Ford, Numerical Experiments on the Stochastic Behavior of a Lennard-Jones Gas System, Phys. Rev. A **8**, 1504 (1973).

[122] C. Taillan, N. Combe, and J. Morillo, Chladni figures at the nanoscale, The European Physical Journal B **88**, 317 (2015).

[123] I. A. Viktorov, *Acoustic surface waves in solids (in Russian)*, (Nauka, Moscow, 1981).

[124] D. Royer and E. Dieulesaint, Rayleigh wave velocity and displacement in orthorhombic, tetragonal, hexagonal, and cubic crystals, J. Acoust. Soc. Am. **76**, 1438 (1984).

[125] A. M. Lomonosov and P. Hess, Impulsive Fracture of Silicon by Elastic Surface Pulses with Shocks, Phys. Rev. Lett. **89**, 095501 (2002).

[126] V. V. Kozhushko and P. Hess, Anisotropy of the strength of Si studied by a laser-based contact-free method, Phys. Rev. B **76**, 144105 (2007).

[127] K. A. Jackson, The Interface Kinetics of Crystal Growth Processes, Interface Sci. **10**, 159 (2002).

[128] Y. Ashkenazy and R. S. Averback, Kinetic stages in the crystallization of deeply undercooled body-centered-cubic and face-centered-cubic metals, Acta Mater. **58**, 524 (2010).

[129] M. I. Mendelev, Molecular dynamics simulation of solidification and devitrification in a one-component system, Modell. Simul. Mater. Sci. Eng. **20**, 17 (2012).

[130] Y. Mishin, Atomistic modeling of the γ and γ'-phases of the Ni–Al system, Acta Mater. **52**, 1451 (2004).

[131] S.-N. Luo, T. J. Ahrens, T. Çağın, A. Strachan, W. A. Goddard, and D. C. Swift, Maximum superheating and undercooling: Systematics, molecular dynamics simulations, and dynamic experiments, Phys. Rev. B **68**, 134206 (2003).

[132] N. I. Polushkin, V. Oliveira, R. Vilar, M. He, M. V. Shugaev, and L. V. Zhigilei, Phase-Change Magnetic Memory: Rewritable Ferromagnetism by Laser Quenching of Chemical Disorder in ${\mathrm{Fe}}_{60}{\mathrm{Al}}_{40}$ Alloy, Phys. Rev. Appl. **10**, 024023 (2018).

[133] J. Ehrler *et al.*, Laser-Rewriteable Ferromagnetism at Thin-Film Surfaces, ACS Appl. Mater. Interfaces **10**, 15232 (2018).

[134] L. V. Zhigilei and B. J. Garrison, Microscopic mechanisms of laser ablation of organic solids in the thermal and stress confinement irradiation regimes, J. Appl. Phys. **88**, 1281 (2000).

[135] J.-M. Savolainen, M. S. Christensen, and P. Balling, Material swelling as the first step in the ablation of metals by ultrashort laser pulses, Phys. Rev. B **84**, 193410 (2011).

[136] A. A. Ionin, S. I. Kudryashov, A. E. Ligachev, S. V. Makarov, L. V. Seleznev, and D. V. Sinitsyn, Nanoscale cavitation instability of the surface melt along the grooves of one-dimensional nanorelief gratings on an aluminum surface, J ETP Lett. **94**, 266 (2011).

[137] S. I. Ashitkov, N. A. Inogamov, V. V. Zhakhovskii, Y. N. Emirov, M. B. Agranat, I. I. Oleinik, S. I. Anisimov, and V. E. Fortov, Formation of nanocavities in the surface layer of an aluminum target irradiated by a femtosecond laser pulse, J ETP Lett. **95**, 176 (2012).

[138] S. V. Starikov and V. V. Pisarev, Atomistic simulation of laser-pulse surface modification: Predictions of models with various length and time scales, J. Appl. Phys. **117**, 135901 (2015).

[139] M. Levy, H. E. Bass, and R. Stern (ed.), *Modern Acoustical Techniques for the Measurement of Mechanical Properties*, (Academic Press, New York, 2001).

[140] P. Hess, Surface Acoustic Waves in Materials Science, Phys. Today **55**, 42 (2002).

[141] M. V. Shugaev and N. M. Bulgakova, Thermodynamic and stress analysis of laser-induced forward transfer of metals, Appl. Phys. A **101**, 103 (2010).

[142] B. S. Yilbas, Short-pulse laser heating of gold-chromium layers: thermo-elasto-plastic analysis, J. Phys. D **35**, 1210 (2002).

[143] D. Y. Tzou and E. J. Pfautsch, Ultrafast heating and thermomechanical coupling induced by femstosecond lasers, Journal of Engineering Mathematics **61**, 231 (2008).

[144] Y.-M. Lee and T.-W. Tsai, Effect of interfacial contact conductance on thermo-elastic response in a two-layered material heated by ultra-fast pulse-laser, J. Phys. D **41**, 045308 (2008).

[145] Y. P. Meshcheryakov and N. M. Bulgakova, Thermoelastic modeling of microbump and nanojet formation on nanosize gold films under femtosecond laser irradiation, Appl. Phys. A **82**, 363 (2005).

[146] J. E. Vidale and R. W. Clayton, A stable free-surface boundary condition for two-dimensional elastic finite-difference wave simulation, GEOPHYSICS **51**, 2247 (1986).

[147] E. Vanagas *et al.*, *Glass cutting by femtosecond pulsed irradiation*, (SPIE, 2004), Vol. 3, 2.

[148] L. V. Zhigilei and B. J. Garrison, Microscopic simulation of short-pulse laser damage of melanin particles, Proc. SPIE **3254**, 135 (1998).

[149] M. V. Shugaev, I. Gnilitskyi, N. M. Bulgakova, and L. V. Zhigilei, Mechanism of single-pulse ablative generation of laser-induced periodic surface structures, Phys. Rev. B **96**, 205429 (2017).

[150] K. Han, J. P. Hirth, and J. D. Embury, Modeling the formation of twins and stacking faults in the ag-cu system, Acta Mater. **49**, 1537 (2001).

[151] X. Zhang, A. Misra, H. Wang, T. D. Shen, M. Nastasi, T. E. Mitchell, J. P. Hirth, R. G. Hoagland, and J. D. Embury, Enhanced hardening in Cu/330 stainless steel multilayers by nanoscale twinning, Acta Mater. **52**, 995 (2004).

[152] S. Xue, Z. Fan, Y. Chen, J. Li, H. Wang, and X. Zhang, The formation mechanisms of growth twins in polycrystalline Al with high stacking fault energy, Acta Mater. **101**, 62 (2015).

[153] R. C. Nelson, T. L. Einstein, S. V. Khare, and P. J. Rous, Energies of steps, kinks, and defects on Ag{100} and Ag{111} using the embedded atom method, and some consequences, Surf Sci. **295**, 462 (1993).

[154] T. Frolov and M. Asta, Step free energies at faceted solid-liquid interfaces from equilibrium molecular dynamics simulations, J. Chem. Phys. **137**, 214108 (2012).

[155] J. J. Hoyt, M. Asta, and A. Karma, Method for Computing the Anisotropy of the Solid-Liquid Interfacial Free Energy, Phys. Rev. Lett. **86**, 5530 (2001).

[156] J. R. Morris, Complete mapping of the anisotropic free energy of the crystal-melt interface in Al, Phys. Rev. B **66**, 144104 (2002).

[157] R. E. Rozas and J. Horbach, Capillary wave analysis of rough solid-liquid interfaces in nickel, EPL (Europhysics Letters) **93**, 26006 (2011).

[158] A. R. Honerkamp-Smith, P. Cicuta, M. D. Collins, S. L. Veatch, M. den Nijs, M. Schick, and S. L. Keller, Line Tensions, Correlation Lengths, and Critical Exponents in Lipid Membranes Near Critical Points, Biophys. J. **95**, 236 (2008).

[159] F. P. Kuhl and C. R. Giardina, Elliptic Fourier features of a closed contour, Comput. Vison Graph. **18**, 236 (1982).

[160] J. R. Morris and X. Song, The melting lines of model systems calculated from coexistence simulations, J. Chem. Phys. **116**, 9352 (2002).

[161] N. Amenta, M. Bern, and D. Eppstein, The Crust and the β-Skeleton: Combinatorial Curve Reconstruction, Graph. Model Im. Proc. **60**, 125 (1998).

[162] G. J. Gloor, G. Jackson, F. J. Blas, and E. de Miguel, Test-area simulation method for the direct determination of the interfacial tension of systems with continuous or discontinuous potentials, J. Chem. Phys. **123**, 134703 (2005).

[163] R. W. Zwanzig, High-Temperature Equation of State by a Perturbation Method. I. Nonpolar Gases, J. Chem. Phys. **22**, 1420 (1954).

[164] M. I. Mendelev, T. L. Underwood, and G. J. Ackland, Development of an interatomic potential for the simulation of defects, plasticity, and phase transformations in titanium, J. Chem. Phys. **145**, 154102 (2016).

[165] H. Okumura and F. Yonezawa, Liquid–vapor coexistence curves of several interatomic model potentials, J. Chem. Phys. **113**, 9162 (2000).

[166] H. Okumura and F. Yonezawa, Reliable Determination of the Liquid-Vapor Critical Point by the NVT Plus Test Particle Method, J. Phys. Soc. Jpn. **70**, 1990 (2001).

[167] S. R. Wilson, K. G. S. H. Gunawardana, and M. I. Mendelev, Solid-liquid interface free energies of pure bcc metals and B2 phases, J. Chem. Phys. **142**, 134705 (2015).

[168] D. W. Bäuerle, *Laser Processing and Chemistry*, (Springer Science & Business Media, Berlin, 2013).

[169] M. von Allmen and A. Blatter, *Laser Beam Interactions with Materials*, (Springer, Berlin, 1998).

[170] J. Kaspar and A. Luft, Microstructure Formed in Body Centred Cubic Metals by Laser Shock Processing, Surf. Eng. **17**, 379 (2001).

[171] J. G. Hoekstra, S. B. Qadri, J. R. Scully, and J. M. Fitz-Gerald, Laser Surface Modification of a Crystalline Al-Co-Ce Alloy for Enhanced Corrosion Resistance, Advanced Engineering Materials **7**, 805 (2005).

[172] L. Xie, K. Funatani, and G. E. Totten (ed.), *Handbook of Metallurgical Process Design*, (CRC Press, 2004).

[173] R. Le Harzic, N. Huot, E. Audouard, C. Jonin, P. Laporte, S. Valette, A. Fraczkiewicz, and R. Fortunier, Comparison of heat-affected zones due to nanosecond and femtosecond laser pulses using transmission electronic microscopy, Appl. Phys. Lett. **80**, 3886 (2002).

[174] V. Margetic, K. Niemax, and R. Hergenröder, Application of Femtosecond Laser Ablation Time-of-Flight Mass Spectrometry to In-Depth Multilayer Analysis, Anal. Chem. **75**, 3435 (2003).

[175] Q. Feng, Y. N. Picard, H. Liu, S. M. Yalisove, G. Mourou, and T. M. Pollock, Femtosecond laser micromachining of a single-crystal superalloy, Scr. Mater. **53**, 511 (2005).

[176] T. H. R. Crawford, J. Yamanaka, G. A. Botton, and H. K. Haugen, High-resolution observations of an amorphous layer and subsurface damage formed by femtosecond laser irradiation of silicon, J. Appl. Phys. **103**, 053104 (2008).

[177] X. Sedao, C. Maurice, F. Garrelie, J.-P. Colombier, S. Reynaud, R. Quey, and F. Pigeon, Influence of crystal orientation on the formation of femtosecond laser-induced periodic surface structures and lattice defects accumulation, Appl. Phys. Lett. **104**, 171605 (2014).

[178] C. A. Becker, F. Tavazza, and L. E. Levine, Implications of the choice of interatomic potential on calculated planar faults and surface properties in nickel, Philos. Mag. **91**, 3578 (2011).

[179] Dislocation Extraction Algorithm (DXA) tool, http://ovito.org/dxa/download.html (Accessed 01 2019).

[180] A. Stukowski and K. Albe, Extracting dislocations and non-dislocation crystal defects from atomistic simulation data, Modell. Simul. Mater. Sci. Eng. **18**, 085001 (2010).

[181] E. D. Palik, *Handbook of Optical Constants of Solids*, (Academic Press, San Diego, 1998).

[182] G. P. Purja Pun and Y. Mishin, Development of an interatomic potential for the Ni-Al system, Philos. Mag. **89**, 3245 (2009).

[183] Z. Lin, E. Leveugle, E. M. Bringa, and L. V. Zhigilei, Molecular Dynamics Simulation of Laser Melting of Nanocrystalline Au, J. Phys. Chem. C **114**, 5686 (2010).

[184] D. S. Ivanov and L. V. Zhigilei, Kinetic Limit of Heterogeneous Melting in Metals, Phys. Rev. Lett. **98**, 195701 (2007).

[185] M. He, C. Wu, M. V. Shugaev, G. D. Samolyuk, and L. V. Zhigilei, Computational study of short pulse laser induced generation of crystal defects in Ni-based single-phase binary solid solution alloys, J. Phys. Chem. C **123**, 2202 (2019).

[186] L. Zhibin and L. V. Zhigilei, Temperature dependences of the electron–phonon coupling, electron heat capacity and thermal conductivity in Ni under femtosecond laser irradiation, Applied Surface Science **253**, 6295 (2007).

[187] D. S. Ivanov and L. V. Zhigilei, Combined atomistic-continuum model for simulation of laser interaction with metals: application in the calculation of melting thresholds in Ni targets of varying thickness, Appl. Phys. A **79**, 977 (2004).

[188] B. H. Billings and D. E. Gray, *American Institute of Physics handbook*, 3 ed., (McGraw-Hill, New York, 1972).

[189] C. Wu, E. T. Karim, A. N. Volkov, and L. V. Zhigilei, in *Lasers in Materials Science*, edited by M. Castillejo, P. M. Ossi, and L. Zhigilei (Springer International Publishing, Cham, 2014), pp. 67.

[190] A. Kelly, G. W. Groves, and P. Kidd, *Crystallography and Crystal Defects*, revised ed., (Wiley, Chichester, 2000).

[191] J. R. Rice and G. E. Beltz, The activation energy for dislocation nucleation at a crack, J. Mech. Phys. Solids **42**, 333 (1994).

[192] M. Forsblom and G. Grimvall, How superheated crystals melt, Nature Materials **4**, 388 (2005).

[193] K. M. T. Ahmmed, C. Grambow, and A.-M. Kietzig, Fabrication of Micro/Nano Structures on Metals by Femtosecond Laser Micromachining, Micromachines **5**, 1219 (2014).

[194] T. V. Kononenko, S. V. Garnov, S. M. Klimentov, V. I. Konov, E. N. Loubnin, F. Dausinger, A. Raiber, and C. Taut, Laser ablation of metals and ceramics in picosecond–nanosecond pulsewidth in the presence of different ambient atmospheres, Applied Surface Science **109-110**, 48 (1997).

[195] A. Cunha, A. P. Serro, V. Oliveira, A. Almeida, R. Vilar, and M.-C. Durrieu, Wetting behaviour of femtosecond laser textured Ti–6Al–4V surfaces, Applied Surface Science **265**, 688 (2013).

[196] K. Bazaka, R. J. Crawford, and E. P. Ivanova, Do bacteria differentiate between degrees of nanoscale surface roughness?, Biotechnology Journal **6**, 1103 (2011).

[197] P. T. Mannion, J. Magee, E. Coyne, G. M. O'Connor, and T. J. Glynn, The effect of damage accumulation behaviour on ablation thresholds and damage morphology in ultrafast laser micro-machining of common metals in air, Applied Surface Science **233**, 275 (2004).

[198] G. Raciukaitis, M. Brikas, P. Gecys, and M. Gedvilas, Accumulation effects in laser ablation of metals with high-repetition-rate lasers, Proc. SPIE **7005**, 70052L (2008,).

[199] J. Byskov-Nielsen, J.-M. Savolainen, M. S. Christensen, and P. Balling, Ultra-short pulse laser ablation of metals: threshold fluence, incubation coefficient and ablation rates, Appl. Phys. A **101**, 97 (2010).

[200] Y. Jee, M. F. Becker, and R. M. Walser, Laser-induced damage on single-crystal metal surfaces, J. Opt. Soc. Am. B **5**, 648 (1988).

[201] N. Koumvakalis, C. S. Lee, and M. Bass, *Single And Multiple Pulse Catastrophic Damage In Diamond-Turned Cu And Ag Mirrors At 10.6, 1.06, And 0.532 μm*, (SPIE, 1983), Vol. 22, 4.

[202] S. J. Thomas, R. F. Harrison, and J. F. Figueira, Observations of the morphology of laser-induced damage in copper mirrors, Appl. Phys. Lett. **40**, 200 (1982).

[203] J. E. Sipe, J. F. Young, J. S. Preston, and H. M. van Driel, Laser-induced periodic surface structure. I. Theory, Phys. Rev. B **27**, 1141 (1983).

[204] F. Garrelie, J. P. Colombier, F. Pigeon, S. Tonchev, N. Faure, M. Bounhalli, S. Reynaud, and O. Parriaux, Evidence of surface plasmon resonance in ultrafast laser-induced ripples, Opt. Express **19**, 9035 (2011).

[205] H. Zhang, J.-P. Colombier, C. Li, N. Faure, G. Cheng, and R. Stoian, Coherence in ultrafast laser-induced periodic surface structures, Phys. Rev. B **92**, 174109 (2015).

[206] M. Huang, F. Zhao, Y. Cheng, N. Xu, and Z. Xu, Origin of Laser-Induced Near-Subwavelength Ripples: Interference between Surface Plasmons and Incident Laser, ACS Nano **3**, 4062 (2009).

[207] C. S. R. Nathala, A. Ajami, A. A. Ionin, S. I. Kudryashov, S. V. Makarov, T. Ganz, A. Assion, and W. Husinsky, Experimental study of fs-laser induced sub-100-nm periodic surface structures on titanium, Opt. Express **23**, 5915 (2015).

[208] J. Bonse, J. Krüger, S. Höhm, and A. Rosenfeld, Femtosecond laser-induced periodic surface structures, Journal of Laser Applications **24**, 042006 (2012).

[209] S. Sakabe, M. Hashida, S. Tokita, S. Namba, and K. Okamuro, Mechanism for self-formation of periodic grating structures on a metal surface by a femtosecond laser pulse, Phys. Rev. B **79**, 033409 (2009).

[210] M. Hashida, Y. Miyasaka, Y. Ikuta, S. Tokita, and S. Sakabe, Crystal structures on a copper thin film with a surface of periodic self-organized nanostructures induced by femtosecond laser pulses, Phys. Rev. B **83**, 235413 (2011).

[211] X.-F. Li, C.-Y. Zhang, H. Li, Q.-F. Dai, S. Lan, and S.-L. Tie, Formation of 100-nm periodic structures on a titanium surface by exploiting the oxidation and third harmonic generation induced by femtosecond laser pulses, Opt. Express **22**, 28086 (2014).

[212] J. Reif, F. Costache, O. Varlamova, G. Jia, and M. Ratzke, Self-organized regular surface patterning by pulsed laser ablation, physica status solidi c **6**, 681 (2009).

[213] A. A. Ionin, S. I. Kudryashov, S. V. Makarov, L. V. Seleznev, D. V. Sinitsyn, A. E. Ligachev, E. V. Golosov, and Y. R. Kolobov, Sub-100 nanometer transverse gratings written by femtosecond laser pulses on a titanium surface, Laser Phys. Lett. **10**, 056004 (2013).

[214] M. B. Agranat, S. I. Ashitkov, V. E. Fortov, A. V. Kirillin, A. V. Kostanovskii, S. I. Anisimov, and P. S. Kondratenko, Use of optical anisotropy for study of ultrafast phase transformations at solid surfaces, Appl. Phys. A **69**, 637 (1999).

[215] W.-L. Chan, R. S. Averback, D. G. Cahill, and Y. Ashkenazy, Solidification Velocities in Deeply Undercooled Silver, Phys. Rev. Lett. **102**, 095701 (2009).

[216] S. C. Chen, D. G. Cahill, and C. P. Grigoropoulos, Melting and Surface Deformation in Pulsed Laser Surface Micromodification of Ni-P Disks, Journal of Heat Transfer **122**, 107 (1999).

[217] J. Chen, W.-K. Chen, J. Tang, and P. M. Rentzepis, Time-resolved structural dynamics of thin metal films heated with femtosecond optical pulses, Proc. Natl. Acad. Sci. U.S.A. **108**, 18887 (2011).

[218] J. Wang, N. Li, O. Anderoglu, X. Zhang, A. Misra, J. Y. Huang, and J. P. Hirth, Detwinning mechanisms for growth twins in face-centered cubic metals, Acta Mater. **58**, 2262 (2010).

[219] J. M. Howe, *Interfaces in Materials: Atomic Structure, Thermodynamics and Kinetics of Solid-Vapor, Solid-Liquid and Solid-Solid Interfaces*, (John Wiley & Sons Inc, New York, 1997).

[220] D. R. Lide, *CRC Handbook of Chemistry and Physics*, 85 ed., (CRC Press, Boca Raton, FL, 2004).

[221] Y. S. Touloukian, R. K. Kirby, R. E. Taylor, and P. D. Desai, *Thermal Expansion Metallic Elements and Alloys*, (IFI/Plenum, New York, 1975), Vol. 12, Thermophysical Properties of Matter - the TPRC Data Series.

[222] W. H. Duff and L. V. Zhigilei, Computational study of cooling rates and recrystallization kinetics in short pulse laser quenching of metal targets, J Phys Conf Ser. **59**, 413 (2007).

[223] L. Lu, Y. Shen, X. Chen, L. Qian, and K. Lu, Ultrahigh Strength and High Electrical Conductivity in Copper, Science **304**, 422 (2004).

[224] E. Ma, Y. M. Wang, Q. H. Lu, M. L. Sui, L. Lu, and K. Lu, Strain hardening and large tensile elongation in ultrahigh-strength nano-twinned copper, Appl. Phys. Lett. **85**, 4932 (2004).

[225] M. Dao, L. Lu, Y. F. Shen, and S. Suresh, Strength, strain-rate sensitivity and ductility of copper with nanoscale twins, Acta Mater. **54**, 5421 (2006).

[226] X. Zhang, A. Misra, H. Wang, M. Nastasi, J. D. Embury, T. E. Mitchell, R. G. Hoagland, and J. P. Hirth, Nanoscale-twinning-induced strengthening in austenitic stainless steel thin films, Appl. Phys. Lett. **84**, 1096 (2004).

[227] A. M. Hodge, Y. M. Wang, and T. W. Barbee, Mechanical deformation of high-purity sputter-deposited nano-twinned copper, Scr. Mater. **59**, 163 (2008).

[228] L. Lu, X. Chen, X. Huang, and K. Lu, Revealing the Maximum Strength in Nanotwinned Copper, Science **323**, 607 (2009).

[229] X. Zhang, A. Misra, H. Wang, A. L. Lima, M. F. Hundley, and R. G. Hoagland, Effects of deposition parameters on residual stresses, hardness and electrical resistivity of nanoscale twinned 330 stainless steel thin films, J. Appl. Phys. **97**, 094302 (2005).

[230] T. Zhu, J. Li, A. Samanta, H. G. Kim, and S. Suresh, Interfacial plasticity governs strain rate sensitivity and ductility in nanostructured metals, Proc. Natl. Acad. Sci. U.S.A. **104**, 3031 (2007).

[231] K. A. Afanasyev and F. Sansoz, Strengthening in Gold Nanopillars with Nanoscale Twins, Nano Letters **7**, 2056 (2007).

[232] D. Jang, X. Li, H. Gao, and J. R. Greer, Deformation mechanisms in nanotwinned metal nanopillars, Nature Nanotechnology **7**, 594 (2012).

[233] O. Anderoglu, A. Misra, H. Wang, F. Ronning, M. F. Hundley, and X. Zhang, Epitaxial nanotwinned Cu films with high strength and high conductivity, Appl. Phys. Lett. **93**, 083108 (2008).

[234] O. Anderoglu, A. Misra, H. Wang, and X. Zhang, Thermal stability of sputtered Cu films with nanoscale growth twins, J. Appl. Phys. **103**, 094322 (2008).

[235] C. J. Shute, B. D. Myers, S. Xie, T. W. Barbee, A. M. Hodge, and J. R. Weertman, Microstructural stability during cyclic loading of multilayer copper/copper samples with nanoscale twinning, Scr. Mater. **60**, 1073 (2009).

[236] C. J. Shute, B. D. Myers, S. Xie, S. Y. Li, T. W. Barbee, A. M. Hodge, and J. R. Weertman, Detwinning, damage and crack initiation during cyclic loading of Cu samples containing aligned nanotwins, Acta Mater. **59**, 4569 (2011).

[237] L. E. Murr, E. Moin, F. Greulich, and K. P. Staudhammer, The contribution of deformation twins to yield stress: The Hall-Petch law for inter-twin spacing, Scripta Metallurgica **12**, 1031 (1978).

[238] M. D. Merz and S. D. Dahlgren, Tensile strength and work hardening of ultrafine-grained high-purity copper, J. Appl. Phys. **46**, 3235 (1975).

[239] D. Bufford, Y. Liu, Y. Zhu, Z. Bi, Q. X. Jia, H. Wang, and X. Zhang, Formation Mechanisms of High-density Growth Twins in Aluminum with High Stacking-Fault Energy, Materials Research Letters **1**, 51 (2013).

[240] J. Y. Li, C. Ni, J. Y. Liu, M. J. Jin, W. Li, and X. J. Jin, Extraordinary stability of nano-twinned structure formed during phase transformation coupled with grain growth in electrodeposited Co–Ni alloys, Materials Chemistry and Physics **148**, 1202 (2014).

[241] L. Zhong, J. Wang, H. Sheng, Z. Zhang, and S. X. Mao, Formation of monatomic metallic glasses through ultrafast liquid quenching, Nature **512**, 177 (2014).

[242] D. R. Lide (ed.), *Handbook of Chemistry and Physics*, 84 ed., (CRC Press. Boca Raton, Boca Raton, FL, 2003).

[243] J. Donachie and J. Matthew, *Titanium: A Technical Guide*, 2 ed., (ASM International, Materials Park, OH, 2000).

[244] E. O. Ezugwu and Z. M. Wang, Titanium alloys and their machinability—a review, Journal of Materials Processing Technology **68**, 262 (1997).

[245] in *Surface Engineered Surgical Tools and Medical Devices*, edited by M. J. Jackson, and W. Ahmed (Springer US, Boston, MA, 2007), pp. 533.

[246] H. J. Rack and J. I. Qazi, Titanium alloys for biomedical applications, Materials Science and Engineering: C **26**, 1269 (2006).

[247] R. R. Boyer, An overview on the use of titanium in the aerospace industry, Materials Science and Engineering: A **213**, 103 (1996).

[248] R. R. Boyer and R. D. Briggs, The use of β titanium alloys in the aerospace industry, Journal of Materials Engineering and Performance **14**, 681 (2005).

[249] C. Veiga, J. P. Devim, and A. J. R. Loureiro, Properties and Applications of Titanium Alloys: a Brief Review, Reviews on advanced Materials Science **32**, 133 (2012).

[250] K. Otsuka and X. Ren, Physical metallurgy of Ti–Ni-based shape memory alloys, Prog. Mater Sci. **50**, 511 (2005).

[251] H. Zong, Z. Ni, X. Ding, T. Lookman, and J. Sun, Origin of low thermal hysteresis in shape memory alloy ultrathin films, Acta Mater. **103**, 407 (2016).

[252] H. Zong, X. Ding, T. Lookman, and J. Sun, Twin boundary activated α → ω phase transformation in titanium under shock compression, Acta Mater. **115**, 1 (2016).

[253] A. Serra, D. J. Bacon, and R. C. Pond, Dislocations in interfaces in the h.c.p. metals—I. Defects formed by absorption of crystal dislocations, Acta Mater. **47**, 1425 (1999).

[254] C. Ni, H. Ding, M. Asta, and X. Jin, Computational study of <11¯00> symmetric tilt grain boundaries in Mg and Ti, Scr. Mater. **109**, 94 (2015).

[255] S. Rawat and N. Mitra, Compression twinning and structural phase transformation of single crystal titanium under uniaxial compressive strain conditions: Comparison of inter-atomic potentials, Comput. Mater. Sci. **126**, 228 (2017).

[256] R. R. Zope and Y. Mishin, Interatomic potentials for atomistic simulations of the Ti-Al system, Phys. Rev. B **68**, 024102 (2003).

[257] G. J. Ackland, Theoretical study of titanium surfaces and defects with a new many-body potential, Philosophical Magazine A **66**, 917 (1992).

[258] R. A. Johnson, Many-body effects on calculated defect properties in h.c.p. metals, Philosophical Magazine A **63**, 865 (1991).

[259] X. W. Zhou *et al.*, Atomic scale structure of sputtered metal multilayers, Acta Mater. **49**, 4005 (2001).

[260] Y.-M. Kim, B.-J. Lee, and M. I. Baskes, Modified embedded-atom method interatomic potentials for Ti and Zr, Phys. Rev. B **74**, 014101 (2006).

[261] R. G. Hennig, T. J. Lenosky, D. R. Trinkle, S. P. Rudin, and J. W. Wilkins, Classical potential describes martensitic phase transformations between the α, β and ω titanium phases, Phys. Rev. B **78**, 054121 (2008).

[262] W.-S. Ko, B. Grabowski, and J. Neugebauer, Development and application of a Ni-Ti interatomic potential with high predictive accuracy of the martensitic phase transition, Phys. Rev. B **92**, 134107 (2015).

[263] C. M. Rouleau, C. Y. Shih, C. Wu, L. V. Zhigilei, A. A. Puretzky, and D. B. Geohegan, Nanoparticle generation and transport resulting from femtosecond laser ablation of ultrathin

metal films: Time-resolved measurements and molecular dynamics simulations, Appl. Phys. Lett. **104**, 193106 (2014).

[264] C.-Y. Shih, C. Wu, M. V. Shugaev, and L. V. Zhigilei, Atomistic modeling of nanoparticle generation in short pulse laser ablation of thin metal films in water, Journal of Colloid and Interface Science **489**, 3 (2017).

[265] C. Kittel, *Introduction to Solid State Physics*, 7 ed., (Wiley-Interscience, New York, 1996).

[266] W. B. Pearson, *A Handbook of Lattice Spacings and Structures of Metals and Alloys*, 1 ed., (Pergamon Press, New York, 1958).

[267] E. S. Fisher and C. J. Renken, Single-Crystal Elastic Moduli and the hcp → bcc Transformation in Ti, Zr, and Hf, Phys. Rev. **135**, A482 (1964).

[268] H. W. G. Simmons, *Single Crystal Elastic Constants and Calculated Aggregate Properties*, (MIT, Cambridge, 1971).

[269] A. Tunde Raji, S. Scandolo, R. Mazzarello, S. Nsengiyumva, M. Härting, and D. Thomas Britton, Ab initio pseudopotential study of vacancies and self-interstitials in hcp titanium, Philos. Mag. **89**, 1629 (2009).

[270] M. Benoit, N. Tarrat, and J. Morillo, Density functional theory investigations of titanium γ-surfaces and stacking faults, Modell. Simul. Mater. Sci. Eng. **21**, 015009 (2012).

[271] Interatomic potentials repository project, http://www.ctcms.nist.gov/potentials/Ti.html (Accessed 01 2017).

[272] C. Cheng and X. Xu, Molecular Dynamics Calculation of Critical Point of Nickel, Int. J. Thermophys. **28**, 9 (2007).

[273] A. Ghoufi, P. Malfreyt, and D. J. Tildesley, Computer modelling of the surface tension of the gas–liquid and liquid–liquid interface, Chem. Soc. Rev. **45**, 1387 (2016).

[274] F. Goujon, A. Ghoufi, P. Malfreyt, and D. J. Tildesley, Can we approach the gas–liquid critical point using slab simulations of two coexisting phases?, J. Chem. Phys. **145**, 124702 (2016).

[275] J. S. Rowlinson and B. Widom, *Molecular Theory of Capillarity*, (Clarendon Press, Oxford, 1982).

[276] J. C. Le Guillou and J. Zinn-Justin, Critical exponents from field theory, Phys. Rev. B **21**, 3976 (1980).

[277] A. M. Ferrenberg and D. P. Landau, Critical behavior of the three-dimensional Ising model: A high-resolution Monte Carlo study, Phys. Rev. B **44**, 5081 (1991).

[278] H. Watanabe, N. Ito, and C.-K. Hu, Phase diagram and universality of the Lennard-Jones gas-liquid system, J. Chem. Phys. **136**, 204102 (2012).

[279] J. Pérez-Pellitero, P. Ungerer, G. Orkoulas, and A. D. Mackie, Critical point estimation of the Lennard-Jones pure fluid and binary mixtures, J. Chem. Phys. **125**, 054515 (2006).

[280] N. Tsakiris and L. J. Lewis, Phase diagram of aluminum from EAM potentials, The European Physical Journal B **86**, 313 (2013).

[281] V. E. Fortov and I. T. Lakubov, *The Physics of Non-Ideal Plasma* (World Scientific Publishing Co. Pte. Ltd., Singapore, 2000).

[282] R. W. Ohse and H. von Tippelskirch, The critical constants of the elements and of some refractory materials with high critical temperatures, High Temp. - High Press. **9**, 367 (1977).

[283] K. C. Mills, B. J. Monaghan, and B. J. Keene, Thermal conductivities of molten metals: Part 1 Pure metals, Int. Mater. Rev. **41**, 209 (1996).

[284] OVITO, http://ovito.org/ (Accessed 01 2017).

[285] Interat. Potentials Repos. Proj., http://www.ctcms.nist.gov/potentials/Ti.html (Accessed 01 2017).

[286] S. H. Møller, E. H. Eriksen, P. L. Tønning, P. B. Jensen, J. Chevallier, and P. Balling, Femtosecond-laser-induced modifications of Ge2Sb2Te5 thin films: Permanent optical change without amorphization, Applied Surface Science **476**, 221 (2019).

[287] P. L. Williams, Y. Mishin, and J. C. Hamilton, An embedded-atom potential for the Cu–Ag system, Modell. Simul. Mater. Sci. Eng. **14**, 817 (2006).

[288] S. Lee, M. J. Bluemle, and F. S. Bates, Discovery of a Frank-Kasper σ Phase in Sphere-Forming Block Copolymer Melts, Science **330**, 349 (2010).

[289] S. M. Foiles, Application of the embedded-atom method to liquid transition metals, Phys. Rev. B **32**, 3409 (1985).

[290] M. Engel, P. F. Damasceno, C. L. Phillips, and S. C. Glotzer, Computational self-assembly of a one-component icosahedral quasicrystal, Nature Materials **14**, 109 (2014).

[291] S. M. Foiles, M. I. Baskes, and M. S. Daw, Embedded-atom-method functions for the fcc metals Cu, Ag, Au, Ni, Pd, Pt, and their alloys, Phys. Rev. B **33**, 7983 (1986).

[292] E. T. Karim, Atomistic simulation study of short pulse laser-induced generation of crystal defects in metal targets, PhD thesis, University of Virginia, 2016.

[293] B. P. Fairand, B. A. Wilcox, W. J. Gallagher, and D. N. Williams, Laser shock-induced microstructural and mechanical property changes in 7075 aluminum, J. Appl. Phys. **43**, 3893 (1972).

[294] R. Fabbro, J. Fournier, P. Ballard, D. Devaux, and J. Virmont, Physical study of laser-produced plasma in confined geometry, J. Appl. Phys. **68**, 775 (1990).

[295] P. Peyre and R. Fabbro, Laser shock processing: a review of the physics and applications, Optical and Quantum Electronics **27**, 1213 (1995).

[296] X. Wu, Z. Duan, H. Song, Y. Wei, X. Wang, and C. Huang, Shock pressure induced by glass-confined laser shock peening: Experiments, modeling and simulation, J. Appl. Phys. **110**, 053112 (2011).

[297] J. Bohandy, B. F. Kim, and F. J. Adrian, Metal deposition from a supported metal film using an excimer laser, J. Appl. Phys. **60**, 1538 (1986).

[298] I. Zergioti, S. Mailis, N. A. Vainos, C. Fotakis, S. Chen, and C. P. Grigoropoulos, Microdeposition of metals by femtosecond excimer laser, Applied Surface Science **127-129**, 601 (1998).

[299] M. Domke, S. Rapp, M. Schmidt, and H. P. Huber, Ultra-fast movies of thin-film laser ablation, Appl. Phys. A **109**, 409 (2012).

[300] G. Heise, M. Englmaier, C. Hellwig, T. Kuznicki, S. Sarrach, and H. P. Huber, Laser ablation of thin molybdenum films on transparent substrates at low fluences, Appl. Phys. A **102**, 173 (2011).

[301] G. Heise, M. Domke, J. Konrad, S. Sarrach, J. Sotrop, and H. P. Huber, Laser lift-off initiated by direct induced ablation of different metal thin films with ultra-short laser pulses, J. Phys. D **45**, 315303 (2012).

[302] J.-H. Klein-Wiele and P. Simon, Sub-100nm pattern generation by laser direct writing using a confinement layer, Opt. Express **21**, 9017 (2013).

[303] N. C. Anderholm, Laser-generated stress waves, Appl. Phys. Lett. **16**, 113 (1970).

[304] T. Yabe *et al.*, Microairplane propelled by laser driven exotic target, Appl. Phys. Lett. **80**, 4318 (2002).

[305] J. Sotrop, A. Kersch, M. Domke, G. Heise, and H. P. Huber, Numerical simulation of ultrafast expansion as the driving mechanism for confined laser ablation with ultra-short laser pulses, Appl. Phys. A **113**, 397 (2013).

[306] M. W. Wu and H. Metiu, The effect of strain on the adsorption of CO on Pd(100), J. Chem. Phys. **113**, 1177 (2000).

[307] S. I. Anisimov, V. V. Zhakhovskii, N. A. Inogamov, K. Nishihara, A. M. Oparin, and Y. V. Petrov, Destruction of a solid film under the action of ultrashort laser pulse, Journal of Experimental and Theoretical Physics Letters **77**, 606 (2003).

[308] A. K. Upadhyay and H. M. Urbassek, Melting and fragmentation of ultra-thin metal films due to ultrafast laser irradiation: a molecular-dynamics study, J. Phys. D **38**, 2933 (2005).

[309] B. J. Demaske, V. V. Zhakhovsky, N. A. Inogamov, and I. I. Oleynik, Ablation and spallation of gold films irradiated by ultrashort laser pulses, Phys. Rev. B **82**, 064113 (2010).

[310] Z. Lin and L. V. Zhigilei, Time-resolved diffraction profiles and atomic dynamics in short-pulse laser-induced structural transformations: Molecular dynamics study, Phys. Rev. B **73**, 184113 (2006).

[311] C. F. Richardson and P. Clancy, Picosecond Laser Processing of Copper and Gold, Molecular Simulation **7**, 335 (1991).

[312] C. Cheng and X. Xu, Mechanisms of decomposition of metal during femtosecond laser ablation, Phys. Rev. B **72**, 165415 (2005).

[313] M. Gill-Comeau and L. J. Lewis, Ultrashort-pulse laser ablation of nanocrystalline aluminum, Phys. Rev. B **84**, 224110 (2011).

[314] E. T. Karim, Z. Lin, and L. V. Zhigilei, Molecular dynamics study of femtosecond laser interactions with Cr targets, AIP Conf. Proc. **1464**, 280 (2012).

[315] C. Li, J. Zhang, and X. Wang, Phase change and stress wave in picosecond laser–material interaction with shock wave formation, Appl. Phys. A **112**, 677 (2013).

[316] A. F. Voter and S. P. Chen, Accurate Interatomic Potentials for Ni, Al and Ni3Al, MRS Proc. **82**, 175, 175 (1986).

[317] C. Wu, D. A. Thomas, Z. Lin, and L. V. Zhigilei, Runaway lattice-mismatched interface in an atomistic simulation of femtosecond laser irradiation of Ag film–Cu substrate system, Appl. Phys. A **104**, 781 (2011).

[318] N. W. Ashcroft and N. D. Mermin, *Solid State Physics*, (Holt, Rinehart and Winston, New York, 1976).

[319] M. V. Shugaev, C.-Y. Shih, E. T. Karim, C. Wu, and L. V. Zhigilei, Generation of nanocrystalline surface layer in short pulse laser processing of metal targets under conditions of spatial confinement by solid or liquid overlayer, Applied Surface Science **417**, 54 (2017).

[320] E. Leveugle and L. V. Zhigilei, Molecular dynamics simulation study of the ejection and transport of polymer molecules in matrix-assisted pulsed laser evaporation, J. Appl. Phys. **102**, 074914 (2007).

[321] A. Vogel and V. Venugopalan, Mechanisms of Pulsed Laser Ablation of Biological Tissues, Chem. Rev. **103**, 577 (2003).

[322] V. Amendola and M. Meneghetti, What controls the composition and the structure of nanomaterials generated by laser ablation in liquid solution?, Phys. Chem. Chem. Phys. **15**, 3027 (2013).

[323] S. Ibrahimkutty, P. Wagener, T. d. S. Rolo, D. Karpov, A. Menzel, T. Baumbach, S. Barcikowski, and A. Plech, A hierarchical view on material formation during pulsed-laser synthesis of nanoparticles in liquid, Sci. Rep. **5**, 16313 (2015).

[324] S. Reich *et al.*, Pulsed laser ablation in liquids: Impact of the bubble dynamics on particle formation, Journal of Colloid and Interface Science **489**, 106 (2017).

[325] M. E. Povarnitsyn and T. E. Itina, Hydrodynamic modeling of femtosecond laser ablation of metals in vacuum and in liquid, Appl. Phys. A **117**, 175 (2014).

[326] W. T. Nichols, T. Sasaki, and N. Koshizaki, Laser ablation of a platinum target in water. I. Ablation mechanisms, J. Appl. Phys. **100**, 114911 (2006).

[327] E. V. Zavedeev, A. V. Petrovskaya, A. V. Simakin, and G. A. Shafeev, Formation of nanostructures upon laser ablation of silver in liquids, Quantum Electronics **36**, 978 (2006).

[328] E. Stratakis, V. Zorba, M. Barberoglou, C. Fotakis, and G. A. Shafeev, Laser writing of nanostructures on bulk Al via its ablation in liquids, Nanotechnology **20**, 105303 (2009).

[329] G. K. Podagatlapalli, S. Hamad, S. Sreedhar, S. P. Tewari, and S. Venugopal Rao, Fabrication and characterization of aluminum nanostructures and nanoparticles obtained using femtosecond ablation technique, Chem. Phys. Lett. **530**, 93 (2012).

[330] S. V. Rao, G. K. Podagatlapalli, and S. Hamad, Ultrafast laser ablation in liquids fornanomaterials and applications, Journal of Nanoscience and Nanotechnology **14**, 1364 (2014).

[331] S. Bashir, M. S. Rafique, C. S. Nathala, and W. Husinsky, The formation of nanodimensional structures on the surface of Tin exposed to femtosecond laser pulses in the ambient environment of ethanol, Applied Surface Science **290**, 53 (2014).

[332] R. Kuladeep, M. H. Dar, K. L. N. Deepak, and D. N. Rao, Ultrafast laser induced periodic sub-wavelength aluminum surface structures and nanoparticles in air and liquids, J. Appl. Phys. **116**, 113107 (2014).

[333] E. V. Barmina, G. A. Shafeev, P. G. Kuzmin, A. A. Serkov, A. V. Simakin, and N. N. Melnik, Laser-assisted generation of gold nanoparticles and nanostructures in liquid and their plasmonic luminescence, Appl. Phys. A **115**, 747 (2014).

[334] A. A. Serkov, E. V. Barmina, G. A. Shafeev, and V. V. Voronov, Laser ablation of titanium in liquid in external electric field, Applied Surface Science **348**, 16 (2015).

[335] J. Ihlemann and R. Weichenhain-Schriever, Pulsed laser-induced formation of silica nanogrids, Nanoscale Research Letters **9**, 102 (2014).

[336] R. Z. Valiev, I. V. Alexandrov, Y. T. Zhu, and T. C. Lowe, Paradox of Strength and Ductility in Metals Processed Bysevere Plastic Deformation, J. Mater. Res. **17**, 5 (2002).

[337] M. A. Meyers, A. Mishra, and D. J. Benson, Mechanical properties of nanocrystalline materials, Prog. Mater Sci. **51**, 427 (2006).

[338] T. H. Fang, W. L. Li, N. R. Tao, and K. Lu, Revealing Extraordinary Intrinsic Tensile Plasticity in Gradient Nano-Grained Copper, Science **331**, 1587 (2011).

[339] X. Li, S. James, and P. Lei, Interactions Between α-Synuclein and Tau Protein: Implications to Neurodegenerative Disorders, J. Mol. Neurosci. **60**, 298 (2016).

[340] M. Tabetah, A. Matei, C. Constantinescu, N. P. Mortensen, M. Dinescu, J. Schou, and L. V. Zhigilei, The Minimum Amount of “Matrix” Needed for Matrix-Assisted Pulsed Laser Deposition of Biomolecules, J. Phys. Chem. B **118**, 13290 (2014).

[341] J. Zou, C. Wu, W. D. Robertson, L. V. Zhigilei, and R. J. D. Miller, Molecular dynamics investigation of desorption and ion separation following picosecond infrared laser (PIRL) ablation of an ionic aqueous protein solution, J. Chem. Phys. **145**, 204202 (2016).

[342] C. Deng and F. Sansoz, Fundamental differences in the plasticity of periodically twinned nanowires in Au, Ag, Al, Cu, Pb and Ni, Acta Mater. **57**, 6090 (2009).

[343] C. C. Koch, R. O. Scattergood, K. A. Darling, and J. E. Semones, Stabilization of nanocrystalline grain sizes by solute additions, J. Mater. Sci. **43**, 7264 (2008).

[344] F. Liu and R. Kirchheim, Comparison between kinetic and thermodynamic effects on grain growth, Thin Solid Films **466**, 108 (2004).

[345] K. A. Darling, A. J. Roberts, Y. Mishin, S. N. Mathaudhu, and L. J. Kecskes, Grain size stabilization of nanocrystalline copper at high temperatures by alloying with tantalum, Journal of Alloys and Compounds **573**, 142 (2013).

[346] M. Saber, H. Kotan, C. C. Koch, and R. O. Scattergood, Thermodynamic stabilization of nanocrystalline binary alloys, J. Appl. Phys. **113**, 063515 (2013).

[347] K. A. Darling, M. A. Tschopp, B. K. VanLeeuwen, M. A. Atwater, and Z. K. Liu, Mitigating grain growth in binary nanocrystalline alloys through solute selection based on thermodynamic stability maps, Comput. Mater. Sci. **84**, 255 (2014).

[348] T. Chookajorn, H. A. Murdoch, and C. A. Schuh, Design of Stable Nanocrystalline Alloys, Science **337**, 951 (2012).

[349] K. Lücke and K. Detert, A quantitative theory of grain-boundary motion and recrystallization in metals in the presence of impurities, Acta Metall. **5**, 628 (1957).

[350] M. Hillert and B. Sundman, A treatment of the solute drag on moving grain boundaries and phase interfaces in binary alloys, Acta Metall. **24**, 731 (1976).

[351] A. Y. Vorobyev and C. Guo, Effects of nanostructure-covered femtosecond laser-induced periodic surface structures on optical absorptance of metals, Appl. Phys. A **86**, 321 (2007).

[352] Q.-Z. Zhao, S. Malzer, and L.-J. Wang, Self-organized tungsten nanospikes grown on subwavelength ripples induced by femtosecond laser pulses, Opt. Express **15**, 15741 (2007).

[353] S. Barcikowski, A. Hahn, A. V. Kabashin, and B. N. Chichkov, Properties of nanoparticles generated during femtosecond laser machining in air and water, Appl. Phys. A **87**, 47 (2007).

[354] N. Haustrup and G. M. O'Connor, Impact of wavelength dependent thermo-elastic laser ablation mechanism on the generation of nanoparticles from thin gold films, Appl. Phys. Lett. **101**, 263107 (2012).

[355] A. Miotello and N. Patel, Pulsed laser deposition of cluster-assembled films for catalysis and the photocatalysis relevant to energy and the environment, Applied Surface Science **278**, 19 (2013).

[356] C. J. Lin and F. Spaepen, Nickel-niobium alloys obtained by picosecond pulsed laser quenching, Acta Metall. **34**, 1367 (1986).

[357] X. Sedao *et al.*, Self-Arranged Periodic Nanovoids by Ultrafast Laser-Induced Near-Field Enhancement, ACS Photonics **5**, 1418 (2018).

[358] A. K. Upadhyay, N. A. Inogamov, B. Rethfeld, and H. M. Urbassek, Ablation by ultrashort laser pulses: Atomistic and thermodynamic analysis of the processes at the ablation threshold, Phys. Rev. B **78**, 045437 (2008).

[359] C.-Y. Shih, M. V. Shugaev, C. Wu, and L. V. Zhigilei, Generation of Subsurface Voids, Incubation Effect, and Formation of Nanoparticles in Short Pulse Laser Interactions with Bulk Metal Targets in Liquid: Molecular Dynamics Study, J. Phys. Chem. C **121**, 16549 (2017).

[360] A. Abou-Saleh, E. T. Karim, C. Maurice, S. Reynaud, F. Pigeon, F. Garrelie, L. V. Zhigilei, and J. P. Colombier, Spallation-induced roughness promoting high spatial frequency nanostructure formation on Cr, Appl. Phys. A **124**, 308 (2018).

[361] M. E. Povarnitsyn, K. V. Khishchenko, and P. R. Levashov, Phase transitions in femtosecond laser ablation, Applied Surface Science **255**, 5120 (2009).

[362] D. E. Grady, The spall strength of condensed matter, J. Mech. Phys. Solids **36**, 353 (1988).

[363] Q. An, G. Garrett, K. Samwer, Y. Liu, S. V. Zybin, S.-N. Luo, M. D. Demetriou, W. L. Johnson, and W. A. Goddard, Atomistic Characterization of Stochastic Cavitation of a Binary Metallic Liquid under Negative Pressure, J. Phys. Chem. Lett. **2**, 1320 (2011).

[364] T. T. Bazhirov, G. E. Norman, and V. V. Stegailov, Cavitation in liquid metals under negative pressures. Molecular dynamics modeling and simulation, J. Phys. Condens. Matter **20**, 114113 (2008).

[365] A. V. Neimark and A. Vishnyakov, The birth of a bubble: A molecular simulation study, J. Chem. Phys. **122**, 054707 (2005).

[366] T. Kinjo and M. Matsumoto, Cavitation processes and negative pressure, Fluid Ph. Equilibria **144**, 343 (1998).

[367] D. Turnbull and J. C. Fisher, Rate of Nucleation in Condensed Systems, J. Chem. Phys. **17**, 71 (1949).

[368] H. Okumura and N. Ito, Nonequilibrium molecular dynamics simulations of a bubble, Phys. Rev. E **67**, 045301 (2003).

[369] A. Y. Kuksin, G. E. Norman, V. V. Pisarev, V. V. Stegailov, and A. V. Yanilkin, Theory and molecular dynamics modeling of spall fracture in liquids, Phys. Rev. B **82**, 174101 (2010).

[370] E. Dekel, S. Eliezer, Z. Henis, E. Moshe, A. Ludmirsky, and I. B. Goldberg, Spallation model for the high strain rates range, J. Appl. Phys. **84**, 4851 (1998).

[371] N. Goldenfeld, *Lectures on phase transitions and the renormalization group*, (Addison-Wesley, Advanced Book Program, Reading, Mass., 1992), Frontiers in physics, 85.

[372] I. Egry, E. Ricci, R. Novakovic, and S. Ozawa, Surface tension of liquid metals and alloys - Recent developments, Adv. Colloid Interface Sci. **159**, 198 (2010).

[373] H. M. Lu and Q. Jiang, Surface Tension and Its Temperature Coefficient for Liquid Metals, J. Phys. Chem. B **109**, 15463 (2005).

[374] E. Leveugle and L. V. Zhigilei, Microscopic mechanisms of short pulse laser spallation of molecular solids, Appl. Phys. A **79**, 753 (2004).

[375] D. L. Andrews, G. D. Scholes, and G. P. Wiederrecht, *Comprehensive nanoscience and technology*, 4 ed., (Elsevier, Academic Press, London, 2011).

[376] R. Buividas, M. Mikutis, and S. Juodkazis, Surface and bulk structuring of materials by ripples with long and short laser pulses: Recent advances, Progress in Quantum Electronics **38**, 119 (2014).

[377] J. Bonse, S. Höhm, S. V. Kirner, A. Rosenfeld, and J. Krüger, Laser-Induced Periodic Surface Structures— A Scientific Evergreen, IEEE Journal of Selected Topics in Quantum Electronics **23**, 1 (2017).

[378] S. Wang, K. Liu, X. Yao, and L. Jiang, Bioinspired Surfaces with Superwettability: New Insight on Theory, Design, and Applications, Chem. Rev. **115**, 8230 (2015).

[379] A. Y. Vorobyev and C. Guo, Multifunctional surfaces produced by femtosecond laser pulses, J. Appl. Phys. **117**, 033103 (2015).

[380] G. Rotella, L. Orazi, M. Alfano, S. Candamano, and I. Gnilitskyi, Innovative high-speed femtosecond laser nano-patterning for improved adhesive bonding of Ti6Al4V titanium alloy, CIRP Journal of Manufacturing Science and Technology **18**, 101 (2017).

[381] J. Bonse, R. Koter, M. Hartelt, D. Spaltmann, S. Pentzien, S. Höhm, A. Rosenfeld, and J. Krüger, Femtosecond laser-induced periodic surface structures on steel and titanium alloy for tribological applications, Appl. Phys. A **117**, 103 (2014).

[382] B. Dusser, Z. Sagan, H. Soder, N. Faure, J. P. Colombier, M. Jourlin, and E. Audouard, Controlled nanostructrures formation by ultra fast laser pulses for color marking, Opt. Express **18**, 2913 (2010).

[383] M. Martínez-Calderon, M. Manso-Silván, A. Rodríguez, M. Gómez-Aranzadi, J. P. García-Ruiz, S. M. Olaizola, and R. J. Martín-Palma, Surface micro- and nano-texturing of stainless steel by femtosecond laser for the control of cell migration, Sci. Rep. **6**, 36296 (2016).

[384] J. Bonse, A. Rosenfeld, and J. Krüger, On the role of surface plasmon polaritons in the formation of laser-induced periodic surface structures upon irradiation of silicon by femtosecond-laser pulses, J. Appl. Phys. **106**, 104910 (2009).

[385] Y. Levy, T. J. Y. Derrien, N. M. Bulgakova, E. L. Gurevich, and T. Mocek, Relaxation dynamics of femtosecond-laser-induced temperature modulation on the surfaces of metals and semiconductors, Applied Surface Science **374**, 157 (2016).

[386] J. Reif, O. Varlamova, and F. Costache, Femtosecond laser induced nanostructure formation: self-organization control parameters, Appl. Phys. A **92**, 1019 (2008).

[387] M. Gedvilas, J. Mikšys, and G. Račiukaitis, Flexible periodical micro- and nano-structuring of a stainless steel surface using dual-wavelength double-pulse picosecond laser irradiation, RSC Advances **5**, 75075 (2015).

[388] E. L. Gurevich, Mechanisms of femtosecond LIPSS formation induced by periodic surface temperature modulation, Applied Surface Science **374**, 56 (2016).

[389] I. Gnilitskyi, V. Gruzdev, N. M. Bulgakova, T. Mocek, and L. Orazi, Mechanisms of high-regularity periodic structuring of silicon surface by sub-MHz repetition rate ultrashort laser pulses, Appl. Phys. Lett. **109**, 143101 (2016).

[390] S. D. Brorson, A. Kazeroonian, J. S. Moodera, D. W. Face, T. K. Cheng, E. P. Ippen, M. S. Dresselhaus, and G. Dresselhaus, Femtosecond room-temperature measurement of the electron-phonon coupling constant γ in metallic superconductors, Phys. Rev. Lett. **64**, 2172 (1990).

[391] T. J.-Y. Derrien, T. E. Itina, R. Torres, T. Sarnet, and M. Sentis, Possible surface plasmon polariton excitation under femtosecond laser irradiation of silicon, J. Appl. Phys. **114**, 083104 (2013).

[392] E. L. Gurevich, Y. Levy, S. V. Gurevich, and N. M. Bulgakova, Role of the temperature dynamics in formation of nanopatterns upon single femtosecond laser pulses on gold, Phys. Rev. B **95**, 054305 (2017).

[393] D. S. Ivanov *et al.*, Experimental and Theoretical Investigation of Periodic Nanostructuring of Au with Ultrashort UV Laser Pulses near the Damage Threshold, Phys. Rev. Appl. **4**, 064006 (2015).

[394] L. V. Zhigilei, D. S. Ivanov, E. Leveugle, B. Sadigh, and E. M. Bringa, in *High-Power Laser Ablation*, edited by C. R. Phipps (Proc. SPIE, 2004), pp. 505.

[395] A. J. Manzo and H. Helvajian, Application of a laser heterodyne technique to characterize surface acoustic waves generated via a pulsed laser excitation, Proc. SPIE **8967** (2014).

[396] A. Lomonosov, V. G. Mikhalevich, P. Hess, E. Y. Knight, M. F. Hamilton, and E. A. Zabolotskaya, Laser-generated nonlinear Rayleigh waves with shocks, J. Acoust. Soc. Am. **105**, 2093 (1999).

[397] G. F. Miller and H. Pursey, On the partition of energy between elastic waves in a semi-infinite solid, Proc. Royal Soc. of London. Ser. A, Math. and Phys. Sci. **233**, 55 (1955).

[398] V. P. Lipp, B. Rethfeld, M. E. Garcia, and D. S. Ivanov, Atomistic-continuum modeling of short laser pulse melting of Si targets, Phys. Rev. B **90**, 245306 (2014).

[399] A. Ben-Menahem and S. J. Singh, *Seismic Waves and Sources*, (Springer-Verlag, New York, 1981).

[400] C. E. O'Connell-Rodwell, B. T. Arnason, and L. A. Hart, Seismic properties of Asian elephant (Elephas maximus) vocalizations and locomotion, J. Acoust. Soc. Am. **108**, 3066 (2000).

[401] G. Lehmann, A. M. Lomonosov, P. Hess, and P. Gumbsch, Impulsive fracture of fused quartz and silicon crystals by nonlinear surface acoustic waves, J. Appl. Phys. **94**, 2907 (2003).

[402] A. M. Lomonosov, P. V. Grigoriev, and P. Hess, Sizing of partially closed surface-breaking microcracks with broadband Rayleigh waves, J. Appl. Phys. **105**, 084906 (2009).

[403] I. A. Viktorov, *Rayleigh and Lamb Waves: Physical Theory and Applications* (Plenum Press, New York, 1967).

[404] M. F. Lewis, Rayleigh waves-a progress report, European Journal of Physics **16**, 1 (1995).

[405] Y. J. Liu, X. Ding, S.-C. S. Lin, J. Shi, I. K. Chiang, and T. J. Huang, Surface Acoustic Wave Driven Light Shutters Using Polymer-Dispersed Liquid Crystals, Advanced Materials **23**, 1656 (2011).

[406] C. D. Wood, S. D. Evans, J. E. Cunningham, R. O'Rorke, C. Wälti, and A. G. Davies, Alignment of particles in microfluidic systems using standing surface acoustic waves, Appl. Phys. Lett. **92**, 044104 (2008).

[407] X. Ding, S.-C. S. Lin, B. Kiraly, H. Yue, S. Li, I.-K. Chiang, J. Shi, S. J. Benkovic, and T. J. Huang, On-chip manipulation of single microparticles, cells, and organisms using surface acoustic waves, Proc. Natl. Acad. Sci. U.S.A. **109**, 11105 (2012).

[408] M. Hennig, J. Neumann, A. Wixforth, J. O. Rädler, and M. F. Schneider, Dynamic patterns in a supported lipid bilayer driven by standing surface acoustic waves, Lab on a Chip **9**, 3050 (2009).

[409] S. R. Heron, R. Wilson, S. A. Shaffer, D. R. Goodlett, and J. M. Cooper, Surface Acoustic Wave Nebulization of Peptides As a Microfluidic Interface for Mass Spectrometry, Anal. Chem. **82**, 3985 (2010).

[410] J. Ho, M. K. Tan, D. B. Go, L. Y. Yeo, J. R. Friend, and H.-C. Chang, Paper-Based Microfluidic Surface Acoustic Wave Sample Delivery and Ionization Source for Rapid and Sensitive Ambient Mass Spectrometry, Anal. Chem. **83**, 3260 (2011).

[411] Y. Huang, S. H. Yoon, S. R. Heron, C. D. Masselon, J. S. Edgar, F. Tureček, and D. R. Goodlett, Surface Acoustic Wave Nebulization Produces Ions with Lower Internal Energy than

Electrospray Ionization, Journal of The American Society for Mass Spectrometry **23**, 1062 (2012).

[412] A. A. Kolomenskii, H. A. Schuessler, V. G. Mikhalevich, and A. A. Maznev, Interaction of laser-generated surface acoustic pulses with fine particles: Surface cleaning and adhesion studies, J. Appl. Phys. **84**, 2404 (1998).

[413] D. J. Shull, M. F. Hamilton, Y. A. Il'insky, and E. A. Zabolotskaya, Harmonic generation in plane and cylindrical nonlinear Rayleigh waves, J. Acoust. Soc. Am. **94**, 418 (1993).

[414] M. F. Hamilton, Y. A. Il'inskii, and E. A. Zabolotskaya, Nonlinear surface acoustic waves in crystals, J. Acoust. Soc. Am. **105**, 639 (1999).

[415] M. F. Hamilton, Y. A. Il'insky, and E. A. Zabolotskaya, Evolution equations for nonlinear Rayleigh waves, J. Acoust. Soc. Am. **97**, 891 (1995).

[416] N. Kalyanasundaram, Nonlinear surface acoustic waves on an isotropic solid, International Journal of Engineering Science **19**, 279 (1981).

[417] N. Kalayanasundaram, Nonlinear mode coupling of surface acoustic waves on an isotropic solid, International Journal of Engineering Science **19**, 435 (1981).

[418] N. Kalyanasundaram, R. Ravindran, and P. Prasad, Coupled amplitude theory of nonlinear surface acoustic waves, J. Acoust. Soc. Am. **72**, 488 (1982).

[419] R. W. Lardner, Nonlinear surface waves on an elastic solid, International Journal of Engineering Science **21**, 1331 (1983).

[420] R. W. Lardner, Nonlinear Rayleigh waves: Harmonic generation, parametric amplification, and thermoviscous damping, J. Appl. Phys. **55**, 3251 (1984).

[421] R. W. Lardner, Waveform distortion and shock development in nonlinear rayleigh waves, International Journal of Engineering Science **23**, 113 (1985).

[422] M. Planat, Multiple scale analysis of the nonlinear surface acoustic wave propagation in anisotropic crystals, J. Appl. Phys. **57**, 4911 (1985).

[423] R. W. Lardner, Nonlinear surface acoustic waves on an elastic solid of general anisotropy, Journal of Elasticity **16**, 63 (1986).

[424] R. W. Lardner and G. E. Tupholme, Nonlinear surface waves on cubic materials, Journal of Elasticity **16**, 251 (1986).

[425] V. E. Gusev, W. Lauriks, and J. Thoen, New evolution equations for the nonlinear surface acoustic waves on an elastic solid of general anisotropy, J. Acoust. Soc. Am. **103**, 3203 (1998).

[426] V. E. Gusev, W. Lauriks, and J. Thoen, Theory for the time evolution of nonlinear Rayleigh waves in an isotropic solid, Phys. Rev. B **55**, 9344 (1997).

[427] V. P. Reutov, Use of the averaged variational principle for describing multiwave interactions of elastic surface waves, Radiophysics and Quantum Electronics **16**, 1307 (1973).

[428] L. D. Landau and E. M. Lifshitz, *Theory of Elasticity*, (Pergamon Press, New York, 1986).

[429] N. G. Basov, É. M. Belenov, M. A. Gubin, M. S. Kurdoglyan, V. V. Nikitin, A. N. Oraevskiĭ, and B. N. Chichkov, New ways of obtaining cold atoms and molecules, Soviet Journal of Quantum Electronics **17**, 919 (1987).

[430] H. Nishiyama, N. Saito, H. Chou, K. Sato, and Y. Inoue, Effects of surface acoustic waves on adsorptive properties of ZnO and NiO thin films deposited on ferroelectric substrates, Surf Sci. **433-435**, 525 (1999).

[431] B. L. Holian and G. K. Straub, Molecular dynamics of shock waves in one-dimensional chains, Phys. Rev. B **18**, 1593 (1978).

[432] B. L. Holian and P. S. Lomdahl, Plasticity Induced by Shock Waves in Nonequilibrium Molecular-Dynamics Simulations, Science **280**, 2085 (1998).

[433] K. Kadau, T. C. Germann, P. S. Lomdahl, and B. L. Holian, Microscopic View of Structural Phase Transitions Induced by Shock Waves, Science **296**, 1681 (2002).

[434] L. Koči *et al.*, Simulation of shock-induced melting of Ni using molecular dynamics coupled to a two-temperature model, Phys. Rev. B **74**, 012101 (2006).

[435] D. S. Ivanov, L. V. Zhigilei, E. M. Bringa, M. D. Koning, B. A. Remington, M. J. Caturla, and S. M. Pollaine, Molecular Dynamics Simulations of Shocks Including Electronic Heat Conduction and Electron-Phonon Coupling, AIP Conf. Proc. **706**, 225 (2004).

[436] T. Hatano, Dislocation Nucleation in Shocked fcc Solids: Effects of Temperature and Preexisting Voids, Phys. Rev. Lett. **93**, 085501 (2004).

[437] A. M. Dongare, A. M. Rajendran, B. LaMattina, M. A. Zikry, and D. W. Brenner, Atomic scale studies of spall behavior in nanocrystalline Cu, J. Appl. Phys. **108**, 113518 (2010).

[438] S.-N. Luo, Q. An, T. C. Germann, and L.-B. Han, Shock-induced spall in solid and liquid Cu at extreme strain rates, J. Appl. Phys. **106**, 013502 (2009).

[439] A. Strachan, T. Çağın, and W. A. Goddard, Critical behavior in spallation failure of metals, Phys. Rev. B **63**, 060103 (2001).

[440] J. R. Ray and A. Rahman, Statistical ensembles and molecular dynamics studies of anisotropic solids. II, J. Chem. Phys. **82**, 4243 (1985).

[441] M. I. Rabinovich and D. I. Trubetskov, *Oscillations and waves: in linear and nonlinear systems*, (Kluver Academic Publishers, Dordrecht/Boston/London, 1989).

[442] N. M. Ryskin and D. I. Trubetskov, *Nonlinear waves (in Russian)*, (Fizmatlit, Moscow, 2010).

[443] A. Lomonosov and P. Hess, Effects of Nonlinear Elastic Surface Pulses in Anisotropic Silicon Crystals, Phys. Rev. Lett. **83**, 3876 (1999).

[444] O. V. Rudenko and S. I. Soluyan, *Theoretical Foundations of Nonlinear Acoustics*, (Plenum, New York, 1977).

[445] D. T. Blackstock, *Nonlinear Acoustics (Theoretical)*, 3 ed., (McGraw-Hill, New York, 1972), American Institute of Physics Handbook.

[446] L. K. Zarembo and V. A. Krasil'nikov, Nonlinear phenomena during the propagation of elastic waves in solid, Soviet Physics Uspekhi **13**, 778 (1971).

[447] J. Tersoff, New empirical model for the structural properties of silicon, Phys. Rev. Lett. **56**, 632 (1986).

[448] F. H. Stillinger and T. A. Weber, Computer simulation of local order in condensed phases of silicon, Phys. Rev. B **31**, 5262 (1985).

[449] M. E. Siemens, Q. Li, M. M. Murnane, H. C. Kapteyn, R. Yang, E. H. Anderson, and K. A. Nelson, High-frequency surface acoustic wave propagation in nanostructures characterized by coherent extreme ultraviolet beams, Appl. Phys. Lett. **94**, 093103 (2009).

[450] M. Schubert, M. Grossmann, O. Ristow, M. Hettich, A. Bruchhausen, E. C. S. Barretto, E. Scheer, V. Gusev, and T. Dekorsy, Spatial-temporally resolved high-frequency surface acoustic waves on silicon investigated by femtosecond spectroscopy, Appl. Phys. Lett. **101**, 013108 (2012).

[451] D. Nardi, E. Zagato, G. Ferrini, C. Giannetti, and F. Banfi, Design of a surface acoustic wave mass sensor in the 100 GHz range, Appl. Phys. Lett. **100**, 253106 (2012).

[452] C. Wu, V. Y. Zaitsev, and L. V. Zhigilei, Mechanism of acoustically induced diffusional structuring of surface adatoms, Appl. Phys. Lett. **103**, 221601 (2013).

[453] F. N. Dzegilenko, T. Uzer, and E. Herbst, Classical studies of shock wave-induced desorption for model adsorbates, J. Chem. Phys. **105**, 10868 (1996).

[454] R. Almeida and E. S. Hood, Nonequilibrium dynamics in thermal desorption, J. Phys. Chem. **96**, 3086 (1992).

[455] C. Roland and G. H. Gilmer, Epitaxy on surfaces vicinal to Si(001). I. Diffusion of silicon adatoms over the terraces, Phys. Rev. B **46**, 13428 (1992).

[456] C. Ratsch, A. P. Seitsonen, and M. Scheffler, Strain dependence of surface diffusion: Ag on Ag(111) and Pt(111), Phys. Rev. B **55**, 6750 (1997).

[457] M. Mavrikakis, B. Hammer, and J. K. Nørskov, Effect of Strain on the Reactivity of Metal Surfaces, Phys. Rev. Lett. **81**, 2819 (1998).

[458] M. Schroeder and D. E. Wolf, Diffusion on strained surfaces, Surf Sci. **375**, 129 (1997).

[459] E. Penev, P. Kratzer, and M. Scheffler, Effect of strain on surface diffusion in semiconductor heteroepitaxy, Phys. Rev. B **64**, 085401 (2001).

[460] D. J. Shu, F. Liu, and X. G. Gong, Simple generic method for predicting the effect of strain on surface diffusion, Phys. Rev. B **64**, 245410 (2001).

[461] A. van de Walle, M. Asta, and P. W. Voorhees, First-principles calculation of the effect of strain on the diffusion of Ge adatoms on Si and Ge(001) surfaces, Phys. Rev. B **67**, 041308 (2003).

[462] W. M. Haynes (ed.), *Handbook of Chemistry and Physics*, 94 ed., (CRC Press, Boca Raton, FL, 2014).

[463] H. Coufal, K. Meyer, R. K. Grygier, P. Hess, and A. Neubrand, Precision measurement of the surface acoustic wave velocity on silicon single crystals using optical excitation and detection, J. Acoust. Soc. Am. **95**, 1158 (1994).

[464] S. N. Gurbatov, O. V. Rudenko, and A. I. Saichev, *Waves and Structures in Nonlinear Nondispersive Media*, (Springer-Verlag, Berlin, Heidelberg, 2011).

[465] A. M. Lomonosov, P. Hess, R. E. Kumon, and M. F. Hamilton, Laser-generated nonlinear surface wave pulses in silicon crystals, Phys. Rev. B **69**, 035314 (2004).

[466] Z. Huang, T. Ossenbrüggen, I. Rubinsky, M. Schust, D. A. Horke, and J. Küpper, Development and Characterization of a Laser-Induced Acoustic Desorption Source, Anal. Chem. **90**, 3920 (2018).

[467] U. Sezer, L. Wörner, J. Horak, L. Felix, J. Tüxen, C. Götz, A. Vaziri, M. Mayor, and M. Arndt, Laser-Induced Acoustic Desorption of Natural and Functionalized Biochromophores, Anal. Chem. **87**, 5614 (2015).

[468] A. V. Zinovev, I. V. Veryovkin, and M. J. Pellin, Laser-induced desorption of organic molecules from front- and back-irradiated metal foils, AIP Conf. Proc. **1104**, 200 (2009).

[469] S. J. Stuart, A. B. Tutein, and J. A. Harrison, A reactive potential for hydrocarbons with intermolecular interactions, J. Chem. Phys. **112**, 6472 (2000).

[470] A. V. Sidorenkov, S. V. Kolesnikov, and A. M. Saletsky, Molecular dynamics simulation of graphene on Cu (111) with different Lennard-Jones parameters, The European Physical Journal B **89** (2016).

[471] X. Zhiping and J. B. Markus, Interface structure and mechanics between graphene and metal substrates: a first-principles study, J. Phys. Condens. Matter **22**, 485301 (2010).

[472] LAMMPS Molecular Dynamics Simulator, http://lammps.sandia.gov (Accessed 01 2019).

[473] T. Halicioğlu and G. M. Pound, Calculation of potential energy parameters form crystalline state properties, Physica Status Solidi A **30**, 619 (1975).

[474] L. P. Pitaevskii, E. M. Lifshitz, and J. B. Sykes, *Course of Theoretical Physics: Physical Kinetics*, (Elsevier Science, 2017).

[475] C.-M. Seah, S.-P. Chai, and A. R. Mohamed, Mechanisms of graphene growth by chemical vapour deposition on transition metals, Carbon **70**, 1 (2014).

[476] A. Bosak, M. Krisch, M. Mohr, J. Maultzsch, and C. Thomsen, Elasticity of single-crystalline graphite: Inelastic x-ray scattering study, Phys. Rev. B **75**, 153408 (2007).

[477] N. Mishra, J. Boeckl, N. Motta, and F. Iacopi, Graphene growth on silicon carbide: A review, physica status solidi (a) **213**, 2277 (2016).

[478] S.-J. Chang *et al.*, Graphene growth from reduced graphene oxide by chemical vapour deposition: seeded growth accompanied by restoration, Sci. Rep. **6**, 22653 (2016).